INEEL-EXT-98-00834
Revision 2.4
December 2011

RELAP5-3D Code Manual Volume III: Developmental Assessment

Paul D. Bayless, Editor

INL is a U.S. Department of Energy National Laboratory operated by Battelle Energy Alliance

INEEL-EXT-98-00834
Volume III
Revision 2.4

RELAP5-3D Code Manual
Volume III: Developmental Assessment

Paul D. Bayless, Editor

Idaho National Laboratory
Paul D. Bayless
Nolan A. Anderson
Cliff B. Davis
Peter P. Cebull
Edwin A. Harvego

Information Systems Laboratories, Inc.
Douglas A. Barber
Glen A. Mortensen
Dan A. Prelewicz
Joo Seok Baek
Dean Wang
Robert Beaton
Lance C. Larsen
John Atchison

December 2011

Idaho National Laboratory
Idaho Falls, Idaho 83415

http://www.inl.gov

Prepared for the
U. S. Department of Energy
Under DOE Idaho Operations Office
Contract DE-AC07-05ID14157

The RELAP5-3D manuals are living documents and are being corrected and updated continuously. A printed version of the manuals is frozen and archived when a code version is released. This version of the manual corresponds to RELAP5-3D version 2.4, released June 2005.

ABSTRACT

The RELAP5-3D code has been developed for best-estimate transient simulation of light water reactor coolant systems during postulated accidents. The code models the coupled behavior of the reactor coolant system and the core for loss-of-coolant accidents, and operational transients, such as anticipated transient without scram, loss of offsite power, loss of feedwater, and loss of flow. A generic modeling approach is used that permits simulating a variety of thermal hydraulic systems. Control system and secondary system components are included to permit modeling of plant controls, turbines, condensers, and secondary feedwater systems.

RELAP5-3D code documentation is divided into six volumes: Volume I provides modeling theory and associated numerical schemes; Volume II contains detailed instructions for code application and input data preparation; Volume III provides the results of developmental assessment cases that demonstrate and verify the models used in the code; Volume IV presents a detailed discussion of RELAP5-3D models and correlations; Volume V contains guidelines that have evolved over the past several years through the use of the RELAP5-3D code; and Volume VI discusses the numerical scheme used in RELAP5-3D.

EXECUTIVE SUMMARY

A developmental assessment has been performed for the RELAP5-3D computer code. This assessment used a combination of phenomenological, separate effects, and integral effects cases to investigate how well selected code models perform.

Judgments were made on how well the code calculations predicted the important parameters from each of the assessment cases. These judgments used criteria that evaluated the trends and magnitudes of the data and calculations to determine whether the code results were acceptable or not. Assessment findings of "excellent" or "reasonable" are considered acceptable, while "minimal" or "insufficient" indicate that additional work on the code models may be needed.

The code calculations were performed with both the semi- and nearly-implicit solutions schemes using version 2.4.2is. Assessment judgments for both sets of calculations were made, although no attempts were made to explain differences between the two calculations for a given assessment case. Default code options were generally used, although some card 1 options were required to define specific assessment cases. The calculations were run in 64-bit mode on a personal computer using the Linux operating system.

The phenomenological cases are generally simple problems that test one or two code models. They are thought problems that often have analytical solutions. Seventeen cases were included in the assessment. The code predictions were judged to be in excellent agreement with the data for the following cases (the principal phenomena addressed are also listed):

- Water faucet—momentum equation and gravity
- Fill/drain (semi-implicit)—level tracking
- Manometer (semi-implicit)—oscillations and liquid level
- Core power—decay heat
- Point kinetics ramp—point kinetics
- Pure radial symmetric flow—3-D momentum equations
- Rigid body rotation (semi-implicit)—3-D momentum equations
- R-theta symmetric flow (semi-implicit)—3-D momentum equations
- Conduction enclosure—conduction enclosure
- Conduction enclosure 1-D transient—conduction enclosure
- Conduction enclosure 2-D transient—conduction enclosure.

These cases had assessment findings of reasonable:

- Water over steam, one-dimensional (1-D) case—gravity and liquid level
- Water over steam, three-dimensional (3-D) case (semi-implicit)—gravity and liquid level
- Fill/drain (nearly-implicit)—level tracking
- Bubbling steam through liquid—level tracking
- Gravity wave (1- and 3-D)—horizontal oscillations
- Pryor pressure comparison—water packing.

Assessment judgments of minimal were assigned to the following cases:

- Manometer (nearly-implicit)—oscillations and liquid level
- Rigid body rotation (nearly-implicit)—3-D momentum equations
- R-theta symmetric flow (nearly-implicit)—3-D momentum equations.

An assessment judgment of insufficient was assigned to the following cases:

- Water over steam, three-dimensional (3-D) case (nearly-implicit)—gravity and liquid level
- Point kinetics ramp (very small time step size)—point kinetics.

The separate effects cases are experiments that address one or a few code models. Twenty seven individual tests were included in the assessment. Assessment judgments of excellent were assigned to the following cases:

- Marviken Test JIT 11—saturated vapor critical flow
- Christensen Test 15—void profile and subcooled boiling
- Oak Ridge National Laboratory (ORNL) Thermal-hydraulic Test Facility (THTF) test—void fraction and steam temperature
- Neptunus—pressurizer behavior
- Loss-of-Fluid Test (LOFT) L3-1—accumulator response.

Assessment judgments of reasonable were assigned to the following cases:

- Edwards' pipe—vapor generation and critical flow
- Marviken Test 21—subcooled and saturated liquid critical flow
- Marviken Test 22—subcooled critical flow
- Marviken Test 24—subcooled critical flow
- General Electric (GE) 1-ft level swell—two-phase level and vapor generation
- GE 4-ft level swell—two-phase level and vapor generation
- Bennett heat tube tests—critical heat flux (CHF) and rod heat transfer
- ORNL THTF tests—CHF and film boiling
- Royal Institute of Technology Tube Test 15—CHF
- FLECHT SEASET tests—bundle reflood
- Dukler-Smith air-water flooding—countercurrent flow limitation (CCFL)
- Upper plenum test facility (UPTF) Test 6, Run 131—downcomer CCFL
- Massachusetts Institute of Technology pressurizer test—pressurizer level and thermal stratification
- Model Boiler 2 Test 1712—steady state steam generator behavior
- GE 1/6-scale jet pump—jet pump behavior.

Assessment judgments of minimal were assigned to the following cases:

- Marviken Test 24—mixture density
- Moby Dick air-water—two-component, two-phase critical flow
- ORNL THTF tests—film boiling in Test 3.07.9B.

The integral effects cases use data from large experiment facilities. These cases are generally of greater interest because they provide an indication of how well the code performs overall in modeling transients with a large number of phenomena. Eight specific tests were included in the assessment.

For the LOFT L3-7 small break loss-of-coolant accident (LOCA) test, the code predictions were excellent for the hot leg fluid velocity and high-pressure injection system flow. The calculations were

reasonable for the primary coolant system pressure response, pressurizer liquid level, cladding surface temperature calculations, and coolant temperatures throughout the primary coolant system for the first 1200 s. Minimal assessment judgments were made for the break flow and the densities in the intact and broken loop cold legs, and for most of the coolant temperatures after 1200 s. Improvement of the break flow calculation would likely move most of the minimal judgments to reasonable.

For the ROSA SB-CL-18 small break LOCA test, the nearly-implicit calculation failed early in the simulation. The semi-implicit code predictions were reasonable for the pressure in the primary coolant system, the pressure in the secondary coolant system, the mass flow rates in the hot and cold legs, the accumulator mass flow rates, break flow rate later in the transient, and heater rod temperatures toward the bottom of the core. Minimal judgments were made for most of the loop densities, the break mass flow rate during the initial portion of the transient, heater rod temperatures high in the core, and the core liquid level. The primary deficiency in the calculation was that the code did not predict the clearing of the intact loop loop seal. If this loop seal had cleared as it did in the experiment, the core liquid level would have been better predicted, and the core heatup would have been shorter. A sensitivity study indicated that using the 1995 steam tables resulted in somewhat lower peak heater rod temperatures than using the 1967 or 1984 steam tables, although there were no noticeable differences in other calculated parameters.

For Semiscale natural circulation Tests S-NC-1, S-NC-2, S-NC-3, and S-NC-10, both solution scheme predictions were excellent for single-phase liquid natural circulation. For two-phase natural circulation, the prediction was reasonable when the core power was high (100 kW, Test S-NC-10, Part 4) but became minimal as the power decreased. The code predicted reasonable two-phase natural circulation behavior with the high and intermediate core power (100 kW and 60 kW), but the predictions were minimal at low power (33.54 kW). A reasonable prediction of reflux condenser mode of natural circulation was provided when the core power was 60 kW and the primary system mass inventory was less than 67%. When the secondary system mass inventory was high enough to make the effective heat transfer area larger than around 50%, reasonable natural circulation was predicted. However, when it decreased to be smaller than 50%, the code predictions were in minimal agreement with experiment results.

For LOBI large break LOCA Test A1-04R, both the semi- and nearly-explicit calculations were in excellent agreement for the primary system pressure and in reasonable agreement for the loop mass flow. The rod temperatures were judged to be in excellent agreement for the lower levels where the code predicted nucleate boiling, were judged to be in minimal agreement at the mid-level where the code predicted transition boiling, and were judged to be in reasonable agreement for the upper levels where the code predicted film boiling. The calculated results for the accumulator flow rate were in minimal agreement for both the nearly- and semi-implicit numerical schemes, although it is possible that the data are in error since the code did such an excellent job in predicting the pressure response.

LOFT large break LOCA Experiment L2-5 was modeled using both one-dimensional and multi-dimensional components in the reactor vessel. For the one-dimensional case, the pressures in both the primary and secondary coolant systems were found to be reasonably predicted. The emergency core cooling system behavior was well simulated, with the calculated accumulator level in excellent agreement with the data and the low pressure injection system flow in reasonable agreement. The flow rates in the broken loop hot and cold legs were well predicted (excellent agreement in the broken loop hot leg flow, reasonable agreement in the cold leg), as was the cold leg density (reasonable agreement), but the hot leg density was in minimal agreement with the measured data. In the intact loop, the flow rates were

reasonably simulated, but the calculated densities were in minimal agreement with the data, generally retaining more water in the loops than was measured; also, the pump speed was in minimal agreement for most of the transient, although it was in good agreement during the initial coastdown. Fluid temperatures in the reactor vessel upper and lower plena were predicted reasonably, although the presence of accumulator nitrogen in the calculation reduced the saturation temperature more than was indicated in the experiment. Both the fuel centerline and cladding surface temperatures were judged to be reasonably predicted. In the experiment, there was a partial top-down rewet of some of the fuel rods; this was not predicted by the code. The final quench of the core was both bottom-up and top-down in the experiment and in the calculation. The data showed some early heatup in the center fuel assembly over the entire length of the core, but in the code calculation the top third of the core did not show any early cladding temperature excursions. The peak cladding temperature was predicted to be 93 K below the measured value and occurred earlier in the calculation than was measured (6 vs. 28 s). The assessment findings apply to both the semi- and nearly-implicit calculations.

For the multi-dimensional L2-5 case, the nearly-implicit calculation failed relatively early in the transient and no assessment judgments were made. The results for the semi-implicit calculation were essentially the same as for the one-dimensional case, except that the broken loop hot leg density prediction was judged to be reasonable. The early heatup of the core extended higher than in the one-dimensional case, and the peak cladding temperature was 10 K higher. The three-dimensional effects in the experiment were more pronounced than in the calculation. The essential behavior in the radial variations in the core temperatures was predicted by the code, but the azimuthal variations were not.

Most of the assessment cases showed essentially no differences in results between calculations using either the semi- or nearly-implicit solution scheme. However, there are one or more errors in the nearly-implicit solution scheme associated with the multi-dimensional hydrodynamic component. Until these issues are resolved, users should account for this in determining how best to apply the code to specific facility simulations.

CONTENTS

FIGURES

TABLES

RELAP5-3D Code Manual
Volume III: Developmental Assessment

1. INTRODUCTION

A developmental assessment (DA) of the RELAP5-3D computer code has been performed. The objective of developmental assessment is to provide analysts with sufficient information to determine if the code may be an appropriate tool for a specific application. An assessment of selected code models is presented, along with judgments on how well those models predict experiment or analytical data.

This is not a comprehensive assessment of the code capabilities. It is an assessment of a selected set of code models that are of particular interest in thermal-hydraulic and reactor safety analysis. Information provided here, together with the results of independent assessments of the code and the user guidelines provided in Volume V of the RELAP5-3D code manual, can assist code users in determining the best ways to apply RELAP5-3D to specific problems.

Three categories of assessment cases are addressed. Phenomenological problems are either thought problems or problems with closed-form analytic solutions; they generally address a single code model or capability. Separate effects cases use thermal-hydraulic tests that often model a particular component or geometry that is encountered in full-scale facilities; they are usually relatively simple experiments that address one or a few specific phenomena. Integral effects cases address experiments in facilities that are typically scaled models of a reactor plant; they can address many phenomena in the code, though within the limitations of the measurements that were made.

The specific version used in the assessment was 2.4.2is. The code was compiled using the Intel Fortran Compiler, Version 9.1. The calculations presented were run using 64-bit integers on a personal computer using the Linux operating system.

Calculations were performed using both the semi- and nearly-implicit solution schemes. Assessment judgments were made for both sets of calculations, although no effort was made to investigate or explain the reasons for any differences between the two calculations. Except as noted, there were no differences between the semi- and nearly-implicit input models; they used the same nodalization, options, and time step cards.

The calculations were all performed with the following time step control card options:

- Mass error time step control
- Common hydrodynamic and heat conduction/transfer time step.

In general, time step and nodalization sensitivity studies were not performed; the input files were used as is. Default code options were generally used, although card 1 options were required to define some of the specific cases.

Chapter 2 provides information on the selection of the DA cases, the code model coverage represented by those cases, and the guidelines for comparing the code calculations to the data. Chapters 3, 4, and 5 present the results of the assessments using phenomenological, separate effects, and integral effects cases, respectively. The assessment findings are summarized in Chapter 6. References are provided at the end of each section.

2. DEVELOPMENTAL ASSESSMENT MATRIX

The process used to select the specific cases used for the developmental assessment is described below. The resulting matrix of test cases is presented. The guidelines used to assess the code performance for each of the assessment cases are also described.

2.1 Methodology and Case Selection

When planning a developmental assessment, the principal issue is which cases should be included in the assessment. For RELAP5-3D, a list of potential cases was developed, drawing from previous developmental assessments of RELAP5 and other thermal-hydraulic codes, from RELAP5 test problems that have not been included in previous assessments, and from independent assessments.

For each of these cases, the principal phenomena addressed by the experiment or problem were identified. The list of potential cases was then pared down based on the availability of input models and data. The input models needed to be available and require only minor changes to make them consistent with current modeling guidelines. The data needed to be available and unrestricted.

This reduced list of cases was then reviewed to see how broad the coverage of the code models was. The phenomena of particular interest are those that address the basic capabilities of the RELAP5-3D code with respect to nuclear reactor safety analysis. Some cases were removed because of redundancy, and some new cases were added to address phenomena that were not well covered. Cases were also added that demonstrate some of the newer capabilities in the code, such as the three-dimensional modeling and conduction enclosures.

The final matrix consists of 52 cases: 17 phenomenological problems, 26 separate effects tests, and 9 integral effects tests. The specific cases are provided in the next section.

While the intent was to use only data that were available and unrestricted, some of the cases do present data from proprietary experiments. For these cases, the total data presentation may be sparse, but the data included herein have been presented previously in the open literature. The input files for these cases are not generally available for distribution because of the proprietary information they contain. However, the principal phenomena addressed in these experiments were judged sufficiently useful that the data limitations were worth accommodating.

2.2 Matrix Summary

Table 2.2-1 lists the phenomenological assessment cases and the principal phenomena or code models that each addresses. These analytical or thought problems generally investigate a single code model or behavior. The phenomena addressed include phase separation and entrainment, basic numerics, the momentum equation, point kinetics, and heat structure conduction.

The separate effects cases and the phenomena they address are provided in Table 2.2-2. Many of these tests investigate core behavior, including two-phase level behavior, critical heat flux (CHF), and heat transfer (subcooled, nucleate, post-CHF, reflood). There are several cases that address critical flow. Other

Table 2.2-1. Phenomenological assessment cases.

Case Description	Models Validated
Bubbling steam through liquid	Level tracking, entrainment
Conduction enclosure	Conduction enclosure
Conduction enclosure 1-D transient	Conduction enclosure
Conduction enclosure 2-D transient	Conduction enclosure
Core power	Point kinetics
Fill/drain	Level tracking
Gravity wave 1-D	Stratification, force term
Gravity wave 3-D	Stratification, force term
Manometer	Noncondensables, wall friction, liquid level, oscillations
Point kinetics ramp	Point kinetics
Pryor pressure comparison	Water packing
Pure radial symmetric flow (3-D)	3-D momentum equations
Rigid body rotation (3-D)	3-D momentum equations
R-theta symmetric flow (3-D)	3-D momentum equations
Water faucet	Hydro numerics, gravity, momentum equation
Water over steam (1-D)	Gravitational head, liquid level, gravity
Water over steam (3-D)	Gravitational head, liquid level, gravity

Table 2.2-2. Separate effects assessment cases.

Case Description	Models Validated
Bennett Heated Tube Tests 5358, 5294 and 5394	Non-equilibrium heat transfer, CHF, subcooled boiling, steam cooling
Christensen Test 15	Subcooled boiling heat transfer, void profile
Dukler air-water flooding	CCFL
Edwards' Pipe	Vapor generation, flashing, critical flow, pressure wave propagation
FLECHT-SEASET Test 31504	Reflood model (low reflood rate), two-phase level, natural circulation, subcooled boiling, steam cooling, quench front, interphase evaporation, entrainment, CCFL, condensation heat transfer

Table 2.2-2. Separate effects assessment cases.

Case Description	Models Validated
FLECHT-SEASET Test 31701	Reflood model (high reflood rate), two-phase level, steam cooling, entrainment, CCFL, condensation heat transfer, quench front
GE 1/6-scale jet pump	Jet pump
GE Level Swell, 1 ft. Test 1004-3	Vapor generation, interphase drag, two-phase level
GE Level Swell, 4 ft. Test 5801-15	Vapor generation, interphase drag, two-phase level
LOFT L3-1	Accumulator model
Marviken Test 22	Subcooled choking model, flashing, two-phase level
Marviken Test 24	Subcooled choking model, flashing, two-phase level
Marviken Test CFT 21	Subcooled critical flow, saturated liquid critical flow
Marviken Test JIT 11	Saturated vapor critical flow, interfacial drag in bubbly/slug, pool boiling, void profile
MB2 Test 1712	Steam generator behavior
MIT Pressurizer	Wall condensation, interfacial heat transfer, pressurizer level, thermal stratification
Moby Dick air-water	Critical flow
Neptunus	Pressurizer
ORNL THTF Tests 3.07.9B, 3.07.9N, 3.07.9W	CHF, film boiling, steam cooling
ORNL THTF Test 3.09.10	Void profile in rod bundles, radiation heat transfer
Royal Institute of Technology Tube Test 261	CHF
UPTF Downcomer Countercurrent Flow Test 6, Run 131	Downcomer CCFL, lower plenum refill, condensation, noncondensables, two-phase level, thermal stratification, interphase drag, entrainment

cases address countercurrent flow limitation (CCFL) in pipe and downcomer geometries, and phenomena associated with the pressurizer, steam generator, and jet pump components.

Table 2.2-3 presents the integral effects cases. There are two small break loss-of-coolant accident (LOCA) experiments, two large break LOCA experiments (the Loss-of-Fluid Test [LOFT] experiment L2-5 is modeled with both 1-D and 3-D components), and four loop natural circulation tests from the Semiscale facility. As integral experiments, each of these addresses a large number of phenomena.

Table 2.2-3. Integral effects assessment cases.

Case Description	Experiment Type
LOBI Test A1-04R	Large break LOCA
LOFT L2-5 (1-D)	Large break LOCA
LOFT L2-5 (3-D)	Large break LOCA
LOFT L3-7	1-in. small break LOCA
ROSA-IV Test SB-CL-18	6-in. small break LOCA
Semiscale NC Tests 1, 2, 3, 10	Loop natural circulation

2.3 Assessment Criteria

Judgments of the adequacy of the code models were made, using a standardized and consistent set of criteria that has been previously applied in the assessment of U. S. Nuclear Regulatory Commission-sponsored codes.[2.4-1, 2.4-2, 2.4-3] The terminology is defined below.

Excellent Agreement – Applies when the code exhibits no deficiencies in modeling a given behavior. Major and minor phenomena and trends are correctly predicted. The calculated results are judged to agree closely with the data. The calculation will, with few exceptions, lie within the uncertainty bands of the data. The code may be used with confidence in similar applications. (The term “major phenomena” refers to the phenomena that influence key parameters such as fuel rod cladding temperature, pressure, differential pressure, mass flow rate, and mass distribution. Predicting major trends means that the prediction shows the significant features of the data. Significant features include the magnitude of a given parameter through the transient, slopes, and inflection points that mark significant changes in the parameter.)

Reasonable Agreement – Applies when the code exhibits minor deficiencies. Overall, the code provides an acceptable prediction. All major trends and phenomena are correctly predicted. Differences between calculation and data are greater than deemed necessary for excellent agreement. The calculation will occasionally lie outside the uncertainty bands of the data. However, the correct conclusions about trends and phenomena would be reached if the code were used in similar applications. The code models and/or facility model noding should be reviewed to see if improvements can be made.

Minimal Agreement – Applies when the code exhibits significant deficiencies. Overall, the code provides a prediction that is only conditionally acceptable. Some major trends or phenomena are not predicted correctly, and some calculated values lie considerably outside the uncertainty bands of the data. Incorrect conclusions about trends and phenomena may be reached if the code were used in similar applications, and an appropriate warning needs to be issued to users. Selected code models and/or facility model noding need to be reviewed, modified, and assessed before the code can be used with confidence in similar applications.

Insufficient Agreement – Applies when the code exhibits major deficiencies. The code provides an unacceptable prediction of the test. Major trends are not predicted correctly. Most calculated values lie

outside the uncertainty bands of the data. Incorrect conclusions about trends and phenomena are probable if the code is used in similar applications, and an appropriate warning needs to be issued to users. Selected code models and/or facility model noding need to be reviewed, modified, and assessed before the code can be used with confidence in similar applications.

Assessment judgments of “excellent” or “reasonable” are considered to indicate acceptable code performance. While there is a quantitative aspect to the assessment characterizations, the judgments remain mostly qualitative.

The assessment definitions above judge the code performance relative to pertinent data. While some of the phenomenological cases have no data, the pertinent equations for those that do are included in this report. Most of the separate and integral effects experiment data were obtained from the NRC Data Bank.[2.4-4] For those cases not included in that data bank, the data were obtained from experiment data reports or other reports describing the results of the tests. The data source for each of the cases is identified in the individual assessment sections of the report.

2.4 References

2.4-1. *2D/3D Program Work Summary Report*, prepared jointly by Japan Atomic Energy Research Institute, Gesellschaft fuer Anglagen-und Reaktorsicherheit, Siemens AG, UB KWU, U. S. Nuclear Regulatory Commission, Los Alamos National Laboratory, and MPR Associates, Inc., International Agreement Report NUREG/IA-0126, also GRS-100 and MPR-1345, June 1993.

2.4-2. U. S. Nuclear Regulatory Commission, *Compendium of ECCS Research for Realistic LOCA Analysis*, NUREG-1230, p. 4-126, December 1988.

2.4-3. R. R. Schultz, *International Code Assessment and Applications Program: Summary of Code Assessment Studies Concerning RELAP5/MOD2, RELAP5/MOD3, and TRAC-B*, Idaho National Engineering Laboratory, NUREG/IA-0128, EGG-EAST-8719, December 1993.

2.4-4. U. S. Nuclear Regulatory Commission, *Reactor Safety Data Bank*, August 2004.

3. PHENOMENOLOGICAL CASES

The phenomenological cases are simple problems that have been used to demonstrate qualitatively, and in some cases quantitatively, that the RELAP5-3D code is performing as expected. Each case generally addresses a single phenomenon or code model. A total of 17 cases are included:

- Three cases addressing basic numerics and gravity
- Two cases addressing level tracking
- Three cases with flow oscillations in either vertical or horizontal pipes
- One case addressing water packing
- Two cases involving the point kinetics or decay heat models
- Three cases demonstrating the three-dimensional hydrodynamics
- Three cases addressing the conduction enclosure model.

Details of the assessments for each of the cases are provided in the remainder of this chapter.

3.1 Water Faucet

This is a conceptual problem in which water with an initial downward velocity falls through a vertical pipe under the influence of gravity. With some simplifying assumptions, an analytical solution for the liquid velocity can be obtained and compared to the computational results. This test case has been used in the past to check the correctness of the conservation equations and the numerical solution scheme in RELAP5.[3.1-1]

3.1.1 Code Models Assessed

The performance of the numerics, gravitational force term, and momentum equation was evaluated.

3.1.2 Problem Description

Assuming a negligible pressure gradient and steady state, the liquid momentum equation can be integrated from the pipe inlet to an arbitrary point, resulting in

$$\frac{1}{2}\rho_f v_f^2 = \left(\frac{1}{2}\rho_f v_f^2\right)_{inlet} + \rho_f g z, \tag{3.1-1}$$

where z is the distance from the top of the pipe. Since the liquid is nearly incompressible, Equation (3.1-1) can be rearranged to give

$$v_f = \sqrt{2gz + v_o^2}, \tag{3.1-2}$$

where v_o is the initial liquid velocity, and g is the acceleration due to gravity. This equation can then be used to calculate the liquid velocity at any location in the pipe.

Assuming a constant liquid density, the continuity equation gives

$$\alpha_f A v_f = (\alpha_f A v_f)_o, \tag{3.1-3}$$

where the subscript o indicates the initial condition. Rearranging Equation (3.1-3) and knowing the pipe flow area is constant, it is then possible to calculate the liquid fraction at a point based on conditions at the inlet and the liquid velocity calculated from Equation (3.1-2):

$$\alpha_f = \frac{(\alpha_f v_f)_o}{v_f}. \tag{3.1-4}$$

3.1.3 Input Model Description

The water faucet problem nodalization diagram is shown in Figure 3.1-1. The model consists of a vertical pipe which is 12 m long (twelve volumes, each 1 m in length) and has a diameter of 1.128 m (flow area of 1 m^2). Time-dependent volumes at 1 MPa and a static quality of 0.00149 are attached to the top and bottom of the pipe. A time-dependent junction at the top of the pipe sets the inlet liquid velocity to 10 m/s. The problem is run for 10 s, when a steady state condition has been achieved.

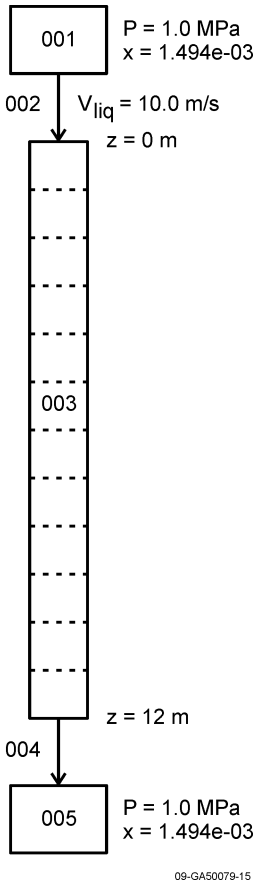

Figure 3.1-1. RELAP5-3D nodalization for the water faucet test case.

Card 1 option 14 is used to turn off interfacial drag, wall friction, and the virtual mass force term. This allows the computational results to be compared with the analytical solution developed above.

3.1.4 Data Comparisons and Results

The steady state junction liquid velocities are plotted in Figure 3.1-2, along with the theoretical values obtained from Equation (3.1-2). As expected, the fluid velocity increases with distance from the inlet due to the acceleration of gravity.

Figure 3.1-3 shows the liquid fractions calculated by RELAP5-3D compared to the analytical solution obtained from Equation (3.1-4). Due to continuity considerations, the liquid fraction decreases with axial distance down the pipe as the liquid velocity increases.

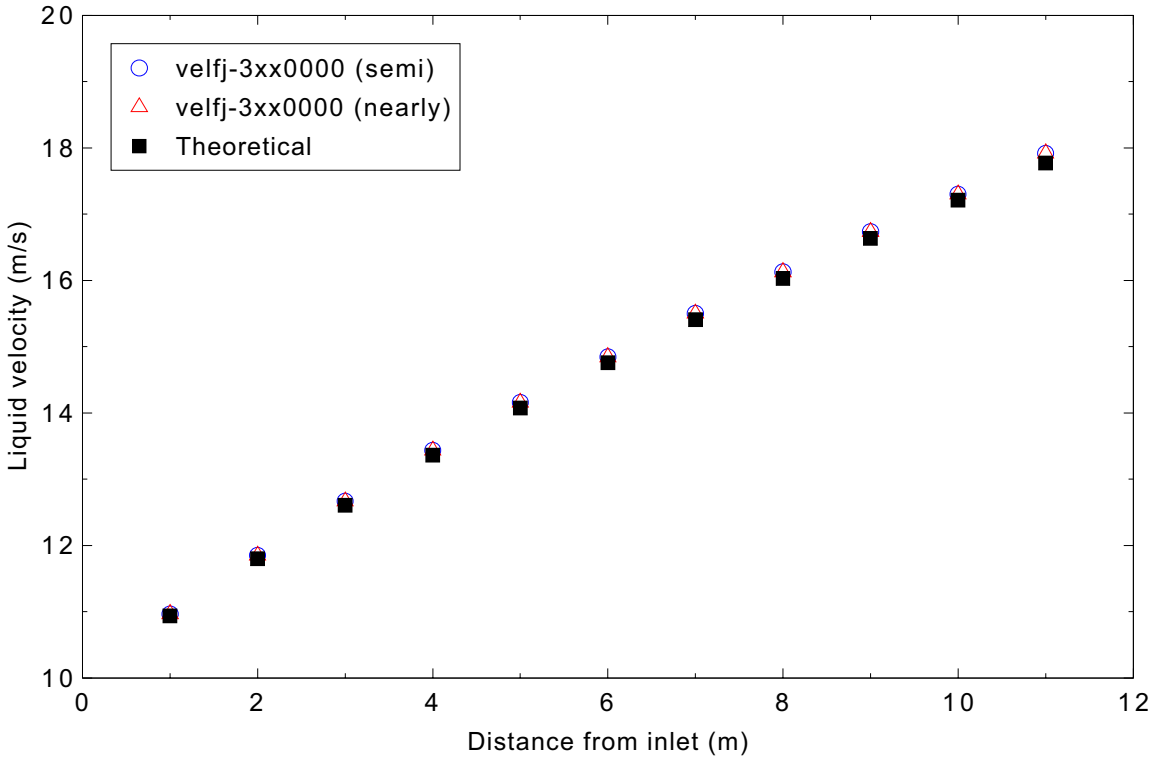

Figure 3.1-2. Comparison of RELAP5-3D calculated liquid velocity with the exact solution for the water faucet case.

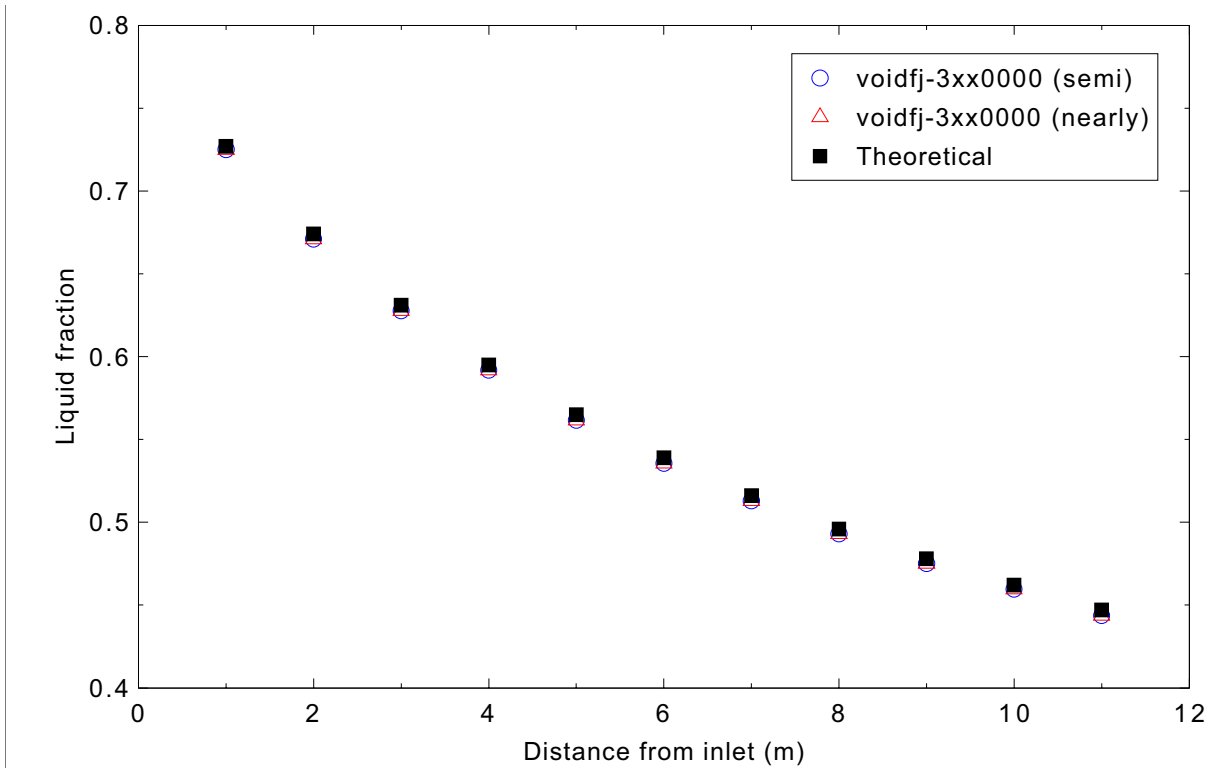

Figure 3.1-3. Comparison of RELAP5-3D calculated liquid fraction with the exact solution for the water faucet case.

The semi-implicit and nearly-implicit results both show excellent agreement with the analytical solution.

3.1.5 Conclusions and Assessment Findings

The RELAP5-3D semi-implicit and nearly-implicit results are in excellent agreement with the analytical solution. Both the fluid velocity and liquid fraction are correctly predicted over the entire pipe length.

3.1.6 References

3.1-1. J. A. Trapp, R. A. Riemke, and R. J. Wagner, *Nearly-Implicit Hydrodynamic Numerical Scheme and Partially-Implicit Hydrodynamic and Heat Slab Coupling for RELAP5/MOD2*, EGG-CMD-6715, September 1984.

3.2 Water over Steam (1-D)

The water over steam problem is simply a vertical pipe with the upper one-third of the pipe filled with water and the lower two-thirds of the pipe filled with steam.

3.2.1 Code Models Assessed

This problem assesses the gravitational head effect in the code.

3.2.2 Problem Description

The top third of a vertical pipe is initially filled with saturated water, below which is saturated steam, both at a pressure of 413 kPa. The pipe is 4.16448 m long and has a flow area of 1.0 m^2. As the transient begins, the water falls, displacing the steam, eventually filling the bottom third of the pipe.

For a free-fall scenario, the time for the liquid to drop a distance h is given by

$$t = \sqrt{\frac{2h}{g}}. \qquad (3.2\text{-}1)$$

With h = 2/3 (4.16448) = 2.77632 m, the drop time t = 0.75 s. This is a lower bound on the drop time, because in this problem the steam must flow through the liquid to get to the top of the pipe.

3.2.3 Input Model Description

3.2-1 shows the RELAP5-3D nodalization diagram. The upward-oriented vertical pipe was modeled using nine equal-length volumes. The upper three volumes are initially filled with saturated water at a pressure of 413 kPa, and the bottom six volumes are filled with saturated steam at a pressure of 413 kPa.

3.2.4 Calculation Results

Both the semi- and nearly-implicit calculations were run with a requested time step of 0.01 s.

The void fraction history of the nine volumes during the transient is seen in Figures 3.2-2 through 3.2-4. The water drains from the upper three volumes in about 8 s, and the lower three volumes are filled by about 10 s. This is slower than the theoretical lower bound time of 0.75 s because of the drag imposed on the liquid as the steam rises, which prevents the liquid from flowing freely. This is especially noticeable in volume 107 (Figure 3.2-2), where the steam initially interacts with the liquid.

The calculated behavior is qualitatively as expected. With such a large flow area, it might be expected that the liquid would fall faster, but there are no data to quantitatively verify the results; the code is judged to perform reasonably. The results from the two calculation schemes are similar, with the liquid in the nearly-implicit calculation falling a little more slowly.

Figure 3.2-1. RELAP5-3D nodalization diagram for the 1-D water over steam problem.

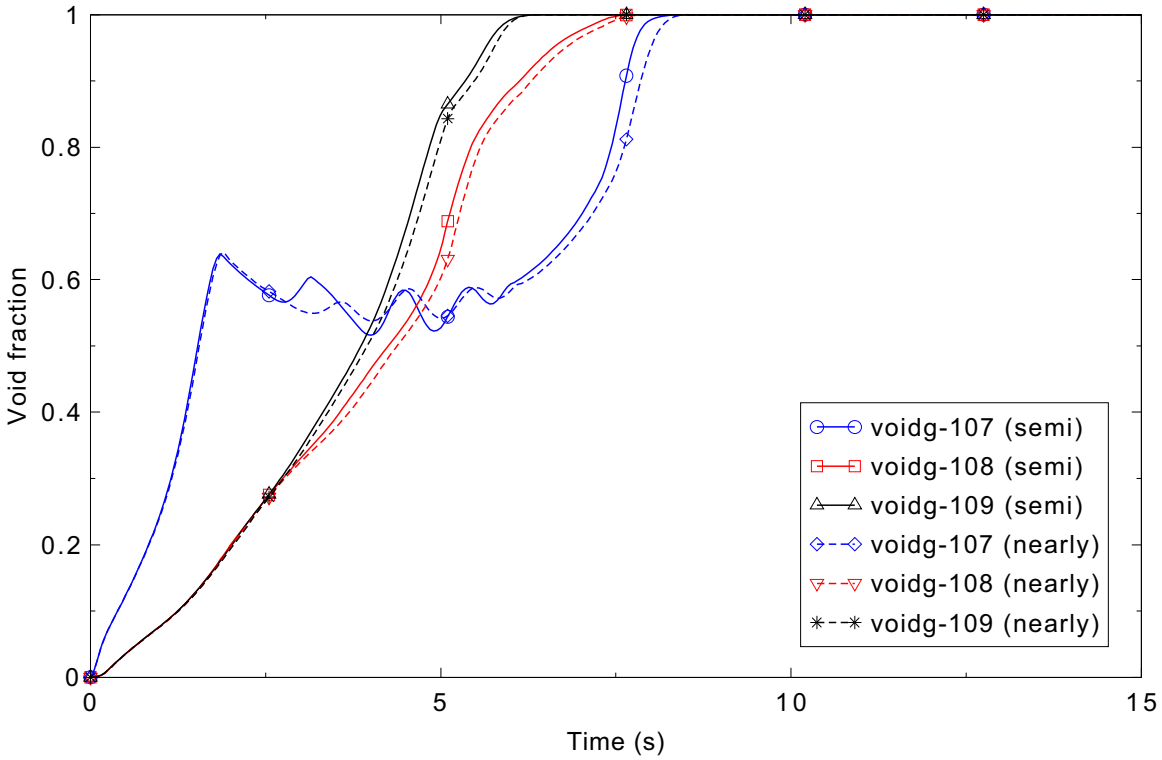

Figure 3.2-2. Void fraction in the top three volumes (7-9) for the 1-D water over steam problem.

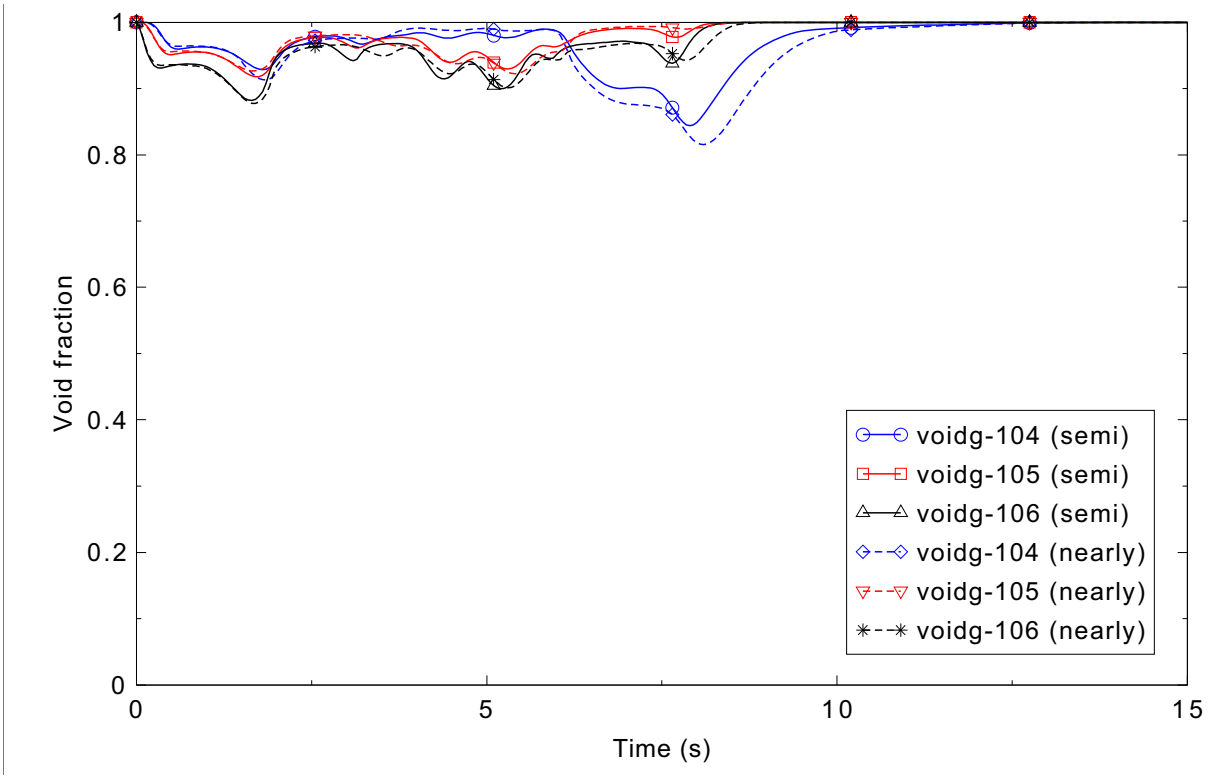

Figure 3.2-3. Void fraction in the middle three volumes (4-6) for the 1-D water over steam problem.

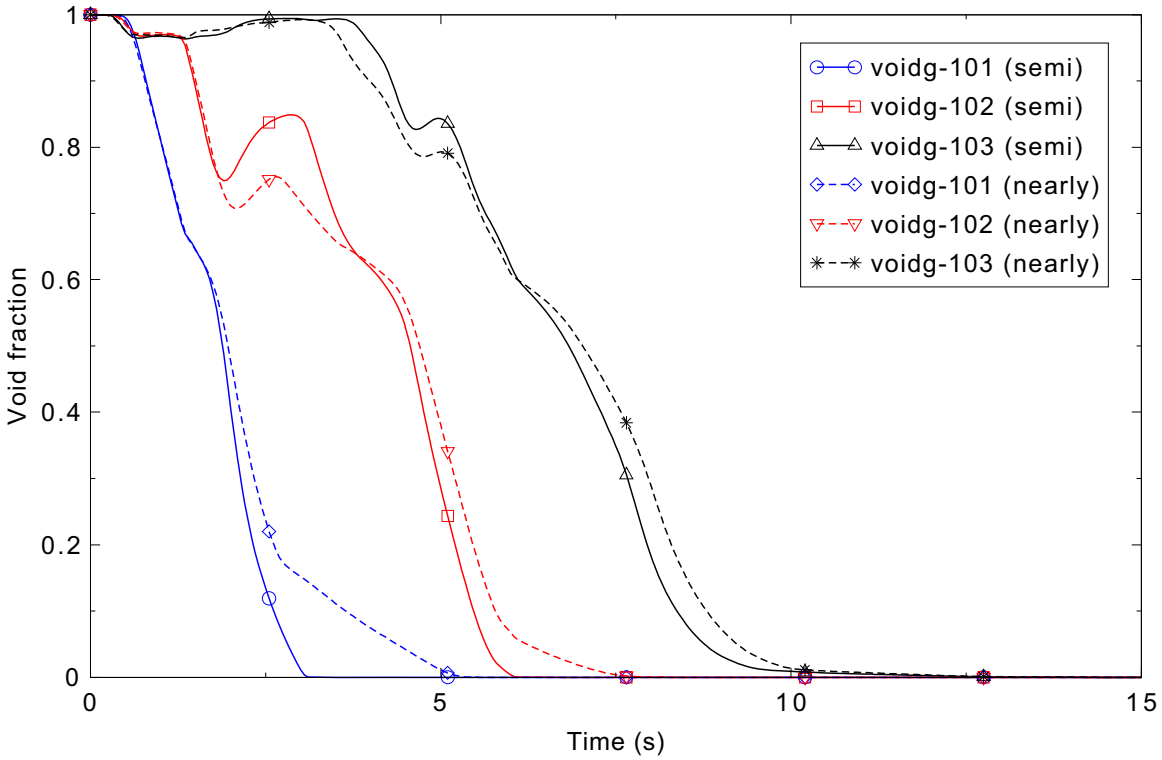

Figure 3.2-4. Void fraction in the bottom three volumes (1-3) for the 1-D water over steam problem.

3.2.5 Conclusions and Assessment Findings

The gravitational head effect in RELAP5-3D causes the liquid to fall to the bottom volumes as it should. The code performance is judged to be reasonable.

3.3 Water over Steam (3-D)

The water over steam problem is simply a vertical pipe with the upper one-third of the pipe filled with water and the lower two-thirds of the pipe filled with steam.

3.3.1 Code Models Assessed

This problem assesses the gravitational head effect and the multi-dimensional component in the code.

3.3.2 Problem Description

The top third of a vertical pipe is initially filled with saturated water, below which is saturated steam, both at a pressure of 413 kPa. The pipe is 4.16448 m long and has a flow area of 1.0 m^2. As the transient begins, the water falls, displacing the steam, eventually filling the bottom third of the pipe.

For a free-fall scenario, the time for the liquid to drop a distance h is given by

$$t = \sqrt{\frac{2h}{g}}. \qquad (3.3\text{-}1)$$

With h = 2/3 (4.16448) = 2.77632 m, the drop time t = 0.75 s. This is a lower bound on the drop time, because in this problem the steam must flow through the liquid to get to the top of the pipe.

3.3.3 Input Model Description

Figure 3.3-1 shows the RELAP5-3D nodalization diagram. The upward-oriented vertical multid component was nodalized with 2 radial regions, 4 azimuthal regions, and 9 axial regions. The radius of the inner cylinder is half that of the pipe. The upper three axial regions are initially filled with saturated water at a pressure of 413 kPa, and the bottom six axial regions are filled with saturated steam at a pressure of 413 kPa.

3.3.4 Calculation Results

Both the semi- and nearly-implicit calculations were run with a requested time step of 0.01 s. The nearly-implicit calculation failed (water property) between 3 and 4 s; using a range of other requested time steps resulted in failures around the same time.

The void fraction history of the nine axial regions during the transient is seen in Figures 3.3-2 through 3.3-4. The void fractions presented were obtained by averaging the eight segments that make up each axial level.

In the semi-implicit calculation, the water in the upper five axial levels drains in about 5 s, and the lower two levels fill by 10 s, but the third level has not quite filled by 20 s, as some liquid is held up in the fourth volume. The draining time is slower than the theoretical lower bound time of 0.75 s because of the drag imposed on the liquid as the steam rises, which prevents the liquid from flowing freely. While there is

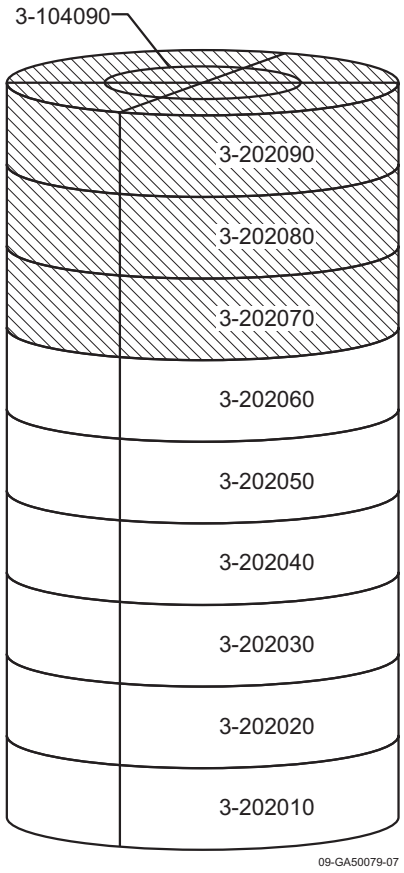

Figure 3.3-1. RELAP5-3D nodalization diagram for the 3-D water over steam problem.

some liquid holdup in the seventh axial level, it is not as pronounced or lengthy as that seen in the one-dimensional case (Section 3.2). Based on the qualitative response, the code calculation is judged to be reasonable; there are no data with which to quantitatively assess the draining time.

Figure 3.3-5 shows the void fraction in each of the eight segments of axial level 5 for the semi-implicit scheme. The water falls in each of the eight segments for axial level 5, some segments more than others, but there are no large differences.

3.3.5 Conclusions and Assessment Findings

The gravitational head effect in RELAP5-3D causes the liquid to fall to the bottom axial levels as it should for the semi-implicit solution scheme, so its performance is judged to be reasonable. Since the nearly-implicit calculation failed to run beyond 4 s, its performance is judged to be insufficient.

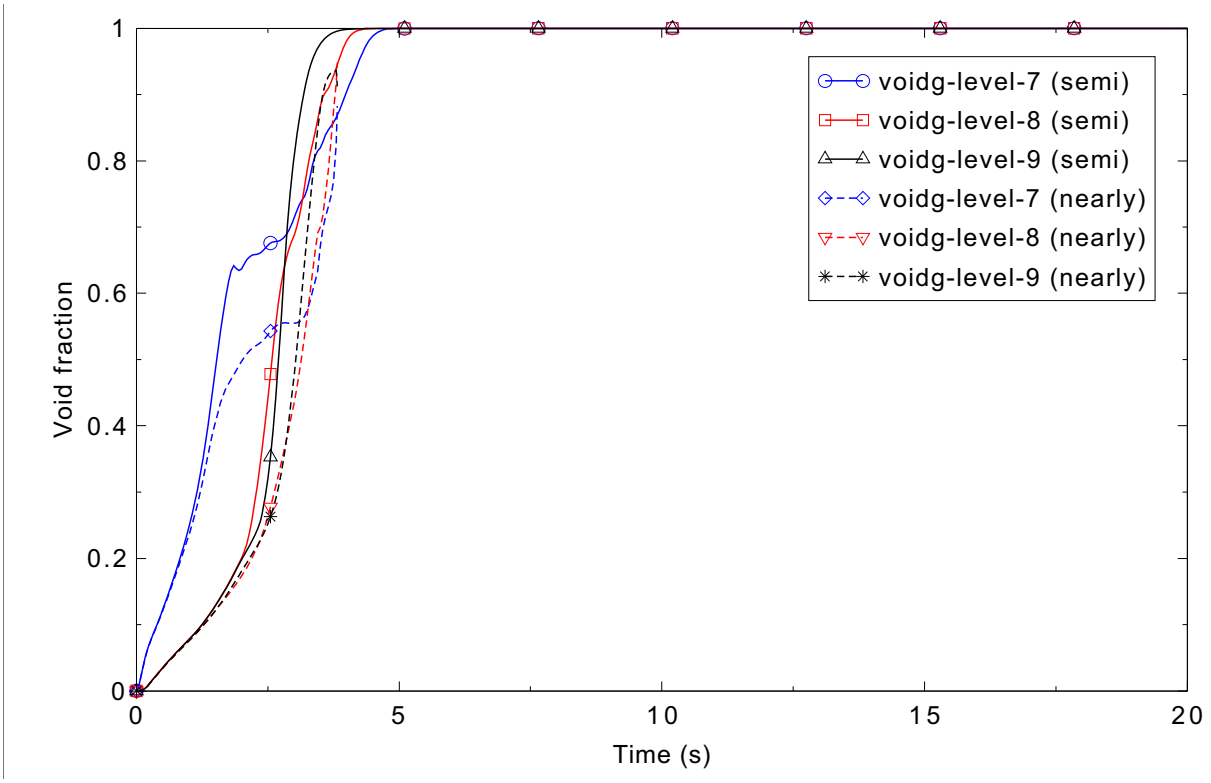

Figure 3.3-2. Void fraction in the top three axial levels (7-9) for the 3-D water over steam problem.

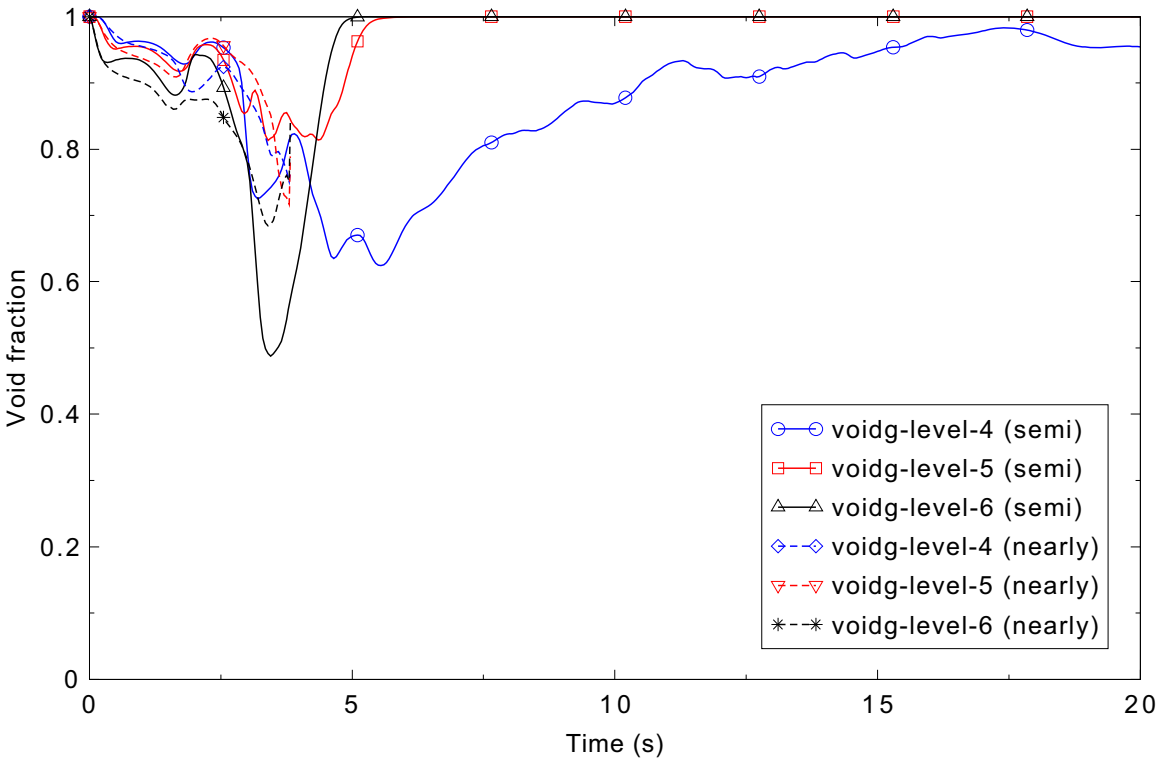

Figure 3.3-3. Void fraction in the middle three axial levels (4-6) for the 3-D water over steam problem.

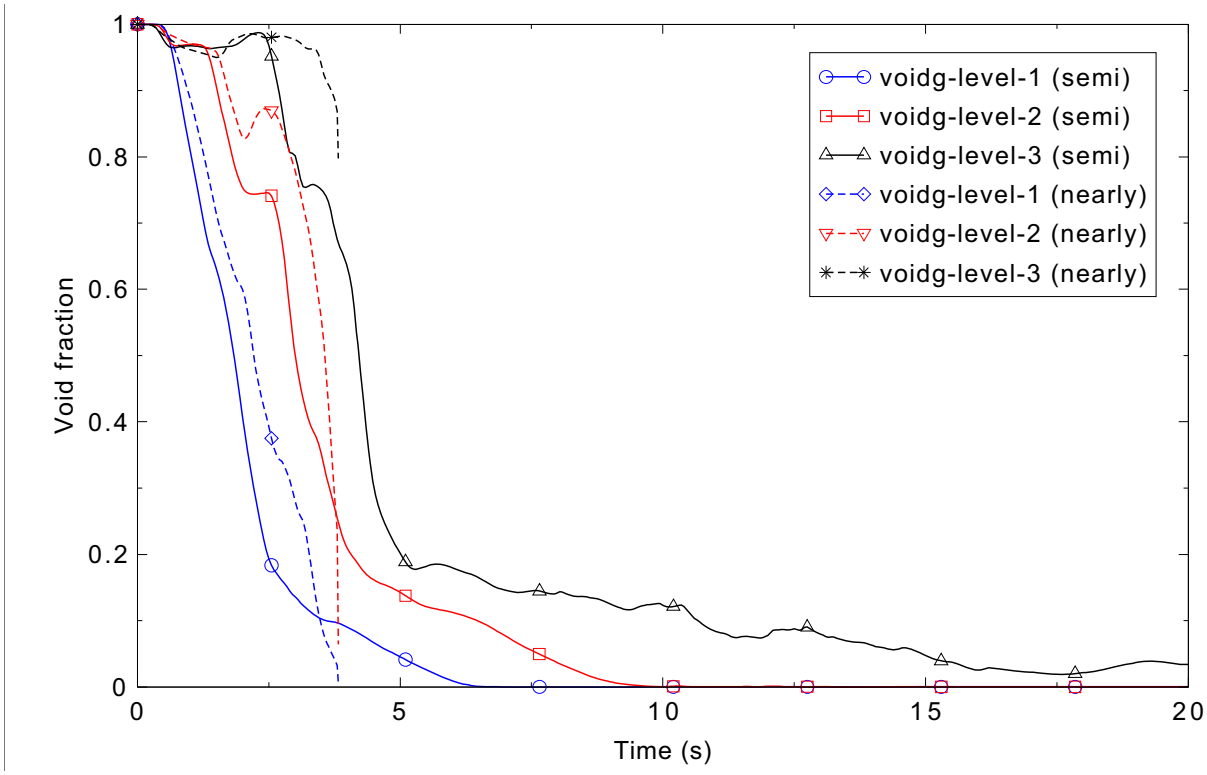

Figure 3.3-4. Void fraction in the bottom three axial levels (1-3) for the 3-D water over steam problem.

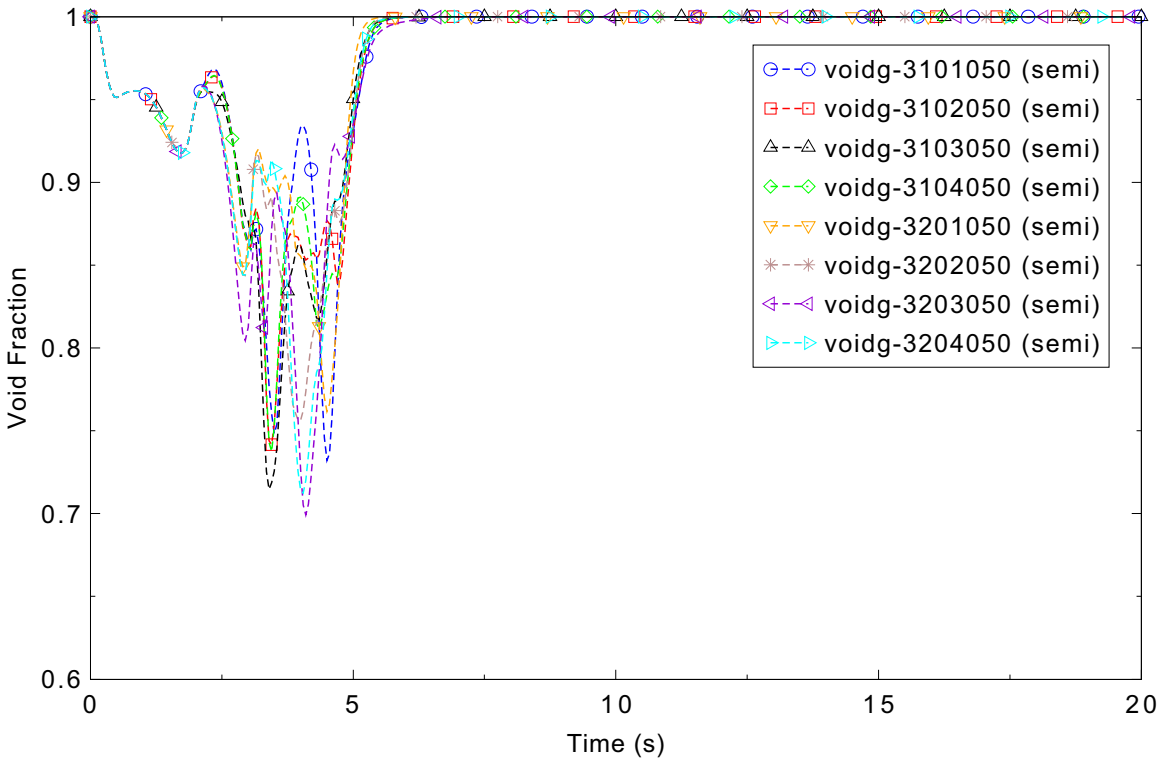

Figure 3.3-5. Void fraction in each of the eight segments of axial level 5 for the 3-D water over steam problem.

3.4 Fill-Drain

The fill-drain assessment problem is an assessment problem for the mixture level tracking model in RELAP5-3D. The mixture level tracking model is essential for modeling gravity-driven cooling systems. This model is used in place of fine nodalization of the component in order to track large changes in void fraction using a relatively small number of volumes in a component. Both normal, void fraction increasing in the vertical direction, and inverted, void fraction decreasing in the vertical direction, mixture levels are located and tracked in the model. An inverted mixture level can appear in places where there is a flow restriction, like a grid spacer or tie plate in a rod bundle.

3.4.1 Code Models Assessed

The fill-drain assessment problem assesses the mixture level tracking model.

3.4.2 Problem Description

A vertical pipe is initially filled with steam at atmospheric pressure. Liquid is then added at the bottom of the pipe, forming a rising level. When the pipe is about half full of liquid, the inlet flow is reversed, and the pipe drains.

3.4.3 Input Model Description

The test problem, shown at the right in Figure 3.4-1, uses a 10-volume vertical pipe (Component 3) with a time-dependent junction (Component 2) adding liquid to and then removing liquid from the bottom volume of the pipe. The top is connected to a time-dependent volume (Component 5) at atmospheric pressure. The pipe is oriented such that volume 1 is at the bottom and volume 10 is at the top. It is initially filled with vapor at atmospheric pressure. The time-dependent junction starts filling the pipe at time 0 and continues to 50 s. Then it reverses direction and starts draining the liquid until 100 s when the problem ends. During the first 50 s, the liquid fills each volume in turn and by 50 s, when the fill reverses, volume 5 is filled to 46%. A time step size of 0.05 s was used for both the semi-implicit and nearly-implicit advancement schemes.

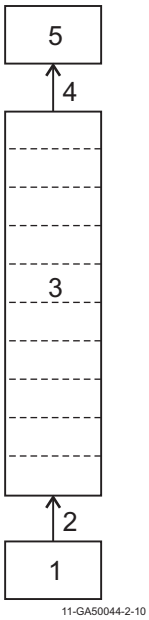

Figure 3.4-1. Nodalization diagram for Fill-Drain test.

3.4.4 Data Comparisons and Results

The liquid velocity at the inlet time-dependent junction is shown in Figure 3.4-2. The change in flow direction is clearly seen to occur at 50 s. The pressure in the bottom of the pipe, volume 1, is shown in Figure 3.4-3.

While the pressure in the bottom volume for the semi-implicit calculation is smooth, that for the nearly-implicit advancement schemes is not; the latter is affected by the level crossing junctions.

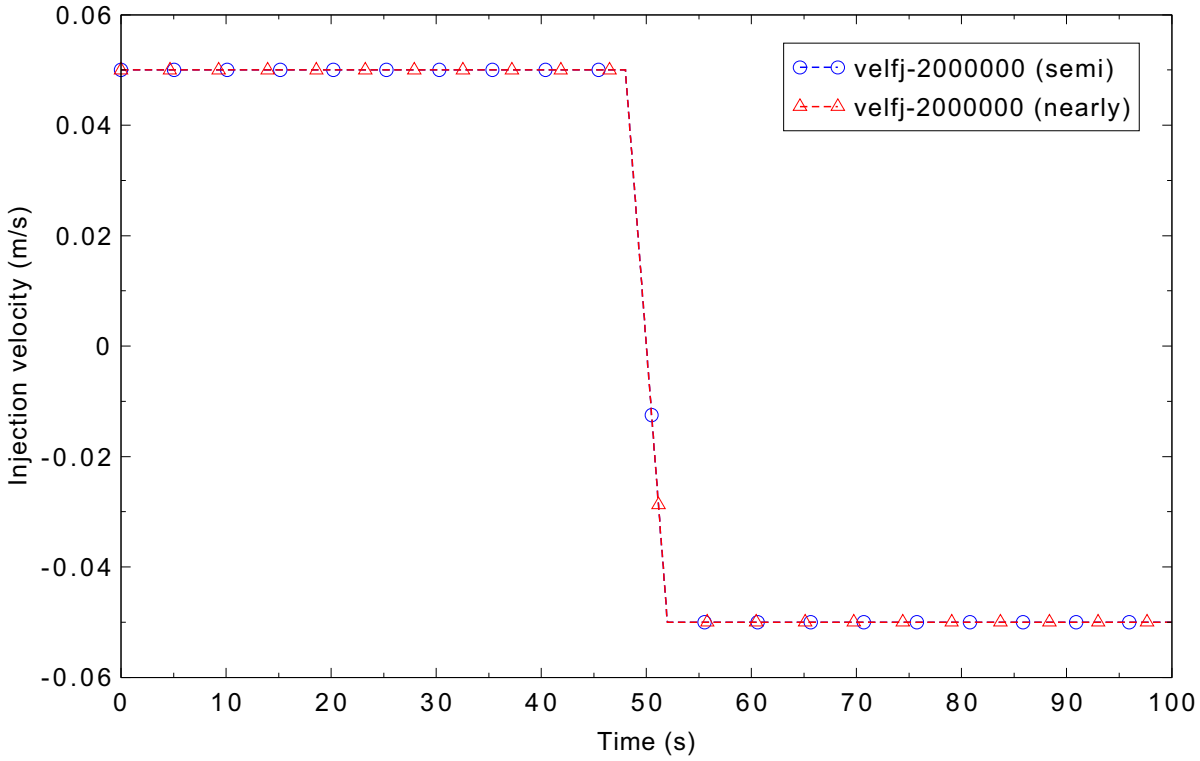

Figure 3.4-2. Injection flow liquid velocity comparison for the Fill-Drain test.

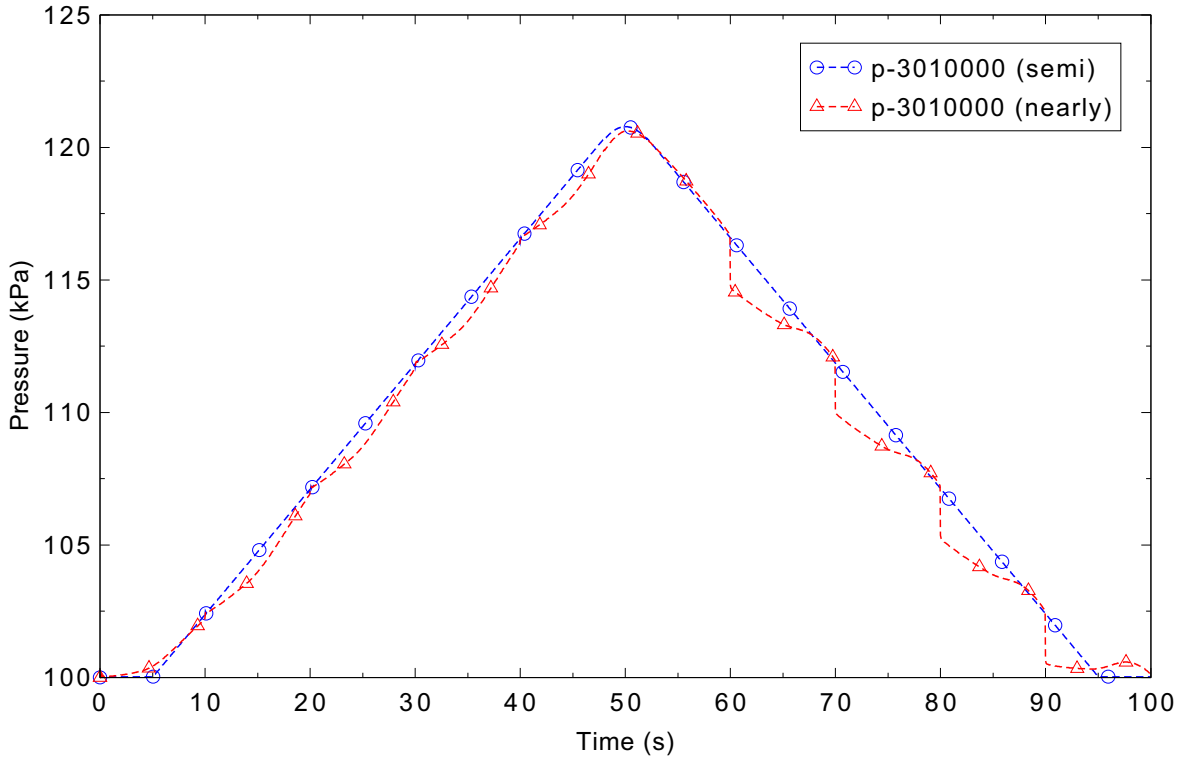

Figure 3.4-3. Bottom volume pressure comparison for the Fill-Drain test.

The next set of five plots shows the mixture level in the bottom five volumes of the pipe compared with analytic data for the semi-implicit and nearly-implicit cases. Figure 3.4-4 shows the mixture level in volume 1, Figure 3.4-5 shows the mixture level in volume 2, Figure 3.4-6 shows the level in volume 3, Figure 3.4-7 shows the mixture level in volume 4, and Figure 3.4-8 shows the mixture level in volume 5. The level peaks in volume 5 and starts down at 50 s. It should be noted that the data only follow the level calculations when it is rising and falling. The code calculations set the level in the volume to zero when it is not in the volume, hence, the sharp drop in the calculated mixture level in these figures when the level crosses into the adjacent volume.

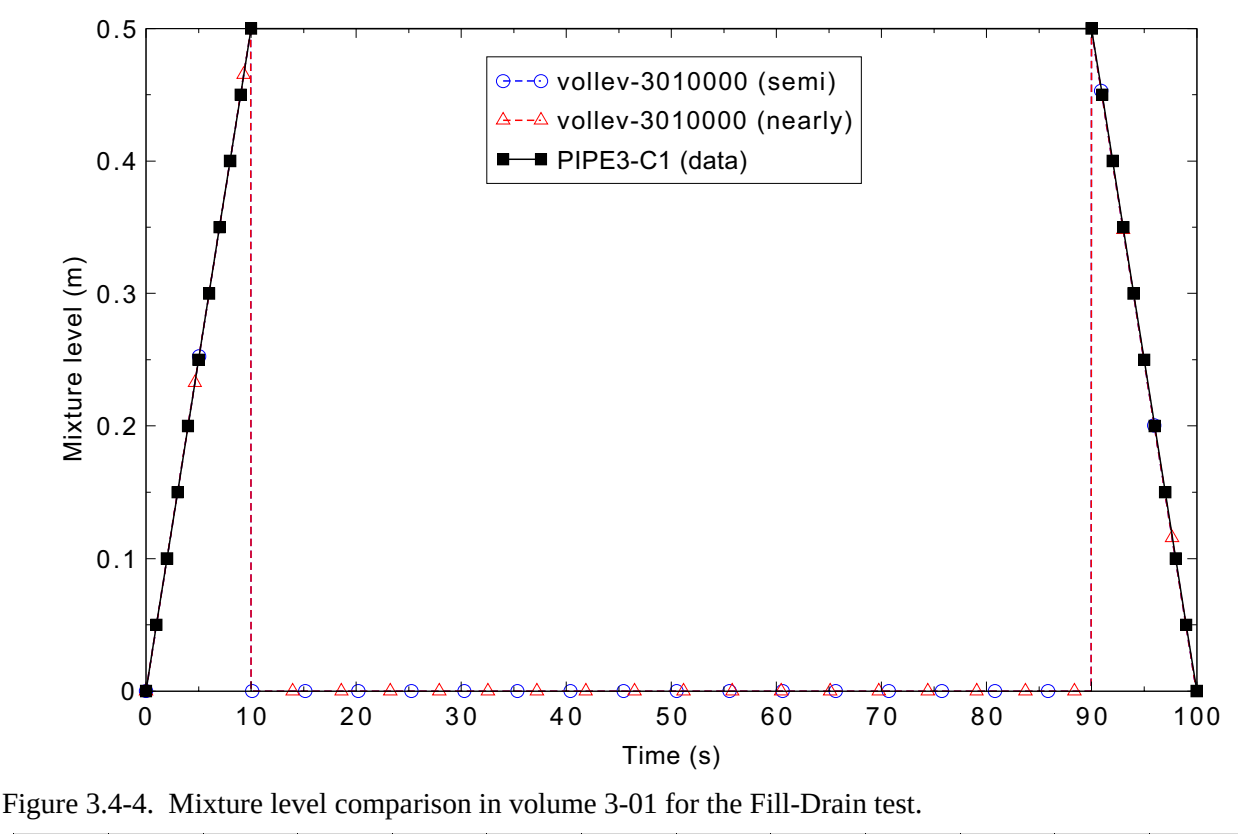

Figure 3.4-4. Mixture level comparison in volume 3-01 for the Fill-Drain test.

3.4.5 Conclusions and Assessment Findings

The level model comparisons for the semi-implicit advancement scheme is excellent, and that for the nearly-implicit advancement scheme is reasonable for this test problem.

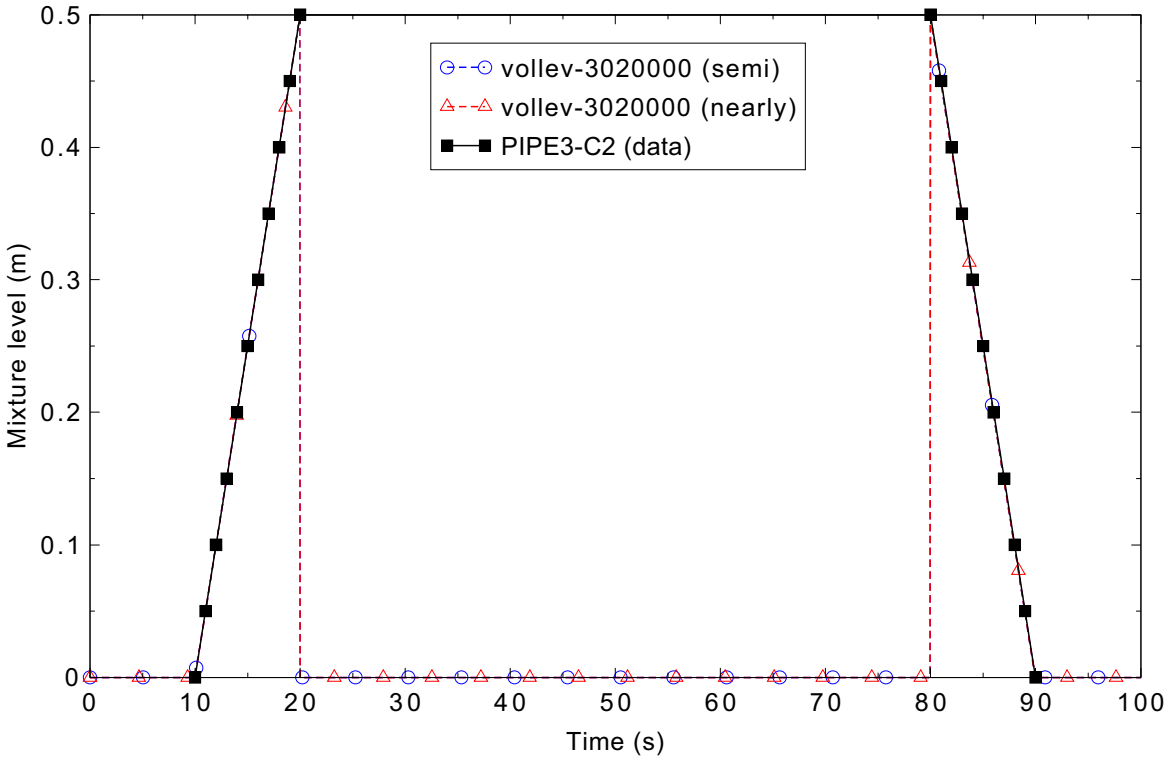

Figure 3.4-5. Mixture level comparison in volume 3-02 for the Fill-Drain test.

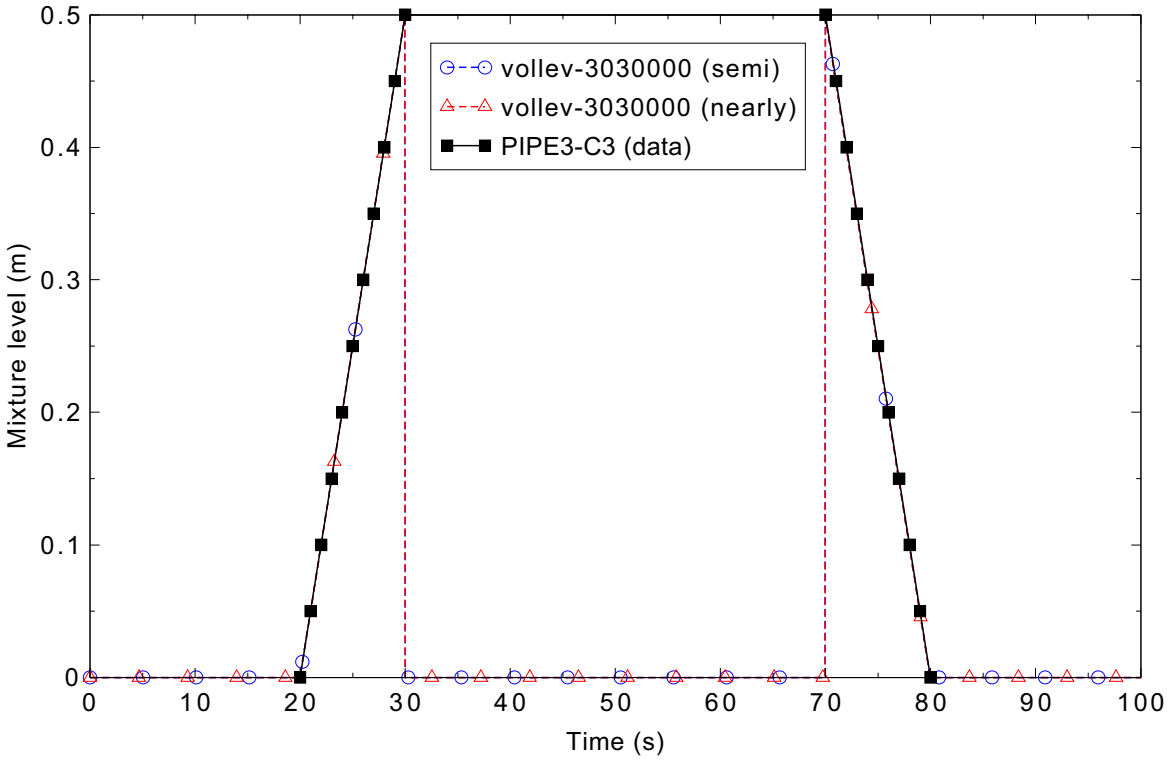

Figure 3.4-6. Mixture level comparison in volume 3-03 for the Fill-Drain test.

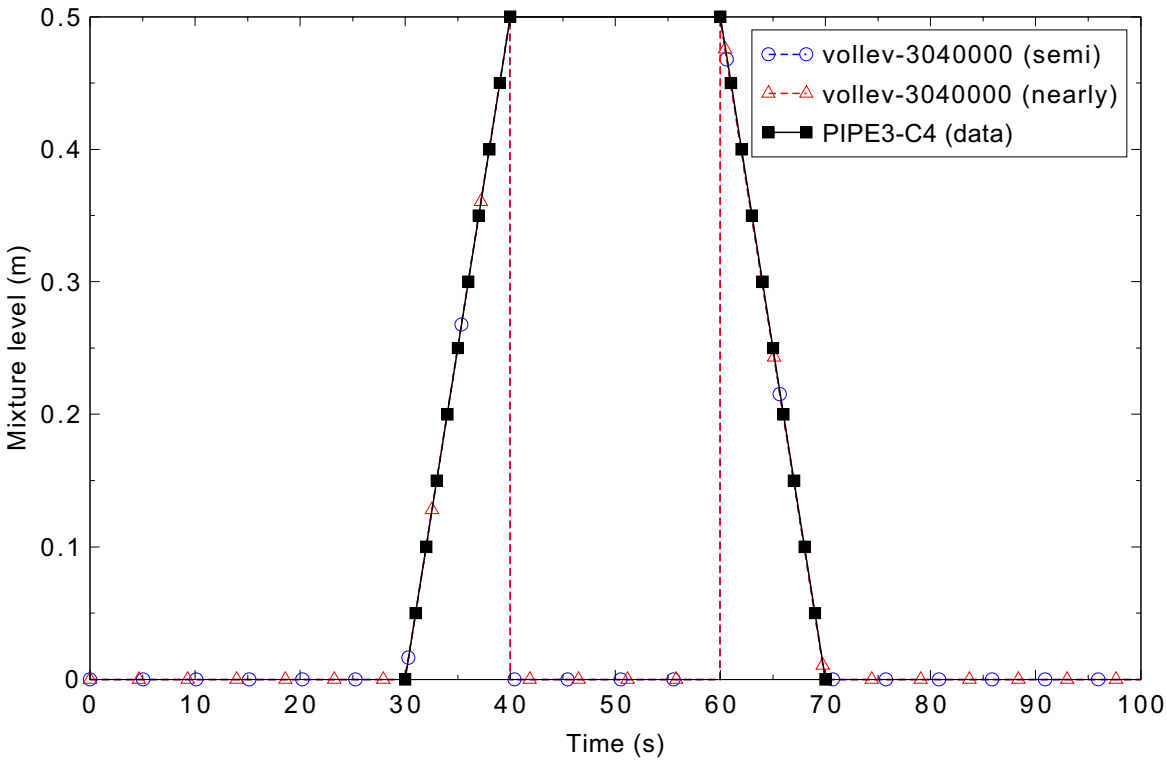

Figure 3.4-7. Mixture level comparison in volume 3-04 for the Fill-Drain test.

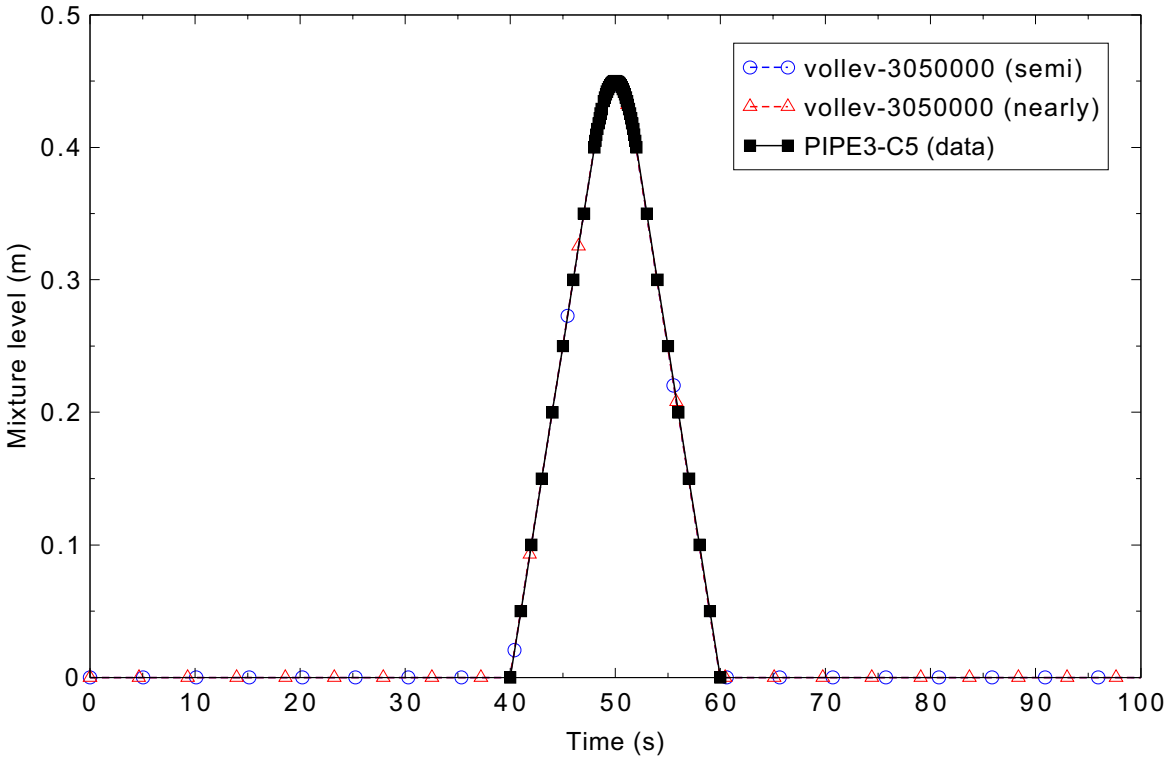

Figure 3.4-8. Mixture level comparison in volume 3-05 for the Fill-Drain test.

3.5 Bubbling Steam through Liquid

This test case was designed to qualitatively examine the progression of mixture liquid levels as a function of steam flow rate and to create conditions in which the entrainment of liquid droplets into the steam flow is established.

3.5.1 Code Models Assessed

The performance of the mixture level tracking and entrainment models was evaluated.

3.5.2 Problem Description

This case is a thought problem in which saturated steam is bubbled up through a column of saturated liquid water. The steam flow rate is increased in steps, allowing quasi-steady conditions to be established. The flow rate is then increased linearly to a value high enough to entrain liquid out of the top of the column.

3.5.3 Input Model Description

The nodalization diagram for this test case is shown in Figure 3.5-1. The model consists of a vertical pipe component with five volumes, each 3 ft long with a flow area of 3 ft^2. The bottom portion of the pipe is initially filled with saturated liquid at 1,000 psia, establishing a liquid level in the second pipe volume. The remainder of the pipe is filled with saturated steam. A time-dependent junction is used to inject saturated steam at 1,000 psia into the bottom volume, and the top pipe volume is connected to a time-dependent volume which is also filled with steam at 1,000 psia.

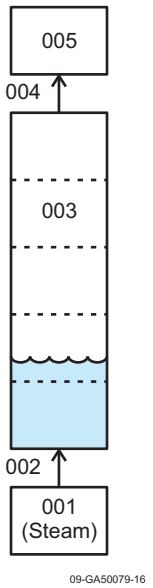

Figure 3.5-1. RELAP5-3D nodalization for the bubbling steam through liquid test case.

The time-dependent junction steam mass flow rate is shown in Figure 3.5-2. The mass flow rate is increased every 100 s in a stepwise fashion, allowing the mixture level to stabilize after each increase. From 600 s to 1,300 s, the flow rate is increased linearly up to a maximum value of 100 lbm/s.

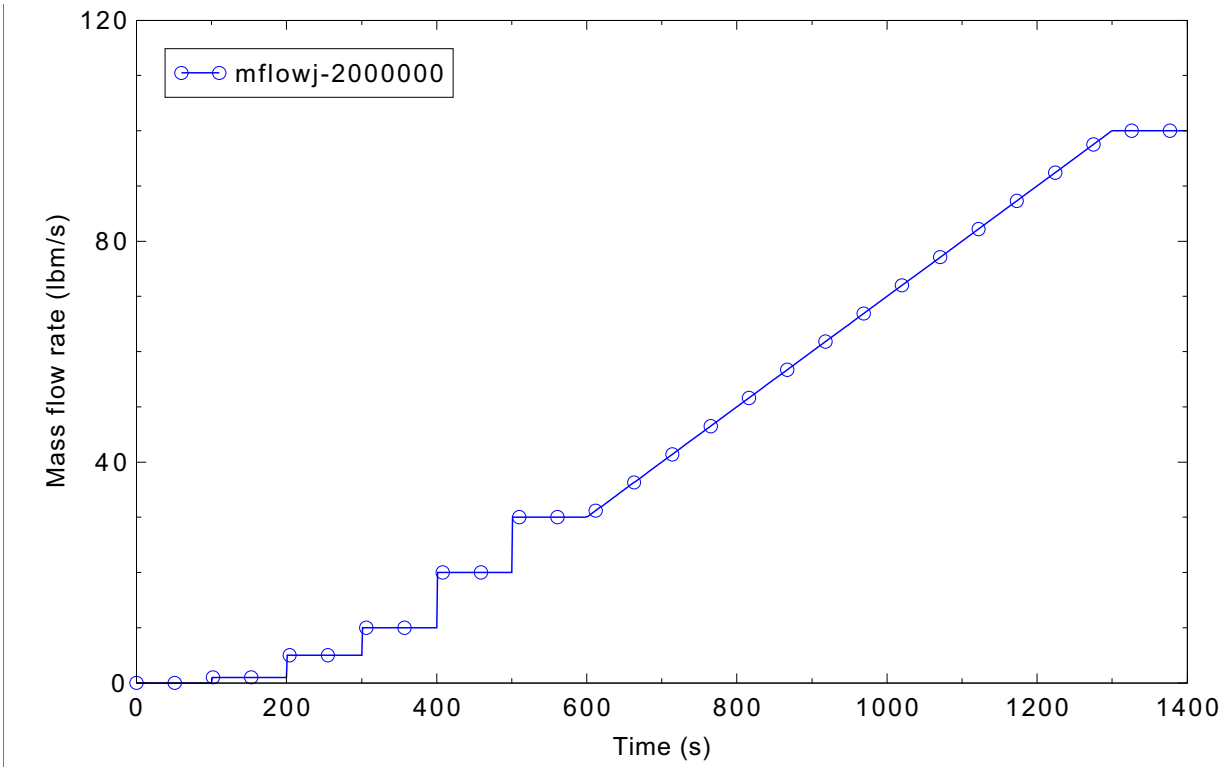

Figure 3.5-2. Steam inlet mass flow rate for the bubbling steam through liquid case.

3.5.4 Data Comparisons and Results

The mixture levels in pipe volumes 2, 3, and 4 are shown in Figures 3.5-3 through 3.5-5. The level in volume 2 is initially at 0.49 ft with no inlet steam flow. The mixture level steadies out at 1.35 ft and 2.60 ft from 100 to 300 s as the steam flow is increased in a stepwise fashion in the semi-implicit calculation, and at somewhat lower values in the nearly-implicit calculation. The increases in steam flow rate at 300 and 400 s cause the mixture level to rise into pipe volume 3 to levels of 0.56 ft and 2.24 ft, respectively, in the semi-implicit calculation, and at slightly higher levels in the nearly-implicit calculation.

After 500 s the mixture level rises into pipe volume 4. The level reached a steady value in the nearly-implicit calculation, but does not in the semi-implicit calculation, instead decreasing linearly as liquid is entrained into the vapor and pulled out of the outlet junction. This loss of liquid mass can be seen in Figure 3.5-6, where the total system mass begins to decrease after 500 s. At 600 s the steam flow rate begins to increase linearly, and the mixture level also increases until the flow becomes too turbulent for a mixture level to be sustained.

The semi-implicit and nearly-implicit results show reasonable behavior in the plots of mixture level. In the total system mass plot of Figure 3.5-6, it is seen that much more liquid is entrained out of the pipe with the semi-implicit advancement scheme until very high steam flows are present. The more gradual loss of

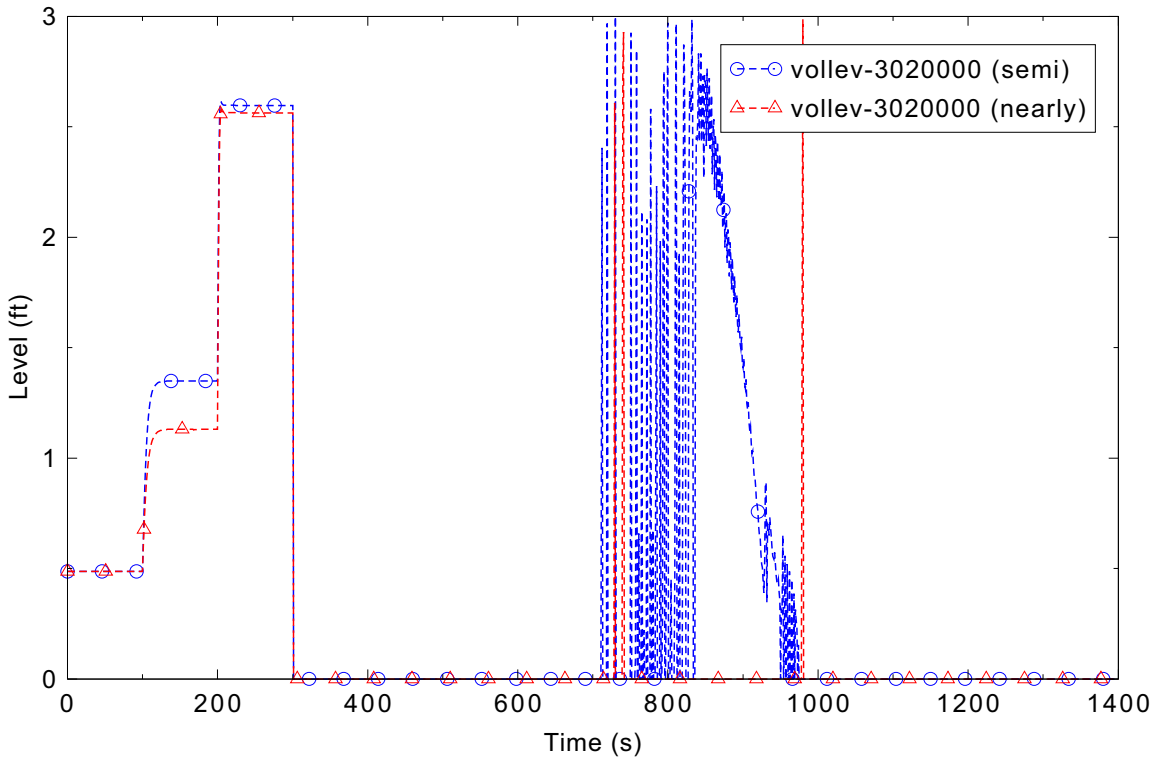

Figure 3.5-3. Mixture level in pipe volume 2 for the bubbling steam through liquid case.

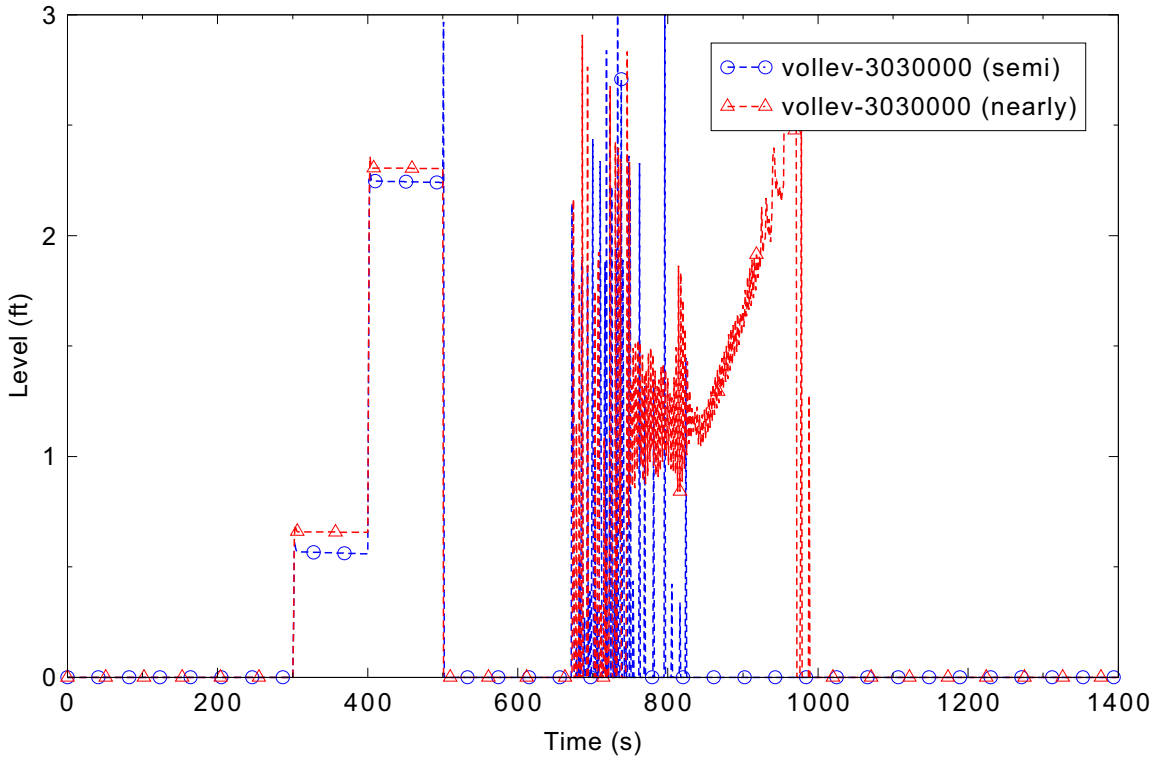

Figure 3.5-4. Mixture level in pipe volume 3 for the bubbling steam through liquid case.

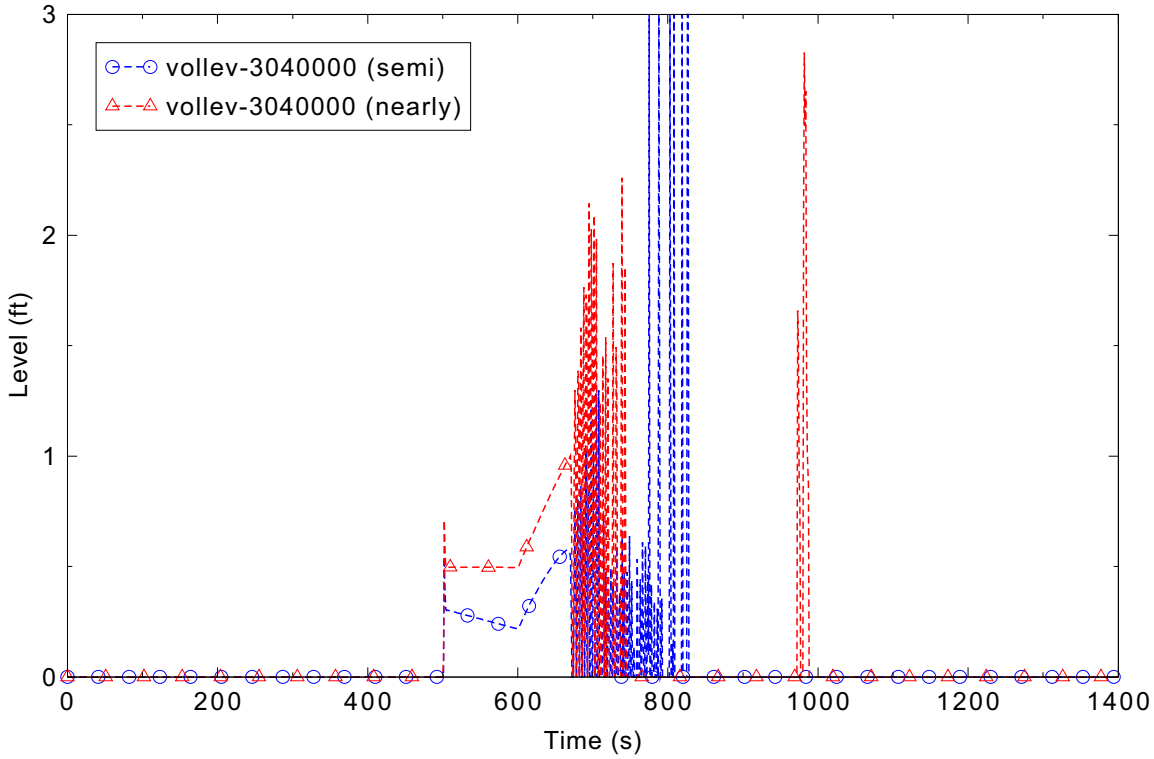

Figure 3.5-5. Mixture level in pipe volume 4 for the bubbling steam through liquid case.

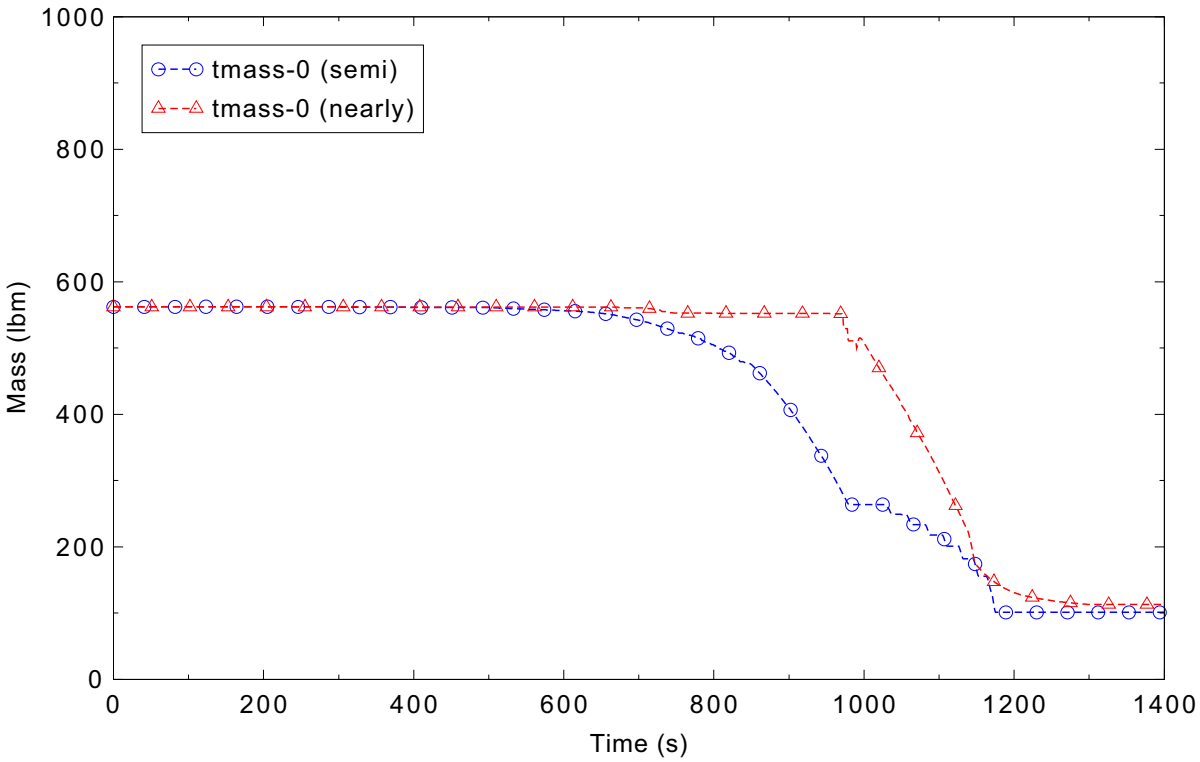

Figure 3.5-6. Total system mass for the bubbling steam through liquid case.

mass predicted using the semi-implicit method appears more reasonable, although there are no data with which to make definitive conclusions.

3.5.5 Conclusions and Assessment Findings

The RELAP5-3D mixture level results have been shown to qualitatively agree with the expected behavior. A series of steady mixture levels is established at lower steam mass flow rates, and an increasing loss of liquid due to entrainment occurs at higher steam flow rates as expected. The code performance is judged to be reasonable using the semi-implicit solution scheme. For the nearly-implicit method, the performance is reasonable except for the range from 800-1100 s, where the entrainment behavior appears suspect, resulting in an assessment judgment of minimal.

3.6 Manometer

The manometer problem is one of several simple problems that have been used to demonstrate qualitatively correct functioning of the code. In some cases the problems have been used to diagnose numerical problems that have been encountered during code development. The rationale for the selection of this particular manometer problem lies in the historical evolution of the code.

3.6.1 Code Models Assessed

The manometer problem is simulated to assess the calculation of the noncondensable state, the code momentum formulation for periodic flow, and the mixture level tracking model.

3.6.2 Problem Description

The analytical solution for the frictionless manometer behavior can be obtained from the governing equation derived by Moody,[3.6-1] page 589, Equation (10.6):

$$\frac{d^2X(t)}{dt^2} + \left(\frac{2g}{L}\right)X(t) = 0. \qquad (3.6\text{-}1)$$

In the equation above, X (t) represents the displacement of the liquid level from its equilibrium level as shown in Figure 3.6-1. The letters g and L stand for the gravitational acceleration and the length of the water column, respectively.

The displacement and liquid velocity are 0.0 m and -1.0 m/s at t = 0.0 s, respectively. The initial velocity of -1.0 m/s means that the liquid flows vertically upward in the left leg. The initial condition for the differential equation can be summarized as shown in Table 3.6-1.

Table 3.6-1. Initial conditions for differential equation of oscillation manometer.

Variable	Initial value
Displacement	X (0) = 0.0 m
Velocity	v (0) = -1.0 m/s

The general solution of the differential equation given in Equation (3.6-1) becomes

$$X(t) = C_1 \sin\left[\left(\sqrt{\frac{2g}{L}}\right)t\right] + C_2 \cos\left[\left(\sqrt{\frac{2g}{L}}\right)t\right]. \qquad (3.6\text{-}2)$$

From the initial condition for the displacement, X (0) = 0.0 m, C_2 becomes zero. The velocity can be obtained by differentiating Equation (3.6-2) with respect to time, and noting that C_2 is zero:

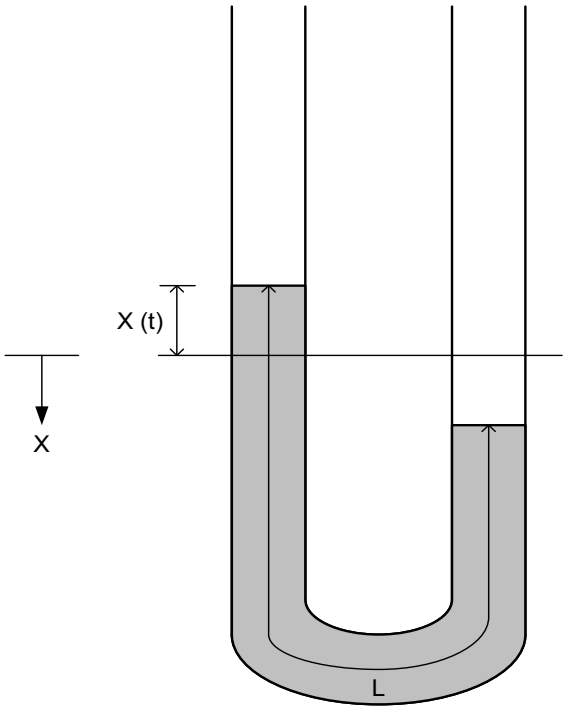

Figure 3.6-1. Schematic of oscillation manometer.

$$v(t) = \frac{dX(t)}{dt} = C_1\left(\sqrt{\frac{2g}{L}}\right)\cos\left[\left(\sqrt{\frac{2g}{L}}\right)t\right]. \quad (3.6\text{-}3)$$

From the initial condition for the velocity, V(0) = -1.0 m/s, the value of C_1 can be obtained as

$$C_1 = -\sqrt{\frac{L}{2g}}. \quad (3.6\text{-}4)$$

Therefore, the analytical solution for the displacement of the oscillation manometer becomes

$$X(t) = -\sqrt{\left(\frac{L}{2g}\right)}\sin\left[\left(\sqrt{\frac{2g}{L}}\right)t\right]. \quad (3.6\text{-}5)$$

The analytical solution for the liquid velocity is

$$v(t) = \frac{dX(t)}{dt} = -\cos\left[\left(\sqrt{\frac{2g}{L}}\right)t\right]. \quad (3.6\text{-}6)$$

From Moody's momentum equation for the right manometer leg, the pressure at the bottom of the leg is given by

$$p_B(t) = p_{atm} + \rho_f X(t)\left[g - \frac{d^2X(t)}{dt^2}\right] = p_{atm} + \rho_f X(t)\left\{g - \left(\sqrt{\frac{2g}{L}}\right)\sin\left[\left(\sqrt{\frac{2g}{L}}\right)t\right]\right\} \quad (3.6\text{-}7)$$

where p_B, p_{atm}, and ρ_f stand for the pressure at the bottom of the manometer, atmospheric pressure, and liquid density, respectively.

The length of the liquid column, L, and the atmospheric pressure, p_{atm}, are 10.0 m and 100,110.0 Pa in this simulation, and the gravitational acceleration, g, is 9.80665 m/s^2. Table 3.6-2 shows the final analytical equations for the liquid height, $h_1(t)$, liquid velocity, $v(t)$, and pressure at the bottom of the manometer, $p_B(t)$. In this table, $\left(\frac{2g}{L}\right) = 1.96133 s^{-2}$. Since the actual length of liquid column in the left leg decreases from its length at rest state (5.0 m in this simulation) when the displacement becomes positive in the coordinate shown in Figure 3.6-1, the analytical solution for the liquid column height in the left leg of the manometer is expressed as

Table 3.6-2. Analytical solutions for oscillation manometer.

Parameter	Analytical Equation
Liquid height (m)	$h(t) = 5.0 + \sqrt{0.50986}\sin[(\sqrt{1.96133})t]$
Velocity (m/s)	$v(t) = -\cos[(\sqrt{1.96133})t]$
Pressure (Pa)	$p_B(t) = 100, 110 + \rho_f[h_l(t) - 0.5](9.80665 - \{\sqrt{1.96133}\sin[(\sqrt{1.96133})t]\})$

$$h_l(t) = 5.0 - X(t) = 5.0 + \sqrt{\left(\frac{L}{2g}\right)}\sin\left[\left(\sqrt{\frac{2g}{L}}\right)t\right]. \quad (3.6\text{-}8)$$

In the equation for the pressure at the bottom of the manometer, the displacement should be replaced by the liquid column height from the center of subcell-10, h (t) - 0.5 m, as shown in the last row of Table 3.6-2. These equations are implemented into the RELAP5-3D input model using control variables.

3.6.3 Input Model Description

Figure 3.6-2 shows the nodalization diagram for the manometer problem input model. The manometer was modeled using a pipe component. Each volume had an area of 0.01 m^2 (0.108 ft^2) and a length of 1.0 m (3.2808 ft). The first 10 volumes were oriented vertically downward and the last 10 volumes were oriented vertically upward. A time-dependent volume and single junction were connected to both the pipe inlet and outlet. The bottom five volumes on the left side (777060000 to 777100000) and the bottom five volumes on the right side (777110000 to 777150000) were filled initially with water at 100.11 kPa (14.5 psi) and 323 K (122°F). The remaining volumes were initialized with dry nitrogen at the same pressure and temperature (including the time-dependent volumes). The wall friction flag was set to 1, to turn off wall friction effects, and the mixture level tracking model was turned on. An initial null problem was run to initialize the pressure gradient in the pipe component to a hydrostatic state. This pressure gradient was used as the initial condition for the transient. To initiate the oscillation, an initial velocity of -1.0 m/s was placed at each junction. A symmetry calculation was also done in which the initial velocity was +1.0 m/s. The expected behavior for this problem is that, without wall friction, the liquid will oscillate back and forth between the two vertical columns with a non-decaying maximum height. The frequency of oscillation is analytically predictable and can be used as a measure of the correctness of the code-calculated ratio of the body force to the inertia.

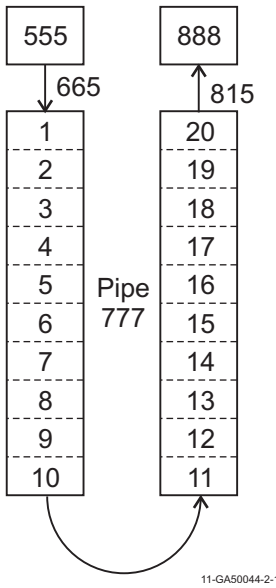

Figure 3.6-2. Nodalization diagram of nitrogen-water Manometer test input model.

A time step size of 0.01 s was used for both the semi-implicit and nearly-implicit advancement schemes.

3.6.4 Data Comparisons and Results

Figure 3.6-3 shows the comparison of the liquid level in the left leg calculated by RELAP5-3D using the semi-implicit numerical scheme with the analytical solution. Both the amplitude and the period of the liquid level oscillation predicted by RELAP5-3D show excellent agreement with the analytical solution.

The nearly-implicit calculation did not run, failing immediately with a Fortran error. This has been corrected in later versions of the code.

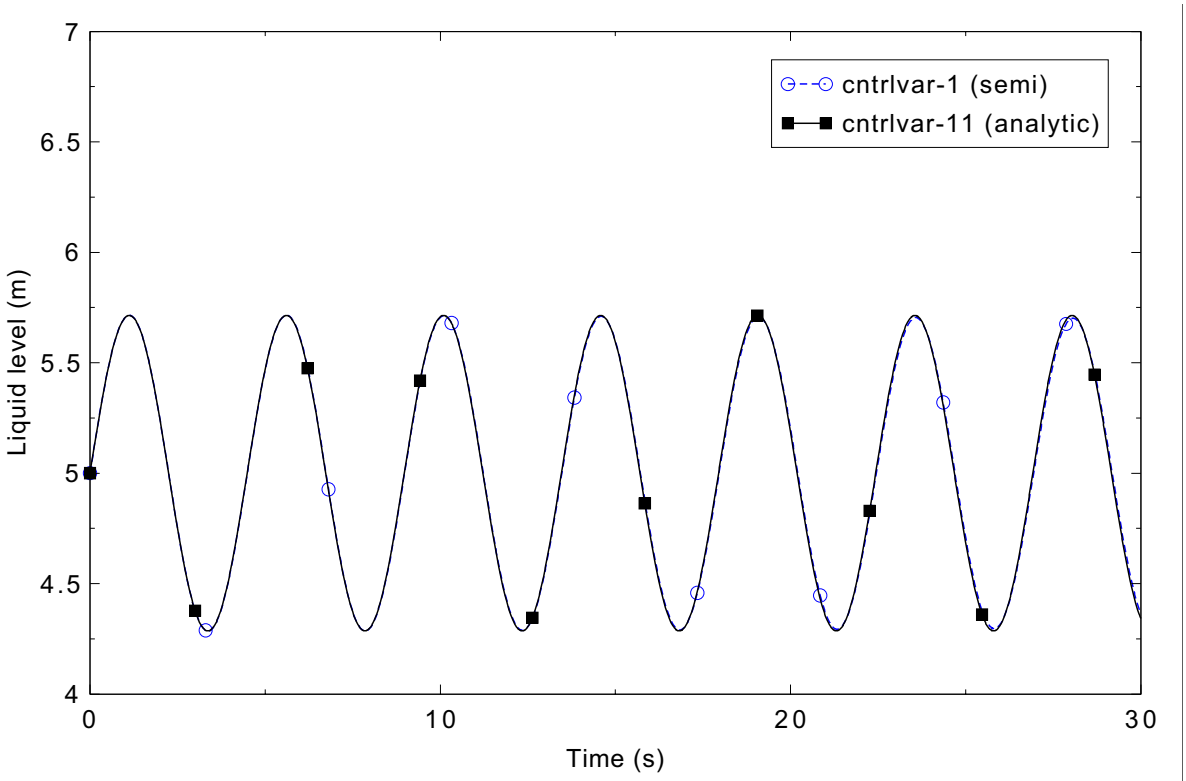

Figure 3.6-3. Comparison of water levels in the left leg for Manometer test.

Similar trends are observed in the comparisons of the predicted liquid velocity and manometer bottom pressure with the analytical solutions, as shown in Figures 3.6-4 and 3.6-5. The calculated amplitudes of the velocity and pressure oscillations are in excellent agreement with the analytical solutions.

In order to check symmetry with respect to the initial velocity, a calculation was made with the initial velocity set to +1.0 m/s instead of -1.0 m/s. For this case, the semi-implicit calculation failed immediately, while the nearly-implicit case ran. Figure 3.6-6 shows the comparison of the liquid level in the right leg calculated by RELAP5-3D with the analytical solution for this case. The period is decreasing, and the amplitude is damping out with the nearly-implicit solution scheme.

A sensitivity calculation was also performed with the mixture level tracking model turned off. Figure 3.6-7 shows the water level in the left leg for this case. The amplitude of the oscillation is only about 20% of the analytical solution, and the period is somewhat longer in the semi-implicit calculation; the nearly-implicit calculation is very over-damped. The theoretical period of the oscillation can be calculated as follows,

$$P = \frac{2\pi}{\sqrt{\left(\frac{2g}{L}\right)}} = \frac{2\pi}{\sqrt{\frac{2 \cdot 9.80665}{10.0}}} = 4.48647\text{s} \qquad (3.6\text{-}9)$$

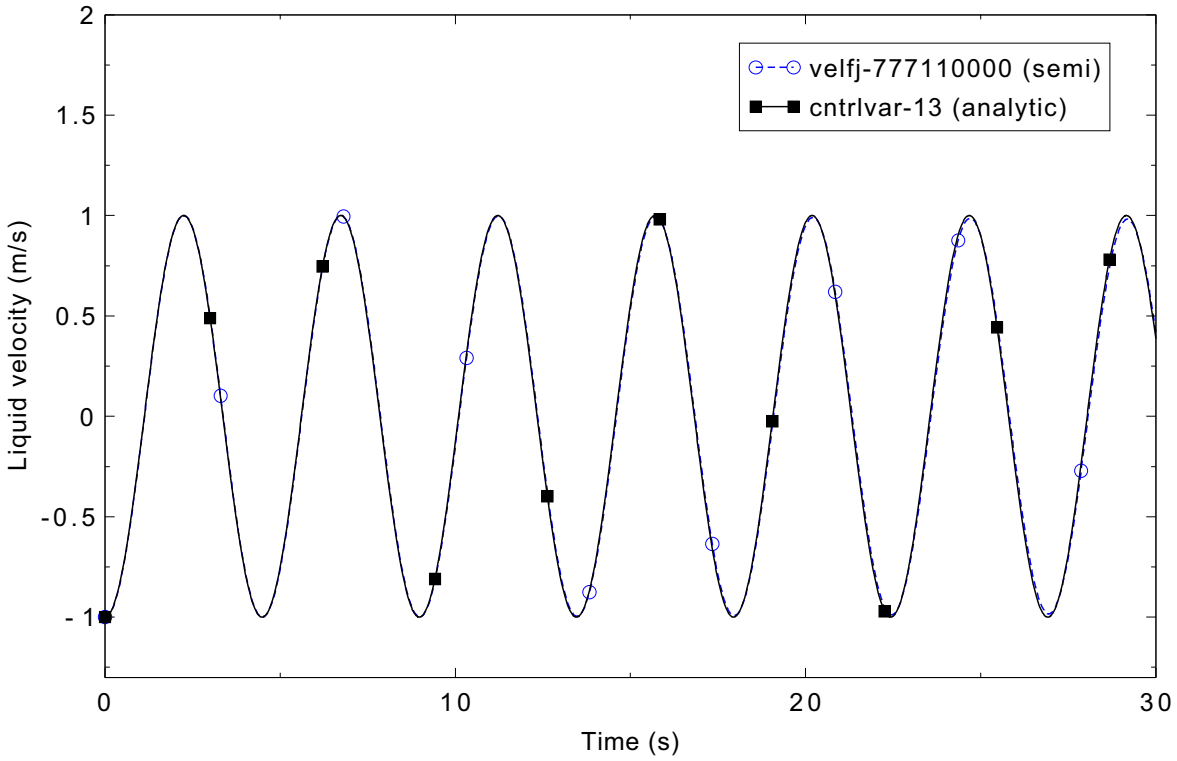

Figure 3.6-4. Comparison of liquid velocities for Manometer test.

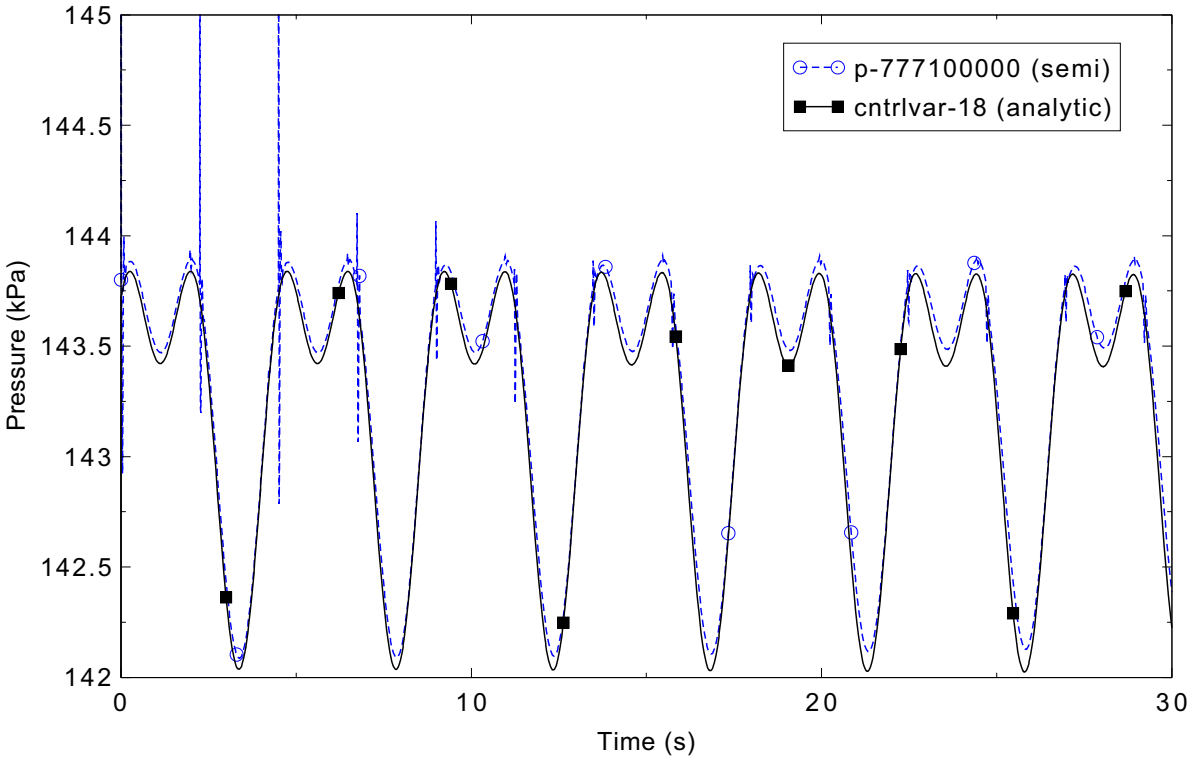

Figure 3.6-5. Comparison of bottom pressure for Manometer test.

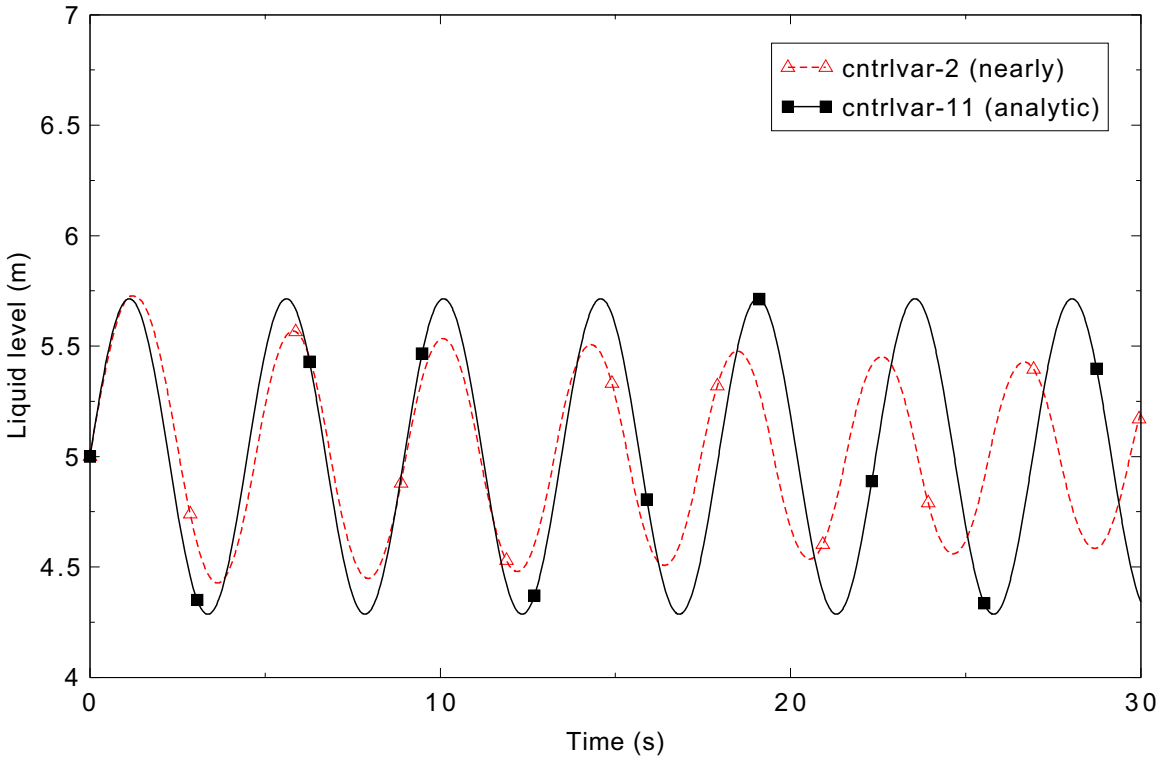

Figure 3.6-6. Comparison of water levels in the right leg for Manometer test.

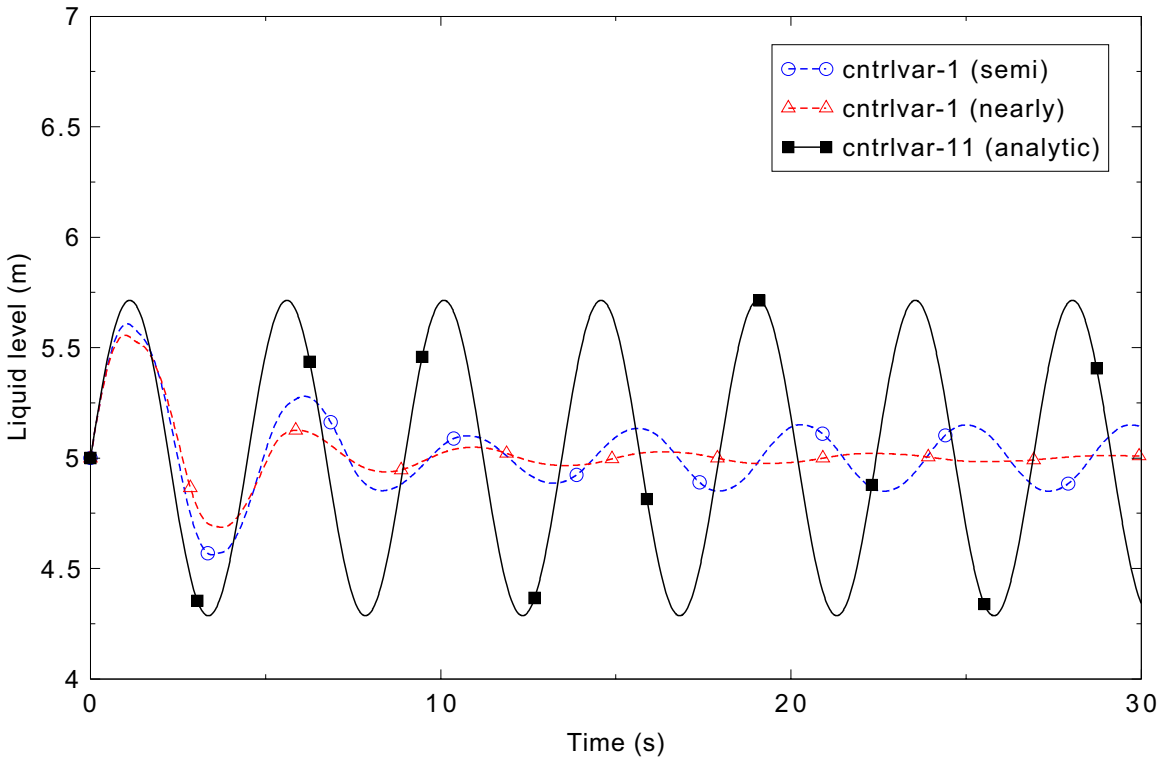

Figure 3.6-7. Comparison of water levels in the left leg for Manometer test without mixture level tracking.

The measured period from the RELAP5-3D calculation is 4.714 s, which is high by 5.07%. The semi-implicit simulation is judged to be in minimal agreement with the exact solution, and the nearly-implicit is judged to be insufficient.

3.6.5 Conclusions and Assessment Findings

Two code failures were encountered in trying to run the various manometer cases. With the flow initialized in reverse, the nearly-implicit calculation failed; with the initial flow positive, the semi-implicit calculation failed. (Both of these cases run successfully in later version of the code.) The semi-implicit simulation was compared with the analytical solutions and was found to be in excellent agreement when the mixture level tracking model was used, accurately predicting both the amplitude and period of the oscillating parameters. The nearly-implicit simulation was in minimal agreement because the oscillations were damping out. When the mixture level tracking model was not used, the semi-implicit code predictions were in minimal agreement with the analytic solution; the amplitude of the level oscillation was too small, and the period was too long. Without the mixture level tracking model, the nearly-implicit calculation was judged to be insufficient because the oscillations are nearly completely damped out.

3.6.6 References

3.6-1. F. J. Moody, *Introduction to Unsteady Thermofluid Mechanics*, John Wiley & Sons, New York, 1990.

3.7 Gravity Wave (1-D)

The gravity wave problem is a conceptual problem involving a horizontal pipe closed at both ends with a linearly graduated liquid level. Due to the gravitational head difference, the liquid tends to flow from the higher level side to the lower level side. The vapor is forced to flow in the opposite direction from the liquid. A countercurrent flow is developed.

3.7.1 Code Models Assessed

This problem was developed to assess the countercurrent flow model and to verify that the speed of propagation for a void wave is qualitatively correct.

3.7.2 Problem Description

The analytical solution for the wave speed in a one-dimensional horizontal circular pipe is presented by Chow[3.7-1] and is expressed as:

$$W = \left[\frac{(\theta - \sin\theta)gD}{8\sin(\theta/2)}\right]^{1/2} \tag{3.7-1}$$

where

g = the gravitational constant
D = the pipe diameter
$\theta = \pi$ radians for $\alpha = 0.5$.

Substituting in $\theta = \pi$ radians, gives:

$$W = \left(\frac{\pi}{8}gD\right)^{1/2} \tag{3.7-2}$$

3.7.3 Input Model Description

Figure 3.7-1 shows the RELAP5-3D nodalization diagram for this case. The pipe was modeled using 20 volumes and 19 junctions (total pipe length = 20 m, pipe flow area = 3.1416 m^2). The pipe is initially filled with a linearly distributed, two-phase, saturated, liquid/vapor mixture at a pressure of 10^7 Pa, and the void fraction varies from 0.47 to 0.53.

The gravity wave problem was performed with Card 1 Option 7 turned on (which sets the interfacial drag and virtual mass force terms to very small values). In addition, the wall friction was turned off (volume control flag f=1 of pipe component card CCC10XX). These conditions were necessary to match the assumptions of the wave equations above.

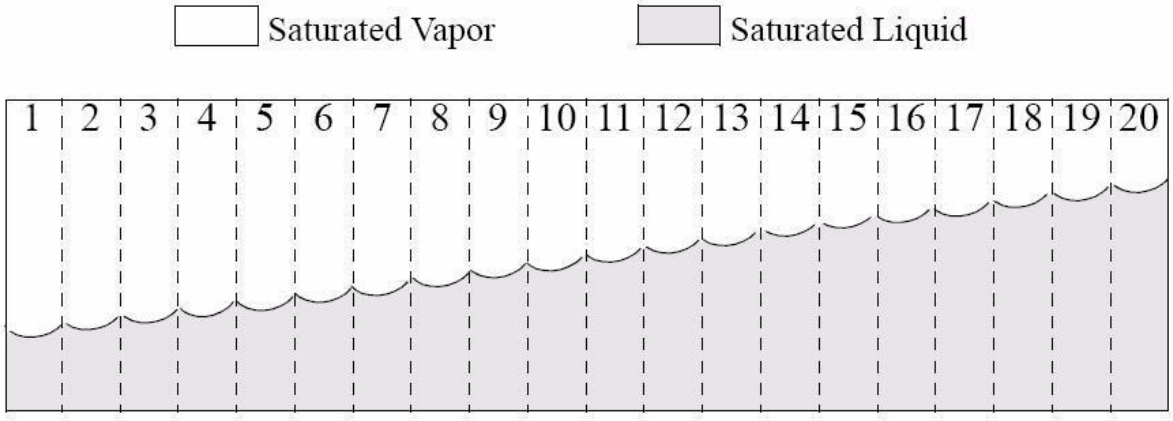

Figure 3.7-1. RELAP5-3D nodalization diagram for the 1-D gravity wave problem.

A second run of the gravity wave problem was performed with the same conditions except Card 1 Option 7 was turned off so that its effect could be evaluated.

3.7.4 Data Comparisons and Results

This problem was run with four time step cards. The first time step card ran to 0.01 s with a requested time step of 0.0001 s, the second time step card ran to 0.1 s with a requested time step of 0.001 s, the third time step card ran to 5.0 s with a requested time step of 0.01 s, and the last time step card ran to 100.0 s with a requested time step of 0.05 s.

The predicted liquid and vapor junction velocities at the middle of the pipe are shown in Figure 3.7-2 for the case with Card 1 Option 7 turned on and in Figure 3.7-3 for the case with Card 1 Option 7 turned off.

The results show that the semi-implicit solution begins to exhibit instability at around 55 s when Card 1 Option 7 is turned on. The nearly-implicit solution shows no instability in the velocity.

When Card 1 Option 7 is turned off for the semi-implicit case the instability in the velocity is not seen.

Based on the dimensions of the pipe, Equation (3.7-2) predicts a wave speed of 2.78 m/s. The RELAP5-3D calculation with Card 1 Option 7 turned on yielded a wave speed of 2.55 m/s, resulting in an 8% difference from the analytic solution, which suggests that there is still some numerical damping present. When Card 1 Option 7 is turned off, the RELAP5-3D calculation yielded a wave speed of 1.49 m/s, resulting in a 46% difference from the analytic solution. This case is lower because the interfacial friction and virtual mass terms inhibit the countercurrent flow.

3.7.5 Conclusions and Assessment Findings

The semi-implicit solution with Card 1 Option 7 turned on eventually exhibits unstable behavior, while the nearly-implicit solution did not. When Card 1 Option 7 is turned off there is no instability in the velocity solution. The code correctly represented a countercurrent flow for this problem as seen in the

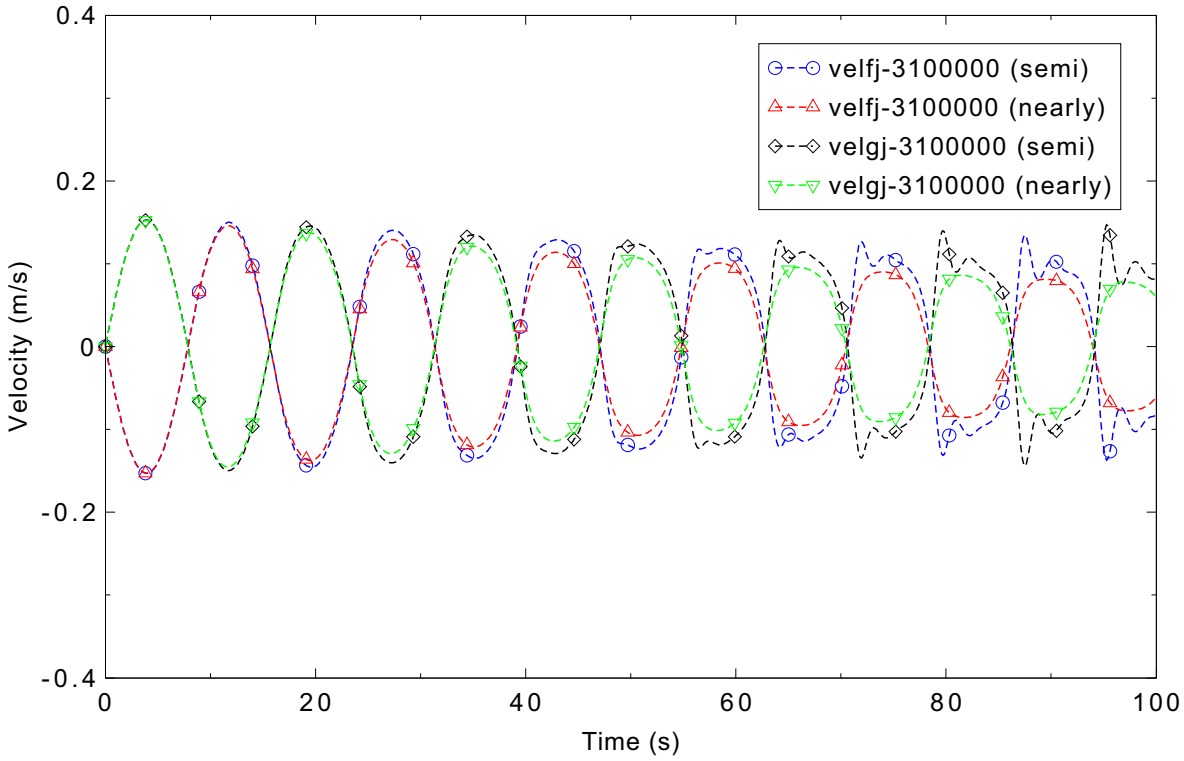

Figure 3.7-2. Calculated liquid and vapor velocities at mid-pipe, gravity wave 1-D, Card 1 Option 7 on.

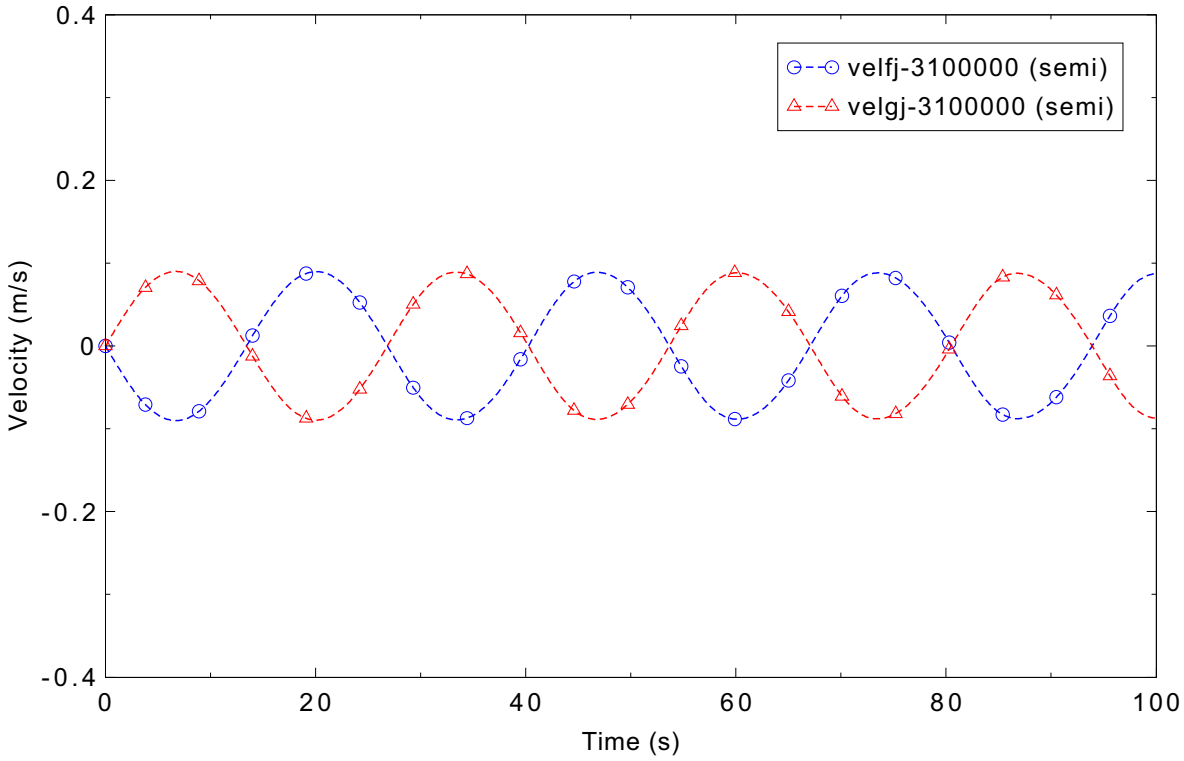

Figure 3.7-3. Calculated liquid and vapor velocities at mid-pipe, gravity wave 1-D, Card 1 Option 7 off.

oscillating wave pattern. The code-calculated the wave speed was 8% below the theoretical value of 2.78 m/s when Card 1 Option 7 is turned on. Overall, the code performance is judged to be reasonable.

3.7.6 References

3.7-1. V. T. Chow, *Open Channel Hydraulics*, McGraw-Hill, New York, NY, 1959.

3.8 Gravity Wave (3-D)

The gravity wave problem is a conceptual problem involving a horizontal rectangular duct closed at both ends with a linearly graduated liquid level. Due to the gravitational head difference, the liquid tends to flow from the higher level side to the lower level side. The vapor is forced to flow in the opposite direction from the liquid. A countercurrent flow is developed.

3.8.1 Code Models Assessed

This problem was developed to assess the countercurrent flow model, the multid component and to verify that the speed of propagation for a void wave is qualitatively correct.

3.8.2 Problem Description

The analytical solution for the wave speed in a one-dimensional horizontal square or rectangular duct case is presented by Chow[3.8-1] and is expressed as:

$$W = [(1-\alpha)gH]^{1/2} \tag{3.8-1}$$

where

α = the void fraction (0.5 for this case)
g = the gravitational constant
H = the cell height.

3.8.3 Input Model Description

Figure 3.8-1 shows the RELAP5-3D nodalization diagram. The 3-D rectangular duct was 30 m wide by 20 m long by 1 m deep. The model used 3 intervals in the x direction, 20 intervals in the y direction, and 1 interval in the z direction. This resulted in a model of 60 volumes and 97 junctions. The internal void fraction was linearly varied (in the y direction) from 0.47 to 0.53.

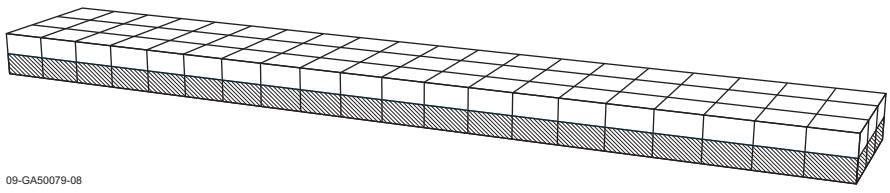

Figure 3.8-1. RELAP5-3D nodalization diagram for the 3-D gravity wave problem.

The gravity wave problem was performed with Card 1 Option 7 turned on (which sets the interfacial drag and virtual mass force terms to very small values). In addition, the wall friction was turned off

(volume control flag f=1 of multi-dimensional component card CCC1NNN). These conditions were necessary to match the assumptions of the wave equation above.

A second run of the gravity wave problem was performed with the same conditions except Card 1 Option 7 was turned off so that its effect could be evaluated.

3.8.4 Data Comparisons and Results

This problem was run with a requested time step of 0.05 s.

The predicted liquid and vapor junction velocities at the middle of the rectangular duct for the three x-intervals are shown in Figures 3.8-2 through 3.8-4 for the case with Card 1 Option 7 turned on and in Figures 3.8-5 through 3.8-7 for the case with Card 1 Option 7 turned off.

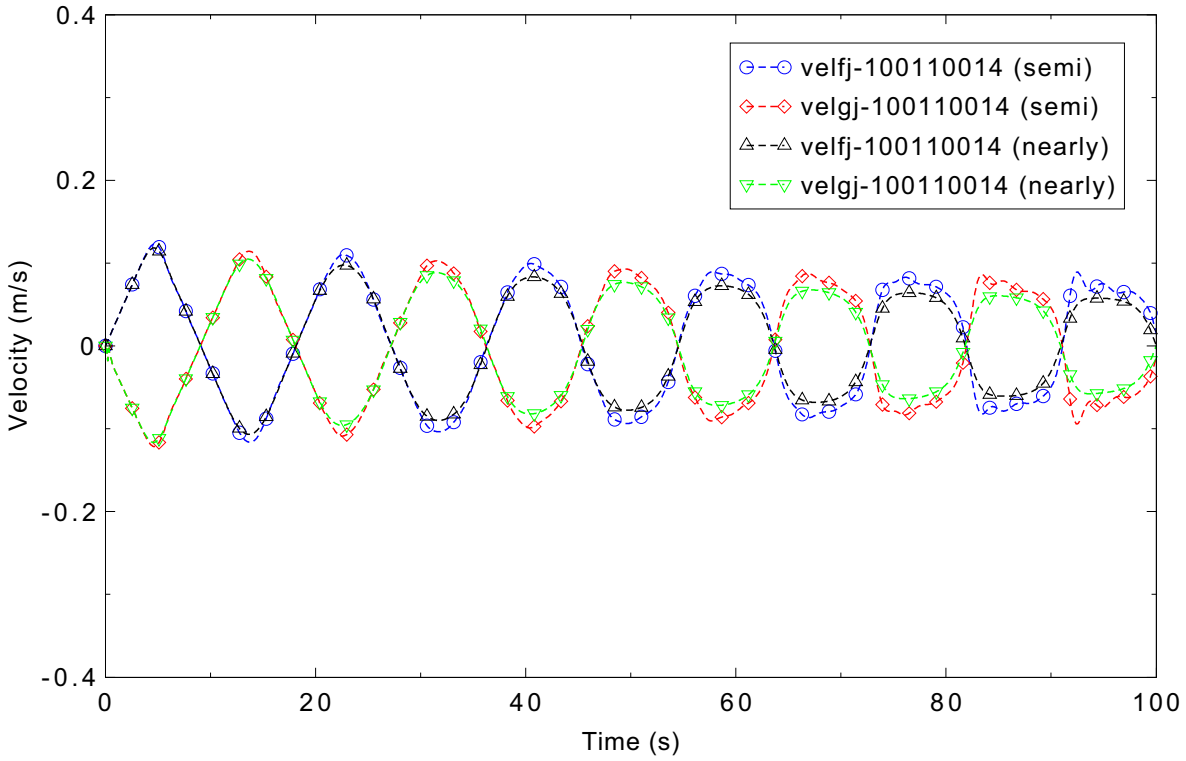

Figure 3.8-2. Calculated liquid and vapor velocities mid-duct, x-interval 1, gravity wave 3-D, Card 1 Option 7 on.

The results show that the semi-implicit solution begins to exhibit instability at around 55 s when Card 1 Option 7 is turned on. The nearly-implicit solution shows no instability in the velocity. Figures 3.8-2 through 3.8-4 show that the velocity solution is the same for each of the three x-intervals. This is because wall friction effects are turned off.

When Card 1 Option 7 is turned off for the semi-implicit case the instability in the velocity is not seen. The decreasing amplitude of the velocity can be attributed to the drag effects from the neighboring cells.

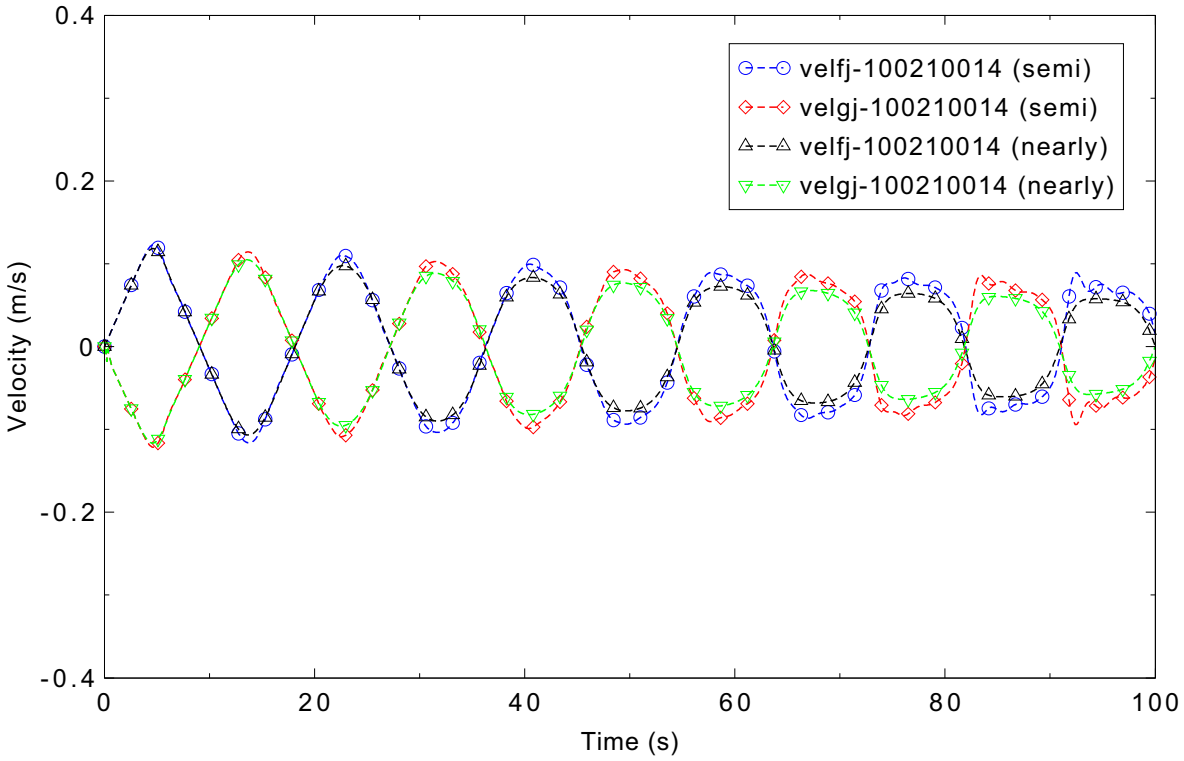

Figure 3.8-3. Calculated liquid and vapor velocities mid-duct, x-interval 2, gravity wave 3-D, Card 1 Option 7 on.

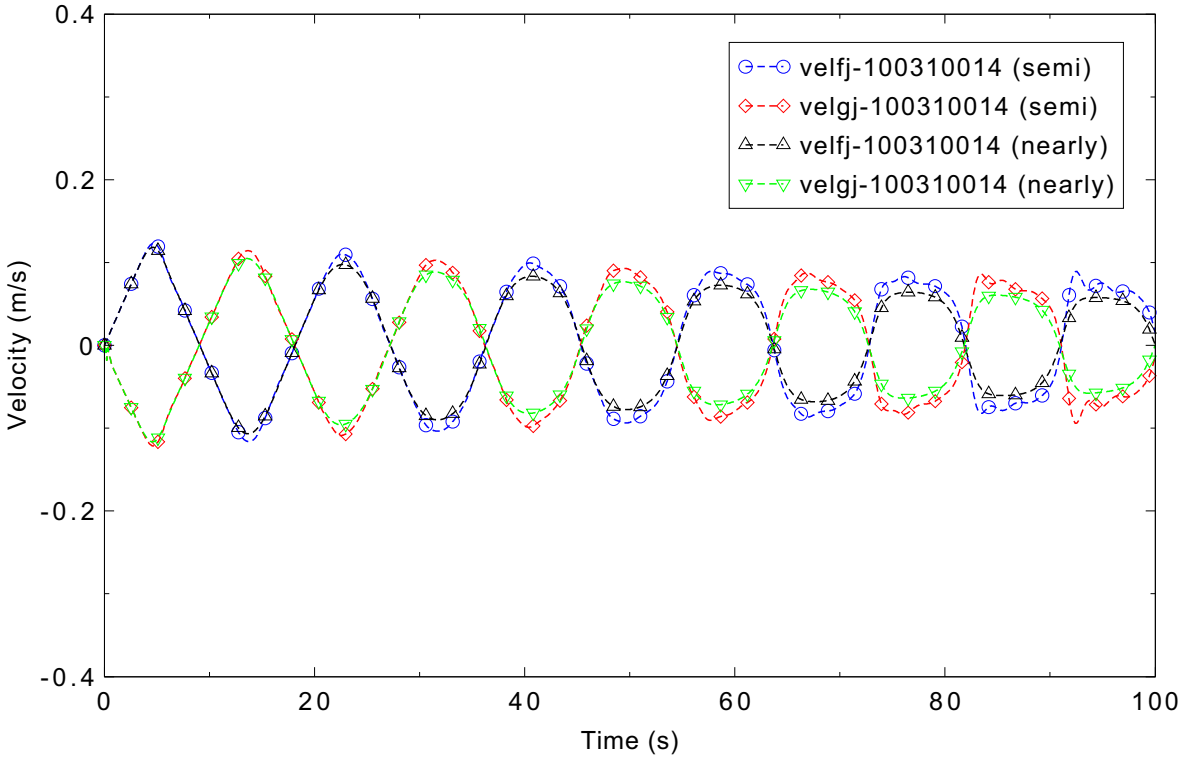

Figure 3.8-4. Calculated liquid and vapor velocities mid-duct, x-interval 3, gravity wave 3-D, Card 1 Option 7 on.

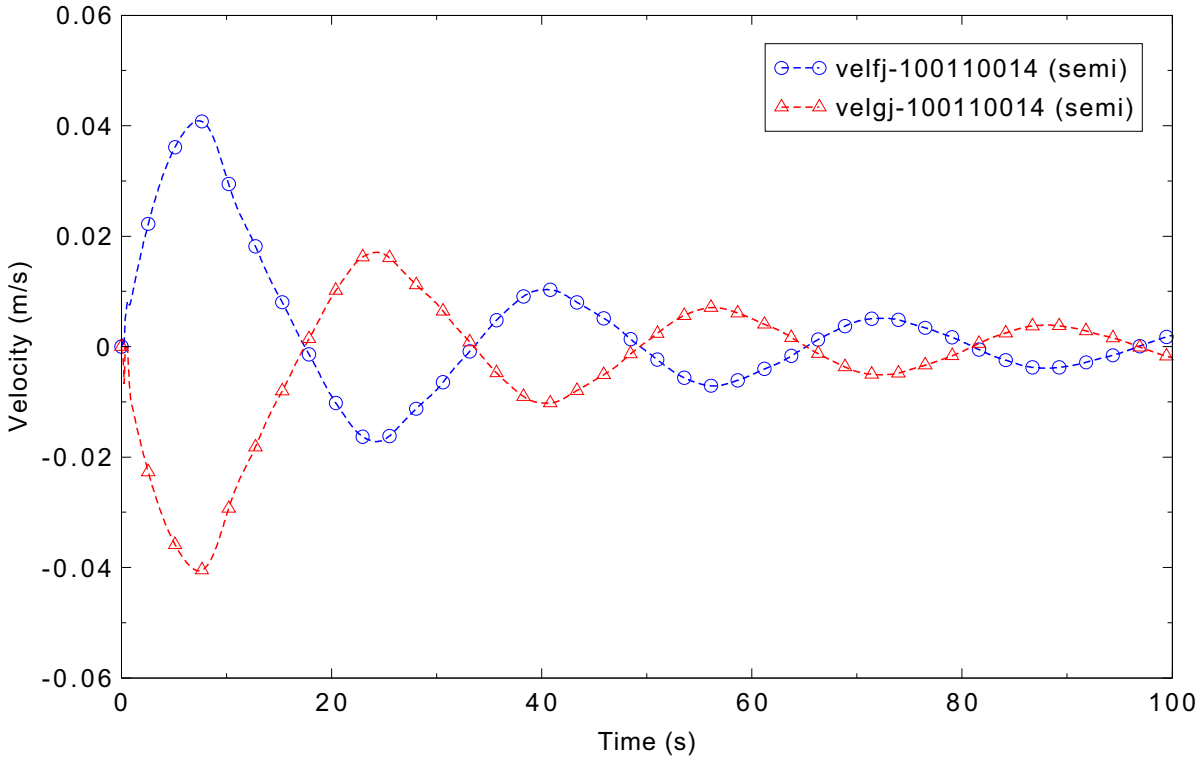

Figure 3.8-5. Calculated liquid and vapor velocities mid-duct, x-interval 1, gravity wave 3-D, Card 1 Option 7 off.

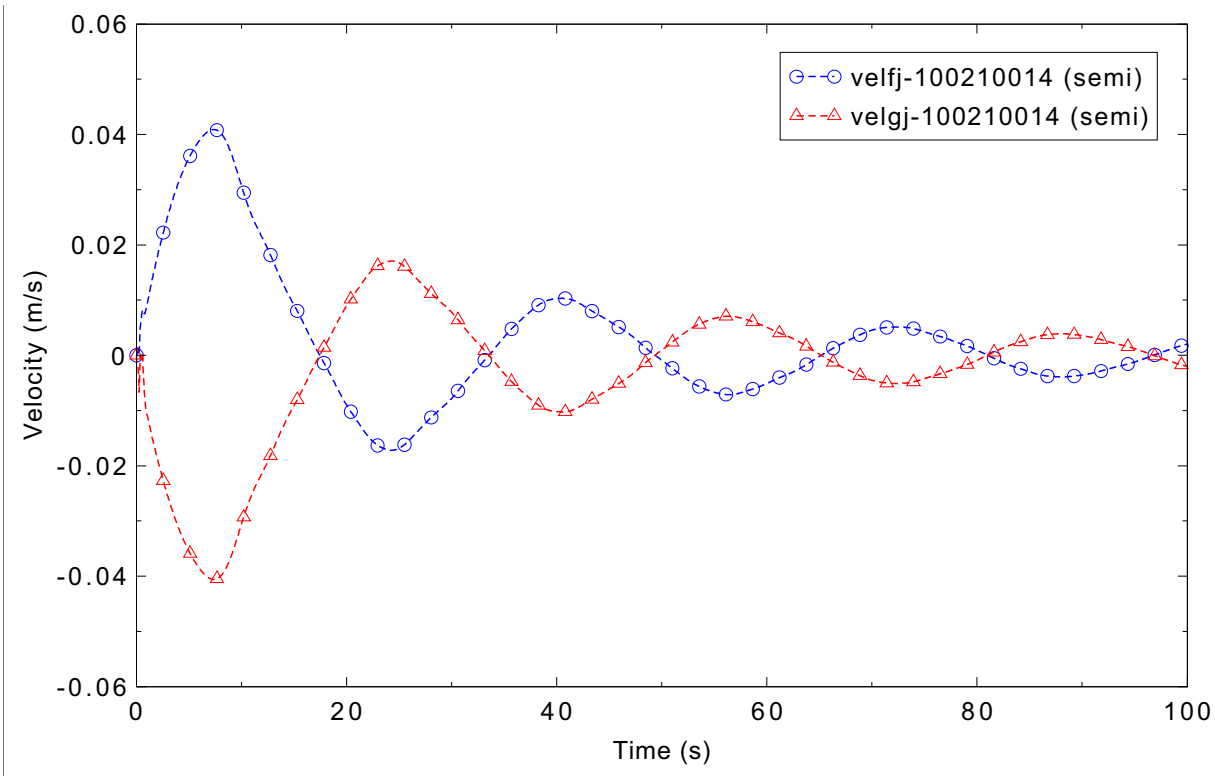

Figure 3.8-6. Calculated liquid and vapor velocities mid-duct, x-interval 2, gravity wave 3-D, Card 1 Option 7 off.

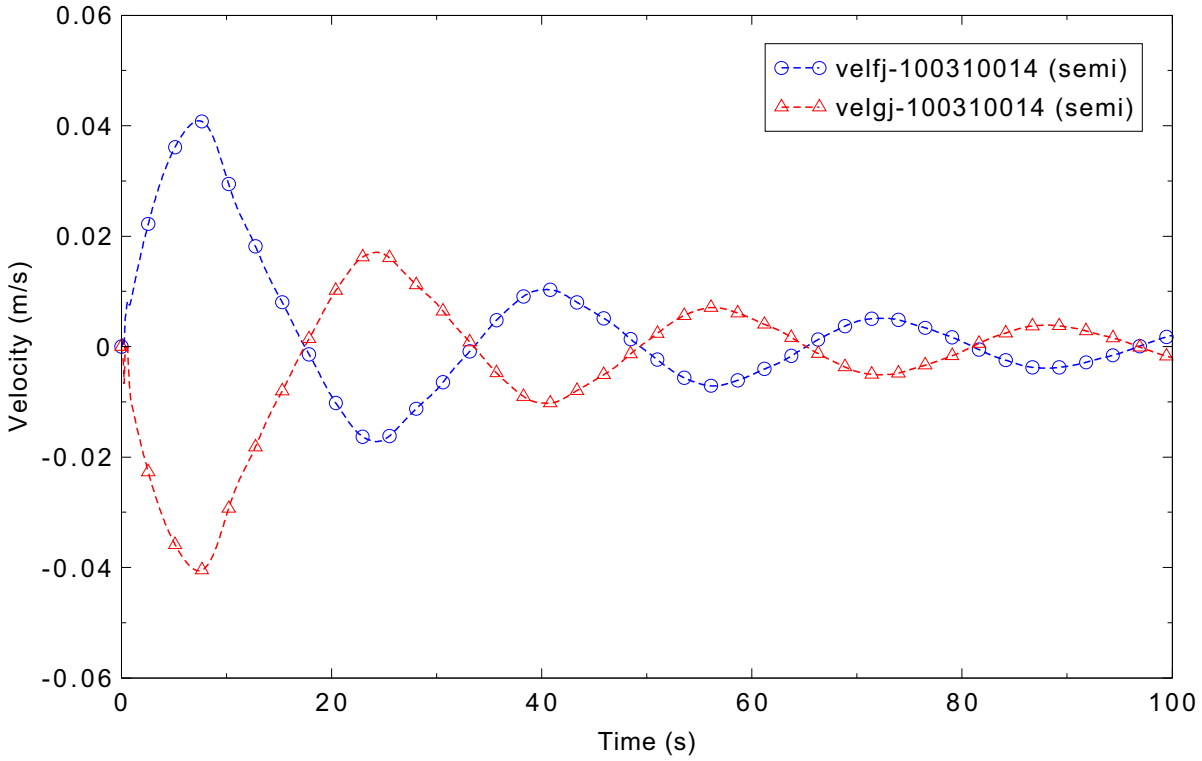

Figure 3.8-7. Calculated liquid and vapor velocities mid-duct, x-interval 3, gravity wave 3-D, Card 1 Option 7 off.

Figures 3.8-5 through 3.8-7 show that the velocity solution is the same for each of the three x-intervals. This is because wall friction effects are turned off.

Based on the dimensions of the rectangular duct, Equation (3.8-1) predicts a wave speed of 2.21 m/s. The RELAP5-3D calculation with Card 1 Option 7 turned on yielded a wave speed of 2.23 m/s, resulting in a less than 1% difference from the analytic solution. When Card 1 Option 7 is turned off, the RELAP5-3D calculation yielded a wave speed of 1.21 m/s, resulting in a 45% difference from the analytic solution. This case is lower because the interfacial friction and virtual mass terms inhibit the counter-current flow.

3.8.5 Conclusions and Assessment Findings

The semi-implicit solution with Card 1 Option 7 turned on eventually exhibits unstable behavior, while the nearly-implicit solution did not. When Card 1 Option 7 is turned off there is no instability in the velocity solution. There is no difference in the velocity solution in the x direction. The code correctly represented a countercurrent flow for this problem as seen in the oscillating wave pattern. The code calculated the wave speed very well when the Card 1 Option 7 is turned on. Overall, the code performance is judged to be reasonable.

3.8.6 References

3.8-1. V. T. Chow, *Open Channel Hydraulics*, McGraw-Hill, New York, NY, 1959.

3.9 Pryor Pressure Comparison

The Pryor pressure comparison problem is an assessment problem for checking the water packing problem which occurs in a finite difference scheme. Water packing occurs in finite difference schemes like that used in RELAP5-3D as a result of adding a relatively incompressible fluid like water to a volume in the explicit part of a time step, subroutine VEXPLT, using the old-time pressure difference across the junction. It the amount of water is excessive as a result of using a large time step, the volume is over filled (water packed) and in the next time step, the pressure in the water packed volume increases dramatically and pushes the water back out in the next time step. Ideally, the code should limit the amount of water added to the volume so that the pressure does not spike.

3.9.1 Code Models Assessed

The Pryor pressure test problem assesses the water packing phenomenon in a horizontal pipe. The code's special model for mitigating water packing is only applied in vertical volumes.

3.9.2 Problem Description

A horizontal pipe is initially filled with slightly superheated steam. Subcooled liquid is added to one end of the pipe, forcing the steam out the other end. The liquid flow rate is high enough that horizontal stratified flow does not occur. The water packing performance is evaluated as successive control volumes fill with liquid.

3.9.3 Input Model Description

The Pryor pressure test problem consists of a 20-volume pipe with water injection at one end as shown in Figure 3.9-1. The pipe is filled with slightly superheated vapor at a pressure of 0.4 MPa and a temperature of 418.2 K. The saturation temperature at 0.4 MPa is 416.77 K. Water at 353 K is added through time-dependent junction 105. The injection velocity starts at 0.0 and ramps up to 2 m/s at 0.5 s. The injection rate after 0.5 s is held constant at 2 m/s until the end of the run at 10 s.

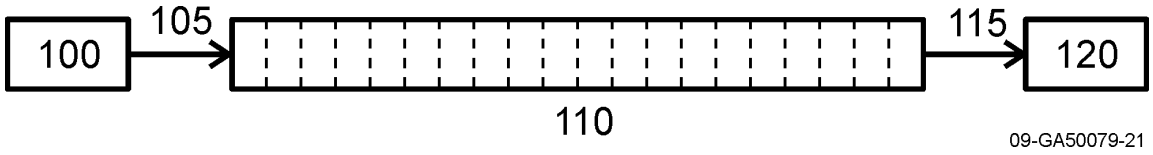

Figure 3.9-1. Nodalization diagram for the Pryor pressure test problem.

3.9.4 Data Comparisons and Results

Comparisons were made of the void fraction in volumes 4, 8, 12, 16 and 20 and the pressure in volume 1 of Pipe 110. Figures 3.9-2 and 3.9-3 show the calculated void fractions in volumes 4, 8, 12, 16 and 20 for the semi-implicit and nearly-implicit cases, respectively. Both advancement schemes yield similar results, including an increase in void fraction in the last volume when the volume is nearly full of liquid, although it was sharper and larger in the semi-implicit calculation. This is caused by a flow reversal

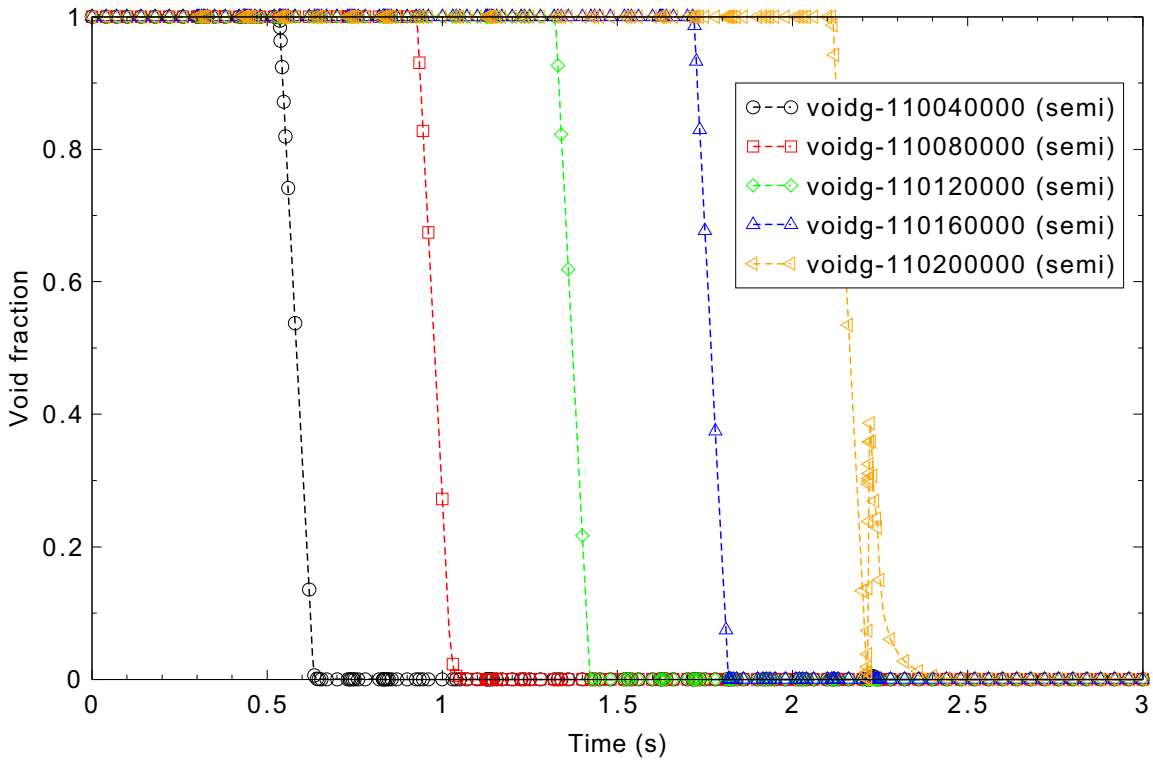

Figure 3.9-2. Void fraction for Pryor pressure test, semi-implicit case with maximum dt = 0.02 s.

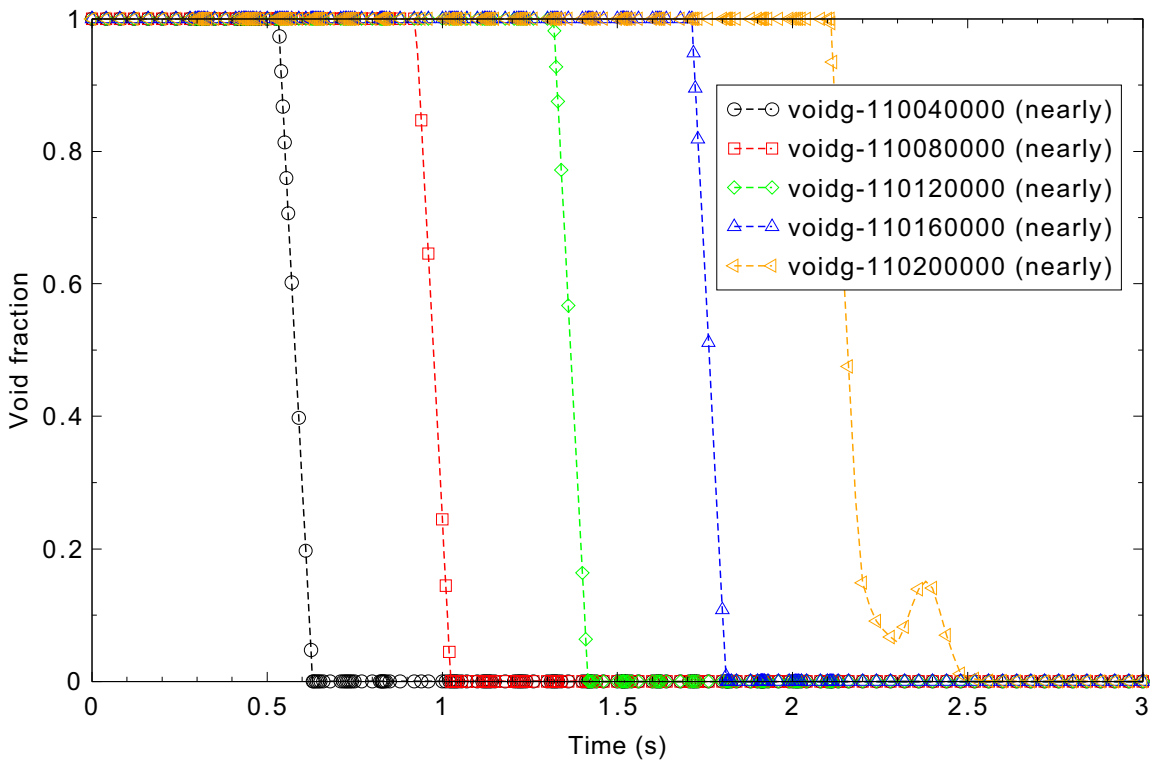

Figure 3.9-3. Void fraction for Pryor pressure test, nearly-implicit case with maximum dt = 0.02 s.

in the last volume which resulted from the volume pressure dropping below the outlet pressure during the water-packing spike.

The pressure response in volume 1 of Pipe 110 is shown in Figures 3.9-4 and 3.9-5 for the semi-implicit and nearly-implicit cases, respectively. Spikes occur in both calculations when each volume fills with liquid. For the semi-implicit case, there was a large difference in the magnitude of the spikes, while the magnitudes were more uniform in the nearly-implicit case. The pressure spikes occur because the code computes over-condensation of the vapor when the volume is nearly full of liquid. The code attempts to account for this by halving the time step size and trying to get through the water pack slowly. This can be seen in the plot of time step size in Figure 3.9-6 (shown only for the semi-implicit case).

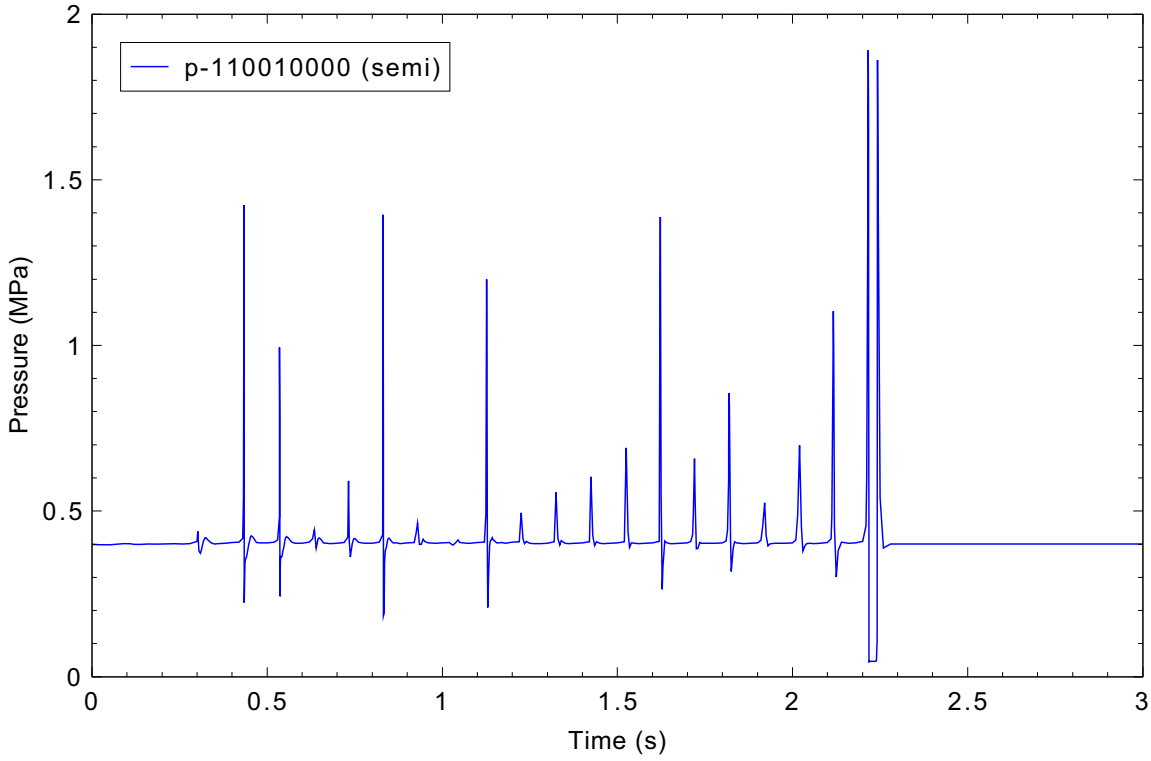

Figure 3.9-4. Volume 1 pressure for Pryor pressure test, semi-implicit case with maximum dt = 0.02 s.

In general, a smaller time step size works well in reducing the magnitude of the pressure spikes during water-packing events. To illustrate this, a separate case was run which fixed the maximum time step size at 0.0001 s for the semi-implicit case. Plots of void fraction and pressure are shown in Figures 3.9-7 and 3.9-8, respectively. The last volume in the pipe does not fill with liquid, as the flow regime was horizontally stratified, allowing the liquid to flow out while still maintaining some steam in the volume. As can be seen in the pressure plot of Figure 3.9-8, most of the spikes are gone with the smaller time step size, although there is a noticeable oscillation in the calculated response.

For most reasonable problems, it is impractical to run at such a small time step size. However, as was shown in Figure 3.9-4, running with a larger time step size and simply cutting the time step in the presence of over-condensation is not sufficient to reduce the magnitude of the pressure spikes. This is due to the use of old-time and new-time weighting of the interfacial heat transfer variables (hif, hig, and hgf) in the code.

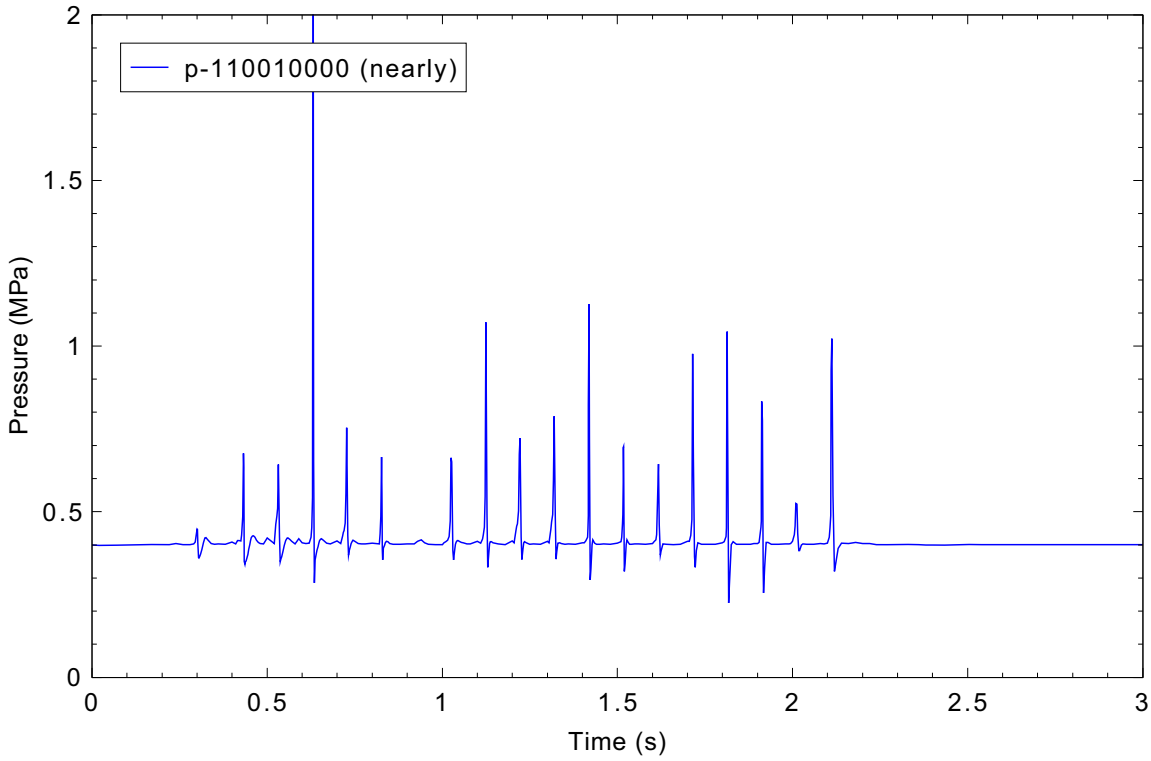

Figure 3.9-5. Volume 1 pressure for Pryor pressure test, nearly-implicit case with maximum dt = 0.02 s.

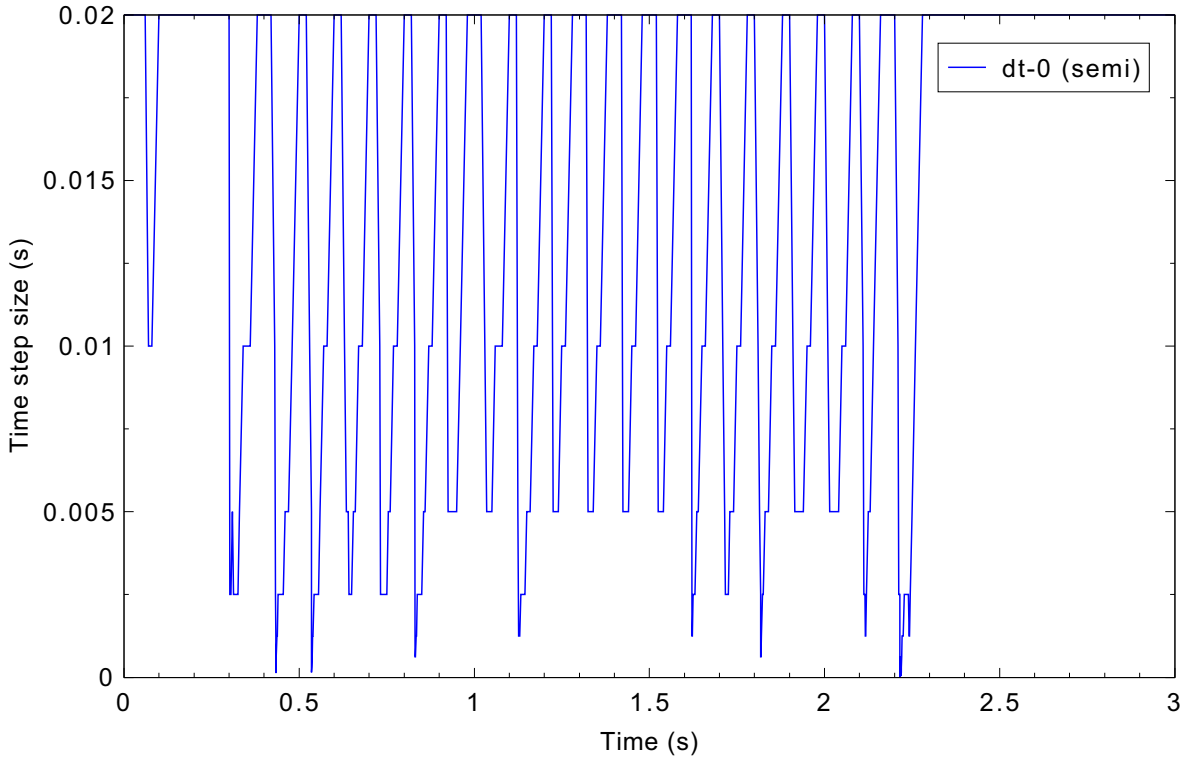

Figure 3.9-6. Time step size for Pryor pressure test, semi-implicit case with maximum dt = 0.02 s.

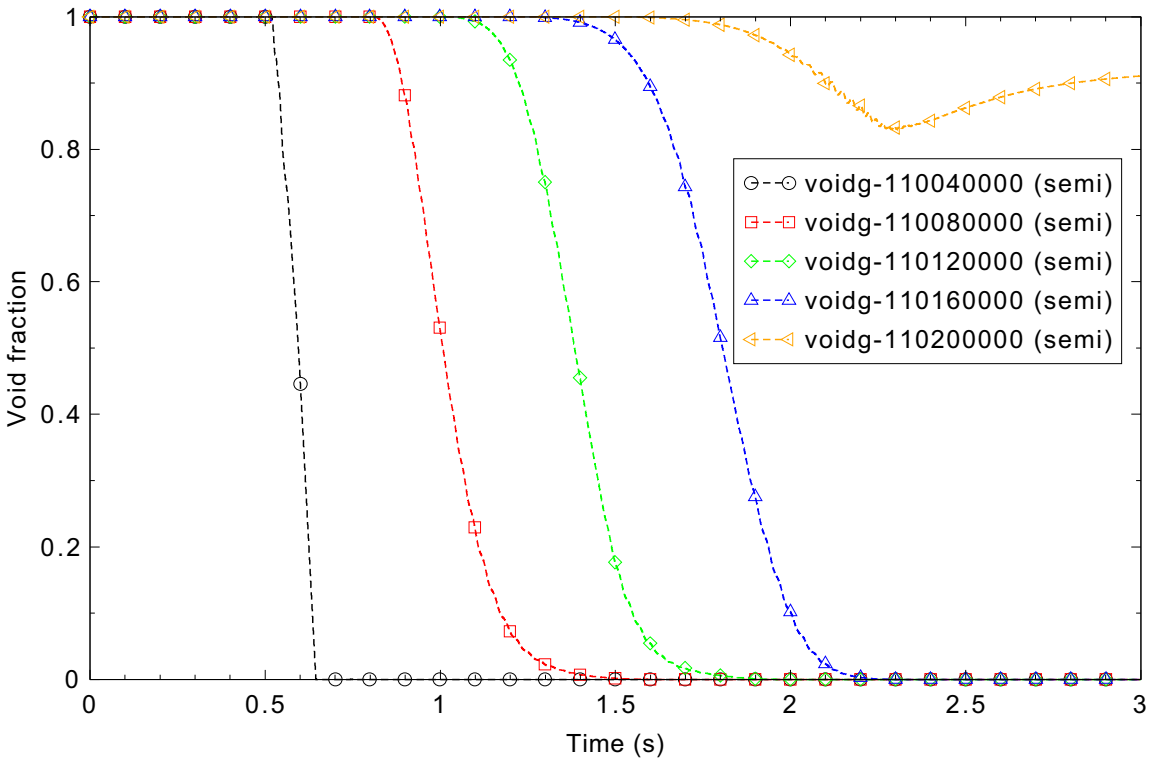

Figure 3.9-7. Void fraction for Pryor pressure test, semi-implicit case with maximum dt = 10^{-4} s.

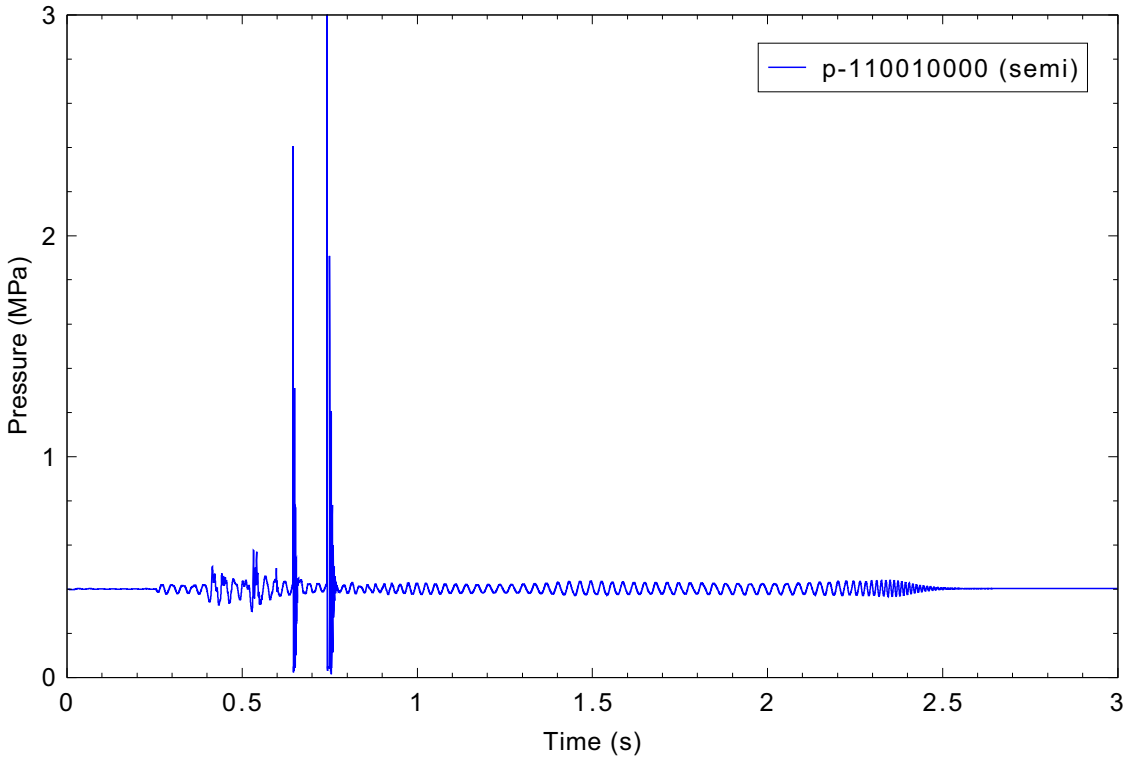

Figure 3.9-8. Volume 1 pressure for Pryor pressure test, semi-implicit case with maximum dt = 10^{-4} s.

As the time step size decreases, the code weights the old-time value more, which increases the final values of hif, hig, and hgf, resulting in still more over-condensation. One suggested technique to address this problem would be to reduce the old time values of hif, hig, and hgf by a factor of ten when over-condensation occurs.

3.9.5 Conclusions and Assessment Findings

For the Pryor pressure test problem, the code is found to generate reasonable results. Pressure spikes were observed for both the semi-implicit and nearly-implicit advancement schemes due to the presence of over-condensation and the resulting water-packing of the volumes. However, it bears mentioning that the code did in fact complete the execution in spite of the pressure spikes.

A suggested work-around for the code to handle the over-condensation problem, which causes the pressure spikes, would be to reduce the old-time weighting of the interfacial heat transfer by a factor of ten. Currently, the code cuts the time step in half when over-condensation occurs, but this does not solve the problem because the code weights the old-time interfacial heat transfer more as the time step size decreases. So, as the time step size decreases, the over-condensation actually becomes worse. Therefore, reducing the old-time weighting of the interfacial heat transfer should be effective in reducing the over-condensation and thereby minimizing the pressure spikes observed in the calculation.

3.10 Core Power

The core power assessment problems are a set of three reactor kinetics test problems for the decay heat models in RELAP5-3D.

3.10.1 Code Models Assessed

The core power problems assess the ANS-79 fission product and actinide decay heat models.

3.10.2 Problem Description

The three test problem models are essentially the same; they model the decay heat from the time the reactor is shutdown out to 100,000 s. They all use the ANS79-1 option, which uses the 1979 ANSI/ANS (ANS-79) Standard.[3.10-1]

3.10.3 Input Model Description

The input for these models is part of the reactor kinetics input, primarily cards 30000001 and 30000002. A minimal hydrodynamic model is used to support the decay power calculation, consisting of a two-volume pipe.

There are three options for the fission product decay type on the 30000001 card:

- NO-GAMMA for no fission product decay calculation,
- GAMMA for standard fission product decay calculation, and
- GAMMA-AC for standard fission product decay plus actinide decay calculations.

The ans79.i and ans79G.i test problems use GAMMA and the ans79ac.i test problem uses GAMMA-AC.

The 30000001 card can also include three additional words (7-9) to input data for computing the G factor as part of the decay heat, as in the ans79G.i input deck. The G factor is a correction factor to the energy from fission product decay to account for the effects of neutron absorption. It can be set via a built-in table that came from the ANS-79 standard or computed using the formula given below:

$$G(t) = 1.0 + (3.24\text{x}10^{-6} + 5.23\text{x}10^{-10}t)T^{0.4}\psi_g \qquad (3.10\text{-}1)$$

where T = the reactor operating time including any periods of shutdown ($T < 1.2614\text{x}10^{8}$ s)

ψ_g = number of fissions per initial fissile atom ($1.0 \le \psi_g \le 3.0$)

t = time since shutdown ($t < 10^{4}$ s)

The corrected decay power is then given by

$$P_\gamma = G(t)P_\gamma' \qquad (3.10\text{-}2)$$

where P_γ' = uncorrected decay power

P_γ = corrected decay power

These three additional words in the ans79G.i test problem on the 30000001 card are -1.0, 1.0E+8, and "sec". The first word is for entering ψ_g, but since it is negative, this signals the code to use the built in table values instead of using the formula in Eq. 3.10-1. The second word is for entering T, and the third word is for the units of T. So the ans79G.i test problem does not use the formula in Eq. 3.10-1.

The actinide decay model describes the production of ^{239}U, ^{239}Np, and ^{239}Pu from neutron capture by ^{238}U. This model is used in the ans79ac.i test problem, which has GAMMA-AC on card 30000001.

All three test problems enter ANS79-1 as word 1 on the 30000002 card. Table 3.10-1 shows the options available for the decay heat models on the 30000002 card. An x in a cell means that the word is not entered, and the x(23) in a cell means that the number of groups defaults to 23.

Table 3.10-1. Reactor kinetics card 30000002 input options.

Word	Reactor Kinetics Card 300000002						
1	ANS73	ANS79-1	ANS79-3		ANS94-1	ANS94-4	
2	MeV/fission						
3	x	x	^{235}U power fraction		x	^{235}U power fraction	
4	x	x	^{238}U power fraction		x	^{238}U power fraction	
5	x	x	^{239}Pu power fraction		x	^{239}Pu power fraction	
6	x	x	x(23)	# ^{235}U groups	x	^{241}Pu power fraction	
7	x	x	x(23)	# ^{238}U groups	x	x(23)	# ^{235}U groups
8	x	x	x(23)	# ^{239}Pu groups	x	x(23)	# ^{238}U groups
9	x	x	x	x	x	x(23)	# ^{239}Pu groups
10	x	x	x	x	x	x(23)	# ^{241}Pu groups

The time step size increased from 0.1 s to 1000.0 s over the course of the 100,000-s transient for both the semi-implicit and nearly-implicit advancement schemes.

3.10.4 Data Comparisons and Results

Three data sets were used to compare with the three test problems that used the semi-implicit and the nearly-implicit advancement schemes. In all these comparisons, control variable 3 (cntrlvar-3) is the normalized decay heat power (rkgapow) multiplied by 200 MeV/fission so that it can be compared with Table 4 (page 12) of the ANS-79 Standard.[3.10-1]

Figures 3.10-1, 3.10-2, and 3.10-3 show the decay heat comparisons for the ans79.i, ans79ac.i, and ans79G.i test problems, respectively. All of the calculations are in excellent agreement with the reference data; there was no discernible difference between the semi-implicit and nearly-implicit calculations.

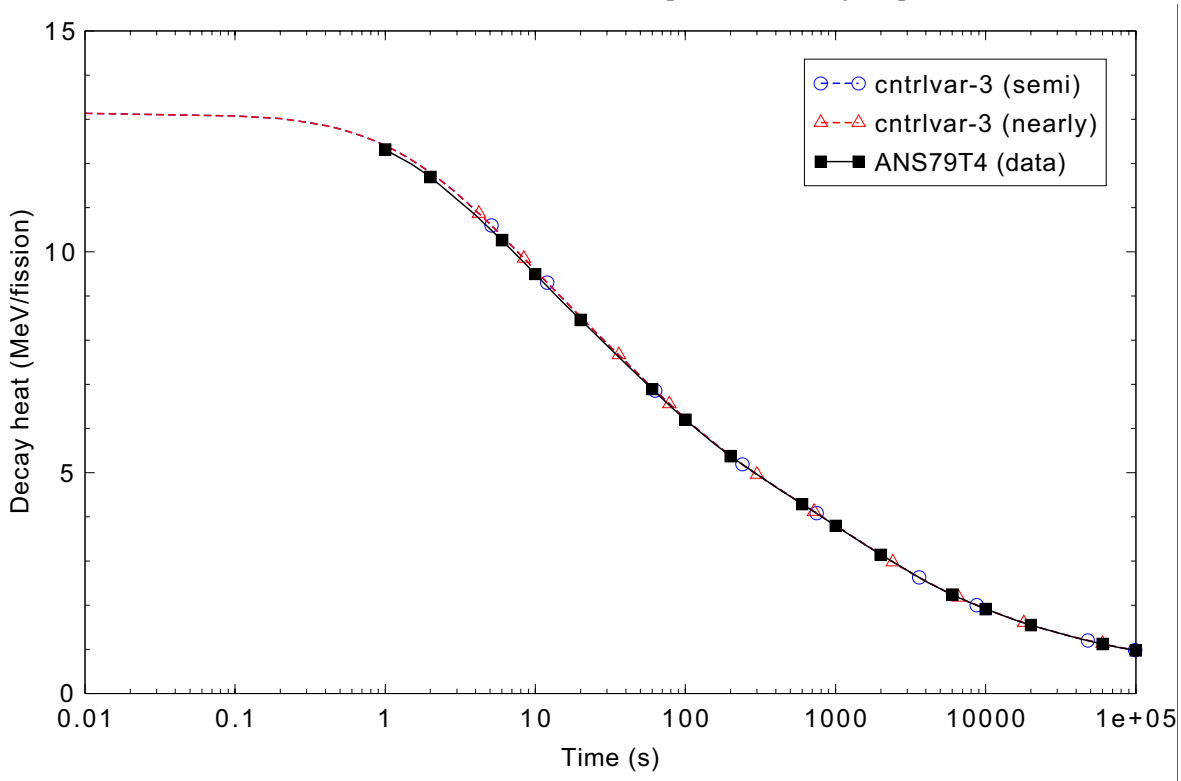

Figure 3.10-1. Decay heat comparison for the ans79.i test problem.

3.10.5 Conclusions and Assessment Findings

The decay heat model assessment is excellent based on these three test problems. It should be noted that the test problems only assessed a small number of the various decay heat options available in the RELAP5-3D code.

3.10.6 References

3.10-1. *American National Standard for Decay Heat Power in Light Water Reactors*, ANSI/ANS-5.1-1979, August 1979.

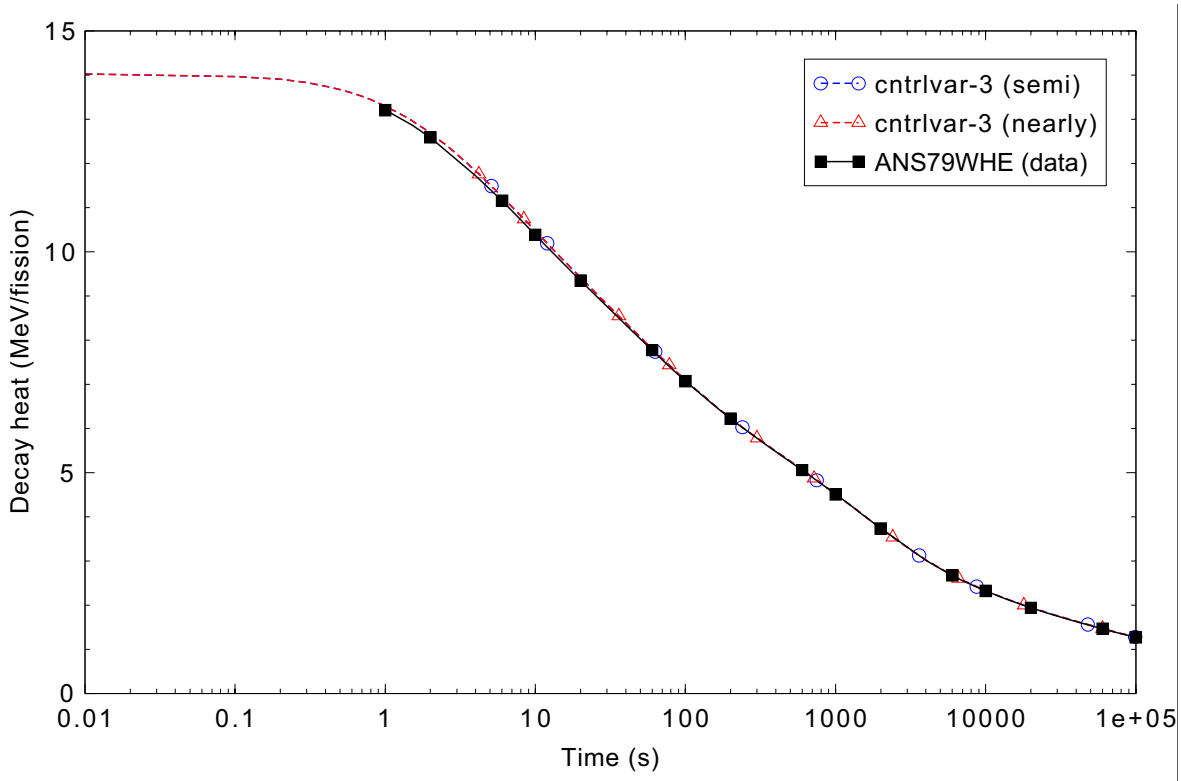

Figure 3.10-2. Decay heat comparison for the ans79ac.i test problem.

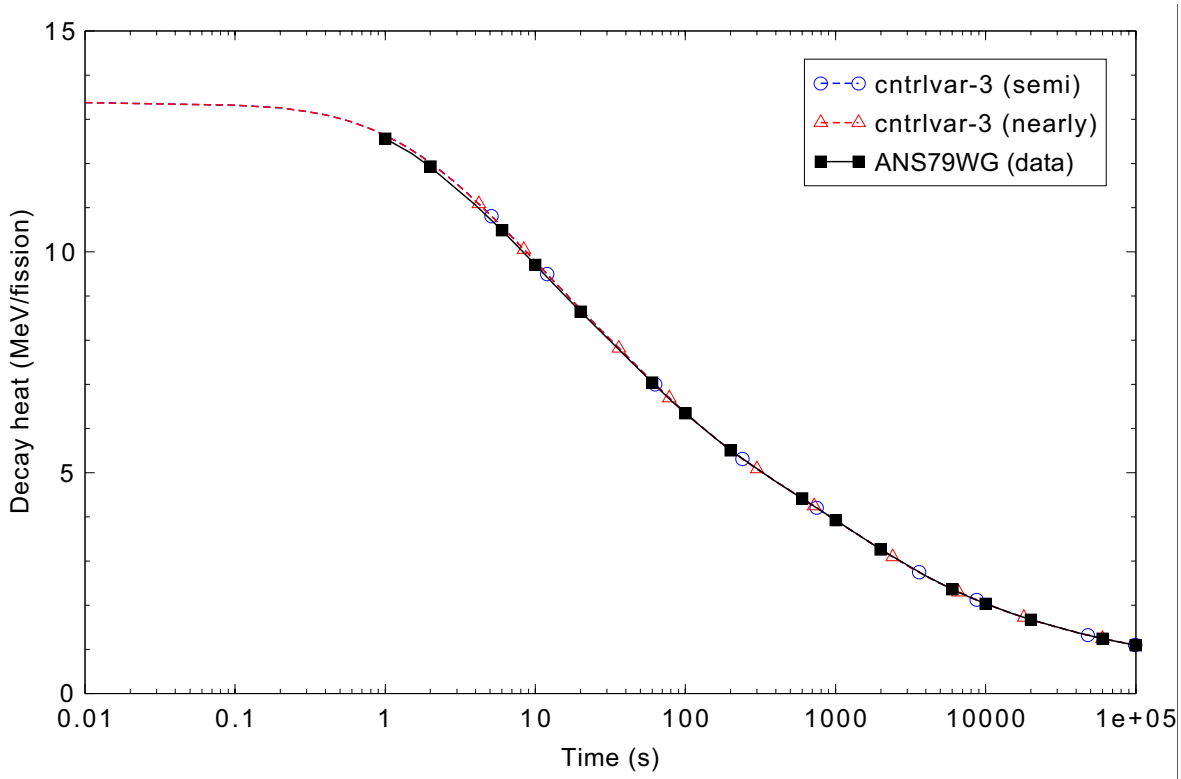

Figure 3.10-3. Decay heat comparison for the ans79G.i test problem.

3.11 Point Kinetics Ramp

The point kinetics ramp problem is an assessment problem for the reactor kinetics model in RELAP5-3D. This case was devised to address a problem identified in RELAP5-3D whereby the point kinetics solution would degrade with increasingly smaller time step sizes. This problem has since been resolved as the results in this section will show.

The point kinetics model in RELAP5-3D originally came from the IREKIN code,[3.11-1] which was written to assess the reactor kinetics experiments at SPERT.[3.11-2] The power is computed using the space-independent or point kinetics approximation, which assumes the power can be separated into space and time functions.

3.11.1 Code Models Assessed

The ramp problem assesses the point reactor kinetics model. Specifically, the prompt and delayed neutron fission power models are assessed.

3.11.2 Problem Description

Reactivity is inserted at a rate of 0.1 $/s and continues for 10 s, when the reactivity is 1 dollar or prompt critical.

3.11.3 Input Model Description

The input deck uses the point kinetics option and the separable feedback option. However, it includes no feedback. It includes no fission product decay calculations. A minimal hydrodynamic model is used to support the kinetics calculation, consisting of a single volume connected to time-dependent volumes on either end. Earlier versions of RELAP5-3D contained an error in the reactor kinetics calculation that showed up for small time steps. For this reason, this assessment was done with two time step sizes, 0.01 and 0.00001 s.

3.11.4 Data Comparisons and Results

Figure 3.11-1 shows a comparison of the ramp reactivity input for the semi-implicit and nearly-implicit runs. Figure 3.11-2 shows a fission power comparison for the semi-implicit and nearly-implicit runs and data for the 0.00001-s time step. The data came from a letter to the editor in Nuclear Science and Engineering.[3.11-3] There are only data points every 0.1 s; hence, the straight line portions of the data curve. Both calculations agree with the data through 9 s, then significantly over predict the power at 10 s. Figure 3.11-3 shows the same fission power comparison for a time step size of 0.01 s. In both cases, the power agrees with the data at points where there are data (every 0.1 s). The power over prediction at the smaller time step is the result of a code error in which there is a non-convergence in the point kinetics model at very small time steps. This error has been corrected in later versions of the code.

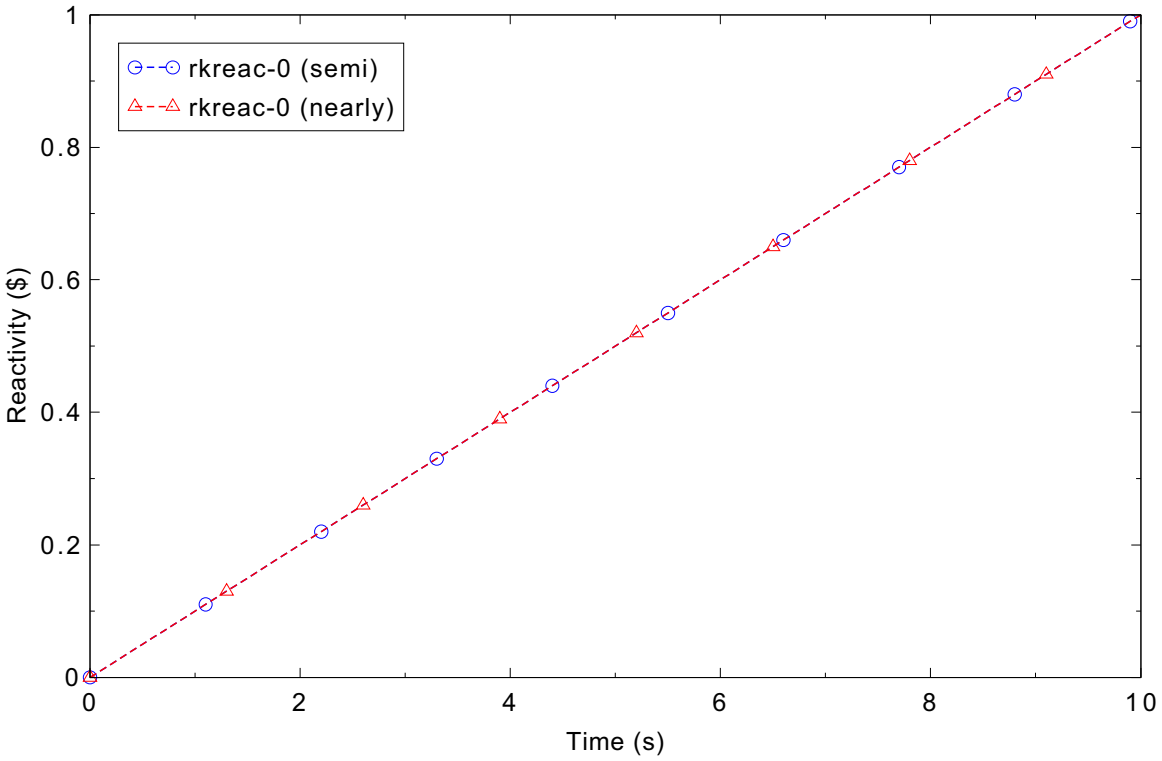

Figure 3.11-1. Reactivity comparison for the point kinetics ramp problem.

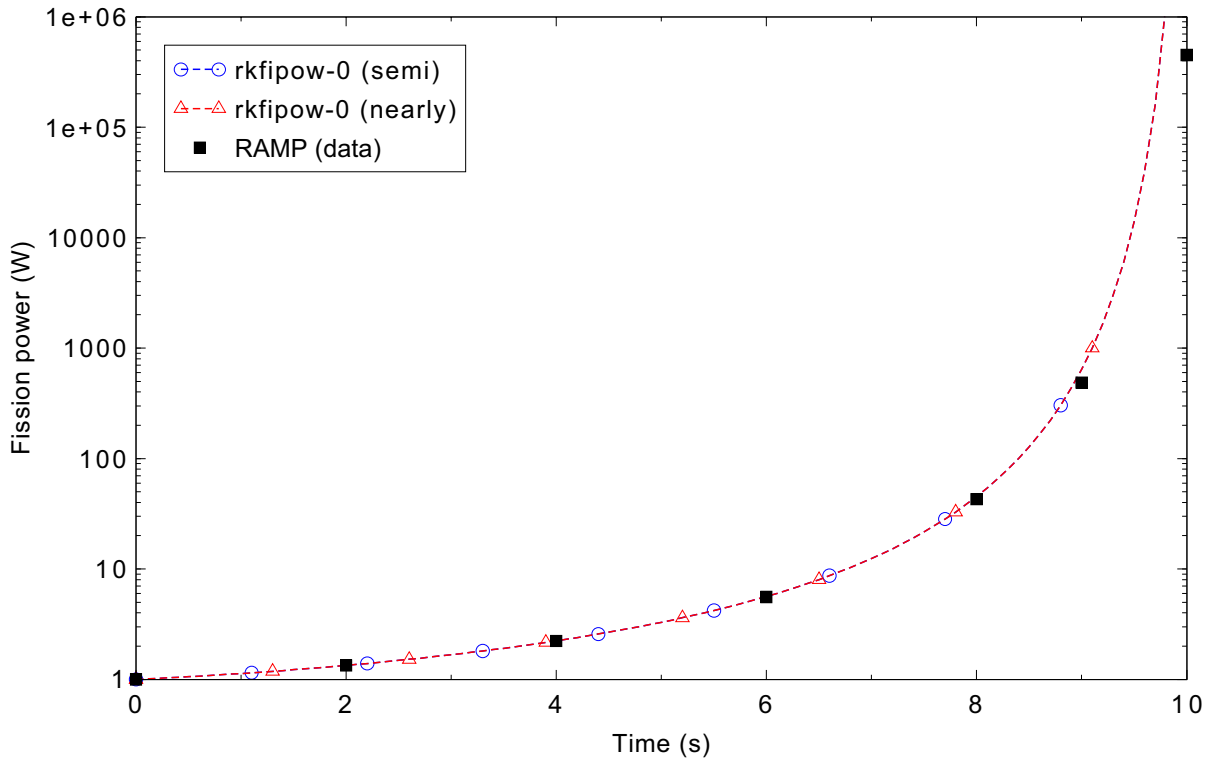

Figure 3.11-2. Fission power comparison for the point kinetics ramp problem with dt = 10^{-5} s.

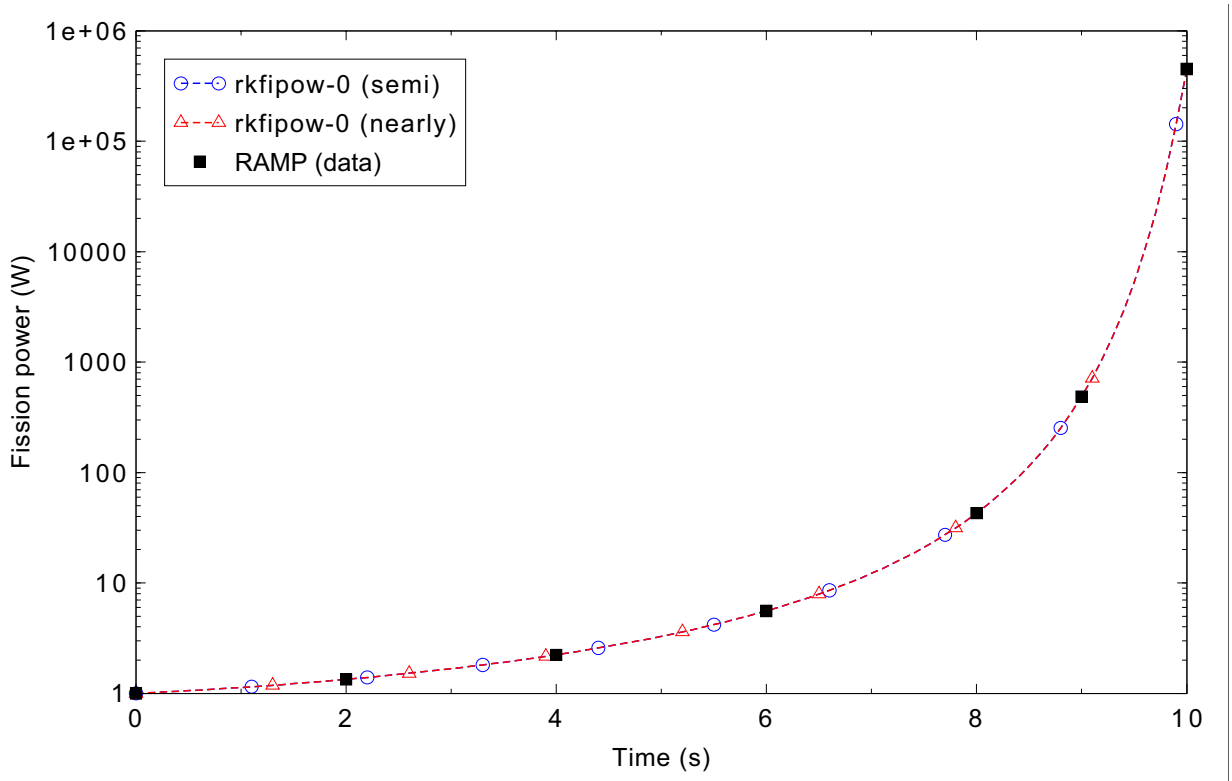

Figure 3.11-3. Fission power comparison for the point kinetics ramp problem with dt = 0.01 s.

3.11.5 Conclusions and Assessment Findings

The assessment of the reactor kinetics for ramp reactivity insertions shows that the code is doing an excellent job if the time step is not too small; at small time steps, a code error results in an insufficient prediction of the core power.

3.11.6 References

3.11-1. R. J. Wagner, *IREKIN -- Program for the Numerical Solution of the Reactor Kinetics Equations*, IDO-17114, National Reactor Testing Station, January 1966.

3.11-2. *Special Power Excursion Reactor Tests, Operated by Phillips Petroleum Co. for Idaho Operations Office*, USAEC, National Reactor Testing Station, 1966.

3.11-3. Gert Van den Eynde, Comments on "A Resolution of the Stiffness Problem of Reactor Kinetics," *Nuclear Science and Engineering*, Vol. 153, 2006, pp 200-202.

3.12 Pure Radial Symmetric Flow (3-D)

This test problem represents a hollow cylinder with a symmetric radial flow pattern. The flow is from the outside radial surface of the cylinder to the inside radial surface. No azimuthal flow is assumed. The test problem is simulated with one cylindrical MULTID component that contains eight rings, six sectors, and one axial level. Flow boundary conditions are applied to the outside radial surface of the cylinder, while pressure boundary conditions are applied to the inside radial surface. A steady-state calculation is performed and results are compared with those from an exact solution.

3.12.1 Code Models Assessed

This problem tests the radial momentum flux terms in the MULTID component.

3.12.2 Problem Description

An exact solution for this problem can be derived assuming steady, incompressible flow without friction, gravity, or azimuthal variation. As described in Reference 3.12-1, the exact solutions for the flow and pressure distributions are given by

$$v_r = \frac{v_{ro}\, r_{ro}}{r} \tag{3.12-1}$$

and

$$P = P_i + \frac{\rho}{2}(v_{ri}^2 - v_r^2) \tag{3.12-2}$$

where v_r is the fluid velocity in the radial direction, r is the radius, P is the pressure, ρ is the density, and the subscripts i and o correspond to the inner and outer radii, respectively (volume-centered or junction radii). The latter equation corresponds to the Bernoulli equation.

The inner and outer volume-centered radii of the cylinder are assumed to be 1.25 and 6.5 m, respectively. The inner and outer junction radii are assumed to be at 1.0 and 7.5 m, respectively. The pressure at the inner boundary volume is 500 kPa. The velocity at the outer junction radius is 0.8667 m/s. The fluid temperature is assumed to be 295.15 K. The exact solutions for the velocity and pressure distributions are given in Table 3.12-1. The radii for the velocity distribution correspond to junctions, while the radii for the pressure distribution correspond to volume centers.

3.12.3 Input Model Description

The geometry assumed in this problem and the nodalization of the RELAP5-3D model are presented in Figure 3.12-1. The model contains a MULTID component with eight rings, six sectors, and one axial level. The figure shows only Sector 1 because of the symmetry in the problem. Six time-dependent volumes are

Table 3.12-1. Exact solutions for the pure radial symmetric flow problem.

Junction Radius (m)	Velocity (m/s)	Volume-centered Radius (m)	Pressure (Pa)
1	6.5003	1.25	507591
1.5	4.3335	1.75	514201
2	3.2501	2.25	516921
2.5	2.6001	2.75	518298
3	2.1668	3.25	519090
3.5	1.8572	3.75	519586
4	1.6251	4.75	520151
5.5	1.1819	6.5	520587
7.5	0.8667		

attached to the outer six sectors by six time-dependent junctions. In addition, six time-dependent volumes are attached to the inner six sectors by a multiple junction component.

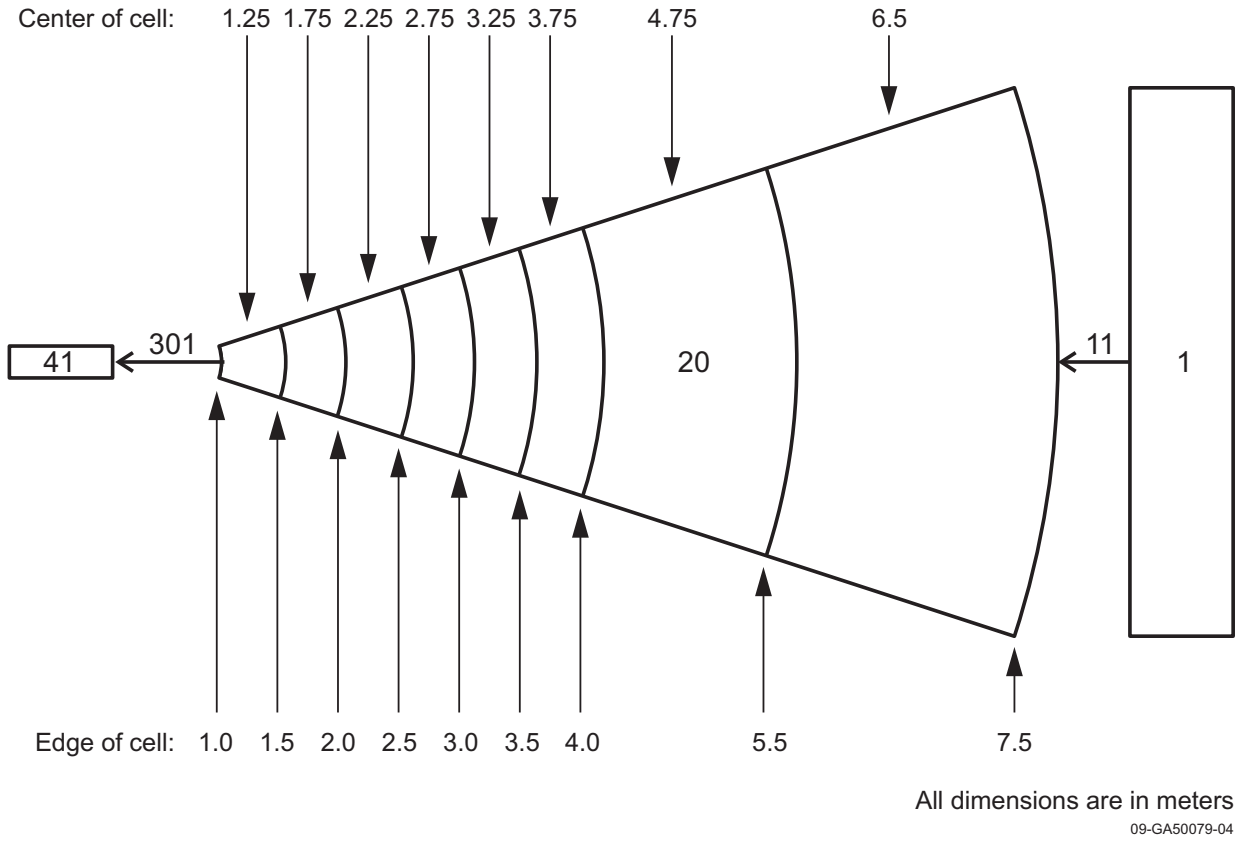

Figure 3.12-1. RELAP5-3D nodalization for the pure radial symmetric flow problem.

3.12.4 Data Comparisons and Results

Two steady-state calculations were performed for this problem, each with a requested time step of 0.02 s. The first calculation used the semi-implicit numerical scheme while the second calculation used the nearly-implicit numerical scheme.

The calculated results at 10 s are plotted against the exact solution for the radial velocity in Figure 3.12-2. The figure presents the magnitude of the calculated velocities. The calculated results within the MULTID component are actually negative because the flow is towards the center. Only results for Sector 1 are presented because of symmetry. The calculated results agreed with the exact solution. This was expected because the radial velocity was determined from the continuity equation and the mass error was very small for this steady problem.

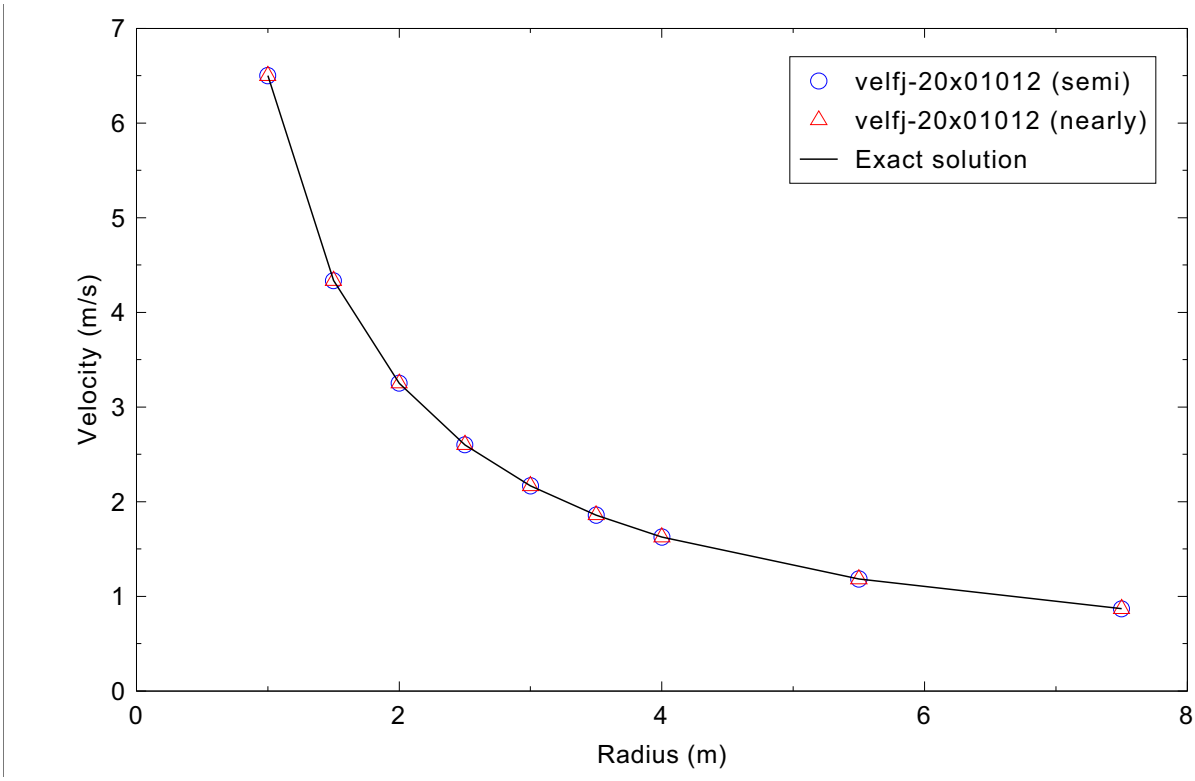

Figure 3.12-2. Radial velocity distribution for the pure radial symmetric flow problem.

The calculated results at 10 s are plotted against the exact solution for the radial pressure in Figure 3.12-3. The calculations agreed with the exact solution.

3.12.5 Conclusions and Assessment Findings

Both RELAP5-3D calculations are in excellent agreement with the exact solution for the radial velocity and pressure distributions in the pure radial symmetric flow problem.

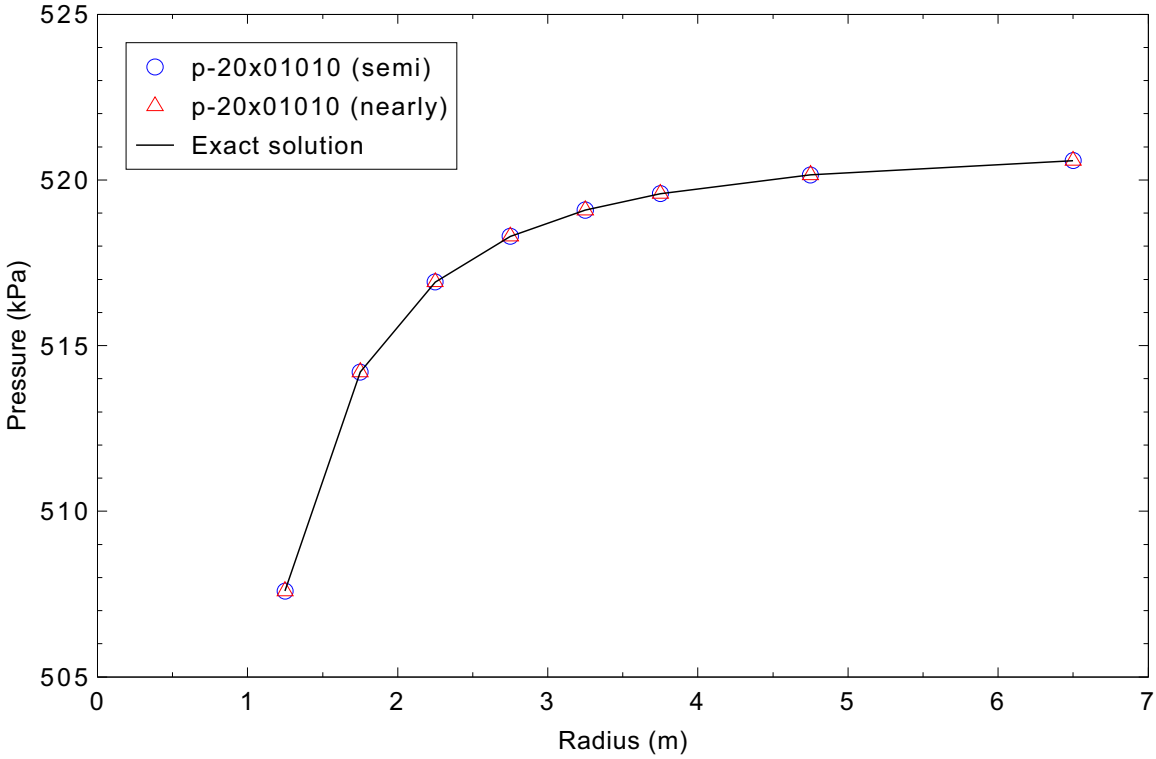

Figure 3.12-3. Radial pressure distribution for the pure radial symmetric flow problem.

3.12.6 References

3.12-1. K. E. Carlson, et al., *Developmental Assessment of the Multidimensional Component in RELAP5 for Savannah River Site Thermal Hydraulic Analysis*, EGG-EAST-9803, Rev. 0, July 1992.

3.13 Rigid Body Rotation (3-D)

This test problem represents a hollow cylinder with a symmetric flow pattern in the azimuthal direction. No radial flow is assumed. The test problem is simulated with one cylindrical MULTID component that contains eight rings, six sectors, and one axial level. Flow boundary conditions of zero are applied to the outside radial surface of the cylinder, while pressure boundary conditions are applied to the inside radial surface. The azimuthal flow pattern is imposed by turning on Card 1 Option 27. This option sets a constant azimuthal velocity at specified junctions. The junction numbers and velocities are given in Appendix B of Reference 3.13-1. A steady-state calculation is performed and results are compared with those from an exact solution.

3.13.1 Code Models Assessed

This problem tests the azimuthal momentum flux terms in the MULTID component.

3.13.2 Problem Description

An exact solution for this problem can be derived assuming steady, incompressible flow without friction, gravity, or azimuthal variation. As described in Reference 3.13-1, the exact solutions for the flow and pressure distributions are given by

$$v_r = 0, \tag{3.13-1}$$

$$v_\theta = r\omega = r\frac{v_{\theta o}}{r_o}, \tag{3.13-2}$$

and

$$P = P_i + \frac{\rho\omega^2}{2}(r^2 - r_i^2). \tag{3.13-3}$$

where v_r is the fluid velocity in the radial direction, v_θ is the fluid velocity in the azimuthal direction, r is the radius, ω is the rotational speed, P is the pressure, ρ is the density, and the subscripts i and o correspond to the inner and outer radii, respectively (volume-centered or junction radii).

The inner and outer volume-centered radii of the cylinder are assumed to be 1.25 and 6.5 m, respectively. The inner and outer junction radii are assumed to be 1.0 and 7.5 m, respectively. The pressure at the inner boundary volume is 500 kPa. The azimuthal velocity at the outer volume-centered radius is 1.0 m/s. The fluid temperature is assumed to be 295.15 K. The exact solutions for the velocity and pressure distributions are given in Table 3.13-1. The radii for the pressure and azimuthal velocity distributions correspond to the volume centers shown in Figure 3.13-1.

Table 3.13-1. Exact solutions for the rigid body rotation problem.

Volume-centered Radius (m)	Azimuthal Velocity (m/s)	Pressure (Pa)
1.25	0.1923	500007
1.75	0.2692	500024
2.25	0.3462	500048
2.75	0.4231	500078
3.25	0.5000	500113
3.75	0.5769	500154
4.75	0.7308	500255
6.5	1.0000	500487

3.13.3 Input Model Description

The geometry assumed in this problem and the nodalization of the RELAP5-3D model are presented in Figure 3.13-1. The model contains a MULTID component with eight rings, six sectors, and one axial level. The figure shows only Sector 1 because of the symmetry in the problem. Six time-dependent volumes are attached to the outer six sectors by six time-dependent junctions. In addition, six time-dependent volumes are attached to the inner six sectors by a multiple junction component.

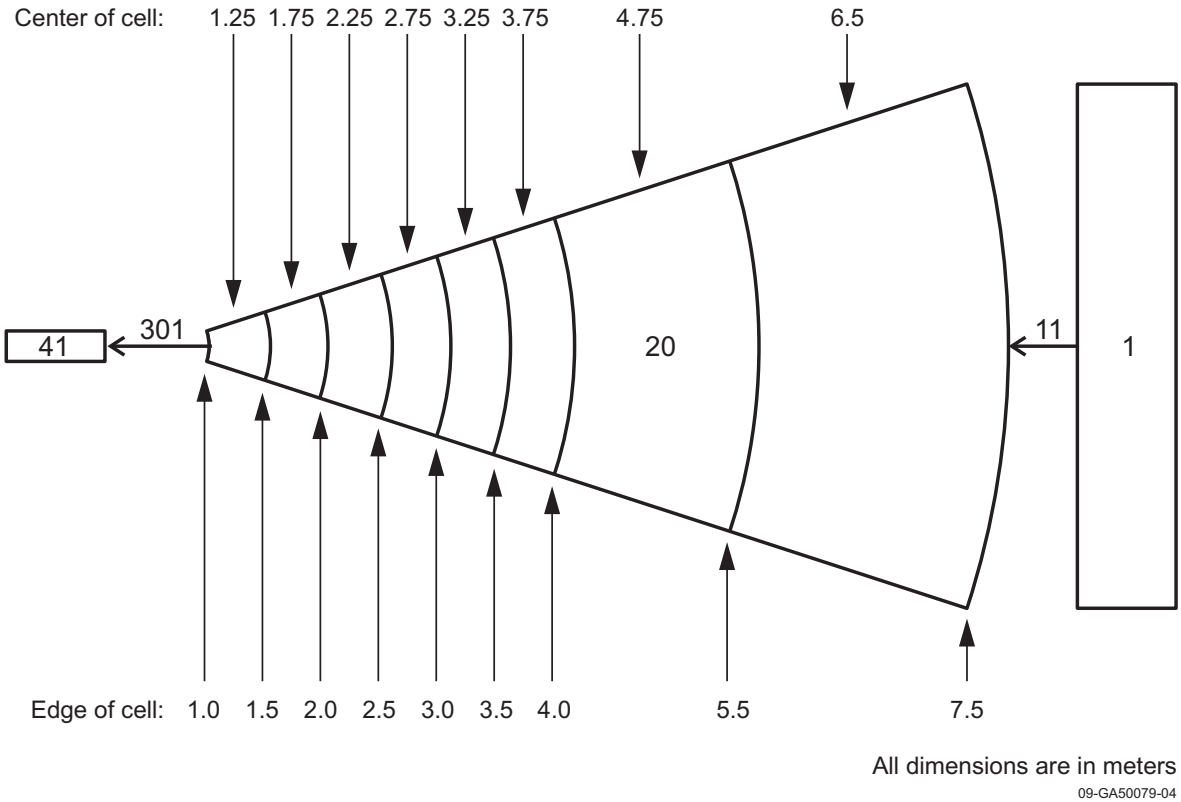

Figure 3.13-1. RELAP5-3D nodalization for the rigid body rotation problem.

The azimuthal velocities in the outermost ring were set to 1.0 m/s using Card 1 Option 27. The initial azimuthal velocities in the inner rings were input consistent with the assumption of rigid body rotation.

3.13.4 Data Comparisons and Results

Two steady-state calculations were performed for this problem; each had a requested time step of 0.02 s. The first calculation used the semi-implicit numerical scheme while the second calculation used the nearly-implicit numerical scheme. The initial discussion will concentrate on the results from the calculation with the semi-implicit scheme.

The calculated results at 50 s are plotted against the exact solution for the azimuthal velocity in Figure 3.13-2. Only results for Sector 1 are presented because of symmetry. The calculated results with the semi-implicit numerical scheme agreed with the exact solution. The radial velocities were essentially zero and thus were also in agreement with the exact solution.

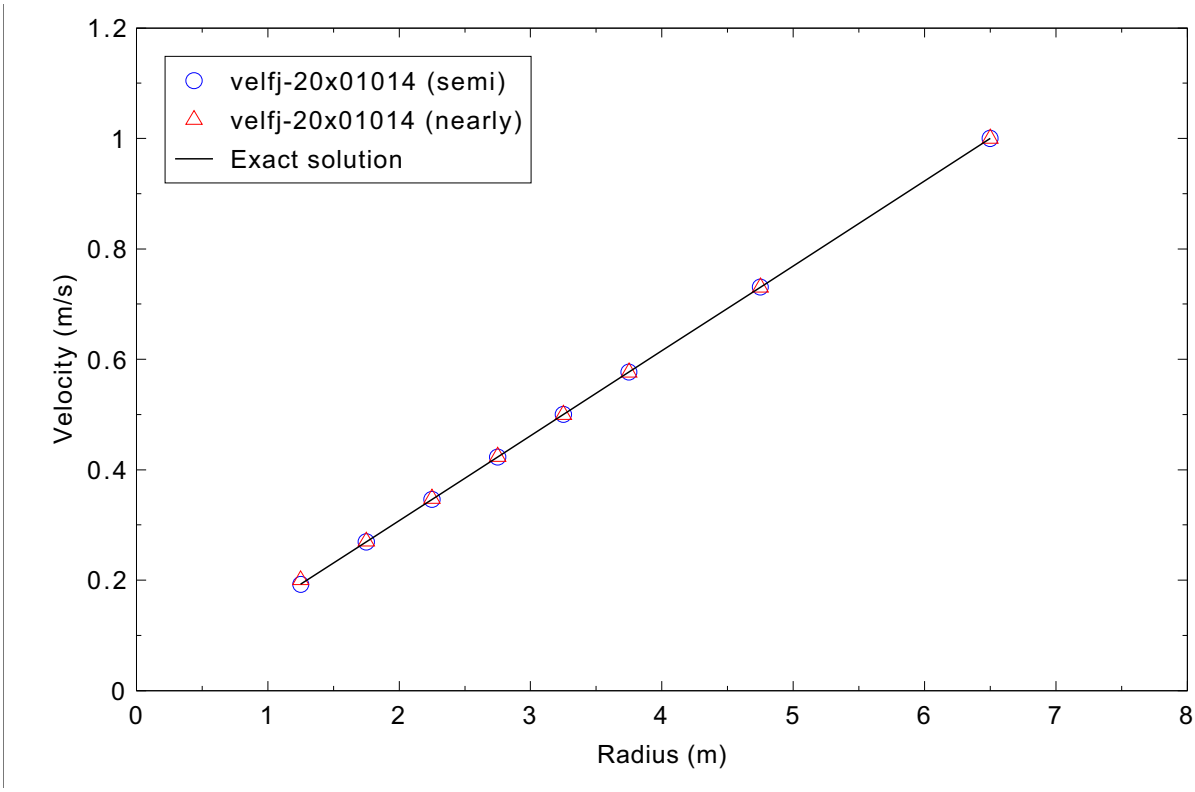

Figure 3.13-2. Azimuthal velocity distribution for the rigid body rotation problem.

The calculated results at 50 s are plotted against the exact solution for the radial pressure in Figure 3.13-3. The calculated pressures with the semi-implicit numerical scheme were consistently about 0.004 kPa higher than the exact solution for all the rings. Thus, the calculated pressures were judged to be in excellent agreement with the exact solution.

Figures 3.13-2 and 3.13-3 also show results calculated with the nearly-implicit numerical scheme. The azimuthal velocities were within 0.5% of the exact solution. However, the calculated radial pressures were in minimal agreement with the exact solution. The trend of the curve and the absolute value of the pressure rise from the center to the outer edge of the cylinder were not in reasonable agreement with the exact solution. In addition, the calculated velocities and pressures were not symmetric in the azimuthal direction.

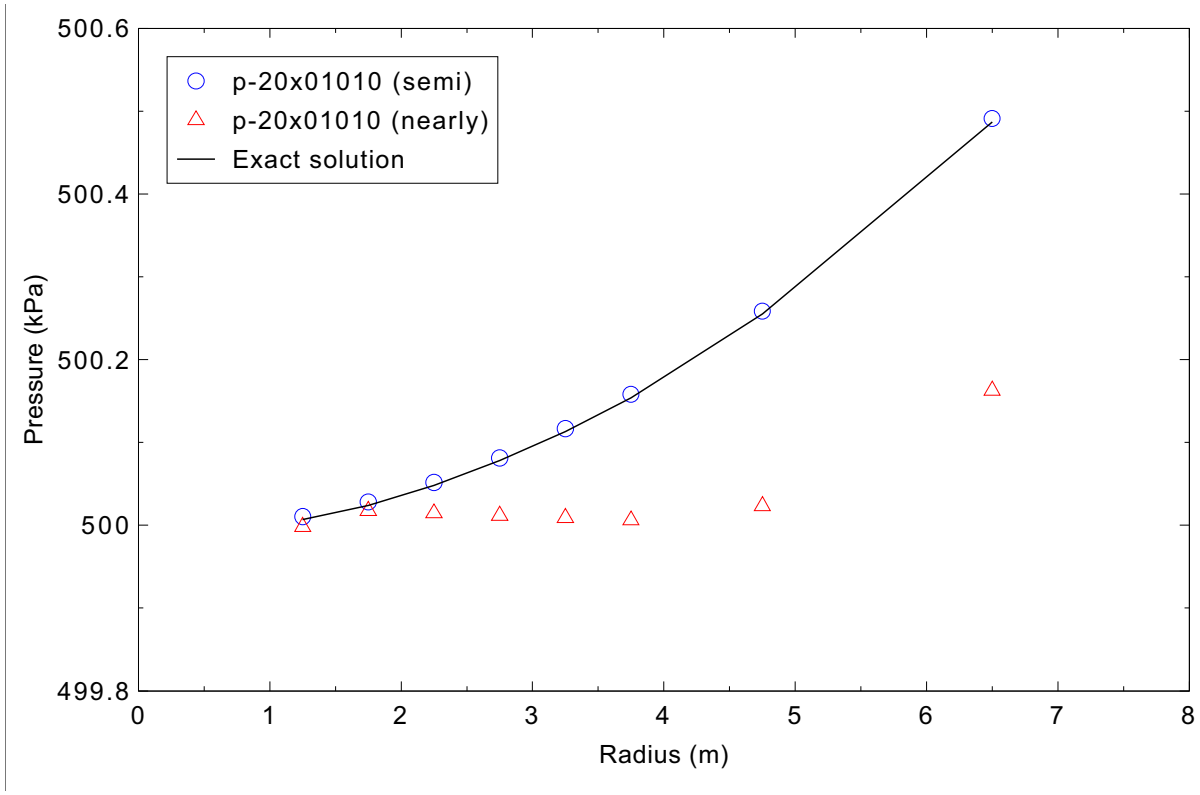

Figure 3.13-3. Radial pressure distribution for the rigid body rotation problem.

3.13.5 Conclusions and Assessment Findings

The RELAP5-3D calculation with the semi-implicit numerical scheme agreed with the exact solution for the radial and azimuthal velocities for the rigid body rotation problem. Although the calculated radial pressure distribution did not exactly match the exact solution, the results were judged to be in excellent agreement.

The RELAP5-3D calculation with the nearly-implicit numerical scheme did not agree with the exact solutions, particularly for the pressure distribution. The results were also not symmetric in the azimuthal direction, which indicates that there is an error in the nearly-implicit numerical scheme for the MULTID component.

3.13.6 References

3.13-1. K. E. Carlson, et al., *Developmental Assessment of the Multidimensional Component in RELAP5 for Savannah River Site Thermal Hydraulic Analysis*, EGG-EAST-9803, Rev. 0, July 1992.

3.14 R-Theta Symmetric Flow (3-D)

This test problem represents a hollow cylinder with a symmetric flow pattern in both the radial and azimuthal directions. The flow is from the outside radial surface of the cylinder to the inside radial surface. The test problem is simulated with one cylindrical MULTID component that contains eight rings, six sectors, and one axial level. Flow boundary conditions are applied to the outside radial surface of the cylinder, while pressure boundary conditions are applied to the inside radial surface. The azimuthal flow pattern is imposed by turning on Card 1 Option 27. This option sets a constant azimuthal velocity at specified junctions. The junction numbers and velocities are given in Appendix B of Reference 3.14-1. A steady-state calculation is performed and results are compared with those from an exact solution.

3.14.1 Code Models Assessed

This problem tests the flow and pressure distributions for a symmetric problem in the MULTID component. This problem tests both the radial and azimuthal terms in the momentum equation.

3.14.2 Problem Description

An exact solution for this problem can be derived assuming steady, incompressible flow without friction, gravity, or azimuthal variation. As described in Reference 3.14-1, the exact solutions for the flow and pressure distributions are given by

$$v_r = \frac{v_{ro} r_o}{r}, \tag{3.14-1}$$

$$v_\theta = \frac{v_{\theta o} r_o}{r}, \tag{3.14-2}$$

and

$$P = P_i + \frac{\rho}{2}(v_{\theta o}^2 + v_{ro}^2)\, r_o^2 \left(\frac{1}{r_i^2} - \frac{1}{r^2} \right), \tag{3.14-3}$$

where v_r is the fluid velocity in the radial direction, v_θ is the fluid velocity in the azimuthal direction, r is the radius, P is the pressure, ρ is the density, and the subscripts i and o correspond to the inner and outer radii, respectively (volume-centered or junction radii).

The inner and outer volume-centered radii of the cylinder are assumed to be at 1.25 and 6.5 m, respectively. The inner and outer junction radii are assumed to be 1.0 and 7.5 m, respectively. The pressure at the inner radius is 500 kPa. The radial velocities at the outer radius (7.5 m) are 0.8667 m/s. The azimuthal velocities at a radius of 6.5 m, which corresponds to the center of the outermost ring shown in Figure 3.14-1, are 1.0 m/s. The fluid temperature is assumed to be 295.15 K. The exact solutions for the

velocity and pressure distributions are given in Table 3.14-1. The radii for the radial velocity distribution correspond to the junctions shown in Figure 3.14-1, while the radii for the pressure and azimuthal velocity distributions correspond to volume centers.

Table 3.14-1. Exact solutions for the r-theta symmetric flow problem.

Junction Radius (m)	Radial Velocity (m/s)	Volume-centered Radius (m)	Azimuthal Velocity (m/s)	Pressure (Pa)
1.0	6.5000	1.25	5.2000	515181
1.5	4.3333	1.75	3.7143	528399
2.0	3.2500	2.25	2.8889	533839
2.5	2.6000	2.75	2.3636	536592
3.0	2.1667	3.25	2.0000	538176
3.5	1.8571	3.75	1.7333	539170
4.0	1.6250	4.75	1.3684	540300
5.5	1.1818	6.5	1.0000	541170
7.5	0.8667			

3.14.3 Input Model Description

The geometry assumed in this problem and the nodalization of the RELAP5-3D model are presented in Figure 3.14-1. The model contains a MULTID component with eight rings, six sectors, and one axial level. The figure shows only Sector 1 because of the symmetry in the problem. Six time-dependent volumes are attached to the outer six sectors by six time-dependent junctions. In addition, six time-dependent volumes are attached to the inner six sectors by a multiple junction component.

3.14.4 Data Comparisons and Results

Two steady-state calculations were performed for this problem; both used a requested time step size of 0.02 s. The first calculation used the semi-implicit numerical scheme while the second calculation used the nearly-implicit numerical scheme. The discussion will initially concentrate on the results from the calculation with the semi-implicit scheme.

The calculated results at 50 s are plotted against the exact solution for the radial velocity in Figure 3.14-2. The figure presents the magnitude of the calculated velocities. The calculated results within the MULTID component are actually negative because the flow is towards the center. Only results for Sector 1 are presented because of symmetry. The calculated results with the semi-implicit numerical scheme agreed with the exact solution. This was expected because the radial velocity was determined from the continuity equation and the mass error was very small for this steady problem.

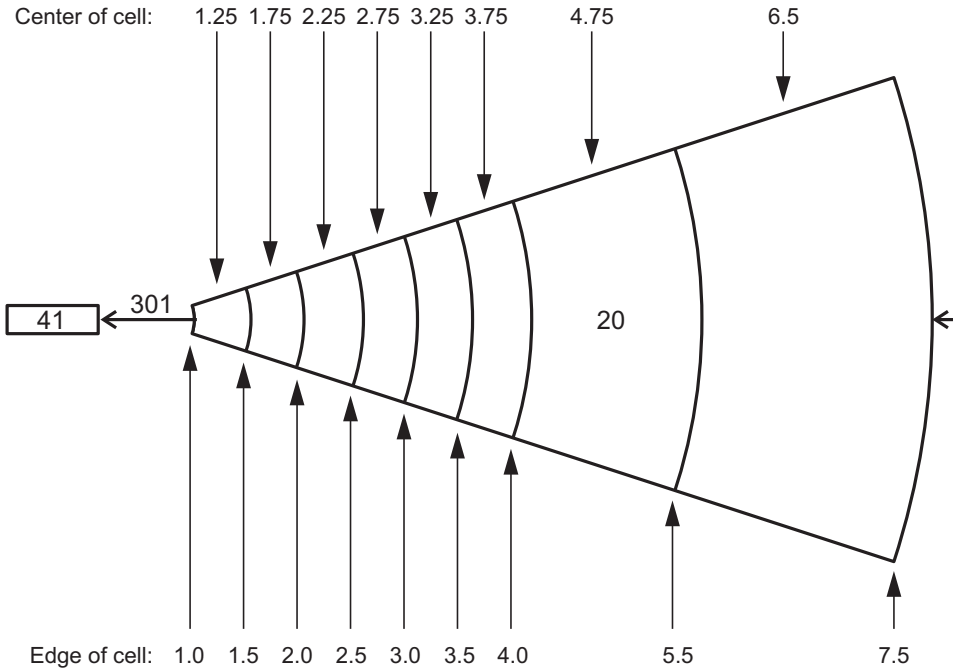

Figure 3.14-1. RELAP5-3D nodalization for the r-theta symmetric flow problem.

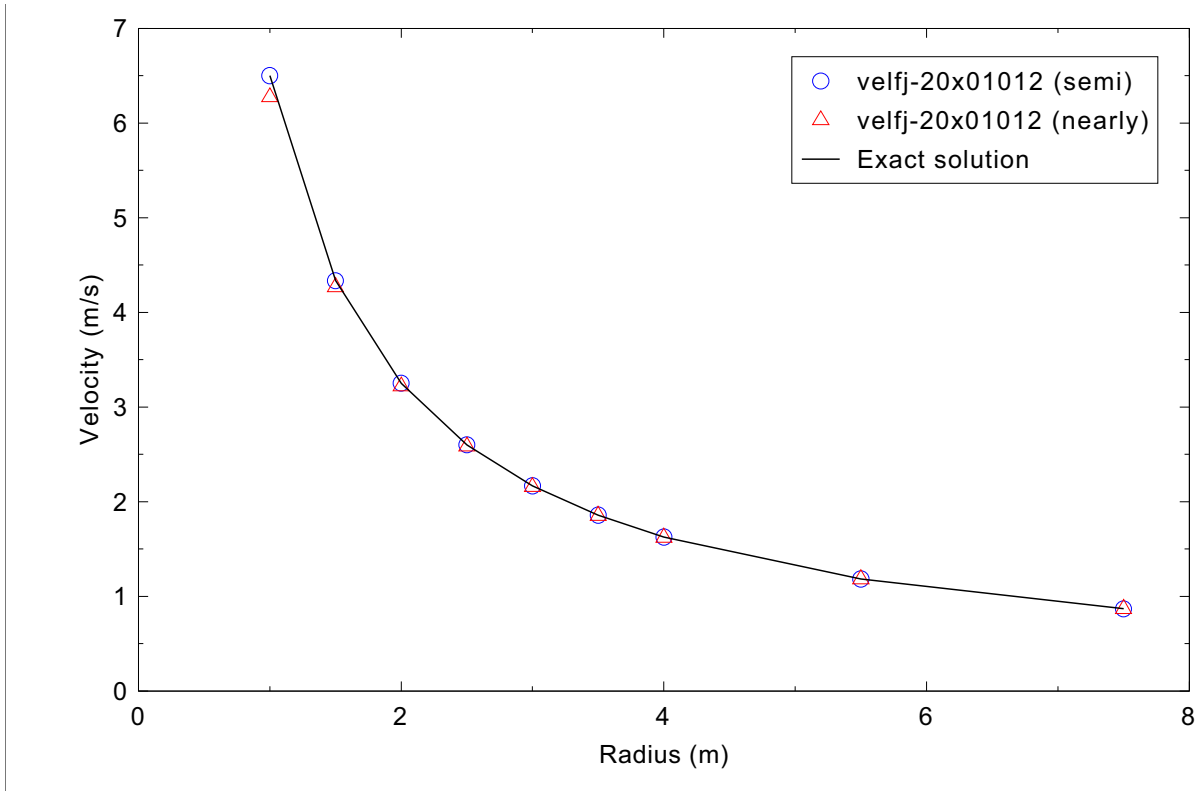

Figure 3.14-2. Radial velocity distribution for the r-theta symmetric flow problem.

The calculated results at 50 s are plotted against the exact solution for the azimuthal velocity in Figure 3.14-3. Only results for Sector 1 are presented because of symmetry. The calculated results with the semi-implicit numerical scheme also agreed with the exact solution.

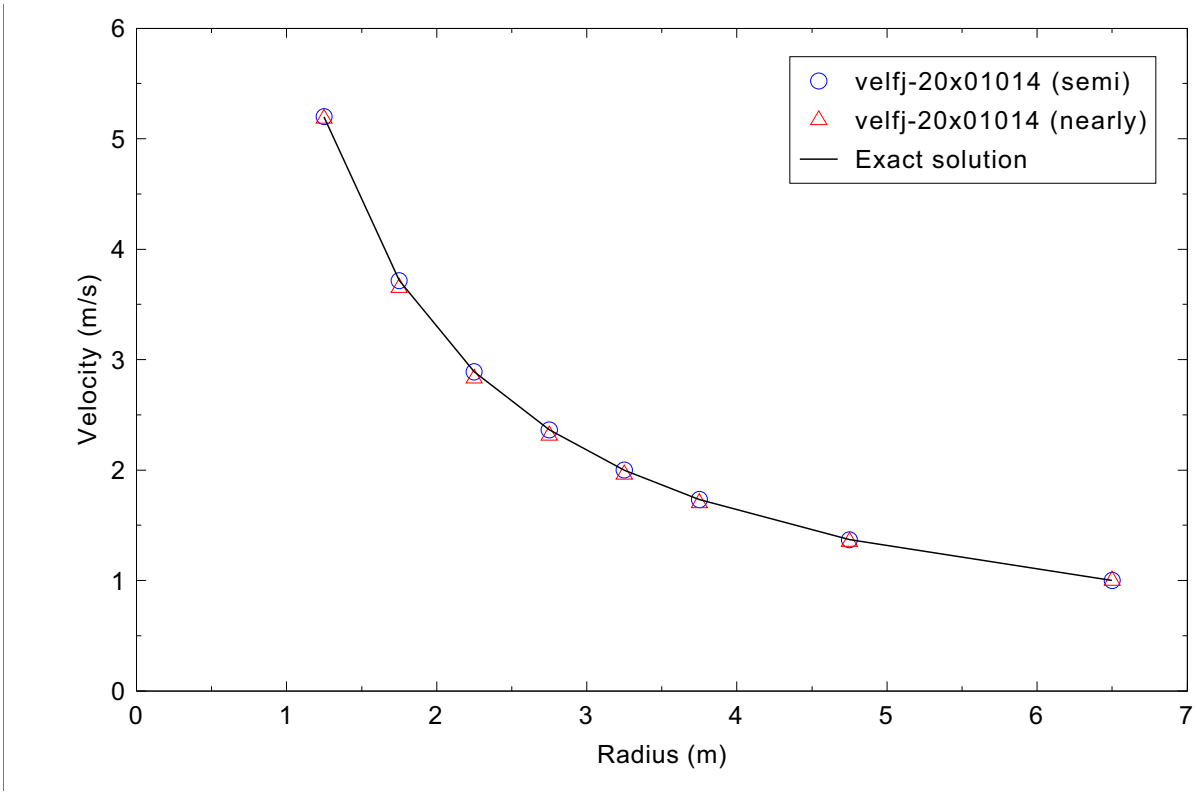

Figure 3.14-3. Azimuthal velocity distribution for the r-theta symmetric flow problem.

The calculated results at 50 s are plotted against the exact solution for the radial pressure in Figure 3.14-4. The calculation with the semi-implicit numerical scheme also agreed with the exact solution.

Figures 3.14-2 through 3.14-4 also show results calculated with the nearly-implicit numerical scheme. The radial and azimuthal velocities were in close agreement with the exact solution, but the calculated pressures were too high. The maximum deviations in the radial and azimuthal velocities in Sector 1 were 3.2% and 2.0%, respectively. The overall pressure rise from the input pressure at the center of the hollow cylinder to the outer edge was 16% too high with the nearly-implicit scheme. The calculated pressures were consistently about 6.8 kPa too high, which indicates that the majority of the error occurred at the junction connecting the inner ring of the MULTID component to the time-dependent volume. An additional problem was that the calculated velocities and pressures were not symmetric in the azimuthal direction.

3.14.5 Conclusions and Assessment Findings

The RELAP5-3D calculation with the semi-implicit numerical scheme is in excellent agreement with the exact solution for the radial velocity, azimuthal velocity, and radial pressure distributions for the r-theta symmetric flow problem.

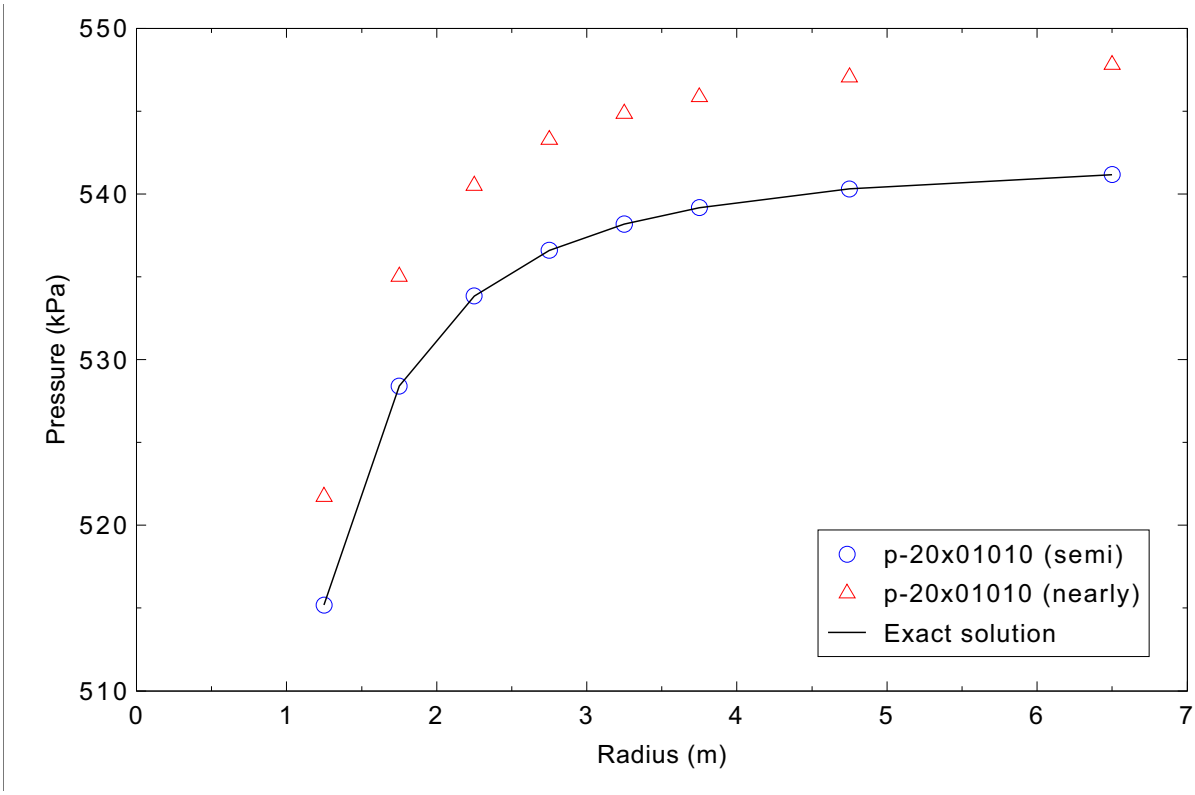

Figure 3.14-4. Radial pressure distribution for the r-theta symmetric flow problem.

The RELAP5-3D calculation with the nearly-implicit numerical scheme did not agree with the exact solutions, particularly for the pressure distribution. The results were also not symmetric in the azimuthal direction, which indicates that there is an error in the nearly-implicit numerical scheme for the MULTID component. The velocity comparisons were judged to be reasonable, while the pressure prediction was minimal.

3.14.6 References

3.14-1. K. E. Carlson, et al., *Developmental Assessment of the Multidimensional Component in RELAP5 for Savannah River Site Thermal Hydraulic Analysis*, EGG-EAST-9803, Rev. 0, July 1992.

3.15 Conduction Enclosure

For typical heat structures used in nuclear plant models, axial heat transfer is negligible compared to the radial convective heat transfer. However, for cases where axial conduction may be important, or where conduction between heat structures is of interest, conduction enclosures provide a means to model axial heat conduction within a heat structure as well as heat conduction due to surface contact between separate heat structures. It should be noted that this assessed version of RELAP5-3D contains an axial conduction model independent of the reflood model, and as such could be used in lieu of the axial conduction enclosure modeling assessed in this section.

For simple geometries with appropriate boundary conditions, the steady state heat conduction problem can be solved analytically using the method of separation of variables. The steady state temperature of a simple 2-D rectangular plate with constant temperature boundary conditions was used as a test case for the heat conduction enclosure model. The results are compared to the analytical solution, which was derived using the method of separation of variables.

For this assessment case, the nearly-implicit solution scheme was not utilized since the hydrodynamic model is immaterial. Therefore, only one set of results is presented.

3.15.1 Code Models Assessed

The ability of the code to model heat conduction between the surfaces of separate heat structures is assessed.

3.15.2 Problem Description

The equation that governs the steady state temperature of the plate is $\nabla^2 T = 0$ (Laplace's Equation). The width of the plate is denoted by 'a' and the height by 'b'. One side of the plate was held at a constant temperature of T_0 while the other three sides were held at a constant temperature of T_∞. The equations that govern the steady state temperature of the plate, in Cartesian coordinates, are the following:

$$\begin{aligned} &\frac{\partial^2 T}{\partial x^2} + \frac{\partial^2 T}{\partial y^2} = 0 \\ &T(0, y) = T_\infty \\ &T(a, y) = T_\infty \\ &T(x, 0) = T_0 \\ &T(x, b) = T_\infty \end{aligned} \qquad (3.15\text{-}1)$$

The heat equation in Equation (3.15-1) can be solved analytically using the method of separation of variables. The solution can be found in Carslaw and Jaeger[3.15-1] and is given by

$$T(x, y) = T_\infty + (T_0 - T_\infty)\sum_{n=0}^{\infty}\frac{4}{Na}\frac{\sinh[N(b-y)]}{\sinh(Nb)}\sin(Nx), \qquad N = \frac{(2n+1)\pi}{a}. \tag{3.15-2}$$

For numerical computation of the solution, the size of the plate and the boundary temperatures were set as follows:

$$a = 0.96\ \text{m}, b = 1\ \text{m}, T_0 = 500\ \text{K}, T_\infty = 300\ \text{K}. \tag{3.15-3}$$

An accurate approximation of the heat plate solution can be obtained by substituting Equation (3.15-3) in Equation (3.15-2) and numerically summing the series using a sufficient number of terms. Practically, the number of terms that can be taken is limited by the sinh function, which grows exponentially with n. While the sinh terms in the numerator and denominator grow exponentially, a careful look at the ratio of sinh terms shows that the ratio is never greater than one for values of y between zero and the plate height of b. The sinh terms can be replaced with a more well behaved expression if sinh is expanded in its exponential form, and the terms are multiplied by the exponential e^{-Nb}. The sinh terms are then expanded as

$$e^{-Nb}\sinh[N(b-y)] = e^{-Nb}\frac{[e^{N(b-y)} - e^{-N(b+y)}]}{2} = \frac{1}{2}[e^{-Ny} - e^{-N(2b-y)}] \tag{3.15-4}$$
$$e^{-Nb}\sinh(Nb) = e^{-Nb}\frac{(e^{Nb} - e^{-Nb})}{2} = \frac{1}{2}(1 - e^{-2Nb})$$

The ratio of the sinh terms can then be written as

$$\frac{\sinh[N(b-y)]}{\sinh(Nb)} = \frac{e^{-Nb}\sinh[N(b-y)]}{e^{-Nb}\sinh(Nb)} = \frac{e^{-Ny} - e^{-N(2b-y)}}{1 - e^{-2Nb}}. \tag{3.15-5}$$

The second exponential term in the numerator of Equation (3.15-5) decays with N when y is less than 2b, so each term is now well behaved. By replacing the sinh ratio with the exponential form derived in Equation (3.15-5), the series can be expanded to a large number of terms to provide an accurate truncated series solution. For comparison with the RELAP5-3D solution, a set of 3,800 terms was included in the truncated series. Values were calculated for an $x \times y$ grid of 25 by 26 nodes, which is consistent with the RELAP5-3D model described below. For the series expansion, the greatest error tends to occur along the 500 K boundary due to the discontinuity that happens where the 500 K boundary meets the 300 K boundaries. With a 3,800-term expansion, the values at nodes along this boundary were 500 ± 0.06 K, which was deemed to be sufficiently accurate for comparison to the RELAP5-3D solution.

3.15.3 Input Model Description

In order to model the heated plate in RELAP5-3D, a series of 25 heat structure geometries with 25 axial cells (heat structures) each was defined. Each cell had a size of $0.04\ \text{m} \times 0.04\ \text{m}$. The 25 heat

structure geometries placed side by side sequentially were associated with the y axis of Equation (3.15-1), and the 25 axial cells of the heat structure geometries were associated with the x axis. Each axial cell in RELAP5-3D includes a right side temperature node (mesh point) and a left side temperature node. To be consistent with the diagrams, these will be referred to as bottom surface and top surface nodes, respectively. As shown in Figure 3.15-1, nodes on the boundary of the square plate model were assigned a fixed temperature consistent with the boundary conditions given in Equation (3.15-3). The top surface nodes of heat structure geometry 1 were assigned a temperature of 500 K. The bottom and top surface nodes for the first and last cells of all 25 heat structure geometries, including heat structure geometry 1, were assigned a temperature of 300 K. To complete the boundary conditions, all bottom surface nodes of heat structure geometry 25 were assigned a temperature of 300 K. Boundary conditions are depicted in Figure 3.15-1.

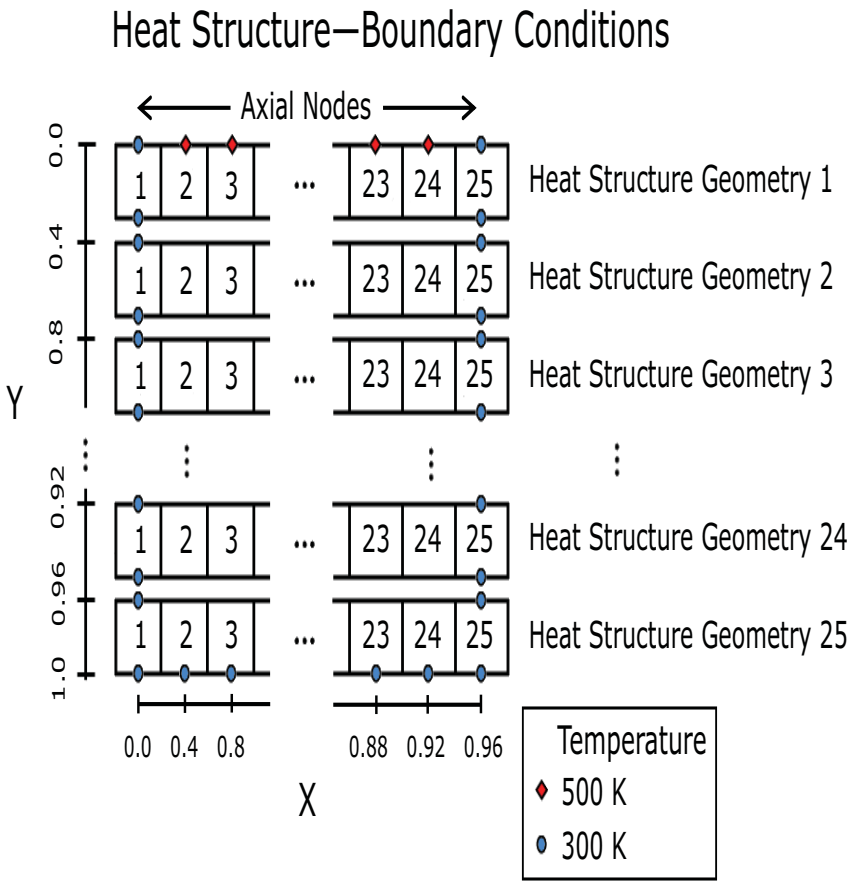

Figure 3.15-1. Heat structure layout with boundary conditions for the conduction enclosure problem.

The thermal conductivity for the heat structures was defined to be 400 W/m-K. Without including conduction enclosures in the model, there is no thermal interaction between the 25 heat structure geometries. In order to model the heat transfer between separate heat structure geometries and to model axial conduction, conduction enclosures were included in the model. The gap conductance (κ) used in conduction enclosures is related to the thermal conductivity (k) used in heat structures by the following formula:

$$\kappa = \frac{k}{dx} \tag{3.15-6}$$

where dx is the distance between thermal nodes. In this axial conduction case, the distance between thermal nodes is 0.04 m, so the axial gap conductance (k) in each of the conduction enclosures was set to 10,000 W/m^2-K.

A conduction enclosure was included between each adjacent heat structure geometry to model the interaction between the heat structure geometries as well as the axial conduction within the individual heat structure geometries. As shown in Figure 3.15-2, the nth conduction enclosure referenced all bottom surface nodes of the nth heat structure geometry, along with the top surface nodes of heat structure geometry n+1. The 25 bottom surface nodes of the nth heat structure geometry were defined as surfaces 1 through 25 in the conduction enclosure, while the 25 top surface nodes of heat structure geometry n+1were defined as surfaces 26 through 50.

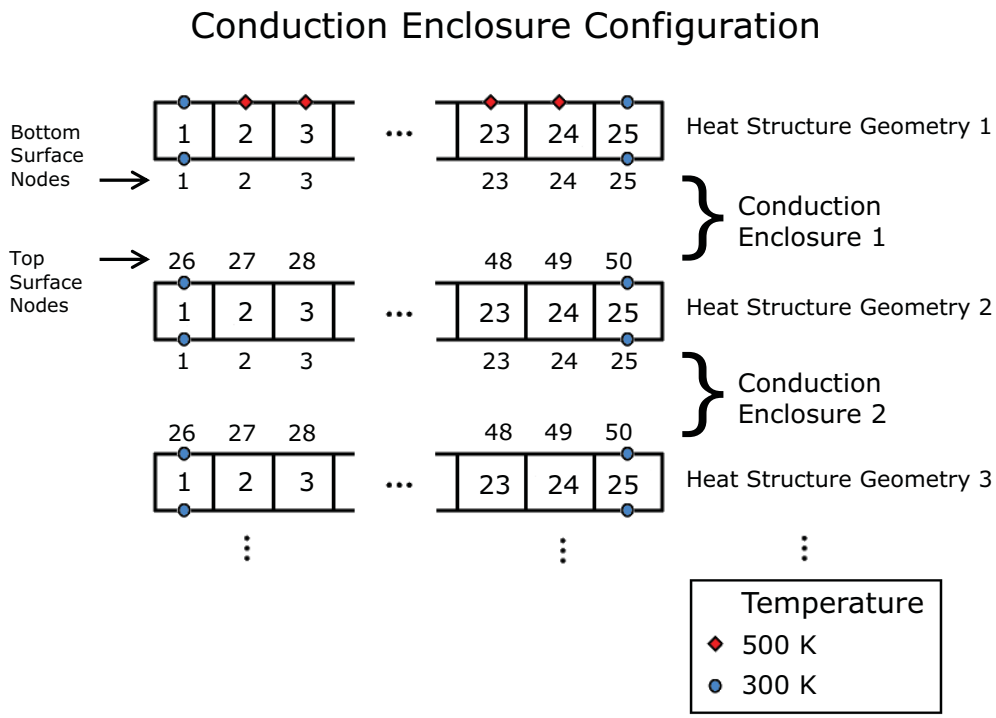

Figure 3.15-2. View of heat structure surfaces included in the conduction enclosures.

In a conduction enclosure, one must define which surfaces included in the conduction enclosure are in contact. Each surface included in the conduction enclosure includes a set of area factors which indicate the amount of contact between that surface and each of the other surfaces included in the conduction enclosure. If the top surface of heat structure cell n is included in the conduction enclosure, the area factor A_{fi} that defines the amount of contact between cell n and surface i is given by

$$A_{fi} = \frac{A_{ci}}{A_{nt}} \tag{3.15-7}$$

where A_{ci} is the area of contact between the two surfaces in the conduction enclosure, and A_{nt} is the top surface area of cell n. If the bottom surface of cell n is included in the conduction enclosure, then A_{nt} in the area factor equation above is replaced by the bottom surface area of cell n (A_{nb}).

Figure 3.15-3 shows the area factors used in the heated plate problem. Note that the contact for bottom surface nodes is different from top surface nodes. Both top and bottom surfaces in the conduction enclosure include contact with cells in the adjacent heat structure (i.e., surface n is in contact with surface n+25 and surface n+25 is contact with surface n). However, only the bottom surface cells include contact with the axial cells to either side in the same heat structure (i.e., cells n-1 and n+1). Note that heat transfer between axial cells occurs through the (internal) left and right surfaces rather than through the bottom surface, which is included in the conduction enclosure. Since the heat structure cells are square, the left and right surfaces each have the same area as the bottom surface, so the area factor is 1.0.

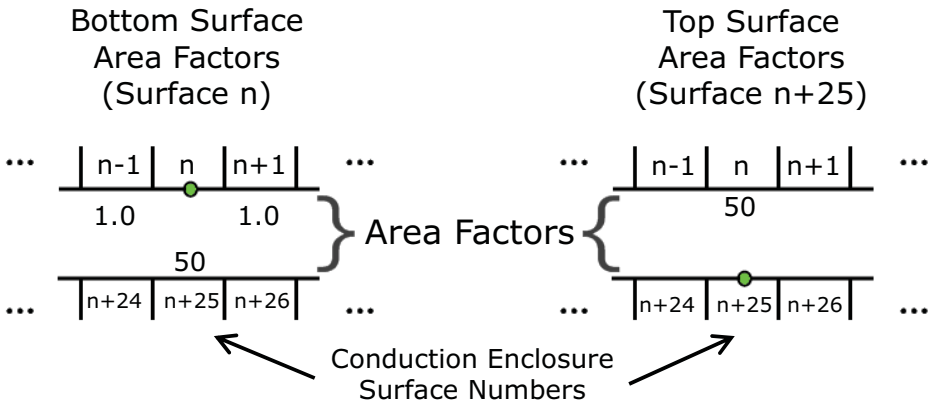

Figure 3.15-3. Area factors used to define axial contact of heat structure cells as well as contact between separate heat structure geometries.

Equation (3.15-7) seems to suggest that the area factor for cells in contact between adjacent heat structure geometries should also be 1.0. Note, however, that the definition of κ in Equation (3.15-6) assumes that the distance between points is 0.04 m. The nodes for surfaces in contact between adjacent heat structure geometries are in much closer proximity than 0.04 m. The thermal conductivity (k) between adjacent heat structures matches the axial thermal conductivity of 400 W/m-K. Since the actual value of dx in Equation (3.15-6) is in fact much smaller than the 0.04-m gap used in the axial direction for nodes in contact from adjacent heat structure geometries, the κ value should be much larger than the κ value along the axial direction. However, only one κ value can be defined for each surface. Therefore, the value of κ is modified indirectly by increasing the area factor between heat structure geometry nodes in contact. A value of 50 was used for the view factor, which had the effect of keeping the temperature difference between nodes that are in contact small (within ±1 K).

A minimal hydrodynamic model was used to support the conduction enclosure calculations, consisting of a single hydrodynamic volume connected to time-dependent volumes on either end. A time step size of 1.0e-4 s was utilized for the calculation.

3.15.4 Data Comparisons and Results

The solution of the heated plate problem is shown in Figure 3.15-4. In order to characterize the local error in the RELAP5-3D model solution, the RELAP5-3D solution was compared to the 3,800-term series solution. With T_R as the local (or point wise) RELAP5-3D steady state temperature, and T_S as the local series solution temperature, the following formula was used for local percent error:

$$\text{Error} = 100\frac{T_S - T_R}{T_0 - T_\infty} \tag{3.15-8}$$

The average percent error based on the error above is given by:

$$\text{AvgError} = \frac{100}{T_0 - T_\infty}\frac{\int |T_S - T_R| dA}{\int dA}. \tag{3.15-9}$$

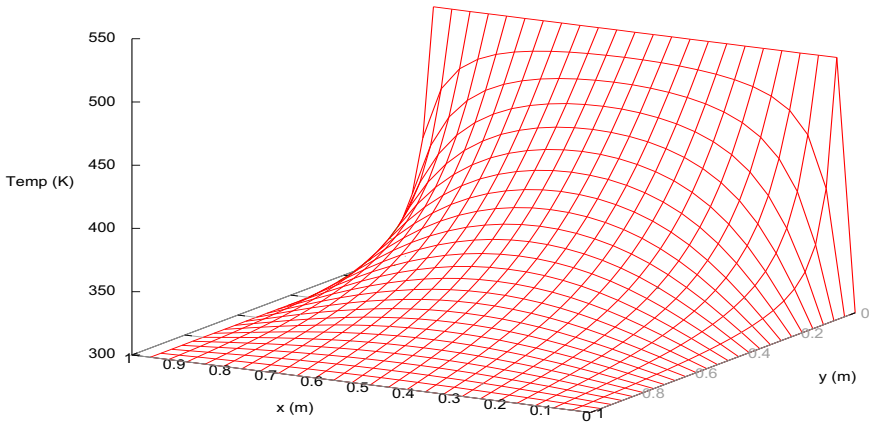

Figure 3.15-4. Steady state temperature for the heated plate problem defined in Equation (3.15-1) based on a 3800-term expansion of the series solution given in Equation (3.15-2).

A plot of the local error is given in Figure 3.15-5. The plot is symmetric about an x value of 0.48 m and shows that the maximum error over the domain is about 0.96%, which equates to a temperature difference between the RELAP5-3D model and the series solution of about 1.92 K. The fact that the error is positive almost everywhere indicates that RELAP5-3D tends to over predict the steady state temperature

of the plate slightly. The average error is 0.23%, which equates to an average temperature difference between the RELAP5-3D solution and the series solution of approximately 0.46 K.

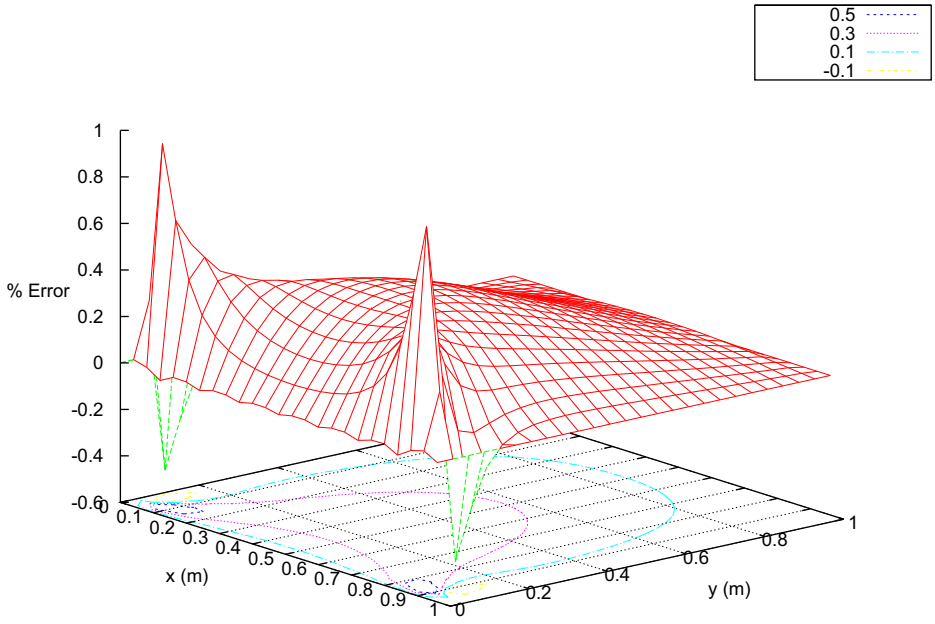

Figure 3.15-5. Local steady state temperature error for the RELAP5-3D solution vs. series solution.

Figure 3.15-6 shows the steady state temperature predicted by RELAP5-3D and the truncated series analytic solution for x equal to 0.04 m, which is the set of nodes closest to the 300 K boundary. FIgure 3.15-7 plots the temperatures for x equal to 0.48 m, which is the line along the center of the plate. These plots show the excellent agreement between the RELAP5-3D solution and the 3,800-term series solution.

3.15.5 Conclusions and Assessment Findings

As seen from the plots, there is excellent agreement between the analytical solution and the RELAP5-3D solution. Notably, a relatively small number of nodes is able to give an approximation for the steady state temperature of the plate with less than 1% error throughout the domain.

3.15.6 References

3.15-1. H. S. Carslaw and J. C. Jaeger, *Conduction of Heat in Solids*, Second Edition, Oxford University Press, 1959.

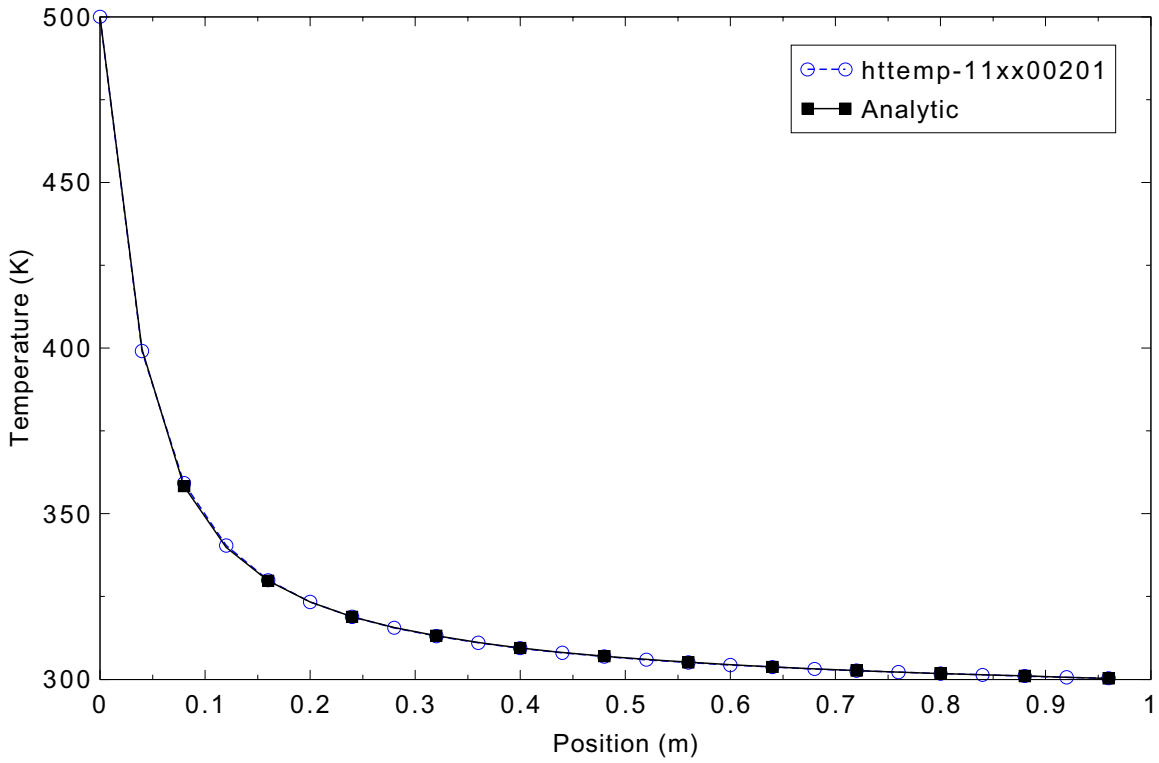

Figure 3.15-6. Heated plate steady state series solution and the RELAP5-3D solution along x equal to 0.04 m.

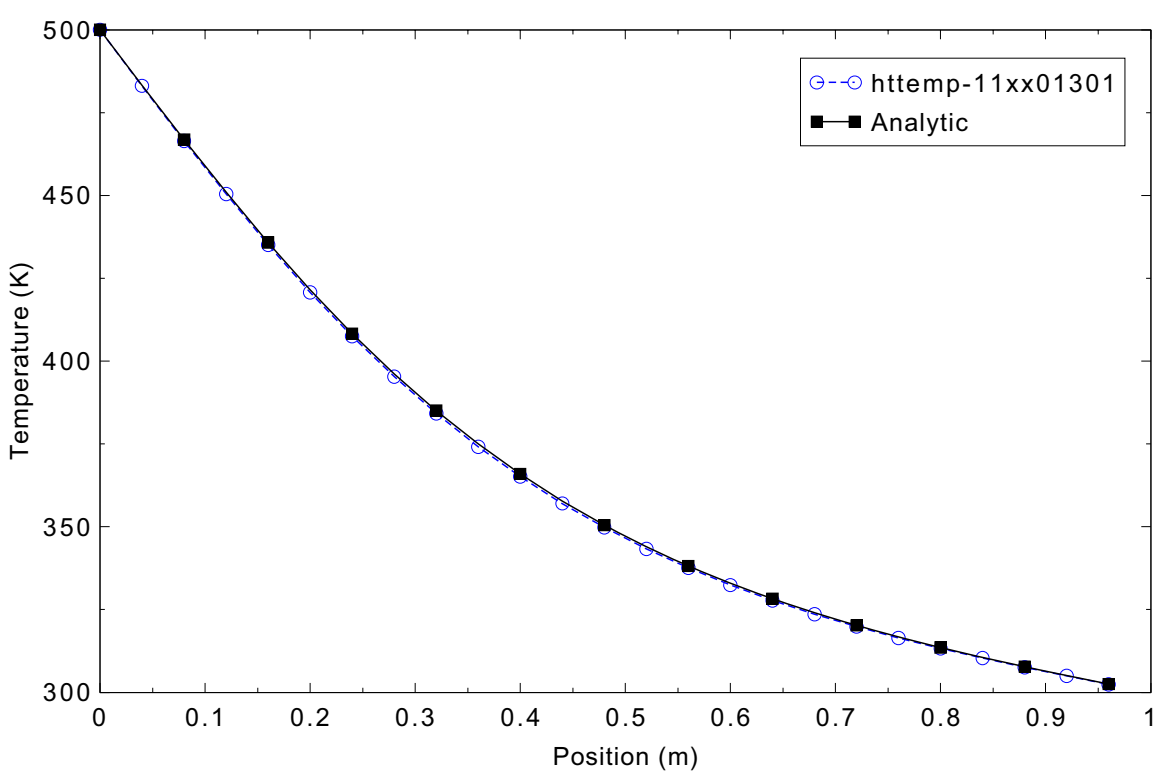

Figure 3.15-7. Heated plate steady state series solution and the RELAP5-3D solution along x equal to 0.48 m.

3.16 Conduction Enclosure: 1-D Transient Model

The RELAP5-3D transient response of a one-dimensional (1-D) rod with axial conduction is compared with the time-dependent analytical solution. It should be noted that this assessed version of RELAP5-3D contains an axial conduction model independent of the reflood model, and as such could be used in lieu of the axial conduction enclosure modeling assessed in this section.

For this assessment case, the nearly-implicit solution scheme was not utilized since the hydrodynamic model is immaterial. Therefore, only one set of results is presented.

3.16.1 Code Models Assessed

The ability of the code to model transient axial heat conduction in a heat structure geometry is assessed.

3.16.2 Problem Description

The model used was a 1-D rod with heated ends and convection along the rod inside the ends. The ends of the rod are held at a fixed temperature (T_0). The convective sink temperature (T_∞) along the rod is also constant. Again an analytical series solution derived using the method of separation of variables is available, and the RELAP5-3D solution is compared to the time-dependent analytical solution.

The following partial differential equation and boundary conditions were used to calculate the temperature response ($T[x, t]$) of the one-dimensional rod with heated ends and convection:

$$\frac{\partial T}{\partial t} - K\frac{\partial^2 T}{\partial x^2} + H(T - T_\infty) = 0 \qquad (3.16\text{-}1)$$

$$T(-L/2, t) = T_0$$

$$T(L/2, t) = T_0$$

$$T(x, 0) = T_\infty$$

The temperature at the ends of the rod (T_0) was chosen as 550 K. The fluid temperature (T_∞) was fixed at 300 K. The length of the rod (L) was 3 m. The coefficients K and H were defined as follows:

$$H = \frac{h}{\rho c_p A} = 2.19 \times 10^{-4} \ \frac{1}{s} \qquad (3.16\text{-}2)$$

$$K = \frac{k}{\rho c_p} = 1.17 \times 10^{-5} \ \frac{m^2}{s}$$

The values above were considered to be constant, and were derived using the physical properties of carbon steel at 478 K, along with the cross sectional area and perimeter of the rod, and an assumed convective heat transfer coefficient. The specific values used are given below:

$$h = 5.68 \frac{W}{m^2 \cdot K} \quad \text{(Convective heat transfer coefficient)} \tag{3.16-3}$$

$$p = 0.08 \text{ m} \quad \text{(Rod perimeter)}$$

$$\rho c_p = 4.15 \times 10^6 \frac{J}{m^3 \cdot K} \quad \text{(Volumetric heat capacity)}$$

$$k = 48.4 \frac{W}{m \cdot K} \quad \text{(Thermal conductivity)}$$

$$A = 0.0005 \text{ m}^2 \quad \text{(Rod cross-sectional area)}$$

The series solution to the heat conduction problem stated in Equation (3.16-1) can be found in Carslaw and Jaeger[3.16-1] and is given by

$$T(x, t) = T_\infty + (T_0 - T_\infty)\frac{\cosh(Vx)}{\cosh\left(\frac{VL}{2}\right)} - 4(T_0 - T_\infty)\sum_{n=0}^{\infty} \frac{(-1)^n e^{-t(H + KP^2)} \cos(Px)}{N\left(1 + \frac{H}{P^2}\right)} \tag{3.16-4}$$

where (3.16-5)

$$V = \sqrt{\frac{H}{K}}, \quad N = 2n + 1, \quad P = \frac{N\pi}{L}.$$

The series solution in Equation (3.16-4) was calculated numerically at 61 nodes (heat structures) along the rod (heat structure geometry) using a 10,000-term expansion for comparison with the RELAP5-3D solution. The discontinuity in initial temperature at the heated ends (i.e., the jump from 300 K along the rod to 550 K at the ends) tends to cause a maximum error in the series solution at time zero. For the 10,000-term expansion, the initial temperature was 550 K at the two end nodes and 300 ± 0.07 K over the 59 interior nodes, which was considered to be sufficiently accurate for comparison with the RELAP5-3D solution.

3.16.3 Input Model Description

The RELAP5-3D model for the rod with heated ends was comprised of a heat structure geometry with 61 cells (heat structures). Cylindrical geometry was specified with an inner radius of 0.0, indicating that the rod is solid, and an outer radius of 0.0127 m.

As shown in Figure 3.16-1, the right surfaces of cells 1 and 61 were assigned a fixed temperature of 550 K. A convective heat transfer condition was specified for right surface nodes 2 through 60. The convective sink temperature T_∞ was defined to be 300 K. The convective heat transfer coefficient was fixed at 5.68 W/m^2-K, the volumetric heat capacity was specified as 4.15x10^6 J/m^3-K, and the thermal conductivity for the heat structure was defined as 48.4 W/m-K, values which are consistent with those defined in Equation (3.16-3).

Axial conduction was included in the model by specifying a conduction enclosure including the right sides of all 61 cells. Equation (3.15-6) in Section 3.15 relates the gap conductance of the conduction enclosure to the thermal conductivity of the heat structure. Figure 3.16-1 shows that the gap between axial temperature nodes is 0.05 m. Dividing the thermal conductivity by the gap between temperature nodes gives a gap conductance of 969 W/m^2-K, which was used in the conduction enclosure.

In the conduction enclosure, each node was defined to be in contact with the nodes to either side. For cylindrical geometry, the right side surface is the outer surface of the rod, and area factors are referenced based on this surface. The surface area for cell n is given by $A_n = 2\pi r dx$, where r is the radius of the rod and dx is the length of the cell. Axial heat transfer does not occur through this surface, but through the circular boundary between adjacent heat structure cells. The area of this surface is $A_c = \pi r^2$. The area factor is the ratio between these and is given by $A_f = A_c/A_n = r/(2dx) = 0.127$. The area factors are shown in Figure 3.16-1.

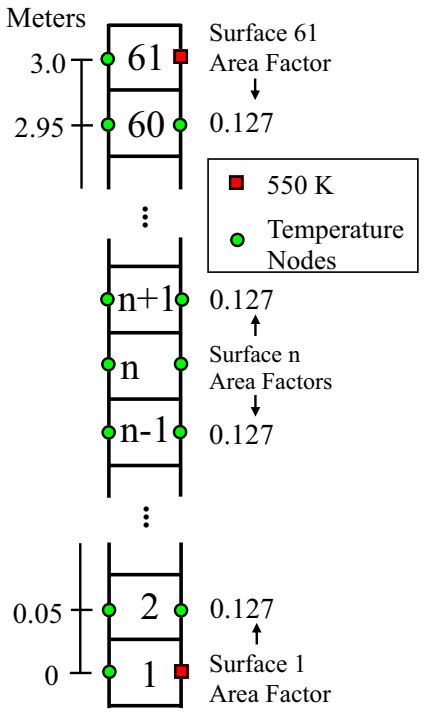

Figure 3.16-1. Rod area factors and end boundary conditions for 1-D conduction enclosure.

A minimal hydrodynamic model was used to support the conduction enclosure calculations, consisting of a single hydrodynamic volume connected to time-dependent volumes on either end. A time step size of 0.25 s was utilized for the calculation.

3.16.4 Data Comparisons and Results

The solution of the rod with heated ends and convection along the right boundary as modeled by Equation (3.16-1) is shown in Figure 3.16-2. In order to characterize the local error in the RELAP5-3D model solution, the RELAP5-3D solution was compared to the 10,000-term series solution. With T_R as the local (or point wise) RELAP5-3D temperature, and T_S as the local series solution temperature, the following formula for local percent error was used:

$$\text{Error} = 100\frac{T_R - T_S}{T_0 - T_\infty}. \qquad (3.16\text{-}6)$$

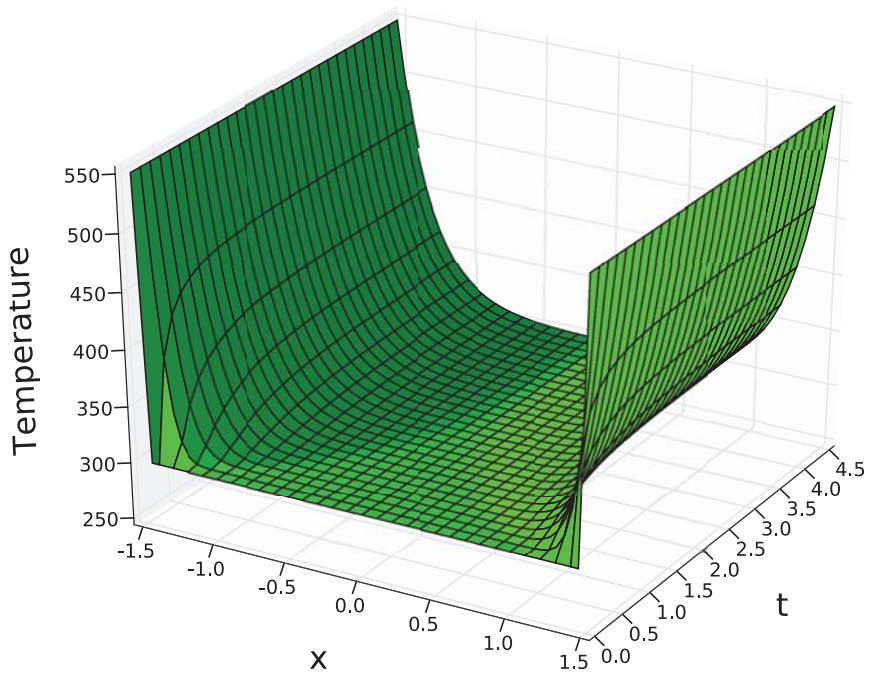

Figure 3.16-2. 1-D conduction enclosure axial temperature vs. time (in hours) based on a 10,000-term expansion of the series solution given in Equation (3.16-4).

Note that temperature is a function of time, so the local percent error defined in Equation (3.16-6) is also a function of time. The average percent error based on the error equation above is given by

$$\text{AvgError} = \frac{100}{T_0 - T_\infty} \frac{\int |T_R - T_S| dA}{\int dA}. \tag{3.16-7}$$

A plot of the local error is given in Figure 3.16-3. The plot is symmetric about the x axis and shows that the maximum error over the domain is approximately 0.3%, which equates to a local temperature difference of about 1 K.

3.16.5 Conclusions and Assessment Findings

Overall the agreement between the RELAP5-3D solution and the analytical solution is excellent. There is a small bias as seen in Figure 3.16-3, but this is on the order of 0.3%, which for most applications is negligible.

3.16.6 References

3.16-1. H. S. Carslaw and J. C. Jaeger, *Conduction of Heat in Solids*, Second Edition, Oxford University Press, 1959.

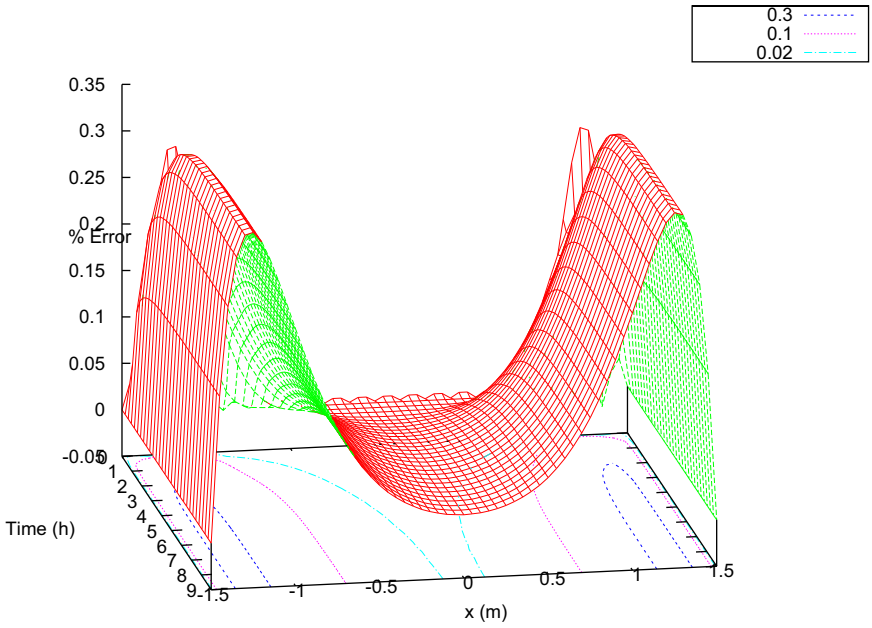

Figure 3.16-3. 1-D conduction enclosure local percent error for the rod with heated ends vs. position along the rod and time.

3.17 Conduction Enclosure: 2-D Transient Model

This assessment case explores the transient response of a 2-D model. It should be noted that this assessed version of RELAP5-3D contains an axial conduction model independent of the reflood model, and as such could be used in lieu of the axial conduction enclosure modeling assessed in this section.

For this assessment case, the nearly-implicit solution scheme was not utilized since the hydrodynamic model is immaterial. Therefore, only one set of results is presented.

3.17.1 Code Models Assessed

The ability of the code to model 2-D transient heat conduction between the surfaces of separate heat structures is assessed.

3.17.2 Problem Description

The model used was an initially hot (higher temperature T_0) two-dimensional plate with all boundaries held at the same fixed lower temperature T_∞. For the simple boundary conditions given, a transient analytical series solution exists which again can be derived using the method of separation of variables. The RELAP5-3D solution is compared to the transient analytical solution.

For the 2-D transient plate, the width was represented by 'a' and height represented by 'b'. For this model, the center of the plate was located at the origin. The following partial differential equation and boundary conditions were used to calculate the temperature response ($T[x, y, t]$) of the two-dimensional plate:

$$\frac{\partial T}{\partial t} = K\left(\frac{\partial^2 T}{\partial x^2} + \frac{\partial^2 T}{\partial y^2}\right) \tag{3.17-1}$$

$$T\left(-\frac{a}{2}, y, t\right) = T_\infty$$

$$T\left(\frac{a}{2}, y, t\right) = T_\infty$$

$$T\left(x, -\frac{b}{2}, t\right) = T_\infty$$

$$T\left(x, \frac{b}{2}, t\right) = T_\infty$$

$$T(x, y, 0) = T_0$$

The initial temperature of the plate (T_0) was chosen as 550 K. The boundary temperature (T_∞) was fixed at 300 K. The coefficient K was defined as follows:

$$K = \frac{k}{\rho c_p} = 1.17 \times 10^{-5} \quad \frac{m^2}{s}. \tag{3.17-2}$$

The values above were considered to be constant, and were derived using the physical properties of carbon steel at 478 K. The specific values used, along with the width and height of the plate, are given below:

$$k = 48.4 \frac{W}{m \cdot K} \quad \text{(Thermal Conductivity)} \tag{3.17-3}$$

$$\rho c_p = 4.15 \times 10^6 \frac{J}{m^3 \cdot K} \quad \text{(Volumetric Heat Capacity)}$$

$$a = 0.96 \text{ m} \quad \text{(Width)}$$

$$b = 1.0 \text{ m} \quad \text{(Height)}$$

$$T_0 = 550 \text{ K} \quad \text{(Initial Temperature)}$$

$$T_\infty = 300 \text{ K} \quad \text{(Boundary Temperature)}$$

The series solution of the heat conduction problem stated in Equation (3.17-1) can be found in Carslaw and Jaeger.[3.17-1] This can be written in the form

$$T(x, t) = T_\infty + 16(T_0 - T_\infty) \sum_{n=0}^{\infty} \frac{(-1)^n e^{-KP^2 t} \cos[P(x - a/2)]}{(2n+1)\pi} \sum_{m=0}^{\infty} \frac{(-1) e^{-KQ^2 t} \cos[Q(y - b/2)]}{(2m+1)\pi} \tag{3.17-4}$$

where

$$P = \frac{(2n+1)\pi}{a}, \; Q = \frac{(2m+1)\pi}{b}. \tag{3.17-5}$$

The series solution in Equation (3.17-4) was calculated numerically on a grid of 25 by 26 nodes on the surface of the plate using a 6,000-term expansion for comparison with the RELAP5-3D solution.

3.17.3 Input Model Description

The heat structure geometry of the RELAP5-3D model for the plate was identical to the steady state heated plate model (see Section 3.15). However, the material properties are different, as well as the boundary conditions used in the model. Boundary conditions are shown in Figure 3.17-1. The boundary of the plate had a fixed temperature of 300 K. The initial temperature of the plate was 550 K. The thermal conductivity for the heat structure was defined as 48.4 W/m-K. As in the steady state heated plate model,

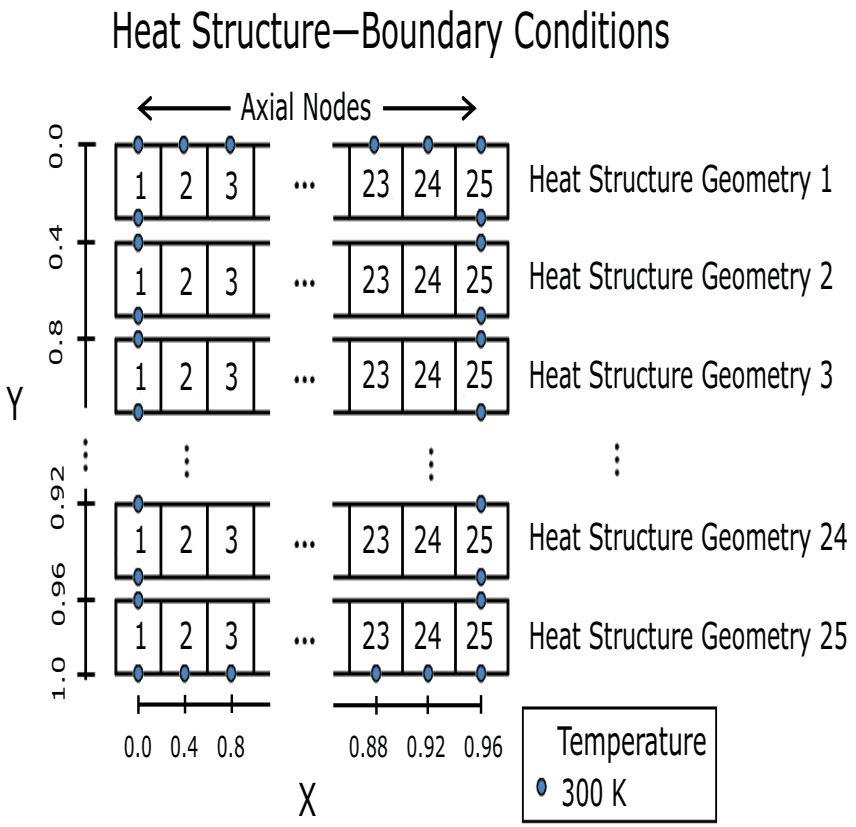

Figure 3.17-1. Boundary conditions for the transient heated plate model for 2-D conduction enclosure.

one conduction enclosure was used between each adjacent heat structure geometry to model heat transfer between the structures. The conduction enclosure also modeled the axial conduction within each heat structure geometry. The gap conductance for the conduction enclosures is related to the thermal conductivity of the heat structure by

$$\kappa = \frac{k}{dx}. \qquad (3.17\text{-}6)$$

Dividing the thermal conductivity (48.4 W/m-K) by the gap between axial thermal nodes (0.04 m) gives the gap conductance of 1,211.2 W/m^2-K. The area factors used for the plate are shown in Figure 3.17-2.

A minimal hydrodynamic model was used to support the conduction enclosure calculations, consisting of a single hydrodynamic volume connected to time-dependent volumes on either end. A time step size of 0.1 s was utilized for the calculation.

3.17.4 Data Comparisons and Results

Because the boundary of the plate is defined as a single fixed temperature of 300 K, the steady state for the plate is simply a uniform temperature of 300 K. Examining the differential equation in Equation (3.17-1) that governs the temperature response of the plate, it is clear that K, which is the ratio of

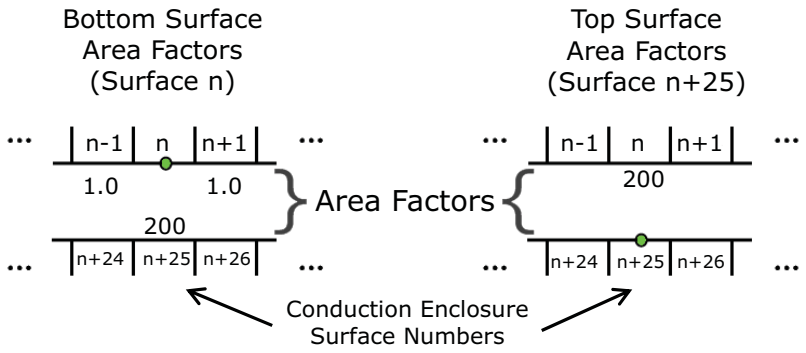

Figure 3.17-2. Area factors for the 2-D plate transient heat conduction model.

thermal conductance to volumetric heat capacity, governs the rate at which the temperature profile approaches steady state. Equation (3.17-2) shows that K is on the order of 10^{-5}, so the change in temperature is relatively slow. Plots of the transient plate temperature at hours one, two, and three are given in Figures 3.17-3, 3.17-4, and 3.17-5, respectively. As expected, the temperature gradually approaches the steady state temperature of 300 K. It takes seven hours for the temperature of the plate to go from being 250 K above the steady state temperature to within 1 K of the steady state temperature. Figure 3.17-6 shows the temperature of a node along the y axis and the analytical solution at the same location. From the figure, it is seen that there is a noticeable discrepancy between the analytical solution and the RELAP5-3D solution approximately over the first 3,000 s. However, this is relatively small and overall the agreement between the analytical solution and RELAP5-3D solution is quite good.

In order to characterize the local error in the RELAP5-3D model solution, the RELAP5-3D solution was compared to the 6,000-term series solution. The definition of percent error used was

$$\text{Error} = 100\frac{T_S - T_R}{T_0 - T_\infty}. \qquad (3.17\text{-}7)$$

The percent errors for times of one, two, and three hours are shown in Figures 3.17-7, 3.17-8, and 3.17-9, respectively.

3.17.5 Conclusions and Assessment Findings

Overall, the agreement between the RELAP5-3D solution and the analytical solution is excellent. At one hour, Figure 3.17-7 shows that the maximum error is less than 0.9%. By three hours, the error has dropped to less than 0.07% as seen in Figure 3.17-9. Note that the maximum error occurs near the center of the plate, so the near mid-plate temperature plots in Figure 3.17-6 provide a comparison of the RELAP5-3D vs. the analytical solution near where the maximum error occurs. As noted, there is a small discrepancy between the RELAP5-3D and analytical temperature responses over the first 3,000 s or so, but the overall agreement of the solutions is good.

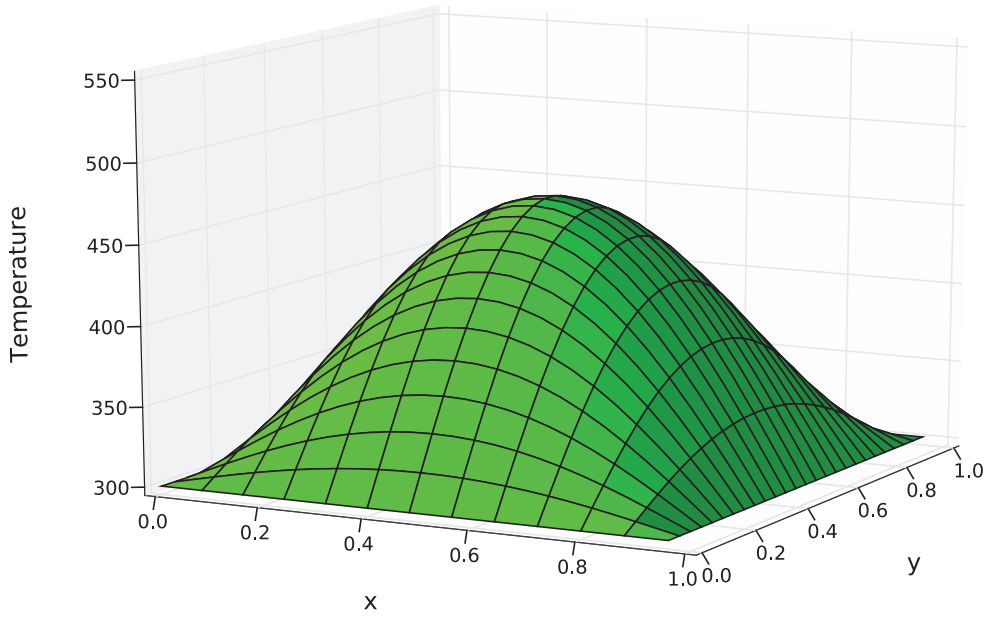

Figure 3.17-3. Plate temperature after one hour for 2-D conduction enclosure.

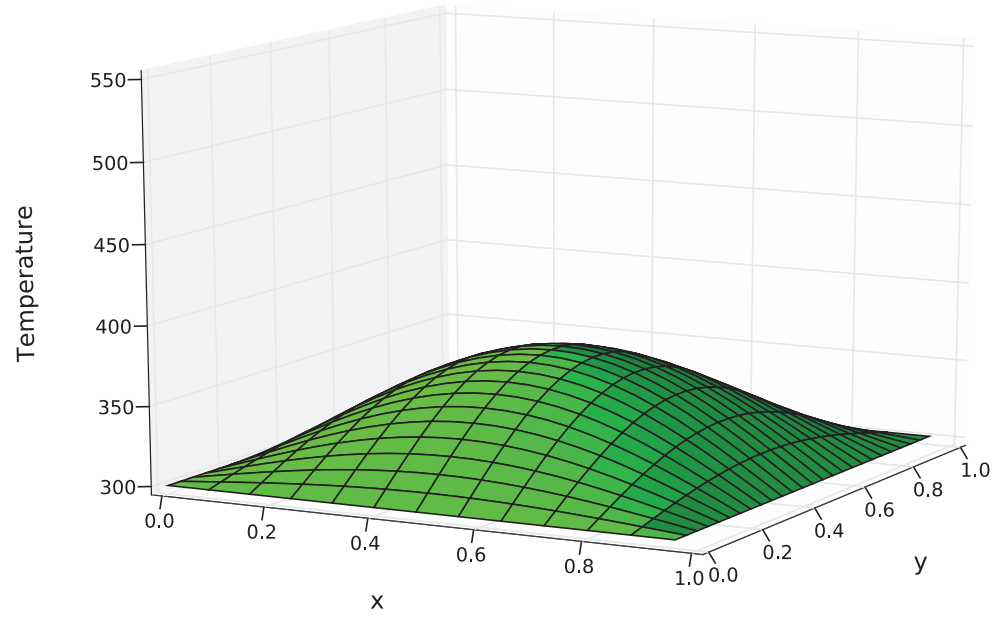

Figure 3.17-4. Plate temperature after two hours for 2-D conduction enclosure.

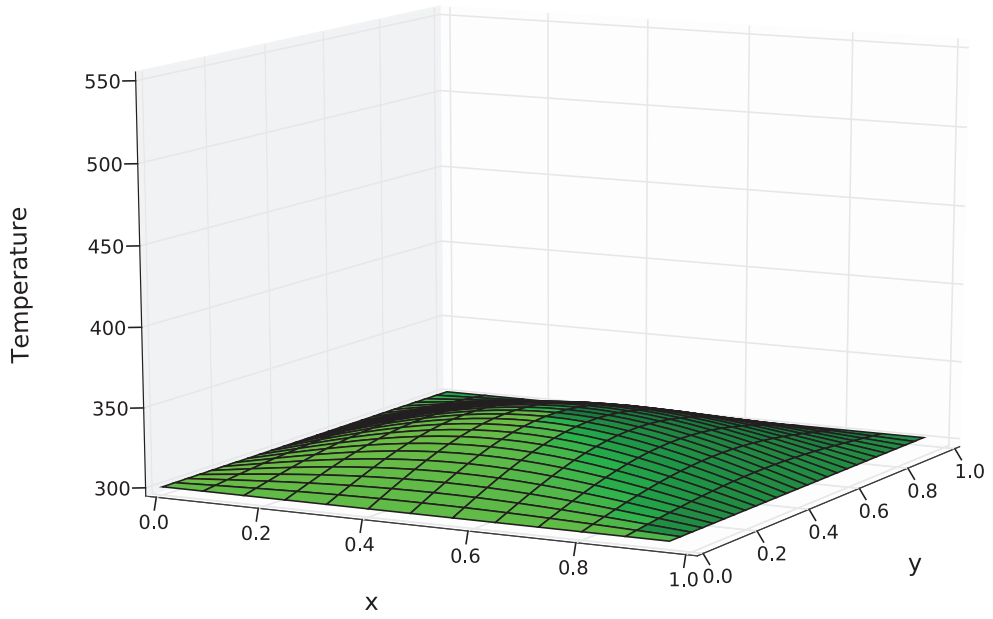

Figure 3.17-5. Plate temperature after three hours for 2-D conduction enclosure.

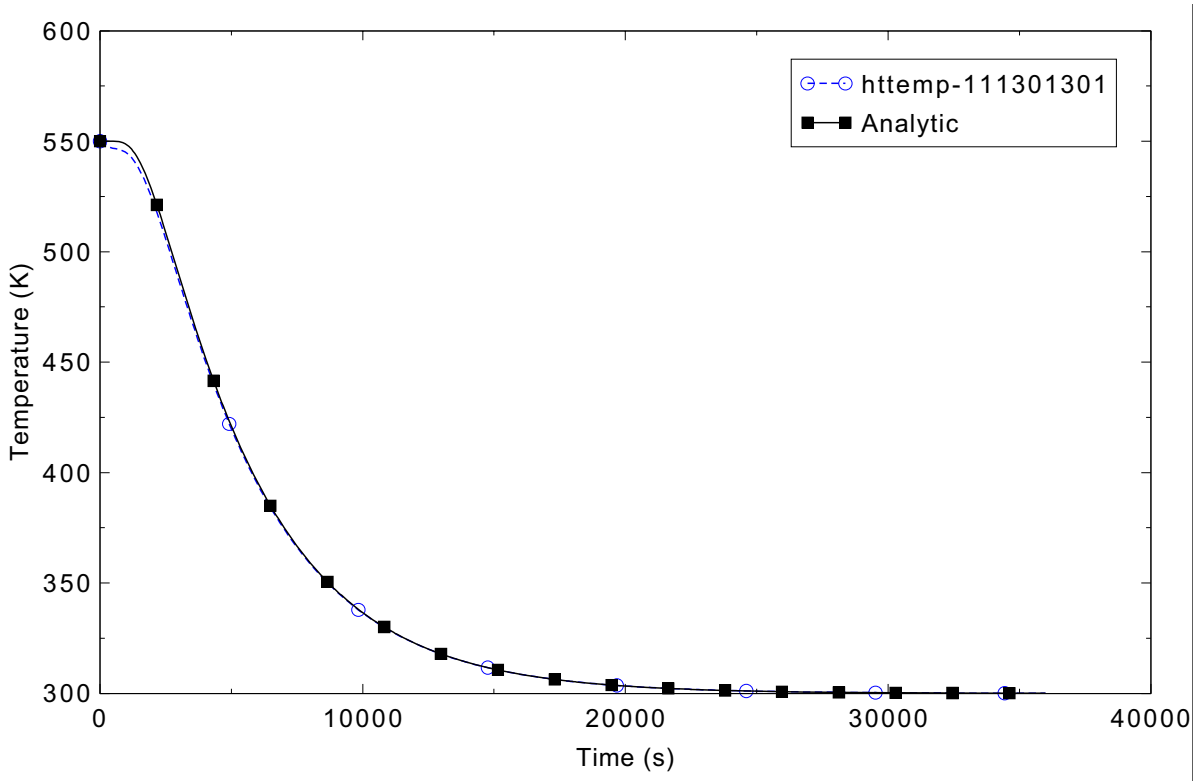

Figure 3.17-6. 2-D conduction enclosure temperature comparison with analytical solution. Temperature is taken at point x=0.2 m, y=0 m.

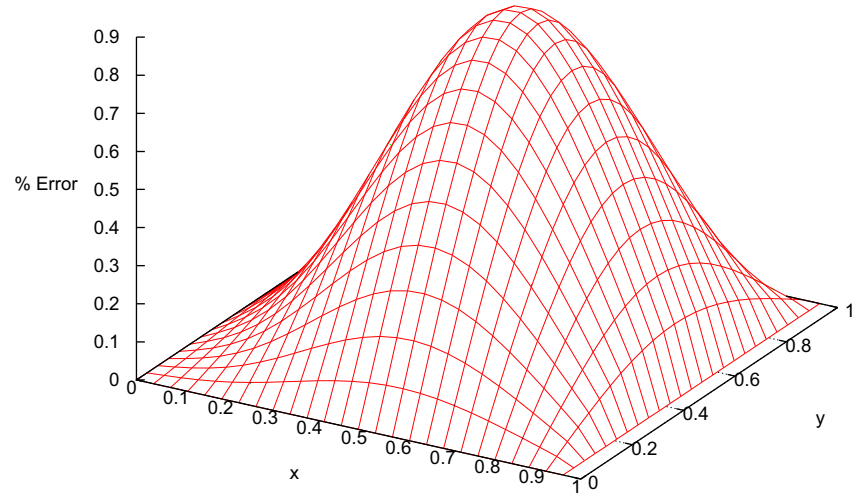

Figure 3.17-7. Local percent error of the transient temperature response for 2-D conduction enclosure at a time of one hour.

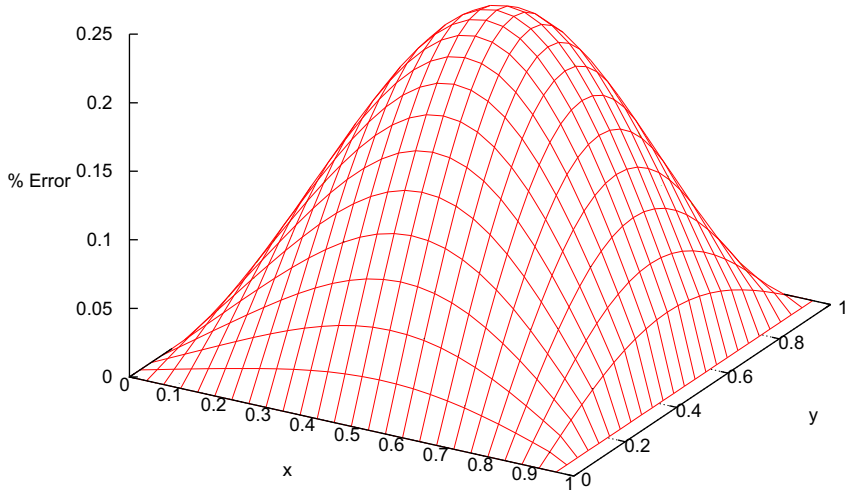

Figure 3.17-8. Local percent error of the transient temperature response for 2-D conduction enclosure at a time of two hours.

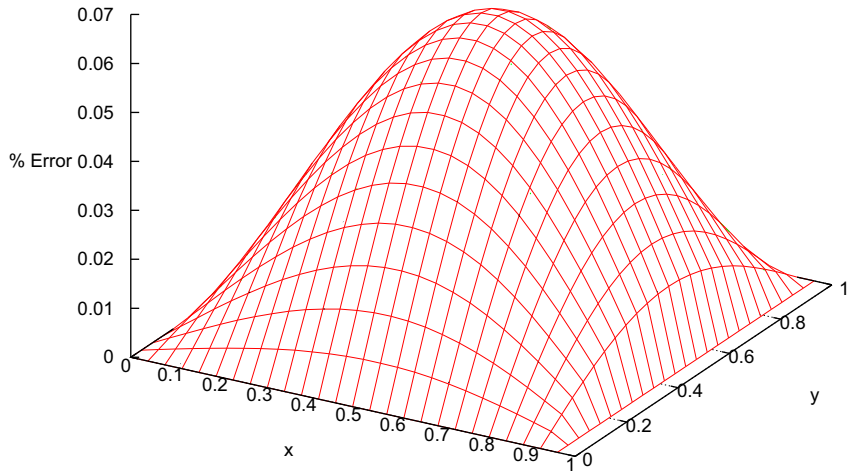

Figure 3.17-9. Local percent error of the transient temperature response for 2-D conduction enclosure at a time of three hours.

3.17.6 References

3.17-1. H. S. Carslaw and J. C. Jaeger, *Conduction of Heat in Solids*, Second Edition, Oxford University Press, 1959.

4. SEPARATE EFFECTS CASES

The separate effects cases compare RELAP5-3D code calculations with data from experiments that typically focused on one or a few physical phenomena. A total of 26 individual tests are included in this collection:

- Six addressing critical flow using the default (Ransom-Trapp) choking model
- Four addressing void profile or two-phase level
- Seven investigating CHF
- Two with reflood
- Two addressing CCFL
- Two investigating pressurizer behavior
- One addressing steady state steam generator performance
- One addressing accumulator injection
- One addressing jet pump performance.

A number of the experiments included assessment data for more than one phenomenon; for example, most experiments investigating CHF also have data on wall-to-fluid heat transfer. The list above provides the primary phenomenon for each test, although others are also addressed in the assessments described in the rest of this chapter.

4.1 Edwards-O'Brien Blowdown Test

The Edwards-O'Brien blowdown test[4.1-1] is a classic separate effects code benchmark problem and is identified as the Committee on the Safety of Nuclear Installations (CNSI) Standard Problem number 1 for performing validation of nuclear reactor safety computer codes.[4.1-2] The test was conducted to investigate and measure pressurized two-phase water blowdown behavior in a straight pipe geometry.

4.1.1 Code Models Assessed

The objective of performing this code benchmark is to validate the code capability to calculate basic rapid blowdown phenomena given a simple straight pipe geometry. The code assessment includes two predominant transient flow regimes and behavior. The initial part of the transient involves single-phase choked flow at the break location while the pipe undergoes rapid depressurization and propagation of a pressure wave along the pipe. As the pipe rapidly depressurizes, flashing occurs along the pipe, resulting in two-phase break flow until the pipe is depressurized and essentially empty.

4.1.2 Experiment Facility Description

A drawing of the Edwards-O'Brien test facility is shown in Figure 4.1-1.[4.1-2] The facility is an electrically-heated straight pipe, filled with water and pressurized. The sealed pipe section is 4.096 m long with a 73 mm inside diameter.[4.1-2] The pipe is instrumented with seven fast response pressure gauges mounted along the length of the pipe and seven temperature transducers with a response time of 15 ms. The pipe is also instrumented with two water density sensors to measure local void fraction during the test.

The initial conditions for this test are 7 MPa and 502 K. The test is initiated by breaking a glass rupture disk located in the end of the pipe, resulting in a break opening time of approximately 1 ms. The effective break flow area is reduced by approximately 13% from the full pipe diameter. Various publications have documented that this reduced break area was due to a small piece of the glass rupture disk remaining at the break location.

4.1.3 Input Model Description

The RELAP5-3D input model is described in Reference 4.1-3 and shown in Figure 4.1-2. The instrumented horizontal pipe section of the test facility is modeled explicitly using a pipe (Component 3) with 24 unequal-length cells and a total length of 4.09651 m. All of the pipe cells have a cross sectional flow area of 4.20269×10^{-3} m^2. The pipe is initialized with zero flow and is full of subcooled water with a non-uniform temperature distribution, which was taken from Reference 4.1-3 and is shown in Figure 4.1-3. The temperature data were taken from the gauge stations and linearly interpolated to obtain the initial temperatures in each cell. Initial pressure in the pipe component is established at 7.0 MPa. A time-dependent volume (Component 5) provides the user-specified atmospheric boundary condition adjacent to the pipe break location for the test simulation. A trip-controlled motor valve (Component 4) is used to connect the pipe to the boundary volume. The valve flow area is set at 3.65654×10^{-3} m^2 to model the effective area of the test rupture disk.

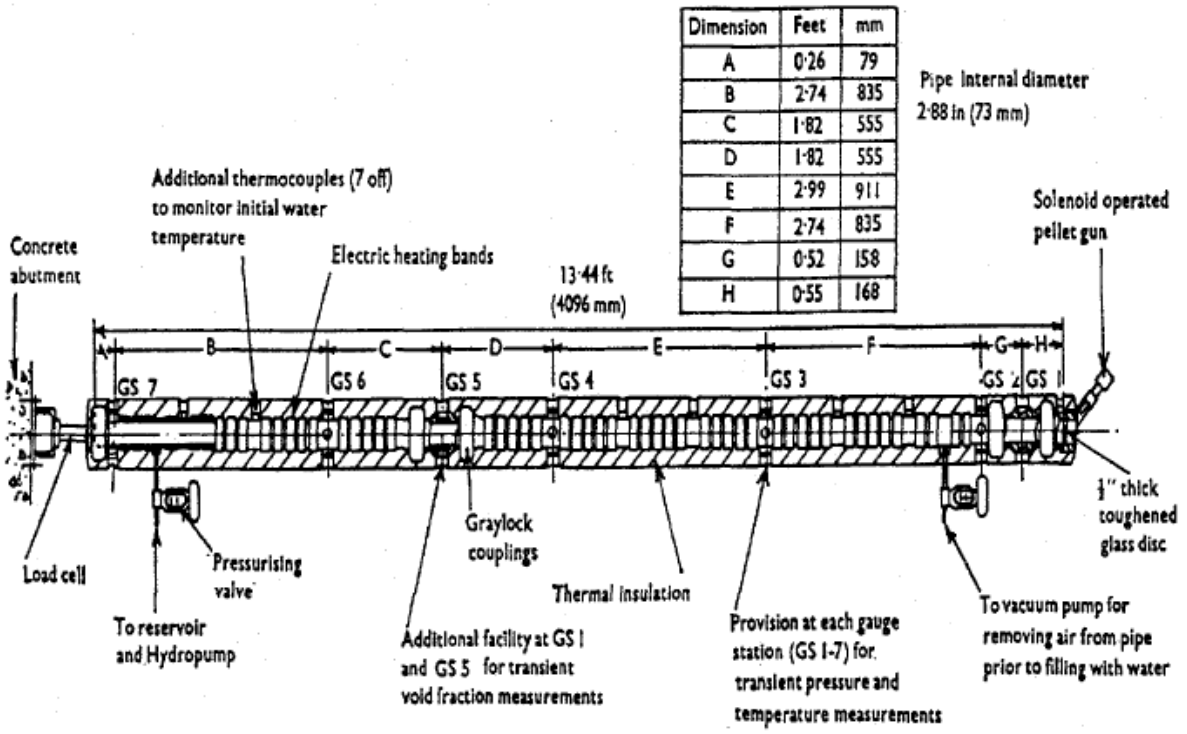

Figure 4.1-1. Edwards-O'Brien test facility.

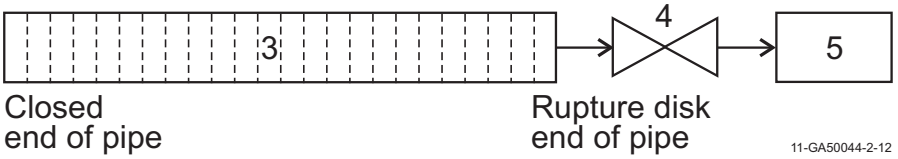

Figure 4.1-2. Diagram of the RELAP5-3D Edwards-O'Brien model.

4.1.4 Data Comparisons and Results

Transient runs were made with the RELAP5-3D code using either the semi-implicit solution option or the nearly-implicit solution option. The transient runs were initiated from a zero flow initial condition. The RELAP5-3D code runs were terminated at 0.5 s. The time step size used for both the semi-implicit and nearly-implicit advancement schemes was 1.0e-4 s.

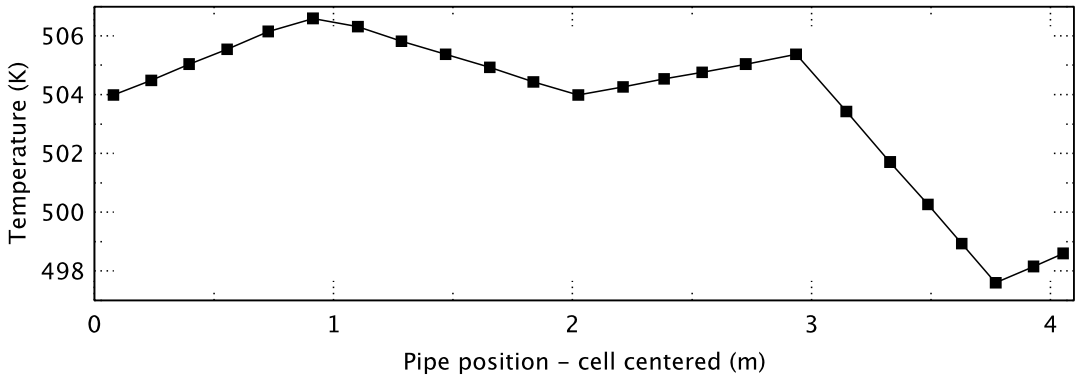

Figure 4.1-3. Non-uniform temperature distribution for Edwards-O'Brien model.

Pressure results from the two calculations are compared to the test data at position GS-5 in Figure 4.1-4. Note that the code-calculated pressure response results are essentially the same for either the semi-implicit or nearly-implicit solution scheme option. The RELAP5-3D calculated pressure response is in good agreement with the Edwards-O'Brien test pressure data, with only an initial undershoot immediately after break initiation and an over prediction of the pressure response in the 0.3 to 0.5 s time period.

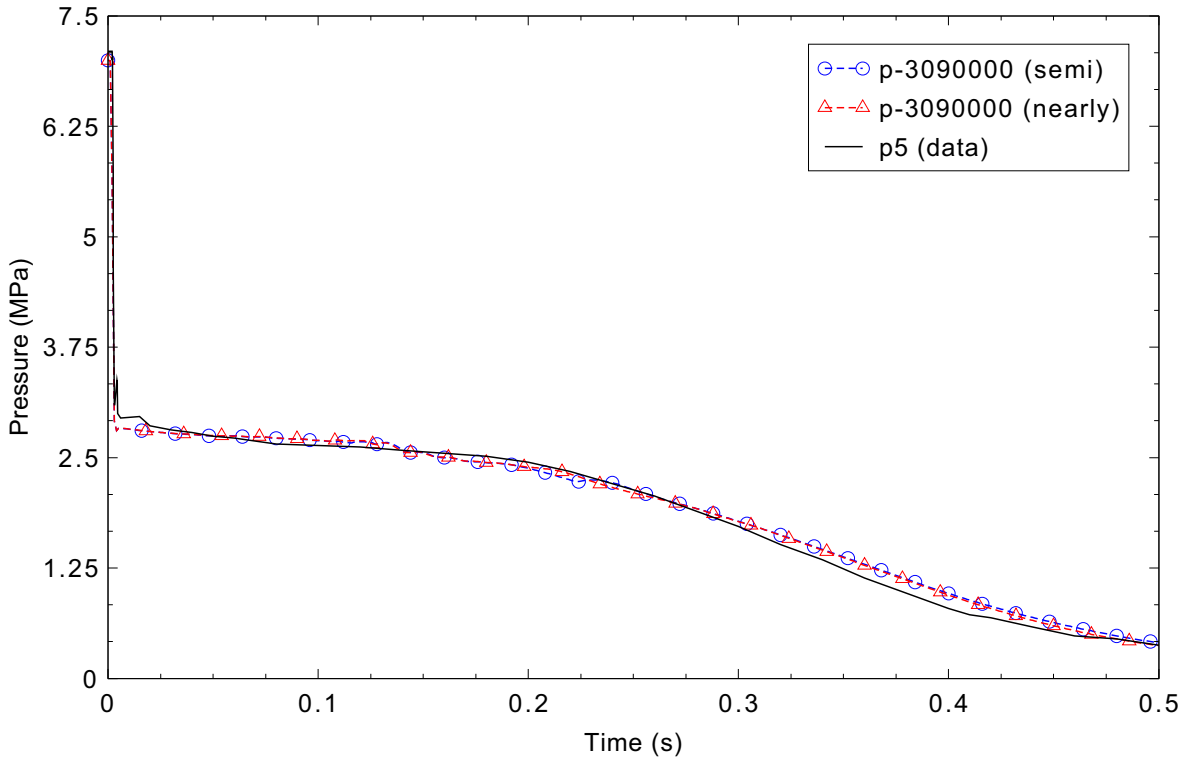

Figure 4.1-4. Measured and calculated pressures for the Edwards-O'Brien blowdown test.

The RELAP5-3D calculated void fraction response is shown in Figure 4.1-5 in comparison to the Edwards-O'Brien test data at position GS-5. The calculated void fractions are in good agreement with the test data. The code-calculated response does not predict the oscillatory behavior shown in the test data in the 0.15 to 0.25 s time period. These void fraction oscillations are also not representative of the test pressure data. The RELAP5-3D code calculations under predict the void fraction in last half of the transient, which is consistent with the code calculations over predicting the pressure in the last half of the transient.

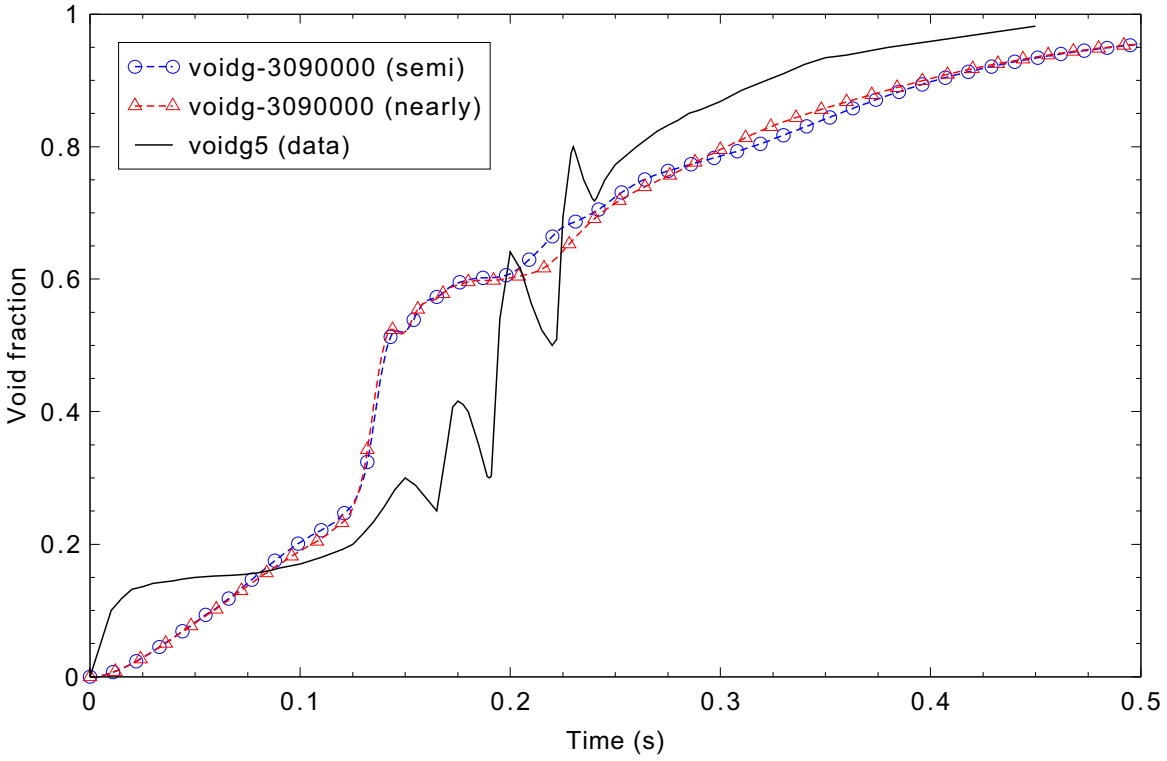

Figure 4.1-5. Measured and calculated void fractions for the Edwards-O'Brien blowdown test.

4.1.5 Conclusions and Assessment Findings

The RELAP5-3D code-calculated pressure results are in reasonable agreement with the Edwards-O'Brien test data. It should be noted that measured break flow data were not available for this test. However, the fact that the pressure is well-calculated indicates that the break flow is likely well-calculated also.

4.1.6 References

4.1-1. A. R. Edwards and T. P. O'Brien, "Studies of Phenomena Connected with the Depressurization of Water Reactors," *Journal of the British Nuclear Energy Society*, pp. 125-135, April 1970.

4.1-2. NEA/CSNI/R(97)3, *International Standard Problems (ISP), Brief Descriptions (1975 - 1997)*, Committee on the Safety of Nuclear Installations, OECD Nuclear Energy Agency, France, July 1997.

4.1-3. E. T. Tomlinson and D. L. Aumiller, “An Assessment of RELAP5-3D Using The Edwards-O’Brien Blowdown Problem,” B-T-3271, Bechtel Bettis, Inc., Bettis Atomic Power Laboratory, *1999 RELAP5 International Users Seminar, Park City, Utah, July 28-30, 1999*.

4.2 Marviken Critical Flow Test 21

Marviken Test 21 was one of the full-scale critical flow tests (CFTs) conducted in Sweden. The 27 experiments were conducted between mid-1977 and December 1979 as a multinational project at the Marviken Power Station. The tests were performed to obtain data for critical flow in short pipes of large diameter at subcooled and low-quality stagnation conditions.

A summary of the Marviken critical flow test program is paraphrased here. The tests were conducted by discharging water and a steam-water mixture from a full sized reactor vessel through a large diameter pipe that was connected to a test nozzle. The test nozzles had rounded entrances and were nominally 0.2, 0.3, or 0.5 m in diameter. The nozzle lengths ranged from 0.166 to 1.809 m. Most tests were conducted with a nominal initial steam dome pressure of 5 MPa with the water subcooled between 1 and 50 K with respect to the steam dome pressure. The vessel, discharge pipe, and nozzle were instrumented to determine the test behavior and to provide a basis for evaluating the stagnation conditions and mass fluxes at the nozzle inlet.

Marviken CFT 21 had a 0.5-meter diameter test nozzle with a length-to-diameter ratio of 1.5. The initial steam dome pressure was 4.94 MPa, and the initial subcooling at the lower vessel was 33°C (relative to the steam dome saturation temperature). The system needed 1.4 s to establish a stable rate of depressurization. Subcooled conditions were observed in the discharge pipe until 28 s. Saturated conditions were present in the discharge pipe from 28 s until the test was terminated at 60 s.

4.2.1 Code Models Assessed

Critical Flow Test 21 (CFT 21) assesses the subcooled choked flow model.

4.2.2 Experiment Facility Description

Marviken CFT 21 was the twenty-first test in a series of full-scale critical flow tests performed as a multinational project at the Marviken Power Station in Sweden. The test equipment consisted of four major components: pressure vessel, discharge pipe, test nozzle, and rupture disk assembly.

The pressure vessel was originally a part of the Marviken nuclear power plant. Of the original vessel internals, only the peripheral part of the core superstructure, the cylindrical wall, and the bottom of the moderator tank remained. Gratings were installed at three levels in the lower part of the vessel prior to the critical flow tests to prevent the formation of vortices which might enter the discharge pipe. The vessel had an inside diameter of 5.22 m and was 24.55 m high from the vessel bottom to the top of the top-cupola. The net available internal volume was 420 m^3.

The discharge pipe consisted of seven elements: axisymmetric inlet section, connection piece, two pipe spools, two instrumentation rings, and an isolation ball valve as shown in Figure 4.2-1. Internal diameters of the connection piece, pipe spools, and instrumentation rings were all 0.752 m. The flow path through the ball valve contained abrupt diameter changes of 0.038 m. The axial distance from the discharge pipe entrance to the end of the discharge pipe (nozzle entrance) is 6.3 m.

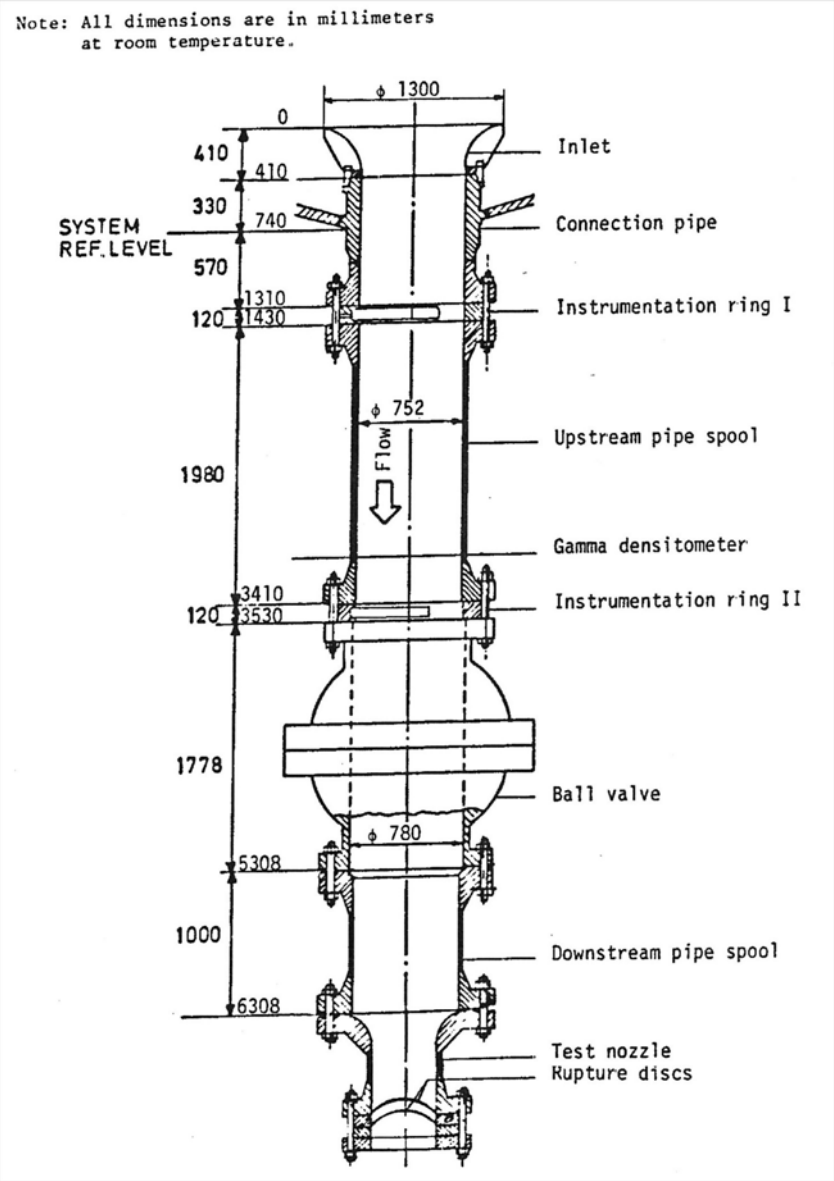

Figure 4.2-1. Marviken Critical Flow Test 21 discharge pipe.

The test nozzle was connected to the lower end of the discharge pipe; a generic nozzle is shown in Figure 4.2-2. The nozzle consisted of a rounded entrance section followed by a constant diameter test section, 0.5 m in diameter, 0.73 m long, giving a length-to-diameter ratio (L/D) of 1.5.

A rupture disk assembly was attached to the downstream end of the test nozzle. The assembly contained two identical rupture disks. The test was initiated by over pressurizing the volume between the two disks. This overpressure resulted in the failure of the outer disk, followed shortly by the failure of the

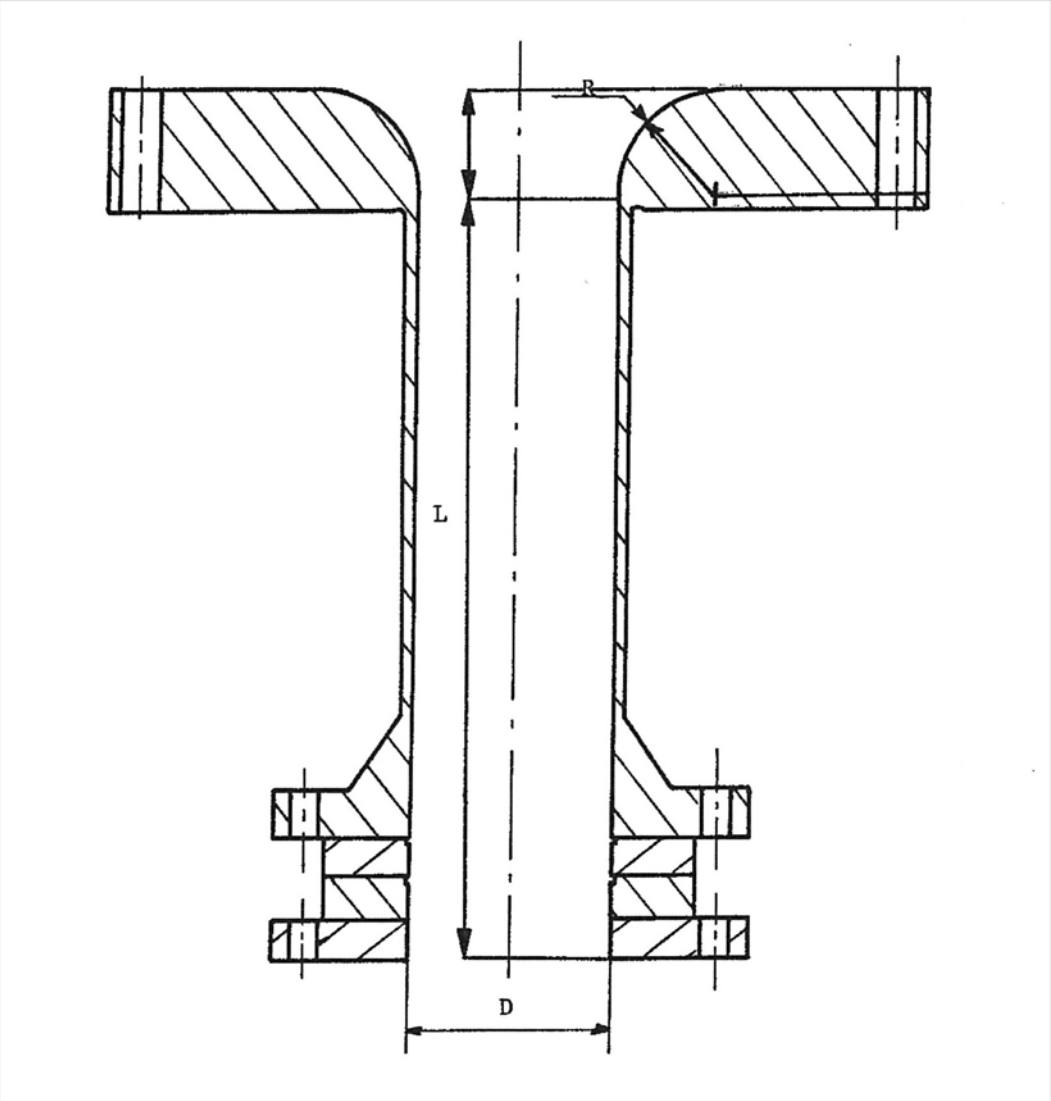

Figure 4.2-2. Marviken critical flow test nozzle.

inner disk. Failure of the disks was designed to occur along the their entire periphery so that they were completely removed from the nozzle exit.

4.2.3 Input Model Description

A nodalization diagram of the input model is shown in Figure 4.2-3. Note that in this analysis, the vessel is not modeled. This allows the analysis to focus on the flow in the discharge pipe. Time-dependent volume 901 represents the fluid conditions in the lower portion of the vessel. Boundary conditions at the vessel bottom were taken from the test data. The pressure history was set using data channel 001M106 and the temperature used an average of channels 001M521 and 001M402.

The discharge pipe (including the test nozzle) is represented by a pipe (Component 402) with seven cells, with the last cell representing the test nozzle volume. The third and fifth junctions (where the flow enters/exits the ball valve and experiences a change in flow area) of the discharge pipe use the abrupt area

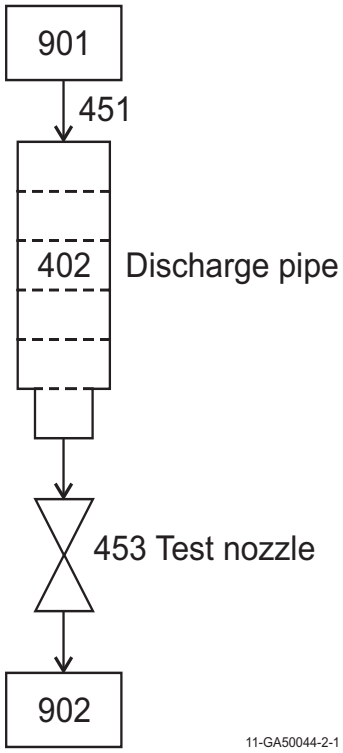

Figure 4.2-3. Marviken Critical Flow Test 21 nodalization diagram.

option. All other junctions use the smooth area option. The test nozzle exit was modeled as a single junction with the smooth area option. No special nodalization was used in the nozzle region. The test nozzle is set to have a diameter of 0.5 m and a length of 0.955 m (which includes the rounded entrance to the test nozzle). All loss coefficients are set to zero and the discharge coefficients are set to the default value of 1.0.

While the experiment was run for 60 s, the RELAP5 simulation was run to 30 s, where the conditions in the discharge pipe remain subcooled.

4.2.4 Data Comparisons and Results

Both the semi- and nearly-implicit solution scheme calculations were run with requested time steps of 0.001 s for the first 1.0 s and 0.10 s for the remainder of the transient. All initial boundary conditions and experiment data are documented in References 4.2-1 and 4.2-2, and the data shown in the plots came from the NRC Data Bank. Table 4.2-1 presents a summary of the initial conditions. Note that since the RELAP5-3D model does not include the vessel, several parameters are marked as not applicable (N/A).

The boundary conditions for the calculations are the pressure and temperature at the bottom of the vessel; these are presented in Figures 4.2-4 and 4.2-5, respectively.

The mass flow rates through the test nozzle are shown in Figure 4.2-6. The experiment mass flow rate was computed using three different methods: the steam dome depressurization method, the vessel mass inventory method, and the pitot-static method. The steam dome depressurization method was applied only

Table 4.2-1. Marviken Critical Flow Test 21 initial conditions.

Parameter	Experiment Data	RELAP5-3D
Steam dome pressure (MPa)	4.94	N/A
Saturation temperature (K)	536	N/A
Degree of nominal subcooling in the lower vessel relative to steam dome saturation temperature (K)	33	N/A
Minimum fluid temperature in vessel (K)	503	503
Initial temperature conditions in the discharge pipe (K)	457 to 503	475
Atmospheric pressure (kPa)	99.75	99.75

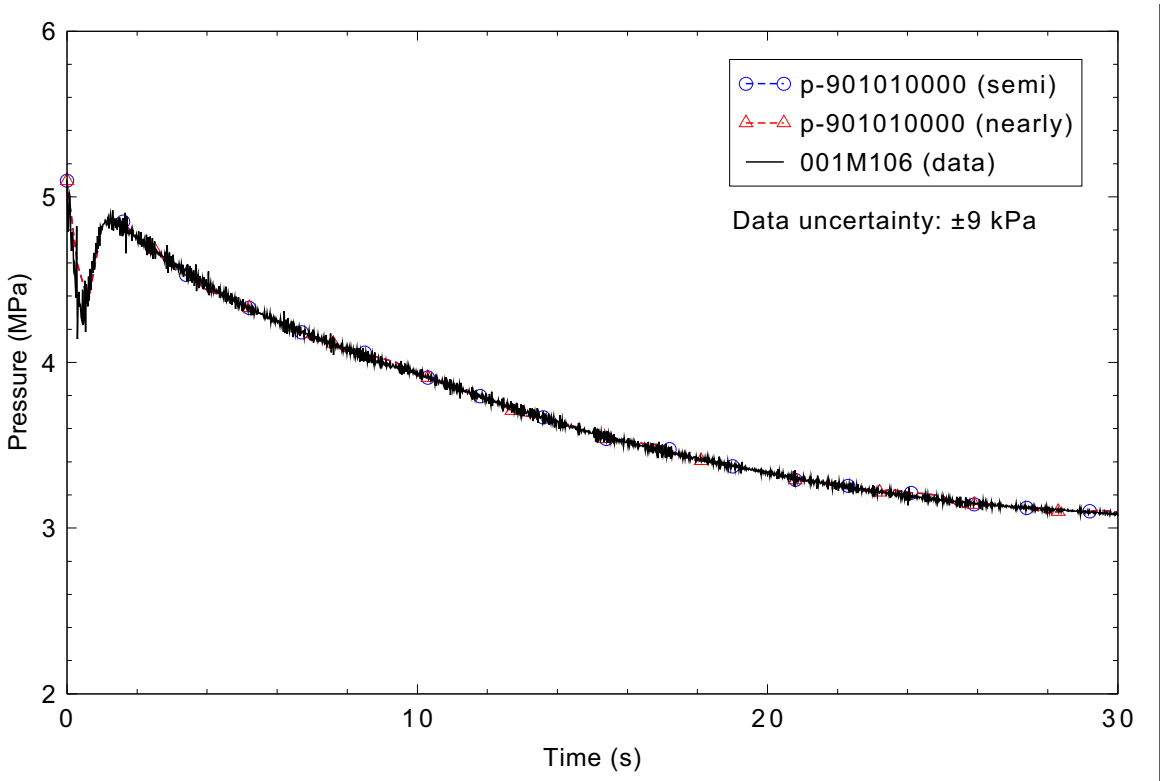

Figure 4.2-4. Marviken CFT 21 pressure at vessel bottom (boundary condition).

for the first 0.5 s and was used to determine a maximum mass flow. The vessel mass inventory method did not give reasonable mass flow results over the first 5 s because of large pressure oscillations that occurred immediately after the initiation of the test. The experiment data indicate the maximum mass flow is anywhere from 10,996 to 12,763 kg/s depending upon whether an equilibrium expansion or an expansion with no condensation occurred. The error associated with this calculation is given as ±15%. The RELAP5-3D predicted peak maximum mass flows are 12,522 kg/s for the semi-implicit case and 12,530 kg/s for the nearly-implicit case. The mass flow rate over the first 15 s of the transient shows that RELAP5-3D is in excellent agreement with data; beyond that, RELAP5-3D under predicts the mass flow.

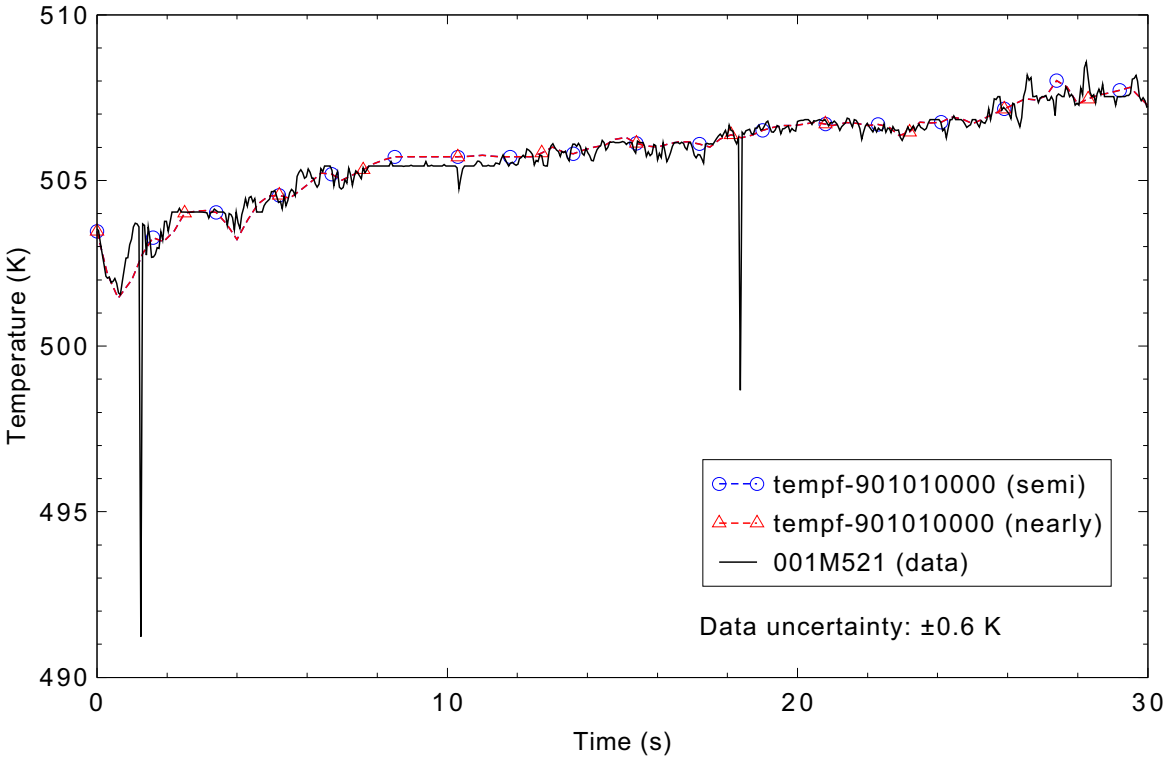

Figure 4.2-5. Marviken CFT 21 temperature at vessel bottom (boundary condition).

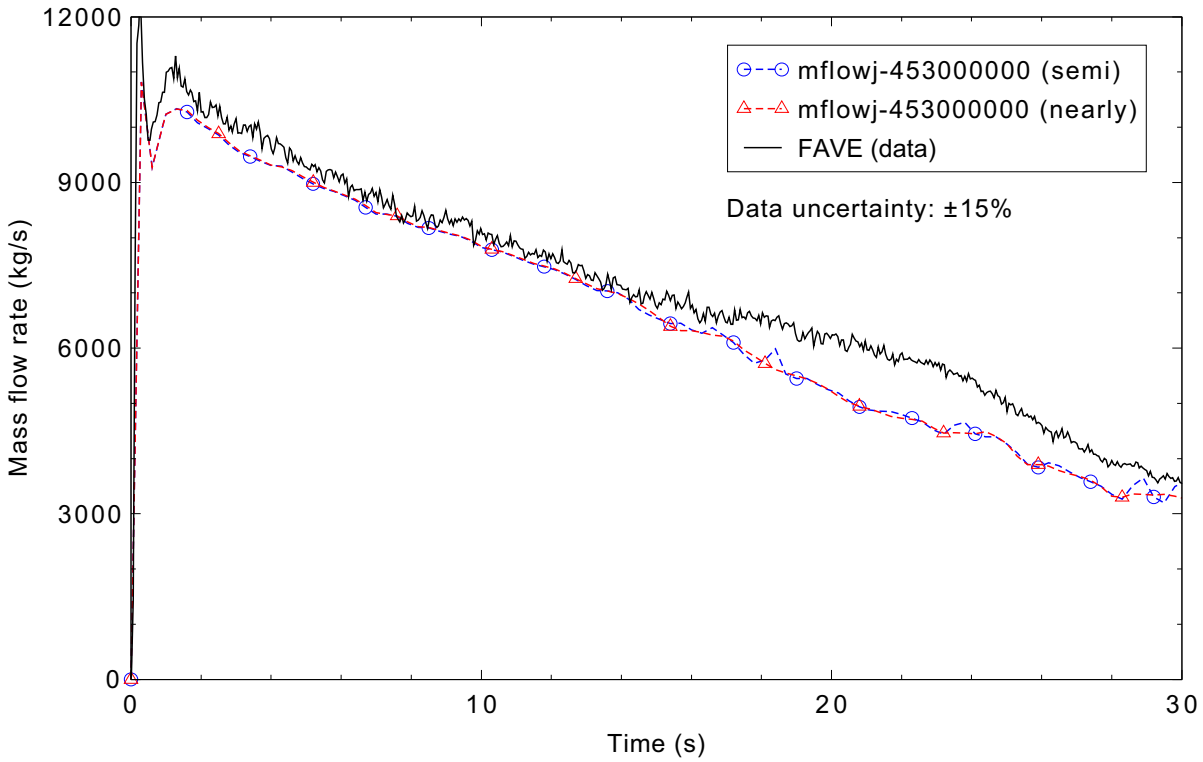

Figure 4.2-6. Measured and calculated mass flow rate for Marviken CFT 21.

A comparison of the mixture density in the exit pipe is shown in Figure 4.2-7. The RELAP5-3D code does a reasonable job predicting the density in the early portion of the transient, and does an excellent job later on when vapor generation begins. The initial drop in density predicted by RELAP5-3D is a result of the discharge pipe being initialized with a temperature of 475 K, which is 25 K lower than the specified inlet boundary condition. When the transient begins, the hotter water from the inlet fills the discharge pipe and causes the density to drop rapidly. It is noted that the uncertainty on the density measurement was ±50 kg/m^3, and the RELAP5-3D result is well within this large uncertainty.

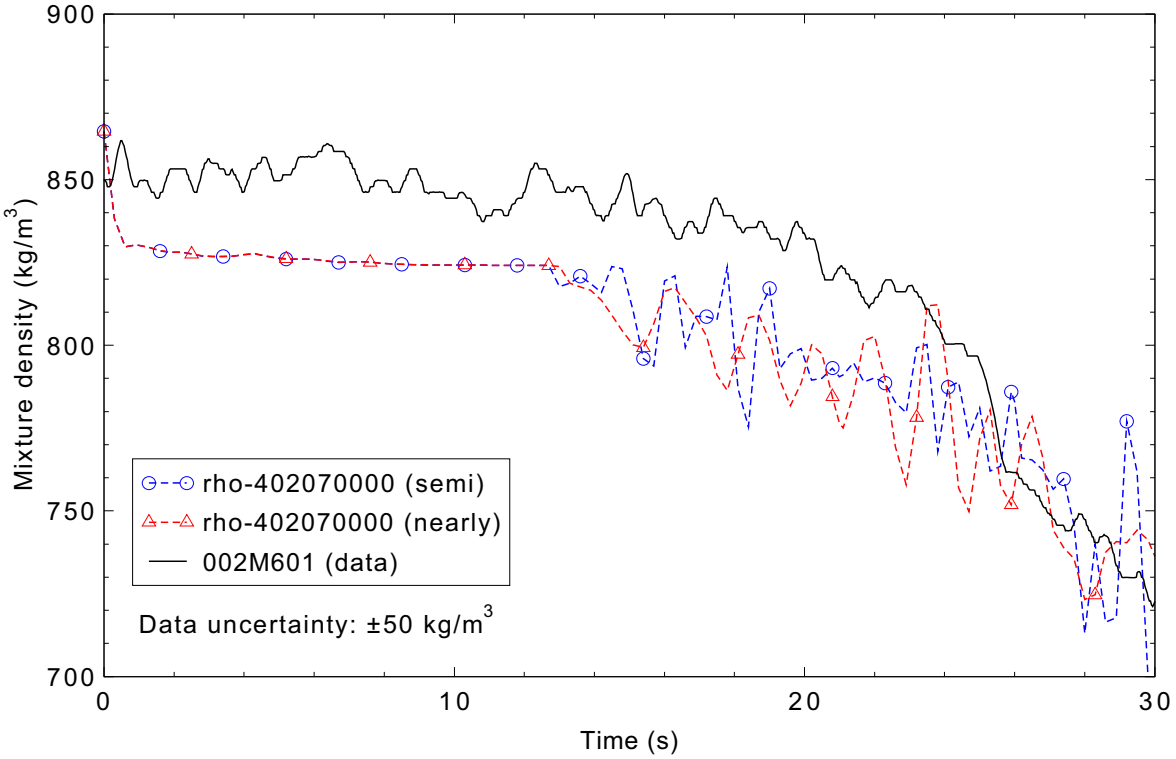

Figure 4.2-7. Measured and calculated mixture density in the discharge pipe for Marviken CFT 21.

4.2.5 Conclusions and Assessment Findings

The RELAP5-3D code was assessed against Marviken Critical Flow Test 21 and overall was found to be in reasonable agreement. The code was run with both the semi-implicit and nearly-implicit solution schemes, and the results for both were very similar.

The RELAP5-3D model includes only the discharge pipe and test nozzle. The mass flow rate over the first 15 s of the transient shows that RELAP5-3D is in excellent agreement with the data, and beyond that RELAP5-3D is in reasonable agreement with the data.

4.2.6 References

4.2-1. *The Marviken Full Scale Critical Flow Tests, Results From Test 21, Joint Reactor Safety Experiments in the Marviken Power Station Sweden*, MXC-221, September 1979.

4.2-2. *The Marviken Full Scale Critical Flow Tests, Summary Report, Joint Reactor Safety Experiments in the Marviken Power Station Sweden*, NUREG/CR-2671, MXC-301, May 1982.

4.2-3. O. Rosdahl and D. Caraher, *Assessment of RELAP5/MOD2 Against Critical Flow Data From Marviken Tests JIT 11 and CFT 21*, NUREG-IA-0007, September 1986.

4.3 Marviken Critical Flow Test 22

Marviken Test 22 was one of the full-scale critical flow tests (CFTs) conducted in Sweden. The 27 experiments were conducted between mid-1977 and December 1979 as a multinational project at the Marviken Power Station. The tests were performed to obtain data for critical flow in short pipes of large diameter at subcooled and low-quality stagnation conditions.

The Marviken tests were conducted by discharging water and a steam-water mixture from a full-sized reactor vessel through a large diameter pipe that was connected to a test nozzle. The test nozzles had rounded entrances and were nominally 0.2, 0.3, or 0.5 m in diameter. The nozzle lengths ranged from 0.166 to 1.809 m. Most tests were conducted with a nominal initial steam dome pressure of 5 MPa with the water subcooled between 1 and 50 K with respect to the steam dome pressure. The vessel, discharge pipe, and nozzle were instrumented to determine the test behavior and to provide a basis for evaluating the stagnation conditions and mass fluxes at the nozzle inlet.

Marviken CFT 22 had a 0.5-m diameter test nozzle with a length-to-diameter ratio of 1.5. The initial steam dome pressure was 4.93 MPa, and the initial subcooling at the nozzle entrance was 52 K. The system needed 1.2 s to establish a stable rate of depressurization. Saturated condition occurrences were recorded in the discharge pipe from 26 to 34 s. Saturated conditions were present everywhere in the discharge pipe from 34 s until the test was terminated at 48 s.

4.3.1 Code Models Assessed

Marviken Critical Flow Test 22 assesses the subcooled and saturated choked flow models.

4.3.2 Experiment Facility Description

Marviken CFT 22 was the twenty-second test in a series of full-scale critical flow tests performed as a multinational project at the Marviken Power Station in Sweden. The test equipment consisted of four major components: pressure vessel, discharge pipe, test nozzle, and rupture disk assembly.

The pressure vessel was originally a part of the Marviken nuclear power plant. Of the original vessel internals, only the peripheral part of the core superstructure, the cylindrical wall, and the bottom of the moderator tank remained. Gratings were installed at three levels in the lower part of the vessel prior to the critical flow tests to prevent the formation of vortices which might enter the discharge pipe. The vessel had an inside diameter of 5.22 m and was 24.55 m high from the vessel bottom to the top of the top-cupola. The net available internal volume was 420 m^3. A diagram of the pressure vessel is shown in Figure 4.3-1.

The discharge pipe consisted of seven elements: axisymmetric inlet section, connection piece, two pipe spools, two instrumentation rings, and an isolation ball valve as shown in Figure 4.3-2. Internal diameters of the connection piece, pipe spools, and instrumentation rings were all 0.752 m. The flow path through the ball valve contained abrupt diameter changes of 0.038 m. The axial distance from the discharge pipe entrance to the end of the discharge pipe (nozzle entrance) is 6.3 m.

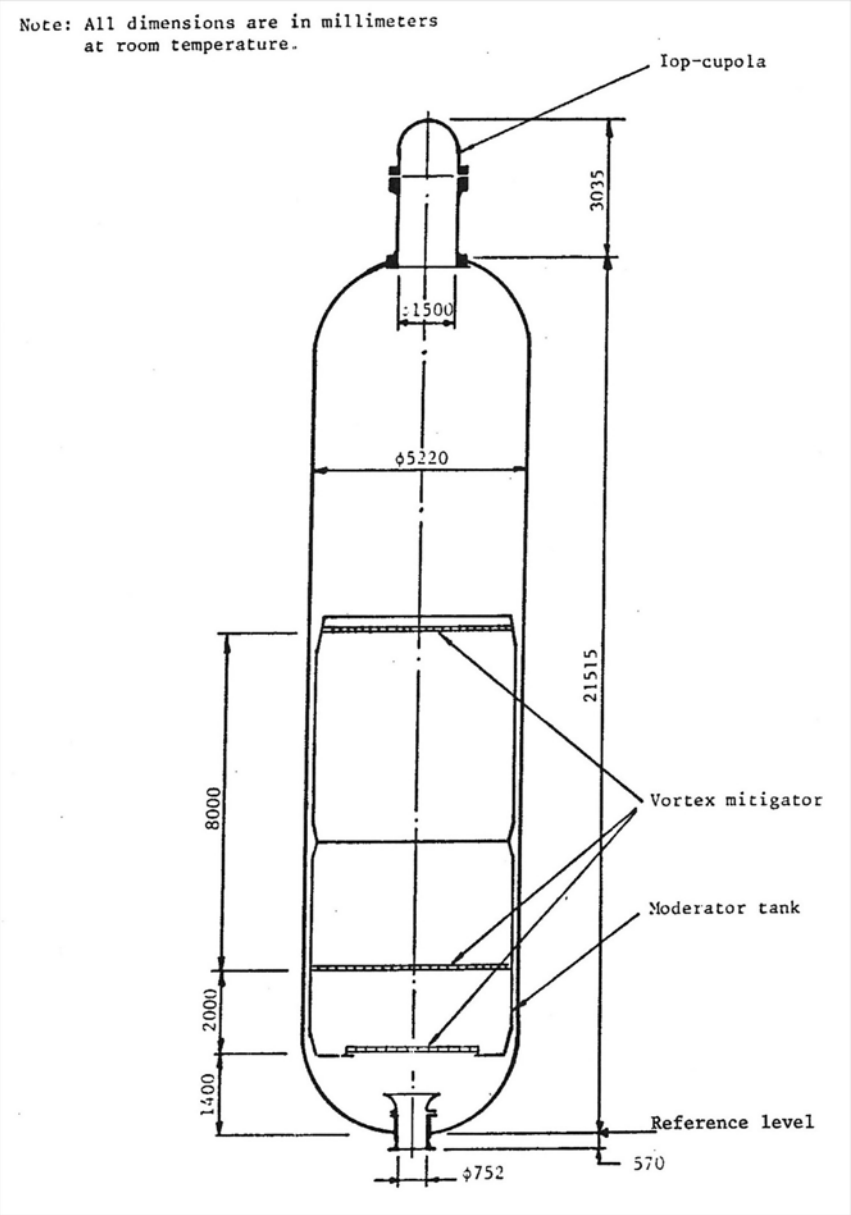

Figure 4.3-1. Marviken Critical Flow Test 22 pressure vessel.

The test nozzle was connected to the lower end of the discharge pipe; a generic nozzle is shown in Figure 4.3-3. The nozzle consisted of a rounded entrance section followed by a constant diameter test section, 0.5 m in diameter, 0.73 m long, giving a length-to-diameter ratio (L/D) of 1.5.

A rupture disk assembly was attached to the downstream end of the test nozzle. The assembly contained two identical rupture disks. The test was initiated by over pressurizing the volume between the two disks. This overpressure resulted in the failure of the outer disk, followed shortly by the failure of the inner disk. Failure of the disks was designed to occur along the their entire periphery so that they were completely removed from the nozzle exit.

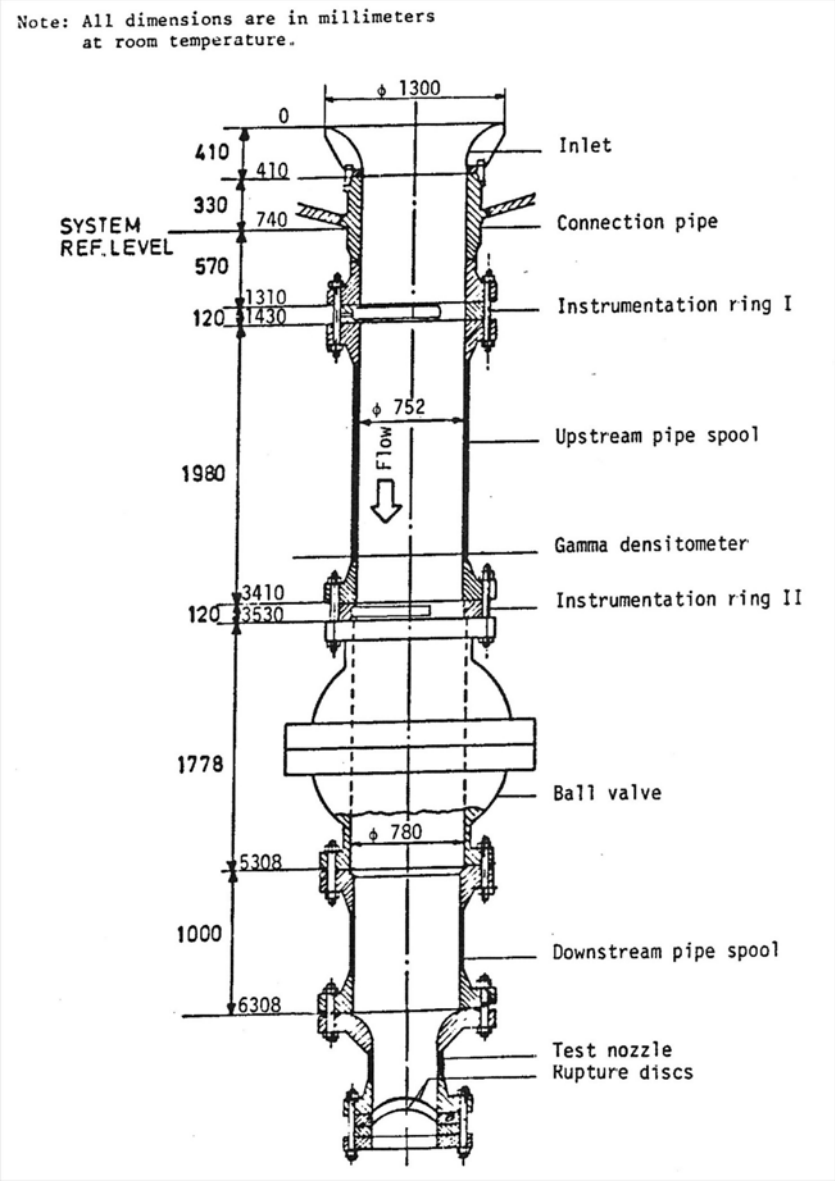

Figure 4.3-2. Marviken Critical Flow Test 22 discharge pipe, test nozzle, and rupture disk assembly.

4.3.3 Input Model Description

A nodalization diagram of the input model is shown in Figure 4.3-4. The vessel is represented by a pipe with 39 cells. This is subdivided as follows: one cell for the top cupola, one cell for the steam dome, 36 equal-length cells for the main portion of the vessel, and one cell for the bottom of the vessel which takes into account the standpipe entrance; the vessel volume below the standpipe entrance is not modeled. All junctions use the smooth area option. The total volume of the vessel is 420 m^3.

The discharge pipe (including the test nozzle) is represented by a pipe with seven cells, with the last cell representing the test nozzle volume. The third and fifth junctions (where the flow enters/exits the ball

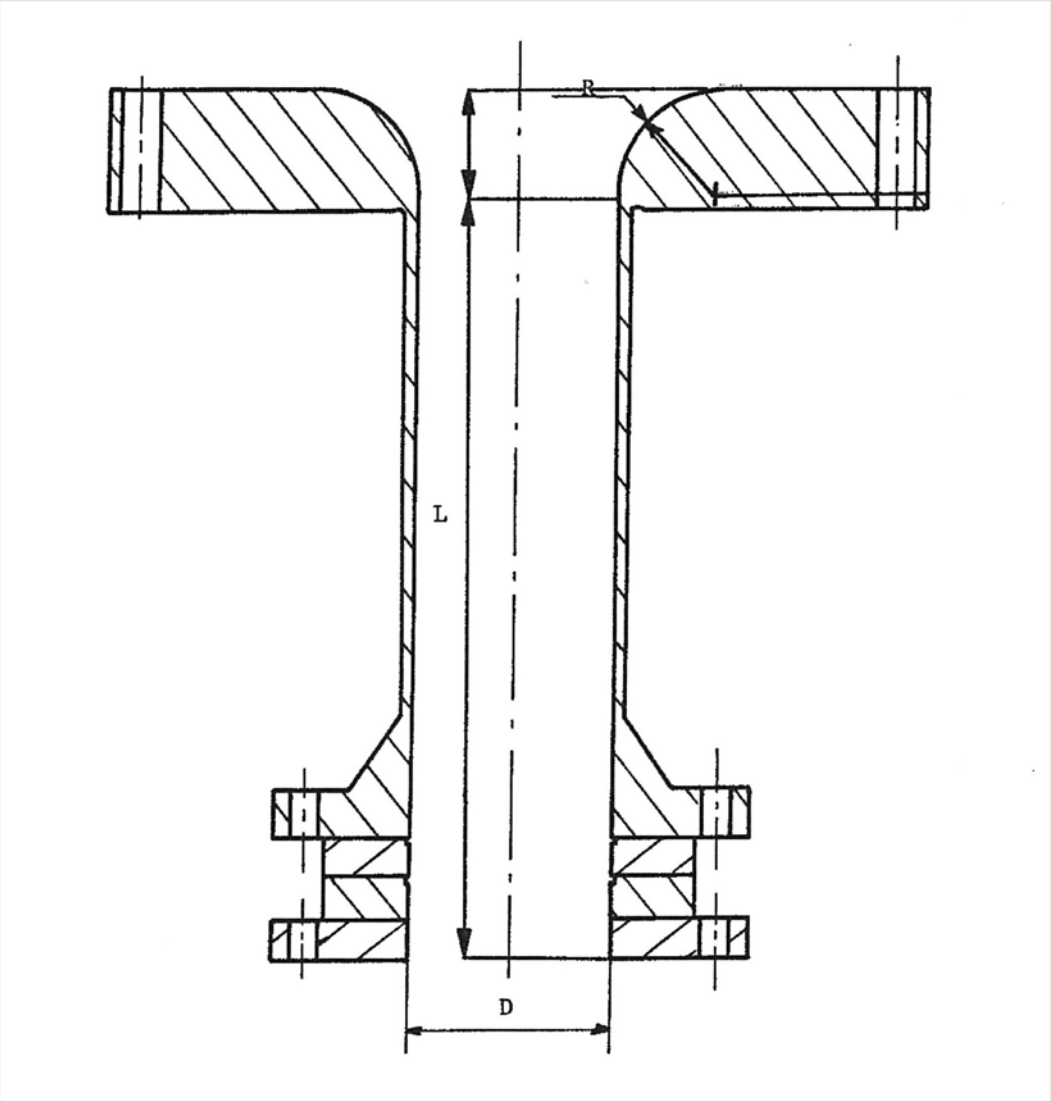

Figure 4.3-3. Marviken critical flow test nozzle.

valve and experiences a change in flow area) of the discharge pipe use the abrupt area option. All other junctions use the smooth area option. The test nozzle was modeled as a single junction with the smooth area option. No special nodalization was used in the nozzle region. The test nozzle is set to have a diameter of 0.5 m and a length of 0.73 m. All loss coefficients are set to zero and the discharge coefficients are set to the default value of 1.0.

4.3.4 Data Comparisons and Results

Both the semi- and nearly-implicit solution scheme calculations were run with requested time steps of 0.5 s for the first 5 s and 0.25 s for the remaining transient time. All initial boundary conditions and experiment data are documented in References 4.3-1 and 4.3-2, and the data shown in the plots came from the NRC Data Bank. Table 4.3-1 presents a summary of the initial conditions.

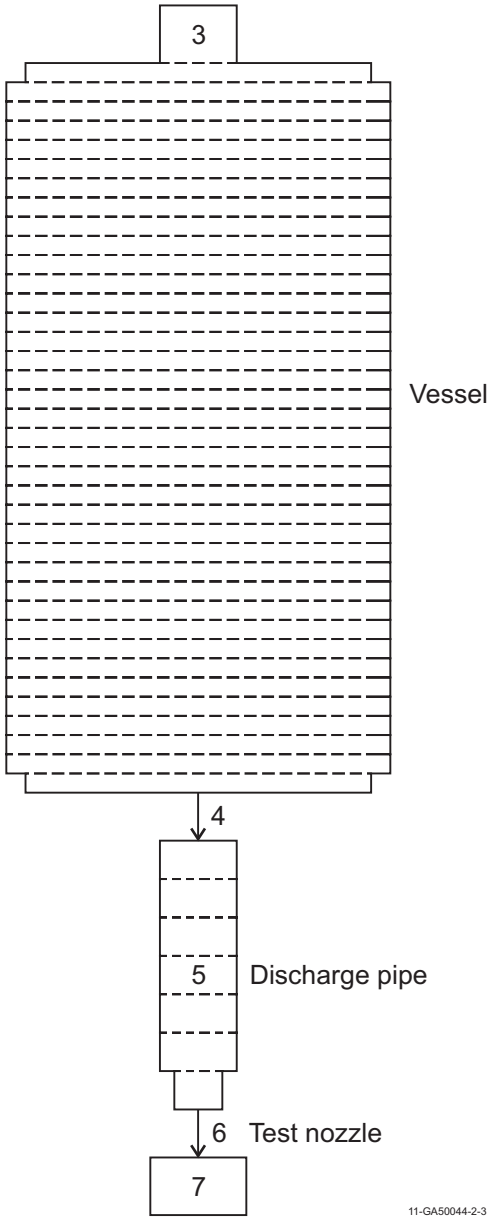

Figure 4.3-4. Marviken Critical Flow Test 22 nodalization diagram.

Upon the rupture disk bursting, the pressure in the vessel begins to decrease, as seen in Figure 4.3-5. The experiment pressure at the top of the vessel drops rapidly for 0.5 s, then increases for 0.5 s. This early pressure response is considered to be a non-equilibrium phase resulting from a delay of the steam production by the saturated water. Following this phase, a rapid depressurization is observed up to 26 s during subcooled flow, and then the depressurization rate slows when some of the flow entering the nozzle becomes saturated. The RELAP5-3D predictions do not match the initial pressure drop and recovery because the interfacial heat transfer in RELAP5-3D is too high, resulting in greater vapor generation which holds the pressure up. It would be possible to better fit the data if the interfacial heat transfer in RELAP5-3D was decreased in order to delay nucleation. Following the initial non-equilibrium phase, RELAP5-3D does a reasonable job of predicting the pressure response.

Table 4.3-1. Summary of initial conditions for Marviken Critical Flow Test 22.

Parameter	Experiment Data	RELAP5-3D
Steam dome pressure (MPa)	4.93	4.93
Saturation temperature (K)	536	536
Degree of nominal subcooling in the lower vessel relative to steam dome saturation temperature (K)	52	51
Minimum fluid temperature in vessel (K)	484	485
Fluid temperature at test nozzle (K)	441	441
Mass of water and steam (kg)	334,000	329,723
Atmospheric pressure (kPa)	101.7	101.7

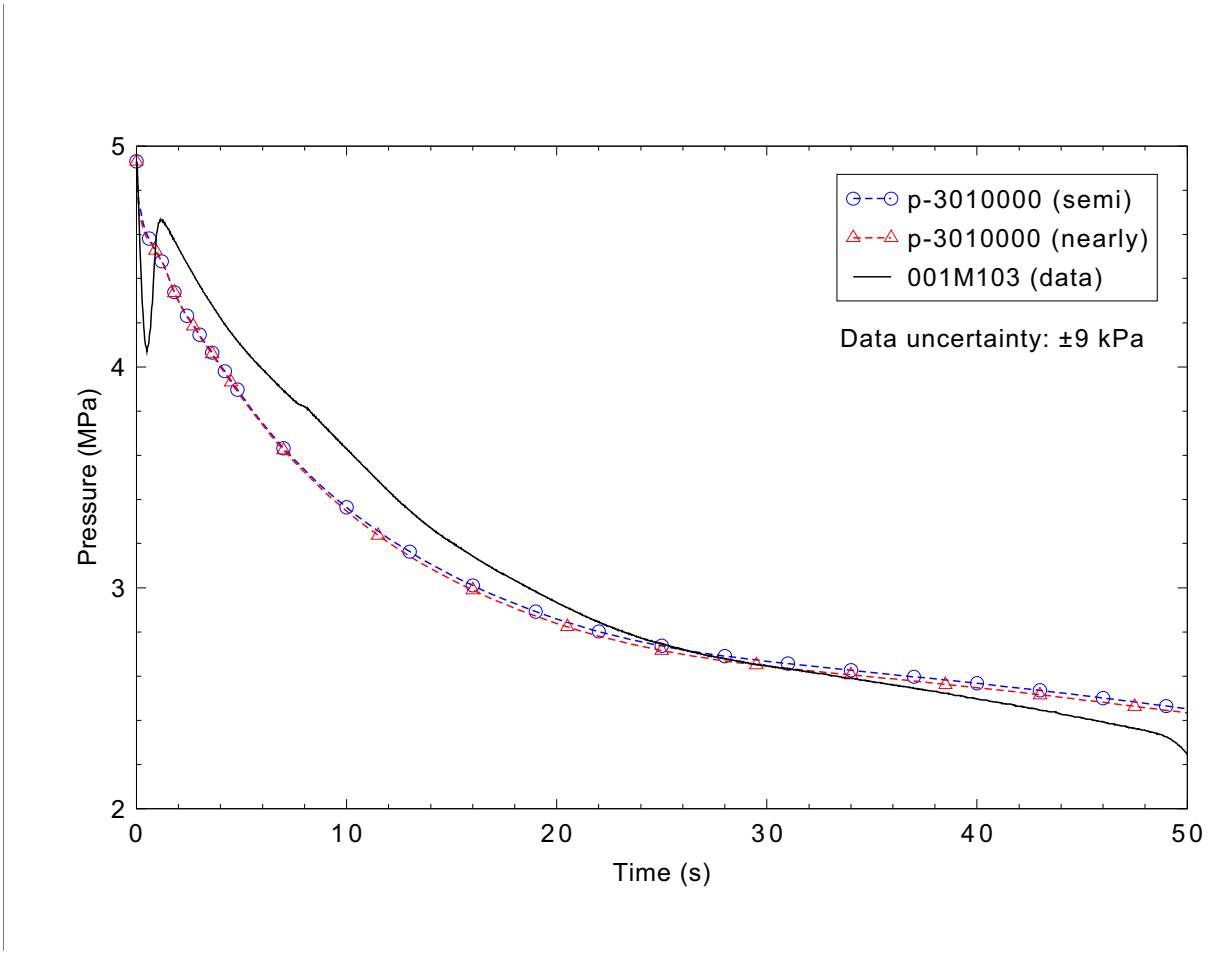

Figure 4.3-5. Measured and calculated vessel pressure for Marviken CFT 22.

The mass flow rates through the test nozzle are shown in Figure 4.3-6. The experiment mass flow rate was evaluated by three independent methods: the steam dome depressurization method, the vessel mass

inventory method, and the pitot-static method. The steam dome depressurization method was applied only for the first 0.5 s and was used to determine a maximum mass flow. The vessel mass inventory method did not give reasonable mass flow results over the first 5 s due to large pressure oscillations that occurred immediately after the initiation of the test. The experiment data indicate the maximum mass flow is anywhere from 13,548 to 15,708 kg/s depending upon whether an equilibrium expansion or an expansion with no condensation occurred. The error associated with this calculation is given as ±15%. The RELAP5-3D predicted peak maximum mass flows are 15,118 and 14,672 kg/s for the semi-implicit and nearly-implicit cases, respectively. The mass flow rate over the transient matches reasonably well between RELAP5-3D and the experiment data. The decrease in mass flow rate from 20 to 30 s was due to increased vapor generation in RELAP5-3D. At 34 s, the flow entering the nozzle became saturated and remained so through the end of the test. The mass flow measurements have an uncertainty of anywhere from ±2% to ±15% depending on which of the three methods was used.

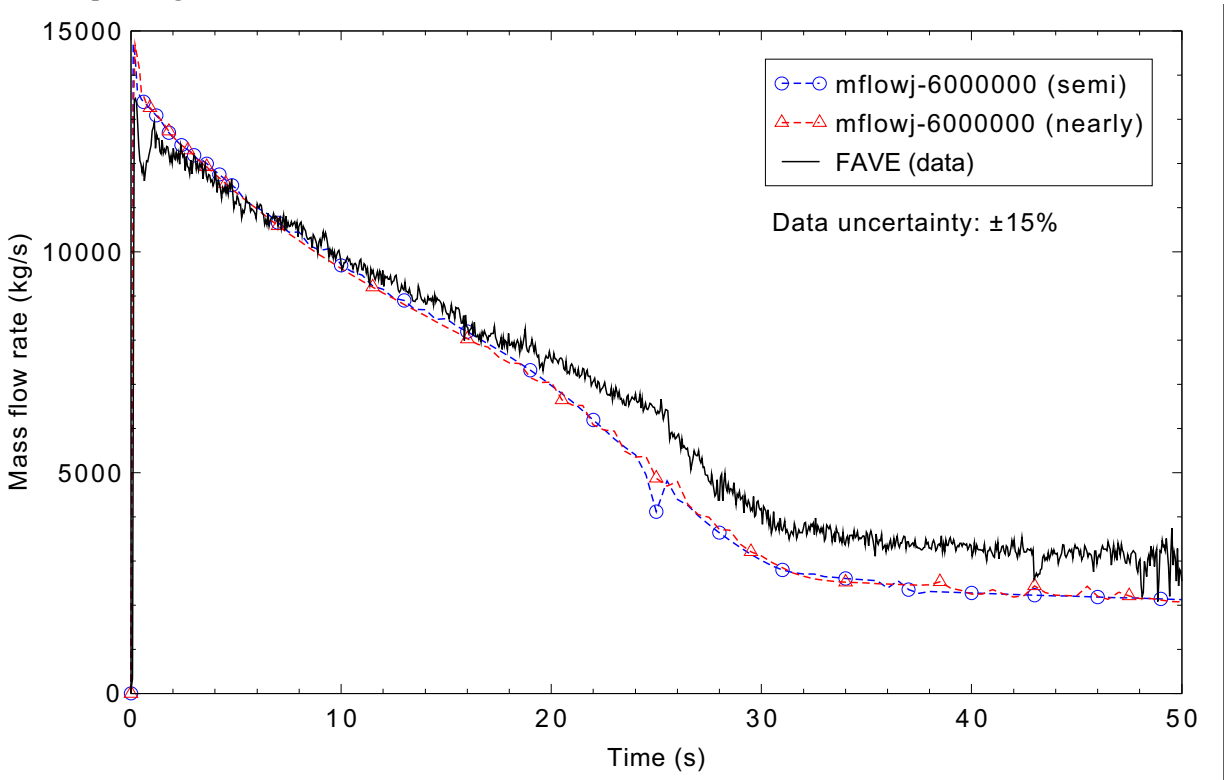

Figure 4.3-6. Measured and calculated mass flow rate for Marviken CFT 22.

A comparison of the temperature profile in the test vessel at 0 and 15 s are shown in Figures 4.3-7 and 4.3-8, respectively. Both calculated temperature profiles are in excellent agreement with the measured profiles.

A comparison of the mixture density in the exit pipe is shown in Figure 4.3-9. The code does a reasonable job predicting the density in the early portion of the transient. Beyond 34 s, the predicted vapor generation was greater than that measured, which resulted in the under prediction of the mixture density. The test ended at 48 s when steam entered the discharge pipe.

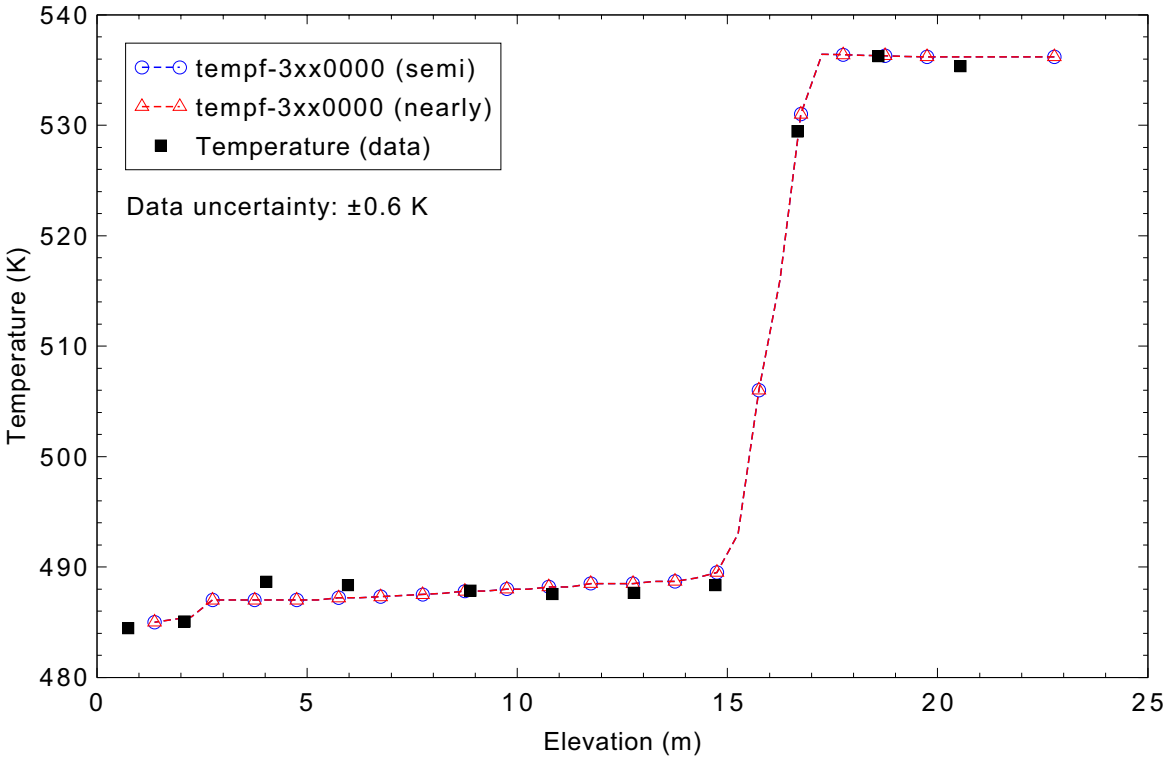

Figure 4.3-7. Measured and calculated temperature profile at 0 s for Marviken CFT 22.

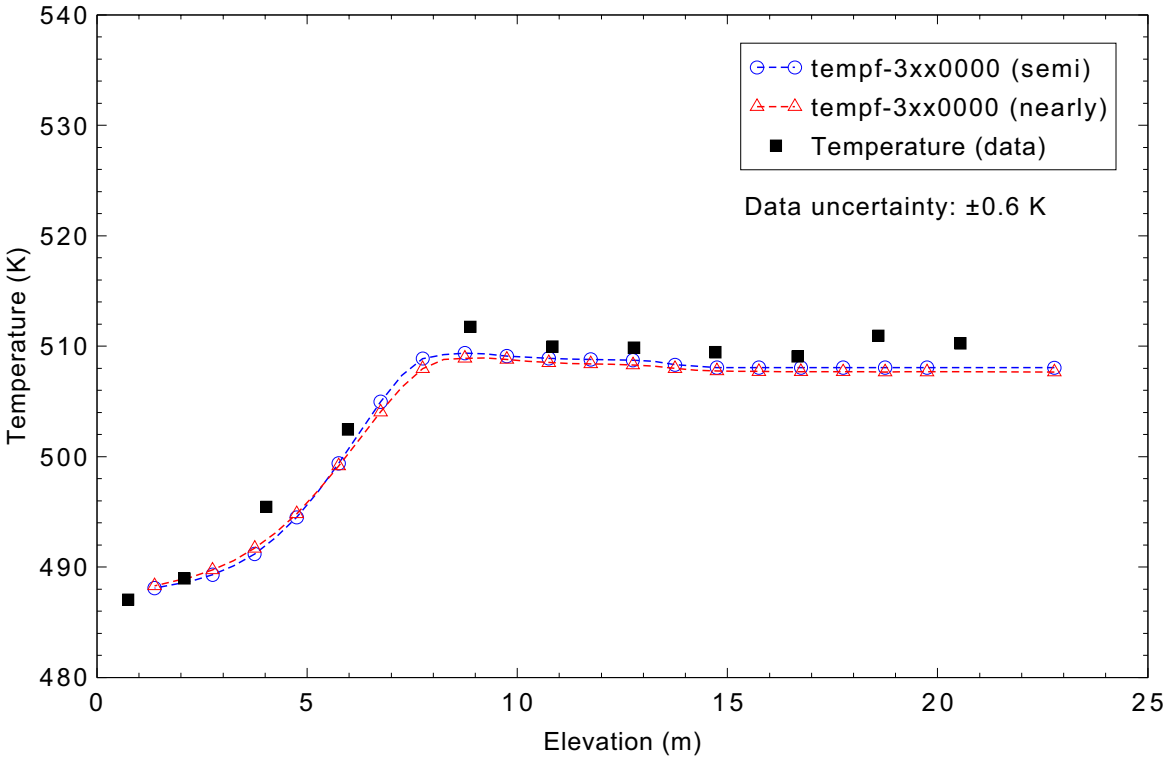

Figure 4.3-8. Measured and calculated temperature profile at 15 s for Marviken CFT 22.

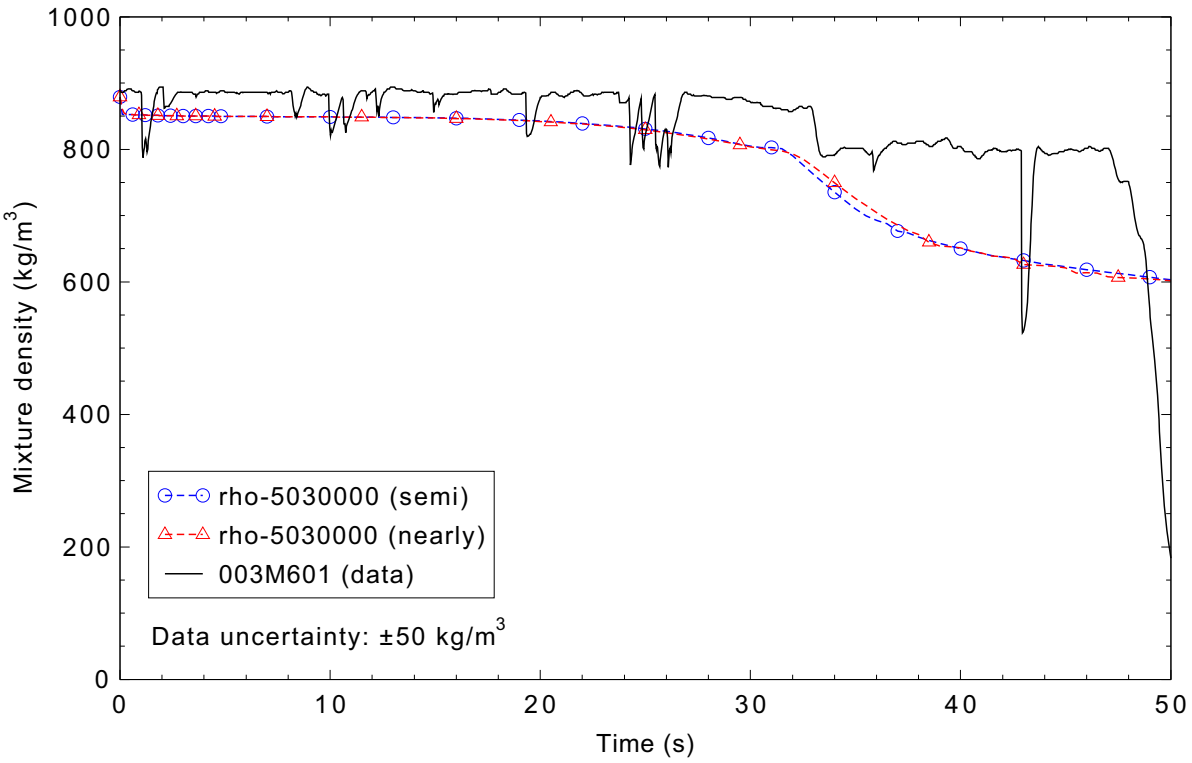

Figure 4.3-9. Measured and calculated mixture density in the discharge pipe for Marviken CFT 22.

4.3.5 Conclusions and Assessment Findings

The RELAP5-3D code was assessed against the Marviken Critical Flow Test 22 and overall was found to be in reasonable agreement. The code was run with both the semi-implicit and nearly-implicit solution schemes, and the results for both were very similar.

The RELAP5-3D code under predicted the vessel pressure in the early portion of the transient (1 to 27 s) and slightly over predicted the pressure during the remaining portion of the test. RELAP5-3D is judged to do a reasonable job predicting the vessel pressure. The predicted mass flow rate was in excellent agreement with the data until 20 s, and in reasonable agreement thereafter. The code did an excellent job predicting the temperature profile in the test vessel, and did a reasonable job predicting the mixture density.

4.3.6 References

4.3-1. *The Marviken Full Scale Critical Flow Tests, Results From Test 22, Joint Reactor Safety Experiments in the Marviken Power Station Sweden*, MXC-222, September 1979.

4.3-2. *The Marviken Full Scale Critical Flow Tests, Summary Report, Joint Reactor Safety Experiments in the Marviken Power Station Sweden*, NUREG/CR-2671, MXC-301, May 1982.

4.4 Marviken Critical Flow Test 24

Marviken Test 24 was one of the full-scale critical flow tests (CFT) conducted in Sweden. The 27 CFT experiments were conducted between mid-1977 and December 1979 as a multinational project at the Marviken Power Station. The tests were performed to obtain data for critical flows in short pipes of large diameter at subcooled and low-quality stagnation conditions.

The Marviken tests were conducted by discharging water and a steam-water mixture from a full-sized reactor vessel through a large diameter pipe that was connected to the test nozzle. The test nozzles had rounded entrances and were nominally 0.2, 0.3, or 0.5 m in diameter. The nozzle lengths ranged from 0.166 to 1.809 m. Most tests were conducted with a nominal initial steam dome pressure of 5 MPa with the water subcooled between 1 and 50 K with respect to the steam dome pressure. The vessel, discharge pipe, and nozzle were instrumented to determine the test behavior and to provide a basis for evaluating the stagnation conditions and mass fluxes at the nozzle inlet.

Marviken CFT 24 had a 0.5-m diameter test nozzle with a length-to-diameter ratio of 0.33. The initial steam dome pressure was 4.96 MPa, and the initial subcooling at the nozzle entrance was 83 K. The system needed 1.3 s to establish a stable rate of depressurization. Saturated condition occurrences were recorded in the discharge pipe from 22 to 30 s. Saturated conditions were present everywhere in the discharge pipe from 30 s until the test was terminated at 54 s.

4.4.1 Code Models Assessed

CFT 24 assesses the subcooled and saturated choked flow models.

4.4.2 Experiment Facility Description

Marviken CFT 24 was the twenty-fourth test in a series of full-scale critical flow tests performed as a multinational project at the Marviken Power Station in Sweden. The test equipment consisted of four major components: pressure vessel, discharge pipe, test nozzle, and rupture disk assembly.

The pressure vessel was originally a part of the Marviken nuclear power plant. Of the original vessel internals, only the peripheral part of the core superstructure, the cylindrical wall, and the bottom of the moderator tank remained. Gratings were installed at three levels in the lower part of the vessel prior to the critical flow tests to prevent the formation of vortices which might enter the discharge pipe. The vessel has an inside diameter of 5.22 m and was 24.55 m high from the vessel bottom to the top of the top-cupola. The net available internal volume was 420 m^3. A diagram of the pressure vessel is show in Figure 4.4-1.

The discharge pipe consisted of seven elements: axisymmetric inlet section, connection piece, two pipe spools, two instrumentation rings, and isolation ball valve as shown in Figure 4.4-2. Internal diameters of the connection piece, pipe spools, and instrumentation rings were all 0.752 m. The flow path through the ball valve contained abrupt diameter changes of 0.038 m. The axial distance from the discharge pipe entrance to the end of the discharge pipe (nozzle entrance) was 6.3 m.

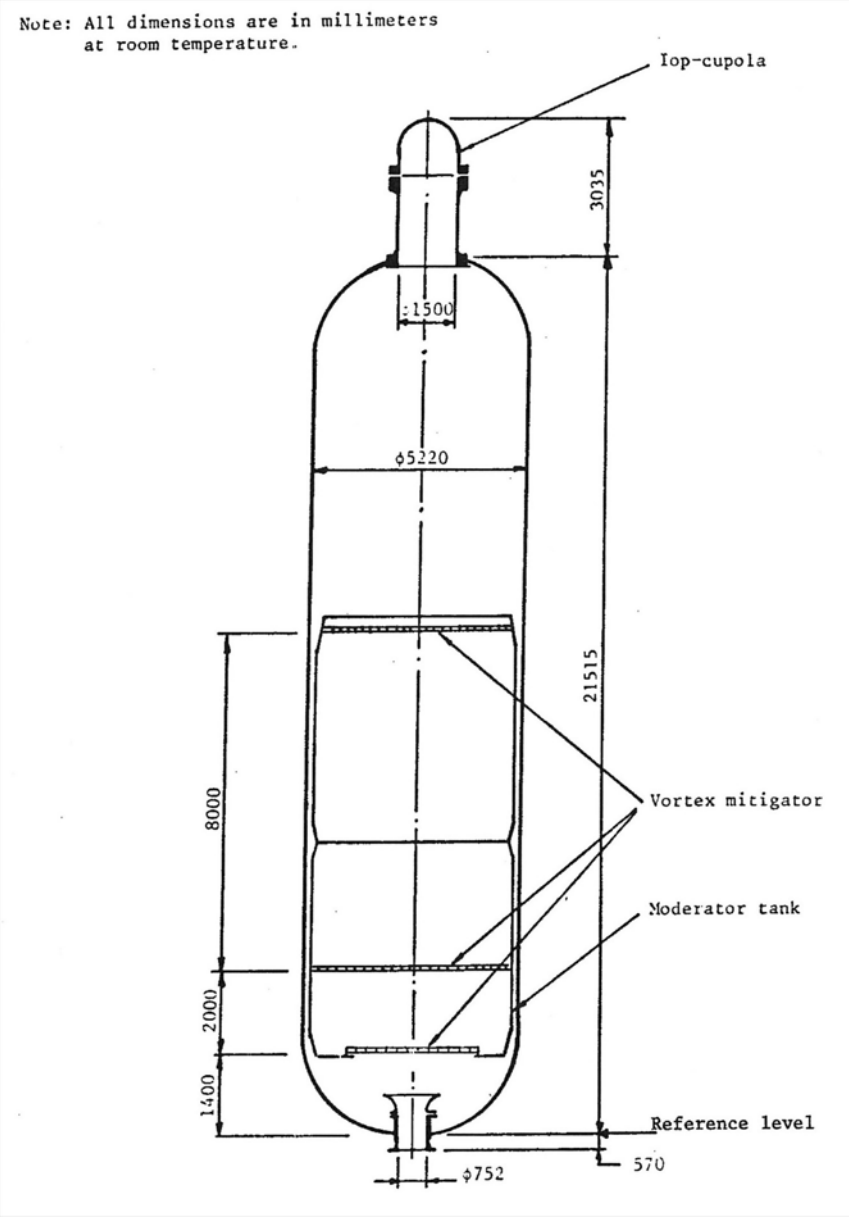

Figure 4.4-1. Marviken Critical Flow Test 24 pressure vessel.

The test nozzle was connected to the lower end of the discharge pipe; a generic nozzle is shown in Figure 4.4-3. The nozzle consisted of a rounded entrance section followed by a constant diameter test section, 0.5 m in diameter, 0.166 m long, giving a length-to-diameter ratio (L/D) of 0.33.

A rupture disk assembly was attached to the downstream end of the test nozzle. The assembly contained two identical rupture disks. The test was initiated by over pressurizing the volume between the two disks. This over pressure resulted in the failure of the outer disk, followed shortly by the failure of the inner disk. Failure of the disks was designed to occur along the their entire periphery so that they were completely removed from the nozzle exit.

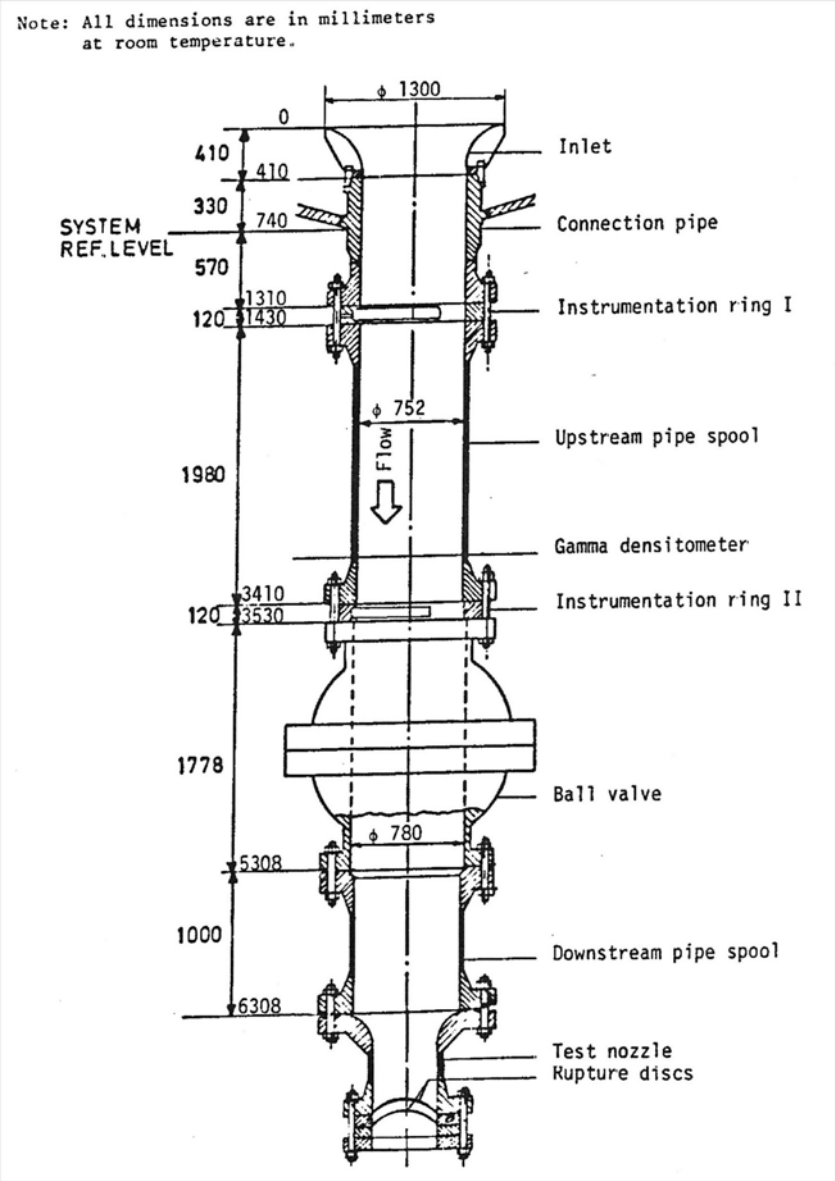

Figure 4.4-2. Marviken Critical Flow Test 24 discharge pipe, test nozzle, and rupture disk assembly.

4.4.3 Input Model Description

A nodalization diagram of the input model is shown in Figure 4.4-4. The vessel is represented by a pipe with 39 cells. This is subdivided as follows: one cell for the top-cupola, one cell for the steam dome, 36 equal-length cells for the main portion of the vessel, and one cell for the bottom of the vessel above the standpipe entrance; the vessel volume below the standpipe entrance is not modeled. All junctions use the smooth area option. The total volume of the vessel is 420 m^3.

The discharge pipe (not including the test nozzle) is represented by a pipe with six cells. The nozzle is not included in the pipe, in accordance with RELAP5-3D modeling guidelines, which state that short nozzles should not be modeled explicitly. The third and fifth junctions (where the flow enters/exits the ball

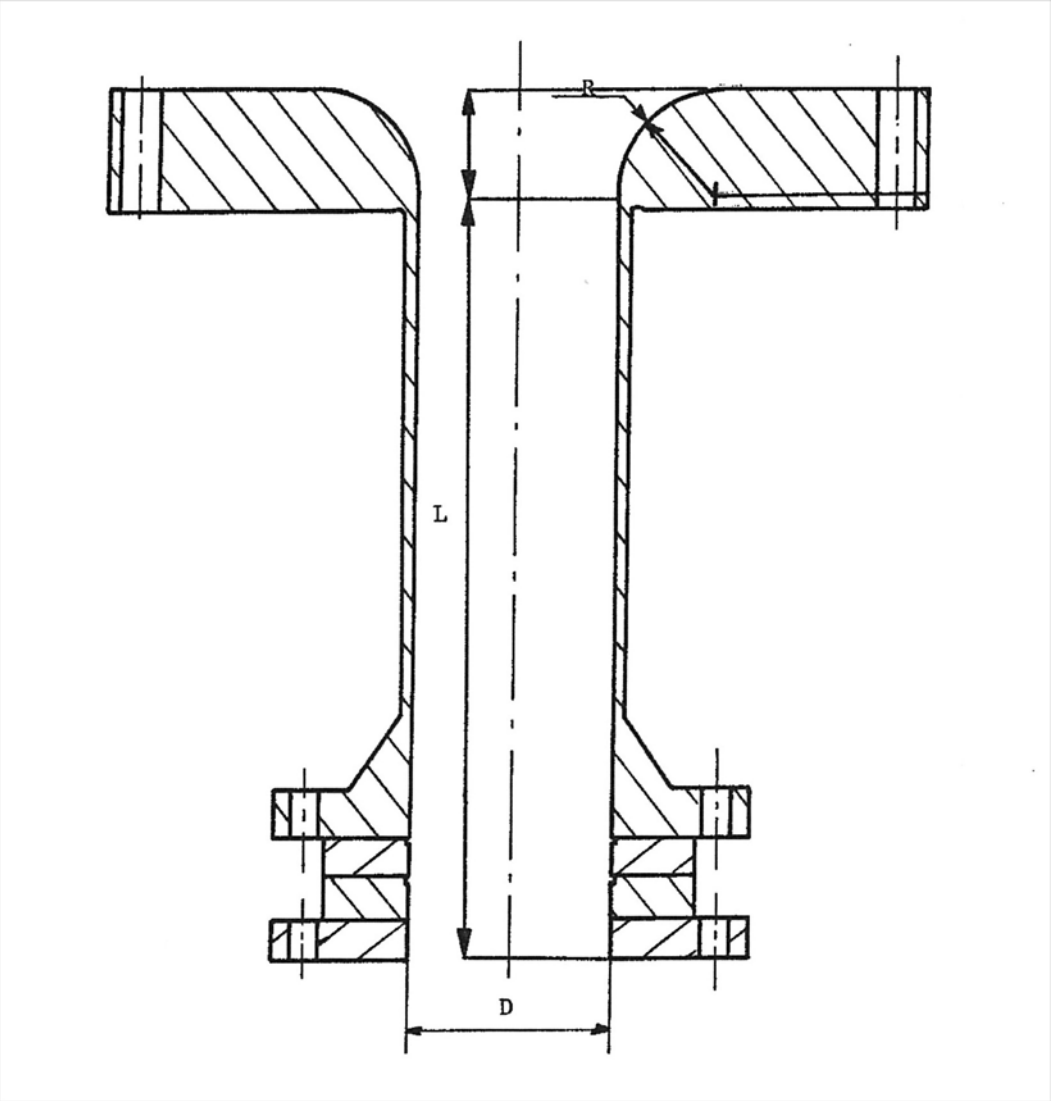

Figure 4.4-3. Marviken critical flow test nozzle.

valve and experiences a change in flow area) of the discharge pipe use the abrupt area option. All other junctions use the smooth area option. The test nozzle was modeled as a single junction with the smooth area change option. No special nodalization was used in the nozzle region. All loss coefficients are set to zero and the discharge coefficients are set to the default value of 1.0.

4.4.4 Data Comparisons and Results

RELAP5-3D calculations were performed using both the semi- and nearly-implicit solution schemes. The requested time step size was 0.05 s for the first 5 s and 0.25 s thereafter. All initial boundary conditions and resulting experiment data results are documented in References 4.4-1 and 4.4-2, and the data shown in the plots came from the NRC Data Bank. Table 4.4-1 presents a summary of the initial conditions.

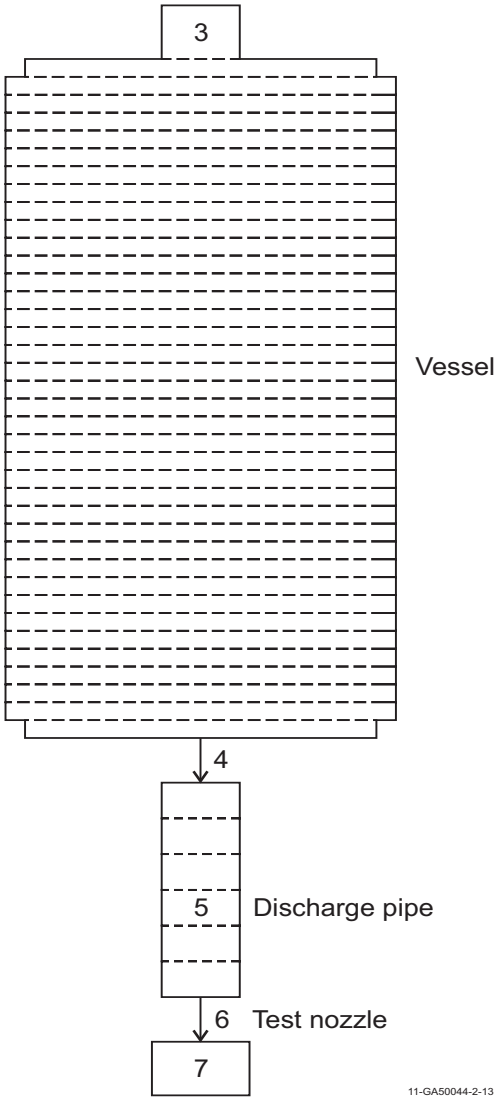

Figure 4.4-4. Marviken Critical Flow Test 24 nodalization diagram.

Table 4.4-1. Summary of initial conditions for Marviken Critical Flow Test 24.

Parameter	Experiment Data	RELAP5-3D
Steam dome pressure (MPa)	4.96	4.96
Saturation temperature (K)	536	537
Degree of nominal subcooling in the lower vessel relative to steam dome saturation temperature (K)	33	33
Minimum fluid temperature in vessel (K)	503	504
Fluid temperature at test nozzle (K)	453	462
Mass of water and steam (kg)	330,000	325,531
Atmospheric pressure (kPa)	101.5	101.5

Upon the rupture disk bursting, the pressure in the vessel begins to decrease as seen in Figure 4.4-5. The experiment pressure at the top of the vessel drops rapidly for 0.5 s, then increases for 0.5 s. This early pressure response is considered to be a non-equilibrium phase resulting from a delay of the steam production by the saturated water. Following this phase, a rapid depressurization is observed up to 22 s during subcooled flow, and then the depressurization rate slows when some of the flow entering the nozzle becomes saturated. The RELAP5-3D predictions do not match the initial pressure drop and recovery because the interfacial heat transfer in RELAP5-3D is too high, resulting in greater vapor generation which holds the pressure up. It would be possible to better fit the data if the interfacial heat transfer in RELAP5-3D was decreased in order to delay nucleation. Following the initial non-equilibrium phase, RELAP5-3D does a reasonable job of predicting the pressure response.

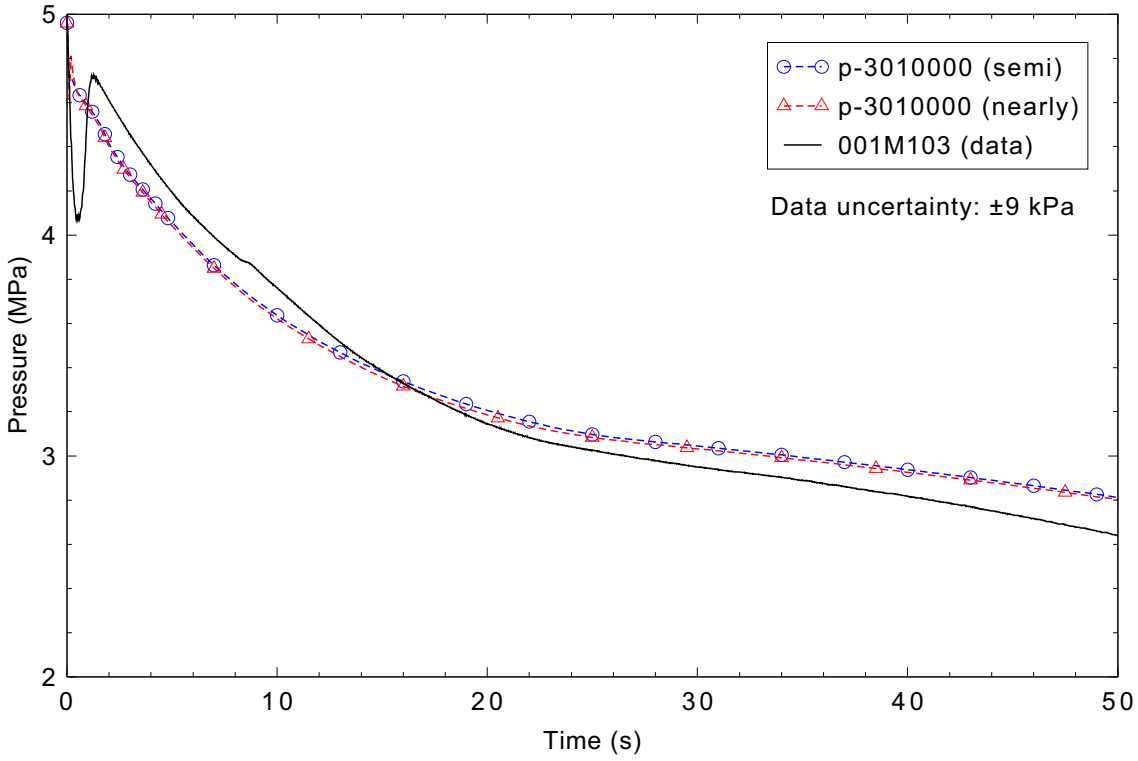

Figure 4.4-5. Measured and calculated vessel pressure for Marviken CFT 24.

The mass flow rates through the test nozzle are shown in Figure 4.4-6. The experiment mass flow rate was evaluated by three independent methods: the steam dome depressurization method, the vessel mass inventory method, and the pitot-static method. The steam dome depressurization method was applied only for the first 0.5 s and was used to determine a maximum mass flow. The vessel mass inventory method did not give reasonable mass flow results over the first 5 s due to large pressure oscillations that occurred immediately after the initiation of the test. The experiment data indicate the maximum mass flow is anywhere from 12,959 to 15,119 kg/s depending upon whether an equilibrium expansion or an expansion with no condensation occurred. The error associated with this calculation is given as ±15%. The RELAP5-3D predicted maximum mass flows are 14,544 and 21,266 kg/s for the semi-implicit and nearly-implicit cases, respectively. The calculated mass flow rate over the transient matches the data reasonably well. The decrease in mass flow rate from 20 to 25 s in the experiment data was caused by increased vapor generation; the calculated decrease was a little later and larger. At 34 s, the flow entering

the nozzle became saturated and remained so through the end of the test. The mass flow measurements have an uncertainty of anywhere from ±2% to ±15% depending on which of the three methods was used.

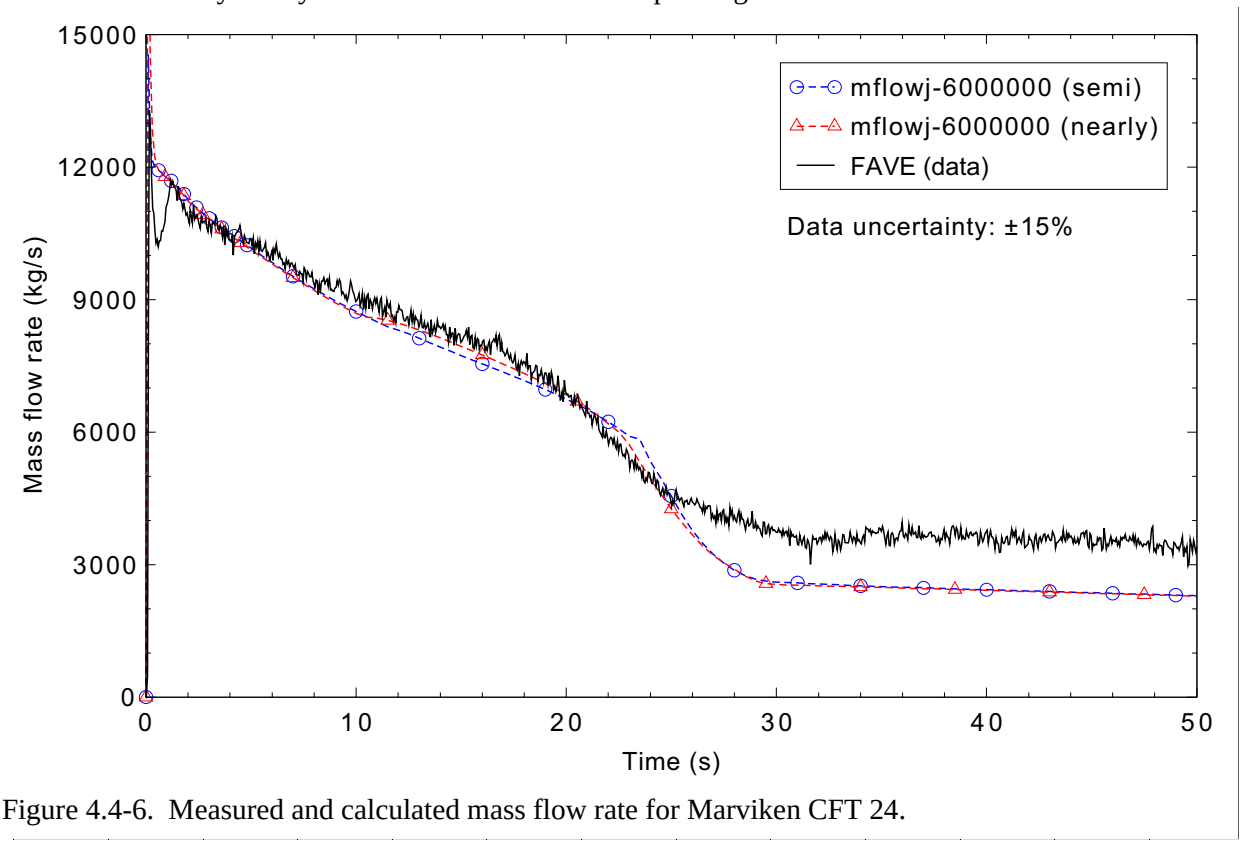

Figure 4.4-6. Measured and calculated mass flow rate for Marviken CFT 24.

A comparison of the temperature profile in the test vessel at time zero is shown in Figure 4.4-7. The temperature profiles at 15 s are presented in Figure 4.4-8. The calculated temperatures at 15 s are in reasonable agreement with the measured data.

A comparison of the mixture density in the exit pipe is shown in Figure 4.4-9. The RELAP5-3D code does a reasonable job predicting the density in the early portion of the transient. Beyond 24 s, both RELAP5-3D and the experiment data show increased vapor generation which resulted in the decreased mixture density. However, the vapor generation predicted by RELAP5-3D was much greater. The test ended at 54 s when steam entered the discharge pipe.

4.4.5 Conclusions and Assessment Findings

The RELAP5-3D code was assessed against the Marviken Critical Flow Test 24 and overall was found to be in reasonable agreement. The code was run with both the semi-implicit and nearly-implicit solution schemes, and the results for both were very similar.

The RELAP5-3D code under predicted the vessel pressure in the early portion of the transient (1 to 12 s) and over predicted the pressure during the remaining portion of the test, but is nonetheless judged to do a reasonable job predicting the vessel pressure. The code was judged to be in excellent agreement with the break flow rate while the flow was subcooled, and in reasonable agreement with the data following the

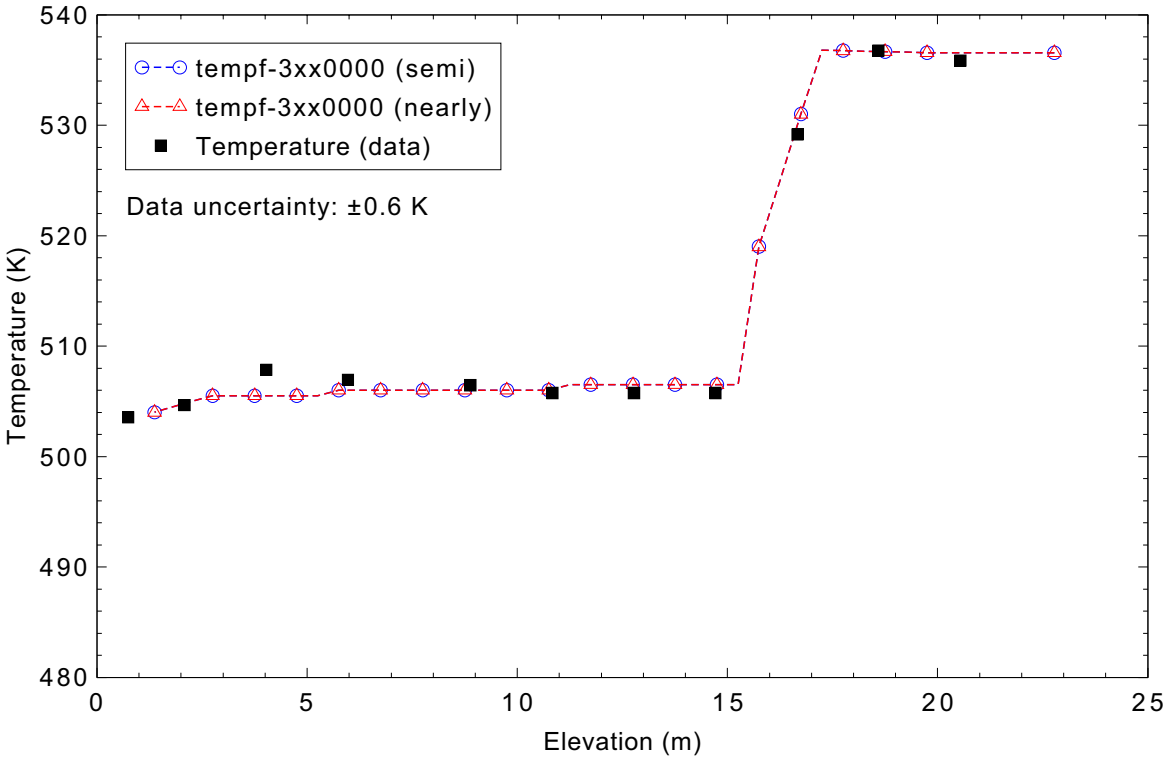

Figure 4.4-7. Measured and calculated vessel temperature profile at 0 s for Marviken CFT 24.

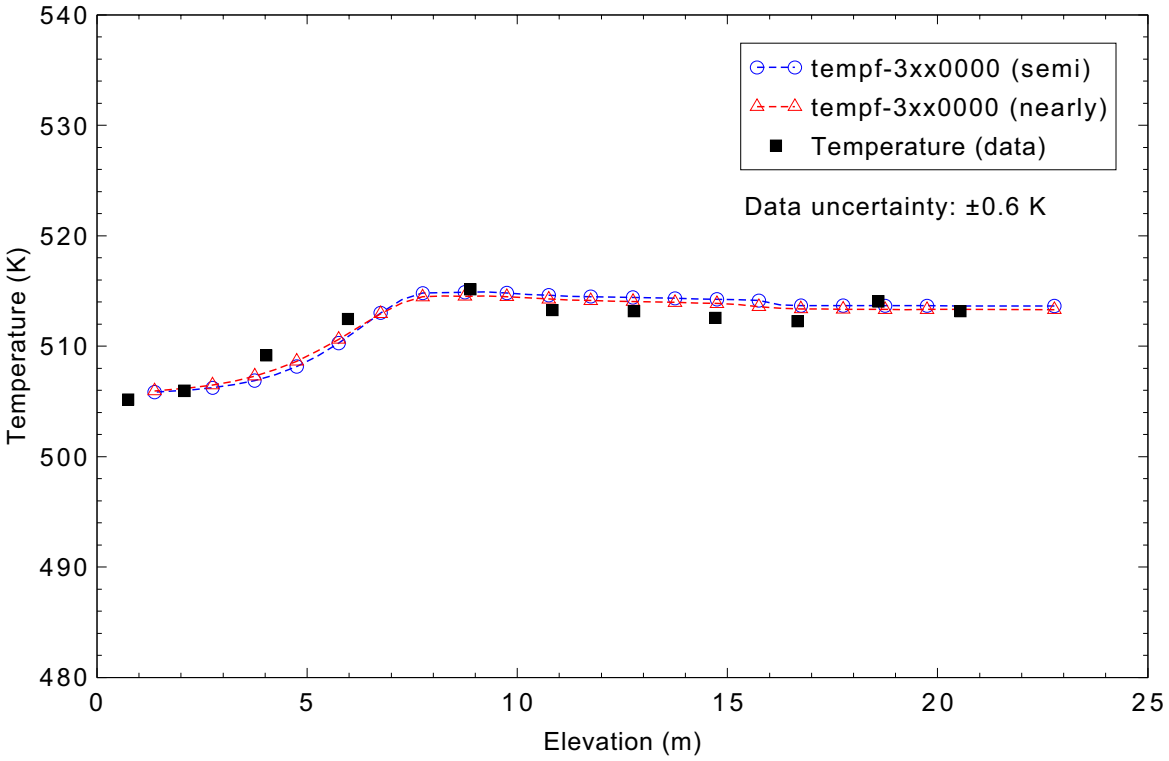

Figure 4.4-8. Measured and calculated vessel temperature profile at 15 s for Marviken CFT 24.

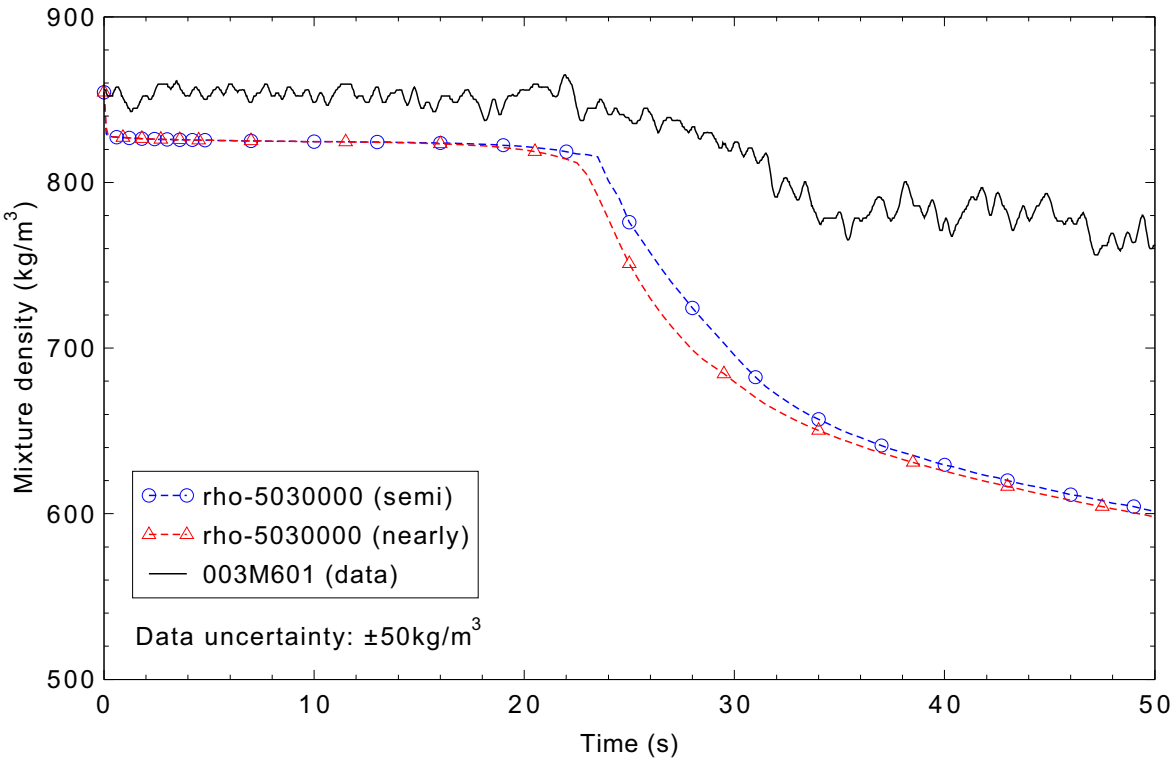

Figure 4.4-9. Measured and calculated mixture density in the discharge pipe for Marviken CFT 24.

transition to saturated flow, a regime in which the flow was under predicted. The RELAP5-3D code also does a reasonable job predicting the temperature profile in the test vessel, and does a reasonable job predicting the mixture density until 24 s, after which the code is in minimal agreement with the data.

4.4.6 References

4.4-1. *The Marviken Full Scale Critical Flow Tests, Results From Test 24, Joint Reactor Safety Experiments in the Marviken Power Station Sweden*, MXC-224, September 1979.

4.4-2. *The Marviken Full Scale Critical Flow Tests, Summary Report, Joint Reactor Safety Experiments in the Marviken Power Station Sweden*, NUREG/CR-2671, MXC-301, May 1982.

4.5 Marviken Jet Impingement Test 11

The Jet Impingement Test (JIT) program was initiated to collect data on jet behavior using test nozzles representative of pipe sizes in a typical nuclear reactor.[4.5-1] The program objectives included collection of data on the spatial distribution of pressure and temperature in free jets, and on the distribution of forces on instrumented targets. The hardware and test facility from the previous Marviken tests were modified to meet these objectives.

The tests were conducted by filling the Marviken pressure vessel with water. After heating the vessel water to a specified temperature and pressure, rupture discs were burst and the vessel contents were discharged through the nozzle to form the jet. The jet discharged into the Marviken containment, which was relieved by exhausting the effluent to the outside atmosphere.

The containment and pressure vessel used in previous Marviken tests were used without significant modifications. However, the nozzles and rupture disc assemblies were modified to meet the test objectives. Test nozzles of 200, 299, and 509 mm diameter were used for the variety of tests. The 299 mm diameter nozzle was used for Test 11.

4.5.1 Code Models Assessed

Marviken Jet Impingement Test 11 (JIT-11) test assesses the high quality vapor choked flow model.

4.5.2 Experiment Facility Description

Marviken JIT-11 was the eleventh test in a series of full-scale jet flow tests performed on August 27, 1981, as part of a multinational project at the Marviken Power Station in Sweden.[4.5-2] The test equipment consisted of four major components: pressure vessel, discharge pipe, ball valve, and test nozzle, as shown in Figure 4.5-1.

The pressure vessel was originally a part of the Marviken nuclear power plant. Of the original vessel internals, only the peripheral part of the core superstructure, the cylindrical wall, and the bottom of the moderator tank remained. The vessel has an inside diameter of 5.22 m and was 24.55 m high from the vessel bottom to the top of the top-cupola. The net available internal volume was 420 m^3, and the initial pressure was 5 MPa. A diagram of the pressure vessel is shown in Figure 4.5-2.

An 18.0 m standpipe was used inside the pressure vessel with its inlet above the liquid level. This was done to ensure saturated steam flow conditions. The standpipe was then connected to the discharge pipe, which consisted of nine elements: axisymmetric inlet section, connection piece, two pipe spools, two instrumentation rings, an isolation ball valve, a rupture disc, and a nozzle, as shown in Figure 4.5-3. Internal diameters of the connection piece, pipe spools, and instrumentation rings were all 0.752 m. The flow path through the ball valve was a constant diameter of 0.780 m. The axial distance from the discharge pipe entrance to the end of the discharge pipe (nozzle entrance) is 9.519 m.

The test nozzle was connected to the lower end of the discharge pipe and is shown in Figure 4.5-4. The nozzle consisted of a rounded entrance section followed by a constant diameter test section, 0.299 m

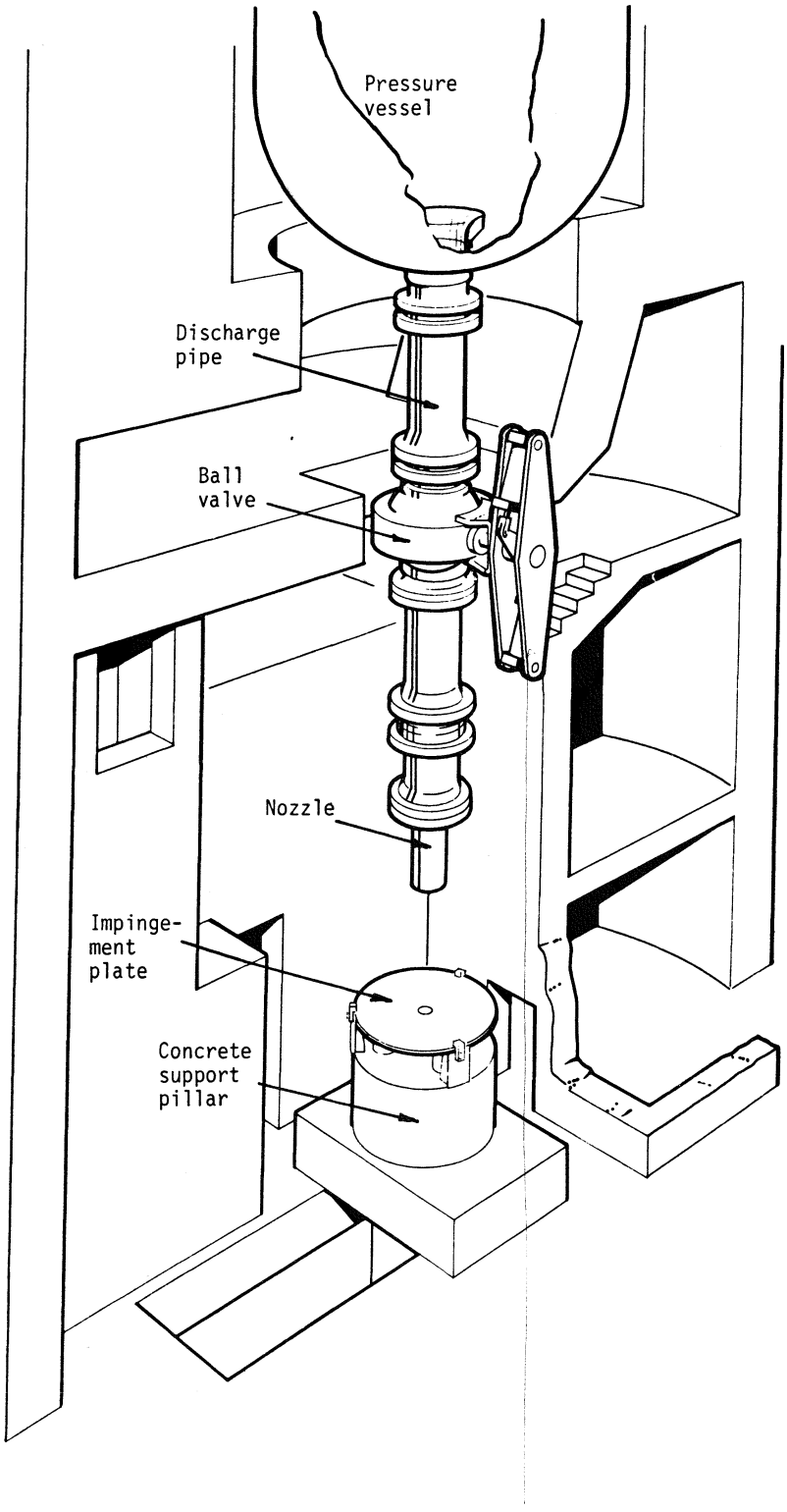

Figure 4.5-1. Test facility for Marviken JIT-11.

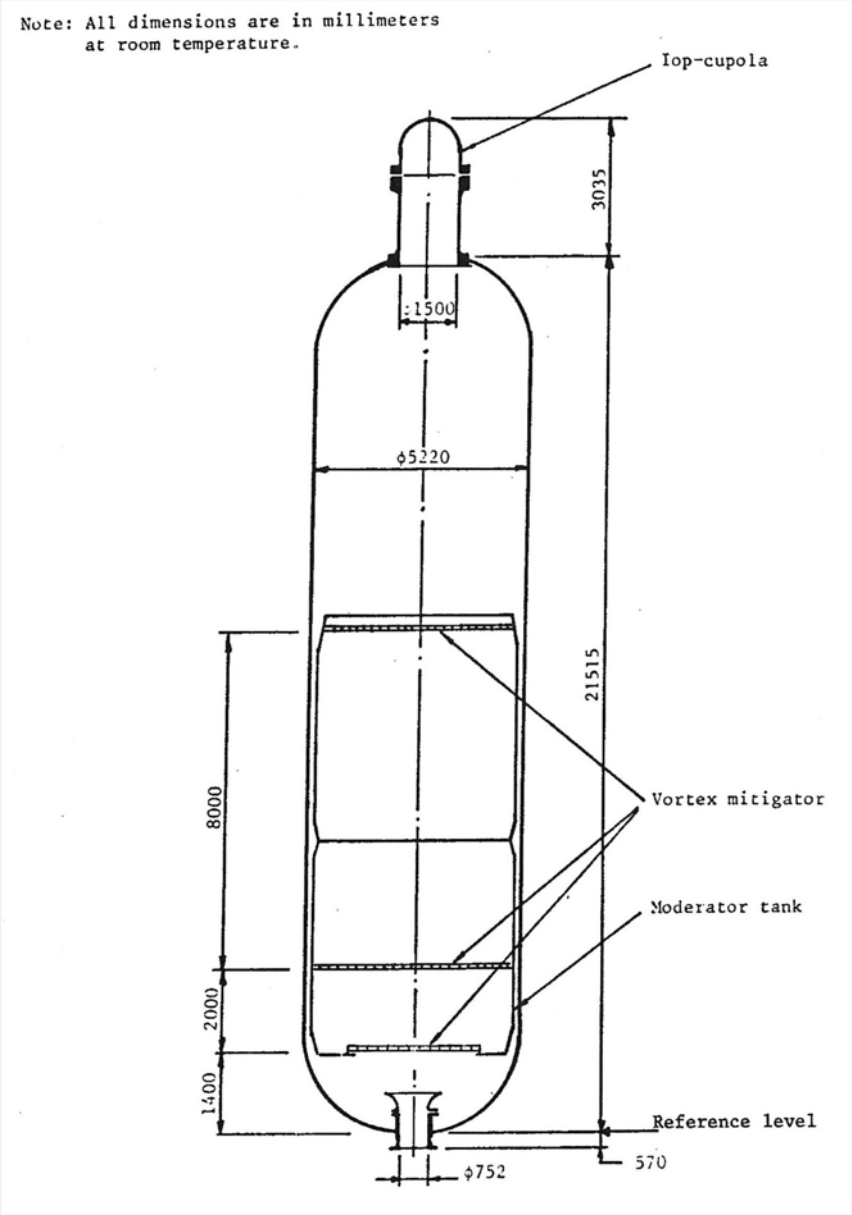

Figure 4.5-2. Pressure vessel for Marviken JIT-11.

in diameter, 1.18 m long, giving a length-to-diameter ratio (L/D) of 3.946. At the nozzle entrance, the fluid was saturated vapor, and the nozzle discharge was steam.

A rupture disk assembly was attached upstream of the test nozzle just below the ball valve. The assembly contained two identical rupture disks. The test was initiated by over pressurizing the volume between the two disks. This over pressure resulted in the failure of the outer disk, followed shortly by the failure of the inner disk. Failure of the disks was designed to occur along the their entire periphery so that they were completely removed from the discharge pipe.

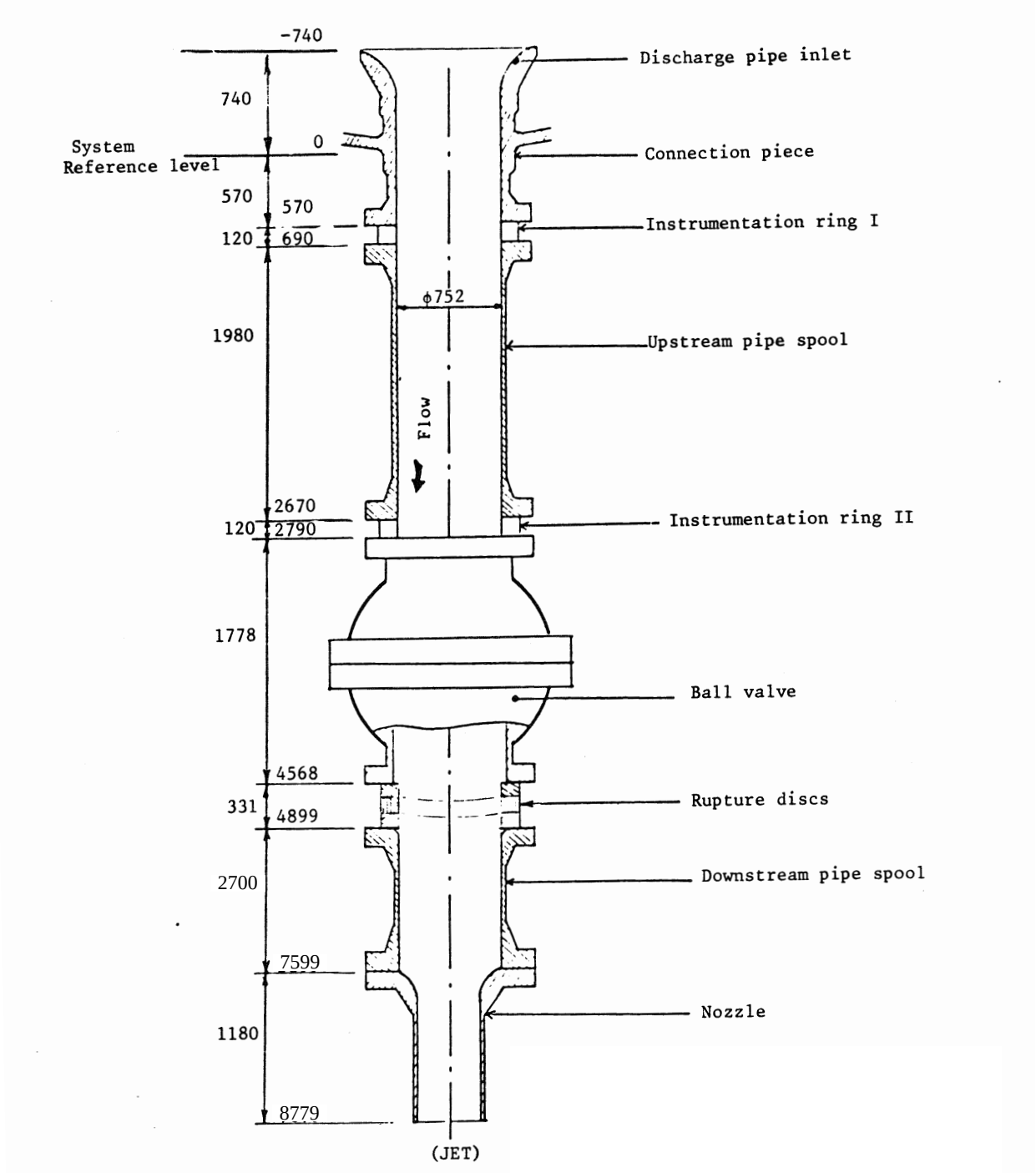

Figure 4.5-3. Discharge pipe for Marviken JIT-11.

4.5.3 Input Model Description

A nodalization diagram of the steady-state input model is shown in Figure 4.5-5.

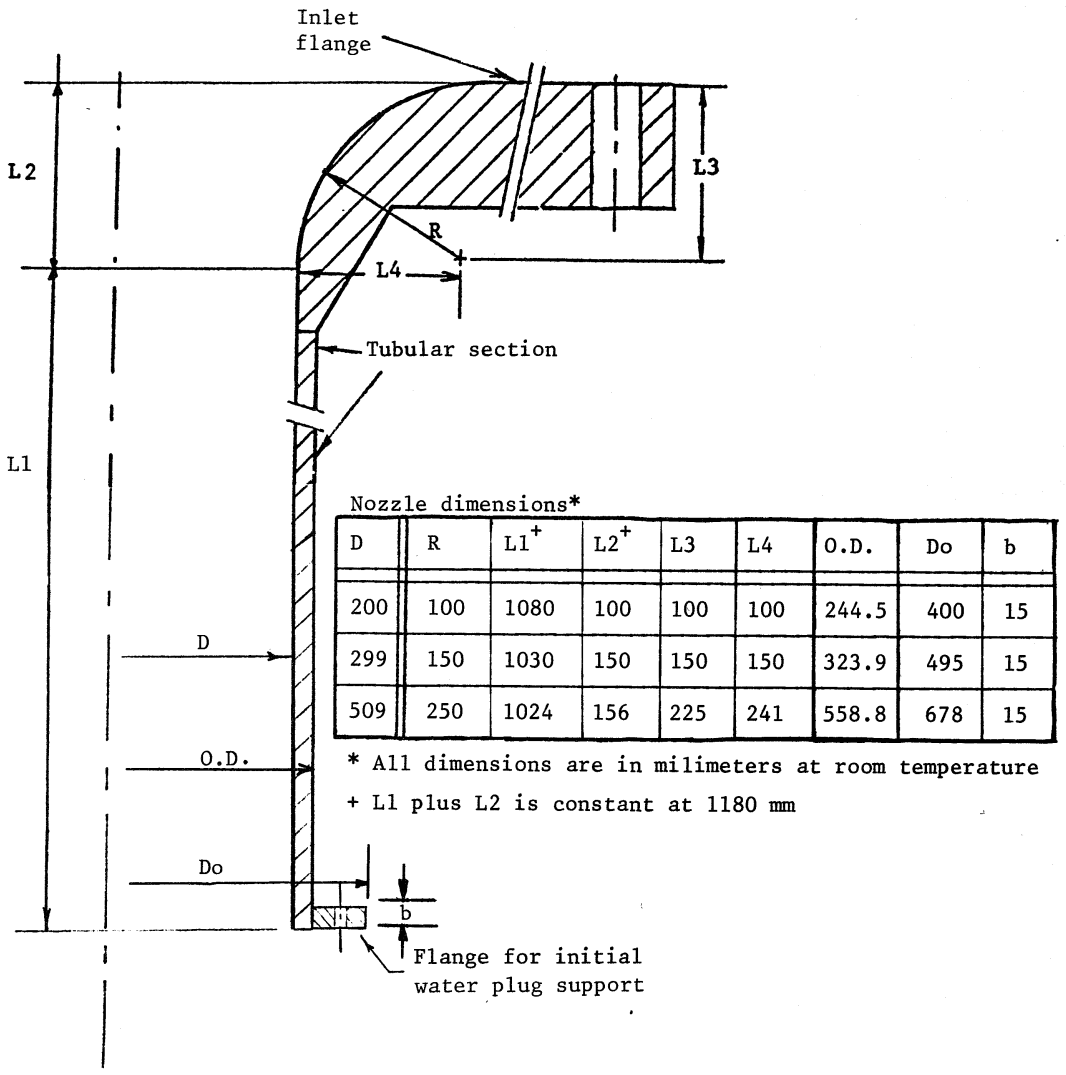

Nozzle dimensions*

D	R	L1+	L2+	L3	L4	O.D.	Do	b
200	100	1080	100	100	100	244.5	400	15
299	150	1030	150	150	150	323.9	495	15
509	250	1024	156	225	241	558.8	678	15

* All dimensions are in milimeters at room temperature

\+ L1 plus L2 is constant at 1180 mm

Figure 4.5-4. Nozzle for Marviken JIT-11.

Only the top portion of the vessel is modeled for this test since the top of the standpipe is above the water level in the vessel. This volume is modeled with saturated vapor and the depressurization rate from the test is used as a boundary condition. The standpipe is modeled as a vertical 18.0-m pipe with 4 equal cells of length 4.5 m and a uniform diameter of 1.0 m.

The standpipe is connected to the discharge pipe with a smooth area change. The discharge pipe is modeled as a vertical 7.929-m pipe with 3 equal cells of length 2.643 m and a uniform diameter of 0.752 m. The various area changes within the discharge pipe described in the test report[4.5-1] and shown in Figure 4.5-3 were considered negligible for this analysis since the dominant physics pertains to the choked flow condition at the nozzle.

The nozzle is modeled in the steady-state input deck with a 1.18-m pipe with 2 equal cells of length 0.59 m and a uniform diameter of 0.299 m. In the transient restart deck, the pipe used to model the nozzle

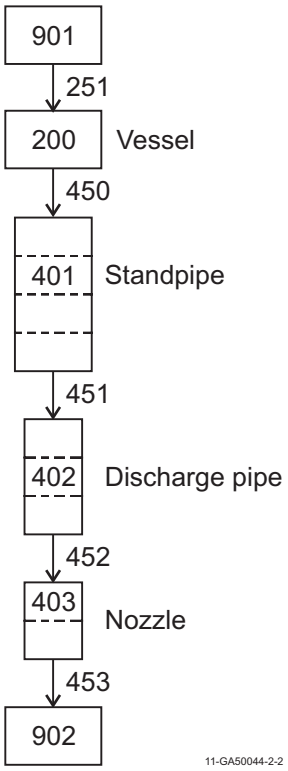

Figure 4.5-5. RELAP5-3D nodalization for Marviken JIT-11.

is discarded and only the single junction representing the abrupt area change of the nozzle is modeled. The default Ransom-Trapp choking model is applied with a discharge coefficient of 0.83. This value was found to be reasonable for matching the critical flow data in previous assessments.

4.5.4 Data Comparisons and Results

RELAP5-3D calculations were performed with both the semi- and nearly-implicit solution schemes. The requested time step sizes were 0.001 s for the first 0.01 s, 0.01 s until 0.5 s, and 0.10 s for the remainder of the calculation. All initial conditions and experiment data are documented in Reference 4.5-2, and the data shown in the plots came from the NRC Data Bank. Table 4.5-1 presents a summary of the initial conditions.

Table 4.5-1. Summary of initial conditions for Marviken JIT-11.

Parameter	Experiment Data	RELAP5-3D
Steam dome pressure (MPa)	5.0	5.0
Saturation temperature (K)	536	537
Degree of nominal subcooling in the lower vessel relative to steam dome saturation temperature (K)	< 3	0.0
Atmospheric pressure (kPa)	103.4	103.4

Upon the rupture disk bursting, the pressure in the vessel begins to decrease as seen in Figure 4.5-6. The experiment pressure at the top of the vessel drops rapidly for the first two seconds, then increases for a second, then shows a steady decrease as expected. The RELAP5-3D input boundary conditions used the same pressure data and thus reproduce identical pressure response, as shown in the figure. This pressure boundary condition was used in order to more accurately compare the critical flow with the test data.

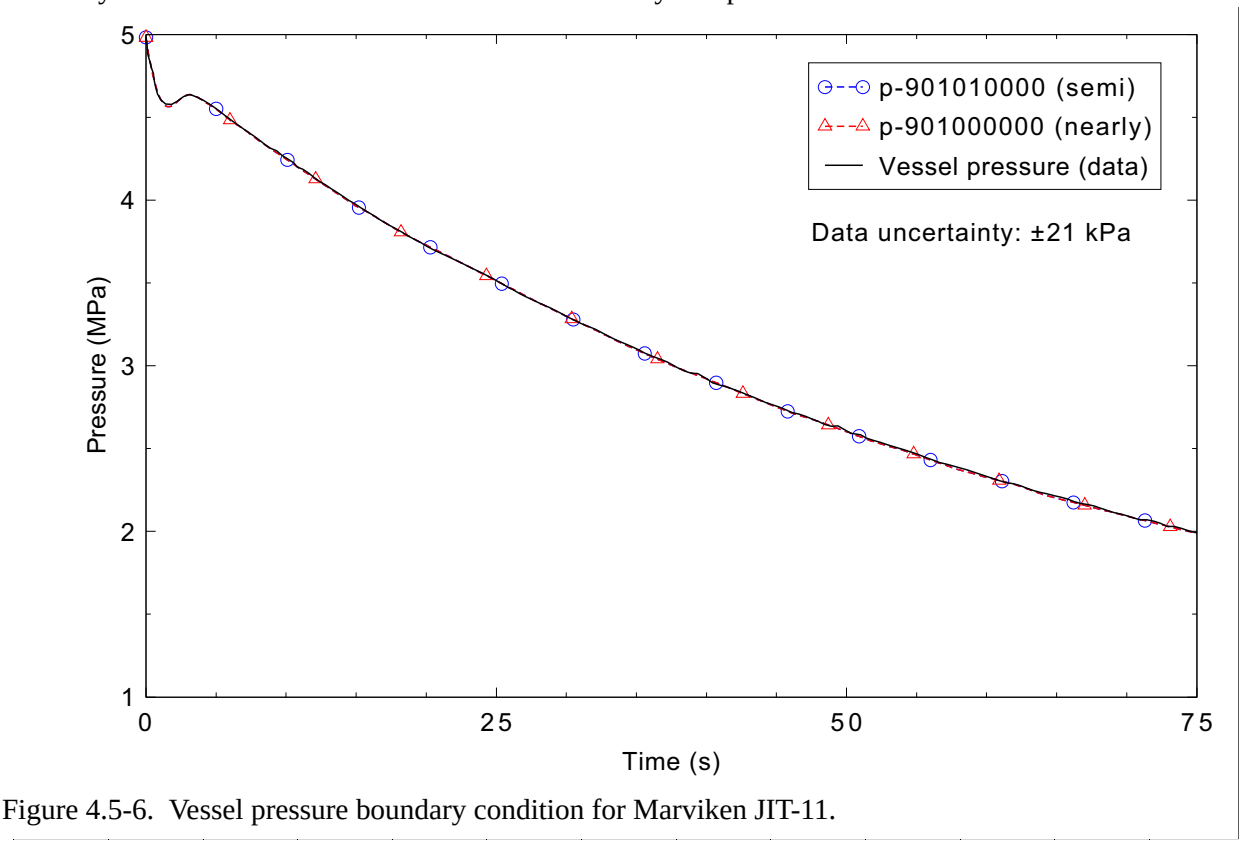

Figure 4.5-6. Vessel pressure boundary condition for Marviken JIT-11.

The mass flow rate through the test nozzle is shown in Figure 4.5-7. The experiment mass flow rate was computed using three different methods: the steam dome depressurization method, the vessel mass inventory method, and the pitot-static method. The mass flow computed by RELAP5-3D was compared against the pitot-static mass flow. The error associated with the data was reported to be between -10% and +15%. The difference between the positive and negative error was due to physical constraints imposed by boundary conditions in the test evaluation model.

The mass flow rate over the transient matches very well between RELAP5-3D and the experiment data. The only exception to this occurs between 15 s and 25 s, at which point the data show an increase in the mass flow. The test report identifies that some liquid spilled over the top of the standpipe and passed through the nozzle, but had negligible impact on the test results. This seems confirmed upon examination of the density measurement.

A comparison of the mixture density in the middle of the discharge pipe is shown in Figure 4.5-8. The RELAP5-3D code does an excellent job predicting the density throughout the transient. The reported error on the density data was ±4 kg/m^3. Between 15 s and 25 s the test data mixture density showed an increase

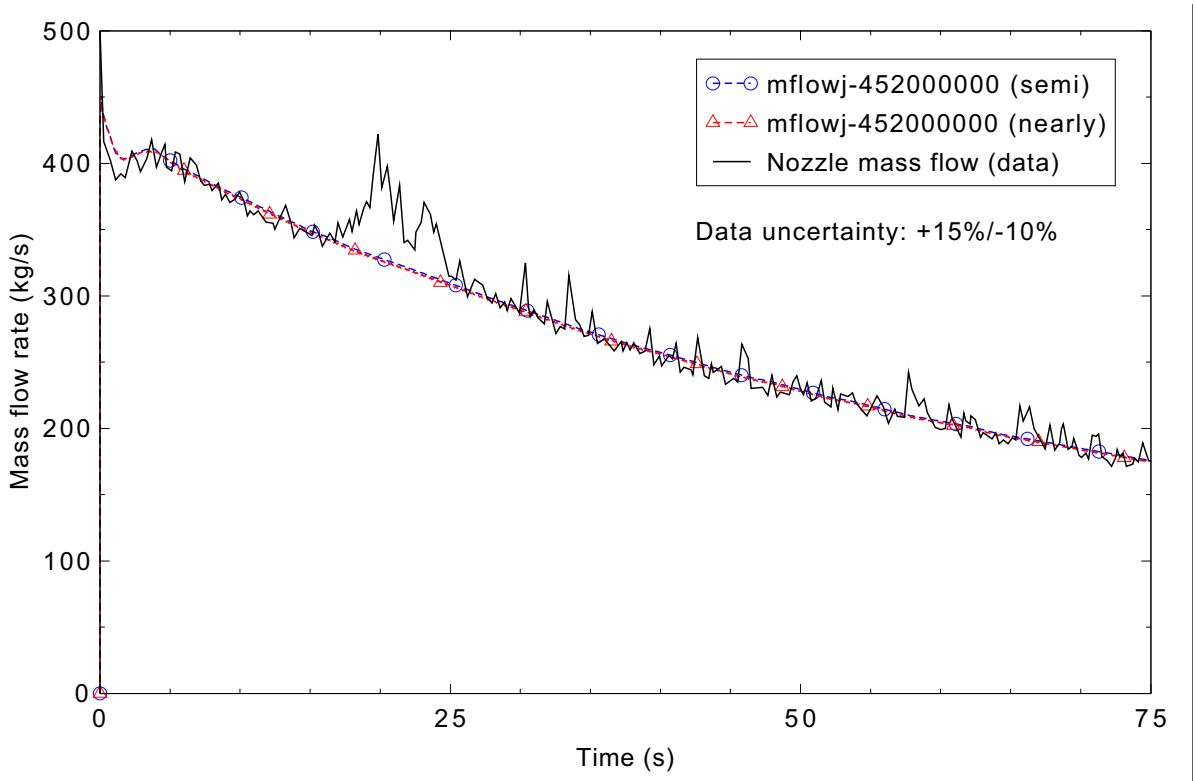

Figure 4.5-7. Measured and calculated mass flow rate for Marviken JIT-11.

consistent with the mass flow increase shown in Figure 4.5-7. This supports the notion that a small amount of liquid spilled into the standpipe from the vessel. This effect could have been accounted for in the RELAP5-3D model, but was not considered important and thus only the top portion of the vessel (vapor-only) was modeled.

4.5.5 Conclusions and Assessment Findings

The RELAP5-3D code was assessed against Marviken Jet Impingement Test 11. The code was run with both the semi- and nearly-implicit solution schemes. The RELAP5-3D results for both the semi- and nearly-implicit solution schemes were very similar. RELAP5-3D is considered to have excellent agreement with the test data.

With the specified pressure boundary condition, RELAP5-3D did an excellent job of matching the critical flow data. Again, the transient pressure boundary condition was specified in order to provide a consistent critical flow comparison. The only significant deviation between the code and data occurred when liquid spilled over the top of the stand-pipe in the test, resulting in a small increase in mass flow between 15 s and 25 s. This was not captured by the code because only the top of the vessel consisting of saturated steam was modeled.

The Ransom-Trapp critical flow model is deemed accurate for this pure steam test case. However, it bears mentioning that the good agreement is due in large part to the choice of discharge coefficient of 0.83.

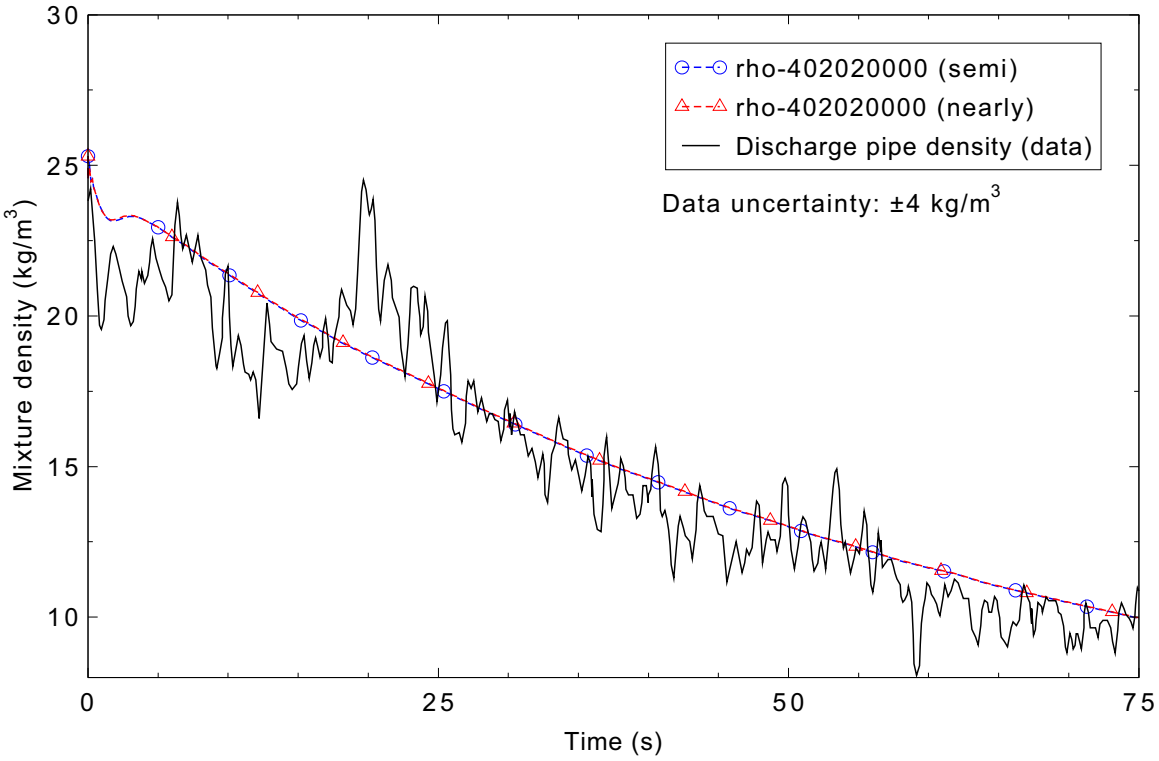

Figure 4.5-8. Measured and calculated mixture density in the discharge pipe for Marviken JIT-11.

4.5.6 References

4.5-1. *The Marviken Full Scale Jet Impingement Tests, Facility Description*, Joint Reactor Safety Experiments in the Marviken Power Station Sweden, MXD-101, February 1982.

4.5-2. *The Marviken Full Scale Jet Impingement Tests, Test 11 Results*, Joint Reactor Safety Experiments in the Marviken Power Station Sweden, MXD-211, March 1982.

4.6 Moby-Dick Air-Water

The Moby-Dick Air-Water Critical Flow Experiment 3141 was performed in the late 1970s at the French Atomic Energy Commission laboratories (Centre d'Etudes Nucleaires de Grenoble). This test was one of a series of experiments to study steady state, two-phase, two-component critical flow in a vertical, divergent nozzle test section. Experiment 3141 was a test with upstream nitrogen injection at low temperature and high flow rate into a low temperature inlet water flow. The test data were obtained under constant inlet flow, steady state conditions.[4.6-1,4.6-2]

4.6.1 Code Models Assessed

The critical flow model was assessed using data from this test.

4.6.2 Experiment Facility Description

The Moby-Dick test facility was comprised of a water and nitrogen supply system, a test section, a catch tank, and measurement instrumentation. The vertical test section includes a 7 degree divergent nozzle as specified test geometry. Axial pressures along the test section were measured by a series of pressure transducers. The flow is choked at the nozzle throat where the minimum pressure is achieved. In the expansion section of the nozzle the pressure recovers to approximately atmospheric pressure before entering the condenser tank. Flashing is experienced in the nozzle recovery section, resulting in increased void fraction. The desired test conditions for each test are obtained by controlling the inlet water and nitrogen flows, pressures and temperatures at the desired steady state conditions. A diagram of the Moby-Dick test loop is shown in Figure 4.6-1.[4.6-2]

Test 3141 used initial conditions selected to examine choked flow conditions with low temperature, high void fraction, high velocity fluid entering the nozzle test section. Test 3141 steady state thermal hydraulic conditions are shown in Table 4.6-1.[4.6-2]

Table 4.6-1. Moby-Dick Test 3141 thermal hydraulic conditions.

Test Parameter	Measured Value
Upstream liquid temperature (K)	308.65
Upstream pressure, P_e (Pa)	561,900
Condenser pressure, P_{cond} (Pa)	103,178
Liquid flow rate (kg/s)	1.222
Liquid entrance velocity (m/s)	7.98
Nitrogen entrance temperature (K)	291.15
Void fraction at test section entrance	0.554
Calculated nitrogen flow rate (kg/s)	0.006101
Choked flow at nozzle?	yes

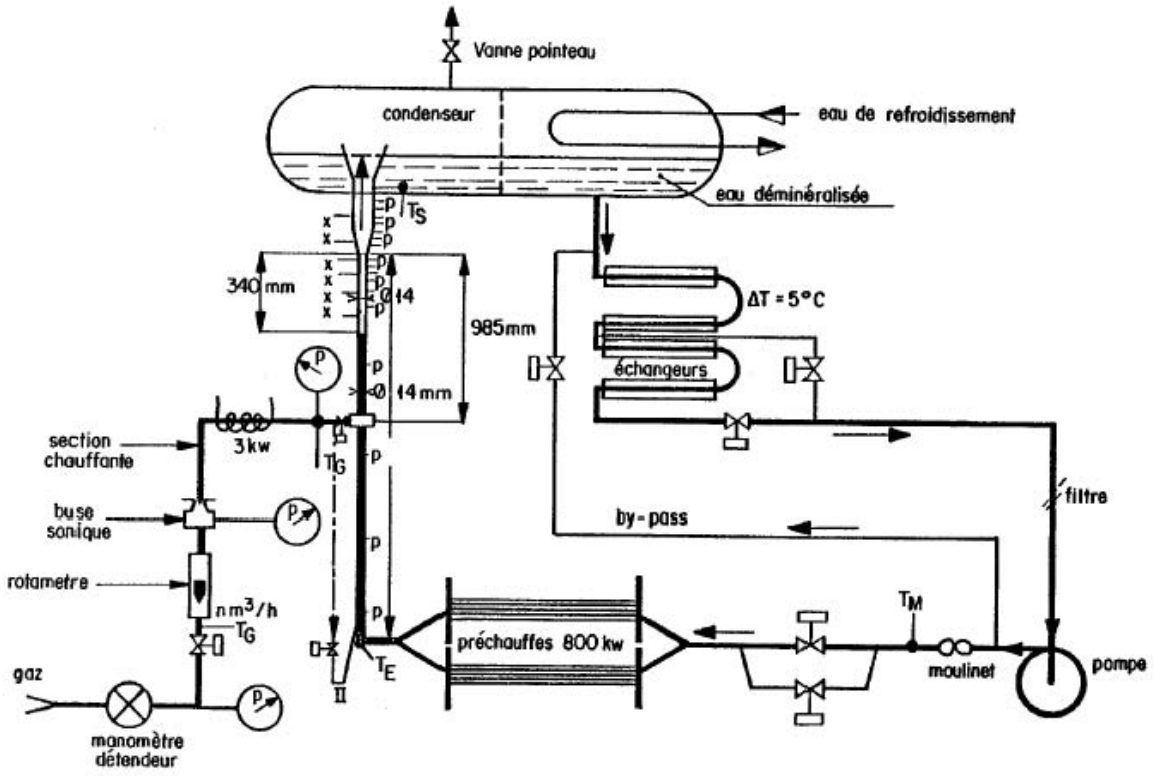

Figure 4.6-1. Moby-Dick test loop.

4.6.3 Input Model Description

A nodalization diagram of the RELAP5-3D input model is given in Figure 4.6-2. The approximately 3-m long test section was modeled. Time-dependent volume and time-dependent junction components provide the user-specified inlet and outlet thermal hydraulic boundary conditions for the test simulation. The entire vertical test section is modeled using a pipe component (Component 110), including the straight pipe nozzle inlet section, the divergent nozzle section, and the straight pipe nozzle exit section; the pipe has 42 cells. The first 20 cells have a cross sectional area of 1.54×10^{-4} m^2 to span the vertical straight pipe inlet section up to the nozzle throat. Over the next 12 cells, the nozzle section area increases to 1.59×10^{-3} m^2, after which the pipe cross sectional area remains constant through the nozzle exit region. The lengths of the cells are chosen proportional to the hydraulic diameter, to have junctions at the correct distance for the nitrogen injection (1.683 m) and the beginning of the nozzle (2.668 m), and to provide cell centers near pressure measurement locations; the pipe total length is 3.3414 m. A drawn tubing wall roughness of 1.524e-6 m was used throughout the test section.

The choking flag was turned off everywhere except junction 20 of Pipe 110, which is the inlet to the nozzle region. Allowing choking in all junctions can result in numerous instances of choking in adjacent junctions, which is not desired and is contrary to current user guidelines.

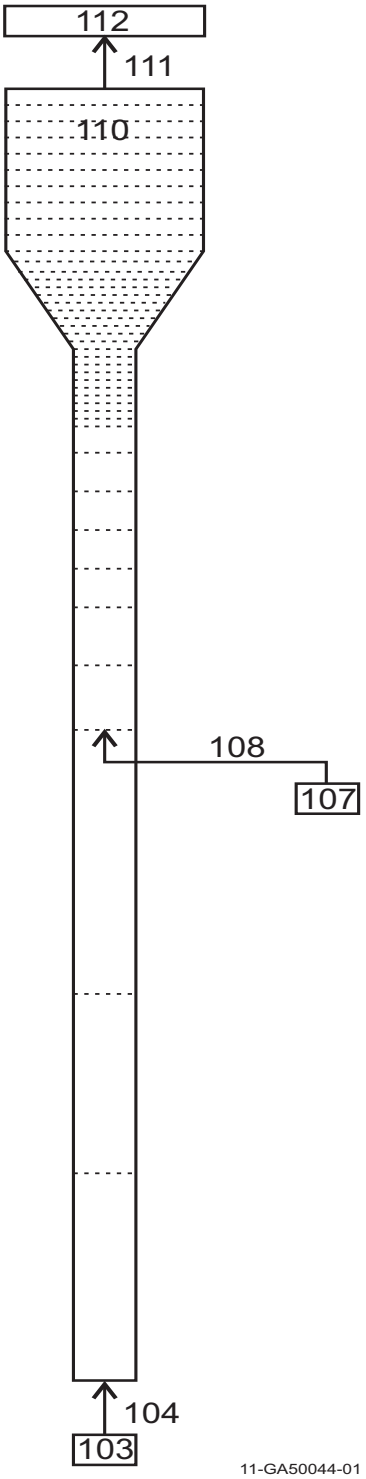

Note: diagram is not to scale.
The width of the test section is
exaggerated versus the length.

Figure 4.6-2. Nodalization diagram of the RELAP5-3D Moby-Dick experiment model.

Time-dependent volume components are used to specify the inlet boundary pressure and temperature conditions for the water (Component 103) and gas (Component 107) injection flows; the conditions used are those in Table 4.6-1. The inlet pressure is 518.9 kPa for the water and 450 kPa for the gas. The steady state liquid flow rate of 1.222 kg/s is injected at the pipe inlet, and the steady state gas flow rate of 6.1×10^{-3} kg/s is injected at the inlet of pipe cell 4. The mixture exits the test pipe section into a condenser sink volume at approximately atmospheric pressure.

4.6.4 Data Comparisons and Results

Transient runs were made with the RELAP5-3D code using both the semi- and nearly-implicit advancement schemes. The time step size for both cases was set to 0.0005 s. The transient runs were initiated with constant flow boundary conditions and user-specified approximate initial pressures and temperatures. The RELAP5-3D calculations quickly converged to a steady state condition at approximately 0.25 s and remained steady. The runs were terminated at 9 s.

Calculations using default code models resulted in a steady state using the nearly-implicit solution scheme, but an unsteady result using the semi-implicit scheme. Steady state conditions were achieved for both solution schemes using Card 1 option 55, which incorporates changes to the annular mist flow regime and map transitions in subroutine phantv. The calculated pressure profile along the test section is compared to the data in Figure 4.6-3. The single-phase liquid pressure drop was calculated very well, as evidenced by the same slope in the pressure up to about 1.7 m (where the nitrogen was injected), but the two-phase pressure drop was significantly under predicted. The pressure undershoot and recovery at the nozzle entrance was predicted reasonably well. The agreement between the calculation and data is judged to be minimal.

One reason for the under prediction of the two-phase pressure drop is that the two-phase multiplier correlation may be outside the range of its applicability. The HTFS correlation used in RELAP5 is based on data sets that have steam-water mass fluxes up to 12,100 kg/m^{2}s and air-water mass fluxes up to 5000 kg/m^{2}s; in this experiment, the nitrogen-water mass flux is nearly 8000 kg/m^{2}s.

The measured void fraction at the test section entrance was noted to be 0.554 for Test 3141. While the test facility elevation where the void fraction was measured is not known, it is believed to be located near cell 11009, where the calculated void fraction is 0.546. For comparison, the calculated void fraction where the nitrogen entered the pipe (cell 110040000) is 0.488 and at the nozzle inlet (cell 110200000) is 0.606. The calculated void fraction appears to be a bit higher than measured.

There was no noticeable difference between the semi- and nearly-implicit calculations.

4.6.5 Conclusions and Assessment Findings

It should be noted that due to the unavailability of a system description report or experiment results report associated with the Moby-Dick critical flow tests, there is considerable uncertainty in correlating the RELAP5-3D model elevations and the experiment thermal-hydraulic conditions. This leads to uncertainty in the comparison of critical flow test data versus the RELAP5-3D calculated results. While the single-phase pressure drop and the pressure undershoot at the choking plane were reasonably simulated,

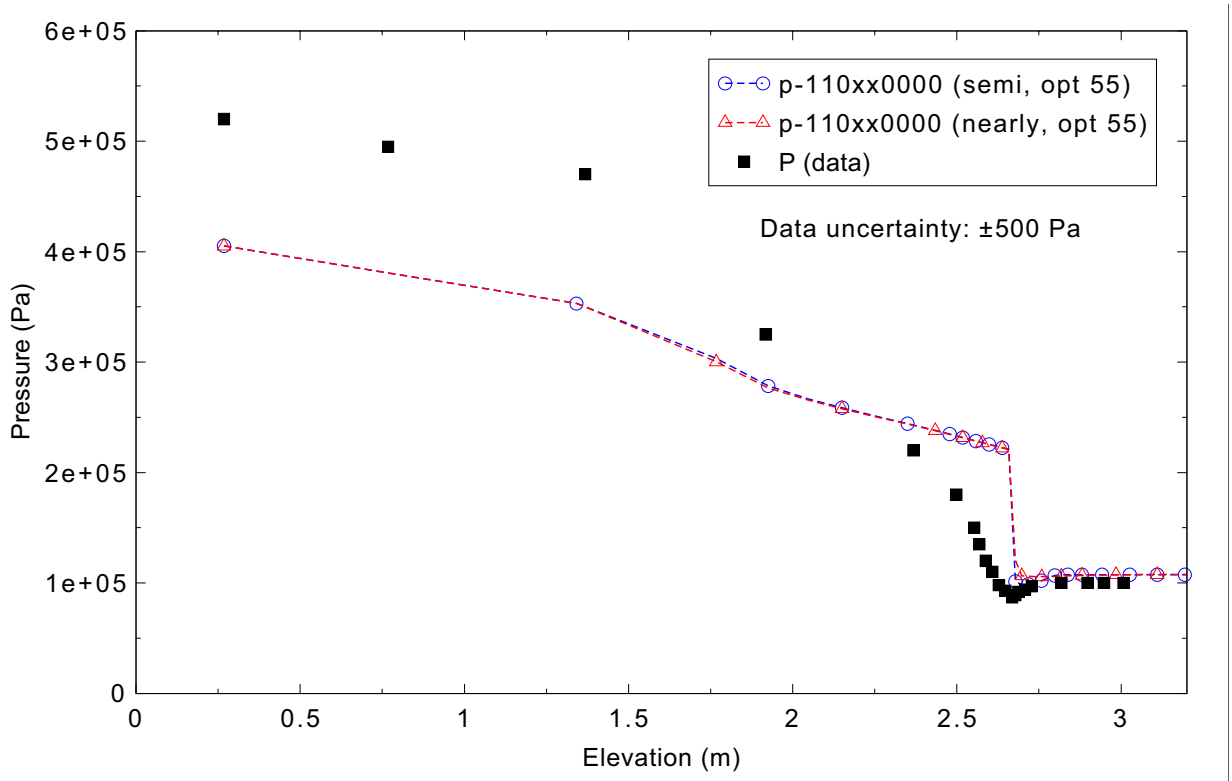

Figure 4.6-3. Measured and calculated axial pressure distribution for Moby-Dick Test 3141.

the significant under prediction of the two-phase pressure drop results in a judgment of minimal agreement in the prediction of the pressure drop near the choking plane in the presence of an air-water mixture.

4.6.6 References

4.6-1. C. Jeandey and G. Barriere, *Etude Experimentale d'Ecoulements Eau-Air a Grande Vitesse*, DTCE/STT/SETRE, January 1979.

4.6-2. William J. Krotiuk, *Analysis Report, TRAC-M Critical Flow Calculation Assessment*, SMSAB-03-01, Office of Nuclear Regulatory Research, Safety Margins and System Analysis Branch, U. S. Nuclear Regulatory Commission, January 2003.

4.7 Christensen Test 15

A series of electrically-heated experiments was performed in the early 1960s to investigate void profiles in vertical tubes using a range of inlet conditions.[4.7-1] Test 15 from that series has been selected to be used in the developmental assessment.

4.7.1 Code Models Assessed

The interphase mass transfer and wall heat flux partitioning models are assessed.

4.7.2 Experiment Facility Description

Figure 4.7-1 is a schematic of the test facility. The test section was a 1.27-m high rectangular tube with a 1.11 x 4.44 cm cross section. The tube was heated by passing an electric current through the tube walls. The void fraction along the test tube was measured by a gamma densitometer. A series of seven tests was conducted investigating the void fraction based on different inlet parameters. The parameters varied were pressure (400-1000 psia) [2.76-6.89 MPa], power (30-70 kW), inlet velocity (0.77-1.15 m/s), and inlet subcooling (2.9-14.4 K). Test 15 was selected for the assessment. The inlet conditions for Test 15 were pressure = 800 psia (5.52 MPa), power = 70 kW, inlet velocity = 1.15 m/s, and inlet subcooling = 12.5 K.

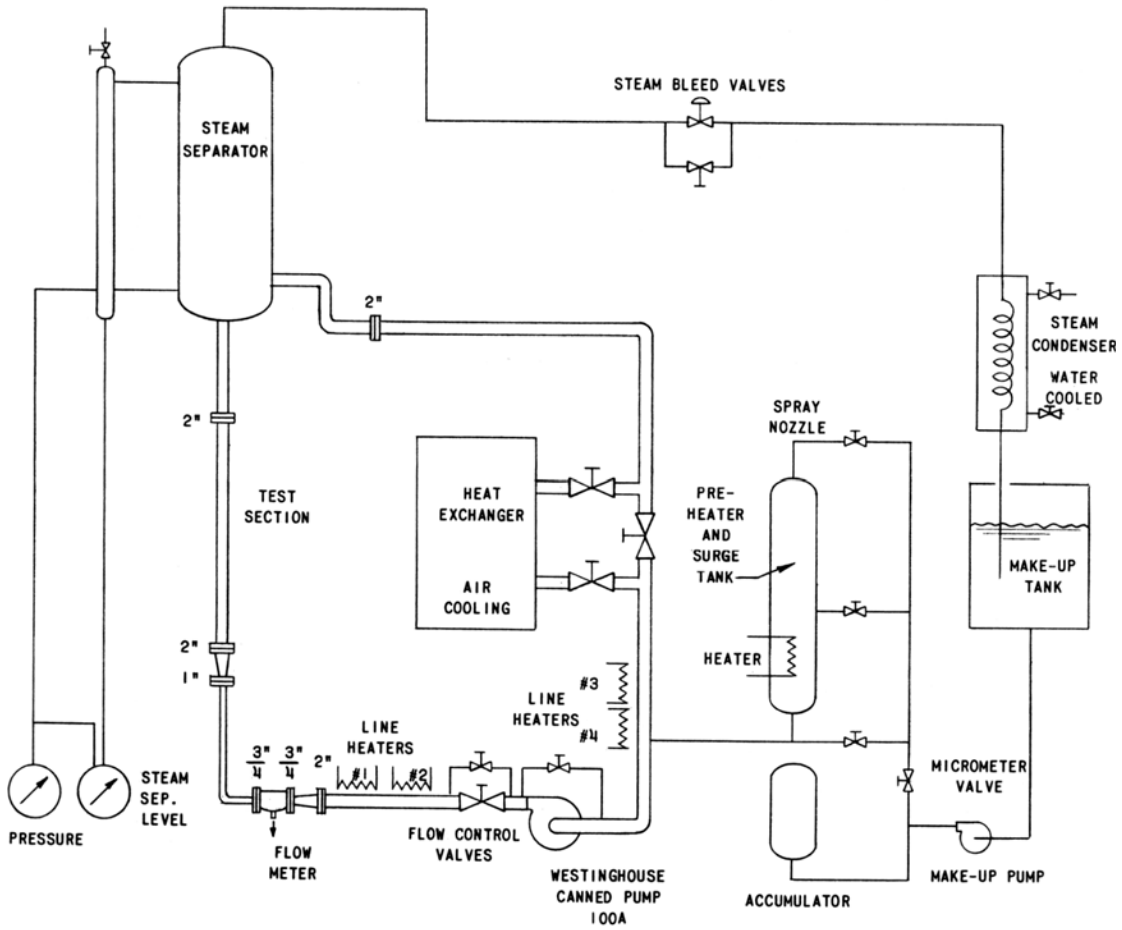

Figure 4.7-1. Test facility schematic for Christensen Test 15.

4.7.3 Input Model Description

The test section was modeled by using a RELAP5-3D pipe component with 17 volumes and 16 junctions. The pipe component dimensions are such that the locations of the pipe internal junctions match the positions where the void fraction was measured for the experiment. At the inlet of the pipe component a time-dependent volume and a time-dependent junction were used to set the boundary conditions for the problem. The outlet was modeled with a single junction component and a time-dependent volume. A heat structure with 17 heat slabs was used to model the heat generated in the walls of the test section. The nodalization is shown in Figure 4.7-2.The RELAP5-3D model was run for 50 s to establish steady-state conditions.

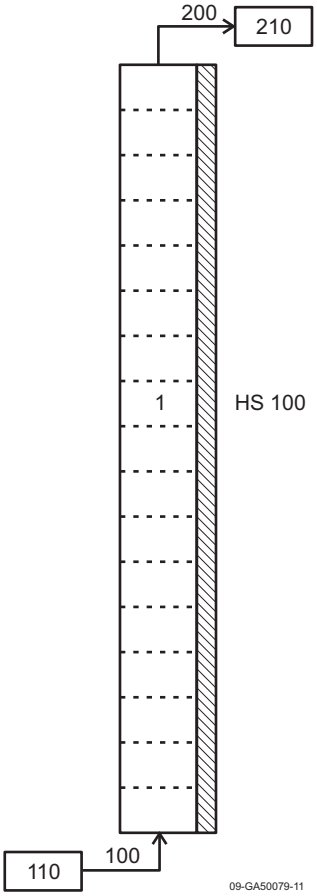

Figure 4.7-2. RELAP5-3D model nodalization for Christensen Test 15.

4.7.4 Data Comparisons and Results

Both the semi- and nearly-implicit calculations were run to 1.0 s with a requested time step of 0.05 s, then to the end of the transient with a requested time step of 0.1 s. The data for this problem come from the NRC Data Bank.

The ability of the code to model the interphase mass transfer and the wall heat flux partitioning was assessed by comparing the measured void fraction in the test section with the RELAP5-calculated void fraction. Figure 4.7-3 presents the measured and calculated void fraction profiles in the test section. The

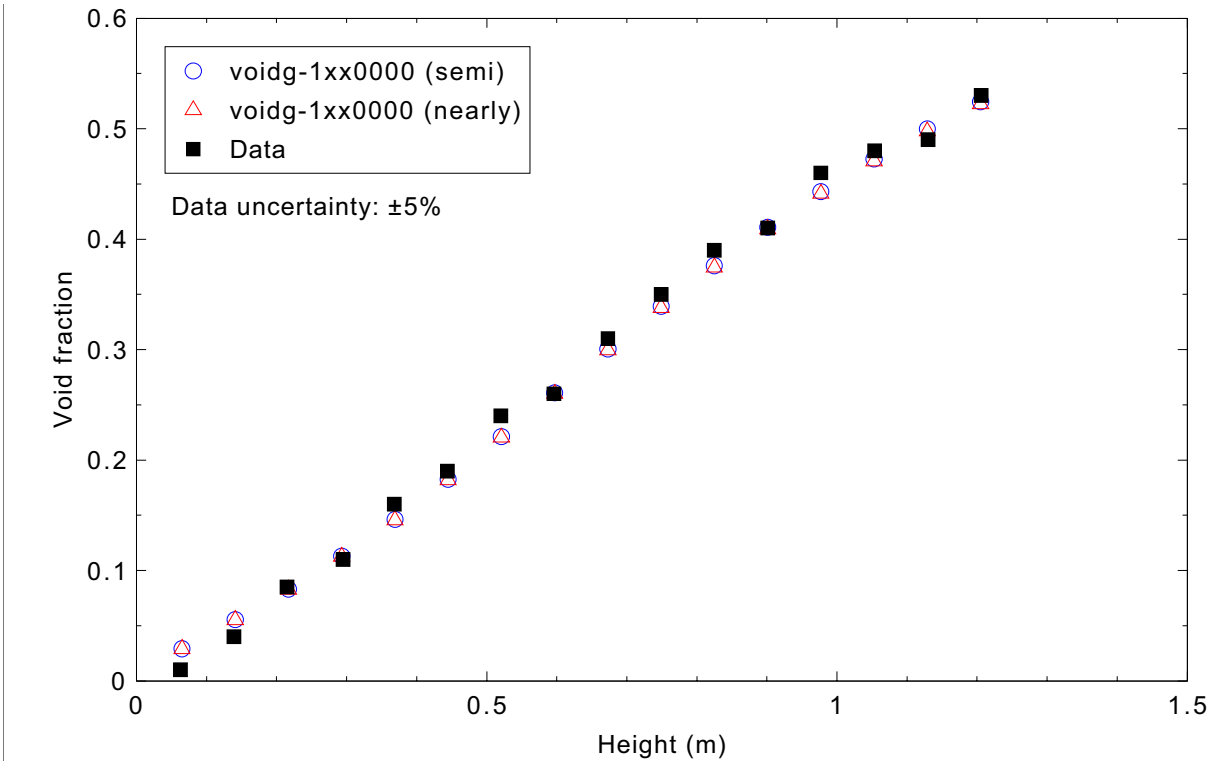

Figure 4.7-3. Measured and calculated test section void profiles for Christensen Test 15.

calculations closely matched the data. There was no difference between the semi- and nearly-implicit void fraction results.

4.7.5 Conclusions and Assessment Findings

The RELAP5-3D calculations are judged to be in excellent agreement with the measured data. The data trend was correctly predicted, and the calculated void fractions were within the data uncertainty band over the entire length of the test section.

4.7.6 References

4.7-1. H. Christensen, *Power-to-Void Transfer Functions*, ANL-6385, 1961.

4.8 GE Level Swell - 1 ft - Test 1004-3

General Electric conducted a series of separate-effects blowdown tests during the 1970s to study transient swell phenomena in two-phase water mixtures. Test number 1004-3 was performed in a one-foot diameter vessel known as the Small Blowdown Vessel. Data collected included absolute and differential pressures, from which void fraction distribution information was derived.[4.8-1]

4.8.1 Code Models Assessed

The performance of the vapor generation, interphase drag, and two-phase level models was evaluated.

4.8.2 Experiment Facility Description

A schematic of the Small Blowdown Vessel is shown in Figure 4.8-1. The vessel is described as being 1 ft (0.3 m) in diameter, 14 ft (4.3 m) long, and having a volume of 10 ft^3 (0.28 m^3). Instrumentation includes an absolute pressure measurement at the top of the vessel as well as differential pressure measurements over two-foot sections of the vessel. A blowdown line runs from near the top of the vessel down to a suppression pool. Orifices of various sizes were inserted into the blowdown line to control the rate of depressurization.

To conduct the blowdown tests, the vessel was partially filled with saturated water. Then the water was heated until the desired initial conditions were obtained. Test 1004-3 had an initial pressure of 1,011 psia (6.97 MPa), an initial liquid level of 10.4 ft (3.2 m), and a blowdown orifice size of 0.375 in. (0.95 cm).

Test results are shown in Reference 4.8-1 as plots of void fraction vs. time for each of the six levels across which differential pressure was measured. Experiment void fractions were determined by assuming that the differential pressure across a section of the vessel (or "node") was due only to the hydrostatic head. An average mixture density for each node i, $\bar{\rho}_i$, was calculated from the hydrostatic head, then the thermodynamic properties at the system pressure were used to calculate an average nodal void fraction:

$$\bar{\alpha}_i = \frac{(\bar{\rho}_i - \rho_f)}{(\rho_g - \rho_f)}. \qquad (4.8\text{-}1)$$

4.8.3 Input Model Description

The nodalization diagram for this test case is shown in Figure 4.8-2. The nodalization of the pressure vessel is the same as that described by Aumiller, Tomlinson, and Clarke[4.8-2] in their assessment of RELAP5-3D. It is represented by a pipe (Component 1) containing 27 volumes. The top and bottom volumes, representing the hemispherical sections of the vessel, are 0.75 ft (0.23 m) in length and have a flow area of 0.5917 ft^2 (0.05497 m^2). The remaining 25 volumes are each 0.5 ft (0.15 m) in length with a flow area of 0.7609 ft^2 (0.07069 m^2). These lengths result in the cell centers being coincident with the locations of the pressure taps, assumed from the test report schematic to be spaced at 2-ft (0.6-m) intervals

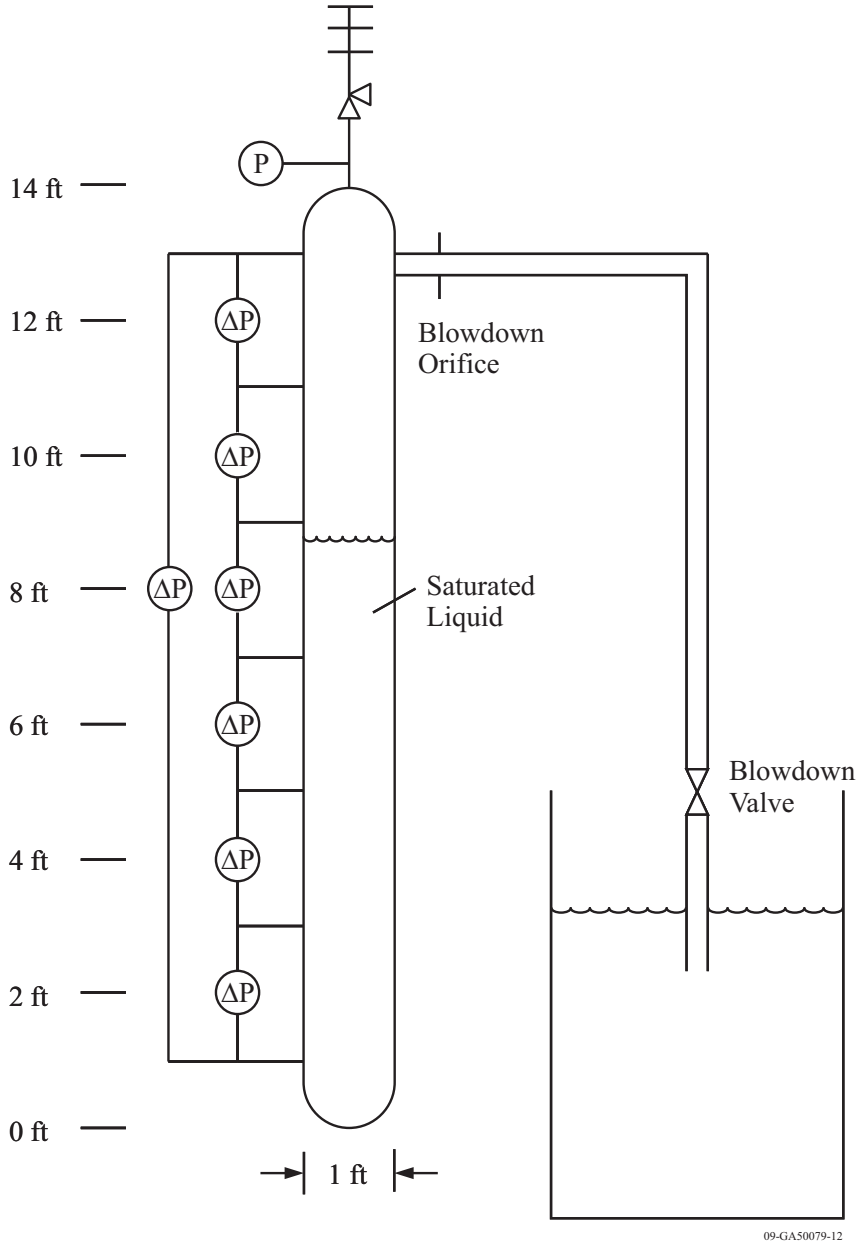

Figure 4.8-1. Test schematic for GE Small Blowdown Vessel test 1004-3.

from 1 to 13 ft (0.3 to 4.0 m). Junction 2, representing the blowdown line, is attached to the side (face 4) of pipe volume 26. It is given a flow area consistent with that of a 2-in. schedule 80 pipe.

Instead of explicitly modeling the discharge line and blowdown orifice, a pressure boundary condition is imposed. Pressure data were extracted from the pressure curve reported in Reference 4.8-1 and are applied in tabular form as the pressure in time-dependent volume 11. This approach has been used previously to eliminate the uncertainties in modeling the choked flow through the blowdown orifice, especially given the fact that the orifice flow rate was not measured and cannot be compared against model output. Implementation of a pressure boundary condition serves to focus the validation on the models of

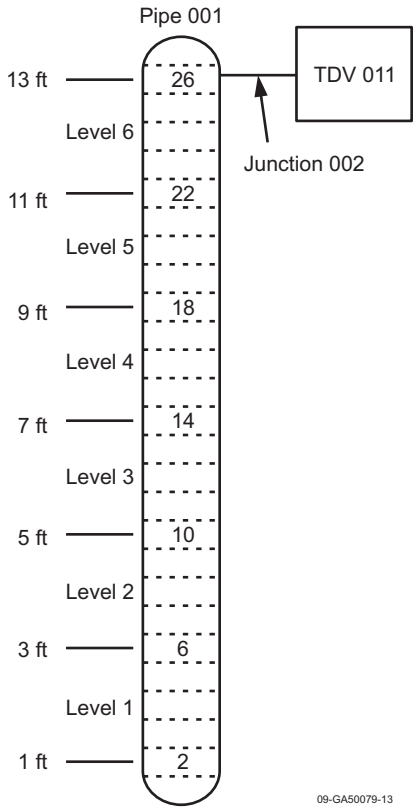

Figure 4.8-2. Nodalization diagram for GE Small Blowdown Vessel test 1004-3.

interest for this case: interphase drag, vapor generation, and two-phase level. Figure 4.8-3 compares the measured pressure data to the calculated pressure imposed by the time-dependent volume.

Void fractions shown in the results section below are calculated using control variables 101-106. Each control variable corresponds to one of the experiment node levels shown in Figure 4.8-2 and is simply a volume-averaged void fraction over the volumes in that level. A previous assessment has indicated that the difference in RELAP5-3D between this volume-averaged void fraction method and the experimental derivation of void fraction from hydrostatic head is small.[4.8-2]

4.8.4 Data Comparisons and Results

Semi- and nearly-implicit calculations were performed, using a requested time step size of 0.1 s. Void fraction predictions are shown in Figures 4.8-4 through 4.8-14. The first six figures are plots of void fraction vs. time for each of the six levels in the experiment. The final five are axial profiles of void fraction at various times during the transient. All data shown in the plots were taken from plots of void fraction vs. time (pressure vs. time in the case of Figure 4.8-3) in Appendix B of Reference 4.8-1. The plots of experiment data in the test document include only an indication of typical uncertainties, not exact values; these are annotated in the figures. With the exception of Figure 4.8-14, all the calculated void fraction values in the plots are volume averaged over each level as described in the Input Model Description section above.

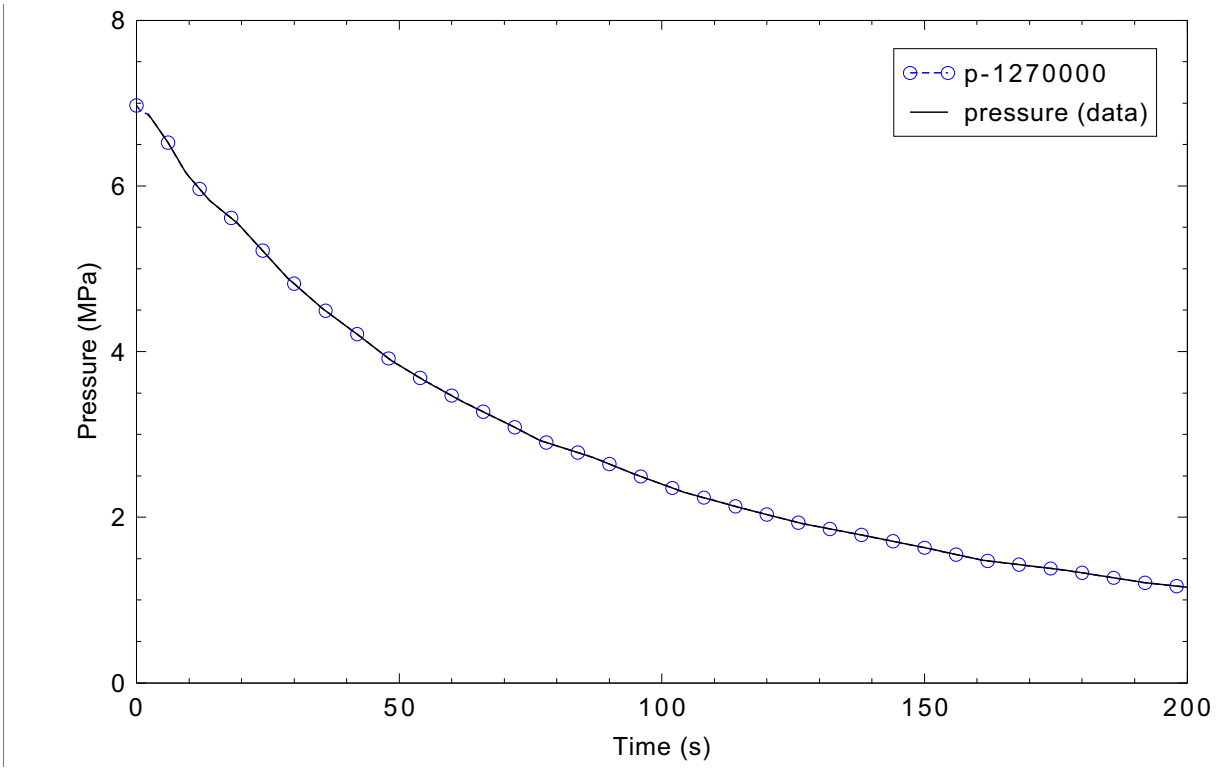

Figure 4.8-3. Comparison of experiment data with the pressure imposed by time-dependent volume 11.

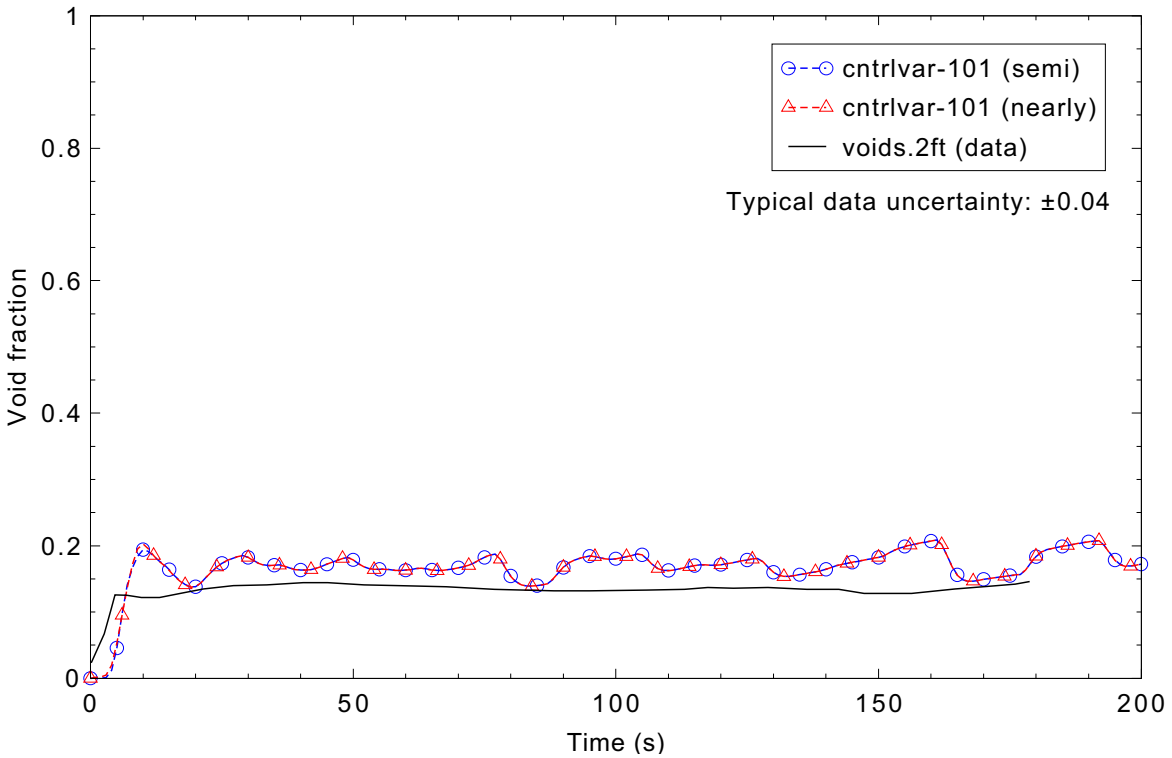

Figure 4.8-4. Measured and calculated void fraction at 2 ft (0.6 m) above the bottom of the vessel (level 1) for GE level swell Test 1004-3.

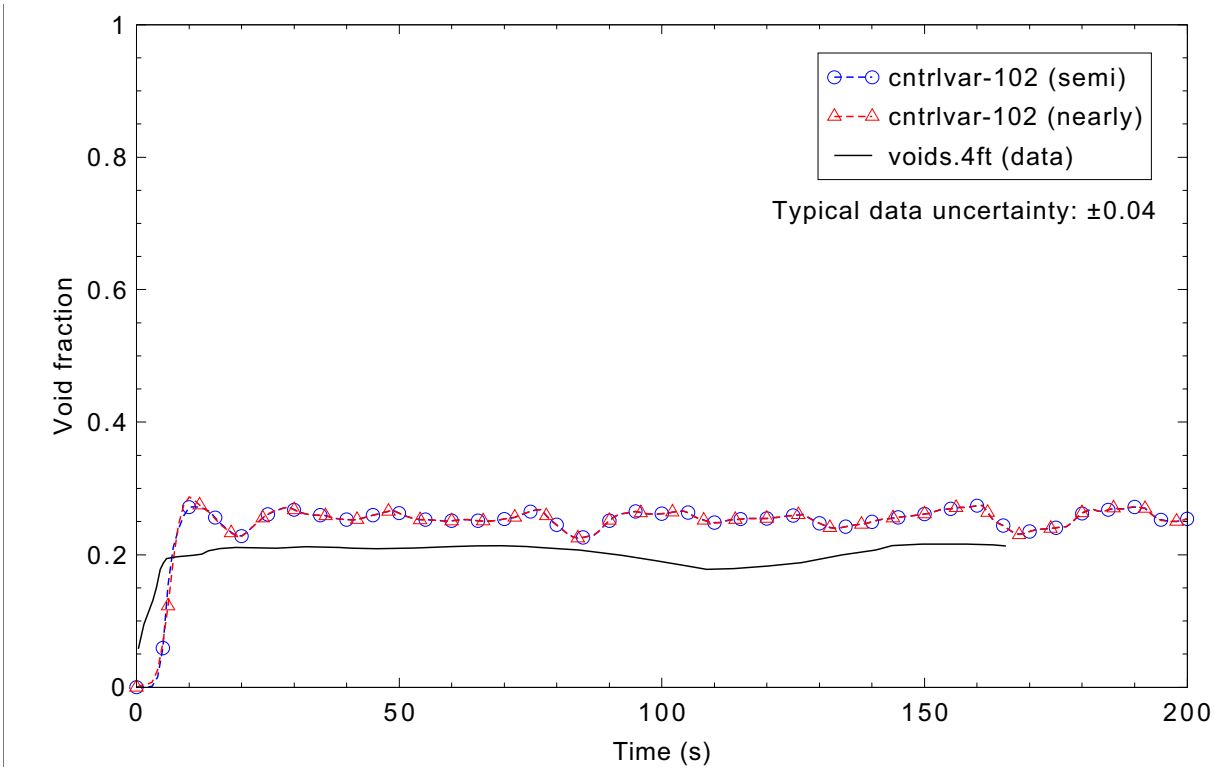

Figure 4.8-5. Measured and calculated void fraction at 4 ft (1.2 m) above the bottom of the vessel (level 2) for GE level swell Test 1004-3.

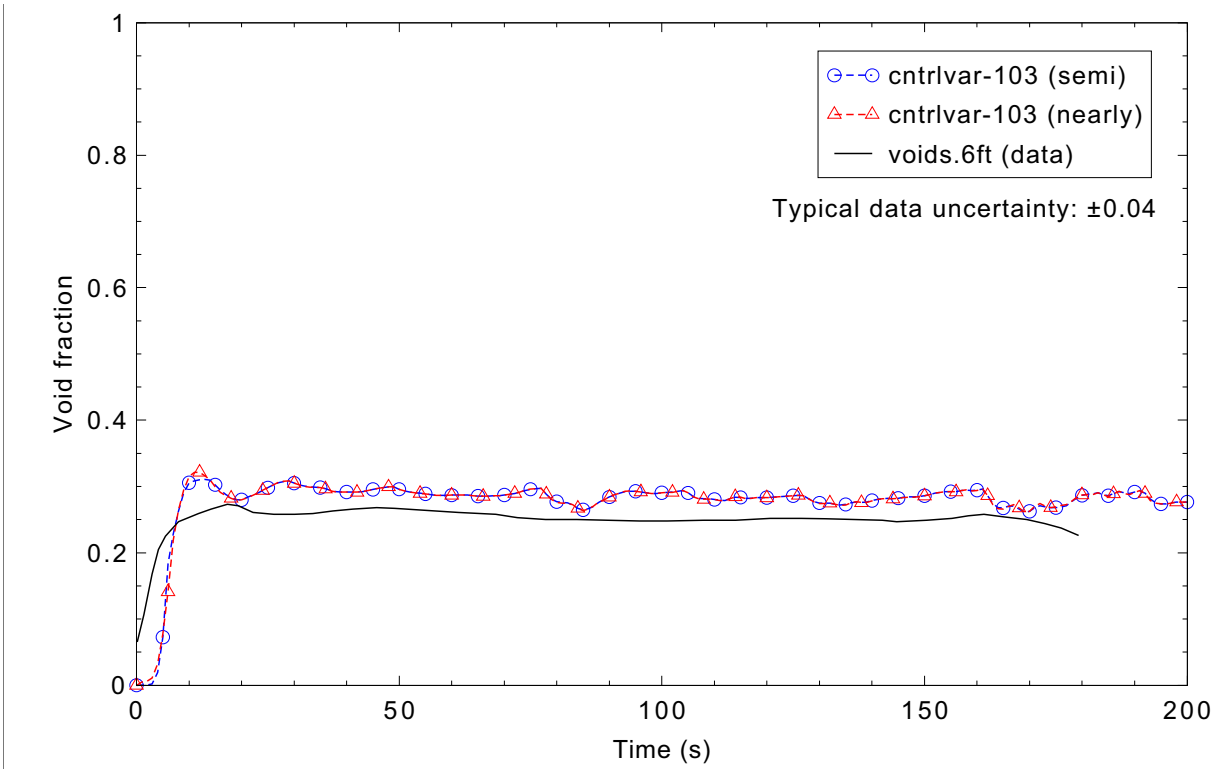

Figure 4.8-6. Measured and calculated void fraction at 6 ft (1.8 m) above the bottom of the vessel (level 3) for GE level swell Test 1004-3.

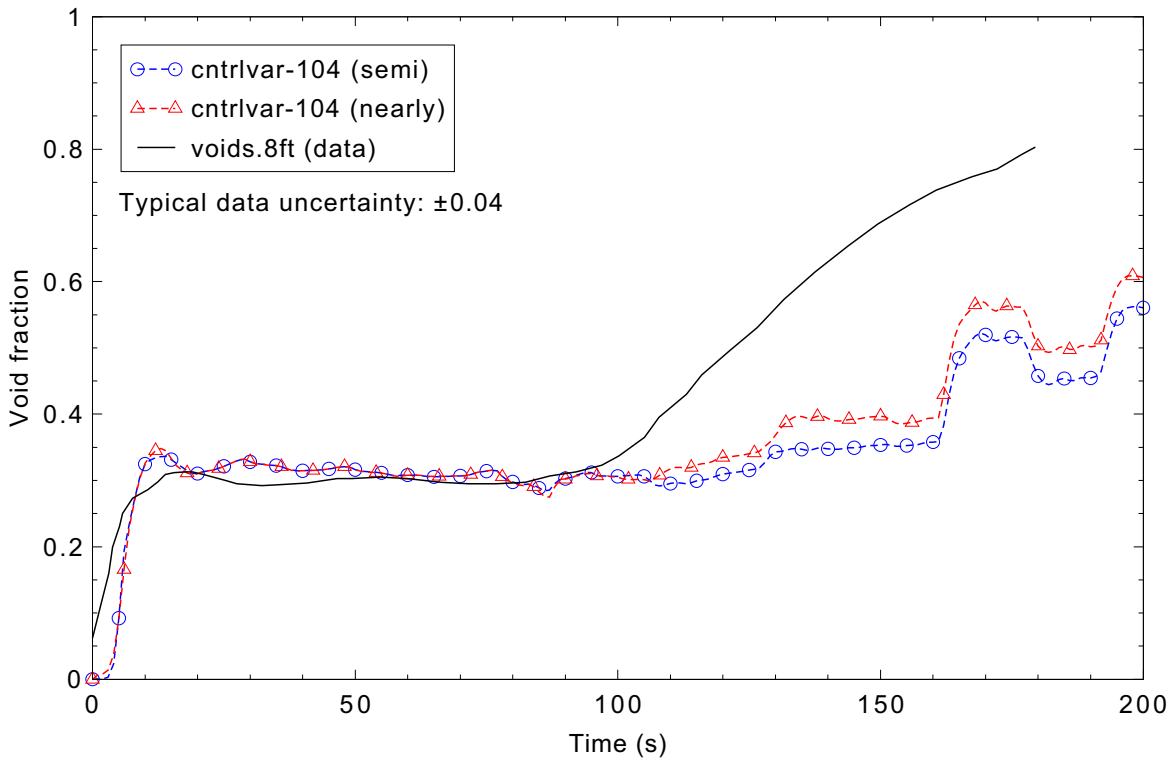

Figure 4.8-7. Measured and calculated void fraction at 8 ft (2.4 m) above the bottom of the vessel (level 4) for GE level swell Test 1004-3.

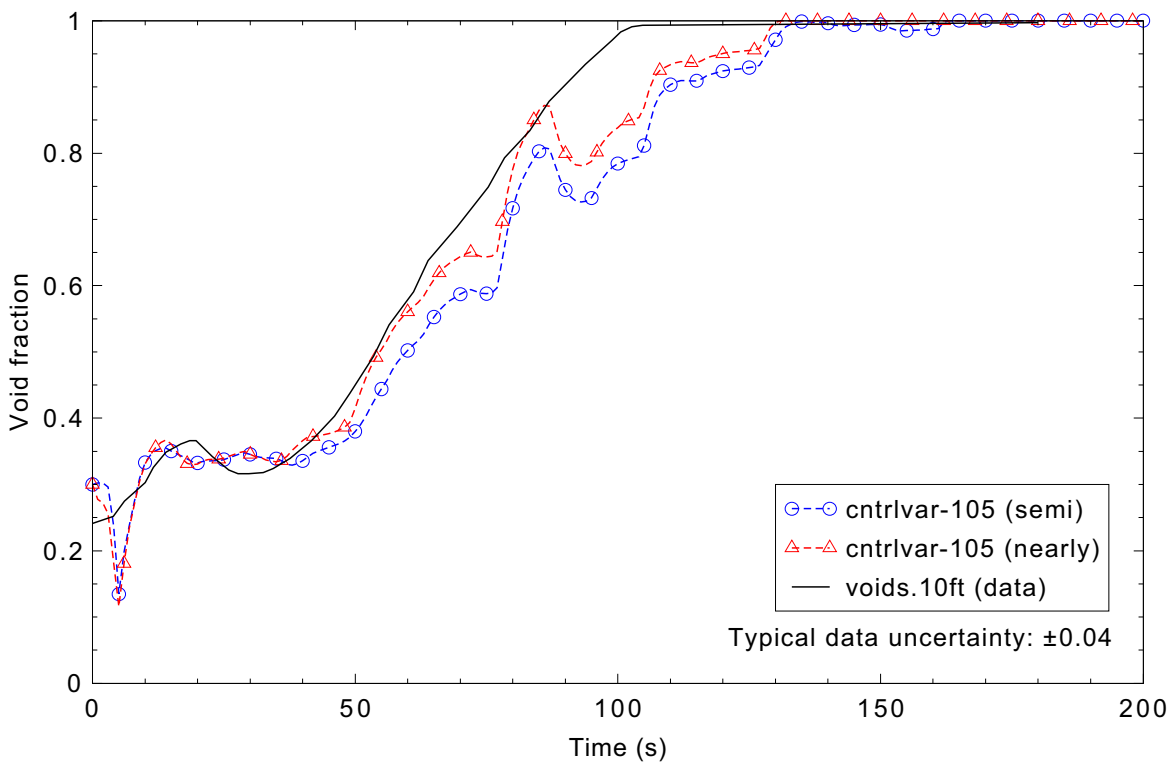

Figure 4.8-8. Measured and calculated void fraction at 10 ft (3.0 m) above the bottom of the vessel (level 5) for GE level swell Test 1004-3.

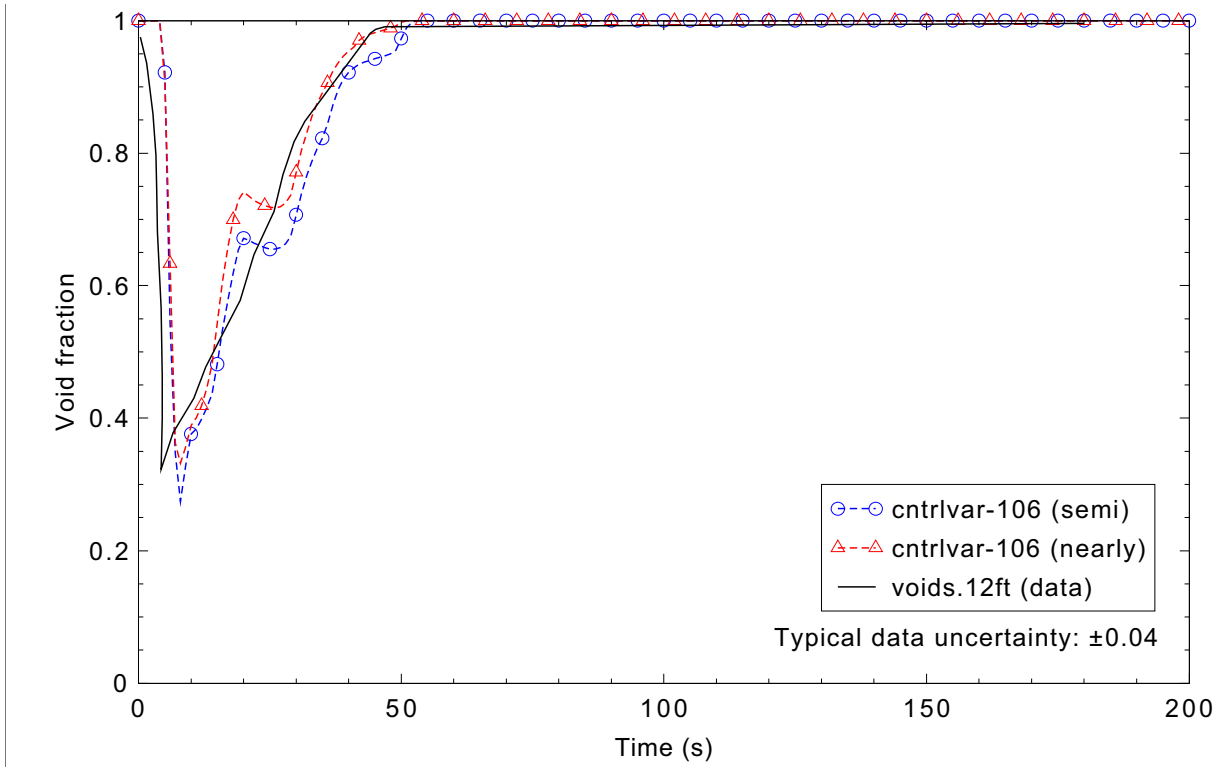

Figure 4.8-9. Measured and calculated void fraction at 12 ft (3.7 m) above the bottom of the vessel (level 6) for GE level swell Test 1004-3.

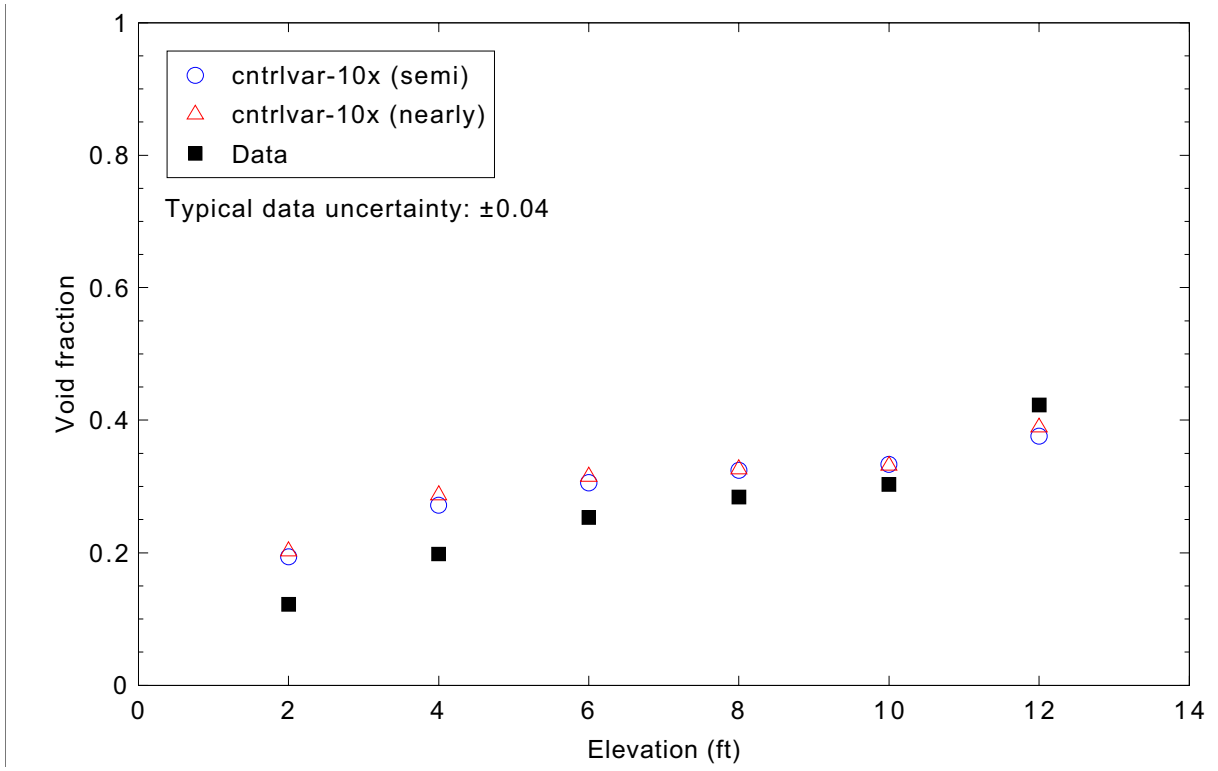

Figure 4.8-10. Measured and calculated void fraction profile in the vessel at 10 s for GE level swell Test 1004-3.

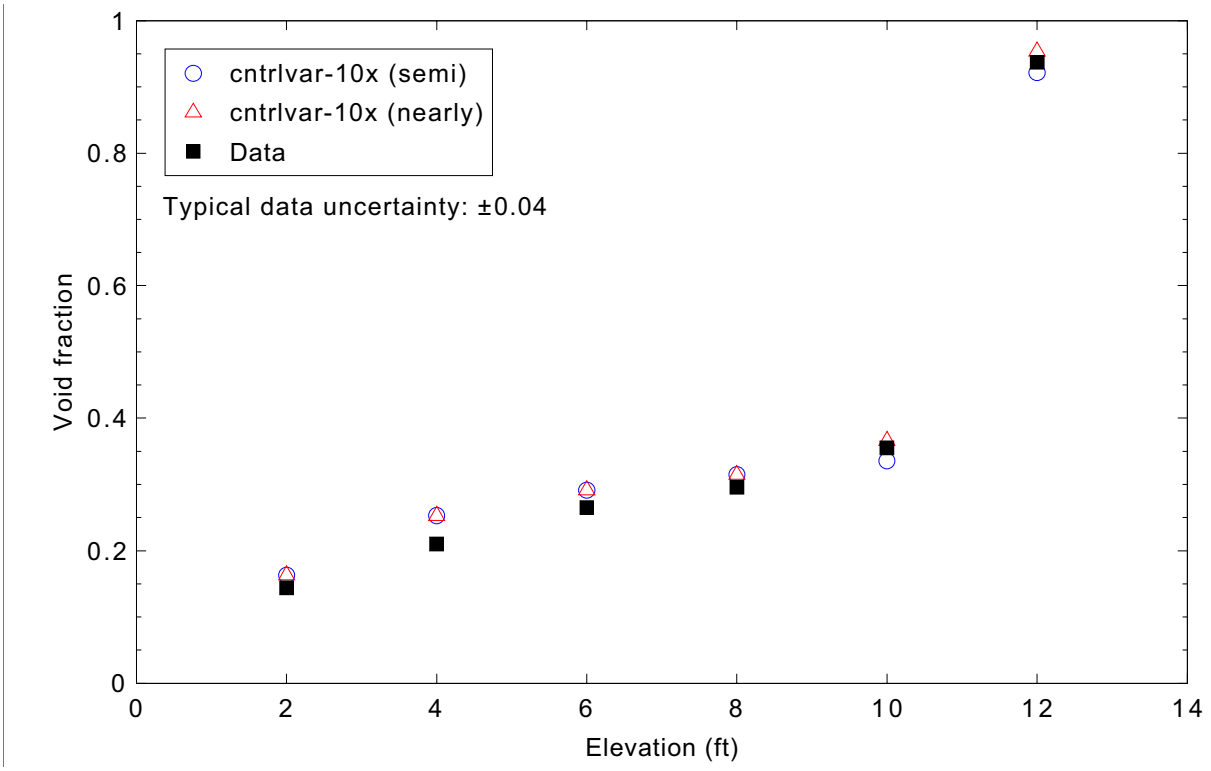

Figure 4.8-11. Measured and calculated void fraction profile in the vessel at 40 s for GE level swell Test 1004-3.

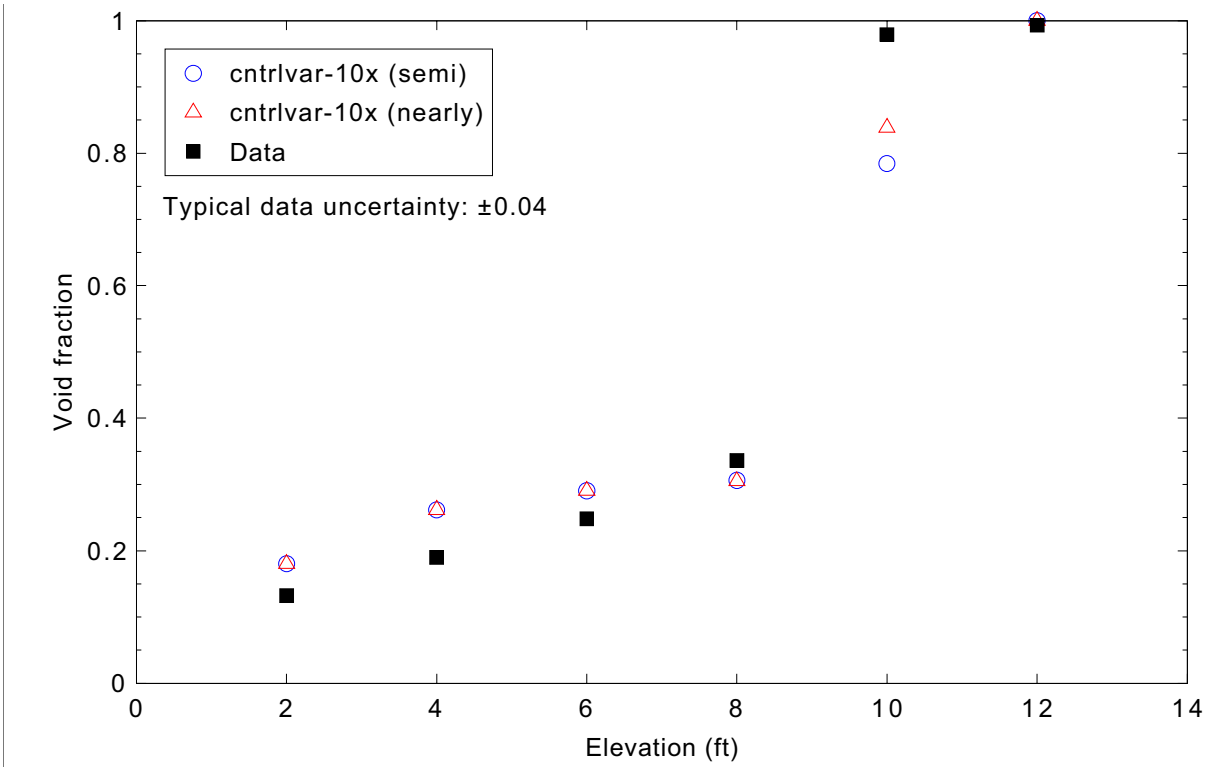

Figure 4.8-12. Measured and calculated void fraction profile in the vessel at 100 s for GE level swell Test 1004-3.

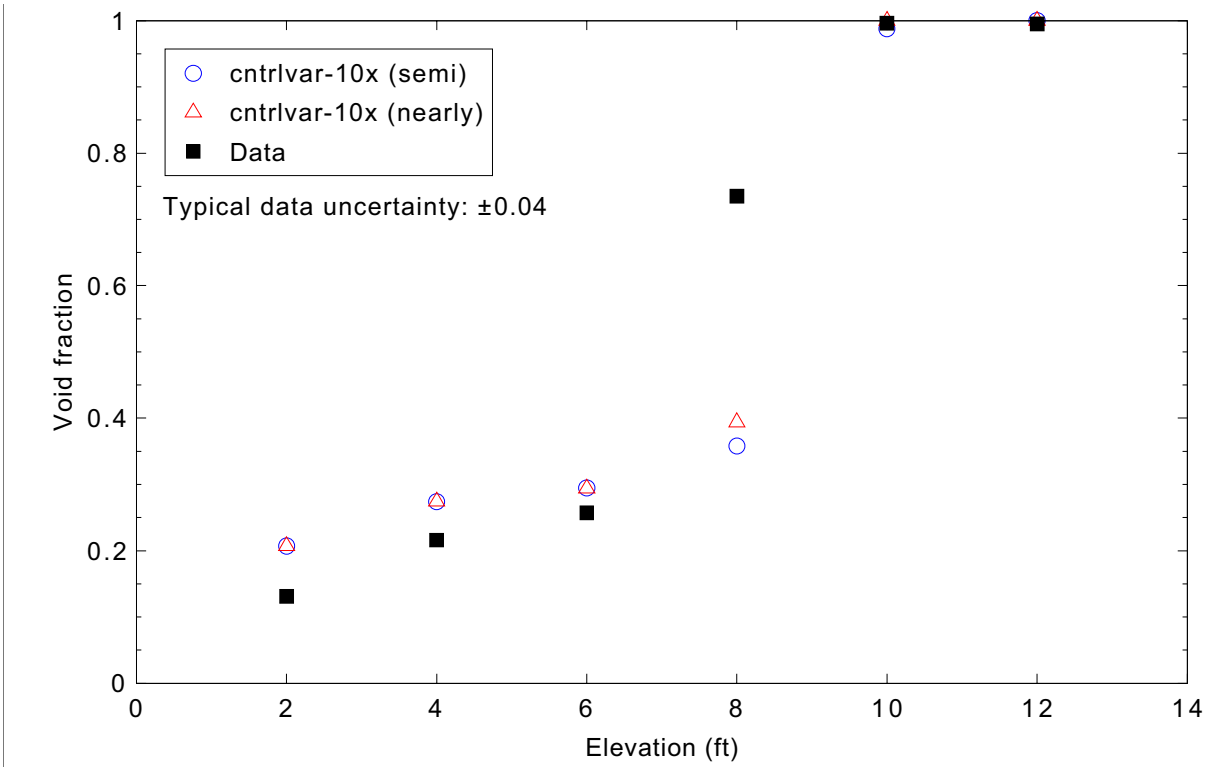

Figure 4.8-13. Measured and calculated void fraction profile in the vessel at 160 s for GE level swell Test 1004-3.

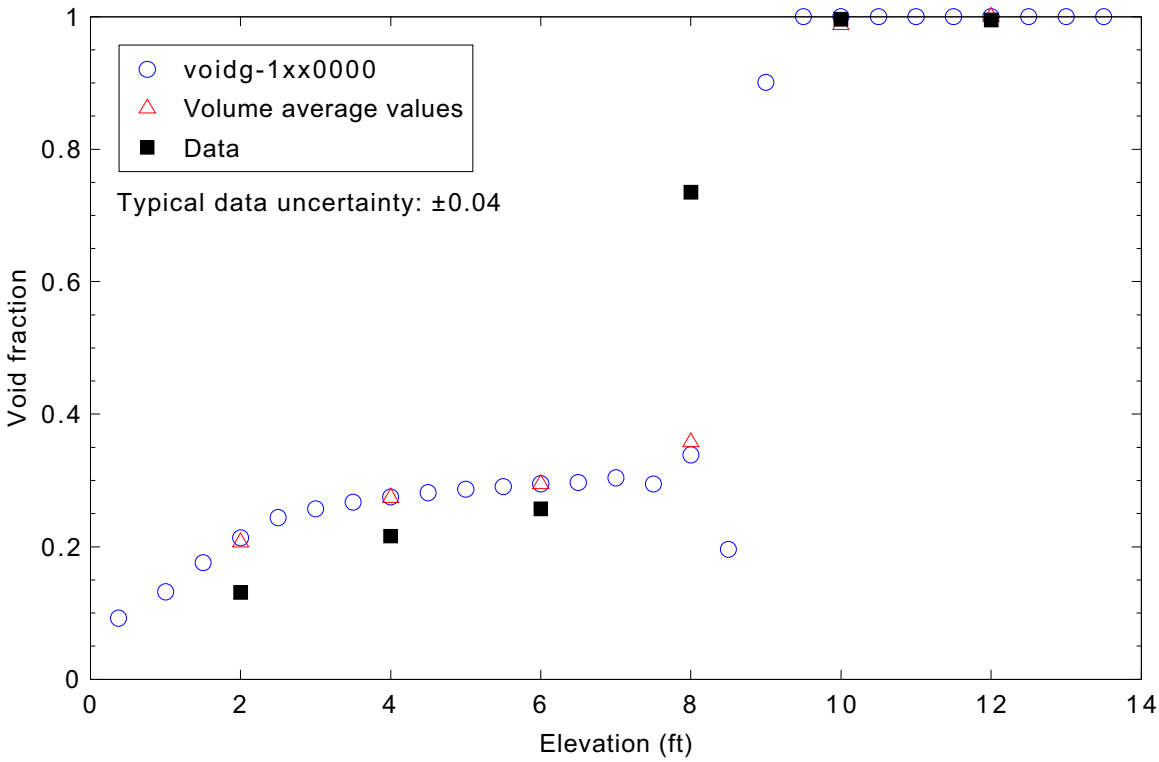

Figure 4.8-14. Volume and volume-average void fractions at 160 s for GE level swell Test 1004-3 (semi-implicit calculations).

The void fraction time history predictions for the pressure vessel nodes below the mixture level (Figures 4.8-4 through 4.8-6) show reasonable agreement with the data. While the liquid region void fraction is slightly over predicted, most of the predicted values lie within the typical range of uncertainty for the experiment data.

Notable discrepancies between the predicted void fraction and the experiment data begin appearing in Figure 4.8-7 after approximately 100 s, when the mixture level (as indicated by major edit void fraction profiles) begins to drop into level 4. At this point the predicted void fraction falls well below the range of uncertainty in the experiment data. Similar behavior is seen in level 5 when the mixture level is in that range (Figure 4.8-8), although the predicted values are much closer to the experiment data. Level 6 results show excellent agreement with the data.

The axial void profile plots in Figures 4.8-10 through 4.8-13 generally show reasonable agreement with the data. Void fraction in the lower levels tends to be slightly over predicted, although the values fall within or close to the uncertainty range in the data. Figures 4.8-12 and 4.8-13 show that, as described previously, the void fraction is under predicted in the vicinity of the mixture level. The sequence of axial profile plots shows that RELAP5-3D qualitatively predicts the initial level swell and subsequent drop in level, although the predicted level lags that indicated by the experiment data.

A closer inspection of the axial void profiles calculated by RELAP5-3D reveals that during the latter half of the transient there are times at which a void fraction inversion occurs (a volume with a lower void fraction on top of a volume with a higher void fraction). This is seen in Figure 4.8-14, which reproduces the results shown in the previous figure but with the more detailed void profile data added. The major edit at 160 s shows that the flow regimes in pipe volumes 16, 17, and 18 (corresponding to elevations of 8.0, 8.5, and 9.0 ft) are slug, bubbly, and annular mist, respectively. Note that the lower void fraction in volume 17 will also slightly reduce the volume average void fraction result for level 4. This behavior has been noted in a previous assessment using RELAP5/MOD3.2.

4.8.5 Conclusions and Assessment Findings

The RELAP5-3D results are in reasonable agreement with the experiment data. The default interphase drag models create good phase separation. All major trends and phenomena are correctly modeled.

Void fractions in the liquid region tend to be slightly over predicted, while the void fraction in the vicinity of the mixture level is generally low. The code correctly reproduces the initial level swell and qualitatively modeled the subsequent level drop, although the level was over predicted in the latter half of the transient.

4.8.6 References

4.8-1. J. A. Findlay and G. L. Sozzi, *BWR Refill-Reflood Program - Model Qualification Task Plan*, EPRI NP-1527, NUREG/CR-1899, GEAP-24898, October 1981.

4.8-2. David L. Aumiller, Edward T. Tomlinson, and William G. Clarke, “A New Assessment of RELAP5-3D Using a General Electric Level Swell Problem,” *Nuclear Technology*, Vol. 137, No. 3, March 2002, pp. 213-227.

4.9 GE Level Swell - 4 ft - Test 5801-15

General Electric conducted a series of separate-effects blowdown tests during the 1970s to study transient swell phenomena in two-phase water mixtures. Test number 5801-15 was performed in a four-foot diameter vessel known as the Large Blowdown Vessel. Data collected included absolute and differential pressures, from which void fraction distribution information was derived.[4.9-1]

4.9.1 Code Models Assessed

The performance of the vapor generation, interphase drag, and two-phase level models was evaluated.

4.9.2 Experiment Facility Description

A schematic of the Large Blowdown Vessel is shown in Figure 4.9-1. The vessel is 47 in. (1.2 m) in diameter, 14 ft (4.3 m) long, and has a volume of 160 ft^3 (4.5 m^3). Instrumentation includes an absolute pressure measurement at the top of the vessel and in the blowdown line venturi, as well as differential pressure measurements over the seven sections ("nodes") of the vessel. The blowdown line has a 10-in. (0.25-m) diameter vertical dip tube that can be attached to allow top blowdown tests to be conducted, or removed for bottom blowdown tests. Test 5801-15 is a top blowdown test.

Test 5801-15 had an initial pressure of 1,060 psia (7.3 MPa), an initial liquid level of 5.5 ft (1.7 m), and a blowdown nozzle size of 2.5 in. (6.4 cm).

4.9.3 Input Model Description

The nodalization diagram for this test case is shown in Figure 4.9-2. The vertical dip tube is represented by pipe 104. It is connected to the pressure vessel (pipe 103) and upper plenum (pipe 101) by branch 102. The nominal flow area for volumes in the cylindrical section of the pressure vessel is 12.048 ft^2 (1.1193 m^3). The flow area for the volumes containing the dip tube is reduced by the area of the corresponding section of the blowdown line.

Instead of explicitly modeling the blowdown venturi, a pressure boundary condition is imposed. Pressure data (measured at the top of the vessel) were extracted from the NRC Data Bank file and are applied in tabular form as the pressure in time-dependent volume 106. Choking did not occur in the blowdown pipe during the transient, and the differences in calculated pressure between the time-dependent volume and pipe volume 101-06 were insignificant. The differences ranged from a couple of percent during the first 2 s to less than 1.0 psi. Imposing a pressure boundary condition in this way eliminates the uncertainties in modeling the choked flow through the blowdown venturi and serves to focus the validation on the models of interest for this case: interphase drag, vapor generation, and two-phase level. Figure 4.9-3 compares the measured pressure data to the calculated pressure imposed by the time-dependent volume.

Void fractions shown in the results section below are calculated using control variables 101-107. Each control variable corresponds to one of the experiment node levels shown in Figure 4.9-2 and is simply a volume-averaged void fraction over the volumes in that level.

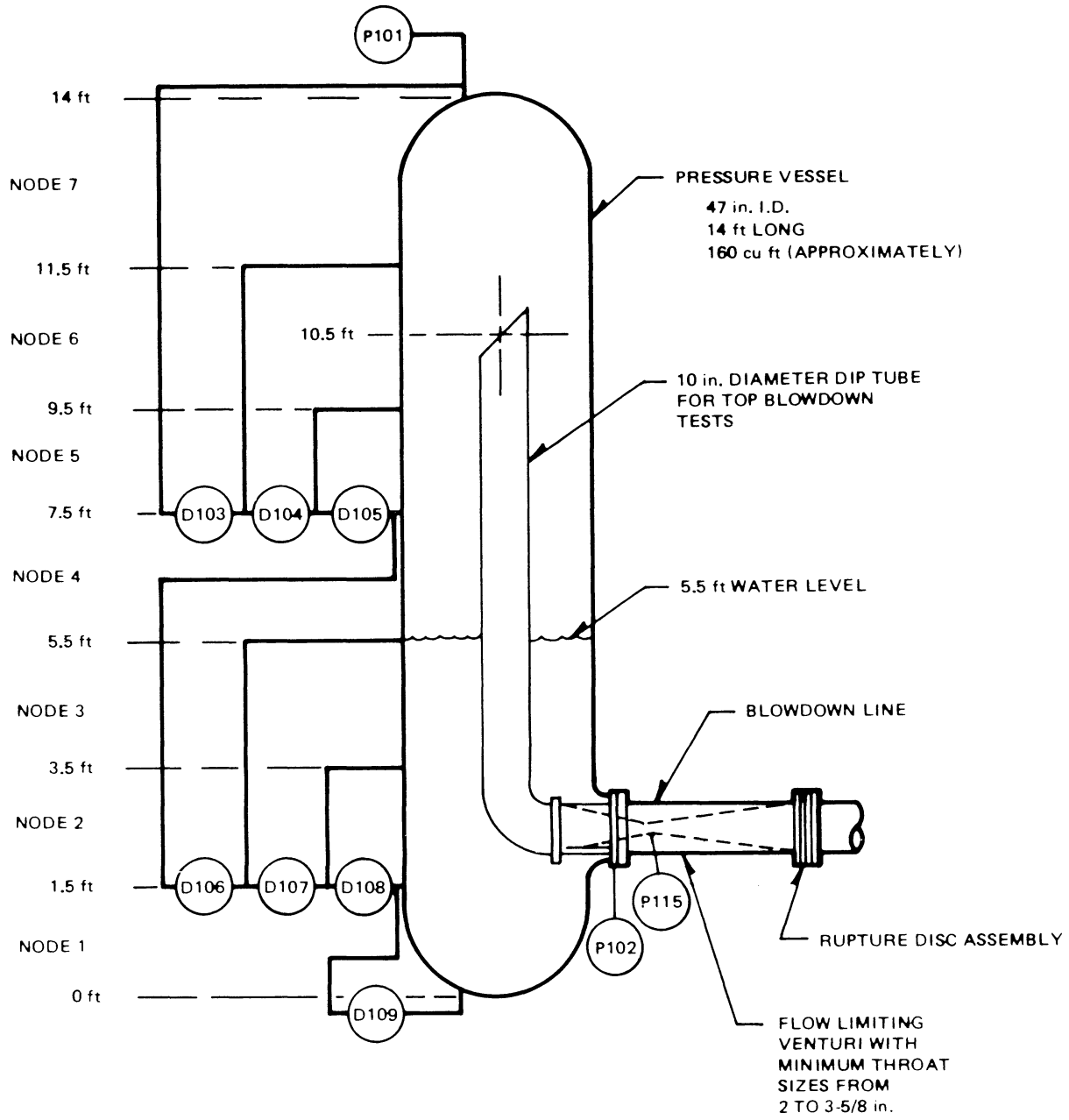

Figure 4.9-1. GE Large Blowdown Vessel schematic diagram.

4.9.4 Data Comparisons and Results

Void fraction axial profiles are shown in Figures 4.9-4 through 4.9-7. Experiment data were obtained from the NRC Data Bank. The plots of experiment data in the test document include only an indication of typical uncertainties, not exact values; this is annotated in the figures. All the calculated void fraction values in the plots are volume averaged over each level as described in the Input Model Description section above. The requested time step sizes were 0.01 s for the first second and 0.2 s for the rest of the transient for both the semi- and nearly-implicit calculations.

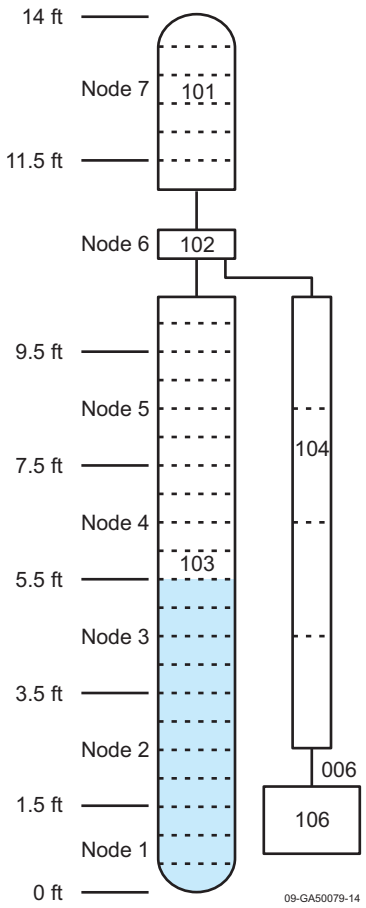

Figure 4.9-2. Nodalization diagram for GE Large Blowdown Vessel test 5801-15.

The axial void fraction profiles calculated by RELAP5-3D generally show reasonable agreement with the data. The results at 2 s lie within the bounds of the data uncertainty, with the exceptions of the nodes immediately below and above the mixture level. The void fraction below the level is slightly under predicted, while that above the level is slightly over predicted. The calculated void fraction actually drops as the elevation increases from level 3 to level 4, in an area predicted to lie within the slug flow regime.

The calculated results for most of the remainder of the transient show a sharper void profile than the experiment data indicate. Void fractions below the mixture level are too low, and those above are too high. By the end of the transient at 20 s, however, the calculated values show excellent agreement with the data.

A limited sensitivity study was performed to judge the effect of the level tracking model on the calculated results. Figures 4.9-8 and 4.9-9 show the semi-implicit results for the bottom five levels, while Figures 4.9-10 and 4.9-11 show the nearly-implicit results. The semi-implicit results show almost no difference in the predicted void fraction, with the exception of some minor differences during the first 2 s of the transient. Similarly, the nearly-implicit results show relatively minor differences, mainly during the first 5 s.

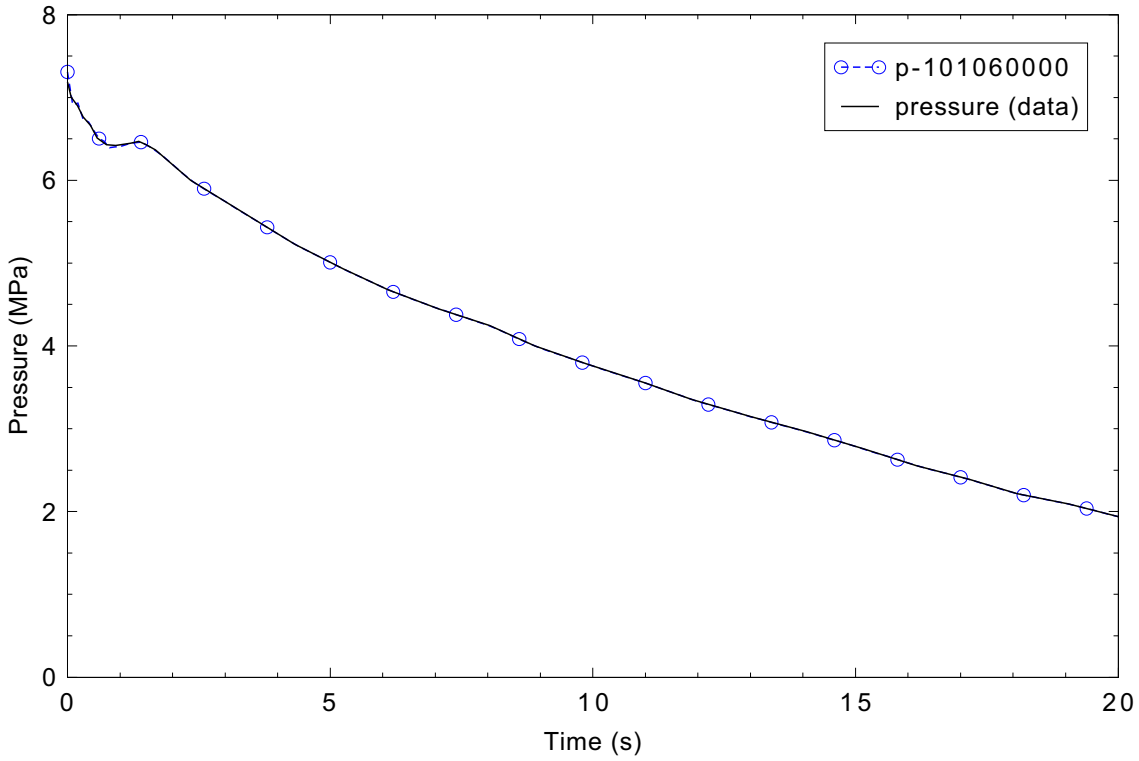

Figure 4.9-3. Comparison of experiment data with the pressure imposed by time-dependent volume 106 for GE level swell Test 5801-15.

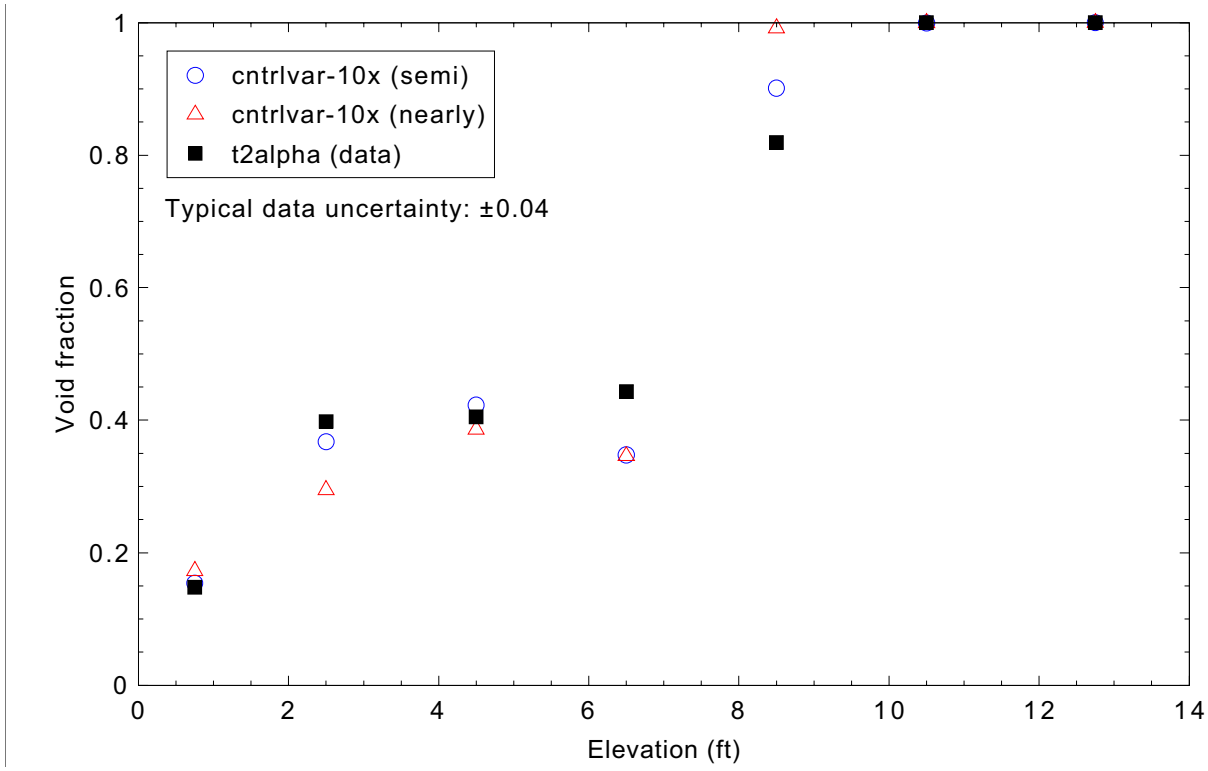

Figure 4.9-4. Measured and calculated void fraction profile in the vessel at 2 s for GE level swell Test 5801-15.

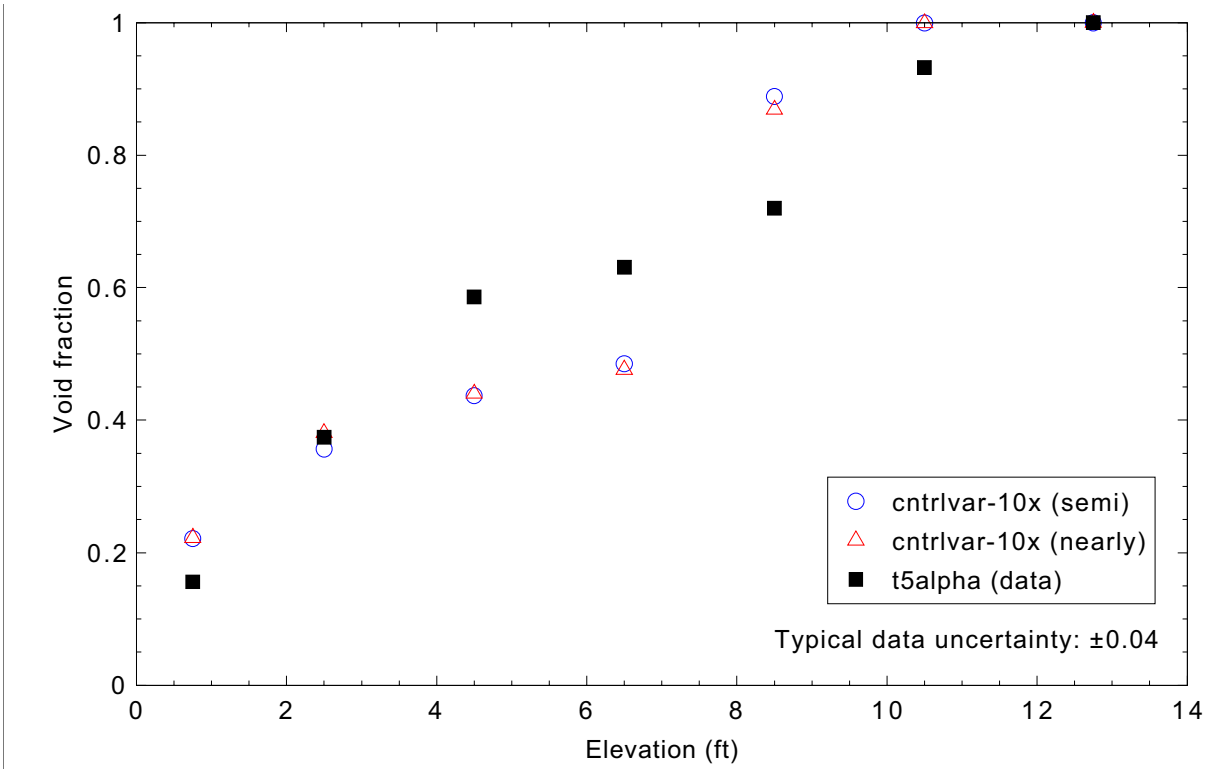

Figure 4.9-5. Measured and calculated void fraction profile in the vessel at 5 s for GE level swell Test 5801-15.

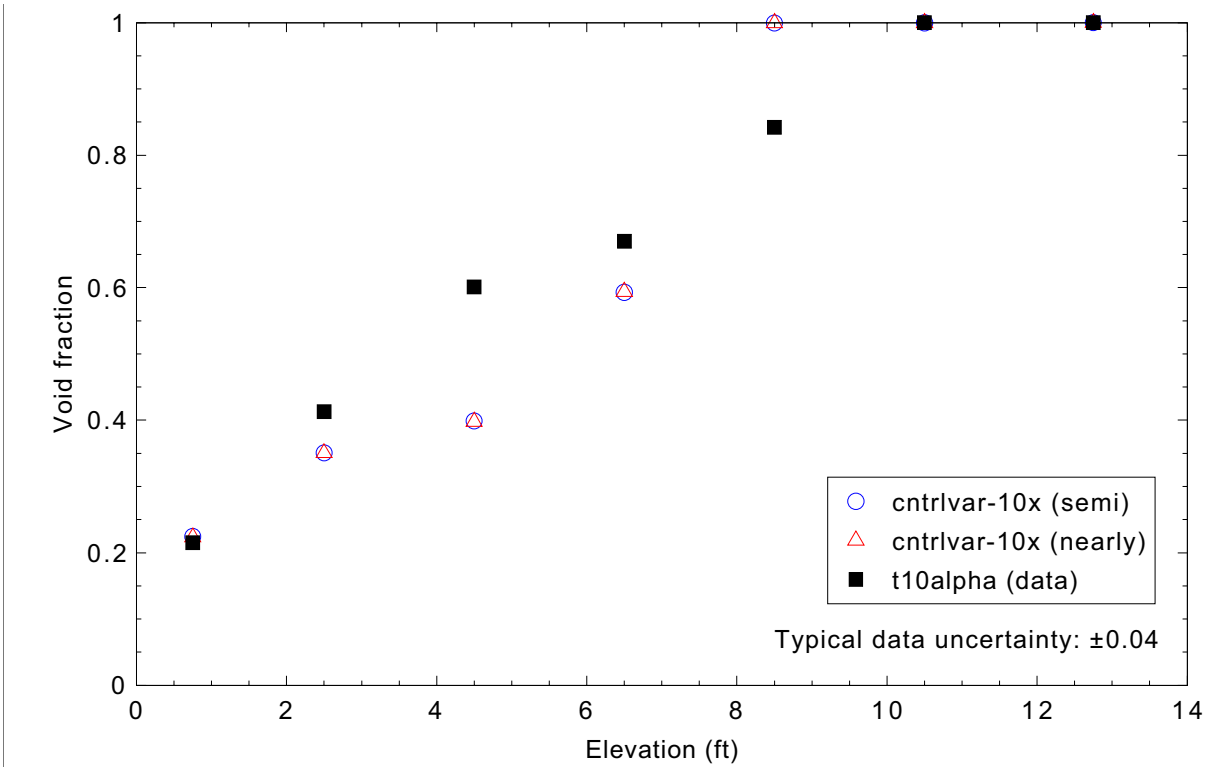

Figure 4.9-6. Measured and calculated void fraction profile in the vessel at 10 s for GE level swell Test 5801-15.

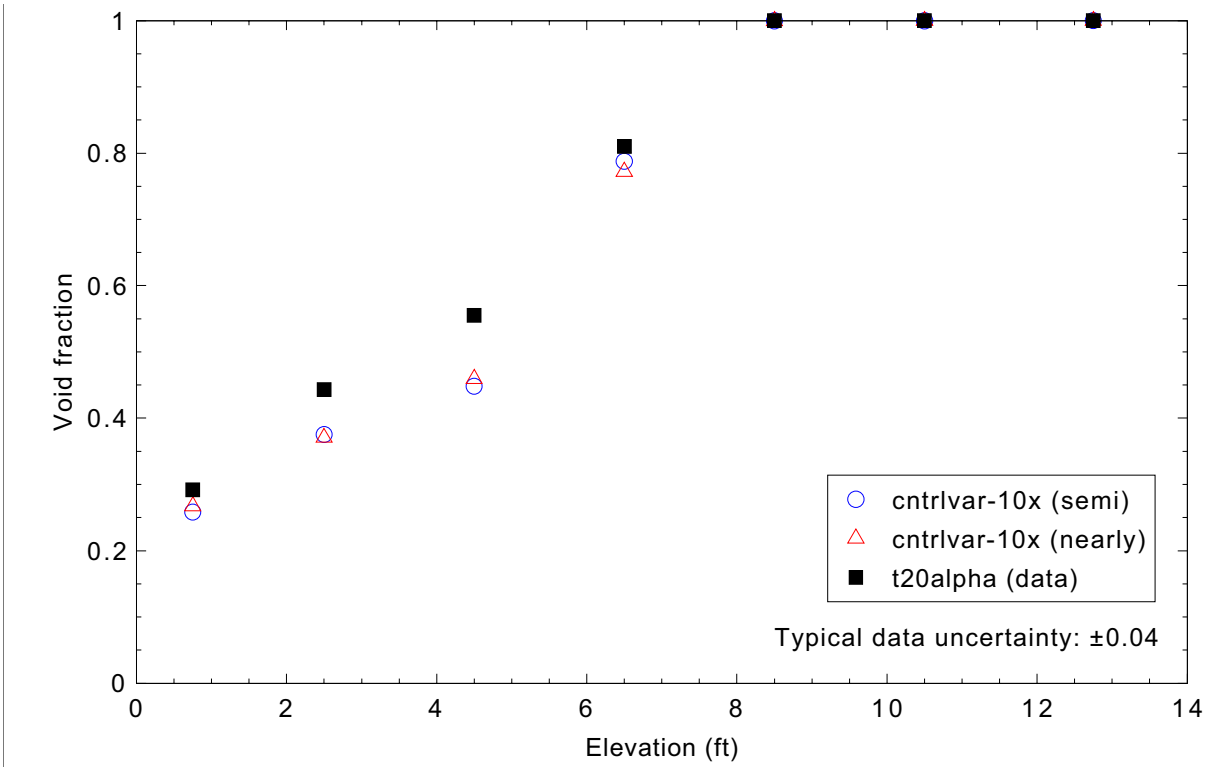

Figure 4.9-7. Measured and calculated void fraction profile in the vessel at 20 s for GE level swell Test 5801-15.

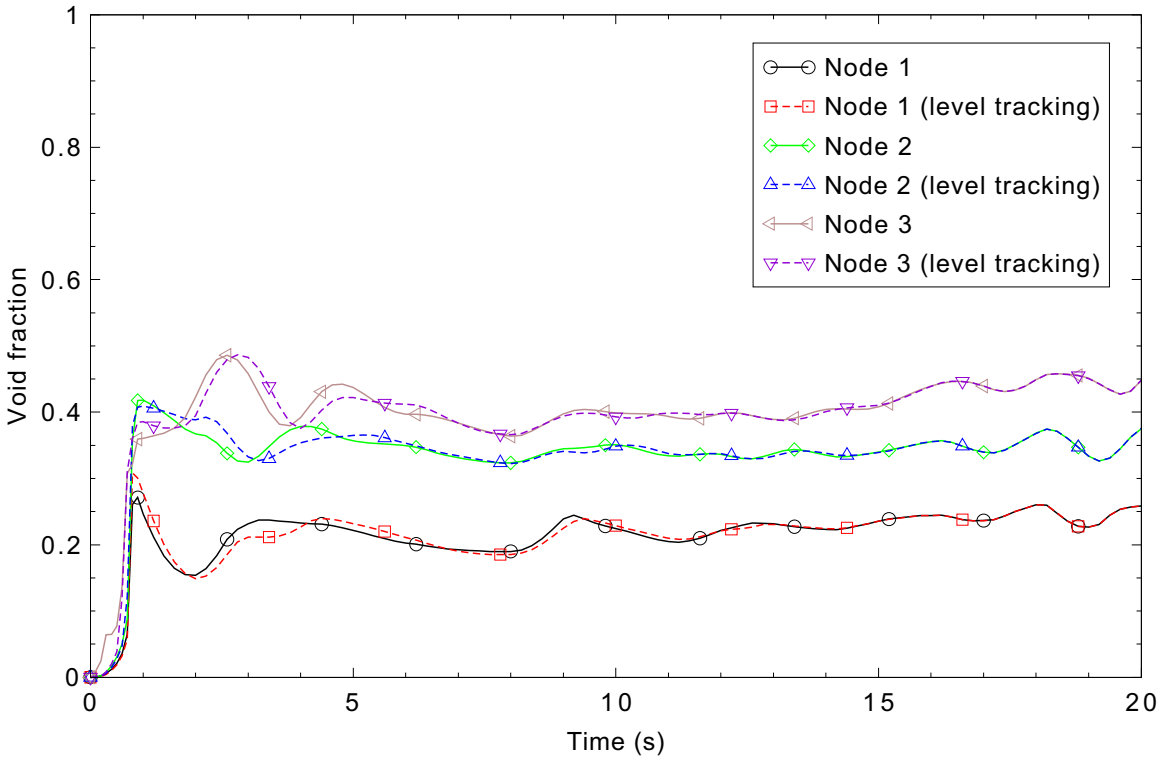

Figure 4.9-8. Effect of level tracking model on calculated void fractions for levels 1-3 using the semi-implicit solution scheme for GE level swell Test 5801-15.

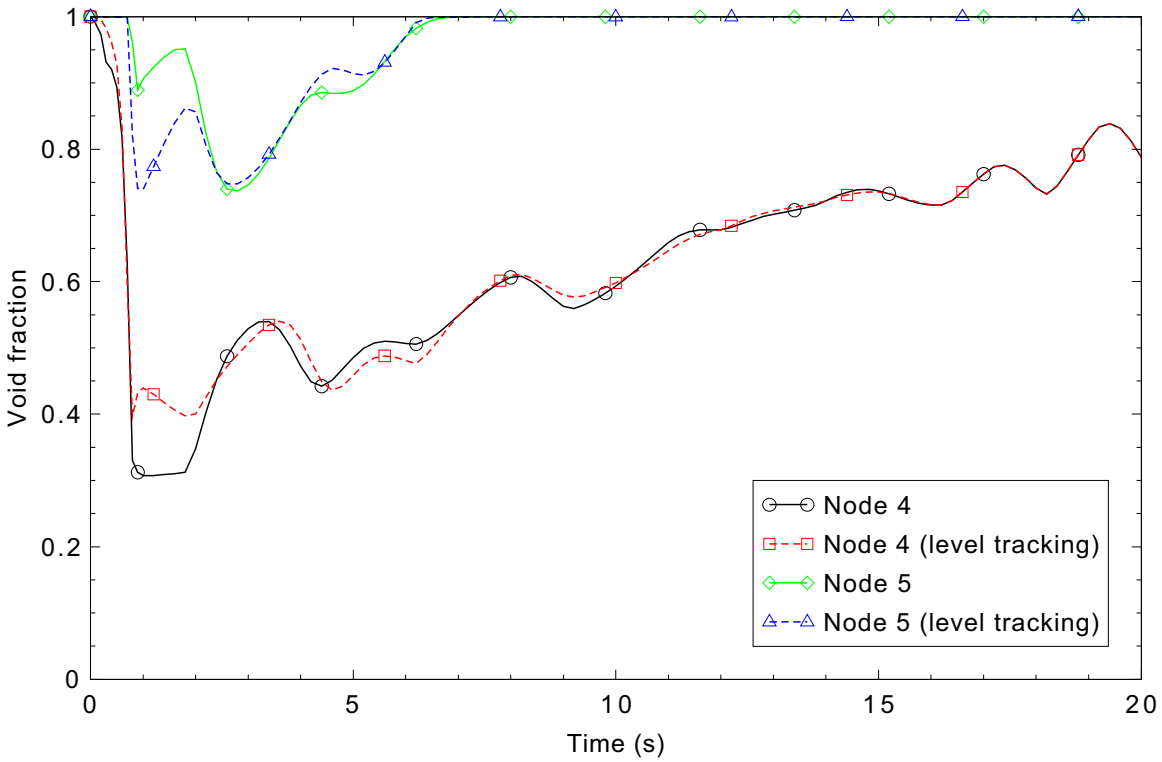

Figure 4.9-9. Effect of level tracking model on calculated void fractions for levels 4 and 5 using the semi-implicit solution scheme for GE level swell Test 5801-15.

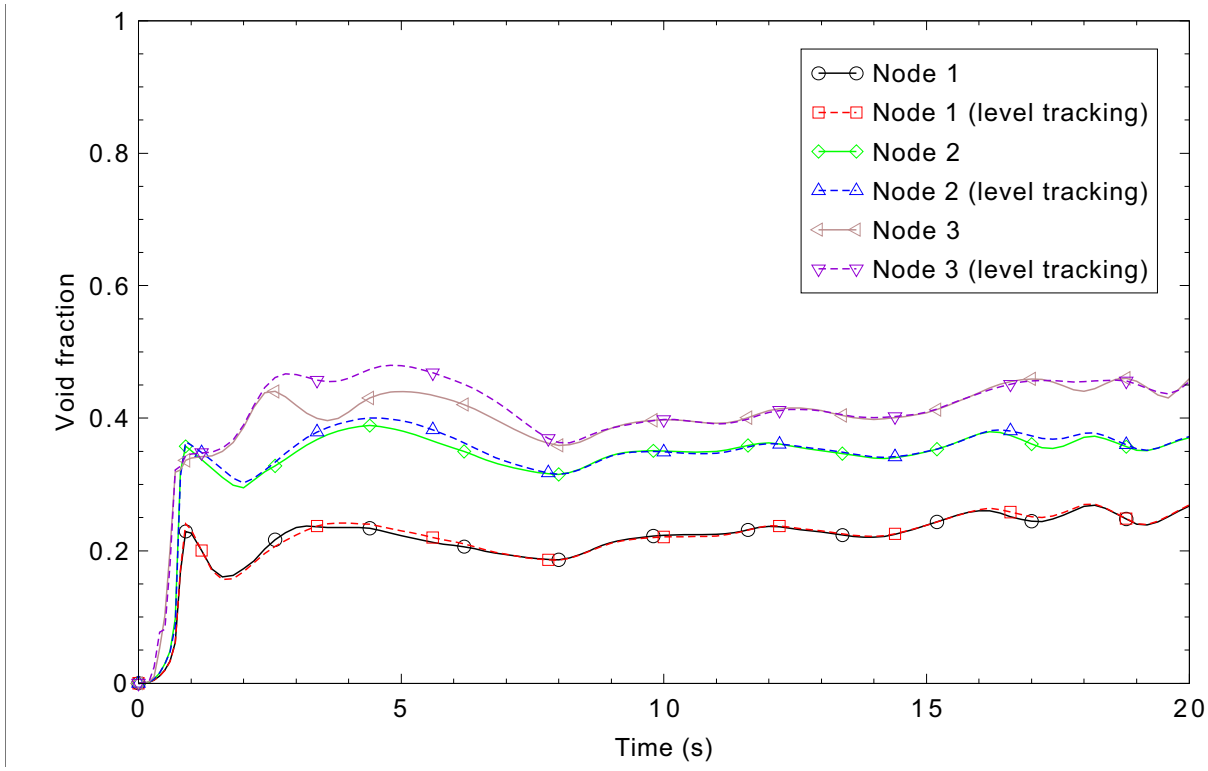

Figure 4.9-10. Effect of level tracking model on calculated void fractions for levels 1-3 using the nearly-implicit solution scheme for GE level swell Test 5801-15.

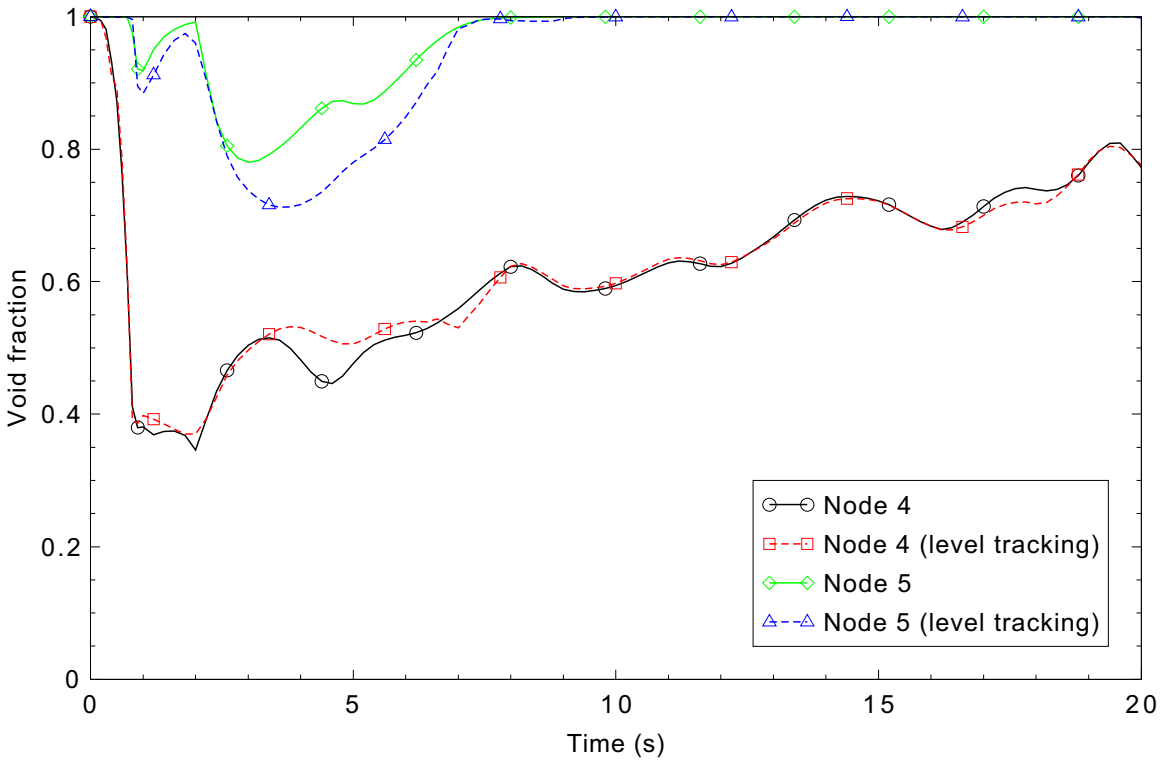

Figure 4.9-11. Effect of level tracking model on calculated void fractions for levels 4 and 5 using the nearly-implicit solution scheme for GE level swell Test 5801-15.

4.9.5 Conclusions and Assessment Findings

Overall, the calculated results are judged to be in reasonable agreement with the experiment data. RELAP5-3D tends to predict a sharper mixture level for most of this transient, with a lower void below the level and a higher void above. However, the major trends are correctly predicted.

A limited sensitivity study was conducted to determine whether the level tracking model produced better results than the default code. The study indicates that the level tracking model does not produce significantly different results for this transient.

4.9.6 References

4.9-1. J. A. Findlay and G. L. Sozzi, *BWR Refill-Reflood Program - Model Qualification Task Plan*, EPRI NP-1527, NUREG/CR-1899, GEAP-24898, October 1981.

4.10 Bennett Heated Tube Tests 5358, 5294, and 5394

The main objectives of the experiment were to measure the dryout location (or critical heat flux [CHF] location) where liquid ceased to adhere to the inside wall and the surface temperature profiles in the region beyond the dryout point. Three experiments were simulated, Bennett Tests 5358, 5294, and 5394.

4.10.1 Code Models Assessed

Bennett heated tube Tests 5358, 5294, and 5394 assess the CHF model.

4.10.2 Experiment Facility Description

The test section was composed of a heated tube with a length and inner diameter of 5.537 m (18.16667 ft) and 0.012624 m (0.041416 ft), respectively. It was vertically oriented. High pressure and high temperature (but slightly subcooled) liquid flowed into the bottom of the test section, boiled passing through the heated tube, and steam (or a two-phase mixture of steam and liquid) flowed to a condenser. The heat flux and mass flux to the test section were constant in each test but their magnitudes varied between experiments.

4.10.3 Input Model Description

Figure 4.10-1 shows the nodalization diagram for the Bennett tube test facility input model. As shown in this figure, the hydraulic components included in this input model are a pipe (test section, Component 1), two time-dependent volumes (Components 110 and 210), a time-dependent junction (Component 100) at the inlet of the test section, and a single junction (Component 200) at the outlet of the test section. A heat structure (Component 1003) is attached to the pipe.

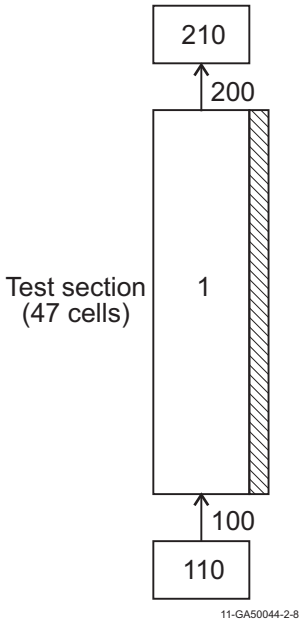

Figure 4.10-1. Nodalization diagram for the Bennett test facility.

The heated test section was nodalized in detail (47 nodes) to simulate Bennett tube Tests 5358, 5294, and 5394. Table 4.10-1 shows the node lengths, flow area, and hydraulic diameter of the test section used in the RELAP5-3D input model. Table 4.10-2 presents the boundary conditions for these three tests.

Table 4.10-1. Geometrical input values of Bennett test section.

Node Number	Length (m)	Flow Area (m^2)	D_H (m)
1	0.3556	0.00012516	0.0126237
2	0.3048	0.00012516	0.0126237
3 to 21	0.1524	0.00012516	0.0126237
22 to 47	0.0762	0.00012516	0.0126237

Table 4.10-2. Boundary conditions for Bennett Tests 5358, 5294, and 5394.

Bennett Test	Pressure (MPa)	Heat Flux (MW/m^2-s)	Mass Flux (kg/m^2-s)	Subcooling (K)
5358	6.9	0.512	380	34.41
5294	6.9	1.09	1953	18.8
5394	6.9	1.75	5181	13.78

4.10.4 Data Comparisons and Results

The simulations for Test 5358 were run for a problem time of 100 s, and those for Tests 5294 and 5394 were run for 20 s in order to reach quasi-steady state conditions. All of the calculations had a requested time step size of 0.1 s. The predicted surface wall temperatures at the end of the calculations are compared with the measured data in Figures 4.10-2 through 4.10-4.

RELAP5-3D predicts the CHF positions earlier in the cases of low and high mass fluxes (Test 5358 and Test 5394) than the measured data. However, it is predicted to occur later than the experiment data in the case of intermediate mass flux (Test 5294). When RELAP5-3D calculates earlier CHF, the peak temperatures have a tendency to be higher than the measured data; conversely, the predicted temperatures are lower than the data when CHF is calculated late.

As shown in Figures 4.10-2 through 4.10-4, the calculated results are the same with the semi- and nearly-implicit numerical models in the lower portion of the tube. The nearly-implicit method predicts lower temperatures than the semi-implicit method in the portion of the tube above where CHF occurs.

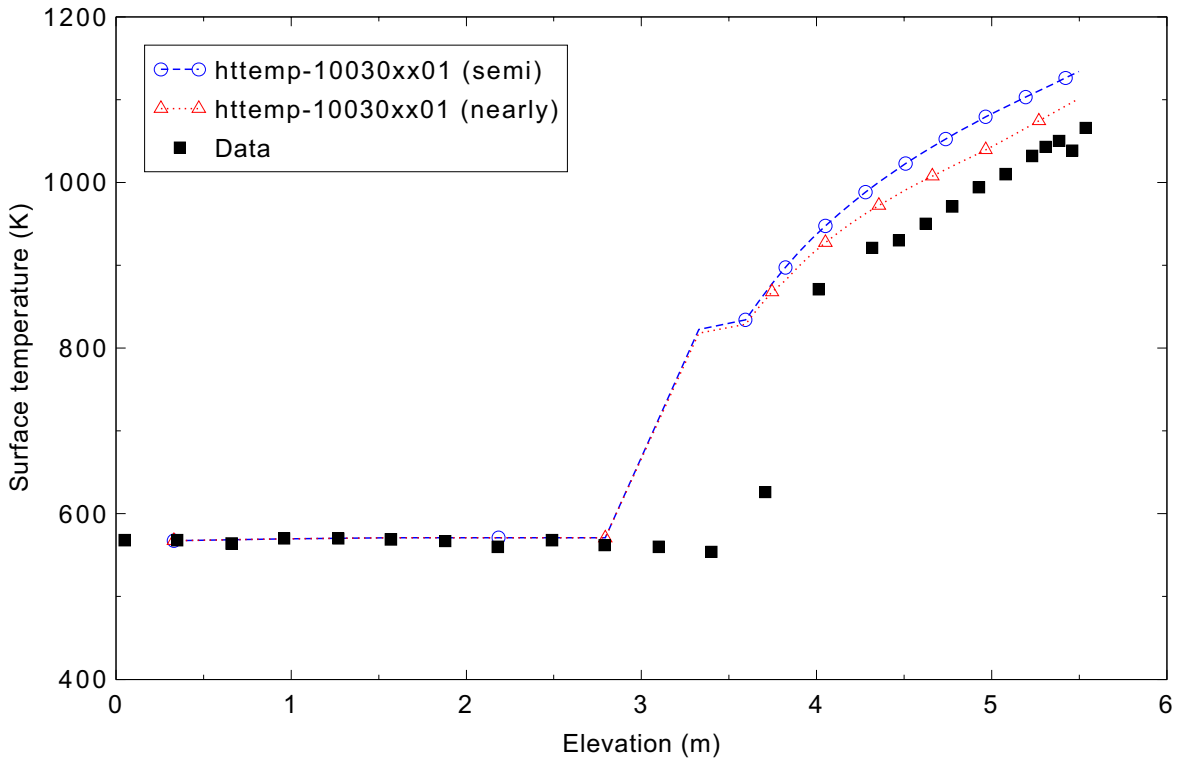

Figure 4.10-2. Measured and calculated axial wall temperatures for Bennett heated tube low mass flux Test 5358.

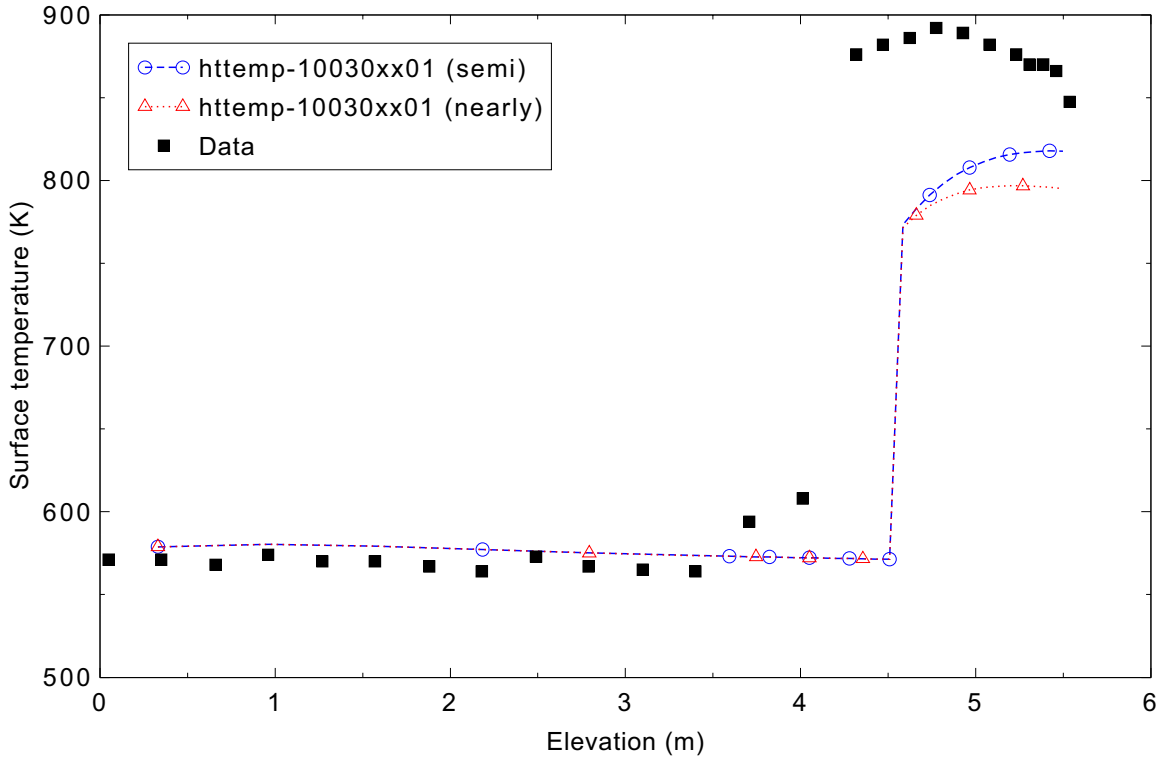

Figure 4.10-3. Measured and calculated axial wall temperatures for Bennett heated tube intermediate mass flux Test 5294.

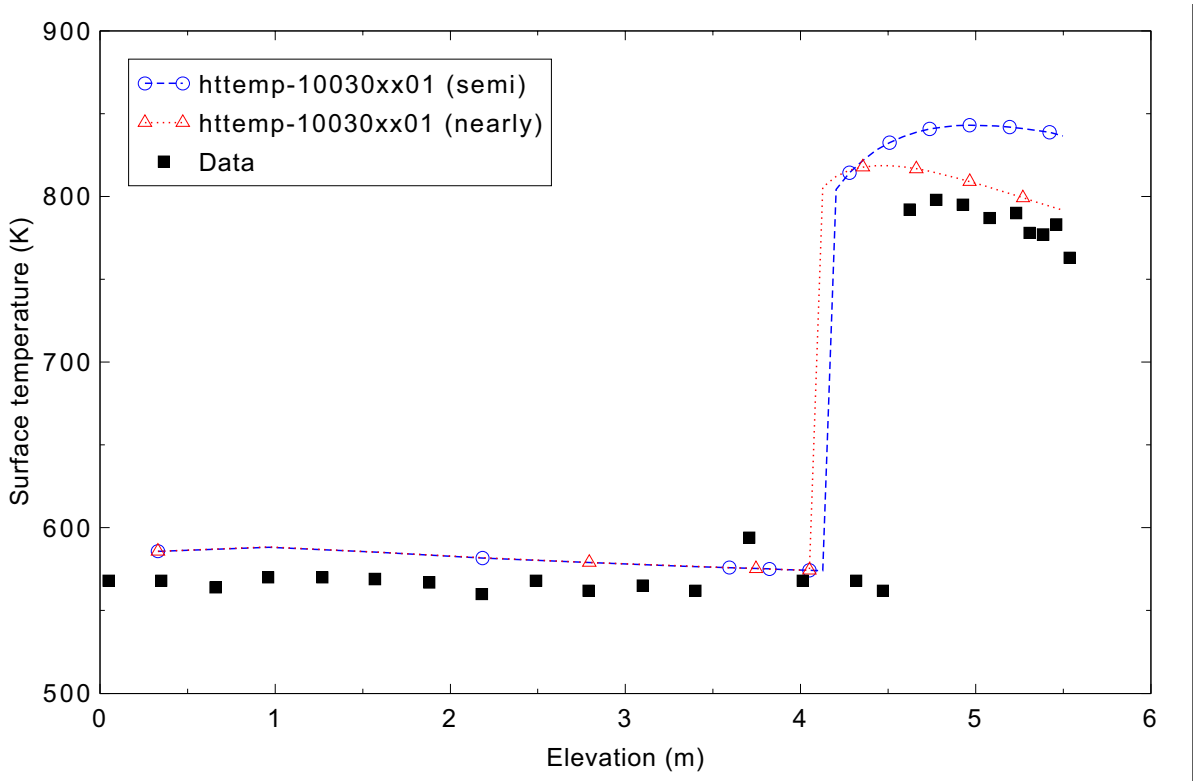

Figure 4.10-4. Measured and calculated axial wall temperatures for Bennett heated tube high mass flux Test 5394.

Table 4.10-3 shows the summary of these comparisons.

Table 4.10-3. Measured and calculated CHF positions from bottom of Bennett heated tube.

Test	Measured CHF Position (m)	Calculated CHF Position (m)
5358	3.708	3.327
5294	4.318	4.585
5394	4.623	4.204 (semi), 4.128 (nearly)

4.10.5 Conclusions and Assessment Findings

RELAP5-3D does a reasonable job in calculating the CHF position even though it predicts the position slightly earlier than the measured data in the cases of the low and high mass fluxes and slightly later in the case of the intermediate mass flux.

4.10.6 References

4.10-1. A. W. Bennett, et al., *Heat Transfer to Steam-Water Mixtures Flowing in Uniformly Heated Tubes in Which the Critical Heat Flux Has Been Exceeded*, AERE-R5373, October 1976.

4.11 ORNL THTF Tests 3.07.9B, 3.07.9N, 3.07.9W and 3.09.10I

The Oak Ridge National Laboratory (ORNL) Pressurized Water Reactor (PWR) Blowdown Heat Transfer (BDHT) Separate-Effects Program was a series of experiments performed in the early 1980s investigating several heat transfer phenomena expected to occur during PWR loss of coolant accidents, including critical heat flux (CHF) and dispersed flow film boiling. Tests 3.07.9B, 3.07.9N, and 3.07.9W were steady state film boiling tests carried out at the ORNL Thermal Hydraulic Test Facility (THTF).[4.11-1] The tests are considered to be low mass flux runs. Test 3.09.10I was a level swell test that used the same experiment facility. The steady state portion of test 3.09.10I was similar to the 3.07.9 tests.

4.11.1 Code Models Assessed

These experiments assess the CHF and film boiling heat transfer models.

4.11.2 Experiment Facility Description

The ORNL THTF is a non-nuclear pressurized water loop comprised of a pump, a vertical test section containing a set of electrically-heated rods, a heat exchanger, and a pressurizer. An isometric view of the facility is shown in Figure 4.11-1.

The test section from the inlet at the bottom to the outlet pipe at the top is 4.5 m in length and contains a set of 64 rods arranged in an 8x8 bundle with a heated length of 3.66 m.[4.11-1] 60 of the rods are electrically heated and 4 rods are unheated. The rod diameter (9.5 mm) and pitch (12. 7mm) are typical of PWR 17x17 fuel rod assemblies. Six spacer grids were located along the heated section of the rods. The test was highly instrumented with numerous thermocouples mounted at specific levels along the rods, thermocouples mounted to grid spacers for in-bundle fluid temperatures, pressure and differential pressure transducers, a gamma densitometer for measuring fluid density, and a current meter for each rod to determine the heat generated by each rod. The number of thermocouples located at each level along the heated test section varied from one in some levels to as many as 55 at one elevation. Several levels along the heated section had from four to seven thermocouples. Grid spacer and instrumentation elevations are shown in Figure 4.11-2. The elevations where sensors were placed are identified by a capital letter or by a capital letter followed by a number (for example, A or F1).

During the tests, subcooled water was pumped into the lower plenum of the test section. Steady state tests 3.07.9B, 3.07.9N, and 3.07.9W had differing rates of inlet flow. Once the inlet flow was established, the power to the rods was increased until the dryout point reached a desired elevation in the test section. The test was run until the operating pressure and rod surface temperatures stabilized. The operating conditions for the 3.07.9 series tests as well as test 3.09.10I are given in Table 4.11-1.

4.11.3 Input Model Description

A nodalization diagram of the input model is given in Figure 4.11-3. Only the heated length of the test section is modeled with RELAP5-3D. Effects of the pump, heat exchanger, and pressurizer were handled as boundary conditions. A time-dependent junction at the inlet provided the mass flow rate through the test section and a time-dependent volume at the outlet enforced the pressure boundary condition. The inlet time-dependent volume specified the temperature of the water entering the test section. The values of

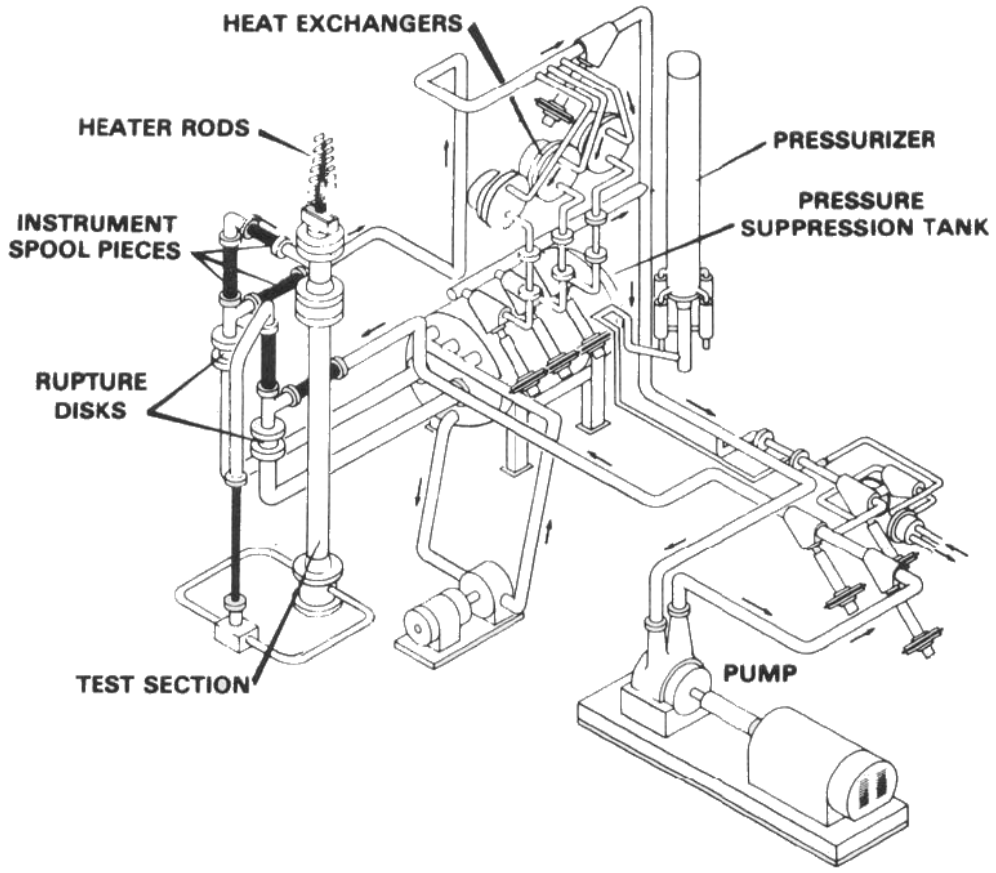

Figure 4.11-1. Experiment setup of the ORNL Thermal Hydraulic Test Facility (THTF) steady state film boiling tests.

Table 4.11-1. Operating conditions for ORNL THTF tests.

Parameter	3.07.9B	3.07.9N	3.07.9W	3.09.10I
Pressure (MPa)	12.8	8.89	12.6	4.5
Water inlet temperature (K)	583	558	567	473
Water mass flow (kg/s)	4.4	4.98	1.58	0.184
Bundle power (MW)	5.96	6.16	2.49	0.487

pressure, temperature, and water flow rate that are used for each of the cases are given in Table 4.11-1. The heated portion of the test section is modeled as a pipe component divided into 24 axial volumes. Each of the sections has a length of 0.15 m, except the last with a length of 0.208 m, to make a total heated pipe of

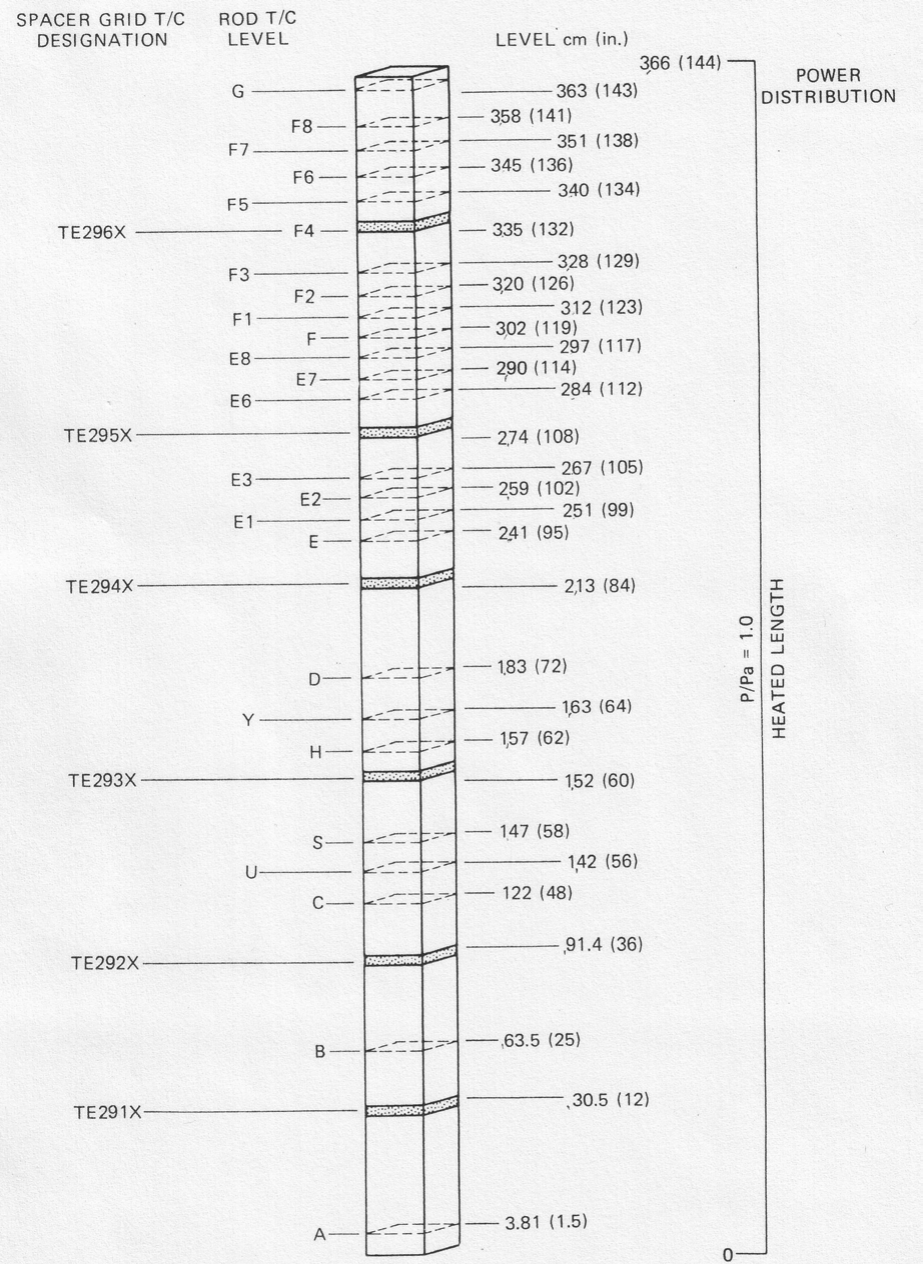

Figure 4.11-2. Test section of the ORNL Thermal Hydraulic Test Facility.

length 3.658 m. A heat structure is attached to the pipe, which models 60 rods. The test facility used 64 rods, but 4 of these rods were unheated. For Test 3.07.9B, one additional rod failed resulting in only 59 heated rods.

The heat structure is modeled as a solid cylinder with 24 axial sections which are attached to the 24 axial pipe volumes. A total power was prescribed for the heat structure. The total power value is also given in Table 4.11-1. The heat flux for each of the 24 sections was proportional to the associated length of the pipe section to which the heat structure is attached. A single junction connects the pipe to the outlet

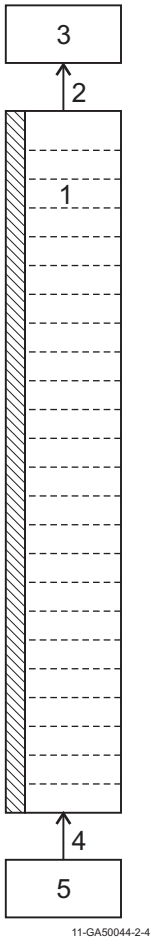

Figure 4.11-3. Nodalization diagram for the ORNL THTF steady state experiments.

time-dependent volume. The grid spacers are not included as part of the hydraulic model, but they are included in the heat structure.

4.11.4 Data Comparisons and Results

Transient runs were made using both the semi-implicit and the nearly-implicit advancement schemes. For the 3.07.9 test calculations, the requested time step size was 0.03 s. For Test 3.09.10I, a requested time step size of 0.05 s was used for both the semi- and nearly-implicit cases.

In order to compare the experiment data from the 3.07.9 tests to the simulation results, the experiment values taken at a particular level were averaged from data obtained from Reference 4.11-2. Averaged temperature values are shown in Figures 4.11-4 through 4.11-6 as black squares. For many levels only one temperature value was recorded. Several levels included between 2 and 6 measurements. A few axial levels had more measured values recorded, with a maximum of 55 temperatures recorded at one level near the dryout point. Along with the average value, the student’s t-distribution was used to calculate a 95% confidence interval based on a 2-sigma deviation. A confidence interval is plotted for several data points (i.e. an interval with 95% probability that the true average temperature value lay within the bounds). No confidence interval was included for axial levels with only one data point (since one cannot be calculated)

or axial levels where too few data points were taken since the confidence interval would be too large to be useful. The instrument uncertainty was also included by taking the square root of the sum of the square of the statistical and instrument uncertainties. For Test 3.09.10I, experiment averaged values for rod surface temperature, gas temperature, and void fraction vs. elevation were compared with simulation results.

Figures 4.11-4 through 4.11-6 show the surface temperature of the heated bundle contained in the test section. The experiment data for all three tests suggest discontinuities in the outer surface temperature for the heated rods around elevations of 2.74 m and 3.35 m, although this is more pronounced in some figures than in others. These elevations correspond to the location of grid spacers in the upper part of the test section, and the effect of the grid spacers is fairly significant, leading to a temperature drop on the order of 50 to 100 K across the grid spacer. The RELAP5-3D input model does take into account the grid spacers, but this only impacts the CHF calculation, and thus no discontinuity is seen in the simulation results. This leads to noticeable differences in the temperature profile of the experiment and simulation, although the overall trend is often consistent.

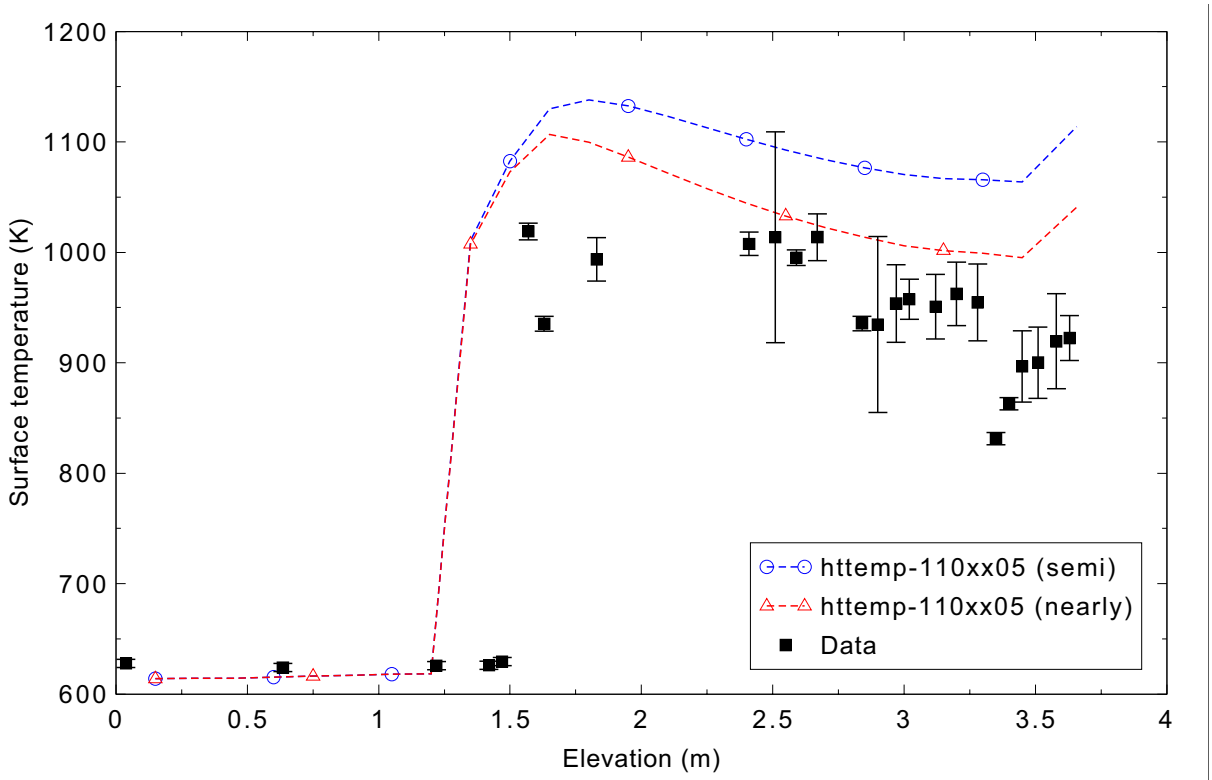

Figure 4.11-4. Measured and calculated steady state rod surface temperatures for ORNL THTF Test 3.07.9B.

The axial rod surface temperature for Test 3.07.9B is shown in Figure 4.11-4. The elevation where transition to film boiling occurs is indicated clearly in 4.11-4 by the sudden jump in rod surface temperature from approximately 600 K to over 1000 K. Aside from the discontinuities near grid spacers noted above, RELAP5-3D seems to accurately predict the temperature trend although it predicts a transition to film boiling at a lower elevation than was measured. The model also over predicts the rod surface temperature in the film boiling region by 80 to 150 K in the semi-implicit calculation, and by 20 to 100 K in the nearly-implicit calculation. The differences between the semi- and nearly-implicit calculations were only noted in the post-CHF region of the bundle.

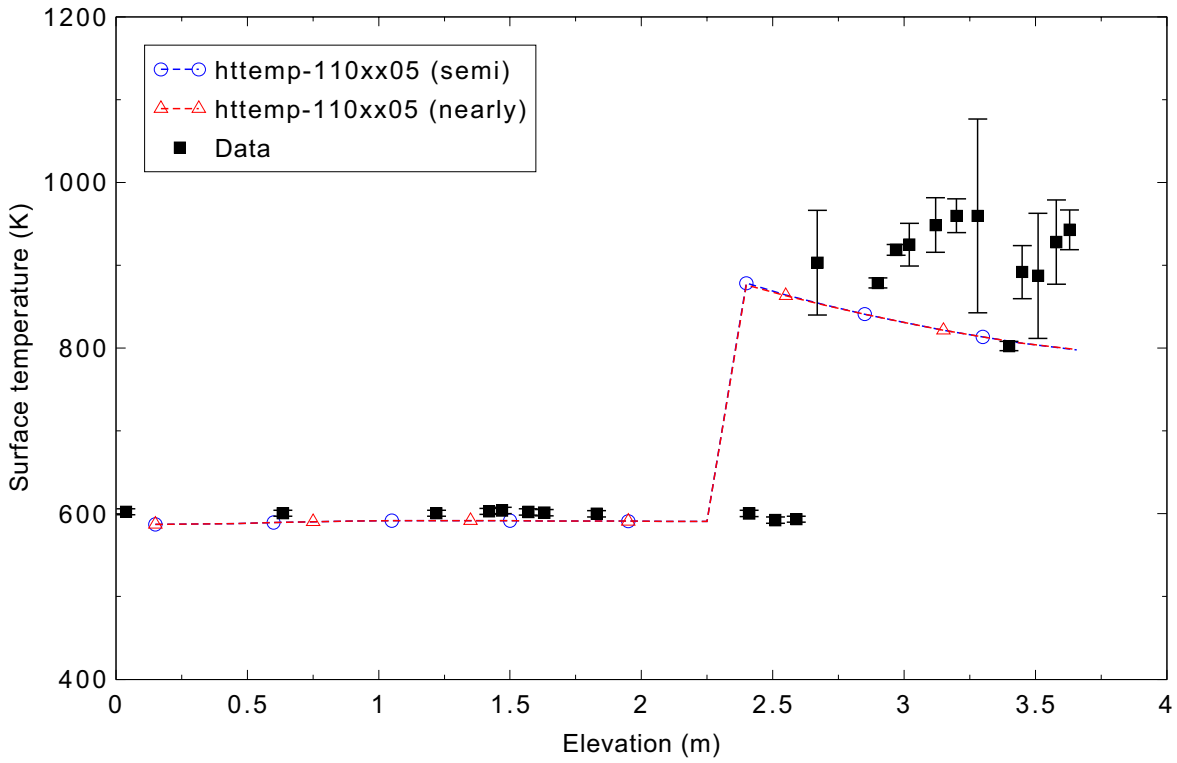

Figure 4.11-5. Measured and calculated steady state rod surface temperatures for ORNL THTF Test 3.07.9N.

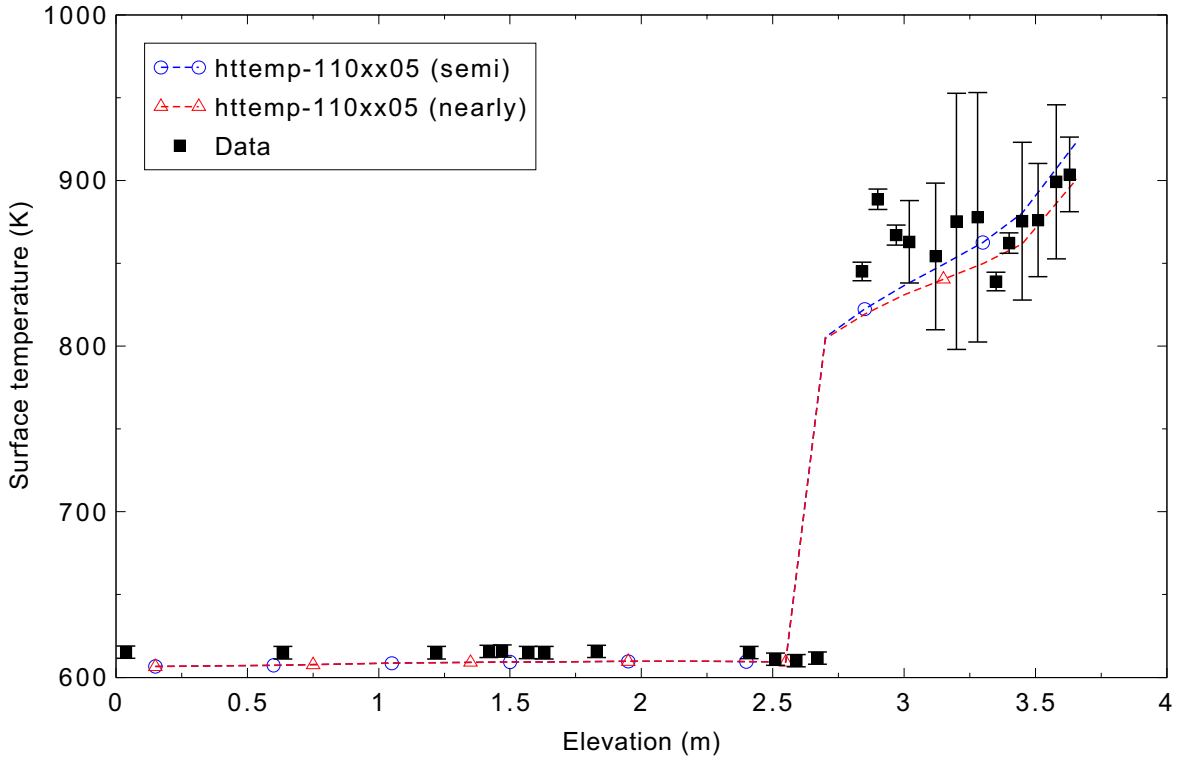

Figure 4.11-6. Measured and calculated steady state rod surface temperatures for ORNL THTF Test 3.07.9W.

Test 3.07.9N had the highest water flux and highest heat flux of the three experiments. The axial rod surface temperatures are shown in Figure 4.11-5. In this case, the rod surface temperature is under predicted by the RELAP5-3D calculation by up to 80 K in the film boiling region. Again the effect of the grid spacers can be seen clearly in the experiment data, and this may account for some of the discrepancy between the experiment data and the RELAP5-3D simulation response. There was no noticeable difference between the semi- and nearly-implicit calculations.

Test 3.07.9W had the lowest water flux and lowest heat flux of the three experiments. The axial rod surface temperatures are shown in Figure 4.11-6. As can be seen in Figure 4.11-6, rod surface temperatures predicted by the RELAP5-3D model agree fairly well with experiment values, with the predicted temperatures tending to stay within the 95% confidence interval bounds. Figure 4.11-6 shows that the rod temperature is slightly under predicted in the lower section (pre-CHF). Effects of the grid spacers are less pronounced in this figure. The nearly-implicit method predicted slightly lower temperatures in the post-CHF region of the bundle.

Rod surface temperatures for Test 3.09.10I are presented in Figure 4.11-7. The effect of the grid spacer can be seen clearly in the experiment profile near the 3.3-m mark, where the greatest deviation occurs, but overall the predicted temperatures are generally within 20 to 30 K of the experiment data. Predicted axial gas temperatures, shown in Figure 4.11-8, match the experiment values very well with little noticeable deviation. Void fractions are shown in Figure 4.11-9. Again the calculated response matches the experiment data fairly well. Dryout appears to occur at a slightly lower elevation in the experiment than is predicted in the simulation, but overall agreement is very good. There were no noticeable differences between the semi- and nearly-implicit calculations.

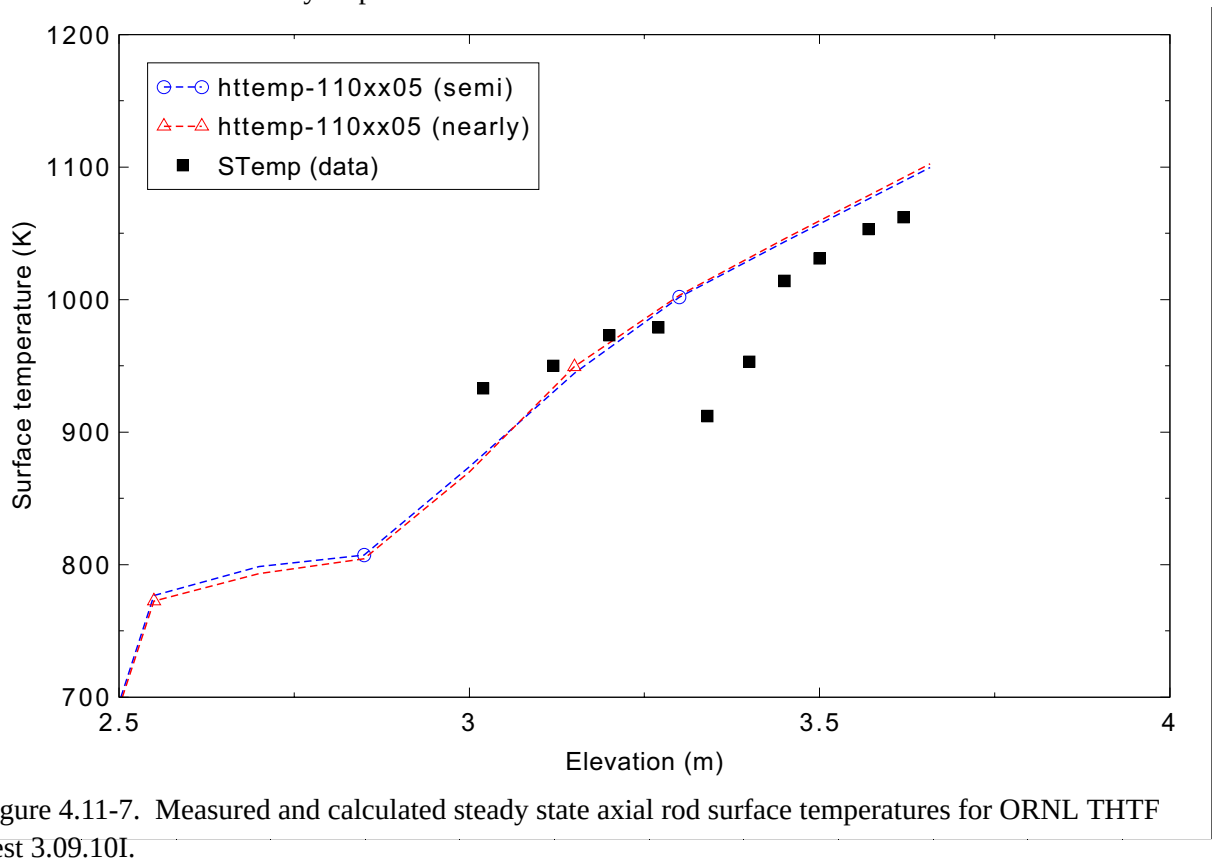

Figure 4.11-7. Measured and calculated steady state axial rod surface temperatures for ORNL THTF Test 3.09.10I.

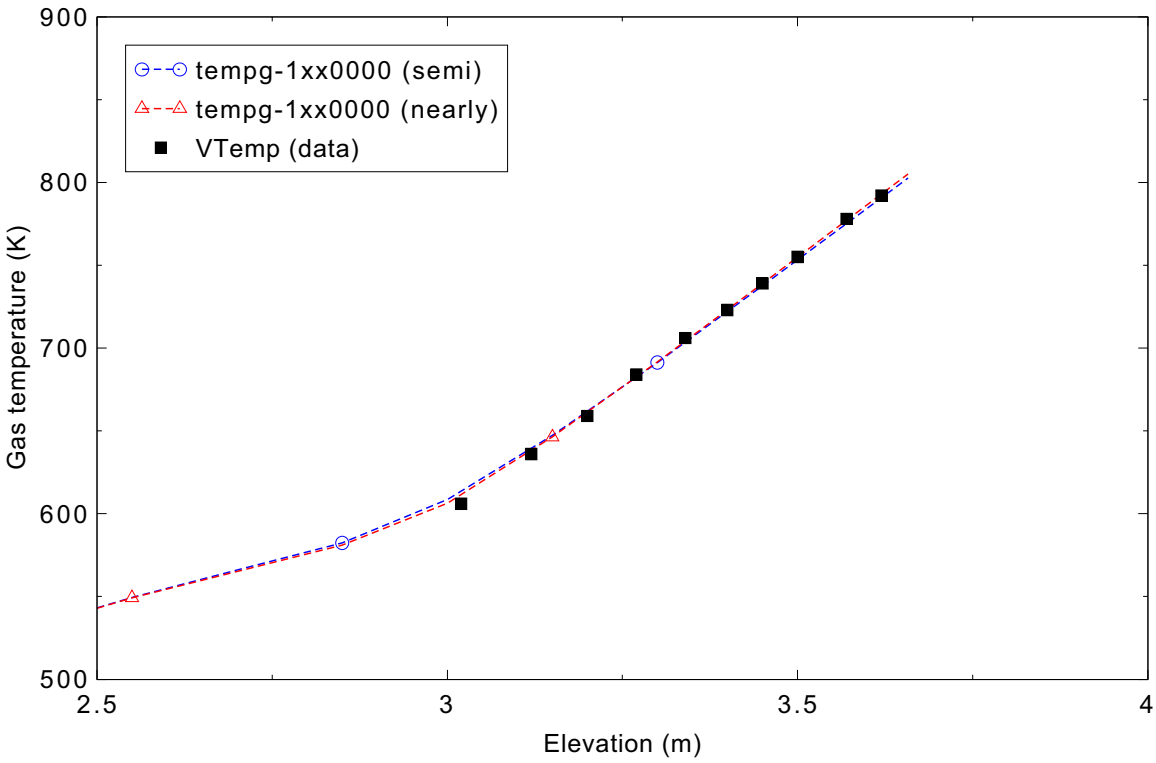

Figure 4.11-8. Measured and calculated steady state axial gas temperatures for ORNL THTF Test 3.09.10I.

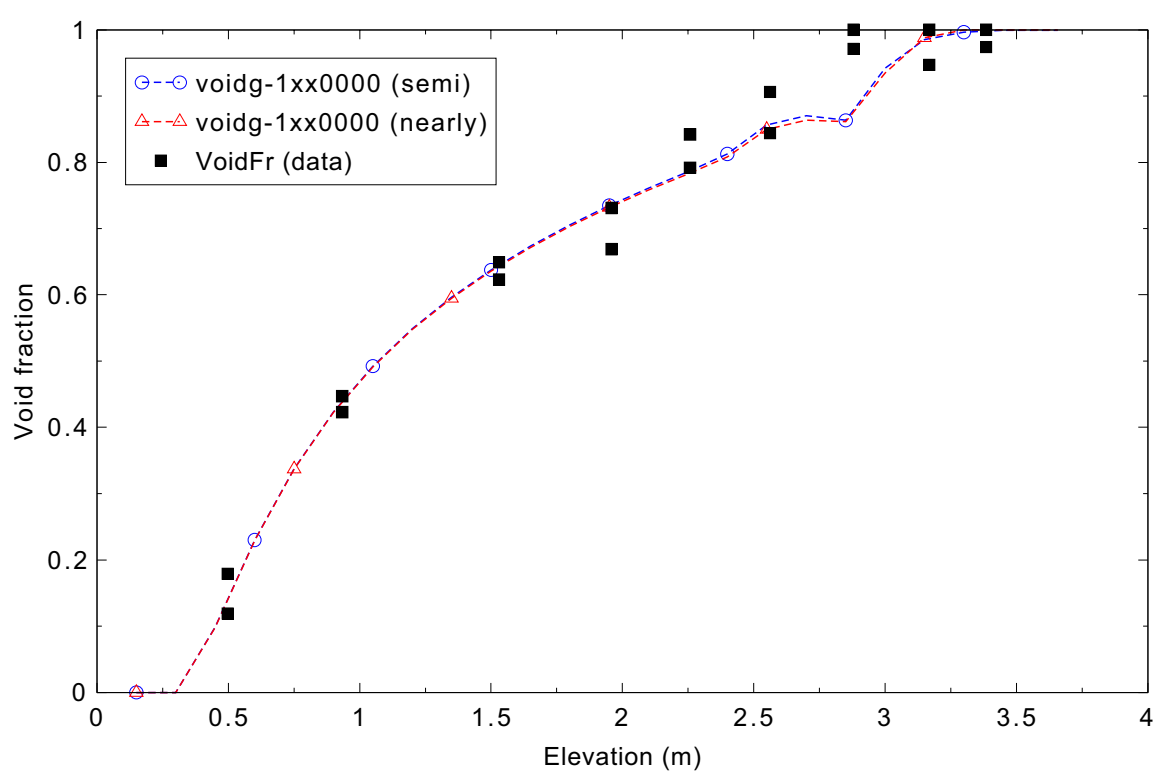

Figure 4.11-9. Measured and calculated steady state axial void fractions for ORNL THTF Test 3.09.10I.

4.11.5 Conclusions and Assessment Findings

With one exception, the CHF and film boiling heat transfer predicted by RELAP5-3D were in reasonable agreement with the experiment data for the four ORNL THTF tests that were assessed.

For the ORNL 3.07.9N and 3.07.9W test cases, the predicted rod temperatures were in reasonable agreement with the experiment data, and RELAP5-3D did a reasonable job of predicting CHF. For the 3.07.9B case, the CHF was reasonably predicted but the rod temperatures were only in minimal agreement with the measured data. Grid spacers were only accounted for in the RELAP5-3D model through the CHF correlation. The grid spacers appeared to have a significant effect on the rod surface temperatures in the ORNL tests, leading to discontinuities in the temperature response.

For the ORNL 3.09.10I test, the predicted void fraction and gas temperature were in excellent agreement with the experiment data, and the rod surface temperature was in reasonable agreement. Again the effect of the grid spacer was pronounced in the experiment data.

4.11.6 References

4.11-1. C. B. Mullins, et al., *ORNL Rod Bundle Heat Transfer Test Data - Volume 7. Thermal-Hydraulic Test Facility Experimental Data Report for Test Series 3.07.9 - Steady-state Film Boiling in Upflow*, NUREG/CR-2525, Vol. 7, ORNL/NUREG/TM-407/V7, May 1982.

4.11-2. G. L. Yoder, et al., *Dispersed Flow Film Boiling in Rod Bundle Geometry - Steady-State Heat Transfer Data and Correlation Comparisons*, NUREG/CR-2435, ORNL-5822, March 1982.

4.12 Royal Institute of Technology Tube Test 261

A total of 510 post-dryout heat transfer experiments were conducted by the Royal Institute of Technology (RIT) in Stockholm, Sweden.[4.12-1] The main purpose of these tests was to study post-critical heat flux (CHF) heat transfer in electrically-heated tubes. The experiment test section was a 7-m long, 1.5-cm diameter heated tube. Experiment pressures ranged from 3 to 20 MPa, mass fluxes ranged from 500 to 2,000 kg/m^2-s, heat fluxes ranged from 10 to 125 W/cm^2, and inlet subcooling ranged from 7 to 13 K. Reference 4.12-1 was not available, so Reference 4.12-2 was used to obtain a detailed description of the RIT experiments along with the experiment data. RIT Tube Test 261 was one of the 510 post-CHF experiments, and it was a steady-state test.

4.12.1 Code Models Assessed

RIT Tube Test 216 assesses the default CHF and PG-CHF ("power" form) models.

4.12.2 Experiment Facility Description

The test facility was designed for the purpose of studying post-CHF heat transfer in electrically-heated tubes. The loop was designed for an operating pressure of 250 bar. Figure 4.12-1 shows a simplified diagram of the RIT test facility. Test sections with heated lengths of up to 7.0 m were accommodated. Power was supplied from a direct current generator.

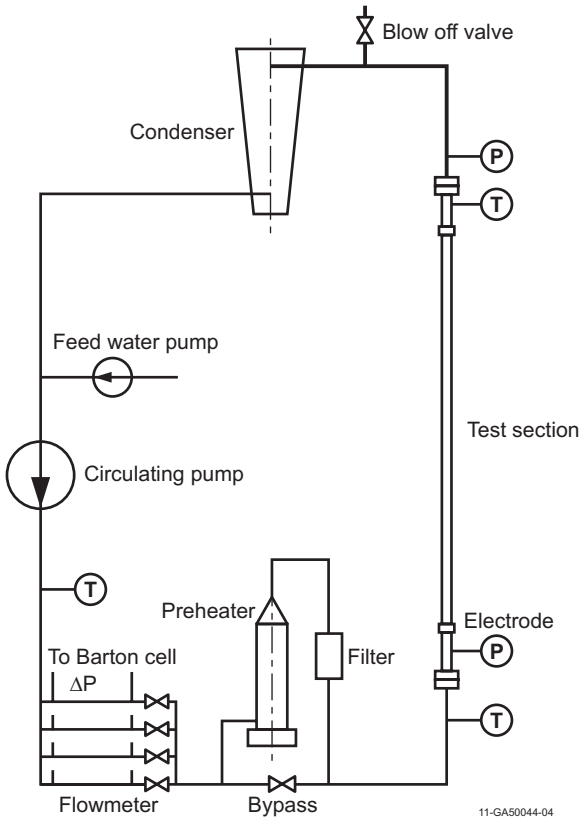

Figure 4.12-1. RIT Tube Test facility diagram.

A total of 55 Chromel-Alumel thermocouples were placed along the heated length of the test section, as shown in Figure 4.12-2 for RIT Tube Test 261. These thermocouples were used to determine the CHF location, evidenced by a sudden and significant temperature increase.

Table 4.12-1 shows a summary of the geometry and initial conditions for RIT Tube Test 261.

Table 4.12-1. Summary of the geometry and initial conditions for RIT Tube Test 261.

Parameter	Geometrical/Initial Value
Heated length	7.0 m
Inner diameter of test section tube	14.9 mm
Outer diameter of test section tube	20.8 mm
Pressure	7.02 MPa
Mass flux	1,988.2 kg/m^2-s
Inlet temperature	548.45 K
Heat flux	1.053 MW/m^2

The mass and heat fluxes are converted to mass flow rate and total power to the test section as follows:

$$\dot{m} = \dot{m}'' \cdot A_f = 1988.2 \frac{kg}{m^2 \cdot s} \times 0.000174366\ m^2 = 0.3467 \frac{kg}{s} \quad (4.12\text{-}1)$$

and

$$Q = q'' \cdot A_{h-OD} = 1,053,000 \frac{W}{m^2} \times 0.457416\ m^2 = 481,658.9\ W \quad (4.12\text{-}2)$$

where A_f and $A_{h\text{-}OD}$ stand for the flow area and the heat transfer area at the outer surface of the test section, respectively.

4.12.3 Input Model Description

Figure 4.12-3 shows the nodalization diagram for the RIT tube test facility. As shown in this figure, the hydraulic components included in this input model are a pipe (test section, Component 1), two time-dependent volumes (Components 110 and 210), a time-dependent junction (Component 100) at the inlet of the test section, and a single junction (Component 200) at the outlet of the test section. A heat structure (Component 1003) is attached to the test section.

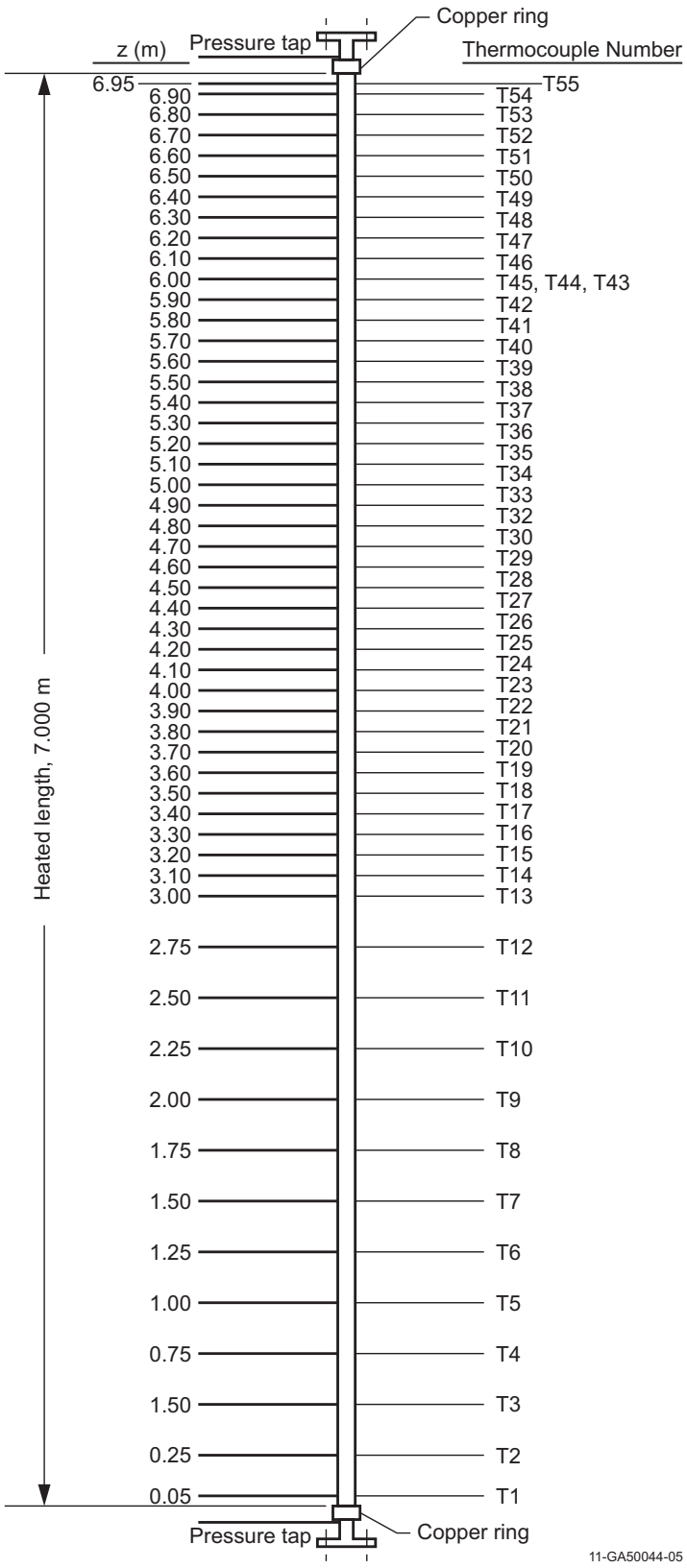

Figure 4.12-2. Locations of temperature measurements for RIT Tube Test 261.

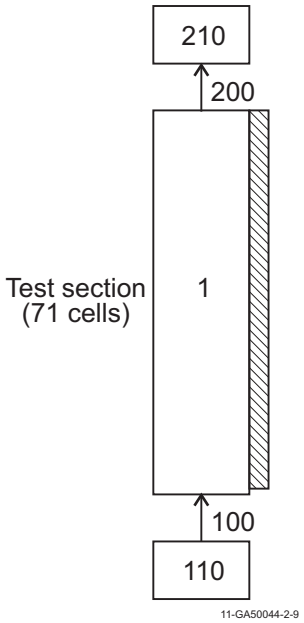

Figure 4.12-3. Nodalization diagram for the RIT test facility.

The heated test section was nodalized in detail (71 nodes, 70 nodes for the heated section and 1 node for part of the inlet pipe) to simulate RIT Tube Test 261. Table 4.12-2 shows the node lengths of the test section and the connection of axial nodes of the heat structure to the test section.

Table 4.12-2. Node lengths and connection of heat structures for RIT Tube Test 261.

Node Number	Length (m)	Connected Node Number of Heat Structure Component
1	0.01	None
2 to 71	0.1	1 to 70

4.12.4 Data Comparisons and Results

Transient runs were made using both the semi-implicit and the nearly-implicit advancement schemes. The time step size was set to 0.001 s for both cases. Figures 4.12-4 and 4.12-5 show the measured and predicted surface temperatures along the heated length with the default CHF model and the PG-CHF model, respectively.

The measured CHF position was 4.65 m. The measured peak temperature of 874 K occurred at 5.4 m. It can be seen from Figures 4.12-4 and 4.12-5 that the CHF location is affected by the CHF model, but not the numerical scheme, and that the semi-implicit numerical scheme predicts higher temperatures in the post-CHF region than does the nearly-implicit numerical scheme. When the default CHF model is used, the CHF occurs higher than in the experiment. However, it occurs lower than the measured data when the PG-CHF model is chosen. The predicted peak temperatures are lower than measured with both CHF

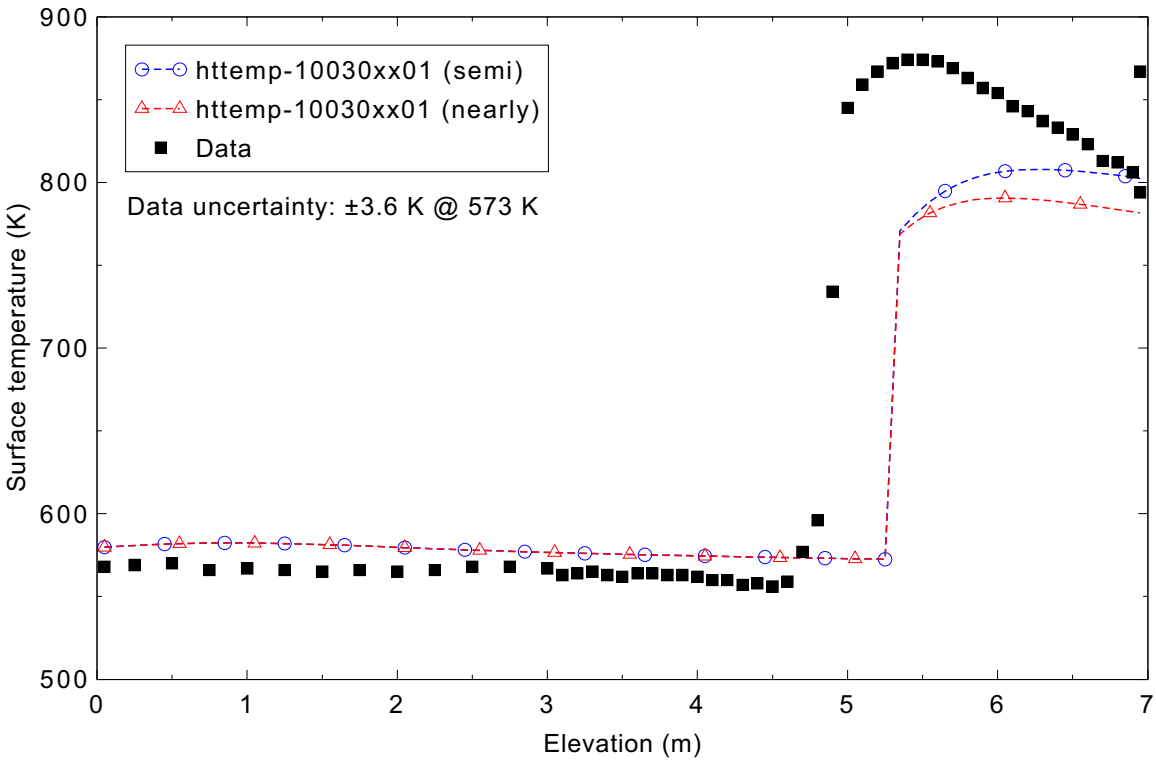

Figure 4.12-4. Measured and calculated tube surface temperatures for RIT Tube Test 261 with the default CHF model.

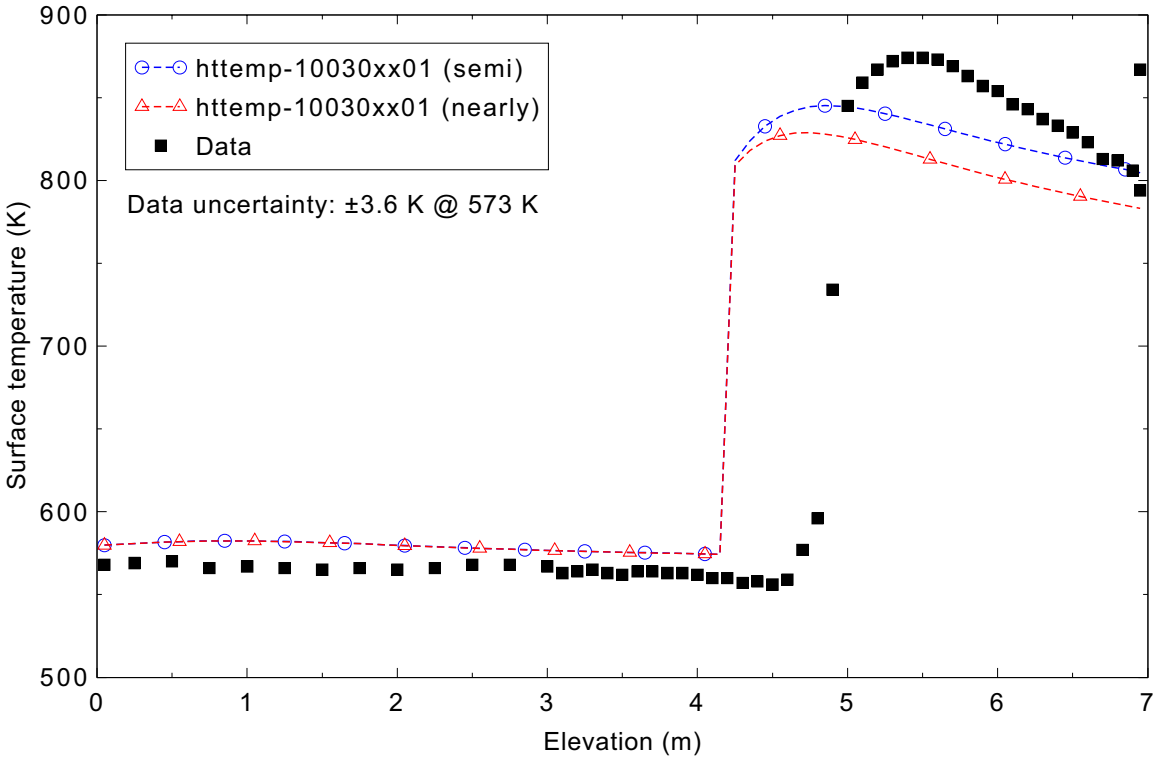

Figure 4.12-5. Measured and calculated tube surface temperatures for RIT Tube Test 261 with the PG-CHF model.

models. Table 4.12-3 shows the summary of the comparison of the simulation results with the experiment data.

Table 4.12-3. Measured and calculated CHF positions and peak temperatures for RIT Tube Test 261.

Case	CHF Position	Peak Temperature
Experiment	4.65 m	874.0 K at 5.4 m
Default CHF Model, semi-implicit	5.35 m	807.9 K at 6.25 m
Default CHF Model, nearly-implicit	5.35 m	790.5 K at 6.05 m
PG-CHF Model, semi-implicit	4.25 m	845.1 K at 4.85 m
PG-CHF Model, nearly-implicit	4.25 m	828.8 K at 4.75 m

4.12.5 Conclusions and Assessment Findings

RELAP5-3D does a reasonable job in calculating the measured CHF position even though it predicts the position slightly higher using the default CHF model and slightly lower using the PG-CHF model.

4.12.6 References

4.12-1. K. M. Becker, et al., *An Experimental Investigation of Post Dryout Heat Transfer,* KTH-NEL-33, Royal Institute of Technology, Stockholm, Sweden, May 1983.

4.12-2. A. Sjoberg and D. Caraher, *Assessment RELAP5/MOD2 against 25 Dryout Experiments Conducted at the Royal Institute of Technology,* International Agreement Report, NUREG/IA-0009, October 1986.

4.13 FLECHT SEASET Test 31504

A forced reflood experiment at a flooding rate of 24.6 mm/s (0.97 in./s) was performed in the 161-rod Full Length Emergency Core Heat Transfer Separate Effects and Systems Effects Tests (FLECHT SEASET) Facility.[4.13-1] The facility's electrically-heated rod configuration was typical of a full-length 17 x 17 rod bundle in a Westinghouse pressurized water reactor (PWR). The experiment provided data on PWR core reflood behavior following a hypothetical loss-of-coolant accident (LOCA).

4.13.1 Code Models Assessed

The performance of the reflood model at a low flooding rate was evaluated.

4.13.2 Experiment Facility Description

Figure 4.13-1 shows the flow diagram for the FLECHT SEASET unblocked bundle configuration used in the forced reflood experiment. The flow diagram also shows the location of instruments used in the experiment. The bundle cross section for the forced reflood experiment is shown in Figure 4.13-2.

Facility design features for the forced reflood experiment included:

- A cylindrical low mass bundle housing to minimize housing heat releases
- Housing differential pressure cells every 0.30 m (12 in.) to obtain void fraction measurements along the heated length of the bundle
- Steam probes in each of 11 thimble tubes to measure steam superheat radially and axially across the bundle
- 177 heater rod thermocouple computer channels
- Housing windows at the 0.91, 1.83, and 2.74 m elevations.

Within the bundle, the dimensions are full scale, compared to a typical PWR, with the exception of the overall radial dimension. The low mass housing used in the forced reflood experiment was designed to minimize the wall effects such that the rods one row or more away from the housing are representative of any region in a PWR core. To preserve proper thermal scaling of the experiment facility with respect to a PWR, the power to flow area ratio in the experiment facility is nearly the same as that for a PWR fuel assembly.

The reflood phase of a typical PWR design basis large break LOCA transient is predicted to start approximately 30 s after initiation of a hypothetical break. To simulate the expected conditions in a PWR at the start of reflood, the initial conditions for the forced reflood experiment were:

- Initial clad temperature – 863°C (1585°F)

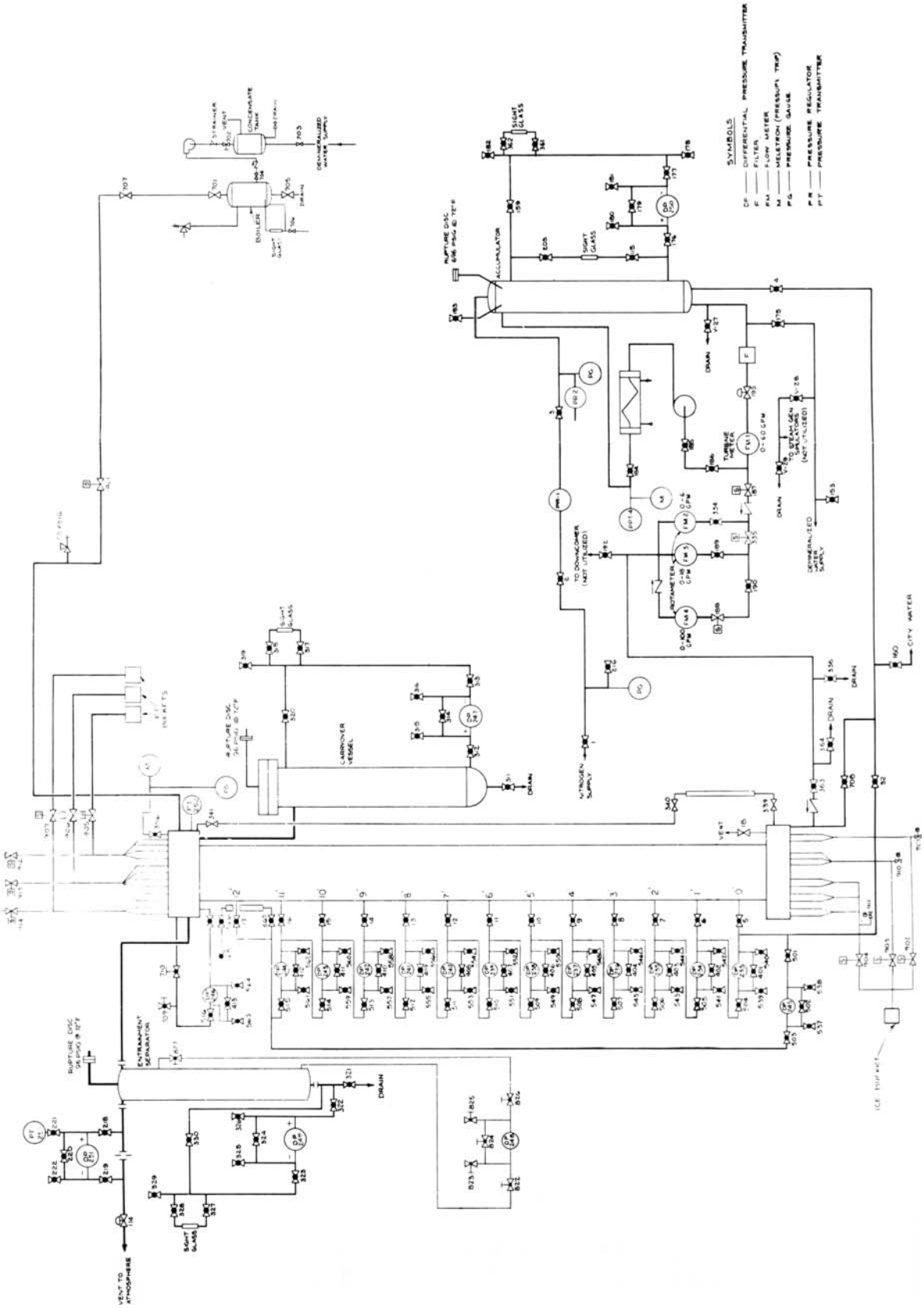

Figure 4.13-1. FLECHT SEASET unblocked bundle flow diagram for forced reflood.

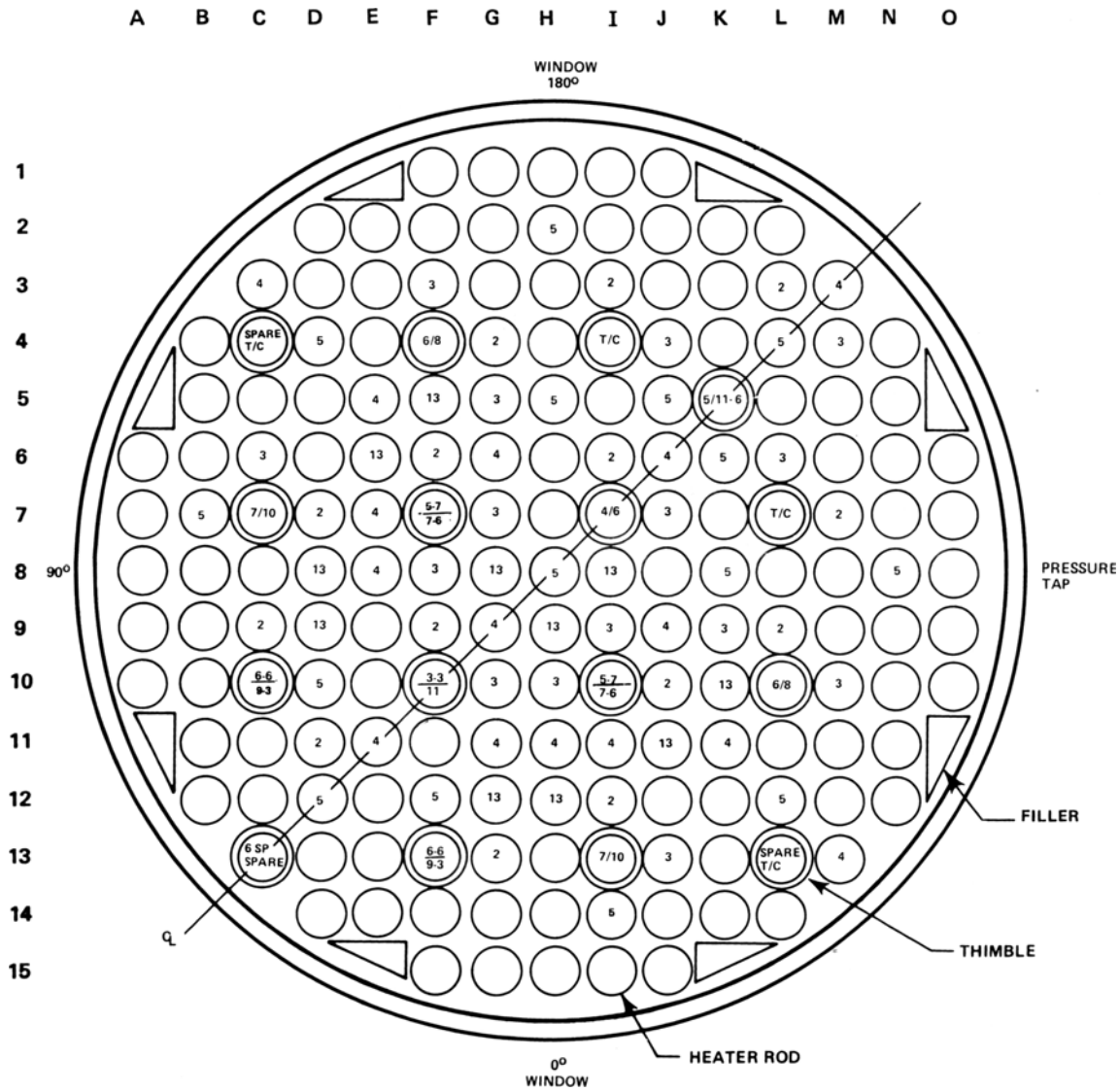

Figure 4.13-2. FLECHT SEASET bundle cross section.

- Peak power – 2.3 kW/m (0.7 kW/ft)
- Upper plenum pressure – 0.28 MPa (40 psia)
- Injection rate (lower plenum initially full) – 24.6 mm/s (0.97 in./s)
- Flooding water temperature entering lower plenum – 51°C (123°F)
- Radial power distribution – uniform
- Axial power shape – cosine (1.66 peak-to-average power ratio).

The power to the heater rods decreased during the experiment following the ANS plus 20 percent power decay curve 30 s after initiation of a LOCA. The heater rods had a uniform radial power profile, and a built-in modified cosine axial power profile with a peak-to-average power ratio of 1.66.

4.13.3 Input Model Description

The test section for the forced reflood experiment was modeled using 20 cells (Component 6) as shown in Figure 4.13-3. Measured fluid conditions were used to define the conditions in the upper and lower time dependent volumes (Components 7 and 5), which represent the upper and lower plenums, respectively. The measured flow injection velocity was used to define the flow conditions at the time-dependent junction (Component 301) that connected the lower plenum and the pipe, which represented the low mass housing. The measured power, which decreased during the test, was used as input to the heat structures representing the rods.

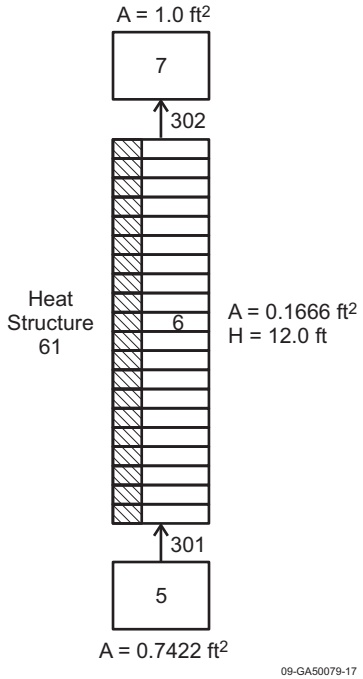

Figure 4.13-3. RELAP5-3D nodalization for the FLECHT SEASET forced reflood experiments.

4.13.4 Data Comparisons and Results

RELAP5-3D calculations were performed for FLECHT SEASET forced reflood Test 31504 using both the semi-implicit and nearly-implicit hydrodynamic advancement schemes; the requested time step size was 0.25 s. The nearly-implicit calculation failed (water property) early in the transient. Comparisons of measured and calculated rod surface temperature histories are presented in Figures 4.13-4 through 4.13-10; the data are from the NRC Data Bank. The results were plotted for 700 s following test initiation to encompass the entire test duration including termination of power to the test bundle at approximately 630 s, which accounts for the drop in temperature in each of the plots at that time. The legend for the rod temperature data is the rod number followed by the elevation in inches; i.e., 7J-072 was from a thermocouple in a rod near the center of the bundle at the axial mid-plane, 1.83 m (72 in.) from the inlet.

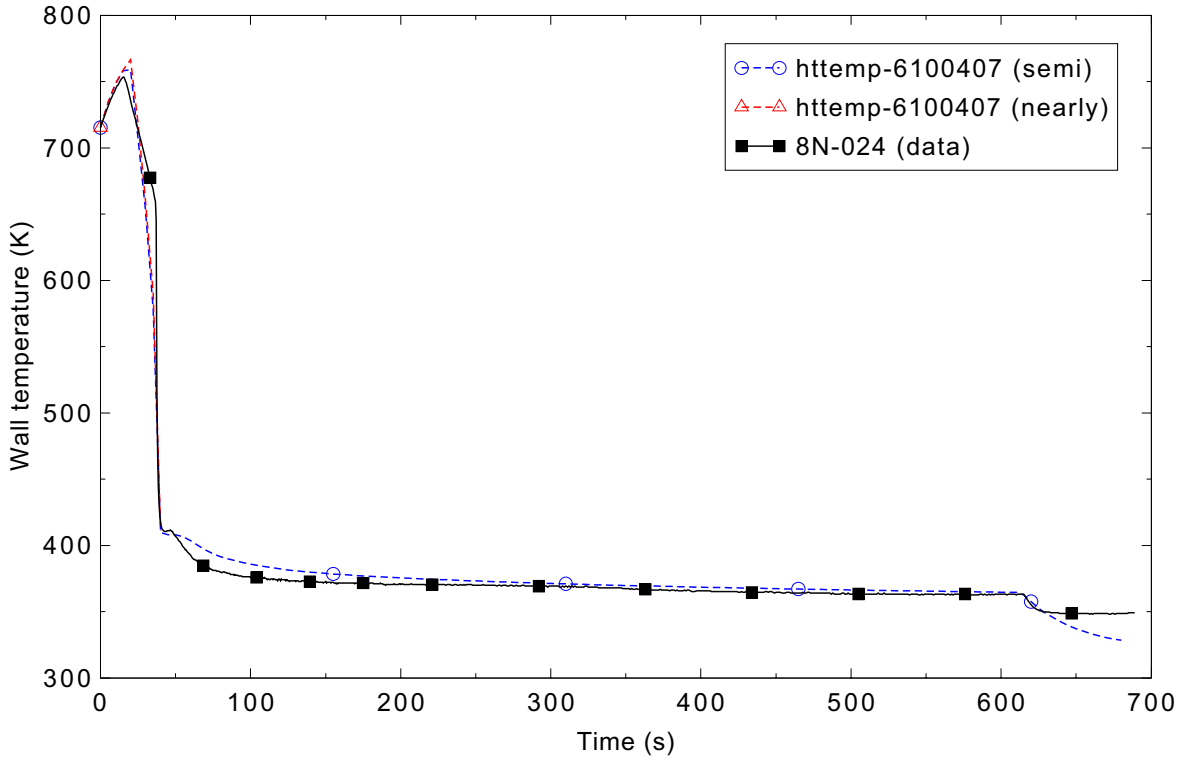

Figure 4.13-4. Measured and calculated rod surface temperatures for FLECHT SEASET forced reflood Test 31504 at the 0.62-m (24-in.) elevation.

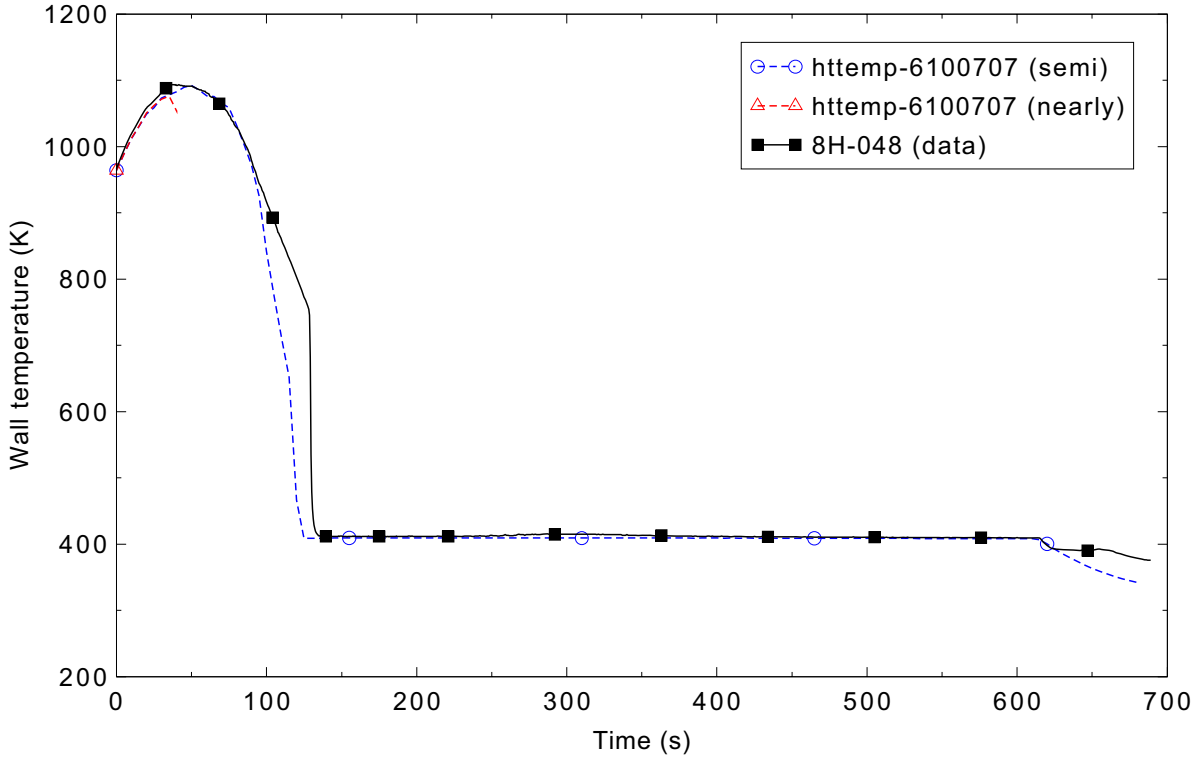

Figure 4.13-5. Measured and calculated rod surface temperatures for FLECHT SEASET forced reflood Test 31504 at the 1.23-m (48-in.) elevation

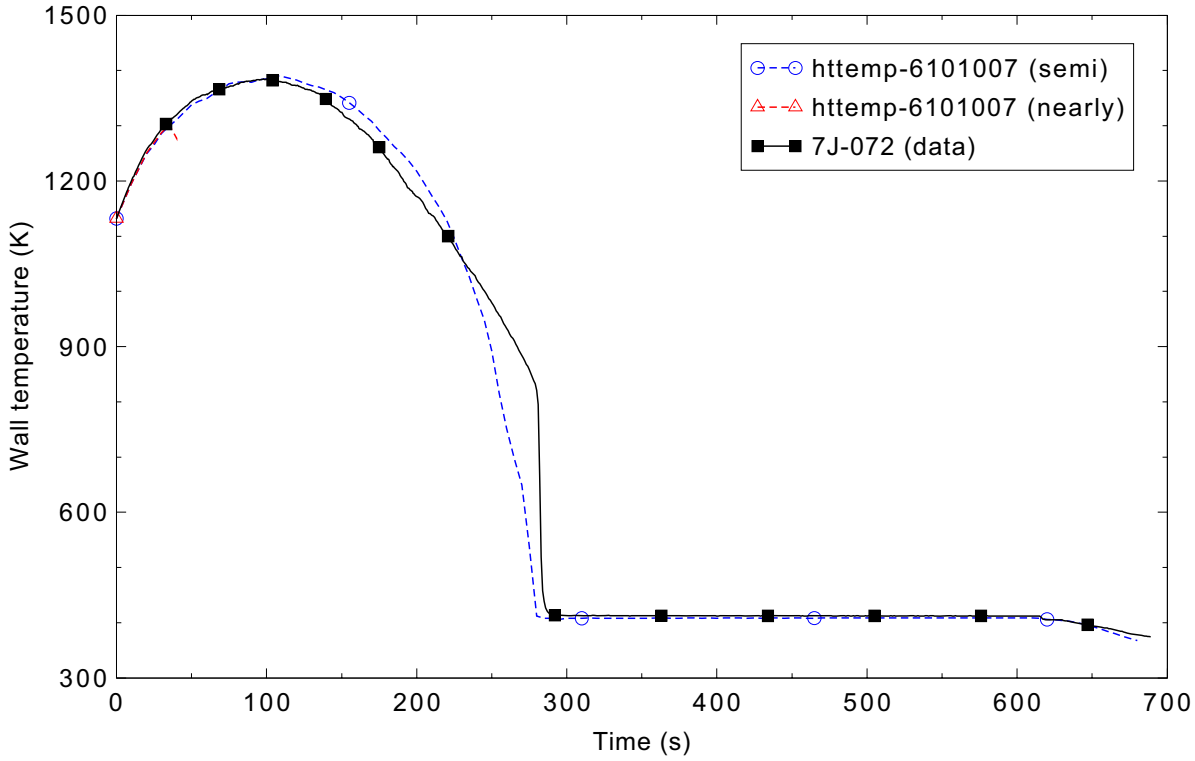

Figure 4.13-6. Measured and calculated rod surface temperatures for FLECHT SEASET forced reflood Test 31504 at the 1.85-m (72-in.) elevation.

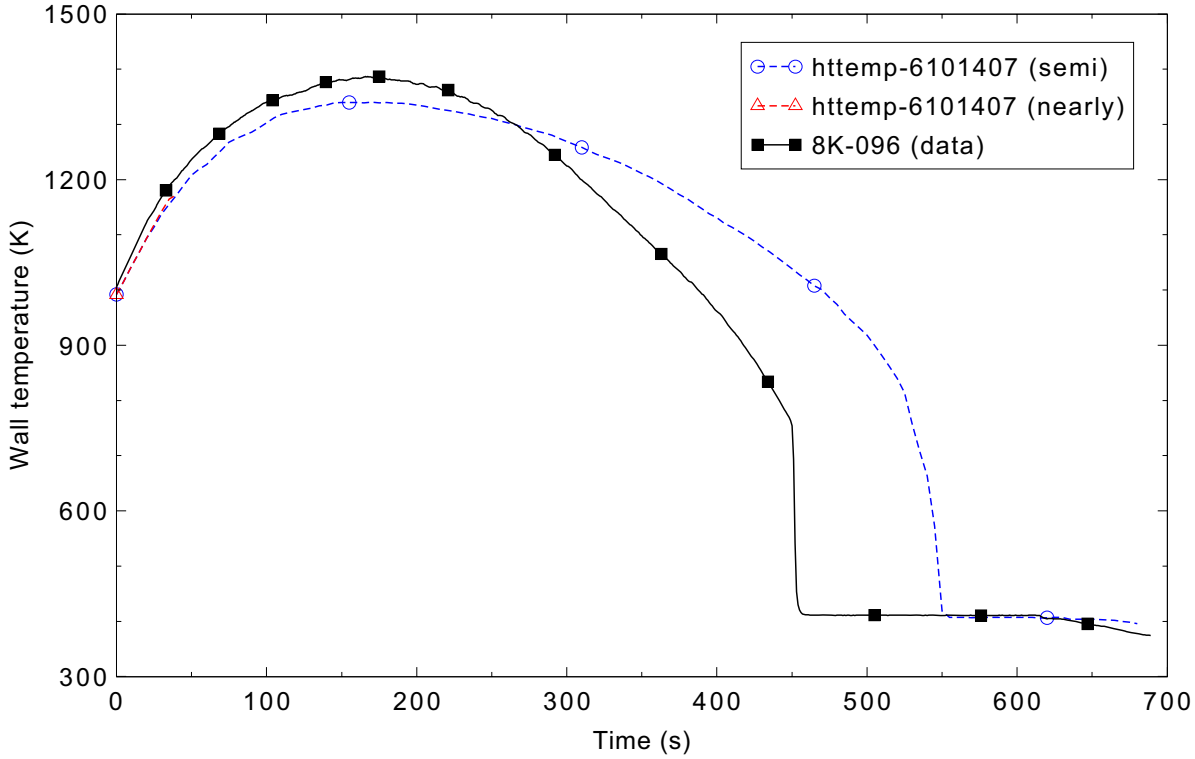

Figure 4.13-7. Measured and calculated rod surface temperatures for FLECHT SEASET forced reflood Test 31504 at the 2.46-m (96-in.) elevation.

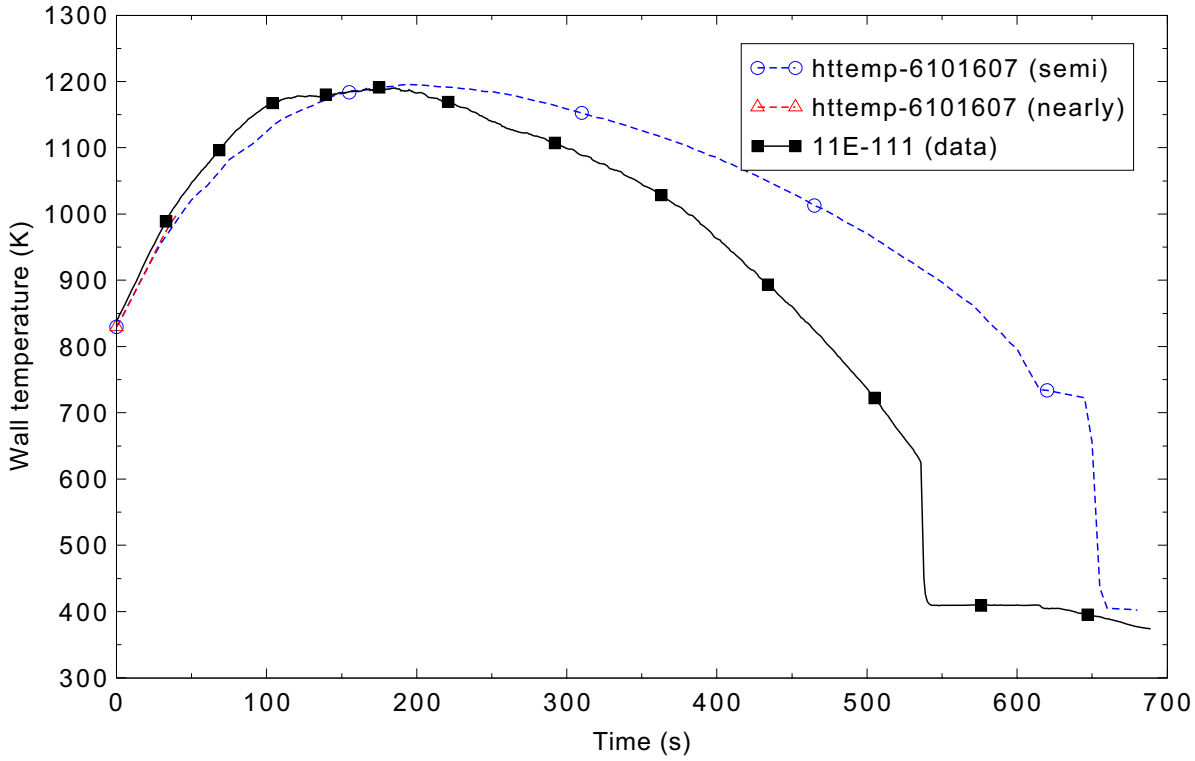

Figure 4.13-8. Measured and calculated rod surface temperatures for FLECHT SEASET forced reflood Test 31504 at the 2.85-m (111-in.) elevation.

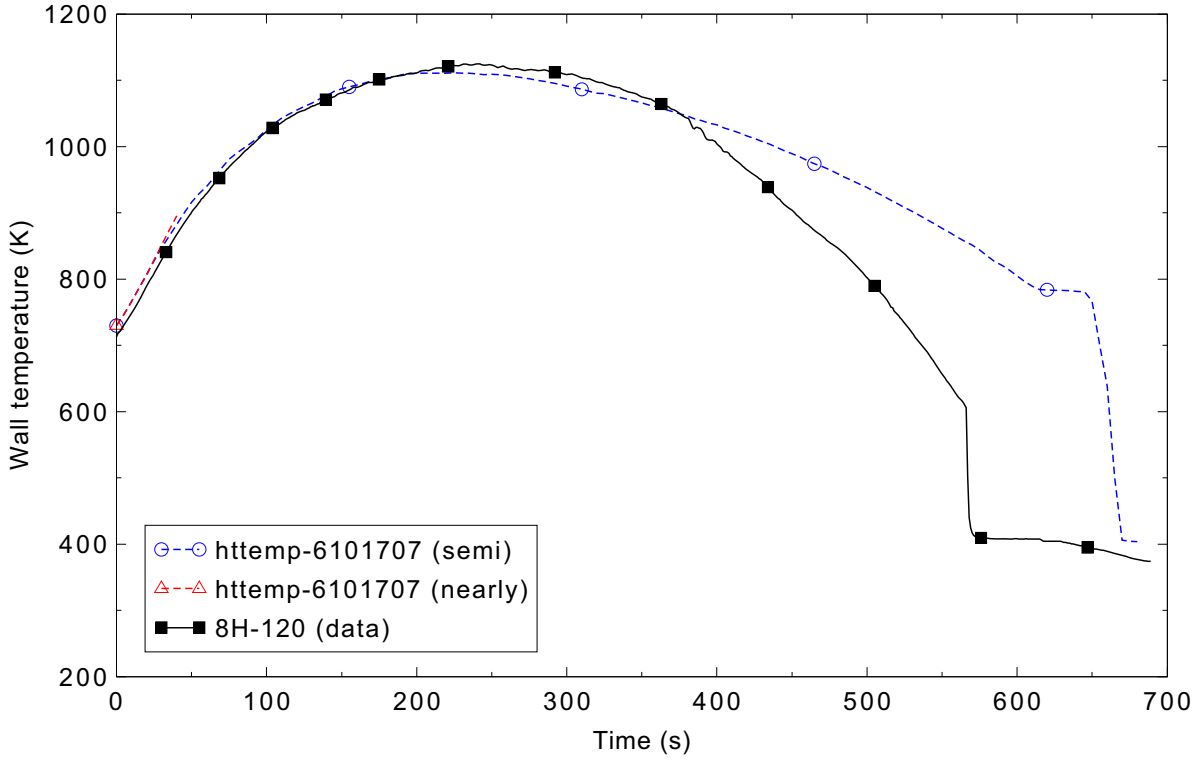

Figure 4.13-9. Measured and calculated rod surface temperatures for FLECHT SEASET forced reflood Test 31504 at the 3.08-m (120-in.) elevation.

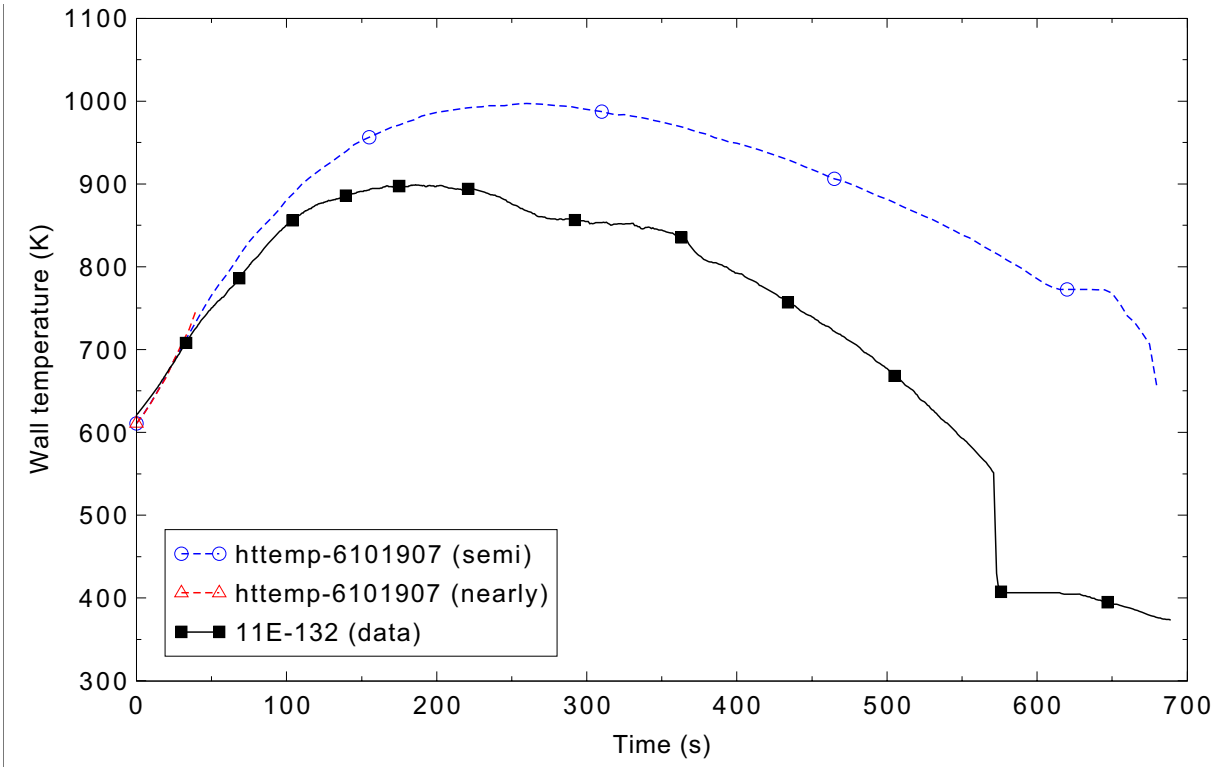

Figure 4.13-10. Measured and calculated rod surface temperatures for FLECHT SEASET forced reflood Test 31504 at the 3.38-m (132-in.) elevation.

The calculated and measured cladding temperatures in the lower portion of the bundle up to the axial midplane were in excellent agreement. As shown in Figures 4.13-4 through 4.13-6, the code accurately calculated the initial temperature rise, peak cladding temperature, temperature turnaround, cool down, and rod quench. Above the bundle axial mid-plane, Figures 4.13-7 to 4.13-9 show that the code adequately predicted the initial cladding temperature rise and peak temperature, but under predicted the cool down and rod quench behavior. At the top of the bundle, Figure 4.13-10 shows that the predicted peak temperature was about 100 K higher than measured, and occurred about 100 s later, with no quench of the heater rods. Quenching was not predicted to occur in the top portion of the bundle until the power was reduced at 610 s (see Figures 4.13-8 through 4.13-10). The under prediction of the cool-down and quench behavior of the upper half of the core indicates a weakness in the reflood model at the low reflood rate for this test.

The measured steam temperatures at various elevations are shown in Figures 4.13-11 through 4.13-16. In the higher elevations of the test bundle, the vapor temperature was under predicted in the early part of the test, indicating a lower calculated heat transfer from the rod surface to the coolant flow. As a result, as shown in earlier plots, the calculated quenching of the heater rods in the higher elevations of the bundle occurred later than measured in the test. The calculated temperature increases after 600 s in Figures 4.13-14 through 4.13-16 occurred after the power to the heater rods was reduced. The lower power allowed the heater rods at lower elevations to quench. Some of the liquid from higher in the bundle flowed downward, resulting in a flow stagnation in the upper portion of the bundle. With no flow, the steam temperature increased as heat continued to be transferred from the heater rods. The measured temperature at the 11.5-ft elevation (Figure 4.13-16) seems unusually low, given the much hotter steam that should be flowing up from lower in the bundle.

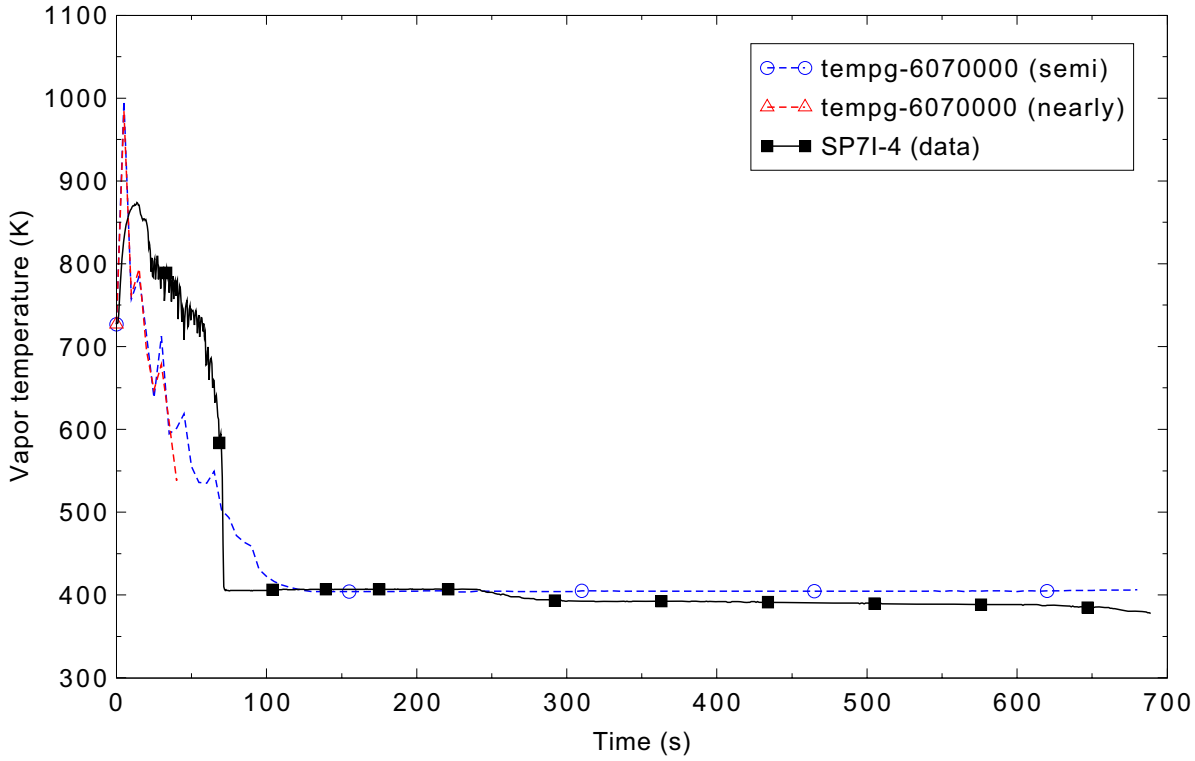

Figure 4.13-11. Measured and calculated steam temperatures for FLECHT SEASET forced reflood Test 31504 at the 1.23-m (4-ft) elevation.

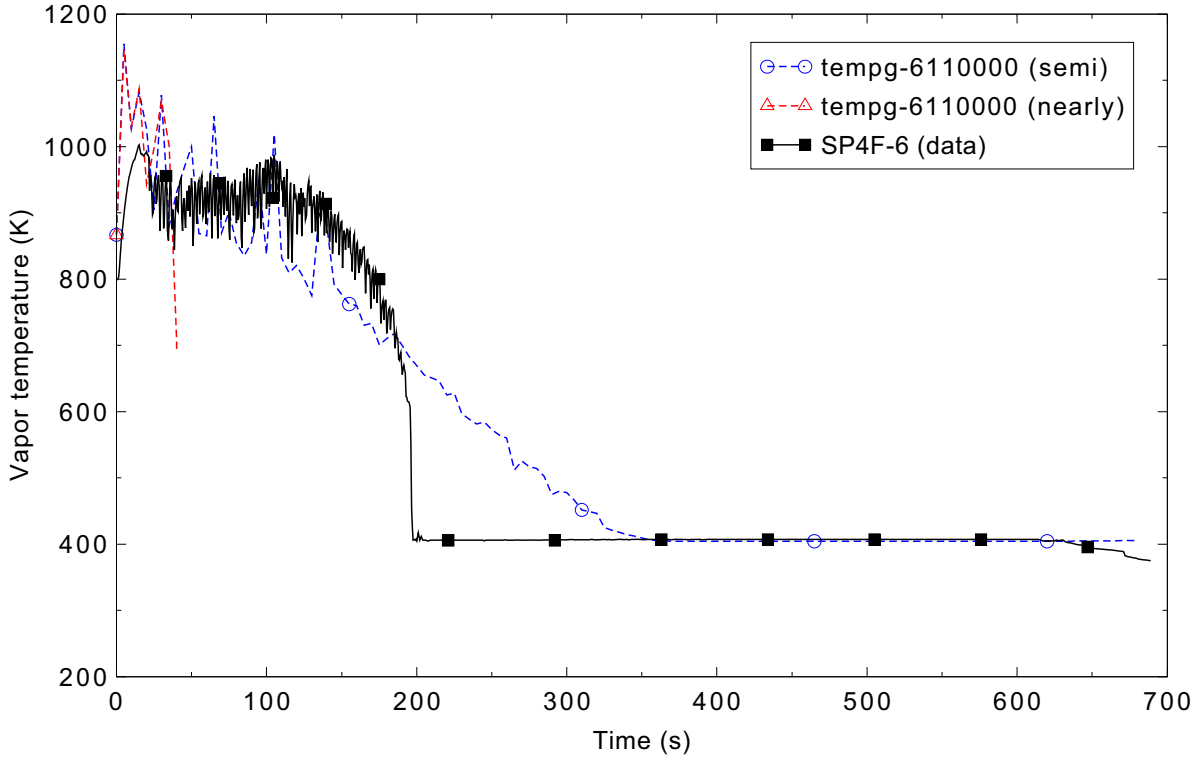

Figure 4.13-12. Measured and calculated steam temperatures for FLECHT SEASET forced reflood Test 31504 at the 1.85-m (6-ft) elevation.

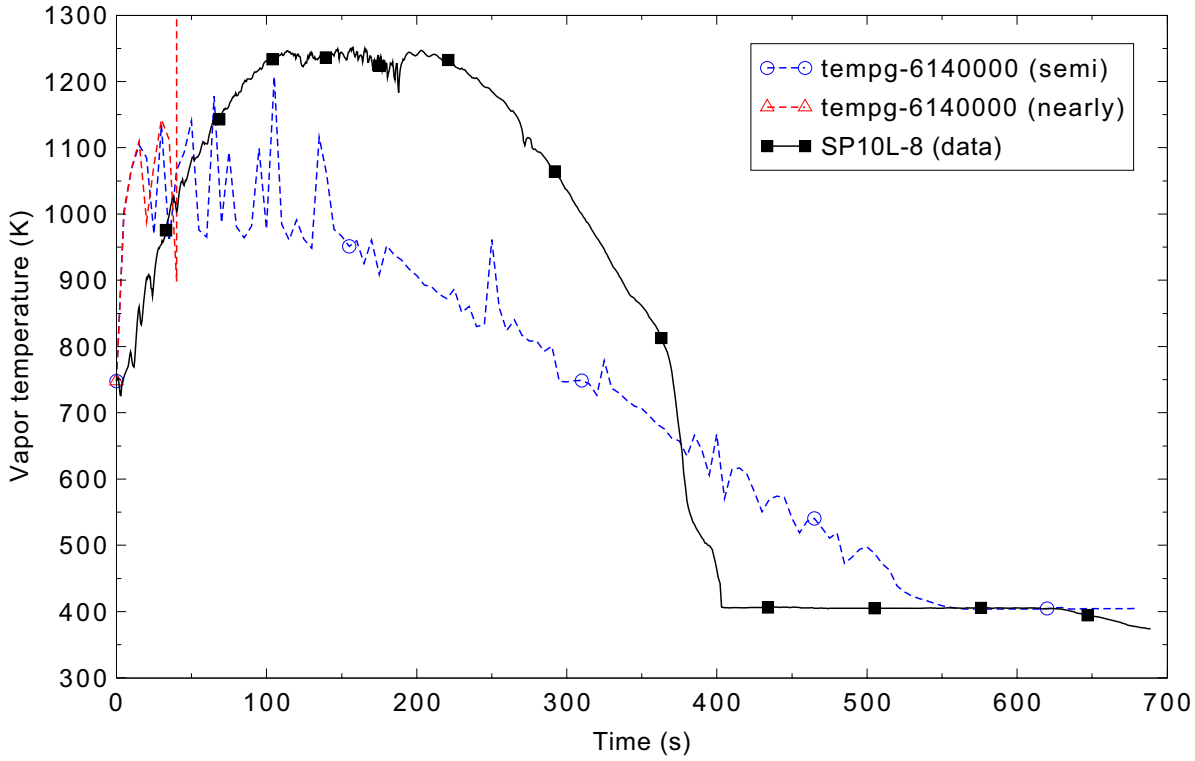

Figure 4.13-13. Measured and calculated steam temperatures for FLECHT SEASET forced reflood Test 31504 at the 2.46-m (8-ft) elevation.

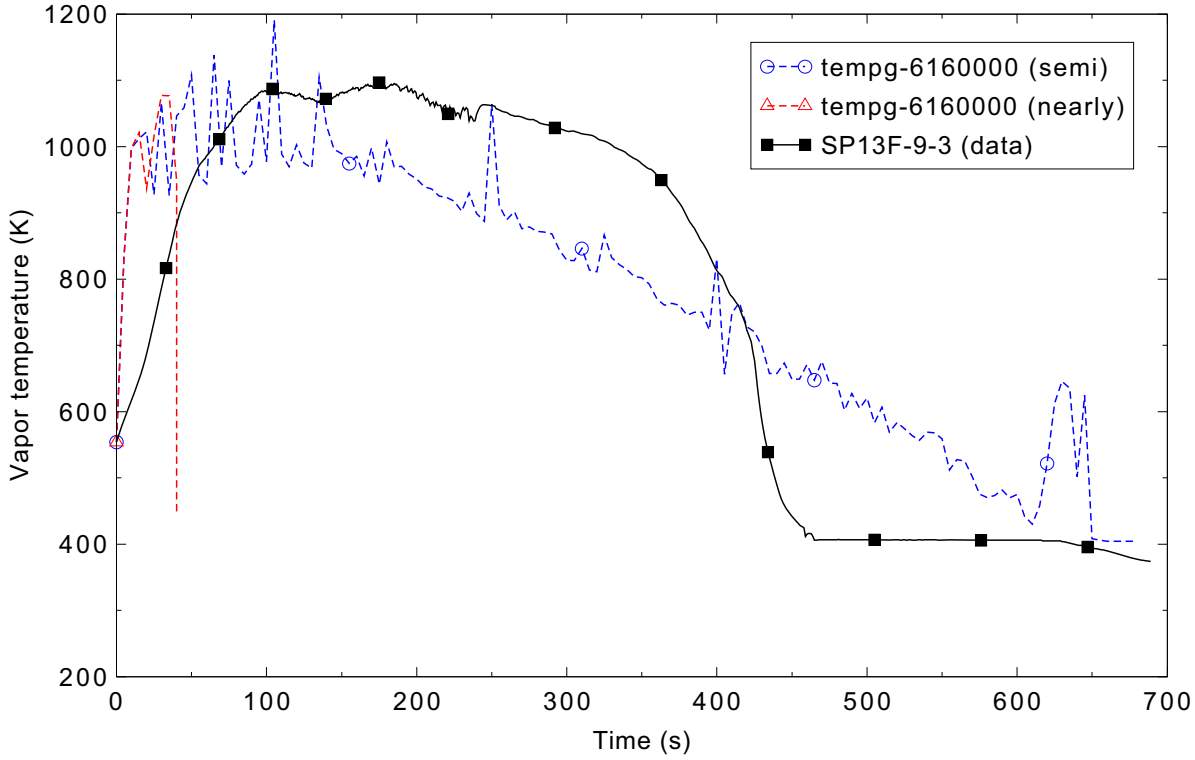

Figure 4.13-14. Measured and calculated steam temperatures for FLECHT SEASET forced reflood Test 31504 at the 2.85-m (9.25-ft) elevation.

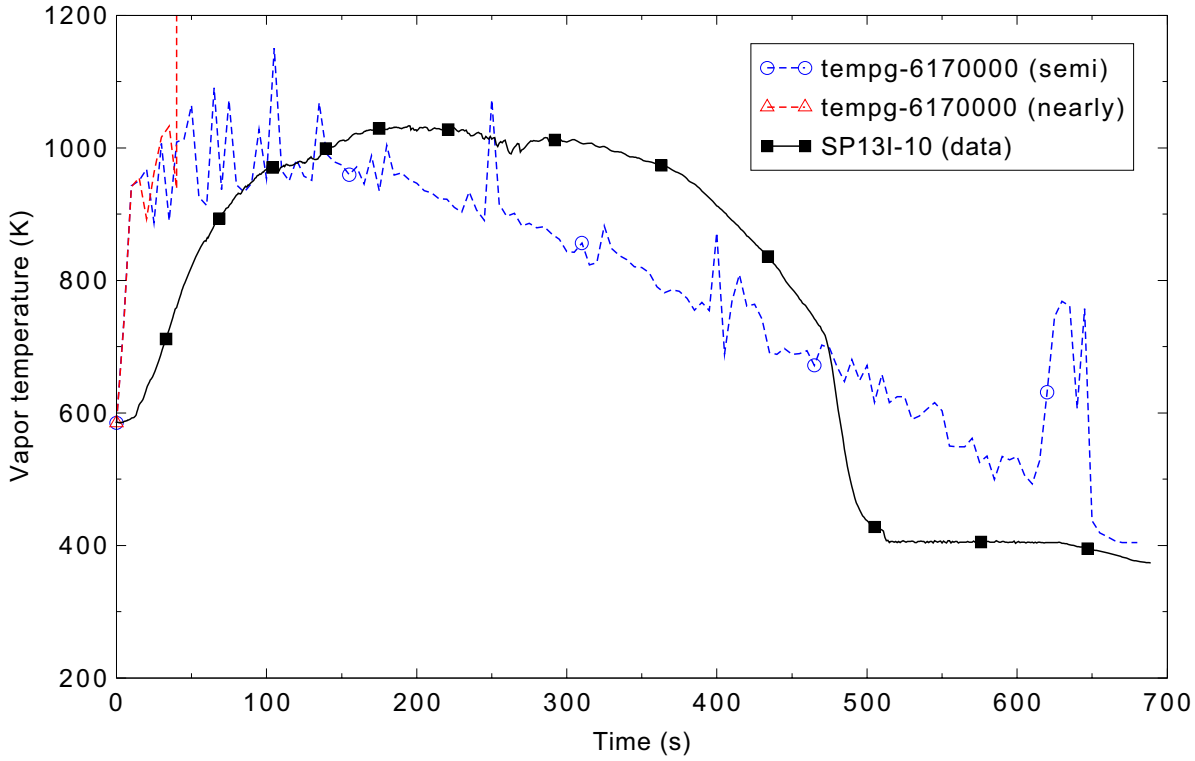

Figure 4.13-15. Measured and calculated steam temperatures for FLECHT SEASET forced reflood Test 31504 at the 3.08-m (10-ft) elevation.

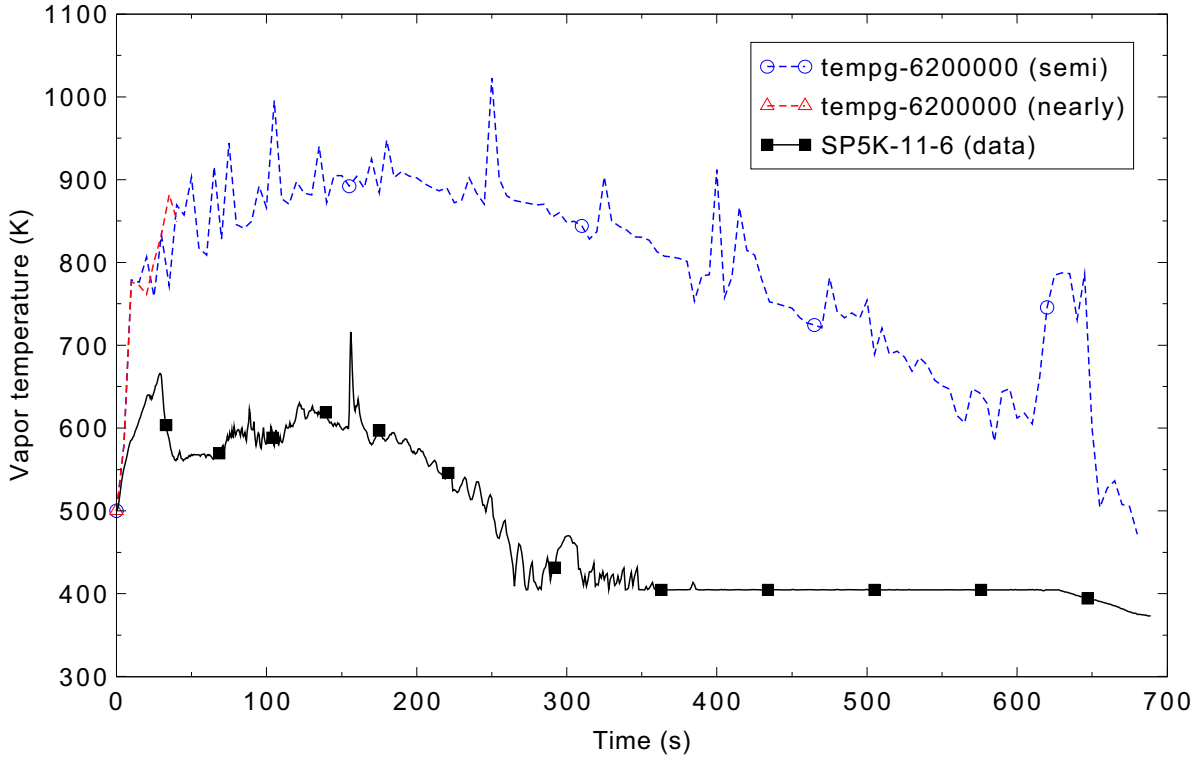

Figure 4.13-16. Measured and calculated steam temperatures for FLECHT SEASET forced reflood Test 31504 at the 3.54-m (11.5-ft) elevation.

The calculated and experimentally-determined mass inventories are compared in Figure 4.13-17. The total calculated mass inventory for the initial 70 s of the transient agrees well with the experiment. However, after 70 s, RELAP5-3D under predicts the mass inventory by about 10%.

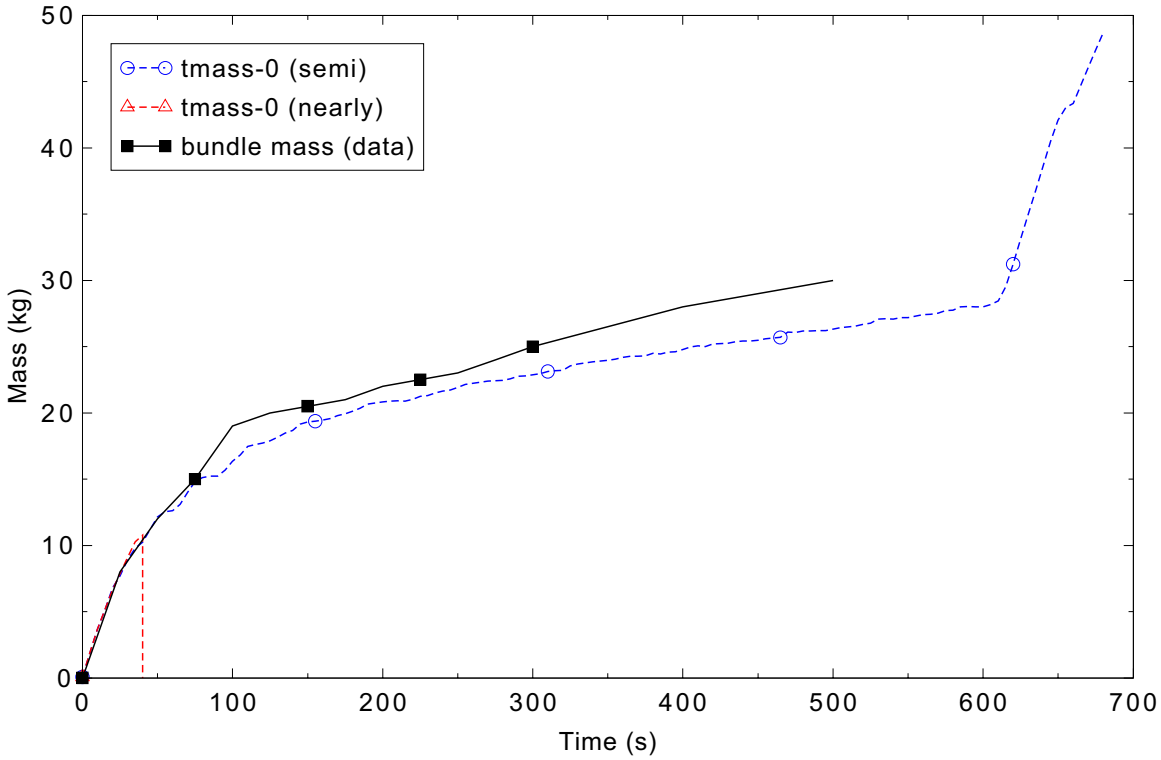

Figure 4.13-17. Measured and calculated total bundle mass inventory for FLECHT SEASET forced reflood Test 31504.

Measured and calculated void fractions at different elevations are compared in Figures 4.13-18 through 4.13-22. The experiment void fraction estimates are obtained from differential pressure cells placed at 0.305-m (1-ft) intervals. The hydraulic cells in the model do not always have a midpoint that exactly matches the midpoint of the differential pressure measurement. Therefore, two predicted void fractions, above and below the measured elevation, are sometimes used in Figures 4.13-18 through 4.13-22 to compare with the measured elevation.

The measured and calculated void fractions at the different elevations appear to be in relatively good agreement, indicating the axial distribution of mass throughout the transient is correctly calculated by RELAP5-3D. This is confirmed by Figure 4.13-23, which shows good agreement between the calculated and measured axial void profile at 300 s into the transient.

4.13.5 Conclusions and Assessment Findings

The RELAP5-3D calculations are judged to be in reasonable agreement with the measured data. Predicted rod surface temperatures in the lower half of the rod bundle were in excellent agreement with the data. Above the core midplane, the code adequately predicted the initial cladding temperature rise and peak temperature, but under predicted the cool down and rod quench behavior. For the most part, the code

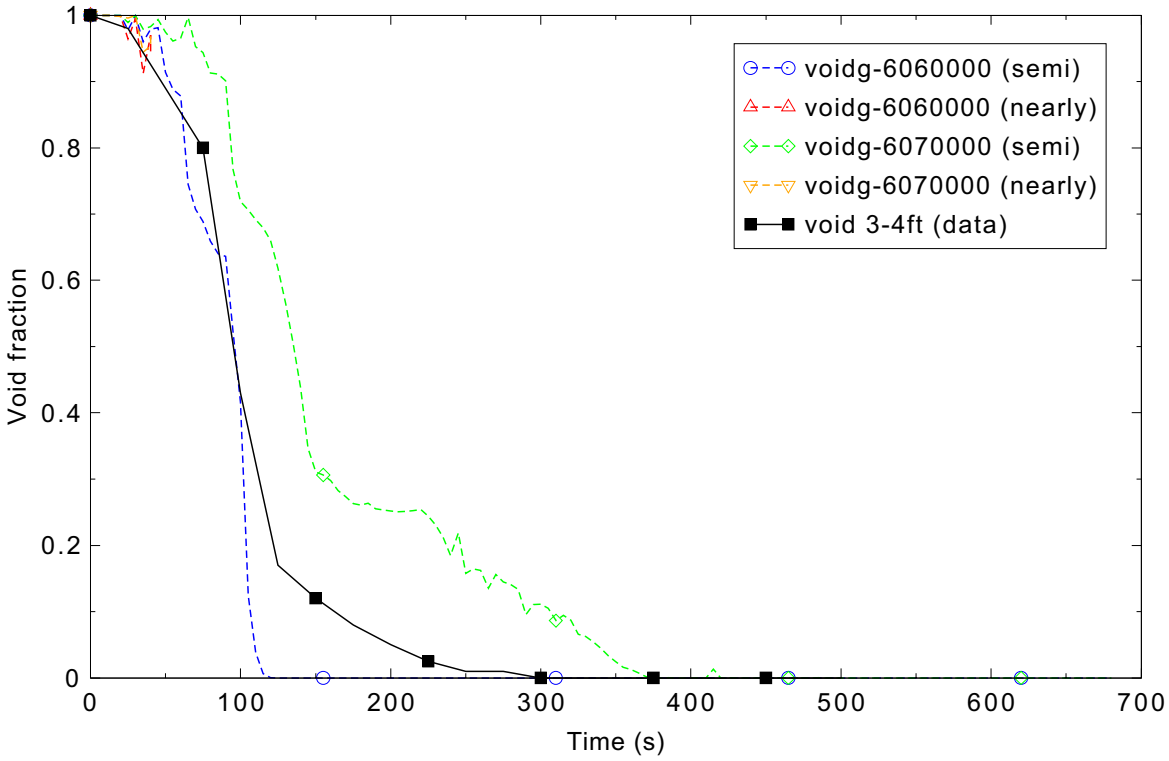

Figure 4.13-18. Measured and calculated void fractions at 0.92 to 1.23-m (3 to 4-ft) elevations for FLECHT SEASET forced reflood Test 31504.

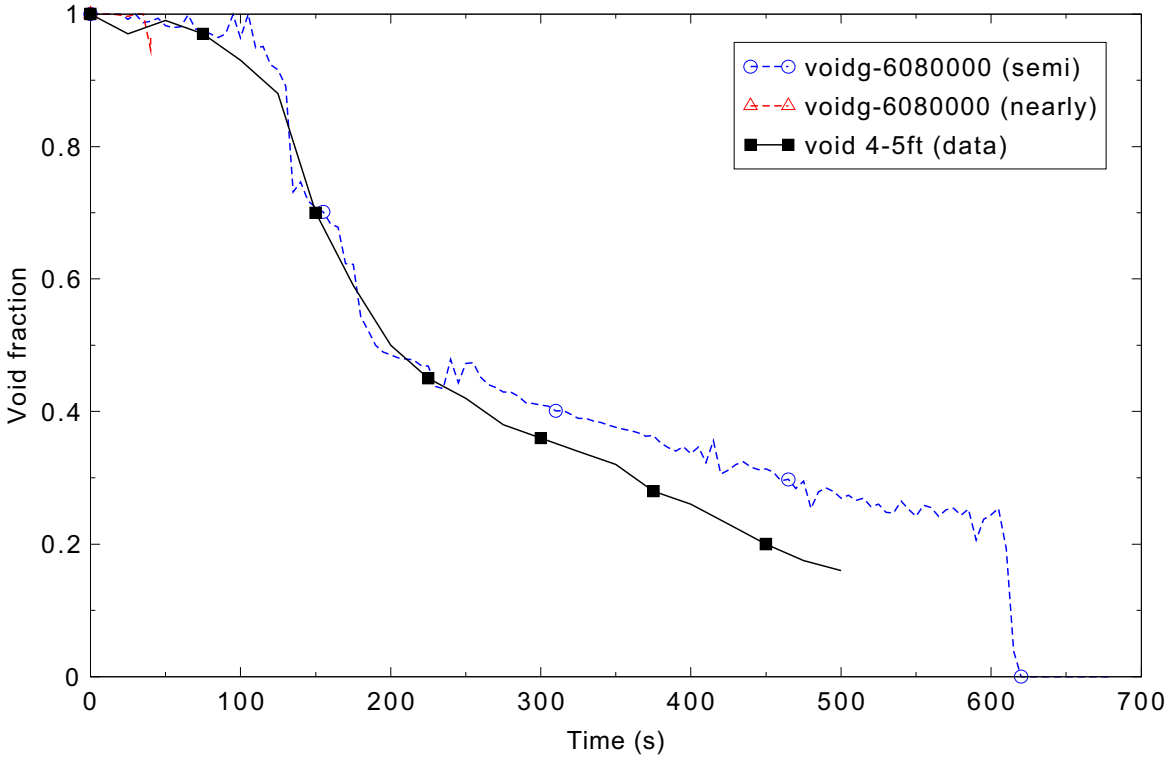

Figure 4.13-19. Measured and calculated void fractions at 1.23 to 1.54-m (4 to 5-ft) elevations for FLECHT SEASET forced reflood Test 31504.

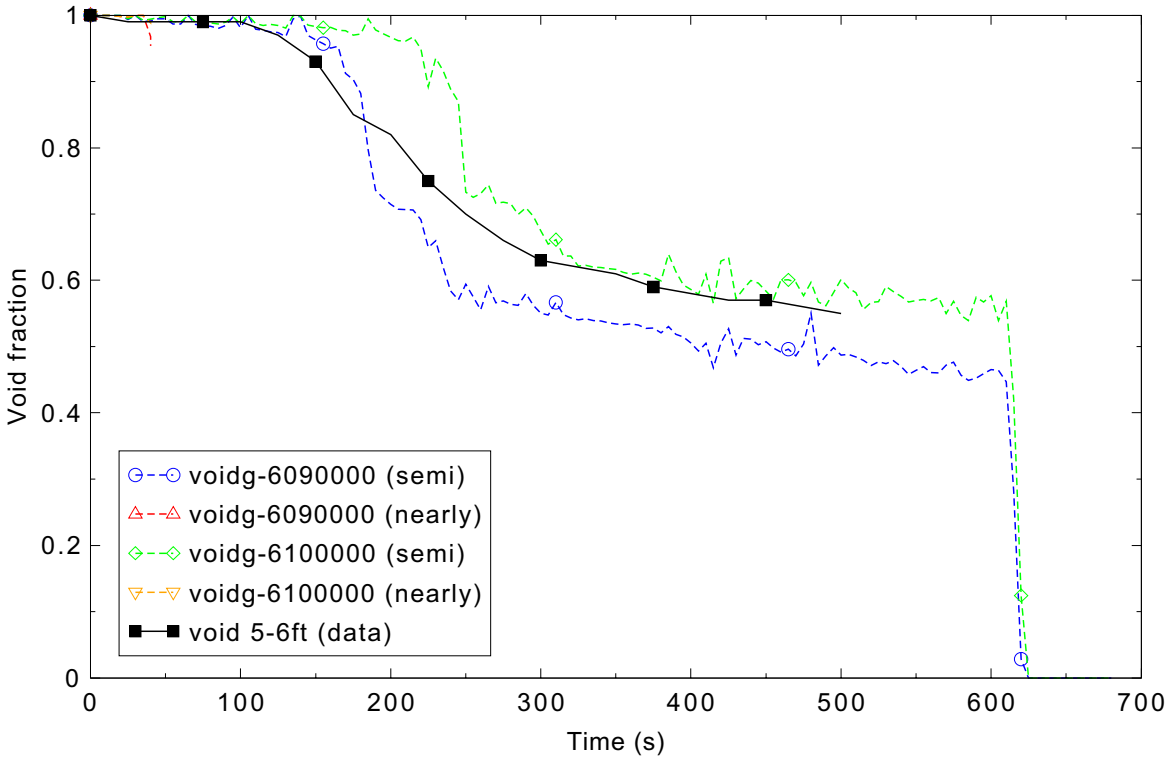

Figure 4.13-20. Measured and calculated void fractions at 1.54 to 1.85-m (5 to 6-ft) elevations for FLECHT SEASET forced reflood Test 31504.

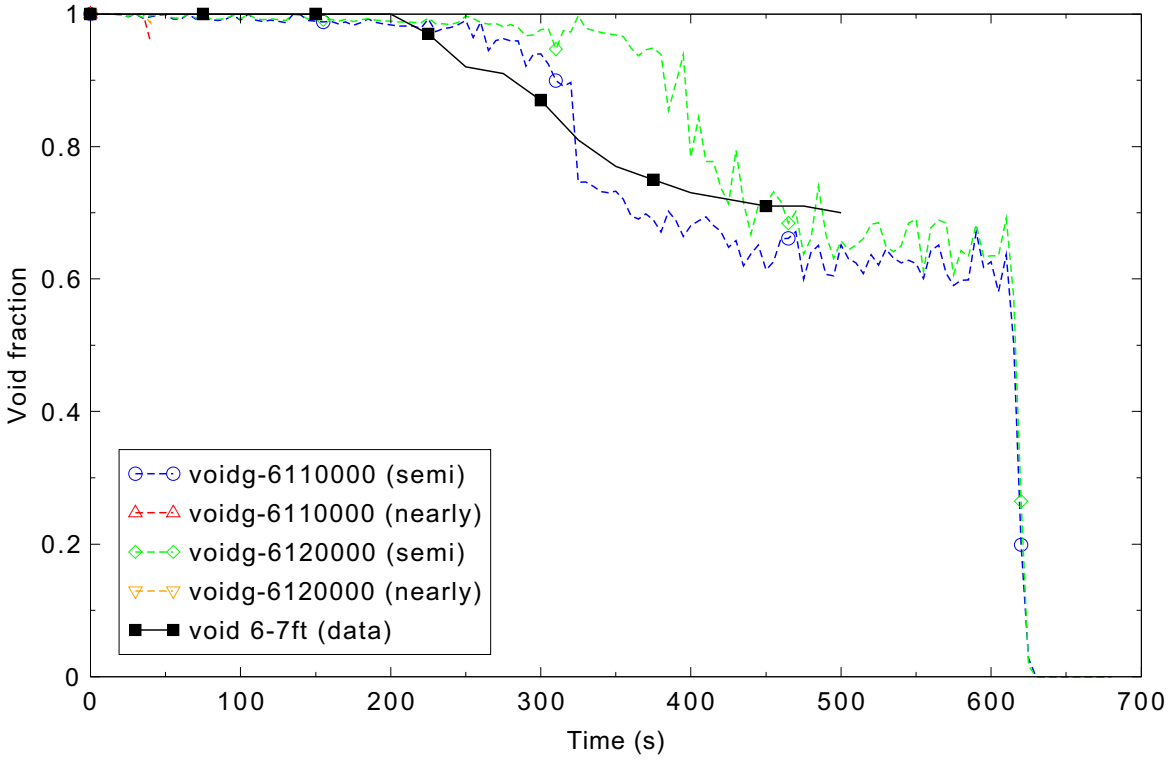

Figure 4.13-21. Measured and calculated void fractions at 1.85 to 2.15-m (6 to 7-ft) elevations for FLECHT SEASET forced reflood Test 31504.

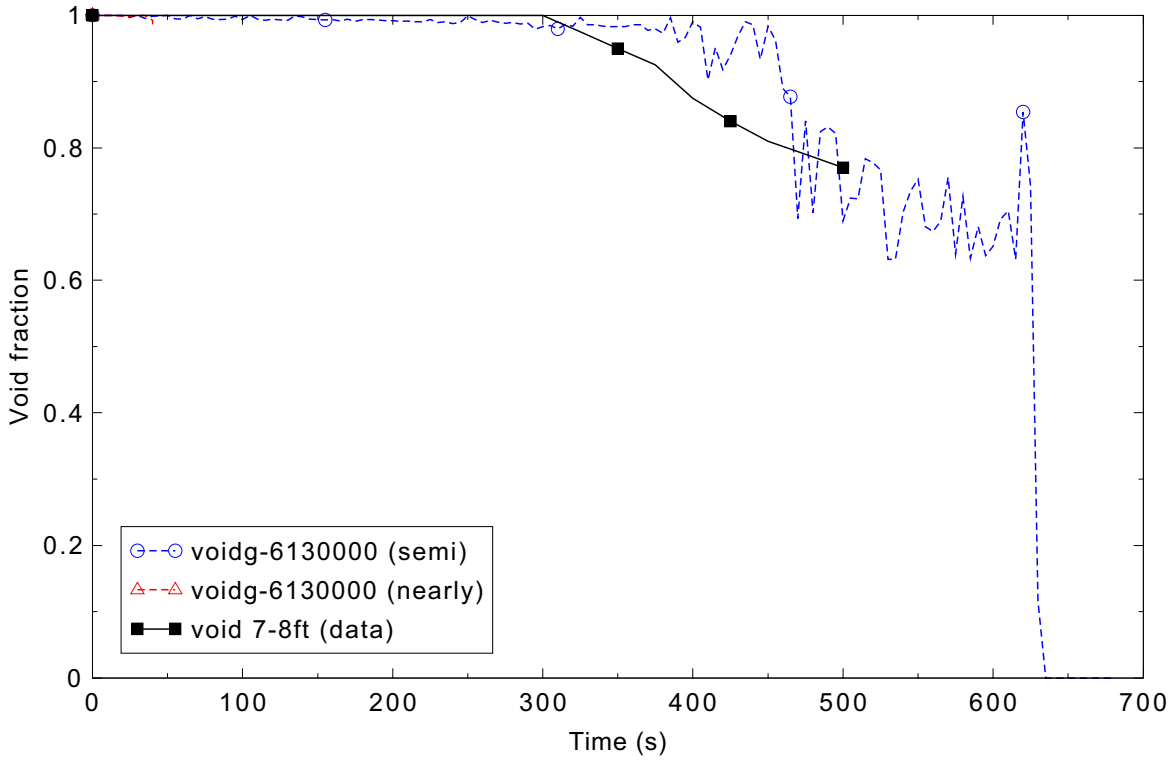

Figure 4.13-22. Measured and calculated void fractions at 2.15 to 2.46-m (7 to 8-ft) elevations for FLECHT SEASET forced reflood Test 31504.

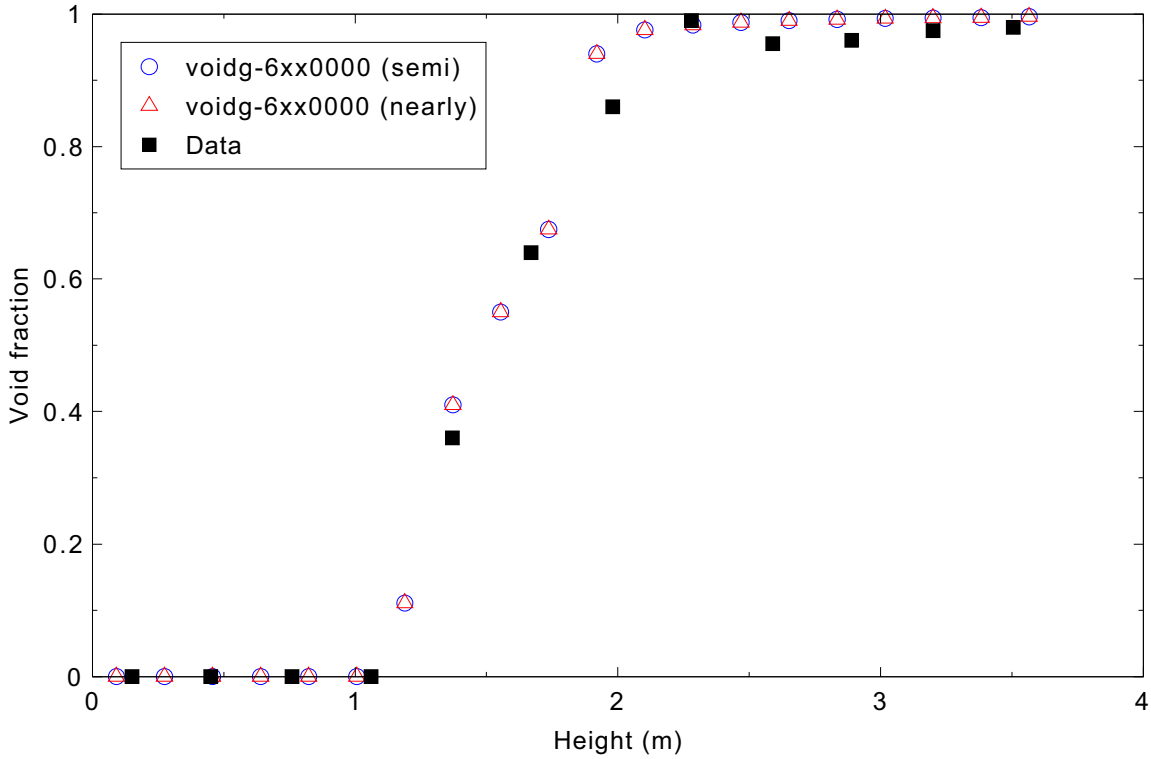

Figure 4.13-23. Measured and calculated axial void profile at 300 s for FLECHT SEASET forced reflood Test 31504.

tended to under predict vapor temperatures in the early part of the transient and over predict vapor temperatures in the latter part of the reflood transient. The under prediction of the cooldown and quench behavior of the upper half of the core, coupled with the under prediction of vapor temperatures in the early part of the transient and the over prediction of vapor temperatures in the latter part of the transient indicates a weakness in the current reflood model that needs to be addressed. Overall, measured and calculated void fractions were generally in good agreement. The code predicted mass inventory and distribution were in excellent agreement during the first 70 s of the transient, but after 70 s, the RELAP5-3D calculated mass inventory was under predicted by about 10%.

4.13.6 References

4.13-1. M. J. Loftus, et al., *PWR FLECHT SEASET Unblocked Bundle, Forced and Gravity Reflood Task Data Report*, NUREG/CR-1532, EPRI NP-1459, WCAP-9699, June 1980.

4.14 FLECHT SEASET Test 31701

A forced reflood experiment at a flooding rate of 155 mm/s (6.1 in./s) was performed in the 161-rod Full Length Emergency Core Heat Transfer Separate Effects and Systems Effects Tests (FLECHT SEASET) Facility.[4.14-1] The facility's electrically-heated rod configuration was typical of a full-length 17 x 17 rod bundle in a Westinghouse pressurized water reactor (PWR). The experiment provided data on PWR core reflood behavior following a hypothetical loss-of-coolant accident (LOCA).

4.14.1 Code Models Assessed

The performance of the reflood model at a high flooding rate was evaluated.

4.14.2 Experiment Facility Description

Figure 4.14-1 shows the flow diagram for the FLECHT SEASET unblocked bundle configuration used in the forced reflood experiment. The flow diagram also shows the location of instruments used in the experiment. The bundle cross section for the forced reflood experiment is shown in Figure 4.14-2.

Facility design features for the forced reflood experiment included:

- A cylindrical low mass bundle housing to minimize housing heat releases
- Housing differential pressure cells every 0.30 m (12 in.) to obtain void fraction measurements along the heated length of the bundle
- Steam probes in each of 11 thimble tubes to measure steam superheat radially and axially across the bundle
- 177 heater rod thermocouple computer channels
- Housing windows at the 0.91, 1.83, and 2.74 m elevations.

Within the bundle, the dimensions are full scale, compared to a typical PWR, with the exception of the overall radial dimension. The low mass housing used in the forced reflood experiment was designed to minimize the wall effects such that the rods one row or more away from the housing are representative of any region in a PWR core. To preserve proper thermal scaling of the experiment facility with respect to a PWR, the power to flow area ratio in the experiment facility is nearly the same as that for a PWR fuel assembly.

The reflood phase of a typical PWR design basis large break LOCA transient is predicted to start approximately 30 s after initiation of a hypothetical break. To simulate the expected conditions in a PWR at the start of reflood, the initial conditions for forced reflood Test 31701 were:

- Initial clad temperature (1.83 m elevation) - 872°C (1601°F)

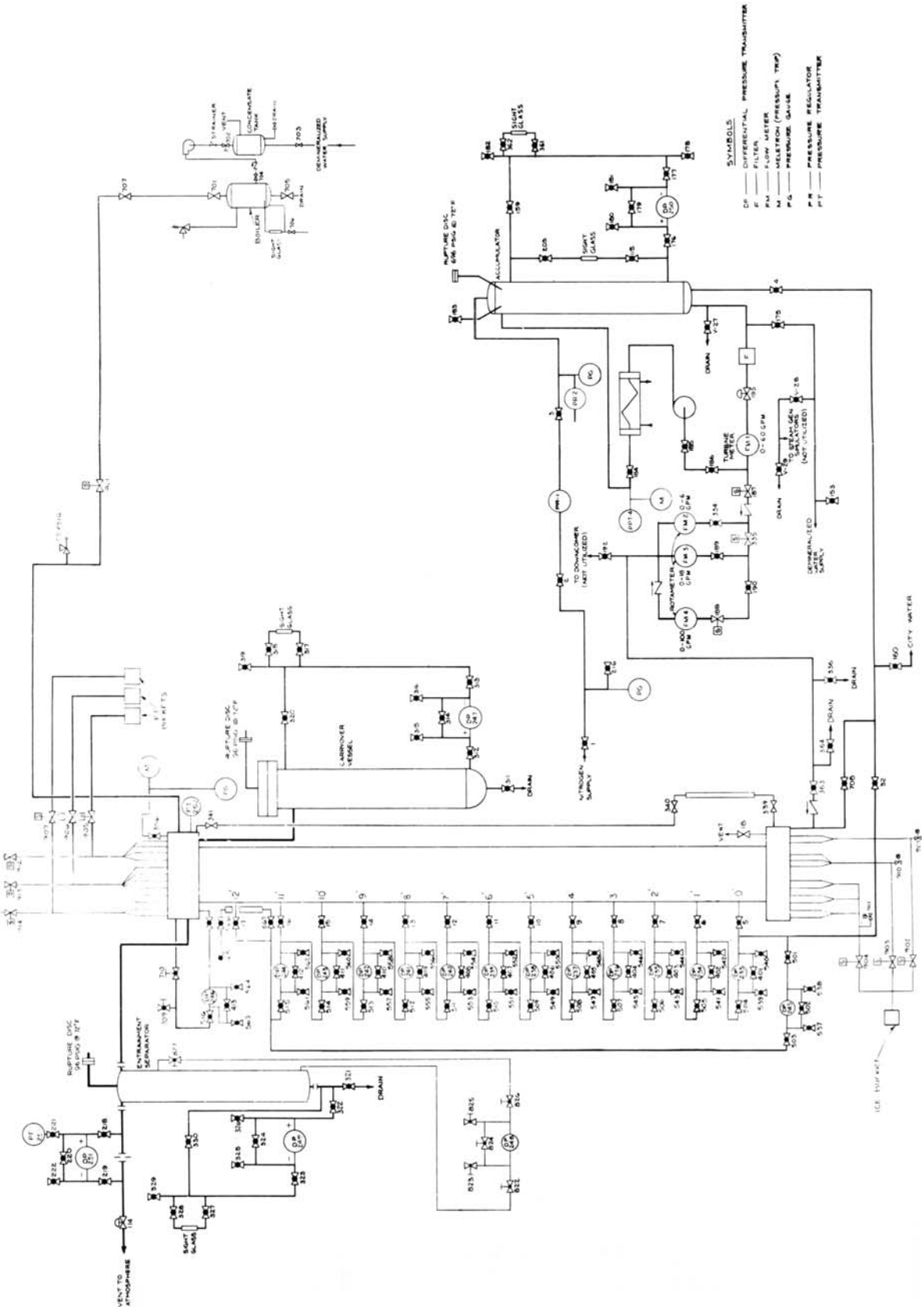

Figure 4.14-1. FLECHT SEASET unblocked bundle flow diagram for forced reflood.

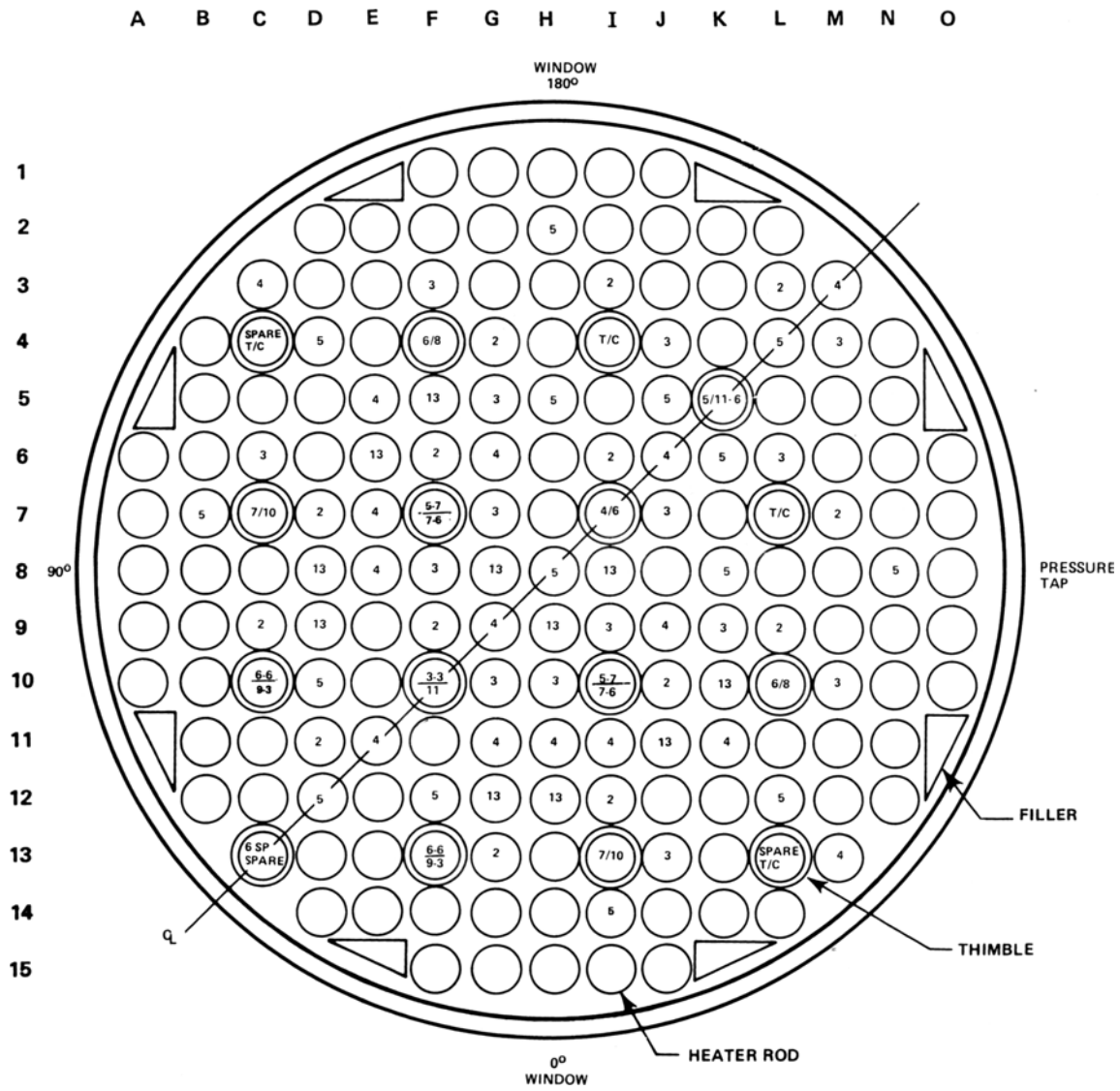

Figure 4.14-2. FLECHT SEASET bundle cross section.

- Peak power - 2.3 kW/m (0.7 kW/ft)
- Upper plenum pressure - 0.28 MPa (40 psia)
- Injection rate (lower plenum initially full) - 155 mm/s (6.1 in./s)
- Flooding water temperature entering lower plenum - 53°C (127°F)
- Radial power distribution - uniform
- Axial power shape - cosine (1.66 peak-to-average power ratio).

The power to the heater rods decreased during the experiment following the ANS plus 20 percent power decay curve 30 seconds after initiation of a LOCA.

4.14.3 Input Model Description

The test section for the forced reflood experiment was modeled using 20 cells (Component 6) as shown in Figure 4.14-3. Measured fluid conditions were used to define the conditions in the upper and lower time dependent volumes (Components 7 and 5), which represent the upper and lower plenums, respectively. The measured flow injection velocity was used to define the flow conditions at the time-dependent junction (Component 301) that connected the lower plenum and the pipe, which represented the low mass housing. The measured power, which decreased during the test, was used as input to the heat structures representing the rods.

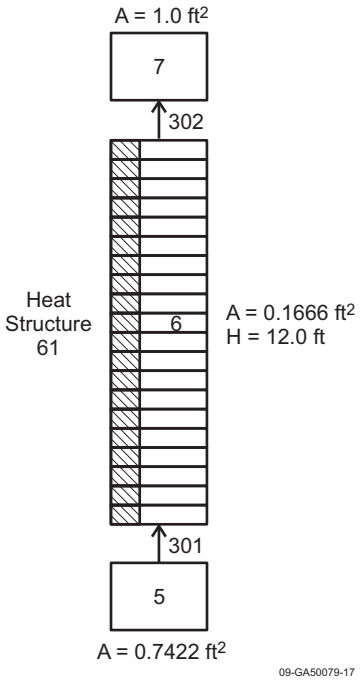

Figure 4.14-3. RELAP5-3D nodalization for the FLECHT SEASET forced reflood experiments.

4.14.4 Data Comparisons and Results

RELAP5-3D calculations were performed for FLECHT SEASET forced reflood Test 31701 using both the semi-implicit and nearly-implicit hydrodynamic advancement schemes; the requested time steps were 0.02 s for the first 80 s, 0.025 s for the next 40 s, and 0.05 s for the final 40 s. Comparisons of measured and calculated rod surface temperatures are presented in Figures 4.14-4 through 4.14-10; the data are from the NRC Data Bank. The results were plotted for 200 s following test initiation to encompass the entire test duration including termination of power to the test bundle at approximately 130 s, which accounts for the drop in temperature in each of the plots at that time. The legend for the rod temperature data is the rod number followed by the elevation in inches; i.e., 7J-072 was from a thermocouple in a rod near the center of the bundle at the axial mid-plane, 1.83 m (72 in.) from the inlet.

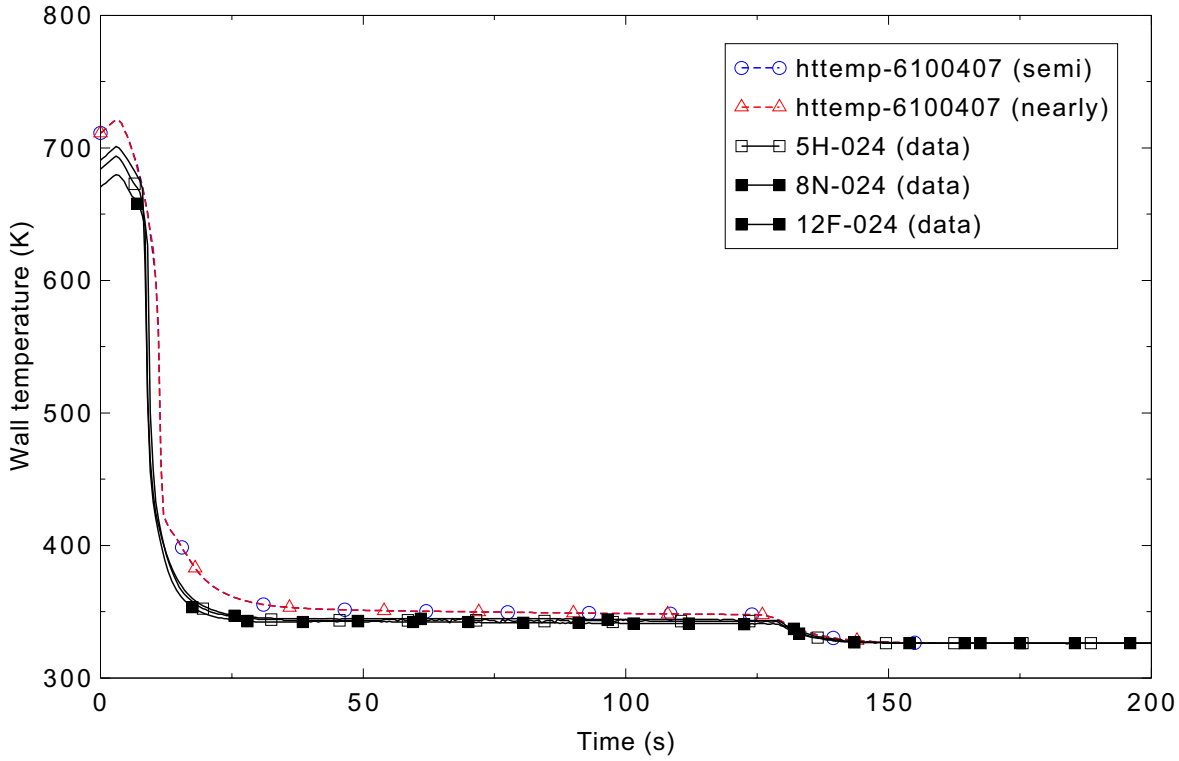

Figure 4.14-4. Measured and calculated rod surface temperatures for FLECHT SEASET forced reflood Test 31701 at the 0.62-m (24-in.) elevation.

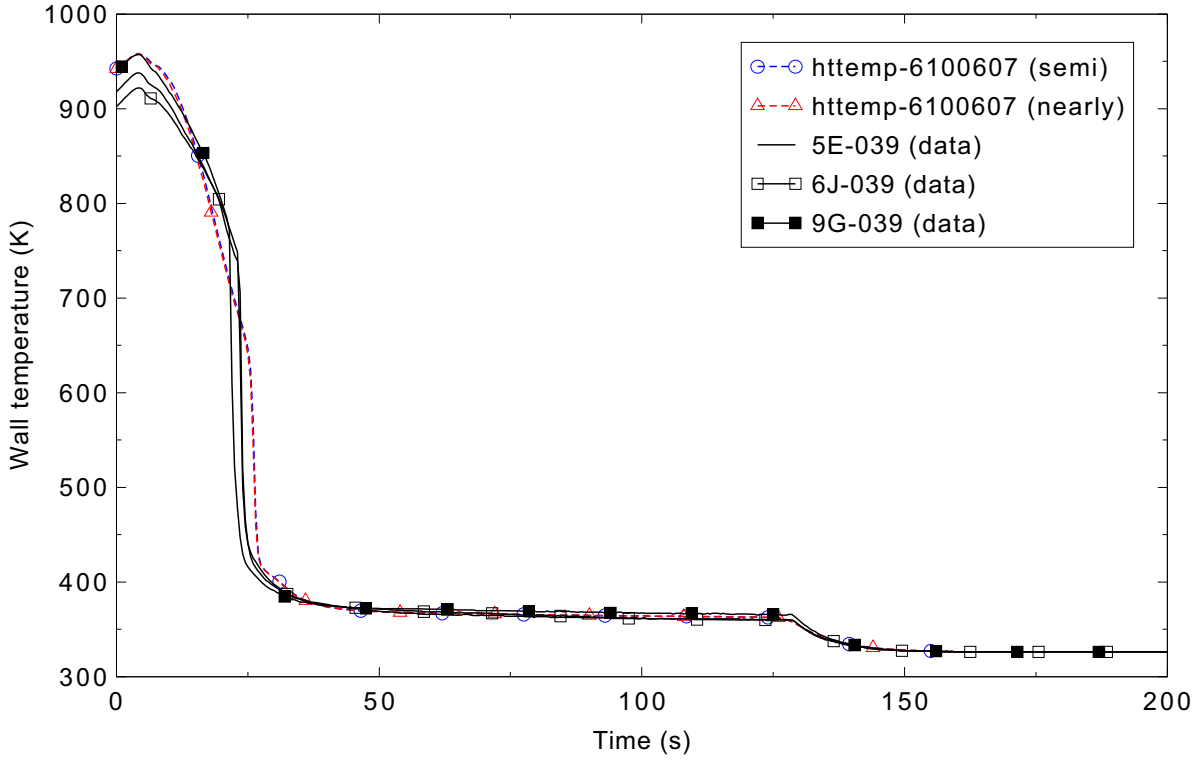

Figure 4.14-5. Measured and calculated rod surface temperatures for FLECHT SEASET forced reflood Test 31701 at the 0.99-m (39-in.) elevation.

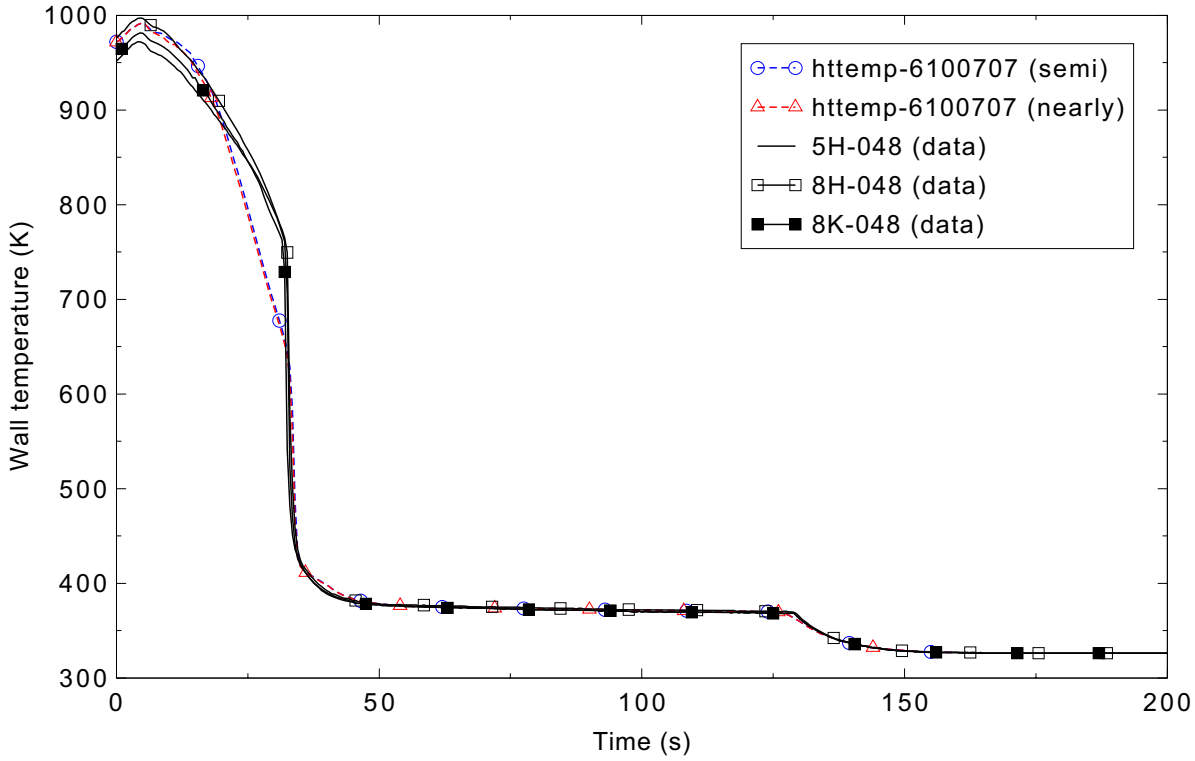

Figure 4.14-6. Measured and calculated rod surface temperatures for FLECHT SEASET forced reflood Test 31701 at the 1.22-m (48-in.) elevation.

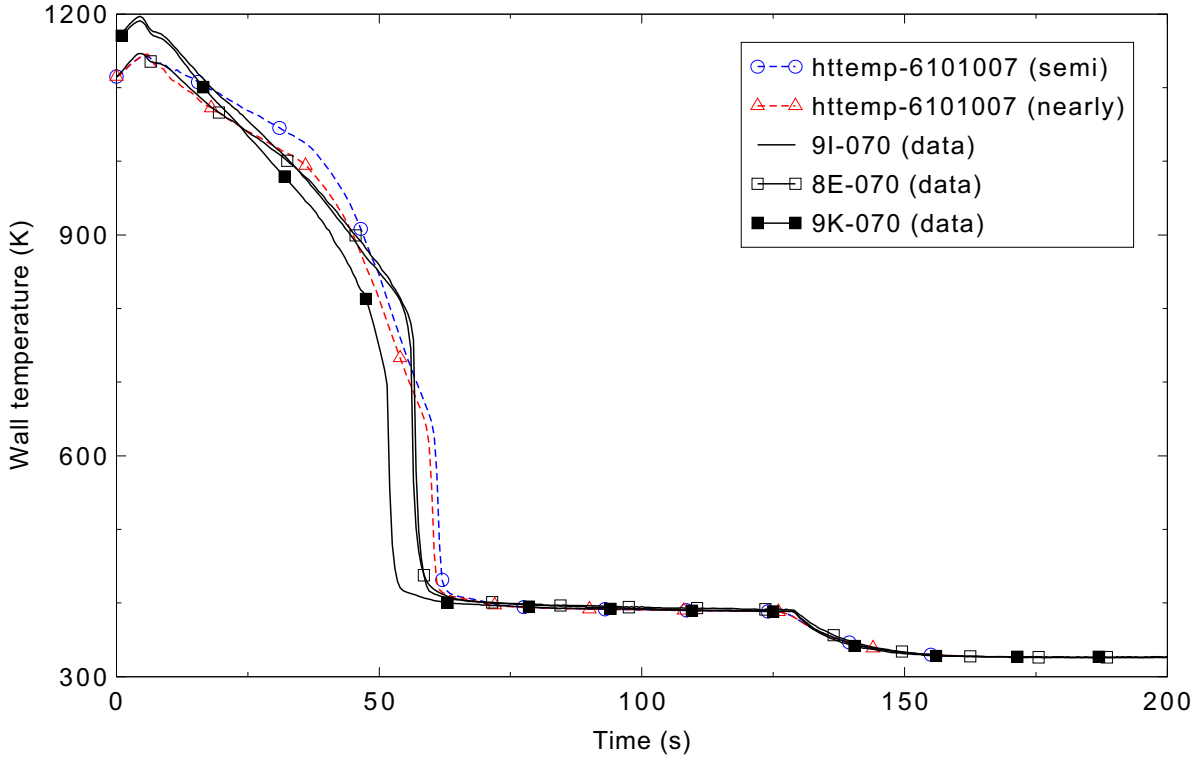

Figure 4.14-7. Measured and calculated rod surface temperatures for FLECHT SEASET forced reflood Test 31701 at the 1.78-m (70-in.) elevation.

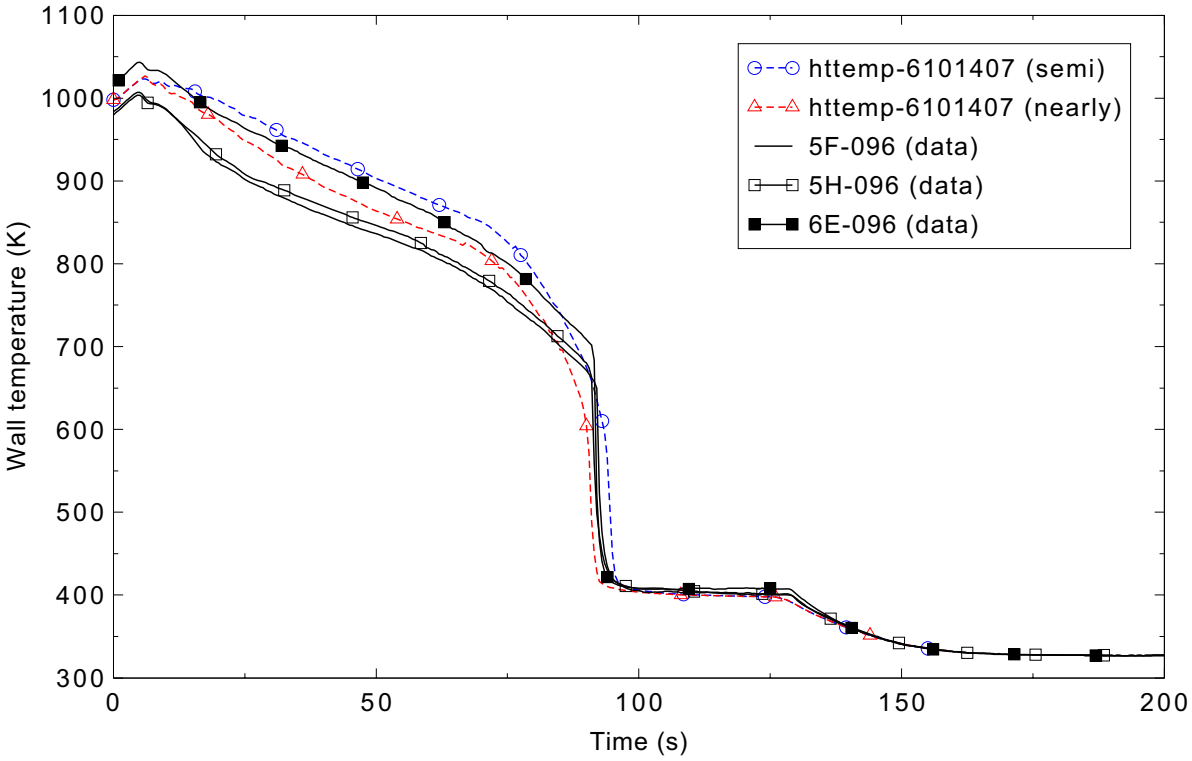

Figure 4.14-8. Measured and calculated rod surface temperatures for FLECHT SEASET forced reflood Test 31701 at the 2.46-m (96-in.) elevation.

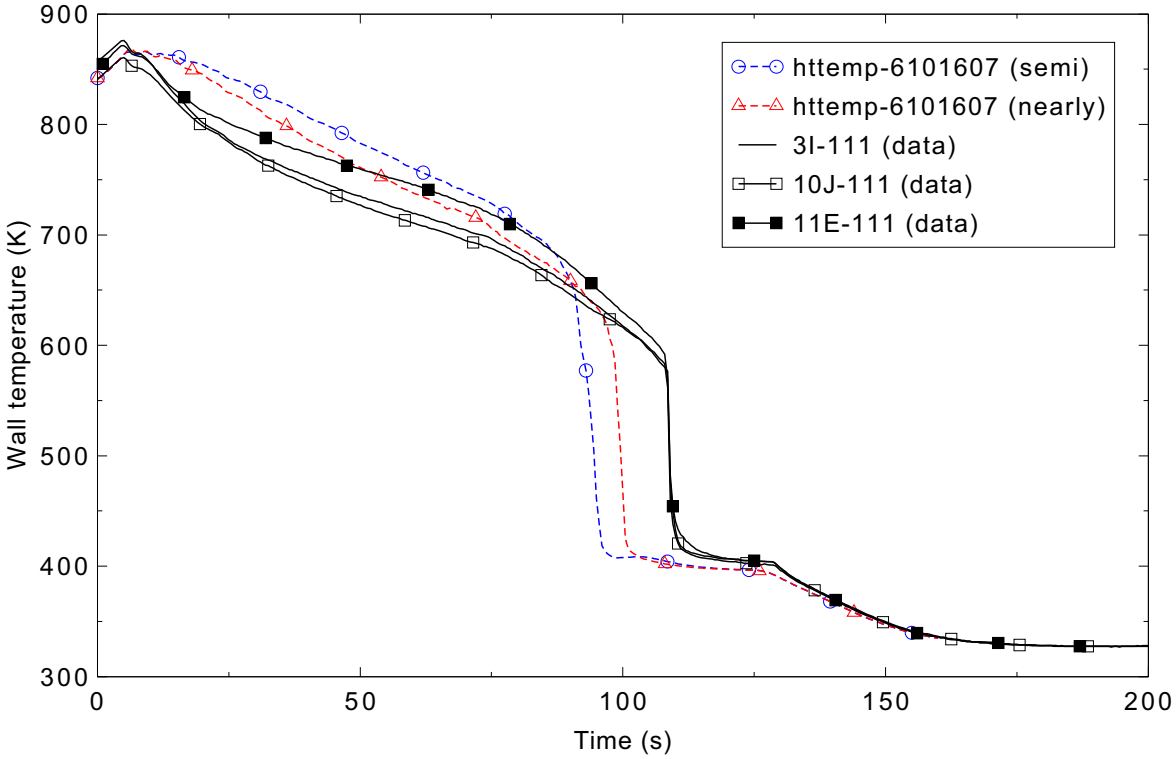

Figure 4.14-9. Measured and calculated rod surface temperatures for FLECHT SEASET forced reflood Test 31701 at the 2.85-m (111-in.) elevation.

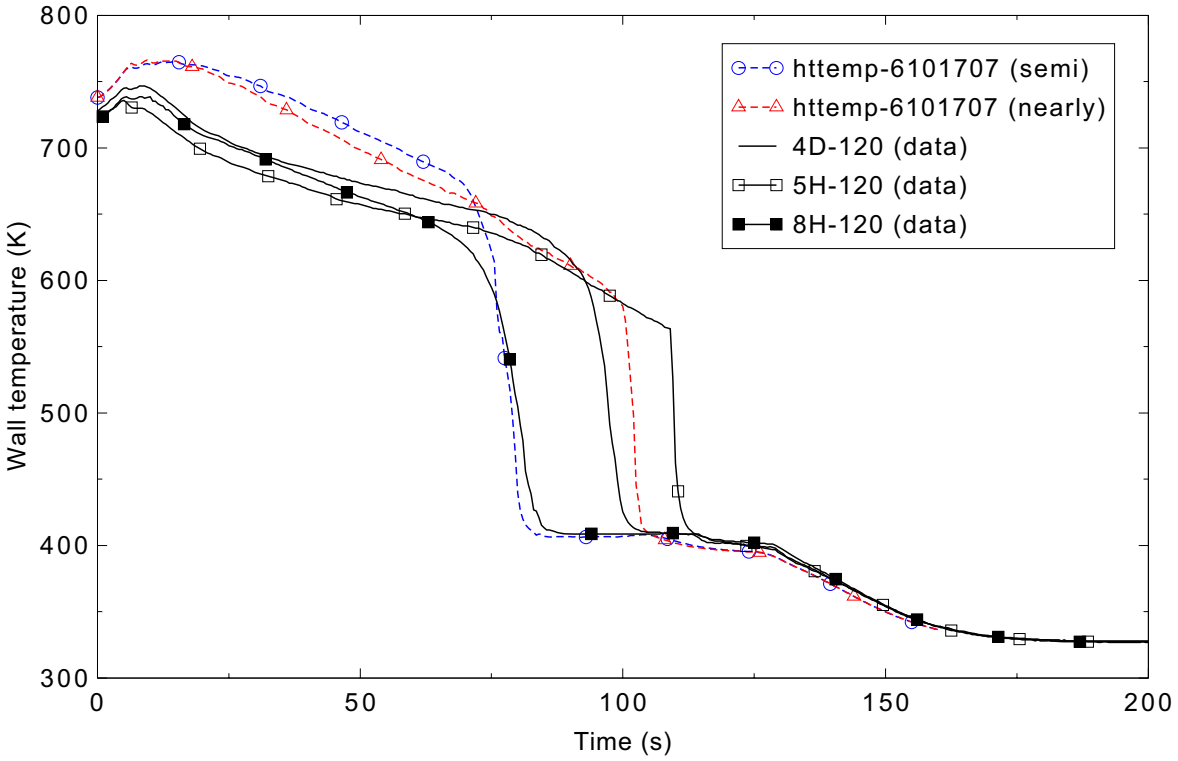

Figure 4.14-10. Measured and calculated rod surface temperatures for FLECHT SEASET forced reflood Test 31701 at the 3.08-m (120-in.) elevation.

The calculated and measured cladding temperatures in the lower portion of the bundle up to the 2.46-m (96-in.) axial elevation were in good agreement. As shown in Figures 4.14-4 through 4.14-8, the code accurately calculated the initial temperature rise, peak cladding temperature, temperature turnaround, cool down, and rod quench using either the semi- or nearly-implicit solution scheme. Above the 2.46-m (96-in.) bundle axial location, Figures 4.14-9 and 4.14-10 show that the code adequately predicted the initial cladding temperature rise and peak temperature, but calculated an earlier quench in the upper portions of the bundle than was measured in the experiment, particularly with the semi-implicit method. This earlier quench in the semi-implicit calculation was the result of a code predicted top-down quenching of the upper portion of the bundle that was not observed in the experiments or in the nearly-implicit calculation. This calculated top-down quenching of the top of the bundle can be seen in Figure 4.14-11, which shows the progression of the quench front from both the bottom and top of the bundle. Although the experiment data did not show the top-down quench behavior observed in the calculations, the large variation in quench times at the 3.08-m (120-in.) elevation in Figure 4.14-10 indicates preferential cooling in some cross-sectional regions of the bundle and a tendency for top-down cooling at this highest elevation.

The measured fluid temperatures and calculated steam temperatures at various elevations are shown in Figures 4.14-12 through 4.14-17. Overall, fluid temperatures throughout the core are not particularly well predicted. At each elevation, measured fluid temperatures reached saturation temperature earlier in the transient than predicted. This may be due in part to thermocouples measuring a combination of superheated steam and saturated liquid as the quench front approaches the measurement locations. Shortly after reaching saturated fluid temperature conditions, the presence of subcooled liquid in the experiment is clearly indicated in Figures 4.14-12 through 4.14-17 by the drop in measured temperature below the

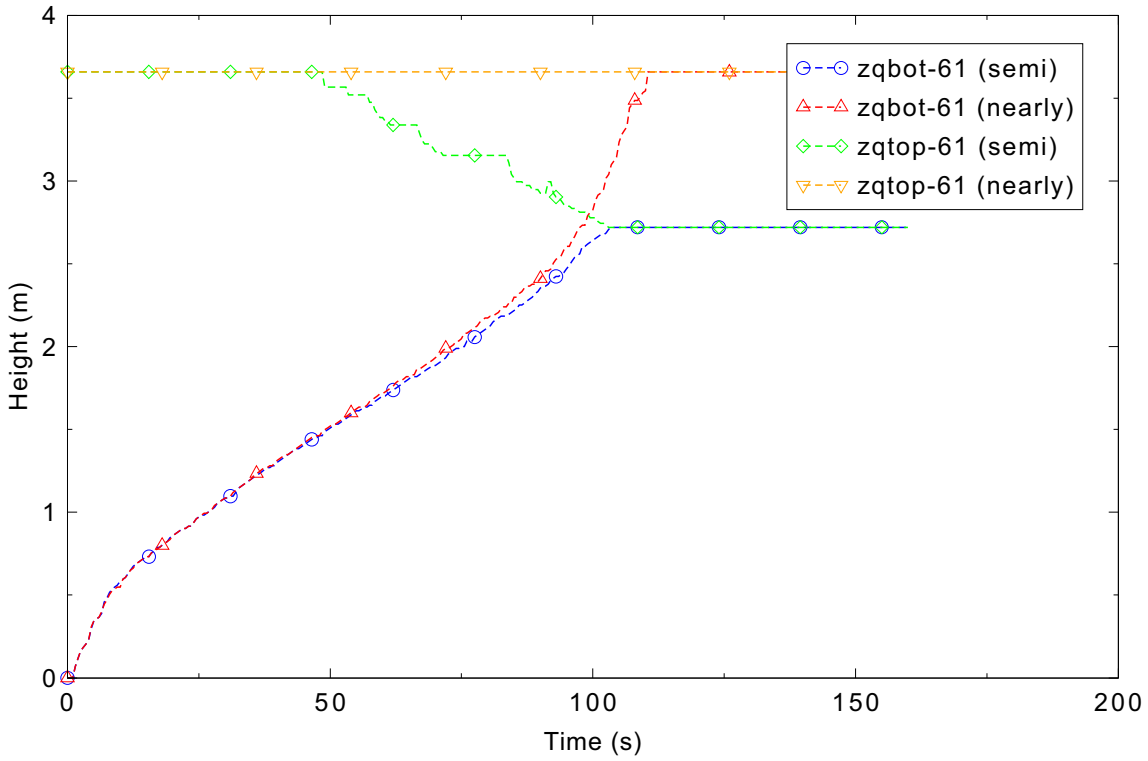

Figure 4.14-11. RELAP5-3D calculated rod bundle bottom and top quench behavior for FLECHT SEASET forced reflood Test 31701.

calculated saturated steam temperature as the liquid front passes each measurement location. The measured data in Figure 4.14-15 are a bit suspect, as the fluid is initially at the saturation temperature, while measurements above and below this elevation show significant superheat. Additionally, the response near the top of the bundle (Figure 4.14-17), in which the steam temperature drops to about 450 K near 10 s and is maintained there, indicates that some liquid may be returning from above the bundle. The large difference between the semi- and nearly-implicit calculations near the top of the bundle (Figure 4.14-17) reflected the top-down quench in the semi-implicit calculation.

The calculated and experimentally-determined mass inventory is compared in Figure 4.14-18. The total calculated mass inventory for the initial 75 s of the transient was under predicted by RELAP5-3D. This may be the result of larger calculated steam generation rates, caused by the RELAP5-3D-calculated top-down and bottom-up bundle quenching. The higher calculated steam generation rates during the initial 75 s of the transient prevented the rapid increase in core mass inventory observed in the early part of the experiment. However, when the entire core was calculated to quench at approximately 100 s, the RELAP5-3D calculations showed a rapid increase in bundle mass inventory, with a complete filling the bundle by about 110 s into the transient.

4.14.5 Conclusions and Assessment Findings

The RELAP5-3D calculations are judged to be in reasonable agreement with the measured data. Predicted rod surface temperatures in the lower two-thirds of the rod bundle (up to the 2.46-m axial elevation) were in good agreement with the data. Above the 2.46-m elevation, the code adequately predicted the initial cladding temperature rise and peak temperature, but calculated an earlier quench in the

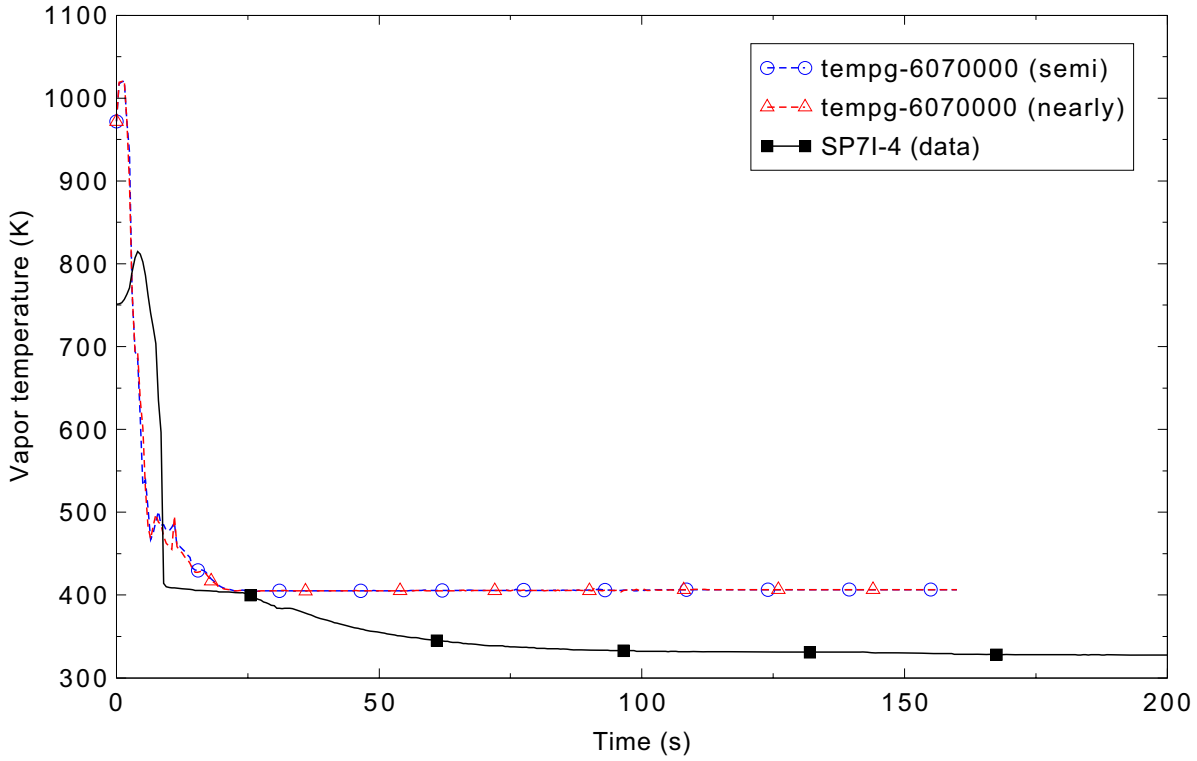

Figure 4.14-12. Measured and calculated steam temperatures for FLECHT SEASET forced reflood Test 31701 at the 1.23-m (4-ft) elevation.

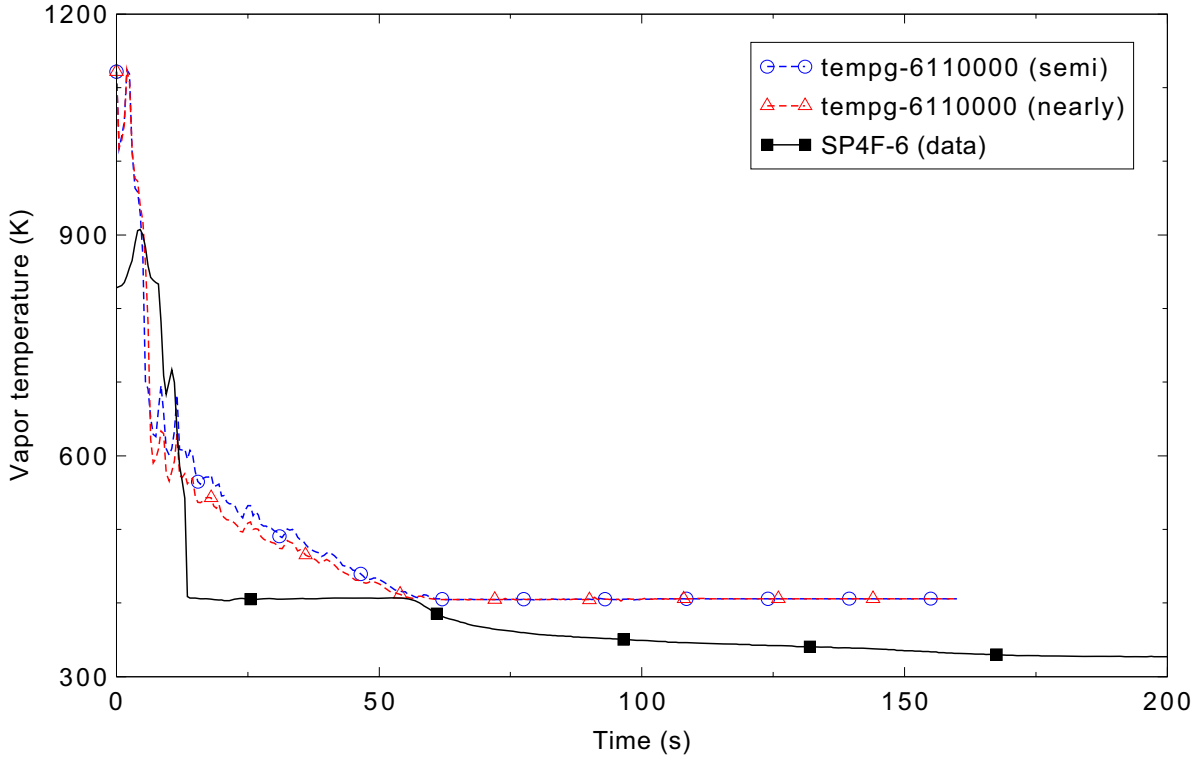

Figure 4.14-13. Measured and calculated steam temperatures for FLECHT SEASET forced reflood Test 31701 at the 1.85-m (6-ft) elevation.

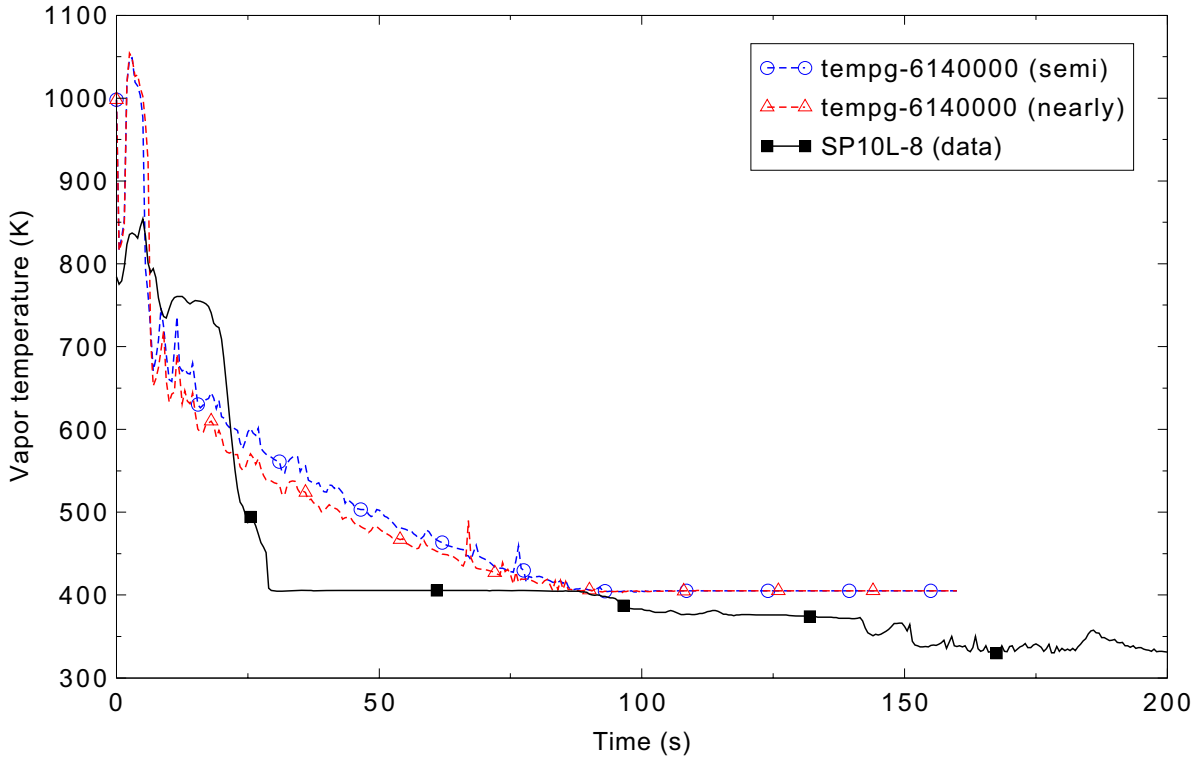

Figure 4.14-14. Measured and calculated steam temperatures for FLECHT SEASET forced reflood Test 31701 at the 2.46-m (8-ft) elevation.

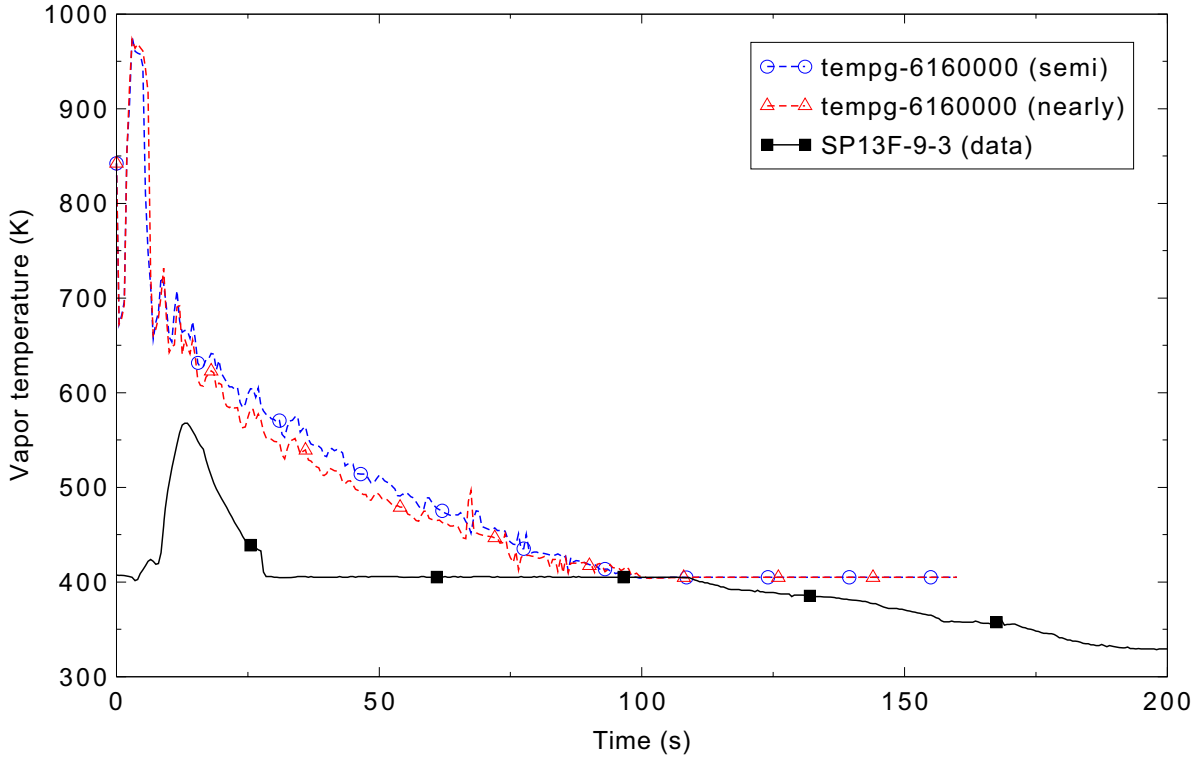

Figure 4.14-15. Measured and calculated steam temperatures for FLECHT SEASET forced reflood Test 31701 at the 2.85-m (9.25-ft) elevation.

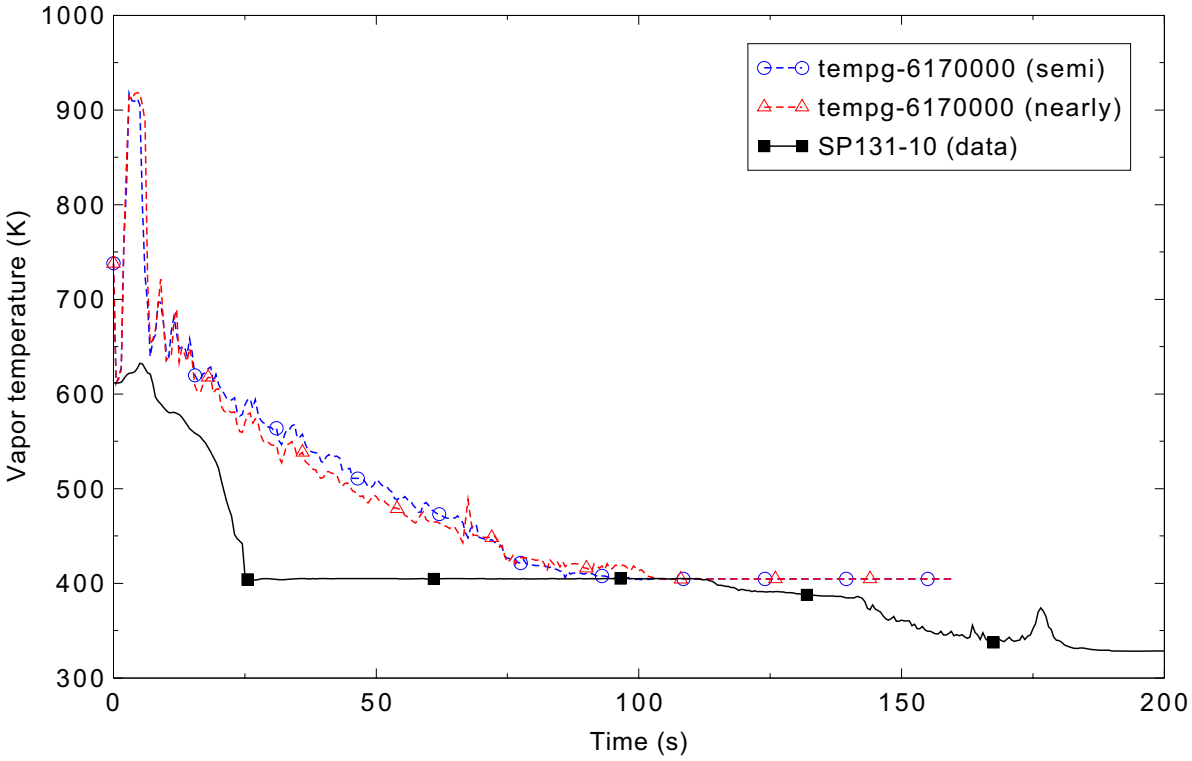

Figure 4.14-16. Measured and calculated steam temperatures for FLECHT SEASET forced reflood Test 31701 at the 3.08-m (10-ft) elevation.

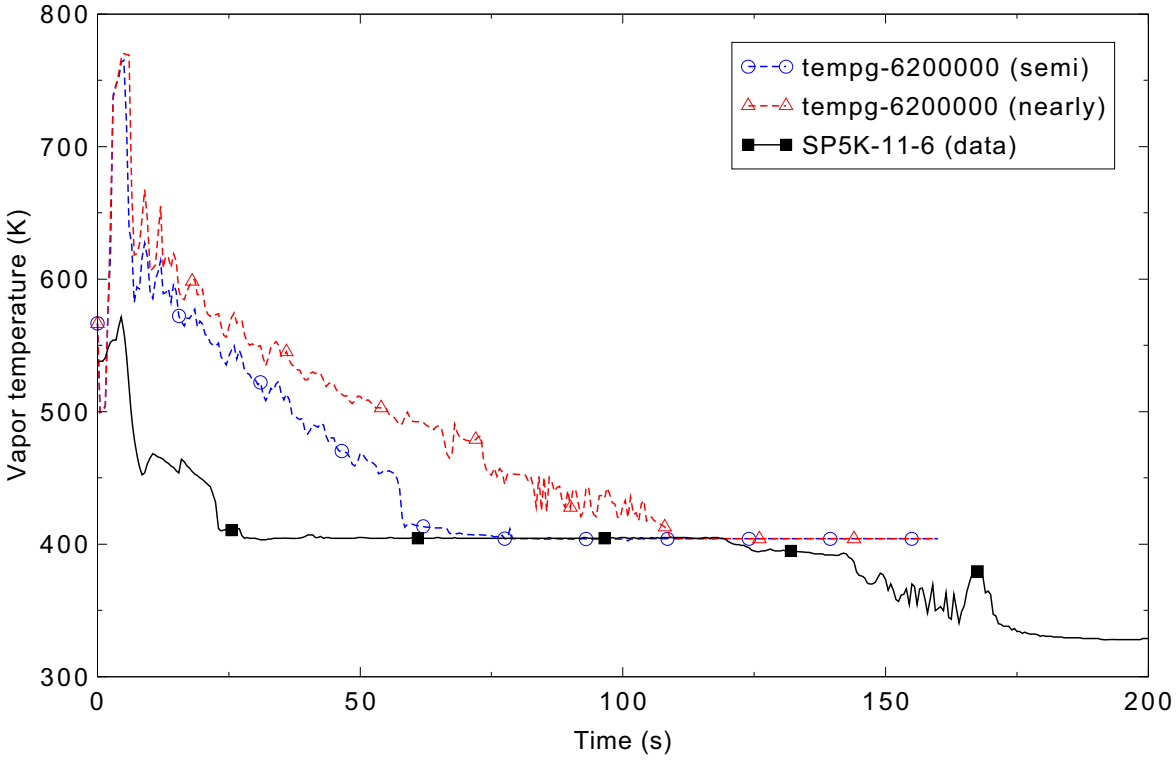

Figure 4.14-17. Measured and calculated steam temperatures for FLECHT SEASET forced reflood Test 31701 at the 3.54-m (11.5-ft) elevation.

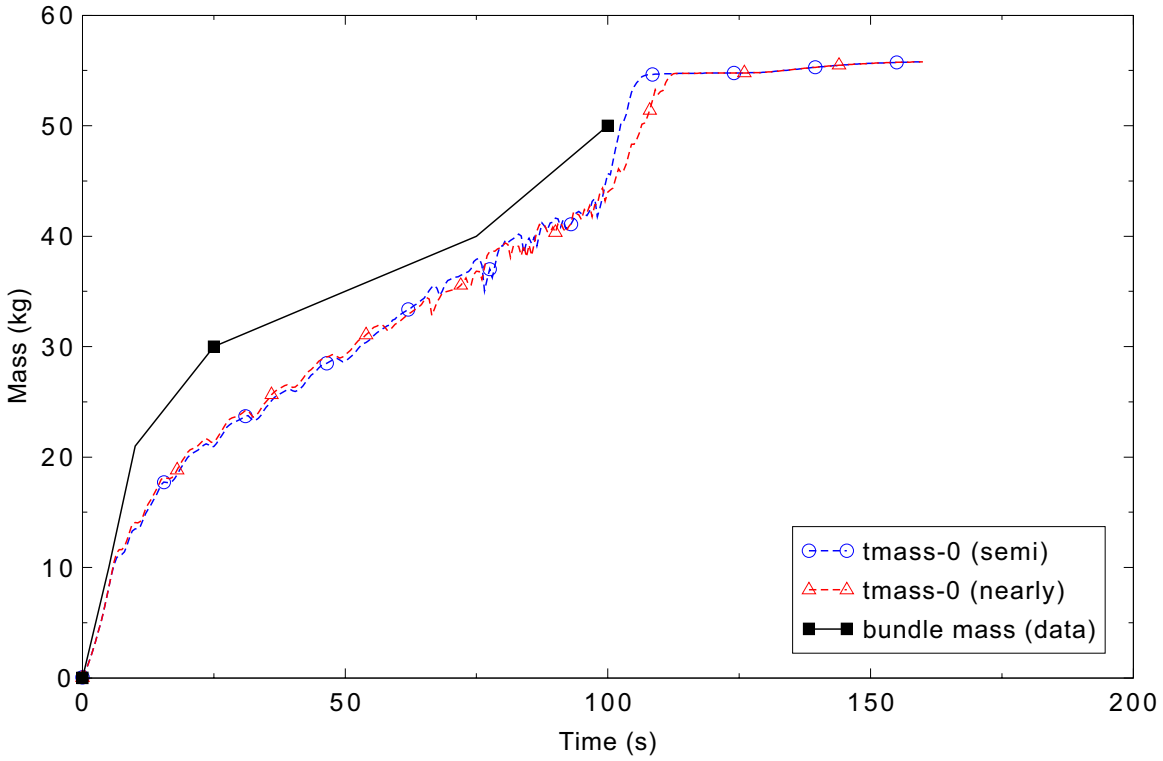

Figure 4.14-18. Measured and calculated total bundle mass inventory for FLECHT SEASET forced reflood Test 31701.

upper portions of the bundle than was measured in the experiment using the semi-implicit solution scheme. The earlier quench of the upper portion of the bundle was the result of a calculated top-down quenching of the upper regions of the bundle that was not observed in the experiment or in the nearly-implicit calculation. For the most part, the code tended to over predict vapor temperatures in the latter part of the reflood transient. The difference between measured and predicted fluid temperatures may be due in part to thermocouples measuring a combination of superheated steam and saturated liquid as the quench front approaches the measurement location. The top-down and bottom-up RELAP5-3D calculated quench behavior resulted in increased steam generation in the bundle and a reduction in the rate of increase in bundle mass inventory compared to that observed during the initial 100 s of the reflood experiment. However, when the entire core was calculated to quench at about 100 s, the calculated core mass inventory rapidly increased, filling the core with liquid by about 110 s into the transient.

4.14.6 References

4.14-1. M. J. Loftus, et al., *PWR FLECHT SEASET Unblocked Bundle, Forced and Gravity Reflood Task Data Report*, NUREG/CR-1532, EPRI NP-1459, WCAP-9699, June 1980.

4.15 Dukler-Smith Air-Water Flooding

Dukler and Smith[4.15-1] conducted a simple flooding experiment at the University of Houston to study the interaction between a falling liquid film with an upflowing gas core. A RELAP5 model for the Dukler-Smith countercurrent flow limitation (CCFL) test facility was developed for earlier assessments using these experiment data. The work of Riemke[4.15-2] and Davis[4.15-3] is representative of these earlier assessments. This work draws heavily on the earlier assessments, basically repeating the assessment for the latest code version.

4.15.1 Code Models Assessed

The Dukler-Smith experiments assess the Wallis countercurrent flow model. Other models are assessed coincidentally as they are used along with the CCFL model.

4.15.2 Experiment Facility Description

A schematic of the Dukler-Smith experiment facility is shown in Figure 4.15-1. The flow system consisted of a 1.52-m (5-ft) length of 0.051-m (2-in.) inner diameter Plexiglas pipe used as a calming section for the incoming air, a 0.305-m (1-ft) diameter section of Plexiglas pipe for both introducing the air to the test section and removing the falling liquid film, a 3.96-m (13-ft) test section consisting of 0.051-m (2-in.) diameter Plexiglas pipe, and an exit section for removing the air, entrainment, and the liquid film flowing up. Measurements were taken of the pertinent flow rates, pressure gradients, and the liquid film thickness over a wide range of gas and liquid flow rates in the flooding region. The liquid film upflow, downflow, and entrainment rates were determined by weighing the liquid flow for a fixed period of time (see discharge lines to weigh tanks labeled B in Figure 4.15-1). Most of the instantaneous measured parameters oscillated once quasi-steady state conditions were reached, and it was necessary to time-average these parameters. Dukler and Smith indicate that the CCFL process is basically an unstable process that is driving the oscillations. In the RELAP5-3D simulations the air and water flow predictions at the measuring point also showed oscillations. The predictions were averaged over 30 s for purposes of showing comparisons to the data.

4.15.3 Input Model Description

The experiment was modeled using the nodalization shown in Figure 4.15-2. The air injection is specified by a time-dependent junction (Component 102) to match the experiment value. The homogeneous (single-velocity momentum equation) option was specified at the air injection point (Junction 10103) to prevent liquid from flowing down the air injection pipe. The falling liquid film drained through Junction 10102. Inlet liquid flow rate was also specified by a time-dependent junction (Component 106) to match the measured value. The falling liquid film drained through a time-dependent junction (Component 195) where the outlet flow was set by a control system to maintain a fixed level in Pipe 190. A pressure of 0.104 MPa was specified for the drain tank (Component 200). Pressure in the test rig was controlled to 0.1 MPa by a time-dependent volume (Component 110).

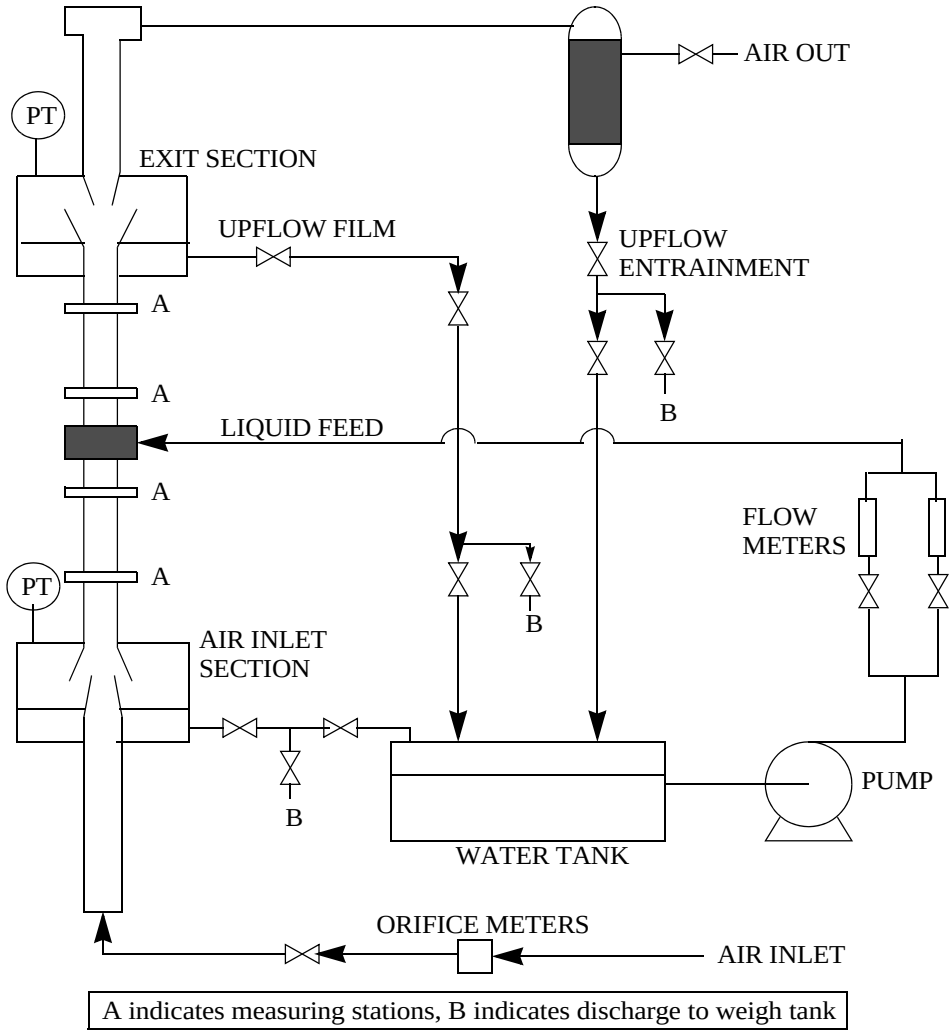

Figure 4.15-1. Schematic of the Dukler-Smith Air-Water Test Facility (from Reference 4.15-3).

Dukler discussed more than one CCFL correlation, but the one that appeared to be best for his test is a Wallis[4.15-4] form of the correlation: $j_g^{1/2} + m j_f^{1/2} = C$, where *j* is defined as the non-dimensional superficial velocity, subscripts *g* and *f* refer to gas and liquid respectively, *m* is the slope, and *C* is the gas intercept constant. This correlation was found to be reasonable for air/water systems where standing waves appeared on the surface of the liquid film. Dukler found this to occur in his experiment. Wallis[4.15-4] indicated that $m = 1$ and *C* varied between 0.88 and 1.0 for small diameter round tubes. The RELAP5-3D input model activated the CCFL model at the junction between Components 104 and 105. The CCFL input data for this junction used the following values: junction hydraulic diameter = 0.0508 m, flooding correlation form $\beta = 0.0$ (Wallis CCFL form), gas intercept $C = 0.88$, and slope $m = 1.0$.

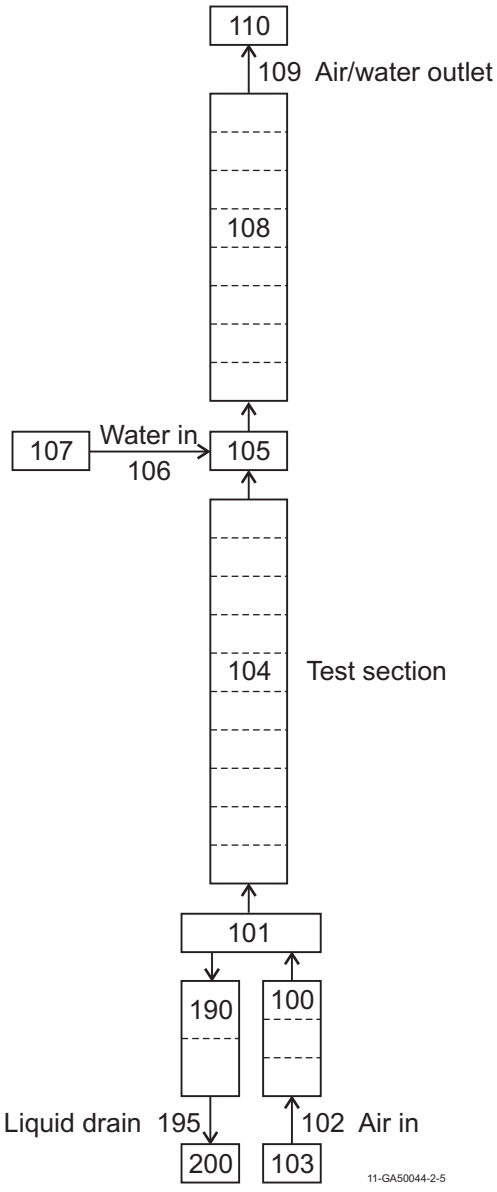

Figure 4.15-2. Nodalization diagram for the Dukler-Smith test facility.

4.15.4 Data Comparisons and Results

The requested time step size for both the semi-implicit and nearly-implicit advancement scheme calculations was 0.005 s. Calculations were run with values of liquid and air injection flows consistent with the data. Figure 4.15-3 compares the calculated liquid downflow rates with data at the given liquid injection flow rate. Good agreement with the data is observed in the predictions with both the semi-implicit and nearly-implicit advancement schemes. At the higher liquid injection rates, the calculated liquid downflow was less than the data, indicating more of the injected liquid was entrained and exited through the top. A possible reason for the under-calculated liquid downflow is that the values for the gas intercept and slope do not fit the data. As shown in Figure 4.15-4, the semi-implicit calculated results are in excellent agreement with the flooding correlation of Wallis as the x-intercept (square root of superficial

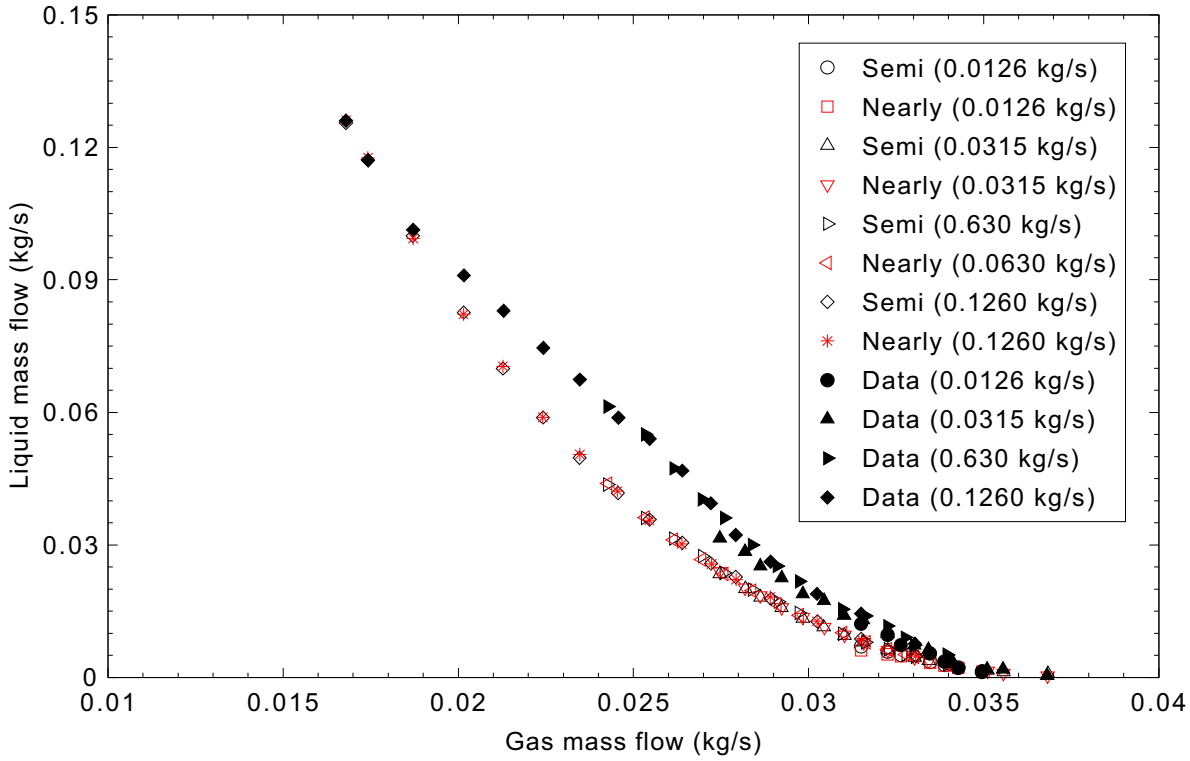

Figure 4.15-3. Comparison of RELAP5-3D predictions to Dukler-Smith data.

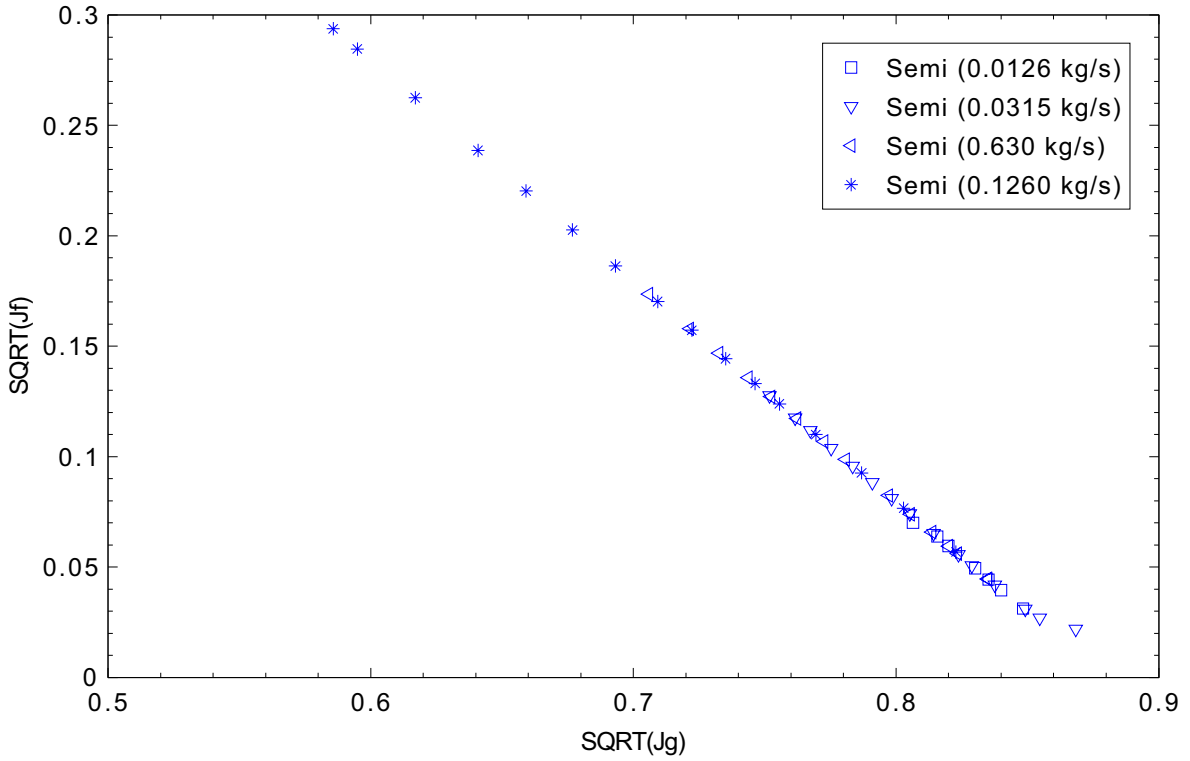

Figure 4.15-4. RELAP5-3D calculated superficial liquid velocity versus superficial gas velocity for the Dukler-Smith test.

vapor velocity) for the predictions is 0.88 and the slope is 1.0. Thus the code is working properly based on the intercept and slope values input to the model.

4.15.5 Conclusions and Assessment Findings

RELAP5-3D predictions are in reasonable agreement with the Dukler-Smith experiment data for countercurrent air-water flow in a single tube over the range of air flows from 0.0126 to 0.126 kg/s. The assessment also shows that the Wallis correlation is implemented correctly.

4.15.6 References

4.15-1. A. E. Dukler and L. Smith, *Two Phase Interactions in Counter-Current Flow: Studies of the Flooding Mechanism*, NUREG/CR-0617, January 1979.

4.15-2. R. A. Riemke, "Countercurrent Flow Limitation Model for RELAP5/MOD3," *Nuclear Technology,* Vol. 93, pp 166-173, February 1991.

4.15-3. C. B. Davis, *Validation Report: RELAP5-3D Flooding Model, Code Version 1.3.5*, R5/3D-01-05, October 2, 2001.

4.15-4. G. F. Hewitt and G. B. Wallis, *Flooding and Associated Phenomena in Falling Film Flow in a Tube*, UKAEA Report AERE-R 4022, 1963.

4.16 UPTF Downcomer CCFL Test 6, Run 131

Experiments were performed in the Upper Plenum Test Facility (UPTF) to obtain full-scale data on downcomer/lower plenum refill behavior during a loss-of-coolant accident initiated by a large break. The experiments provided a counterpart to testing that was done previously in scaled facilities.

4.16.1 Code Models Assessed

The relative performance of the annulus and pipe components for simulating the refill of the lower plenum during a loss-of-coolant accident was compared. The two components are similar except that all the liquid is placed in the film, with no liquid allowed in drops, in the annulus component when in the annular-mist flow regime. Liquid is allowed in both the film and drops in the annular-mist flow regime in the pipe component.

4.16.2 Experiment Facility Description

UPTF is a full-scale model of a four-loop 1300-MWe pressurized water reactor (PWR), including the reactor vessel, downcomer, lower plenum, upper plenum, and coolant loops. Simulators are used to represent the core, primary coolant pumps, steam generators, and containment. A schematic view of the test facility is shown in Figure 4.16-1. Key dimensions are presented in Figure 4.16-2. The test vessel, core barrel, and internals are full-size representations of a PWR, with four full-scale hot and cold legs that simulate three intact loops and one broken loop. Figure 4.16-3 shows the positions of the four loops relative to the downcomer.

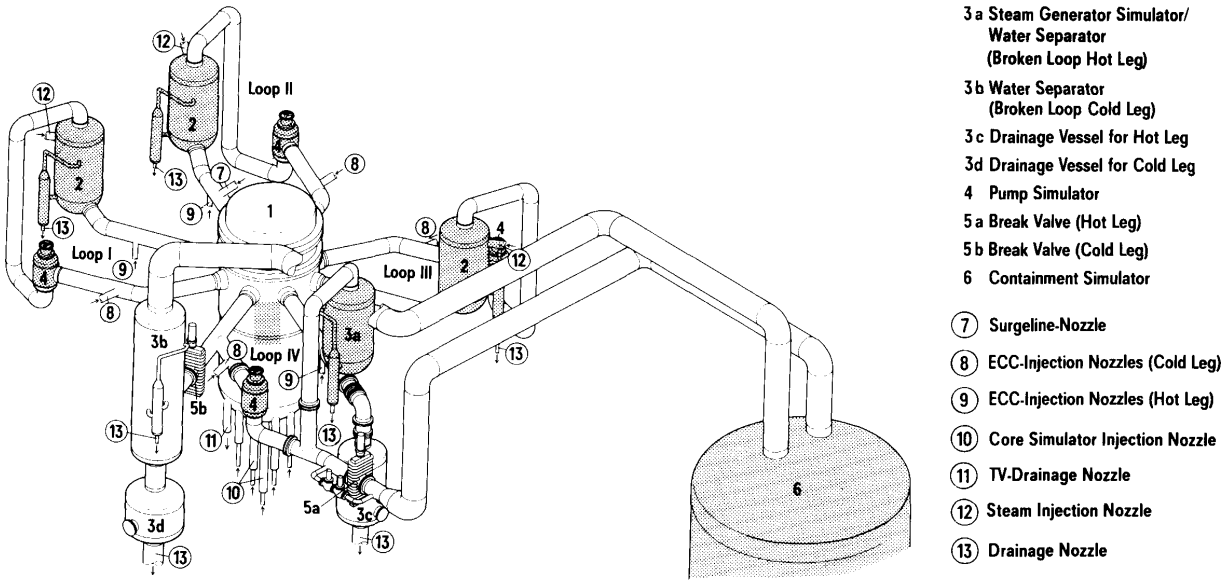

Figure 4.16-1. Schematic of the UPTF.

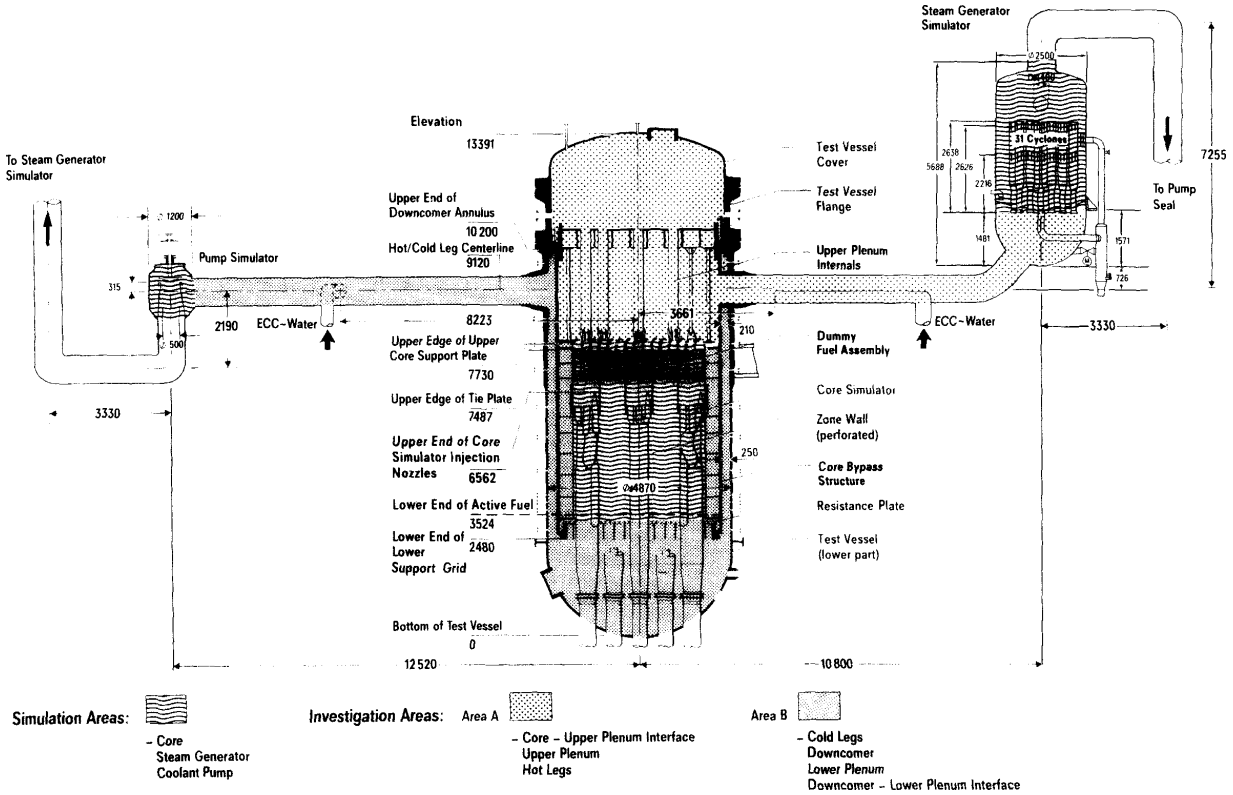

Figure 4.16-2. Key dimensions of the UPTF.

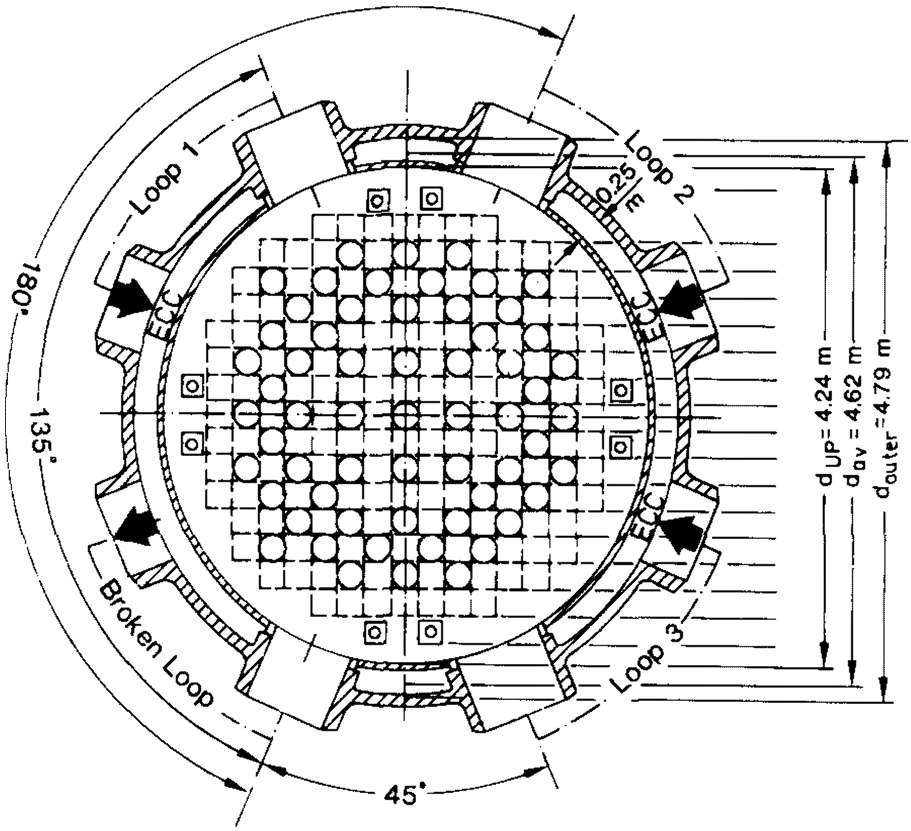

Figure 4.16-3. Cross-section of the UPTF reactor vessel.

Test 6[4.16-1, 4.16-2] was a quasi-steady experiment that was carried out to obtain full-scale data on downcomer/lower plenum refill behavior. Predetermined steam and emergency core cooling (ECC) water flow rates were injected into the system to determine the penetration of ECC water into the downcomer and lower plenum as a function of steam flow up the downcomer. Run 131 was selected for analysis. The system was initially filled with slightly superheated steam at about 2.5E5 Pa. The test was initiated by starting the steam flow from the core and steam generator simulators. ECC injection into the cold legs of the three intact loops began about 12 s later. The temperature of the ECC water was initially near saturated conditions. However, the steam flow caused the pressure to increase during the test, which caused the subcooling to increase. About 1 kg/s of nitrogen was injected along with the ECC to simulate noncondensable coming out of solution. The injection flow rates were terminated near 80 s. The pump simulators were closed during the test so that all the injected steam had to flow through the downcomer. Boundary conditions for Run 131 are summarized in Table 4.16-1.

Table 4.16-1. Summary of Test 6, Run 131 boundary conditions.

Parameter	Value
Total steam injection rate, kg/s	396
Total ECC injection rate, kg/s	1,447
ECC subcooling, K	58

4.16.3 Input Model Description

The RELAP5-3D nodalization used to simulate Run 131 is shown in Figure 4.16-4. The model explicitly represented all four coolant loops. The break (Component 505) connected Loop 4 to the containment simulator (Component 599). The downcomer was divided into two halves, with Components 111 and 112 connected to the “broken” side (Loops 1 and 4) while Components 121 and 122 were connected to the “intact” side (Loops 2 and 3). These downcomer flow paths were connected in crossflow using single and multiple junctions (Components 118 and 119). The lower plenum was divided axially into two control volumes (Components 150 and 160), each containing approximately the same fluid volume. The core and hot legs were combined into a single volume (Component 180). A time-dependent junction (Component 198) supplied steam flow to the core. The ECC and nitrogen flows were supplied by time-dependent junctions (Components 398, 498, and 698).

Standard code options were applied except that the choking model was turned off at all junctions except for the break because of the low pressure at which the test was conducted (in order to prevent unphysical choking at the other junctions).

4.16.4 Data Comparisons and Results

Three RELAP5-3D calculations were initially performed, each with a requested time step of 0.01 s. The first two calculations used the semi-implicit numerical scheme. The downcomer was modeled with four annulus components (111, 112, 121, and 122) in the first calculation and four pipe components in the second calculation. The third calculation was identical to the first one except that it used the nearly-implicit numerical scheme; this calculation failed before reaching 30 s. Figure 4.16-5 shows the calculated pressure

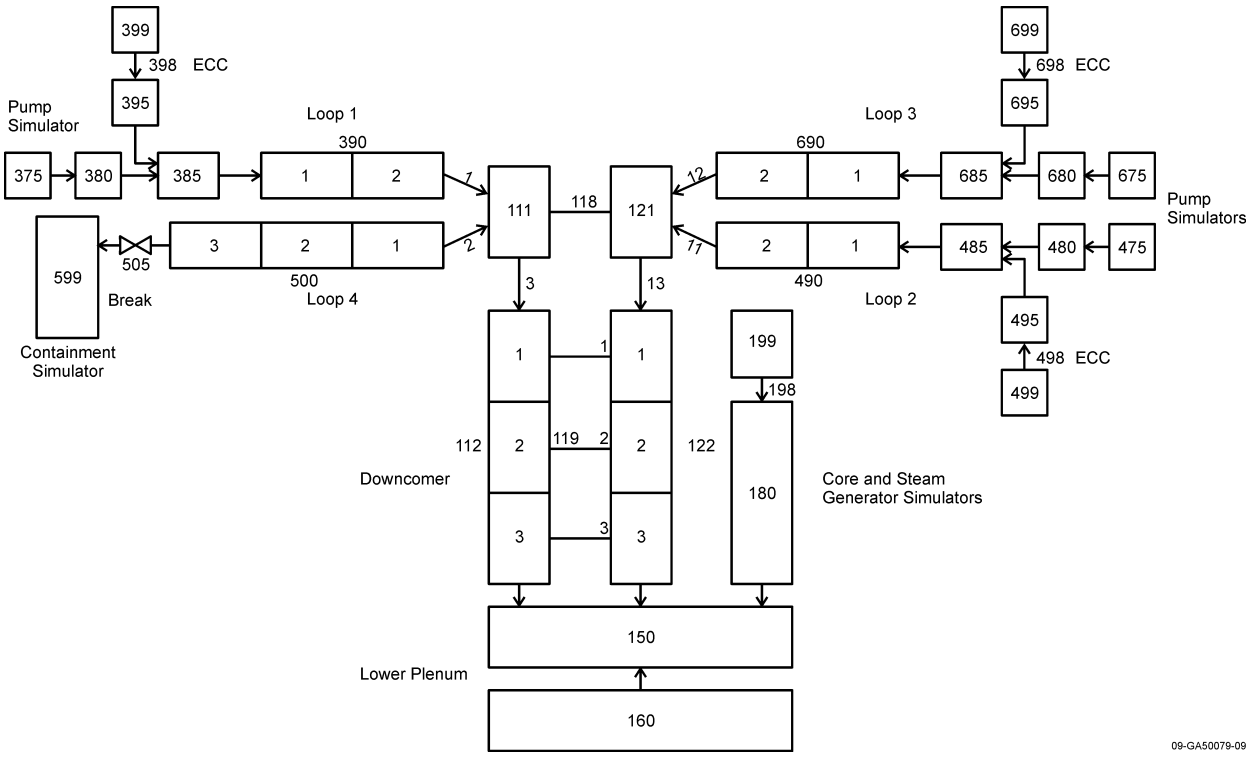

Figure 4.16-4. RELAP5-3D nodalization for UPTF Test 6.

in the downcomer during the test. The initiation of steam flow, which corresponds to 0 s on the figure, caused the pressure to increase. The pressure increased again near 14 s when ECC reached the break, which reduced the volumetric flow out the break. The termination of steam and ECC flows near 80 s caused the pressure to decrease. Measured results are not presented because only limited data for UPTF Test 6 are publicly available.

The capability of the code to calculate the refill of the lower plenum is illustrated in Figure 4.16-6, which shows measured and calculated collapsed liquid levels. The calculated values were obtained from the total liquid volume in the lower plenum and converted to liquid levels after accounting for the curvature of the lower head as well as the internals in the lower plenum. This method accounts for the varying flow area as a function of height and thus allows a more realistic indication of the liquid level than the traditional collapsed liquid level, which is obtained as the liquid volume fraction times the height summed over the number of volumes. The discussion will initially concentrate on the first calculation, which used annulus components and the semi-implicit numerical scheme. The gradual increase in the calculated liquid level prior to 12 s was due to the accumulation of droplets that were formed by condensation of the injected steam from the core. ECC first reached the lower plenum at 15.4 s. The liquid level increased relatively rapidly until 40 s, when the rate of increase decreased significantly until the steam and ECC injection ended near 80 s.The ending of the injection caused the pressure to fall as shown previously in Figure 4.16-5. The subsequent flashing in the lower plenum caused a reduction in the liquid level as the steam produced carried liquid from the lower plenum to the break. The calculated behavior was generally similar to the experiment except that the water began to reach the lower plenum about 7 s earlier than in the test and the level decrease after 80 s was much more pronounced than in the test. The calculated and measured rates of level increase were similar during the refill period. The increase in the indicated

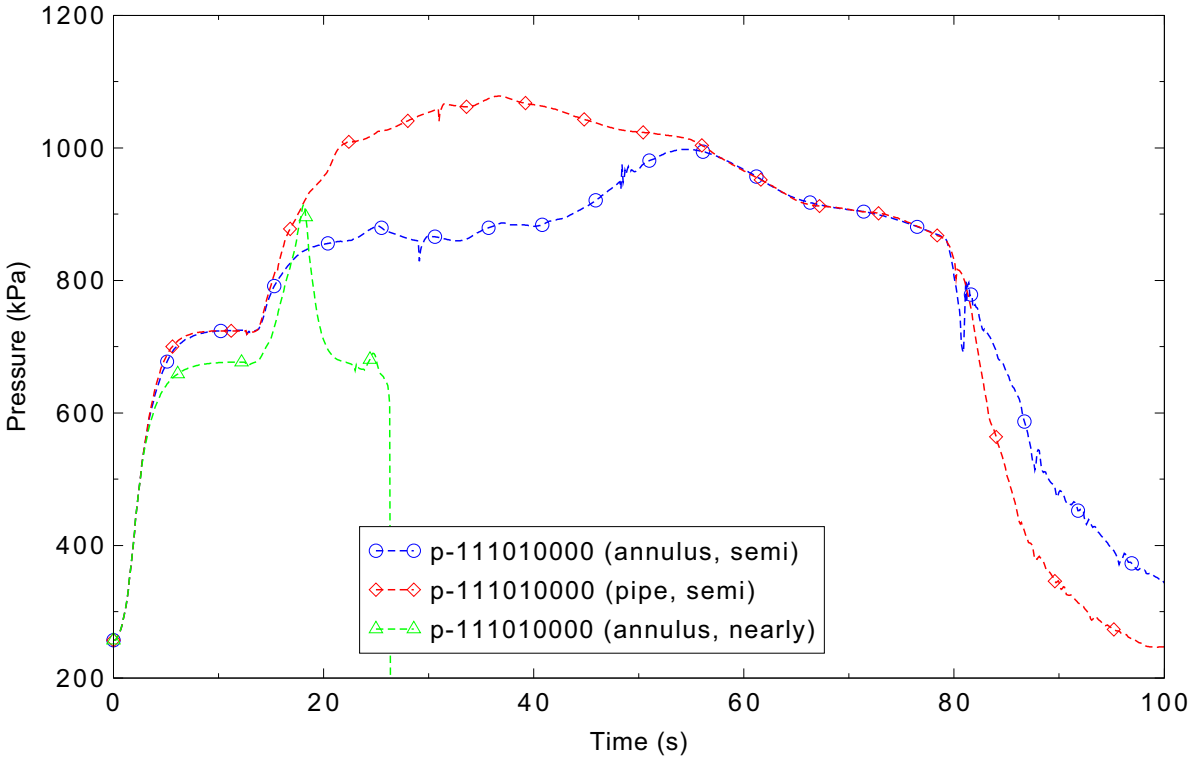

Figure 4.16-5. Calculated downcomer pressure in UPTF Test 6, Run 131.

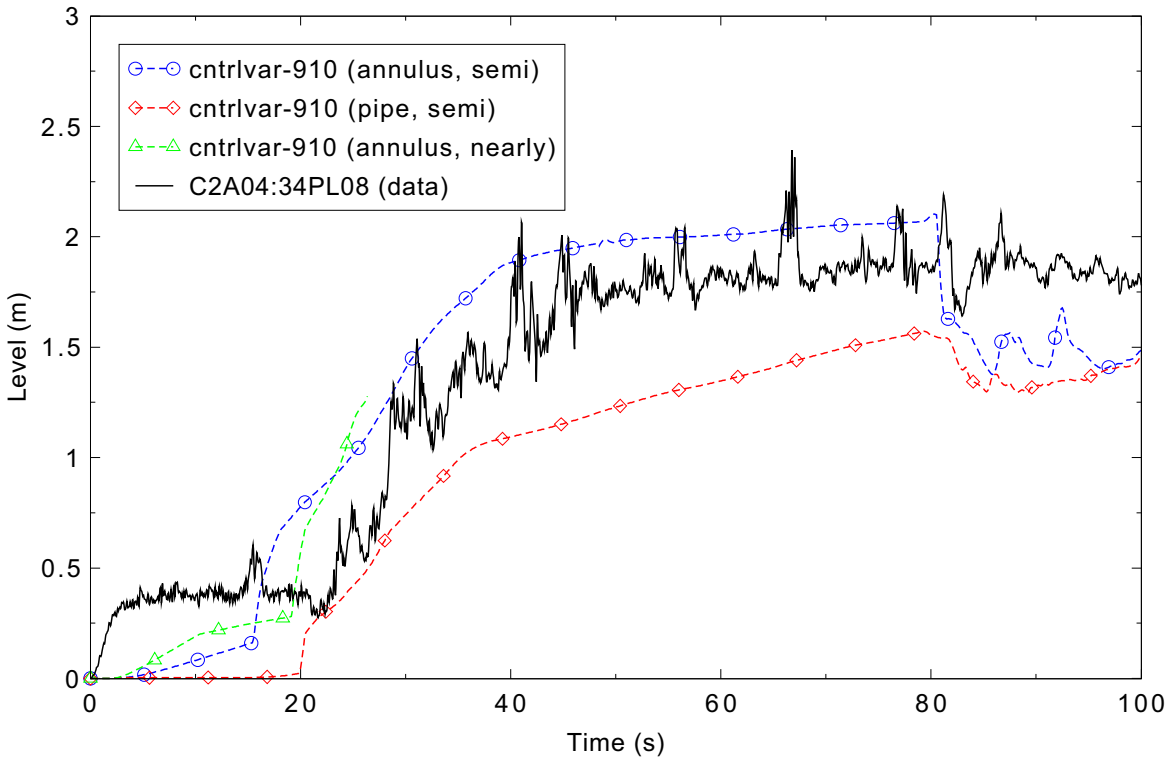

Figure 4.16-6. Measured and calculated collapsed liquid level in the lower plenum in UPTF Test 6, Run 131.

level at the start of the test is attributed to the effect of the steam flow on the differential pressure taps, rather than the presence of actual liquid because ECC flow did not begin until about 12 s. The different flow regime model used in the pipe component resulted in a delay in the liquid reaching the lower plenum and a substantially slower rate of refill.

Figures 4.16-7 and 4.16-8 show the calculated mass flow rate and fluid density in the broken cold leg, respectively. The figures indicate that ECC first reached the break near 14 s. Thereafter the mass flow and density increased substantially due to the bypass of ECC. More bypass was initially obtained in the calculation with the pipe component. The flow rate and density also increased substantially in the annulus calculation when the injection flow rates were terminated near 80 s. The flashing in the lower plenum that was caused by the pressure decrease caused liquid to be entrained from the lower plenum to the break, resulting in an increase in the flow rate and density in the broken loop.

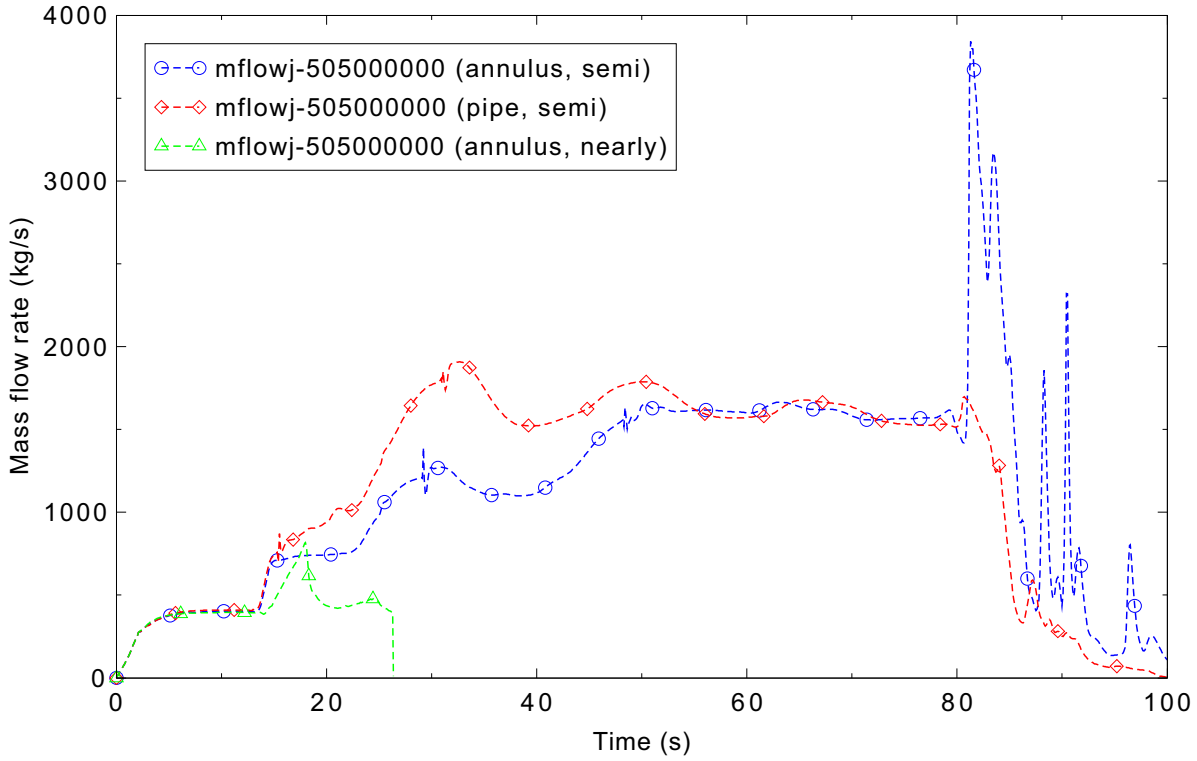

Figure 4.16-7. Calculated break mass flow in UPTF Test 6, Run 131.

An additional sensitivity calculation was performed to investigate the effects of the lower plenum nodalization. In this sensitivity calculation, the lower plenum was modeled with one control volume (Component 150) rather than the two volumes used previously. Figure 4.16-9 shows that the initial refill of the lower plenum was similar with both models. However, the refill of the lower plenum slowed earlier when the single volume was used. The two calculations bracketed the data between 40 and 80 s, with the single volume lower plenum under predicting the level and the two-volume model over predicting it. The sensitivity calculation demonstrates that the total amount of liquid stored in the lower plenum at the end of the refill period depends on the nodalization.

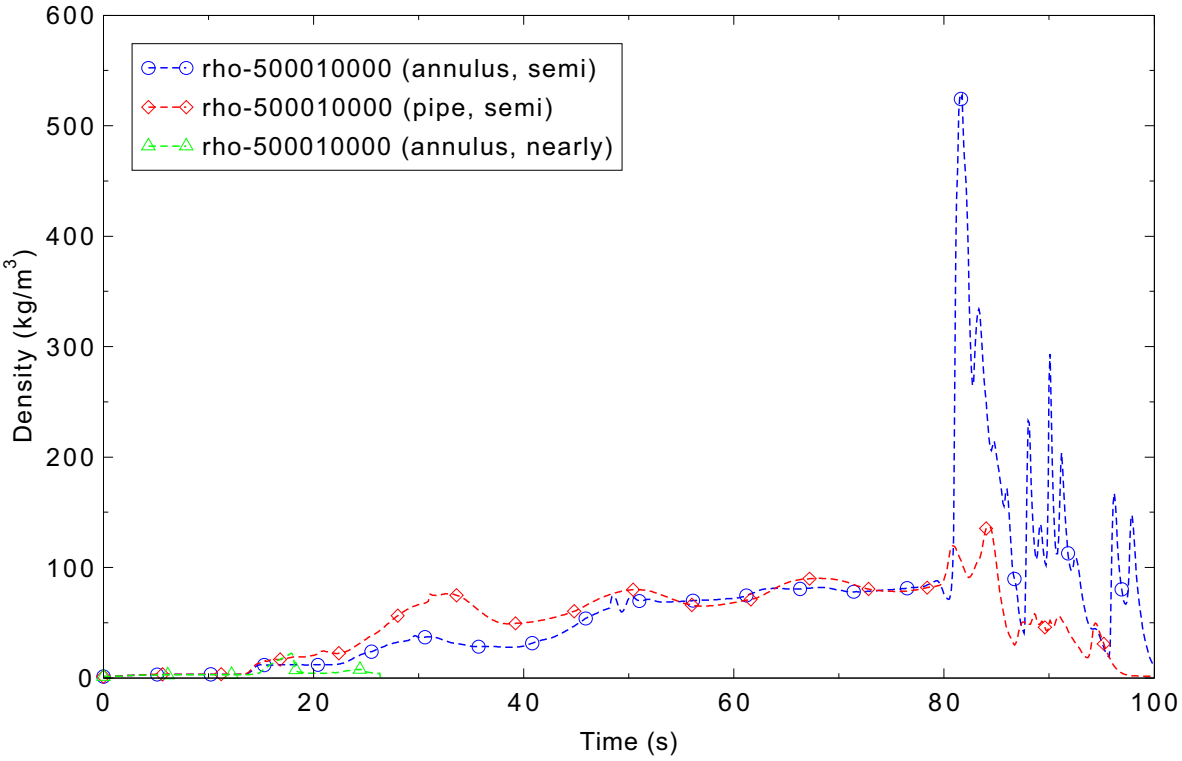

Figure 4.16-8. Calculated fluid density in the broken cold leg in UPTF Test 6, Run 131.

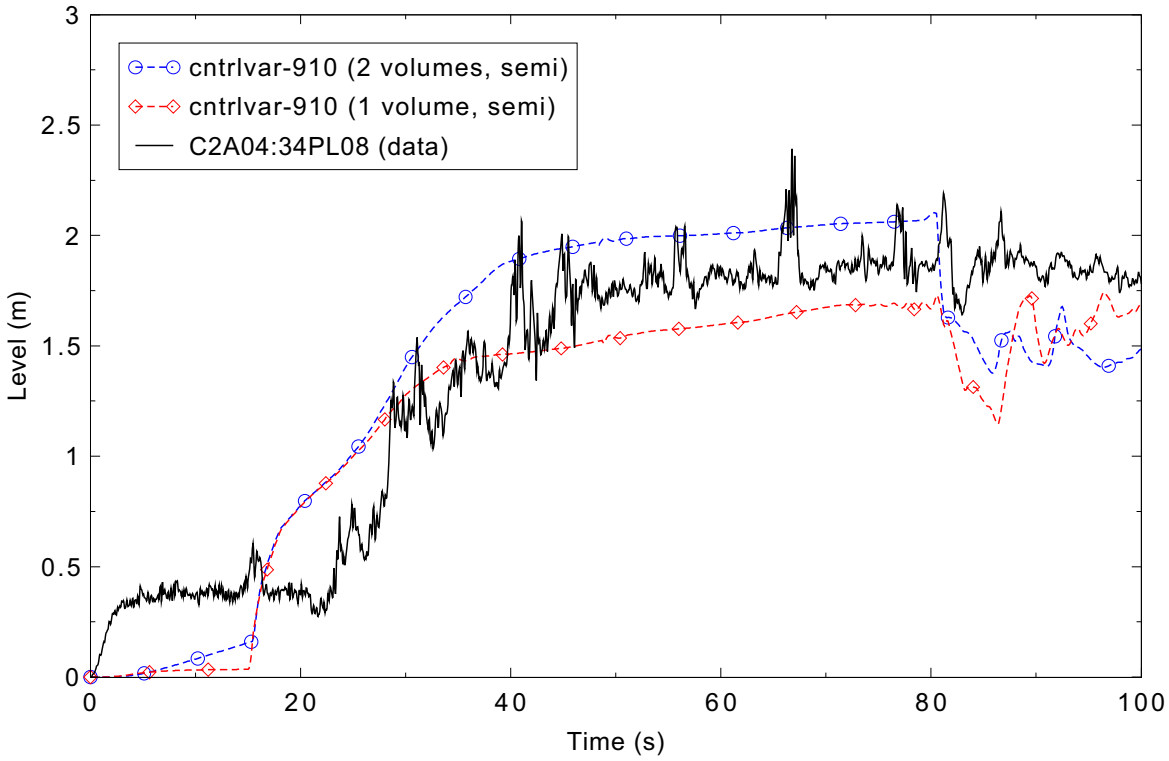

Figure 4.16-9. The effect of nodalization on collapsed liquid level in UPTF Test 6, Run 131.

4.16.5 Conclusions and Assessment Findings

The RELAP5-3D calculations are judged to be in reasonable agreement with the measured liquid level data for UPTF Test 6, Run 131. The calculated refill was similar to that observed in the test, but started about 7 s earlier.

The RELAP5-3D calculation in which the downcomer was modeled with annulus components was in better agreement with the measured results than when pipe components were used. The annular mist flow regime model in the annulus component, which puts all the liquid in the film, resulted in a better prediction of the lower plenum refill for the UPTF test. The pipe component provided a conservative prediction of the amount of liquid in the lower plenum.

The liquid inventory in the lower plenum at the end of the refill period depends on the nodalization.

4.16.6 References

4.16-1. J. Liebert and P. Weiss, "UPTF Experiment Effect of Full-Scale Geometry on Countercurrent Flow Behaviour in PWR Downcomer," *Proceedings of Fourth International Topical Meeting on Nuclear Reactor Thermal-Hydraulics, NURETH-4, Karlsruhe, F.R.G., October 10-13, 1989,* Volume 1, pp. 67 - 74.

4.16-2. H. Glaeser, "Downcomer and tie plate countercurrent flow in the Upper Plenum Test Facility (UPTF)," *Nuclear Engineering and Design*, 133 (1992), pp. 259-283.

4.17 MIT Pressurizer Test ST4

The Massachusetts Institute of Technology (MIT) Pressurizer test[4.17-1,4.17-2] utilized a small-scale, low-pressure representation of a pressurizer. The test used for this assessment case is ST4, which examined wall heat transfer and condensation effects.

4.17.1 Code Models Assessed

The MIT Pressurizer test was used to assess the code capability to simulate pressurizer behavior under inflow conditions. The models tested during this simulation are steam condensation on the pressurizer wall and interfacial heat transfer between the stratified liquid and the vapor above the liquid.

4.17.2 Experiment Facility Description

The MIT Pressurizer facility consisted of two cylindrical steel tanks: the primary tank and the storage tank. The primary tank, which represented the pressurizer, was 1.14 m high with an inner diameter of 0.203 m. It was equipped with six immersion heaters with a total power output of 9 kW. The storage tank was pressurized with nitrogen to force liquid into the bottom of the primary tank. Figure 4.17-1 presents a schematic of the MIT Pressurizer facility.

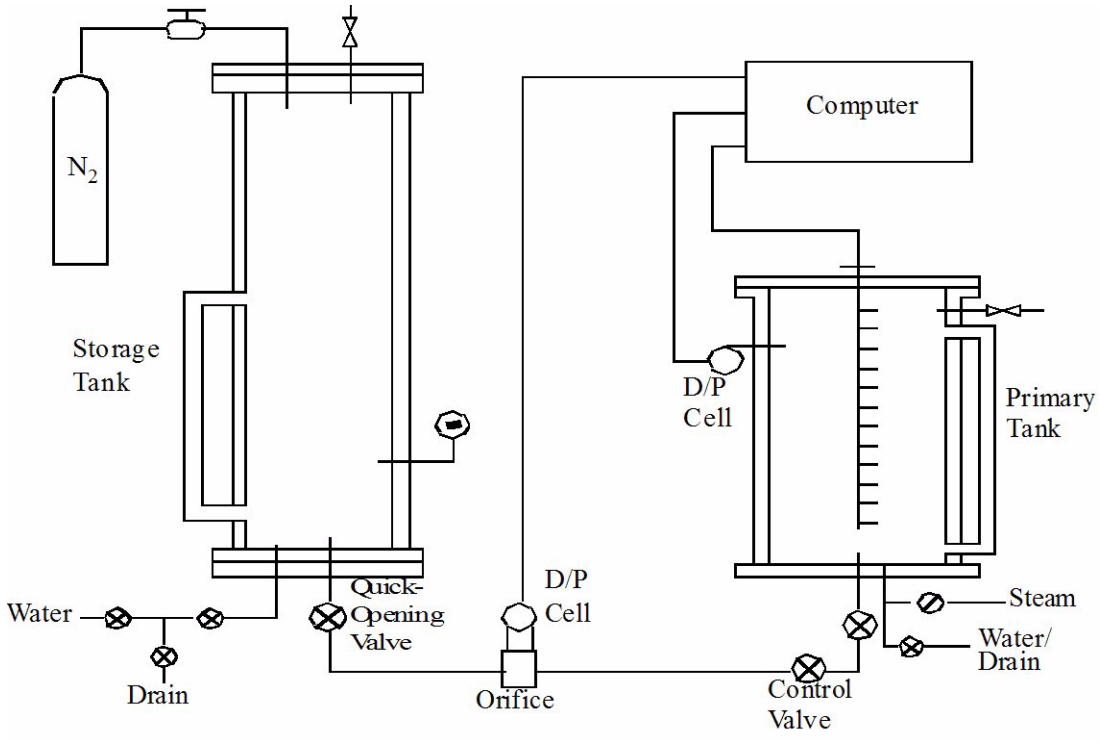

Figure 4.17-1. Schematic of MIT Pressurizer test facility.

Test ST4 was initiated with the liquid level in the primary tank at 0.432 m from the bottom at a pressure of 0.493 MPa under quiescent conditions. Two quick-opening valves were opened, allowing subcooled water to be injected into the primary tank for a time interval of 41 s. The initial water subcooling in the primary tank was 129 K. The water level increased at a rate of 1.15 cm/s over the time interval. As the steam in the upper part of the vessel was compressed and the saturation temperature increased, the vessel walls became subcooled and film condensation occurred.

4.17.3 Input Model Description

The MIT Pressurizer test facility was modeled using a pipe (Component 3) representing the primary tank, as shown in Figure 4.17-2. This pipe component was connected through a time-dependent junction (Component 2) representing the quick-opening valves to a time-dependent volume (Component 1) representing the storage tank. The pipe was oriented vertically and utilized 10 fluid cells. The injection flow through the time-dependent junction was regulated to the rate used during the actual test. The model was initialized with the water level in the fourth cell from the bottom by specifying a void fraction of 0.22 in that cell. The mixture level and thermal front tracking models were turned on in the pressurizer pipe component. The environment surrounding the MIT primary tank (pressurizer) apparatus is modeled as a dry air-filled pipe component at 298 K with a large flow area (10^6 m^2) connected through a heat structure, which is connected along the axial length of both components. This approach was used to account for insulation and environmental heat losses.

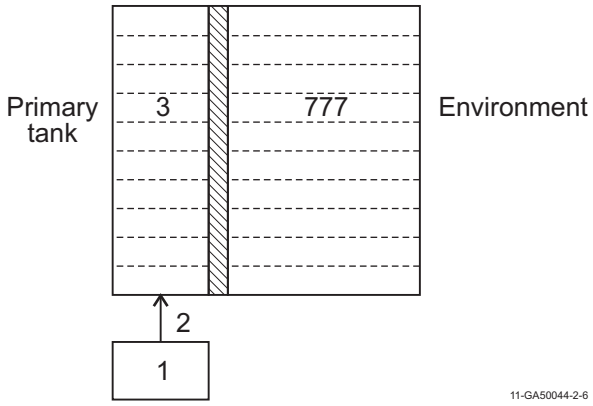

Figure 4.17-2. RELAP5-3D nodalization of MIT pressurizer.

4.17.4 Data Comparisons and Results

Calculations of MIT pressurizer Test ST4 were performed using both the semi- and nearly-implicit hydrodynamic solution schemes; the requested time step size was 0.01 s. Figure 4.17-3 presents a comparison of the measured and calculated pressure response. Initially, the pressure increases due to compression of the steam volume above the water surface as the subcooled water was injected over the 41 s interval. As the pressure increased, the saturation temperature increased. Heat transfer from the vapor through the wall to the surrounding environment and condensation at the liquid/vapor interface slows the rate of the pressure rise. The net result of these effects is that pressure is slightly under predicted by RELAP5-3D. The decline in pressure at about 41 s in both the test data and the code prediction corresponds to the time when the flow into the pressurizer is stopped. The larger pressure decrease

indicates the code may be over predicting the heat loss to the environment or the condensation rate. Overall, RELAP5-3D captures the data trends quite well, although the code slightly under predicts the magnitude of the data.

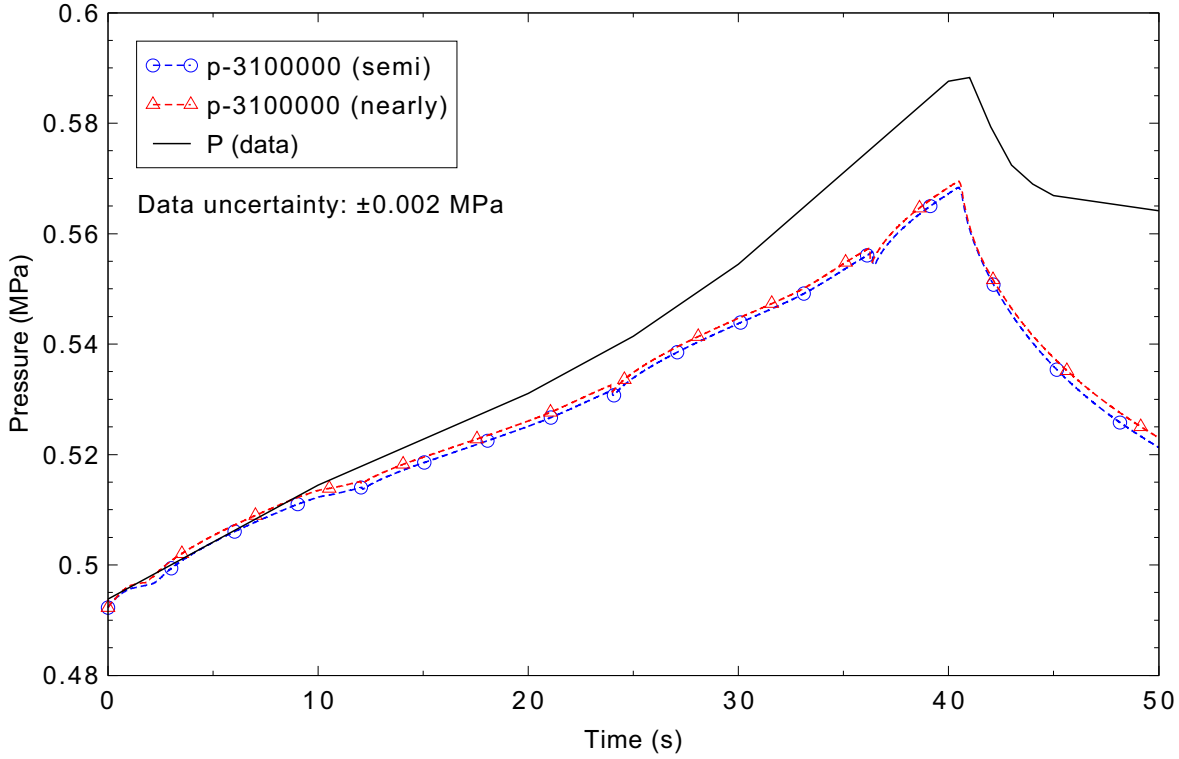

Figure 4.17-3. Measured and calculated pressure at the top of the tank for MIT pressurizer Test ST4.

The measured and predicted axial temperature profiles in the wall and the fluid at 35 s after test initiation (during the fluid insurge) are presented in Figures 4.17-4 and 4.17-5, respectively. Overall, the RELAP5-3D code predicted the temperature profile reasonably well. The differences that do exist have been attributed to numerical mixing in previous assessments, and use of the thermal front tracking model has reduced this difference relative to the results from previous code versions. It is possible finer nodalization may result in improvements in the comparisons.

There were no significant differences between the semi- and nearly-implicit calculations using the base input model.

A sensitivity calculation was also performed in which the mixture level tracking model was turned off. The results are similar to those with the mixture level model enabled. Figure 4.17-6 presents the measured and calculated pressures for these cases, where a difference is noted. The small drops in pressure near 12, 24, and 36 s, which are more pronounced in the semi-implicit calculation, occurred as the liquid level moved into the next volume, causing some condensation that reduced the pressure. As seen in Figure 4.17-3, the mixture level tracking model is effective in mitigating this node boundary crossing behavior.

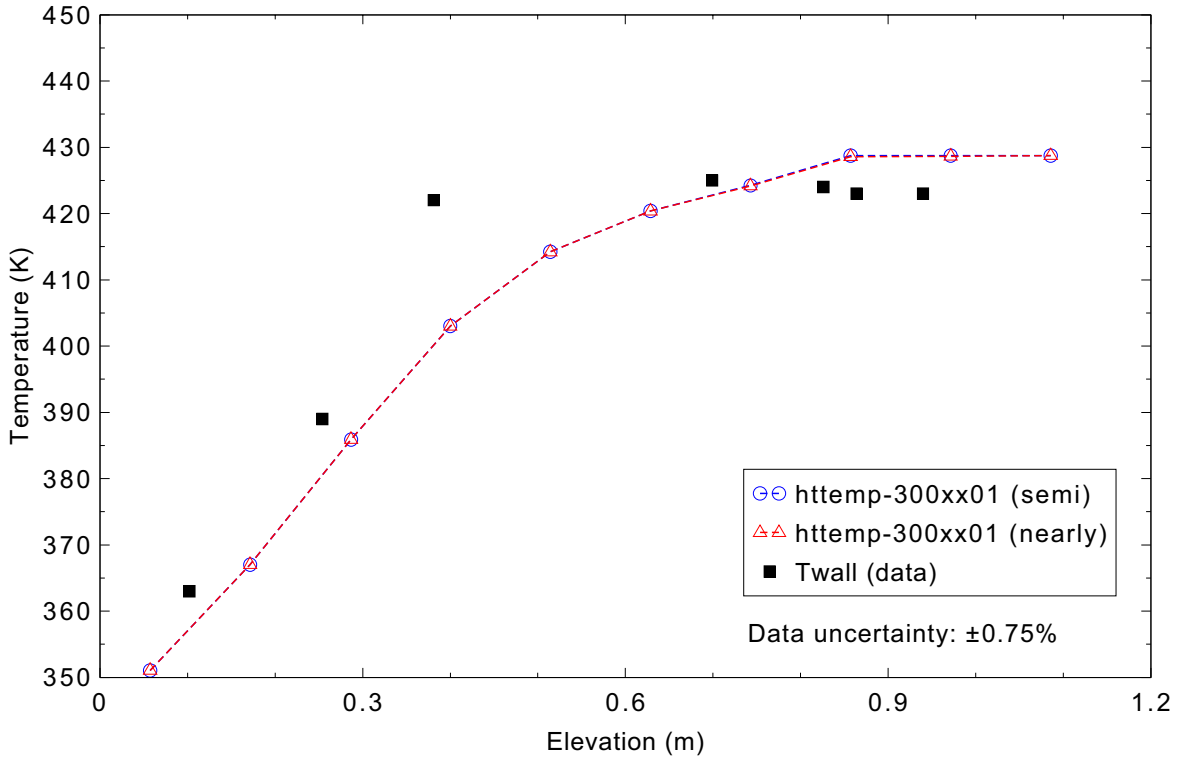

Figure 4.17-4. Measured and calculated wall temperature profile at 35 s for MIT pressurizer Test ST4.

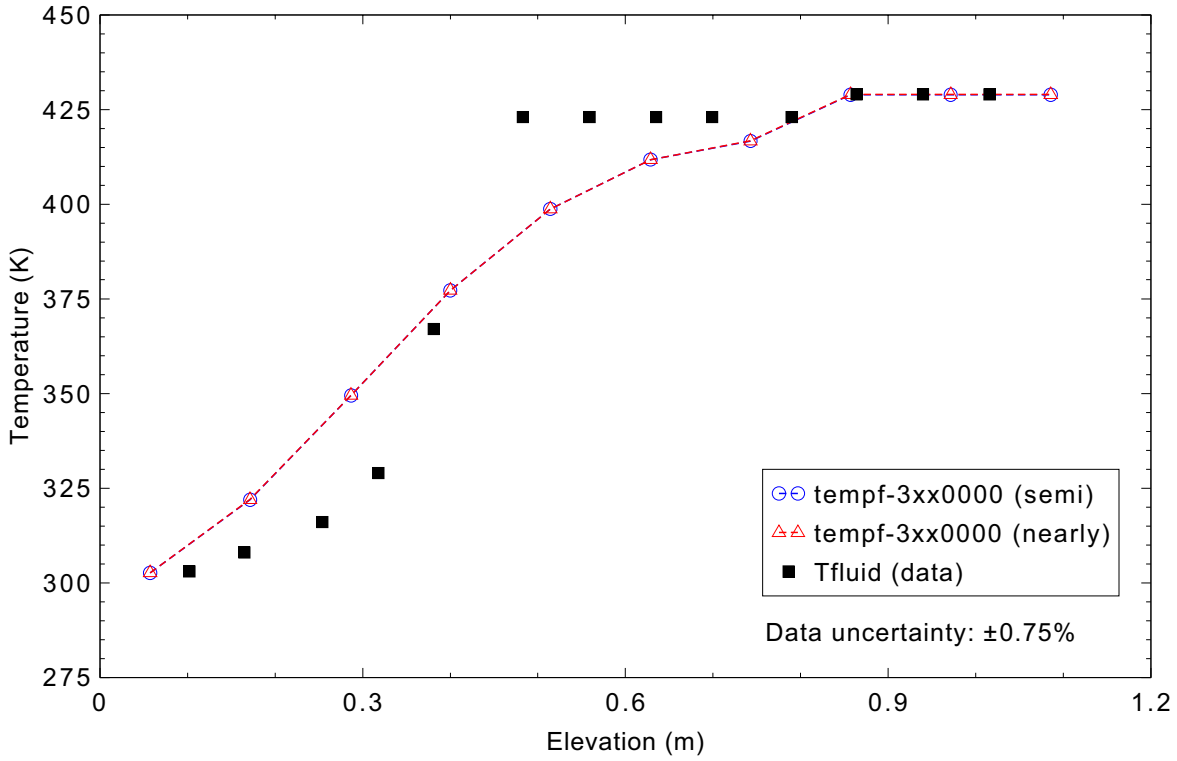

Figure 4.17-5. Measured and calculated fluid temperature profile at 35 s for MIT pressurizer Test ST4.

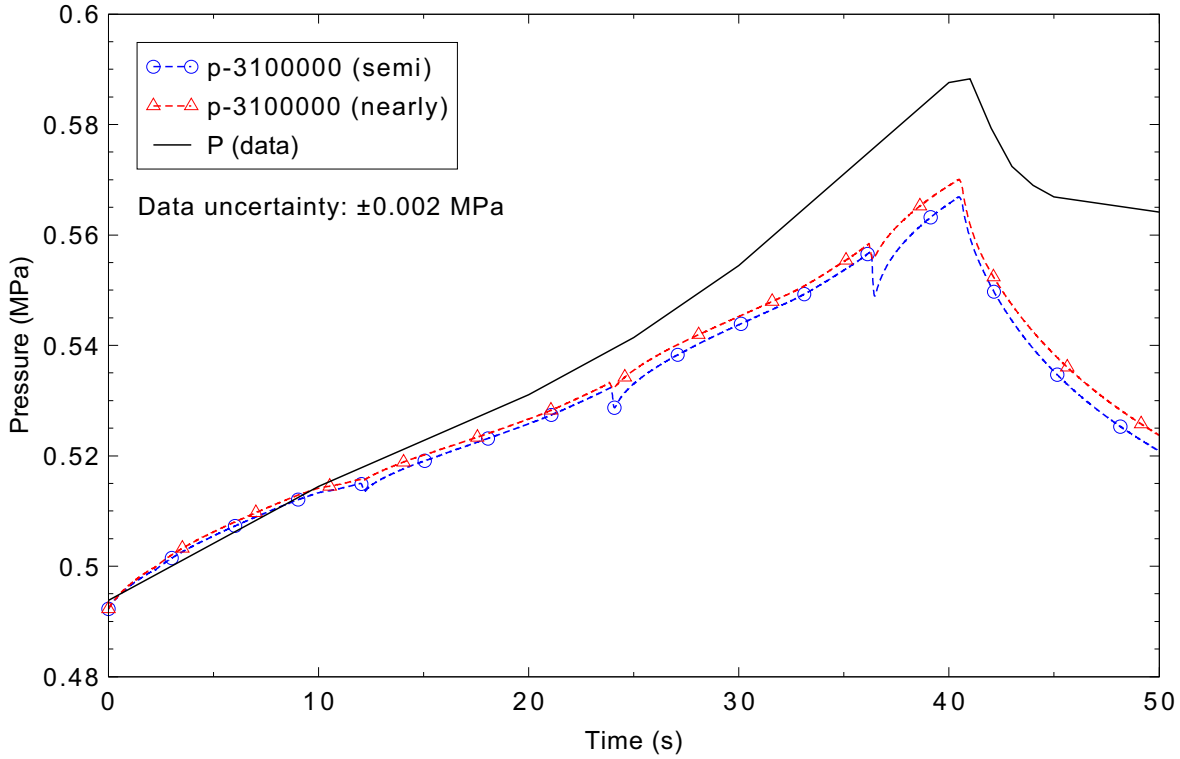

Figure 4.17-6. Measured and calculated pressure at the top of the tank for MIT pressurizer Test ST4 with the mixture level tracking turned off.

4.17.5 Conclusions and Assessment Findings

This assessment finds that RELAP5-3D does a reasonable job of predicting the pressure response along with the axial temperature profile using both the semi-implicit and nearly-implicit advancement schemes. Using the mixture level tracking improved the code performance as the level crossed node boundaries. Improvement in the results may be gained by refining the nodalization or refining the time step size.

4.17.6 References

4.17-1. H. R. Saedi and P. Griffith, "The Pressure Response of a PWR Pressurizer During an Insurge Transient," *Transactions of ANS, 1983 Annual Meeting, Detroit, MI, June 12-16, 1983.*

4.17-2. H. R. Saedi, *Insurge Pressure Response and Heat Transfer for a PWR Pressurizer,* MIT ME Thesis, November 1982.

4.18 Neptunus Test Y05

The Neptunus Test Y05 was performed at the Delft University in the Netherlands. The test was designed to investigate and measure pressurizer thermal hydraulic behavior in response to controlled periodic surge line flow insurges and outsurges in conjunction with pressurizer spray operation. The Neptunus test facility was a $1/40^{th}$-scaled pressurizer.

4.18.1 Code Models Assessed

The pressurizer model and related options are assessed using data from this test.

4.18.2 Experiment Facility Description

The Neptunus test facility pressurizer is a carbon steel pressure vessel 2.51 m high with a 0.8-m inside diameter. The pressurizer surge line attaches to a 0.084-m nozzle located on the bottom of the pressurizer vessel. The pressurizer spray line attaches to a 0.027-m spray nozzle located on the top of the pressurizer vessel. The pressurizer test section is instrumented to record overall pressure and four regional temperatures. The desired test conditions for each test are obtained by establishing the desired initial water level inside the pressurizer at the specified test pressure and temperature. A drawing of the Neptunus pressurizer test facility is shown in Figure 4.18-1.[4.18-1]

4.18.3 Input Model Description

The RELAP5-3D Neptunus pressurizer model uses a multi-cell pressurizer component. Earlier benchmark studies[4.18-1, page 26] performed a sensitivity study using RELAP5 models consisting of three pipe components, two pressurizer components in conjunction with a pipe component, and pressurizer components with varying numbers of cells. The earlier benchmark study concluded that the different modeling techniques did not result in any significant differences in the code-calculated results.

A nodalization diagram of the RELAP5-3D Neptunus pressurizer input model is given in Figure 4.18-2. The pressurizer vessel (Component 2) is modeled using a pressurizer component. Default code values were used for all of the pressurizer component user input options except for the spray mixing coefficient used in the enhanced condensation model. A user-specified spray mixing coefficient of 1.5 was used. The mixture level tracking and thermal stratification models were turned on.

The pressurizer is nodalized with 13 cells in a vertical orientation. The first cell at the bottom of the pressurizer has a cross sectional area of 3.3980×10^{-2} m^2 to simulate the bottom of the lower hemispherical shaped head of the pressurizer. In the next 2 cells, the cross sectional flow area increases to 2.8274×10^{-1} m^2, after which the vessel cross sectional area remains constant at 5.0265×10^{-1} m^2 through the main body of the pressurizer vessel until reaching the vessel's top hemispherical head region. The top head region is composed of 3 cells with a cross sectional area of 4.1169×10^{-1} m^2. The length and number of cells used in this input model were used previously in several code assessments and proven to be adequate.[4.18-1, page 26] The cell lengths are 0.119 m for the first cell, 0.2 m for cells 2 and 3, 0.2295 m for cells 4 through 10, 0.136 m for cell 11, and 0.1245 m for cells 12 and 13. This gives a total length for the

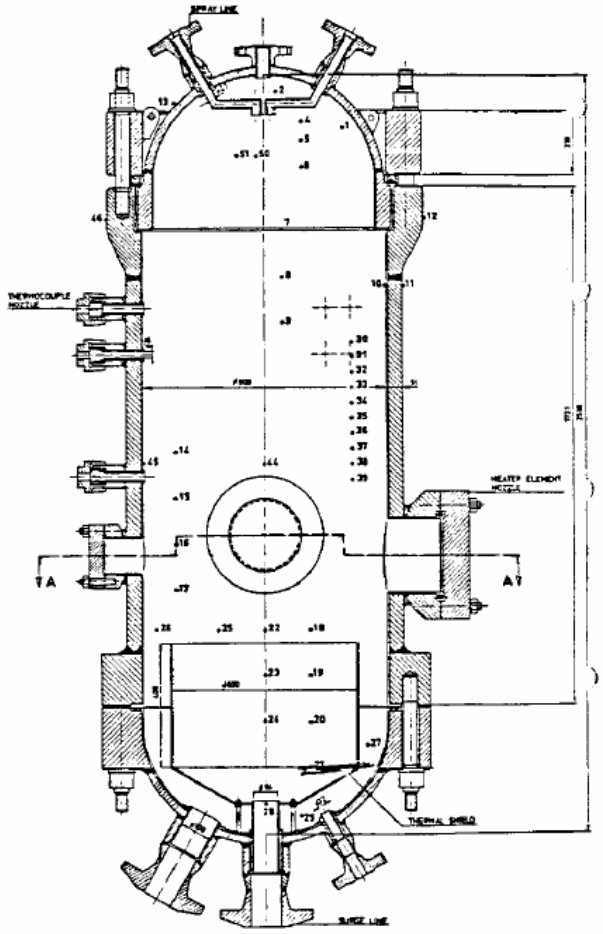

Figure 4.18-1. Neptunus test facility pressurizer.

pressurizer vessel component model of 2.5105 m. The pressurizer wall was modeled as a heat structure with an adiabatic outer boundary.

Time-dependent volume components are used to specify the inlet boundary temperature conditions for the surge line water (Component 6) and spray line water (Component 3) flows. Surge line inlet pressure is 12.5 MPa at 548 K. Pressurizer spray line water conditions are established at a pressure of 12.8 MPa and a temperature that varies between 594 K and 500 K during the transient. The surge line in-surge and out-surge water flow rates are controlled to replicate the test conditions by using a time-dependent junction (Component 4). The pressurizer spray flow rates are controlled by another time-dependent junction (Component 5). The transient boundary condition flow rates for Neptunus Test Y05 are provided on page 88 of Reference 4.18-1 and are shown here in Figure 4.18-3. Figure 4.18-4 shows the boundary flow rates from the RELAP5-3D input model. The surge line was modeled as a very short (0.01-m long) branch (Component 1) so that the pressurizer surge line junction donoring would be correct with the thermal stratification model being used and the desired boundary conditions would be maintained.

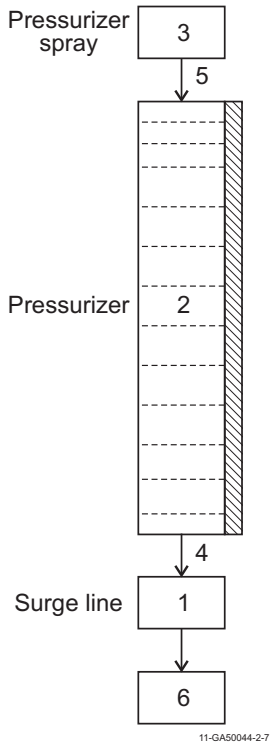

Figure 4.18-2. Nodalization diagram for the Neptunus pressurizer model.

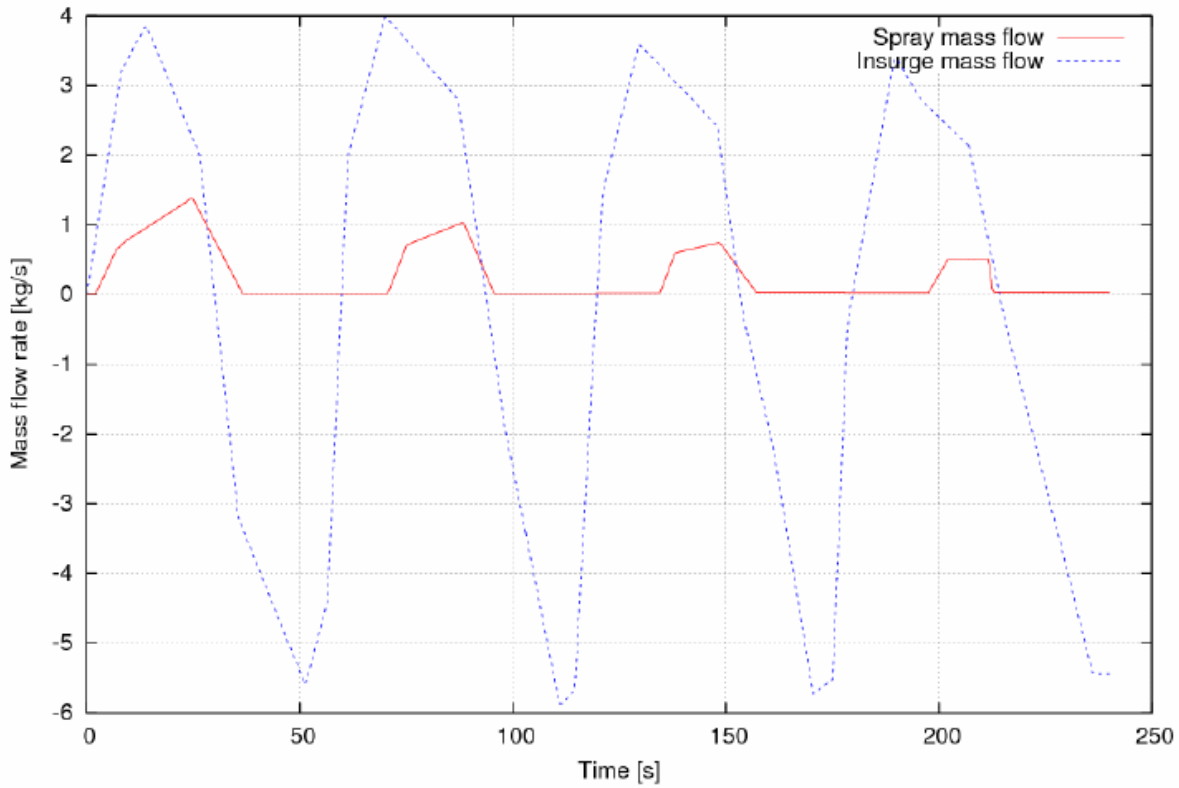

Figure 4.18-3. Transient boundary condition flow rates for Neptunus Test Y05.

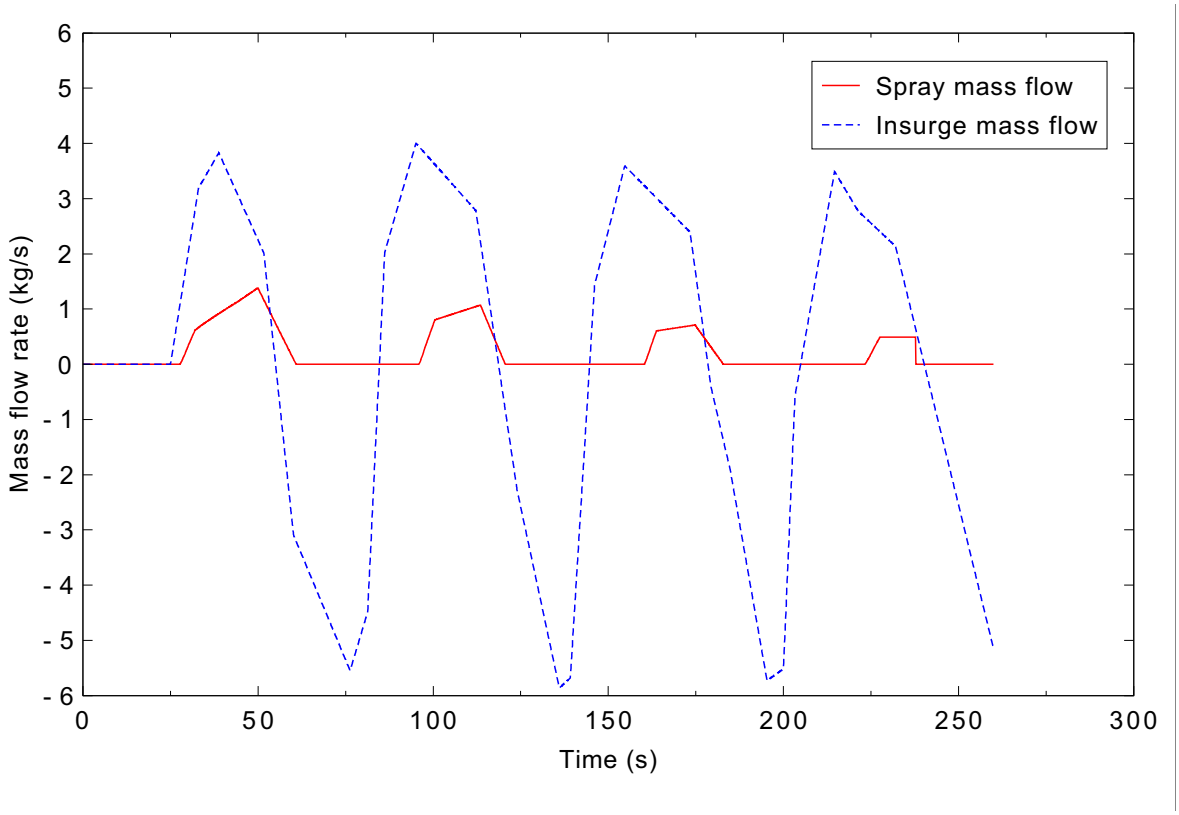

Figure 4.18-4. RELAP5-3D model input boundary flows for Neptunus Test Y05.

The pressurizer is initialized with zero flow and a water level of 1.12 m (the level is in cell 6). Pressurizer pressure is established at 12.39 MPa and the corresponding saturation temperature of 600.25 K.

4.18.4 Data Comparisons and Results

Transient runs were made with the RELAP5-3D code using both the semi-implicit and the nearly-implicit advancement schemes. The requested time step size was 0.05 s for both cases. The transient runs are initiated with user-specified flow boundary conditions at the surge line and spray line. The RELAP5-3D runs have a built-in null transient from time zero until 25 s to ensure the code-calculated pressurizer conditions are stable prior to initiating the transient. The RELAP5-3D code runs are terminated at 260 s.

The two base case runs were made and the pressurizer pressure results are shown in Figure 4.18-5 together with the Neptunus test data. The calculation of the first two pressure cycles is in excellent agreement with the data, reproducing both the peak pressure and the pressurization/depressurization rate. In the subsequent pressure cycles, while the pressure rate of change is well-calculated, the maximum and minimum pressure values are under predicted, with the difference between calculated and measured values increasing with each cycle. Overall, the predicted pressure is judged to be in reasonable agreement with the measured data. Note that the code-calculated pressure response results are essentially the same for both the semi-implicit and nearly-implicit solution schemes.

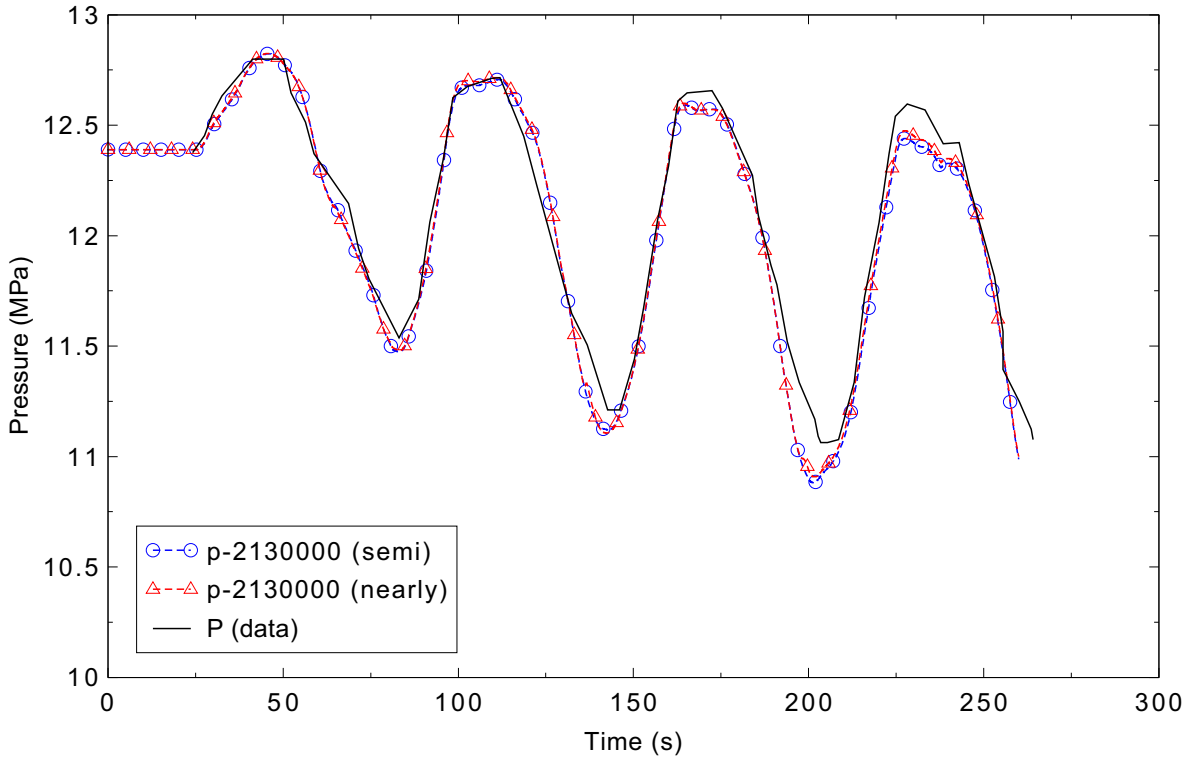

Figure 4.18-5. Measured and calculated pressurizer dome pressure for Neptunus Test Y05.

The RELAP5-3D calculated pressurizer steam temperature response is compared with the Neptunus data in Figure 4.18-6. As for the pressure, the initial temperature cycle and the temperature rate of change through all of the cycles are in excellent agreement with the measured data. The minimum temperatures in each cycle are slightly under predicted. The peak temperatures for the second and third cycles are over predicted, while that for the final cycle is slightly under predicted. Overall, the calculated pressurizer steam space temperatures are judged to be in reasonable agreement with the Neptunus test data.

Unfortunately, there were no water level data available from Neptunus pressurizer Test Y05.

4.18.5 Conclusions and Assessment Findings

The code-calculated pressurizer pressure and temperature results are judged to be in reasonable agreement with the Neptunus pressurizer data for Test Y05. It can be concluded that the RELAP5-3D pressurizer model appropriately calculates the expected two-phase, two-region, non-equilibrium behavior required to simulate pressurizer transient response.

4.18.6 References

4.18-1. Eveliina Takasuo, *Modeling of Pressurizer Using APROS and TRACE Thermal Hydraulic Codes*, VTT Research Notes 2339, VTT Technical Research Center, Finland, 2006.

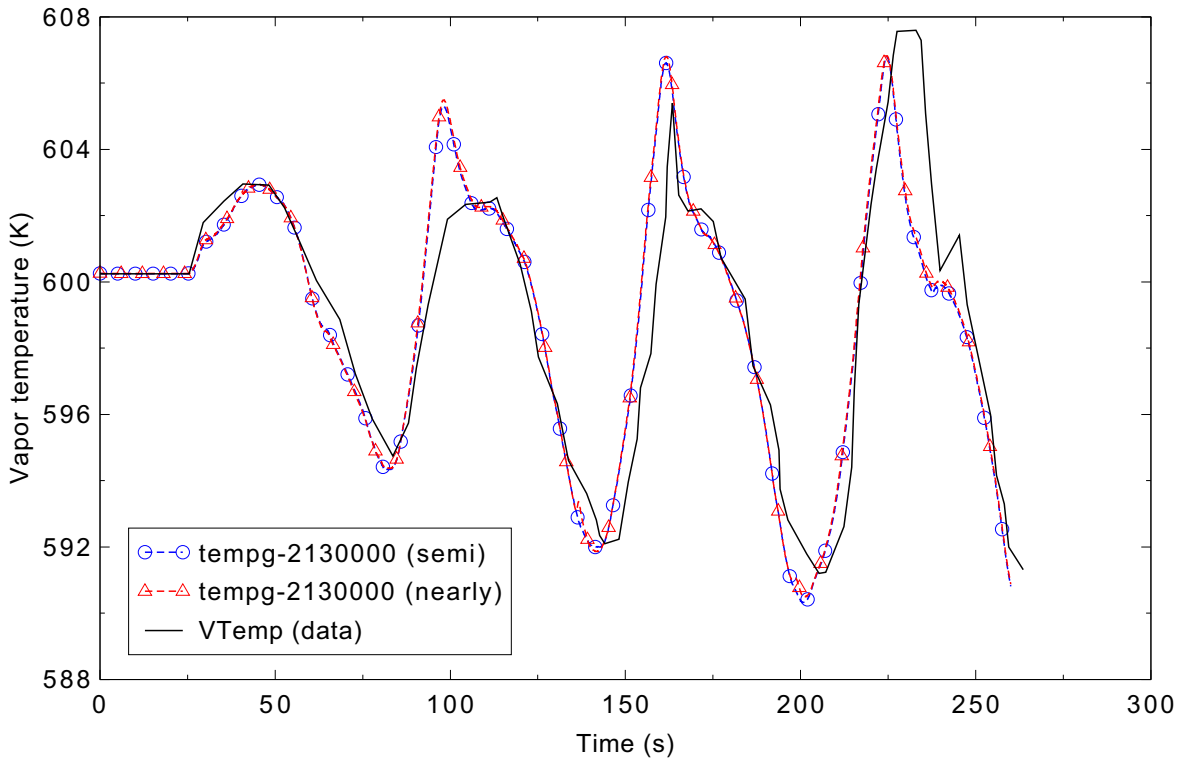

Figure 4.18-6. Measured and calculated pressurizer steam temperature for Neptunus Test Y05.

4.18-2. N. Aksan, et al., *Separate Effects Test Matrix for Thermal-hydraulic Code Validation, Volume 1, Phenomena Characteristics and Selection of Facilities and Tests*, Organization for Economic Co-operation and Development, Paris, OCDE/GD (94)/82, 1993.

4.18-3. A. C. Peterson, *TRAC-PF1/MOD1 Independent Assessment: NEPTUNUS Pressurizer Test Y05*, NUREG/CR-3919, Sandia National Laboratories, 1984.

4.19 MB2 Test 1712

Westinghouse Electric Corporation performed a series of experiments using a power-scaled model of a Model F steam generator. Called the Model Boiler No. 2 (MB-2), this test facility was used to simulate loss of feed (LOF), steam generator tube rupture, and steam line break transients.[4.19-1, 4.19-2]

4.19.1 Code Models Assessed

The performance of the code in modeling steady-state steam generator behavior was evaluated.

4.19.2 Experiment Facility Description

The MB-2 test facility is an approximately 1% power-scaled model of a Westinghouse Model F steam generator. At 100% power (6.67 MWt), the MB-2 produces steam at a pressure of 6.9 MPa. To make the MB-2 as prototypical as possible, the U-tubes were made of the same material, dimensions, and pitch as the Model F. Also, secondary pressures, temperatures, and flow rates were chosen to be consistent with the full size steam generator.

The design of the MB-2 steam generator is shown in Figure 4.19-1. There are 52 U-tubes in a rectangular square-pitch array which is surrounded by a wrapper box, as shown in Figure 4.19-2. Steam from the tube bundle region passes through the transition cone into the primary riser, and then enters a centrifugal separator. The steam and entrained liquid pass through a vane-type separator before exiting the steam generator as dry vapor. Liquid from the two separators and the injected main feedwater travels down two downcomer pipes and enters the wrapper box just above the tube sheet.

Test 1712 was one of a series of test runs which were part of LOF Test No. 1, the purpose of which was to determine steam generator behavior as the secondary water was boiled off under full power conditions.[4.19-2] Since the current assessment deals only with steady-state steam generator behavior, the initial steady-state data from Test 1712 are used for comparison with the conditions calculated by the RELAP5-3D model. The actual steady-state conditions measured at the test facility prior to the LOF transient are shown in Table 4.19-1.

Table 4.19-1. Test 1712 full power steady state conditions.

Plant Parameter	Initial Condition
Primary system pressure	15.51 MPa (2250 psia)
Primary fluid T_{hot}	598 K (618°F)
Primary fluid flow rate	41.3 kg/s (91 lbm/s)
Secondary-side pressure	6.87 MPa (996 psia)
Feedwater temperature	498 K (437°F)
Water level (from top of tube sheet)	11.18 m (440 in.)

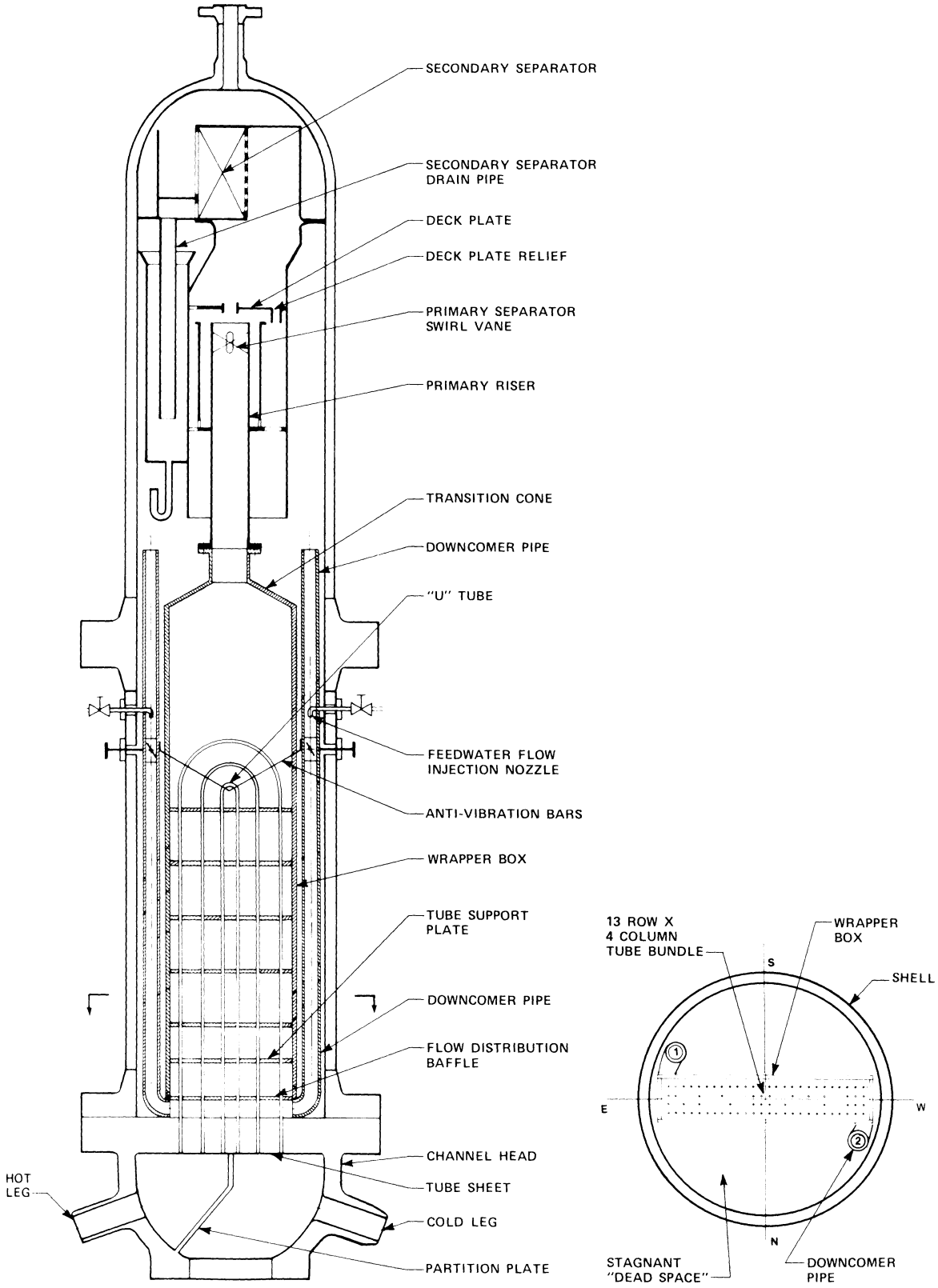

Figure 4.19-1. MB-2 schematic diagram.

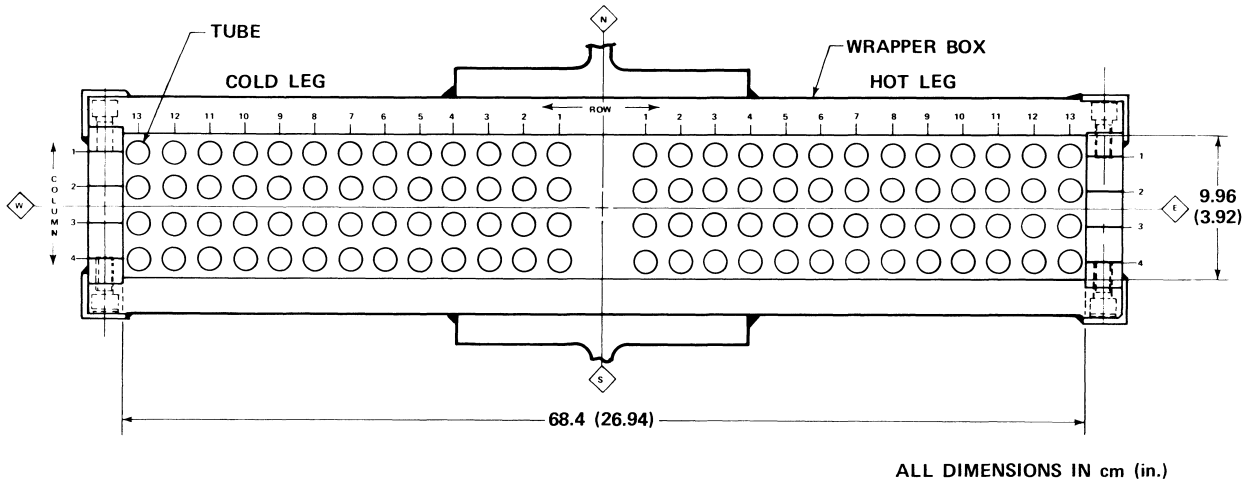

Figure 4.19-2. MB-2 tube bundle cross section.

4.19.3 Input Model Description

The MB-2 nodalization diagram is shown in Figure 4.19-3. The primary-side boundary conditions are established by time-dependent volume 100 and time-dependent junction 102. Pipe 104 contains 10 volumes, with the first and tenth volumes representing the inlet and outlet plenums, respectively. Pipe volumes 2 through 9 represent the tube bundle region.

The secondary side has two components representing the boiler region below the centrifugal separator. Branch 206 is used to connect the junctions coming from the two lower downcomers; the other component is pipe 208, consisting of six volumes. Volume 210 is a separator component, and various branch and pipe components are used to represent the disengagement tank and downcomers. The separator liquid return and vapor outlet junction loss coefficients were adjusted to establish a reasonable amount of liquid in the separator (~30%). The feedwater flow rate is controlled during steady-state initialization to maintain a target mass of 594.1 lbm (269.5 kg) in the secondary, and time-dependent volume 220 is used to impose a pressure boundary condition in the turbine header.

Another loop, which is not shown in Figure 4.19-3, represents the volume inside the shell between the drier support plate and tube sheet and outside of all internal components. This “dead space” is pressurized because the wrapper box cannot withstand the full secondary-to-atmosphere differential pressure during steam line break transients. A separate control system is required to maintain an appropriate pressure in the dead space during operation. The dead space volume is hydraulically independent of the primary and secondary systems, but heat structures are used to represent the heat transfer between the secondary and dead space volumes. Other heat structures are also used to model heat transfer from the primary to the secondary and between the various internal components.

4.19.4 Data Comparisons and Results

The calculated steady-state results are compared to the experiment data in Figures 4.19-4 through 4.19-10. The LOF Test No. 1 transient was initiated at 45 s, so only the first 40 s of experiment data (obtained from the NRC Data Bank) are shown in the figures. The RELAP5-3D calculation was run for

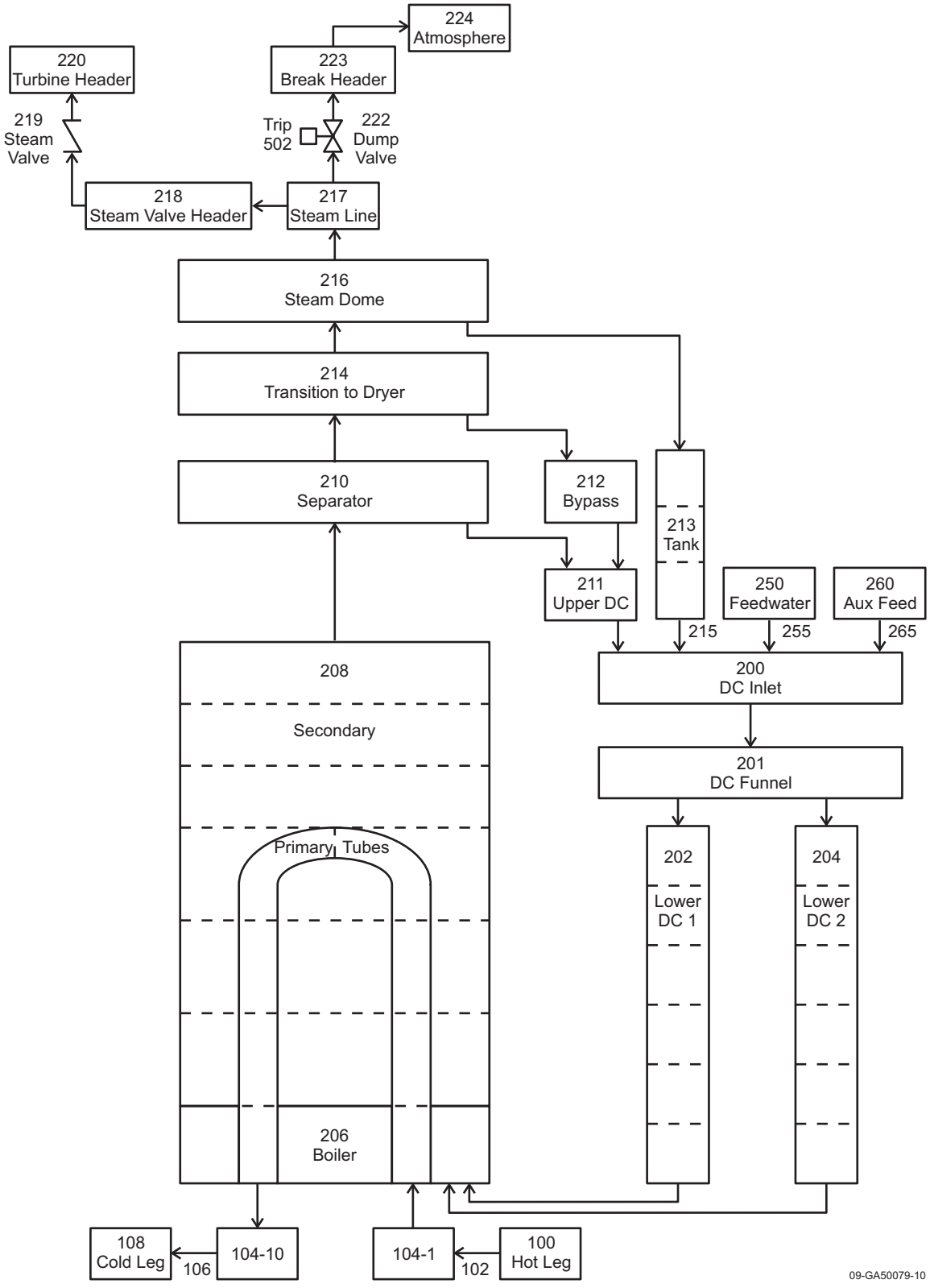

Figure 4.19-3. Nodalization diagram for MB-2 LOF Test 1712.

400 s with a requested time step of 0.1 s, so the calculated results shown in the figures have been offset to display only the last 40 s. This allows a more direct comparison of the final calculated steady-state results to the initial test conditions.

The primary mass flow rate is shown in Figure 4.19-4, and the main feedwater temperature is shown in Figure 4.19-5; both are boundary conditions in the calculations. The steady-state main feedwater flow rate, calculated to maintain the secondary mass at the set point, is shown in Figure 4.19-6, and the calculated mass flow rate of steam through the steam valve is presented in Figure 4.19-7. The calculated flow rates are slightly below the measured values in both cases. Note that the measured steam flow rate was slightly higher than the main feedwater flow rate during the initialization leading up to the transient.

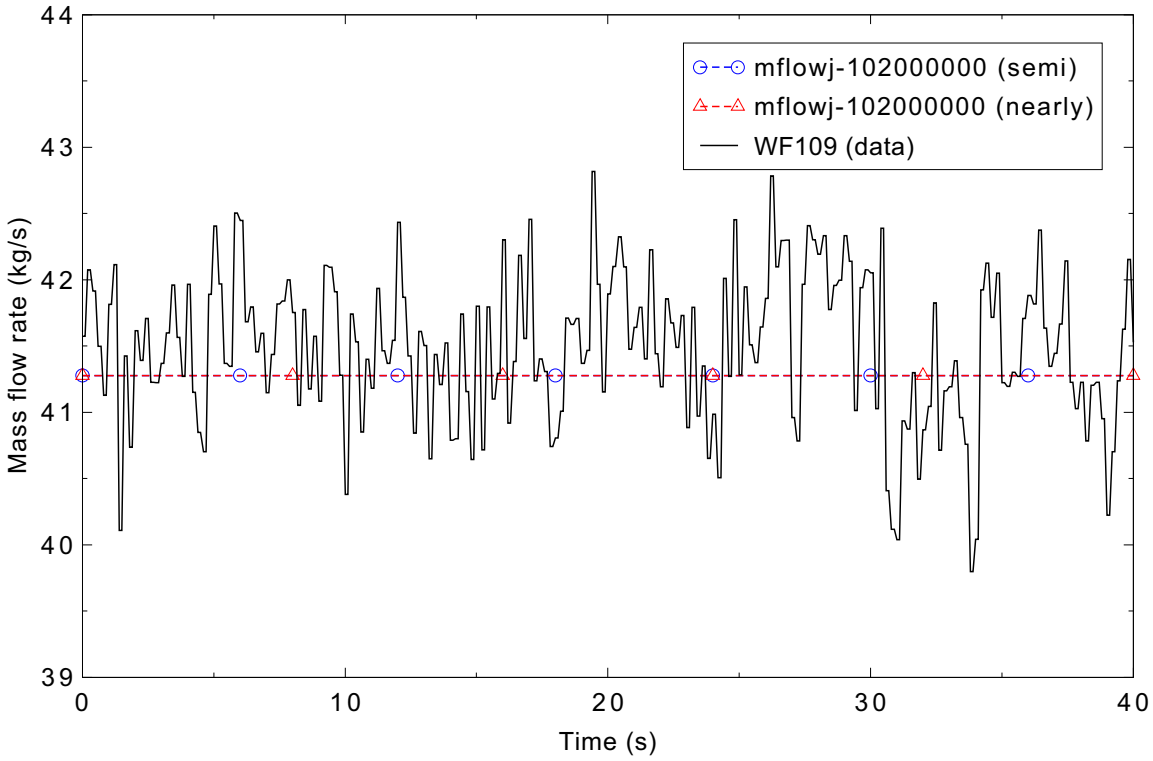

Figure 4.19-4. Measured and input primary flow rate during MB-2 steady state Test 1712.

Figure 4.19-8 shows pressure in the steam line just above the steam dome. The calculated pressure shows excellent agreement with the data. The narrow-range level is shown in Figure 4.19-9. The calculated level is higher than the experiment data indicate. This level depends on obtaining the proper pressure distribution in the steam generator secondary, and is particularly sensitive to the loss coefficients in the outlet and liquid fallback junctions of the separator component. The measured level dropped slightly during the course of the experiment initialization due to the mismatch between feed and steam flows mentioned above.

Figure 4.19-10 shows the primary fluid temperature as a function of elevation above the tube sheet. The calculated results show reasonable agreement with the data. Most temperatures fall within the range of uncertainty of the thermocouple data, although the total calculated primary temperature drop is slightly lower than the data indicate.

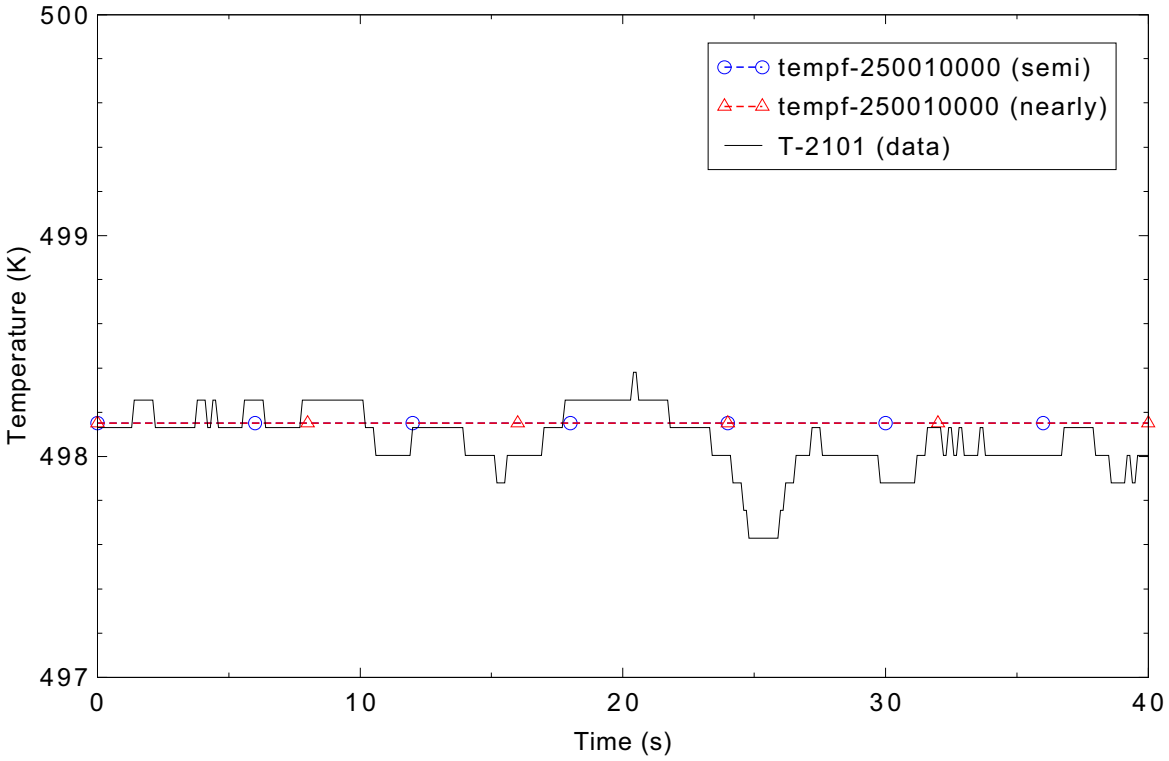

Figure 4.19-5. Measured and input main feedwater temperature during MB-2 steady state Test 1712.

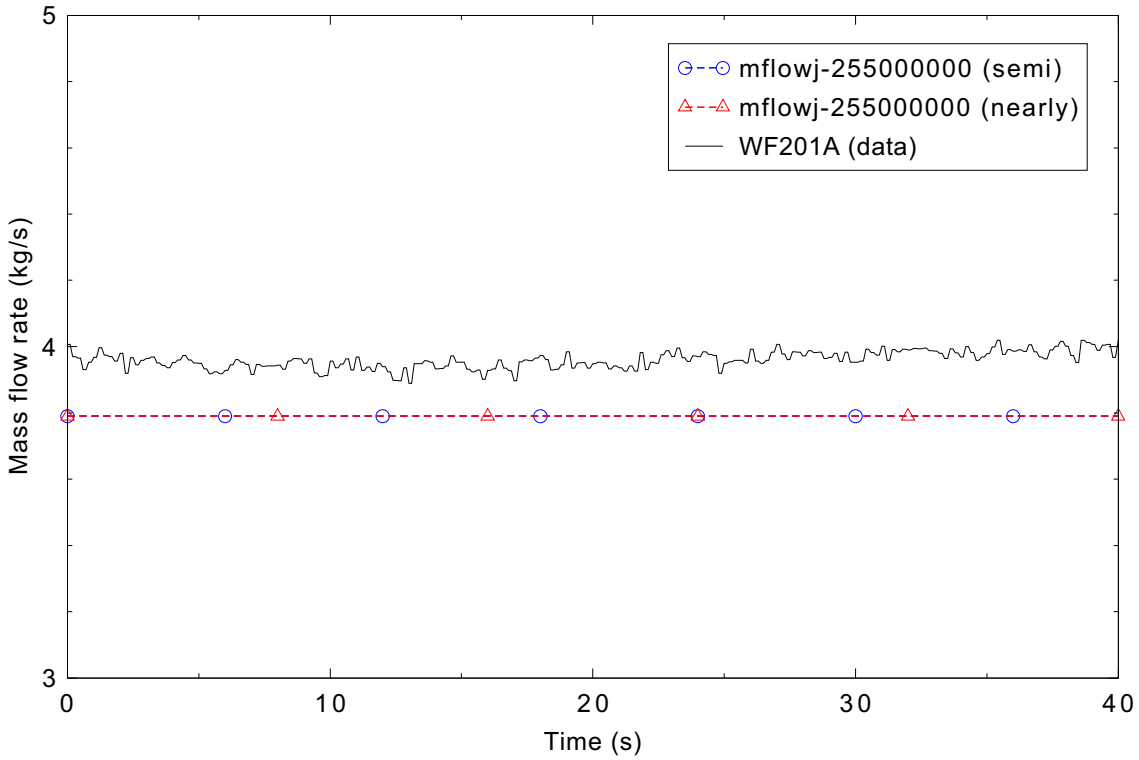

Figure 4.19-6. Measured and calculated main feedwater flow rate during MB-2 steady state Test 1712.

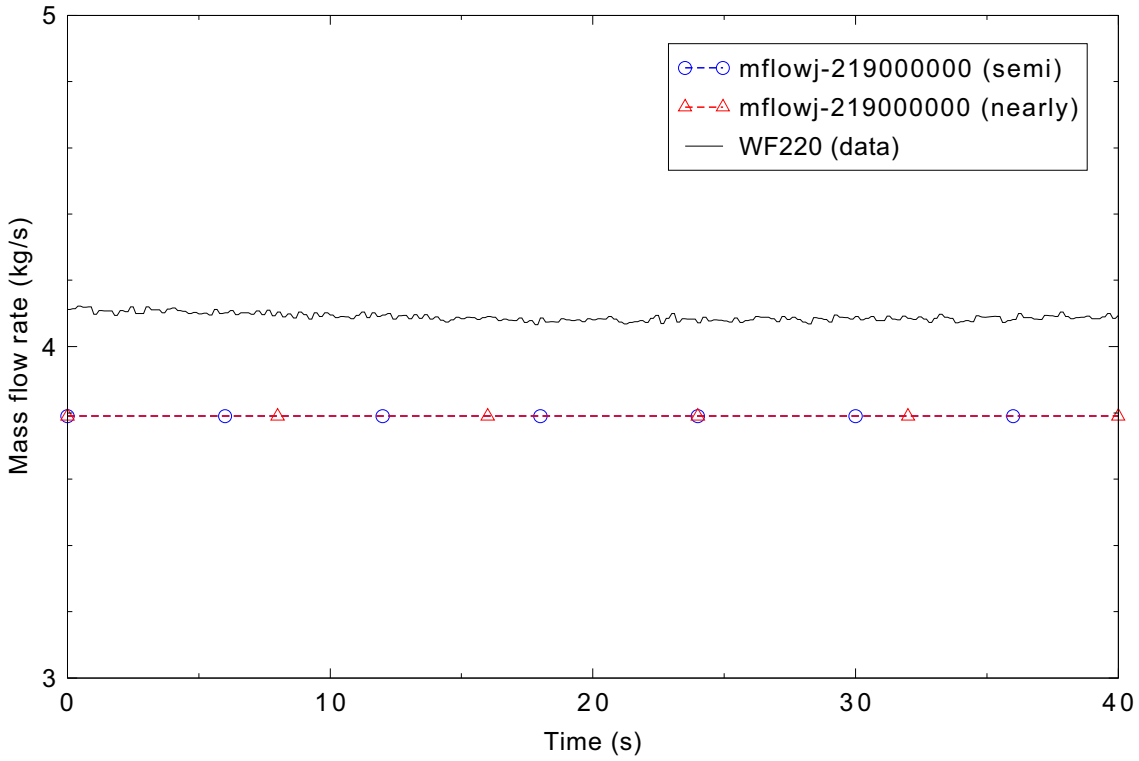

Figure 4.19-7. Measured and calculated steam flow rate during MB-2 steady state Test 1712.

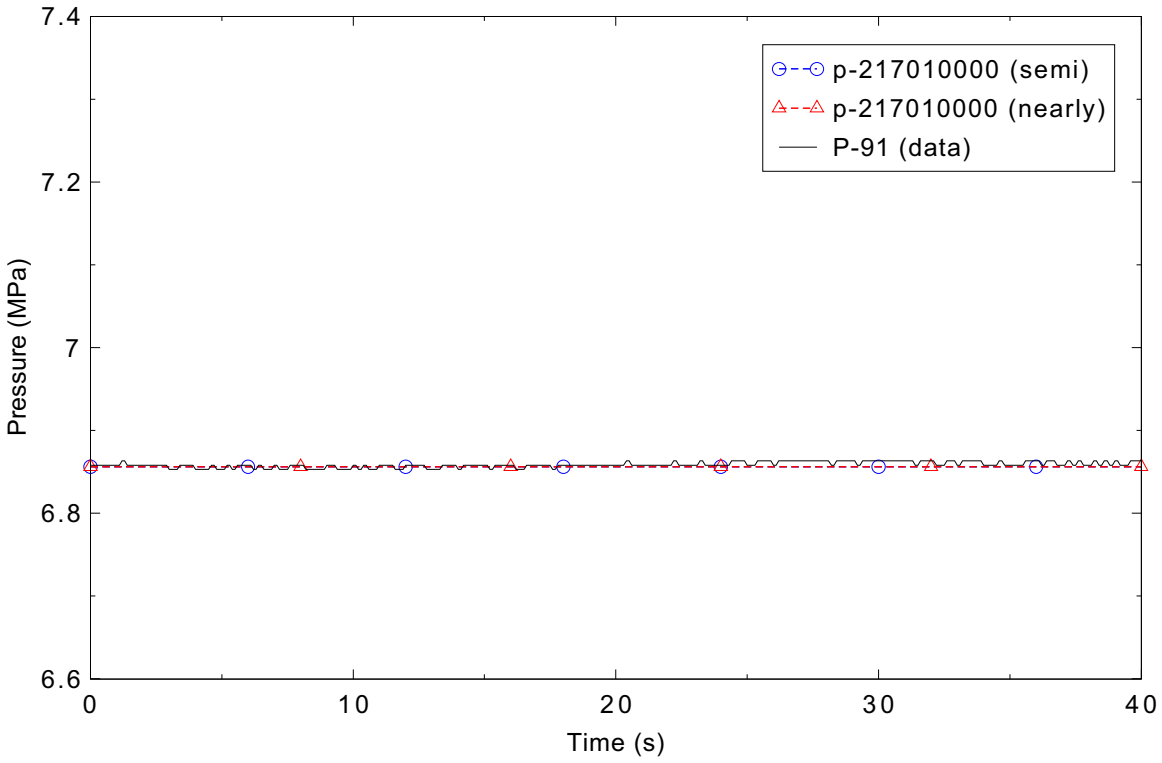

Figure 4.19-8. Measured and calculated steam line pressure during MB-2 steady state Test 1712.

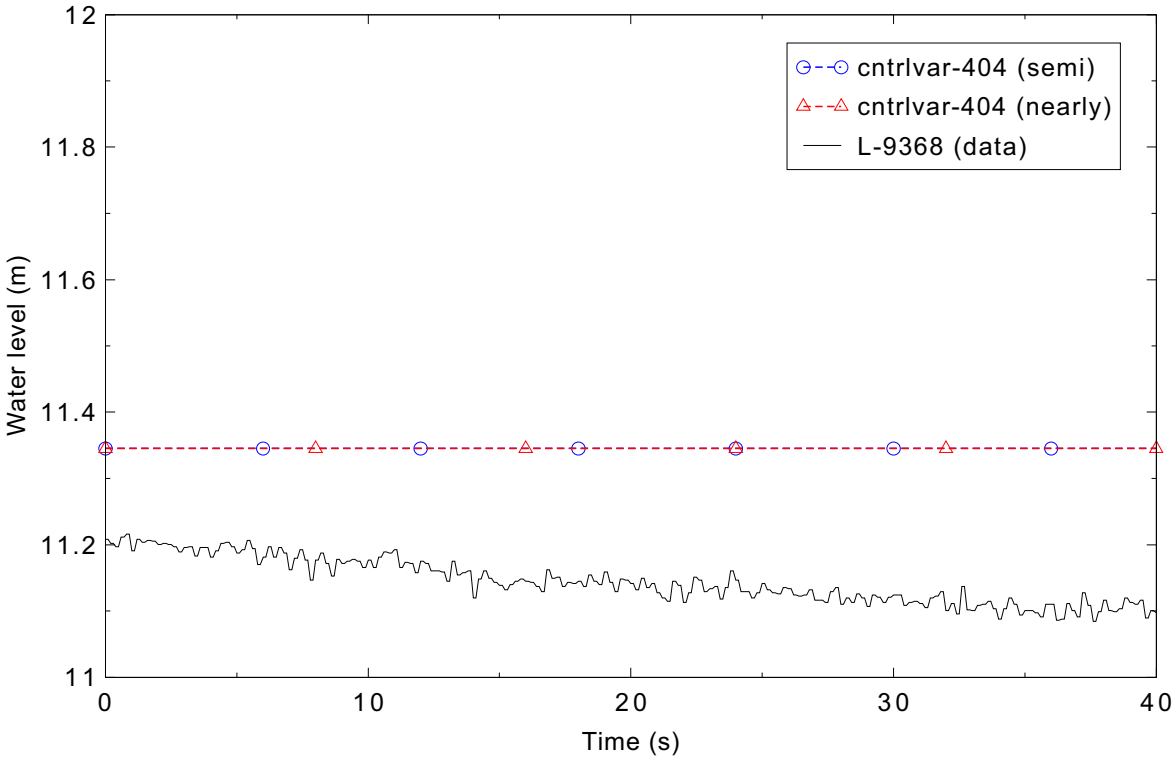

Figure 4.19-9. Measured and calculated narrow range water level during MB-2 steady state Test 1712.

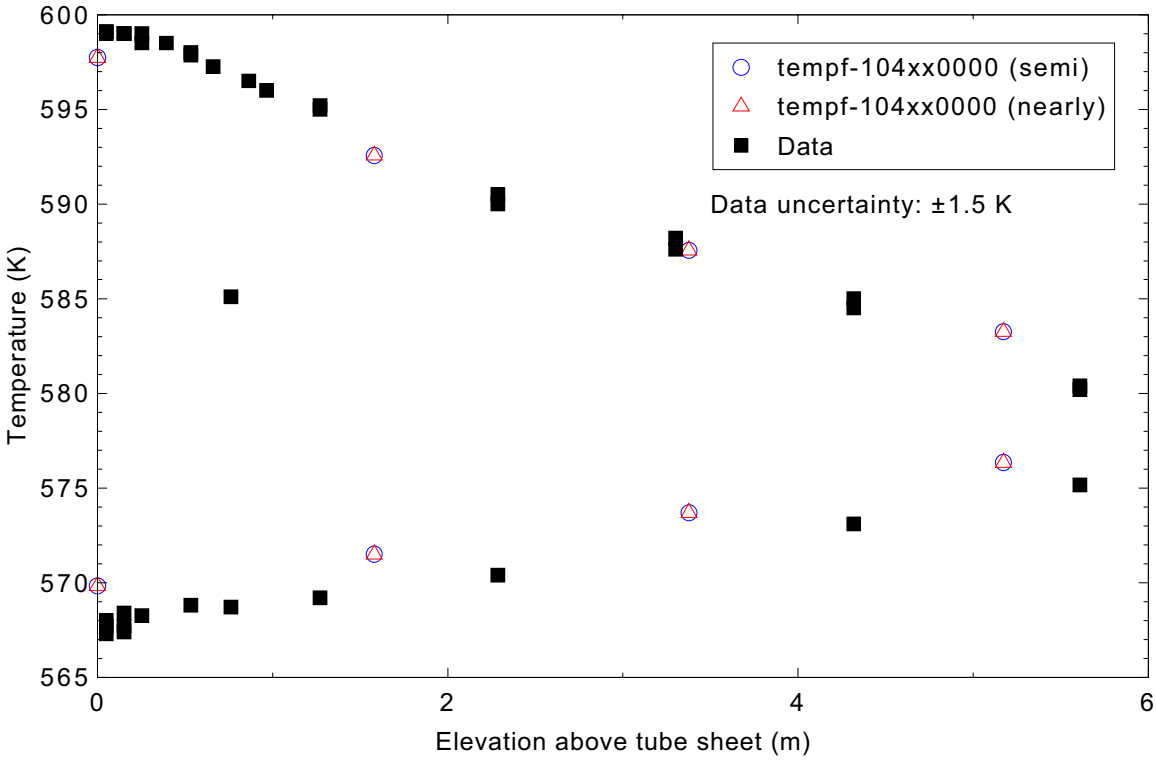

Figure 4.19-10. Measured and calculated primary side fluid temperatures during MB-2 steady state Test 1712.

4.19.5 Conclusions and Assessment Findings

The overall results from the calculation are in reasonable agreement with the data. The primary temperature drop through the U-tube bundle shows reasonable agreement, indicating that the model correctly predicts the amount of energy transferred from the primary to the secondary. Some other calculated steady-state conditions (e.g., narrow range level) lie outside the uncertainty range of the data. The level is particularly sensitive to the separator junction loss coefficients. It is likely that further adjustments to the model could be made to better match the pressure distribution on the secondary side, resulting in initial conditions that are closer to the experiment data.

4.19.6 References

4.19-1. M. Y. Young, et al., *Prototypical Steam Generator Transient Testing Program: Test Plan/Scaling Analysis*, EPRI NP-3494, NUREG/CR-3661, WCAP-10475, September 1984.

4.19-2. O. J. Mendler, K. Takeuchi, and M. Y. Young, *Loss of Feed Flow, Steam Generator Tube Rupture and Steam Line Break Thermohydraulic Experiments: MB-2 Steam Generator Transient Response Test Program*, NUREG/CR-4751, EPRI NP-4786, WCAP-11206, October 1986.

4.20 LOFT Experiment L3-1

Experiments were performed in the 1970s and 1980s in the Loss-of-Fluid Test (LOFT) facility, a 50 MWt power/volume-scaled nuclear reactor designed to investigate the response of a commercial pressurized water reactor to loss-of-coolant accidents and operational transients. From Experiment L3-1, the accumulator response during a small break loss-of-coolant accident was isolated to create a separate-effects test.

4.20.1 Code Models Assessed

The purpose of this problem was to assess the performance of the accumulator model during a slow depressurization associated with a small break loss-of-coolant accident.

4.20.2 Experiment Facility Description

This problem simulates the blowdown of the LOFT Accumulator A and surge line during Experiment L3-1. Experiment L3-1 was a nuclear small-break experiment conducted at the LOFT Facility.[4.20-1] During this experiment, the LOFT primary coolant system underwent a blowdown simulating a small break. As the pressure decreased at the intact loop cold leg emergency core cooling (ECC) injection point, it became less than the pressure in the accumulator. At this time, the accumulator also began to blow down, consequently injecting cold water into the primary system cold leg.

Figure 4.20-1 is a schematic showing the arrangement of the LOFT Accumulator A and surge line relative to the cold leg ECC injection point. The accumulator is a 1.25-m (49-in.) diameter cylindrical tank with elliptical ends. The effective volume of liquid and gas available for injection is adjustable by varying the height of a standpipe inside the tank. For Experiment L3-1, the standpipe height was approximately 0.76 m (30 in.), giving an effective liquid-gas volume of approximately 2.88 m^3 (103 ft^3). The length of the combined standpipe and surge line was 32.82 m (107.7 ft), with an average flow area of 0.01 m^2 (0.147 ft^2). There was a 2.13-m (7.0-ft) rise in elevation from the standpipe entrance to the primary system ECC injection point.

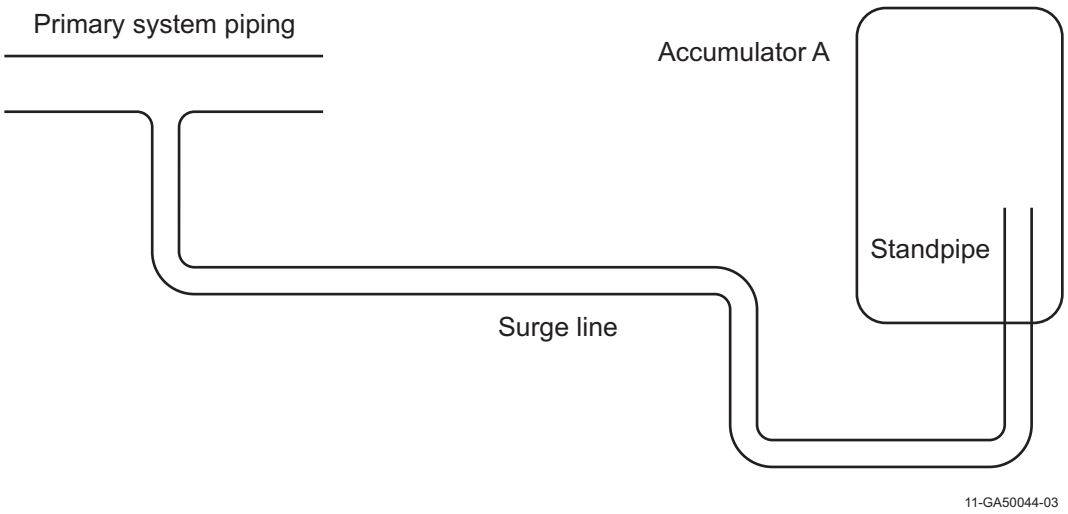

Figure 4.20-1. LOFT L3-1 Accumulator A and surge line schematic.

4.20.3 Input Model Description

Figure 4.20-2 is a schematic of the RELAP5-3D model, which consists of four components. Component 1 is the accumulator component, which represents LOFT Accumulator A. Component 2 is the two-volume pipe component representing the surge line. The first volume of the pipe component accounts for nearly the entire length of the surge line. The second volume of the pipe component accounts for the elevation change that occurs over the length of the surge line. The second volume has an inclination angle of 30 degrees so that the calculation is based on the horizontal flow regime map. Component 3 is a single junction connecting the pipe component to Component 4, which is a time-dependent volume that imposes the pressure history at the LOFT cold leg ECC injection point for LOFT Experiment L3-1. It should be pointed out that the accumulator tank volume is consistent with the accumulator standpipe height for Experiment L3-1. The surge line area and length are consistent with the Experiment L3-1 piping arrangement and include the entire surge line from its entrance in the standpipe to its injection point in the primary system cold leg. All of the surge line orifice, bend, and contraction/expansion losses are accounted for in the forward and reverse loss coefficients in the junction of the pipe component and in the exit single junction.

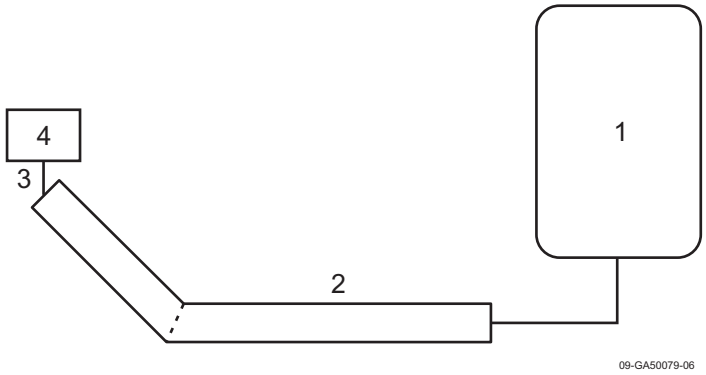

Figure 4.20-2. RELAP5 LOFT L3-1 accumulator model nodalization.

4.20.4 Data Comparisons and Results

This problem was run with a requested time step of 0.5 s. The data for this problem are from the NRC Data Bank.

Calculated results are compared to the experiment data in Figures 4.20-3 through 4.20-5, which are plots of the accumulator gas dome pressure versus volume, the gas dome pressure versus time, and the accumulator liquid level.

In Figure 4.20-3, curves for isothermal (cntrlvar-8) and isentropic (cntrlvar-9) expansion of the gas dome are also shown for comparison. As shown, the calculated results agree very well with the data and lie between the isothermal and isentropic expansion curves as expected. Initially the expansion is nearly adiabatic, and as the gas temperature decreases due to expansion, the heat transfer from the walls and liquid interface cause the expansion to approach isothermal conditions.

The accumulator pressures are shown in Figure 4.20-4. As shown, the calculated accumulator pressure response agreed well with the data. The slow depressurization rate resulted in low flow rates in the surge

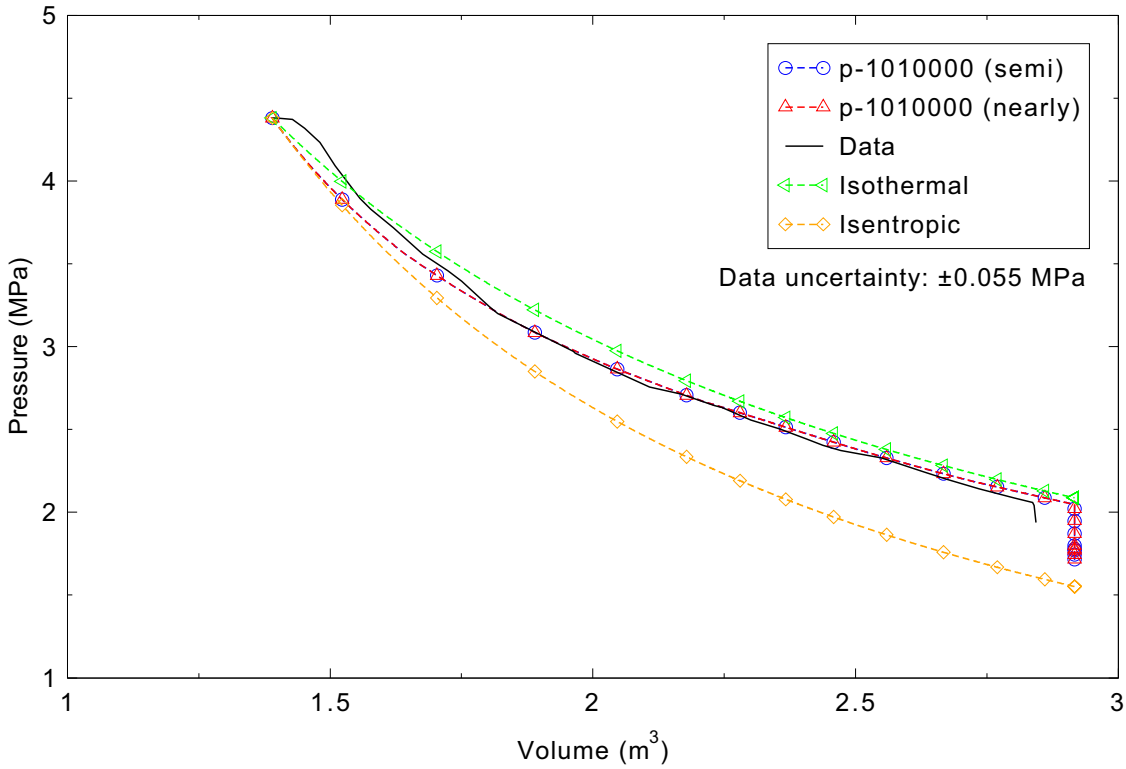

Figure 4.20-3. Measured and calculated accumulator gas dome pressure versus volume for LOFT Experiment L3-1.

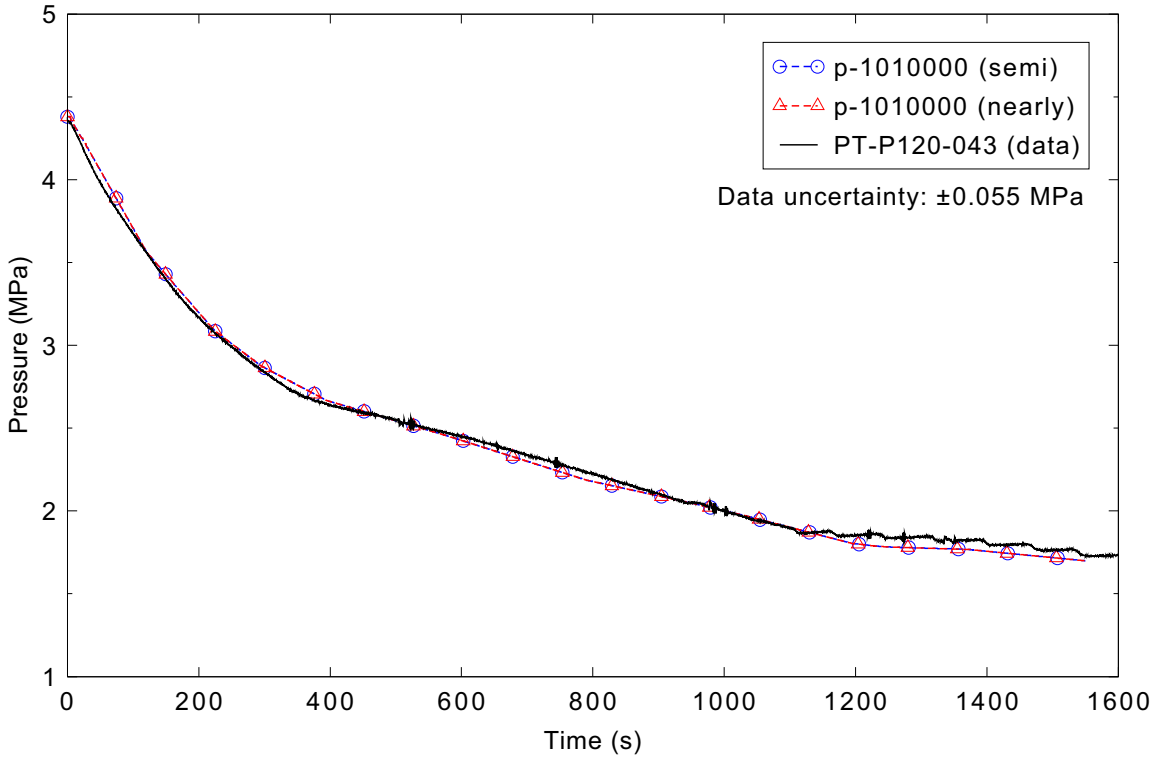

Figure 4.20-4. Measured and calculated accumulator gas dome pressure for LOFT Experiment L3-1.

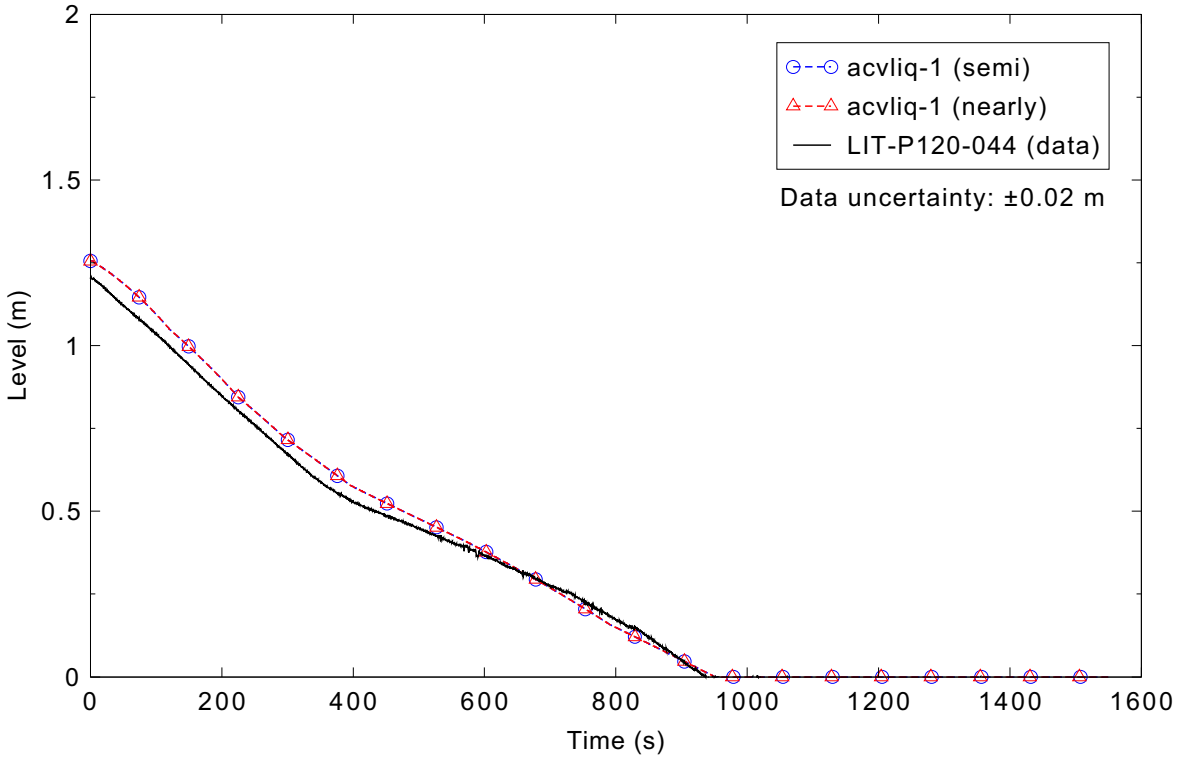

Figure 4.20-5. Measured and calculated accumulator liquid level for LOFT Experiment L3-1.

line, on the order of 0.1 m/s (0.3 ft/s), so that the frictional and form losses in the surge line were not significant to the accumulator response.

The measured and calculated accumulator liquid levels are presented in Figure 4.20-5. The variable acvliq-1 is divided by the cross-sectional area of the accumulator to obtain the displayed results. The calculated response agrees reasonably well with the measured results.

There was no observed difference between the semi- and nearly-implicit results.

4.20.5 Conclusions and Assessment Findings

The RELAP5-3D calculations are judged to be in excellent agreement with the measured data. The data trends were correctly predicted for the LOFT L3-1 test case, and the predictions were generally within the measurement uncertainty bands.

4.20.6 References

4.20-1. P. D. Bayless, J. B. Marlow, and R. H. Averill, *Experiment Data Report for LOFT Nuclear Small Break Experiment L3-1*, NUREG/CR-1145, EGG-2007, January 1980.

4.21 GE 1/6-Scale Jet Pump

Experiments were performed in the late 1970s using a 1/6-scale model of a General Electric Company (GE) jet pump. The experiments were designed to provide data under design and off-design conditions for assisting in the development of computer models for jet pumps.[4.21-1]

4.21.1 Code Models Assessed

The performance of the jet pump model was evaluated.

4.21.2 Experiment Facility Description

The model jet pump is shown in Figure 4.21-1. Figure 4.21-2 provides some additional geometric information. Relevant measurement locations are shown in Figure 4.21-3; fluid flow rate, pressure, and temperature were measured in each of the drive, suction, and discharge lines. The jet pump was installed in the Loss of Fluid Test (LOFT) Technical Support Facility at the Idaho National Laboratory, as illustrated in Figure 4.21-4. The existing components in that facility provided the flow, temperature, and pressure boundary conditions for the experiments.

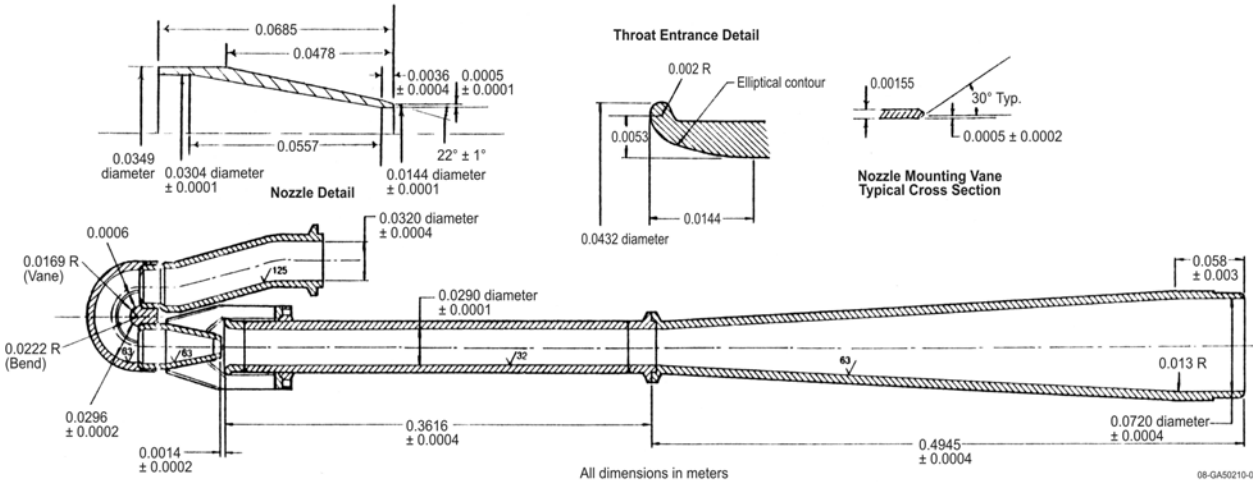

Figure 4.21-1. 1/6-scale model jet pump.

Subcooled, steady state data were obtained for all possible flow patterns that might occur during a loss-of-coolant accident in a boiling water reactor. More than 200 data points were obtained, with pressures ranging from 0.84 to 8.16 MPa, drive flow rates ranging from -4.1 to 4.1 l/s, and suction flow rates ranging from -12.6 to 13.0 l/s. Water temperatures were adjusted to reflect expected values during a blowdown: 540-562 K for the higher pressure (5.80-8.16 MPa) cases, and 302-316 K for the lower pressure (0.84-3.83 MPa) cases. The steady state tests were run as isothermal cases, so that thermal mixing of the fluid streams was not an issue.

The data were reduced using parameters M and N_c: M is a flow ratio, defined as

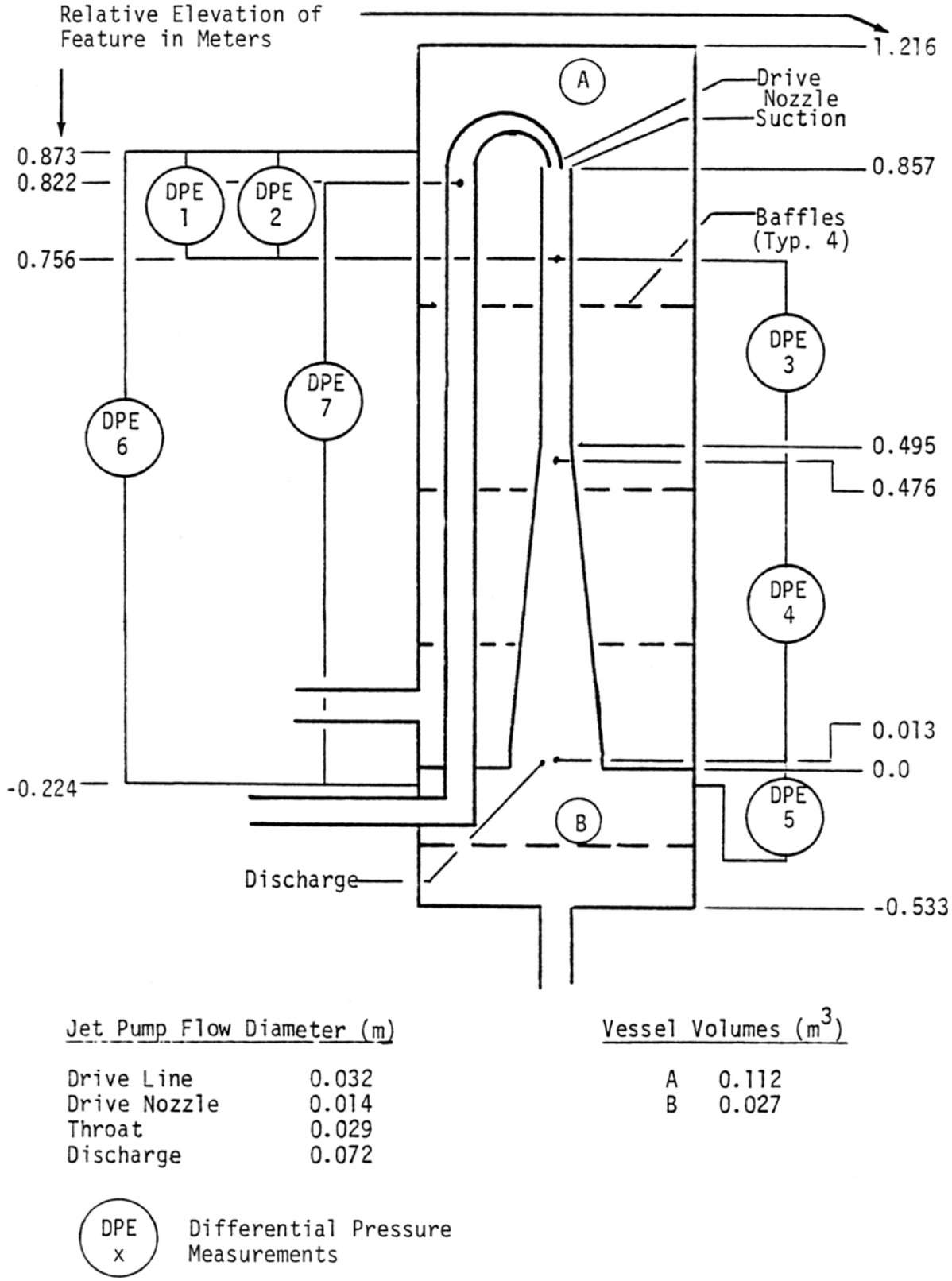

Jet Pump Flow Diameter (m)	
Drive Line	0.032
Drive Nozzle	0.014
Throat	0.029
Discharge	0.072

Vessel Volumes (m^3)	
A	0.112
B	0.027

DPE x — Differential Pressure Measurements

Figure 4.21-2. Schematic of the jet pump and vessel.

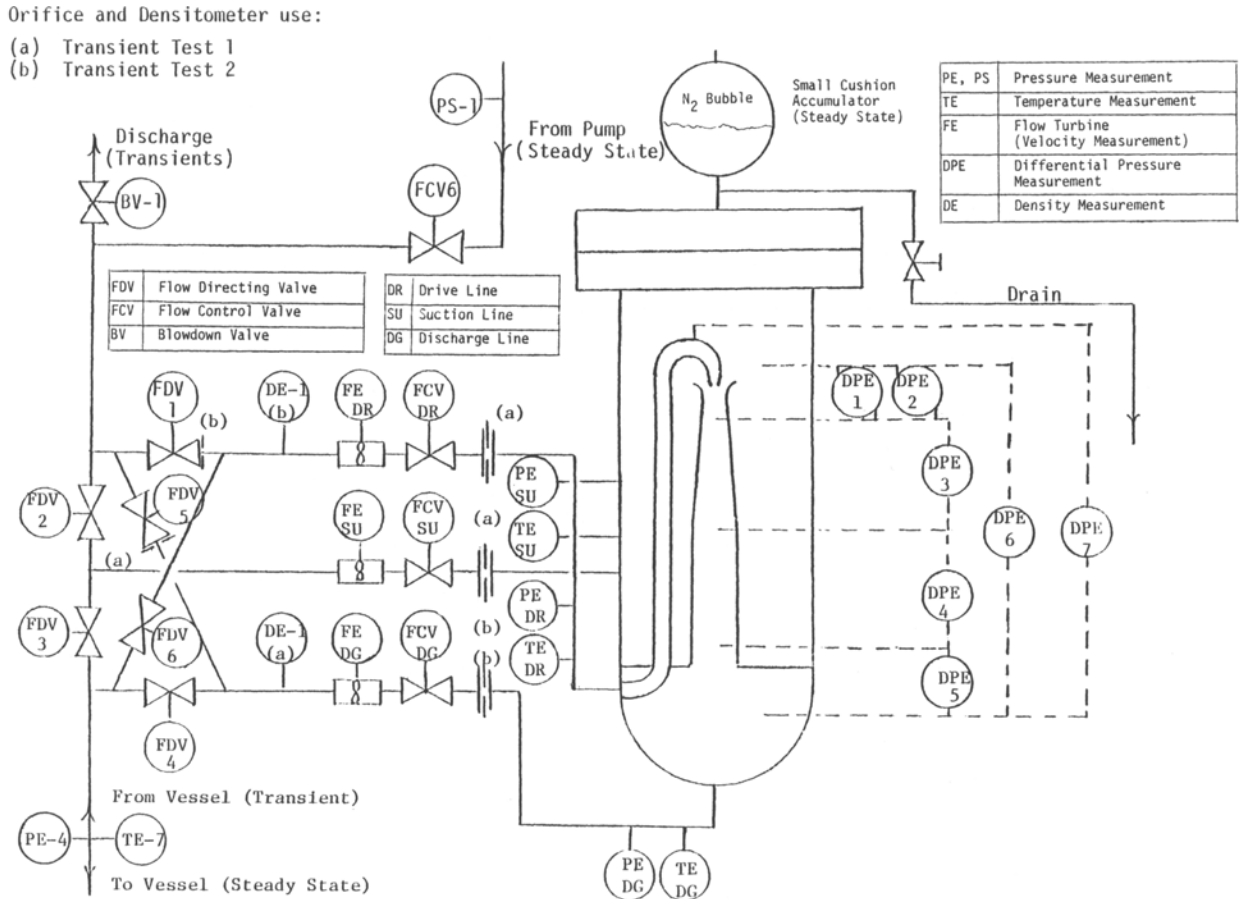

Figure 4.21-3. Jet pump test assembly and instrumentation.

$$M = \frac{\text{Suction Mass Flow}}{\text{Drive Mass Flow}} \tag{4.21-1}$$

and N_c is a differential head ratio, defined as

$$N_c = \frac{\text{Discharge Head} - \text{Suction Head}}{\text{Drive Head} - \text{Discharge Head}}. \tag{4.21-2}$$

Early analysis of the experiment data by Wilson[4.21-2] identified a need for a pressure correction to the differential pressure data. The data presented here have that pressure correction applied, and were taken from Tables A-4 and A-5 in Reference 4.21-2. Wilson also recommended that the data for positive (forward) drive flow with a flow ratio (M) less than -0.8 not be used because of a large scatter in the measurements under those conditions; those data are not included in the assessment described below.

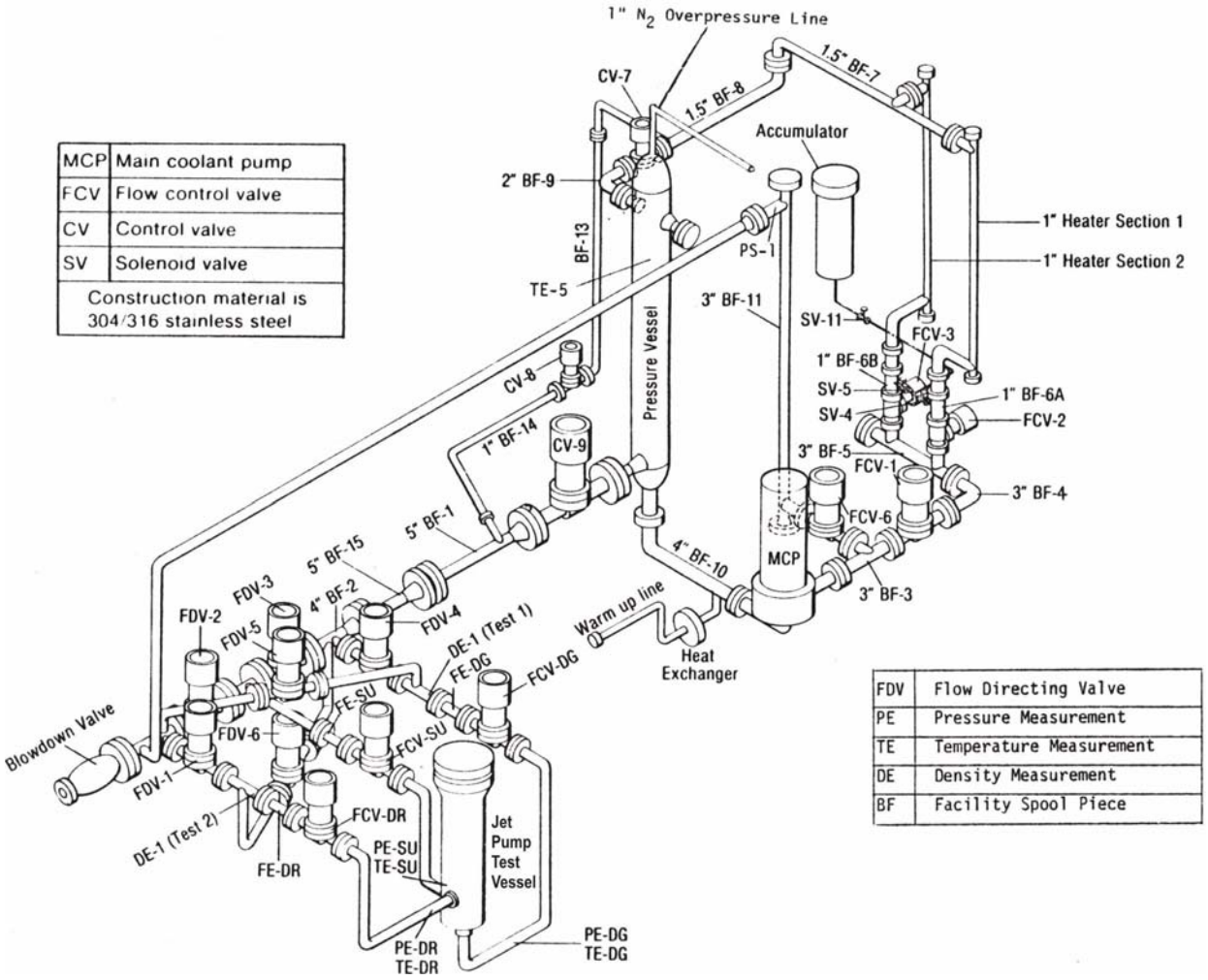

Figure 4.21-4. Jet pump assembly and blowdown facility schematic.

4.21.3 Input Model Description

The RELAP5-3D model of the experiment included only those portions of the system needed to simulate the jet pump behavior. Figure 4.21-5 presents a nodalization diagram. Time-dependent junctions were used for the drive (Component 12) and suction (Component 32) line flows. The region where the drive and suction flows mix is modeled with two components, a jet pump branch (Component 50) and a single volume (Component 55). The jet pump diffuser is modeled as a 3-volume pipe (Component 60). Three time-dependent volumes are used: Components 10 and 30 establish the drive and suction flow temperatures, respectively, and Component 80 sets the pressure. Junction loss coefficients were based on the geometry of the facility, and are summarized in Table 4.21-1. No heat structures were included in the model. Control variables were used to calculate the M and N_c ratios for comparisons with the experiment data.

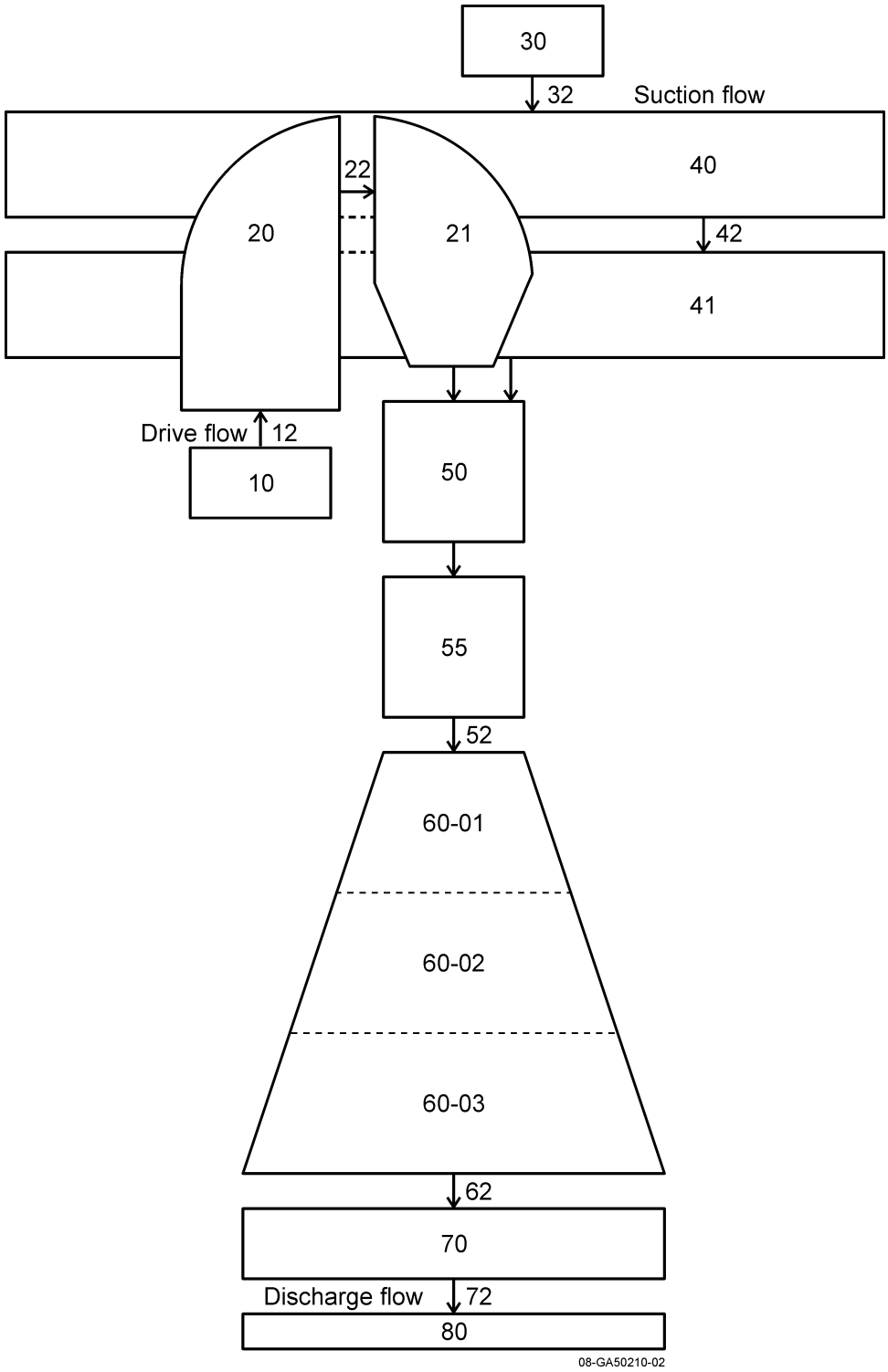

Figure 4.21-5. RELAP5-3D nodalization for the 1/6-scale jet pump test.

Table 4.21-1. Jet pump input model loss coefficients.

"From" Volume	"To" Volume	Forward Loss Coefficient	Reverse Loss Coefficient
20-01	21-01	0.42	0.42
21-01	50-01	0.0	0.238
41-01	50-01	0.02	1.0
50-01	55-01	0.07	0.07
55-01	60-01	0.0919	0.0337

4.21.4 Data Comparisons and Results

RELAP5-3D calculations were performed at a boundary pressure of 7.585 MPa and a temperature of 555 K. Both forward and reverse drive flows of 4.1 l/s were modeled. With the drive flow held constant, the suction flow was varied from -8.1 to 14.2 l/s in increments of about 1.0 l/s. All of the calculations were run with a requested time step of 0.05 s. To check for any pressure or temperature sensitivity in the calculations, a forward case was also run at a pressure of 1.0 MPa and a temperature of 310 K. The results of these two forward flow calculations are presented in Figure 4.21-6, where it is seen that there was almost no difference between the two calculations.

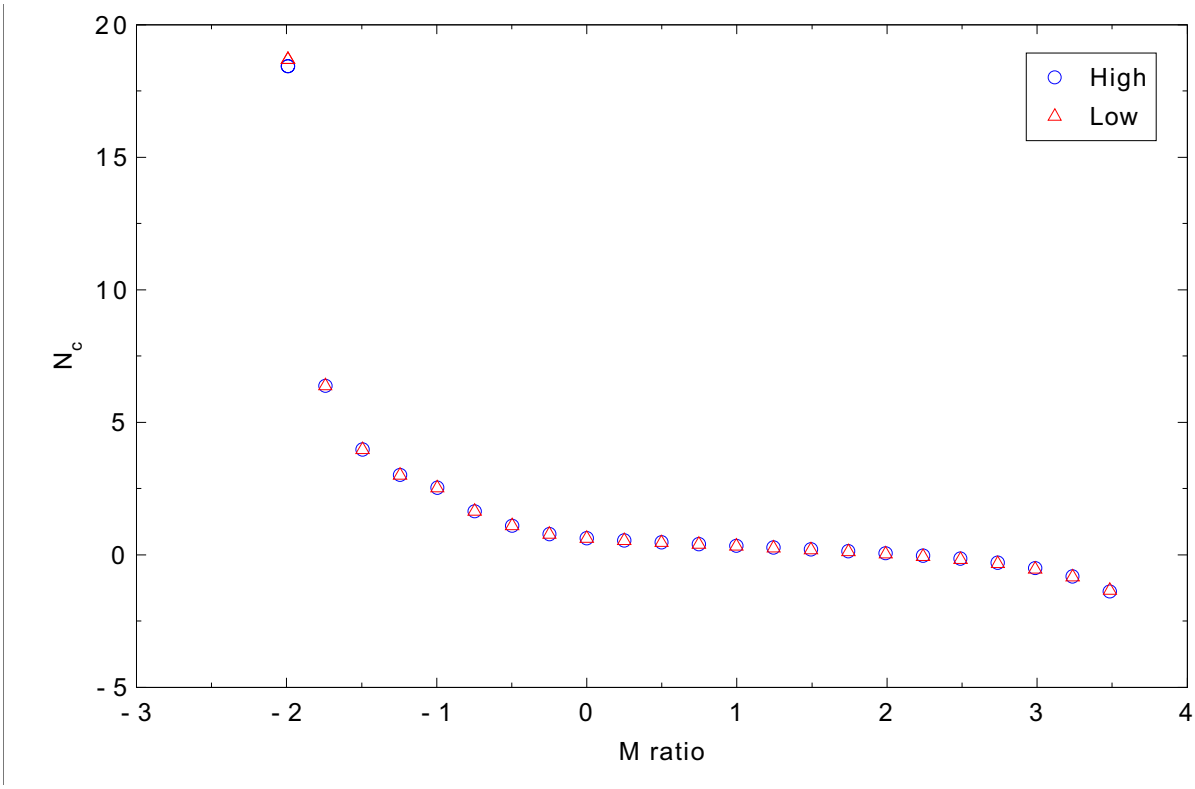

Figure 4.21-6. Calculated flow parameters for forward drive flows at high and low pressure and temperature for the 1/6-scale jet pump case.

Comparisons of measured and calculated high pressure forward drive flow test points are provided in Figure 4.21-7. The figure includes 76 measured values from all of the pressure ranges with error bars indicating the 2-sigma uncertainty. The code-calculated values of the head ratio are in generally excellent agreement with the data. Above a flow ratio of about 2.5, the calculation starts to deviate from the measurements, dropping to values below the measurement uncertainties near a flow ratio of 2.8. There was no difference between the semi- and nearly-implicit calculations.

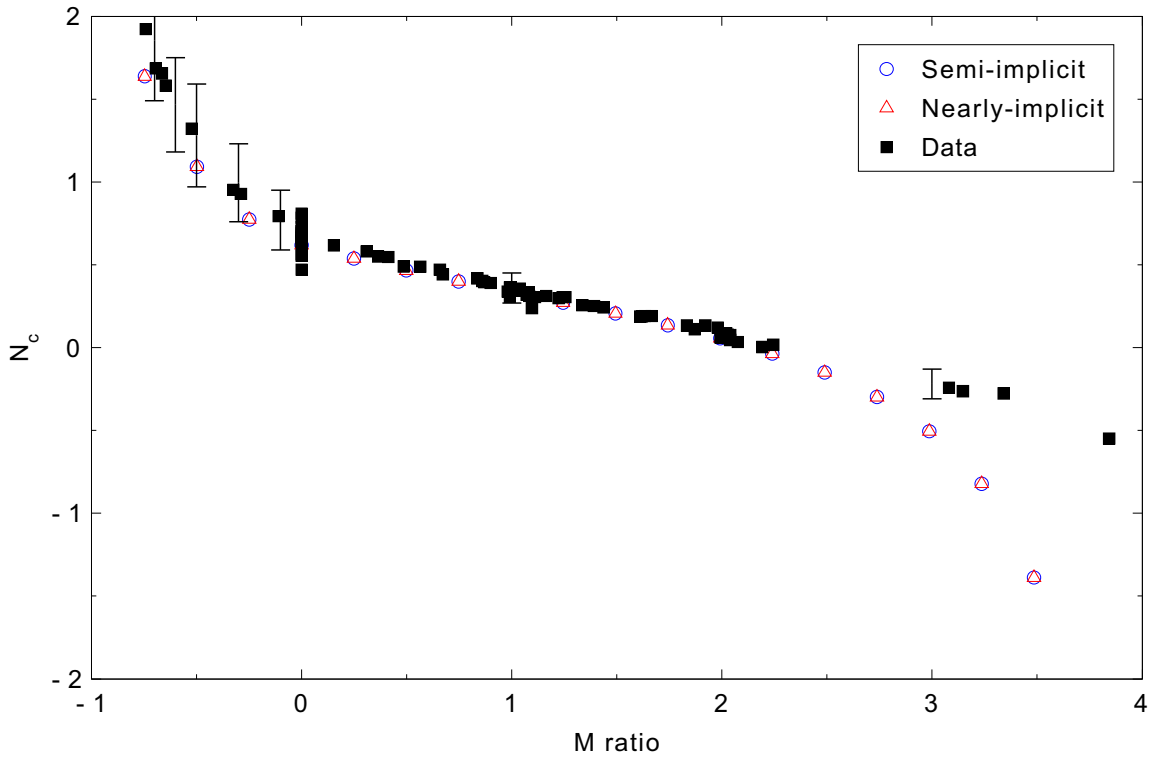

Figure 4.21-7. Measured and calculated flow parameters for forward drive flows for the 1/6-scale jet pump case.

Figure 4.21-8 presents comparisons of measured and calculated reverse drive flow test points. The figure includes 99 measured values with error bars indicating the 2-sigma uncertainty; the uncertainty values seem unrealistically small for values of M less than about 0.5. The code-calculated values of the head ratio are in excellent agreement with the data for flow ratios greater than -2.0. Below this, the RELAP5-3D calculation diverges from the experiment data, predicting higher head ratios than were measured. There was no difference between the semi- and nearly-implicit calculations.

4.21.5 Conclusions and Assessment Findings

The RELAP5-3D calculations are judged to be in reasonable agreement with the measured data. For most of the measurement ranges, the code predictions were in excellent agreement with the data. However, for forward drive flows with flow ratios above 3.0, and for reverse drive flows with flow ratios below -2.5, the calculations were outside the measurement uncertainties, and the trends were away from the data. Most of the data taken were within the range that the code was performing well, suggesting that the regions where the code predictions were suspect may be encountered only in extreme cases. However, users should be aware of the potential problem. Improved agreement in specific regions of the curves could be achieved

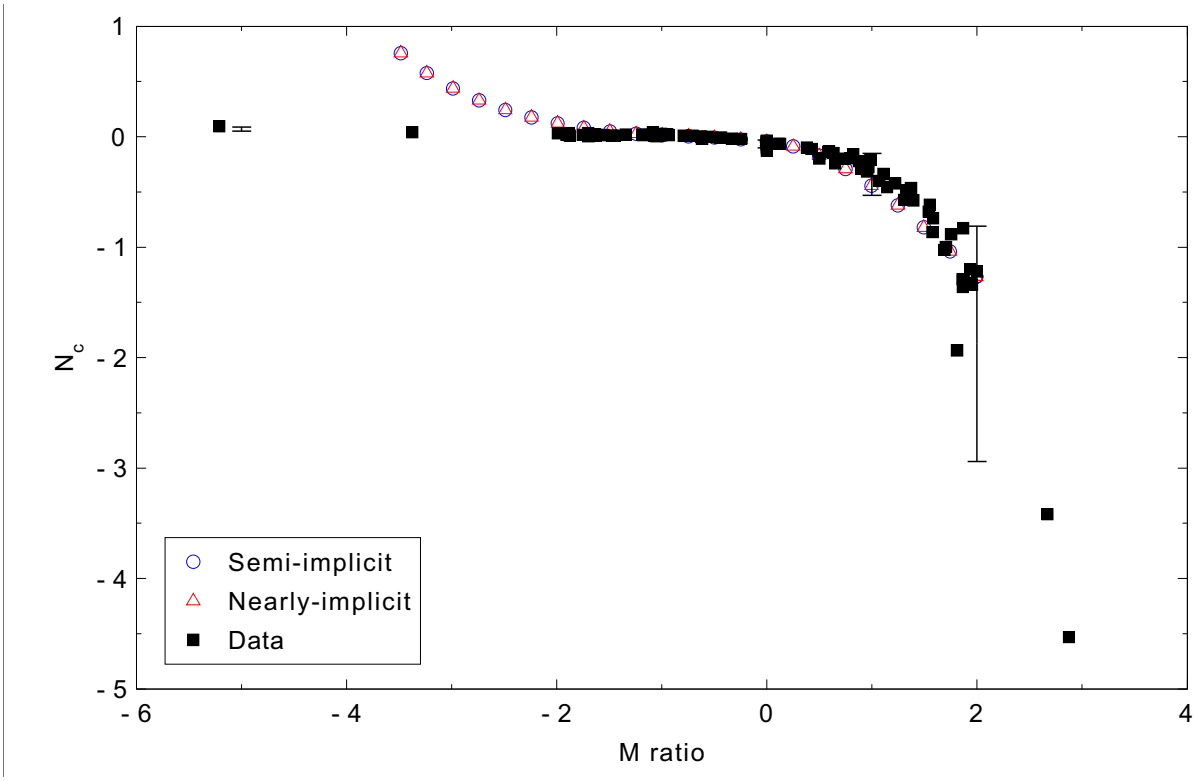

Figure 4.21-8. Measured and calculated flow parameters for reverse drive flows for the 1/6-scale jet pump case.

by altering the various loss coefficients in the input model, although that would likely result in worse predictions in other regions.

4.21.6 References

4.21-1. H. S. Crapo, *LOFT Test Support Branch Data Abstract Report One-Sixth Scale Model BWR Jet Pump Test*, EGG-LOFT-5063, November 1979.

4.21-2. G. E. Wilson, *INEL One-sixth Scale Jet Pump Data Analysis*, EGG-CAAD-5357, February 1981.

5. INTEGRAL EFFECTS CASES

The integral effects cases compare RELAP5-3D code calculations with data from large experimental facilities. These cases are generally of greater interest because they provide an indication of how well the code performs overall in modeling transients with a large number of phenomena. Seven specific tests were included in the assessment:

- Loss-of-Fluid Test (LOFT) Experiment L3-7, which simulated a 1-in. cold leg break
- Rig of Safety Assessment (ROSA)-IV Test SB-CL-18, which simulated a 6-in. cold leg break
- Semiscale Natural Circulation Tests 1, 2, 3, and 10
- Loop Blowdown Investigations (LOBI) Test A1-04R, which simulated a double-ended cold leg break
- LOFT Experiment L2-5, which simulated a double-ended cold leg break.

Details of these assessments are provided in the rest of this chapter. Two different RELAP5-3D input models were used to simulate the LOFT L2-5 experiment, one with one-dimensional components and one with multi-dimensional components in the reactor vessel.

5.1 LOFT Experiment L3-7

Experiments were performed in the 1970s and 1980s in the Loss-of-Fluid Test (LOFT) facility, a 50 MWt power/volume-scaled nuclear reactor designed to investigate the response of a commercial pressurized water reactor (PWR) to loss-of-coolant accidents (LOCAs) and operational transients. Experiment L3-7 simulated a 1-in. diameter cold leg break with a maximum core linear heat generation rate of 52.8 kW/m (16.1 kW/ft).

5.1.1 Code Models Assessed

As an integral test facility, multiple code models are addressed. For this small break LOCA, the interest is in the overall system response, not that of the core, as there is no heatup. Parameters of significance are the break flow rates, system pressure, emergency core coolant (ECC) system response, and system mass distribution.

5.1.2 Experiment Facility Description

The LOFT facility is described in detail in Reference 5.1-1. The nuclear core was 1.68 m high with a 0.61-m diameter. The core contained nine fuel assemblies and 1,300 fuel rods that were representative of a commercial PWR. As shown in Figure 5.1-1, the facility contained two primary coolant loops. The intact loop represented three loops of a commercial plant, containing a hot leg, steam generator, cold leg, two primary coolant pumps, and the pressurizer. The broken loop represented a single loop, and included steam generator and primary coolant pump simulators, which modeled the flow resistance of these components. The broken loop could be configured to model either hot or cold leg breaks. Quick-opening blowdown valves (adjustable opening times of approximately 20 to 50 ms) simulated the initiation of primary coolant pipe ruptures, and orifices were used to model different break sizes. The break effluent was collected in a blowdown suppression tank.

The ECC system included a pumped high-pressure injection system (HPIS), a nitrogen-pressurized accumulator, and a pumped low-pressure injection system (LPIS). The accumulator was equipped with an adjustable height standpipe, which allowed the effective liquid volume to be varied between experiments. The ECC system was designed to allow injection to the intact loop hot leg, intact loop cold leg, reactor vessel upper plenum, lower plenum, or downcomer.

The LOFT facility was extensively instrumented. Fluid pressure, temperature, and flow rate were measured at key locations in the primary coolant, secondary coolant, and ECC systems. Three-beam gamma densitometers were used to measure fluid density at two locations in the intact and broken loops. Thermocouples measured fuel rod cladding and support tube temperatures at 196 core locations. Several fuel rod internal temperatures (fuel and plenum) were also measured. Neutron flux was measured with four fixed detectors, which were designed to measure power transients, and four traversing in-core probes, which were designed to measure steady-state axial flux distributions at four different locations in the core.

Experiment L3-7 simulated a 1-in. diameter break in a cold leg pipe and investigated potential plant recovery methods. The break orifice was located upstream of the quick-opening blowdown valve. For this experiment, the primary coolant pumps were manually tripped following scram. HPIS injection to the intact loop cold leg was the only operating ECC system. HPIS and auxiliary feedwater flows were both

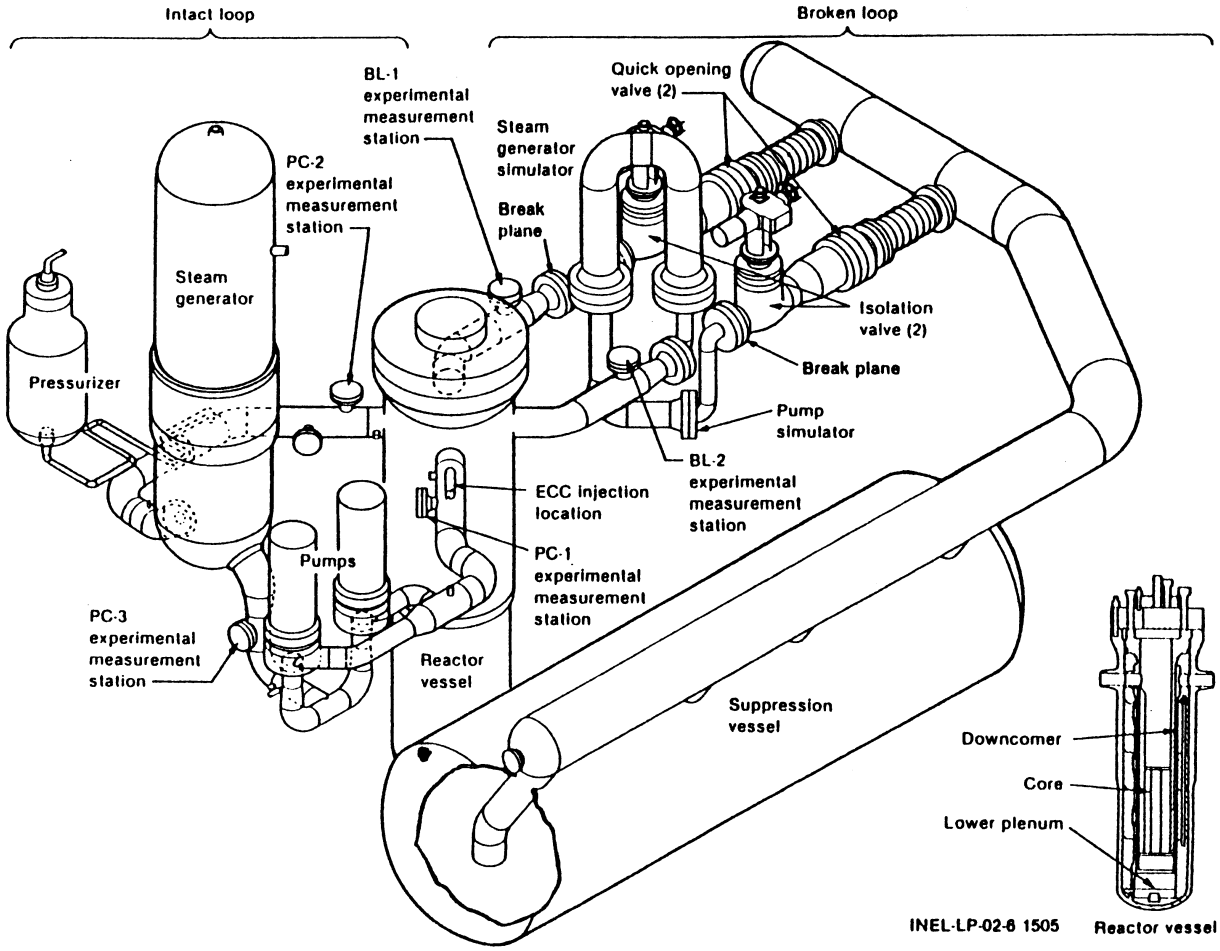

Figure 5.1-1. Schematic of the LOFT facility.

terminated near 1,800 s. Code-to-data comparisons presented below address only the first 2,000 s of the experiment, which was before most of the simulated operator or recovery actions were initiated. Reference 5.1-2 presents the data from this experiment. Reference 5.1-3 noted that there was steam leakage from the secondary side of the steam generators through the steam control valve during the experiment. The temperature response in the broken loop hot and cold legs also indicated that there was flow through the reflood assist bypass line during the test; this is a pipe with normally closed valves connecting the broken loop hot and cold legs.

5.1.3 Input Model Description

The RELAP5-3D input model used for the L3-7 simulation is shown in Figure 5.1-2. It includes the reactor vessel, the intact and broken loops, the intact loop steam generator secondary side, the pressurizer, and the ECC systems. The model contains 131 control volumes, 137 junctions, and 138 heat structures.

The reactor vessel includes representations of the downcomer (Component 210), lower plenum (Components 215-220), core inlet (Component 225), core (Component 230), and upper plenum (Components 240-260). The core was modeled with six axial nodes. Two core bypass paths were modeled:

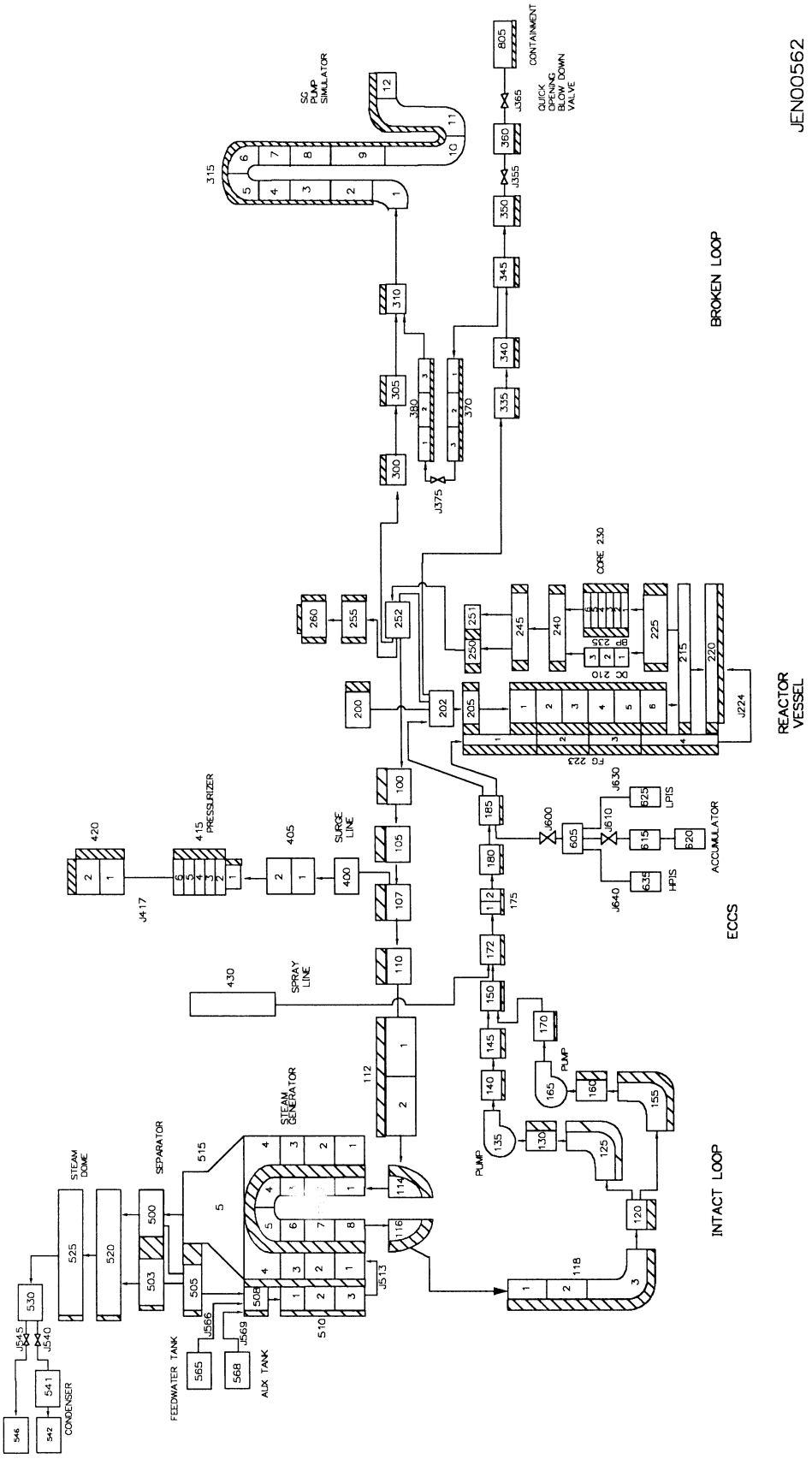

Figure 5.1-2. RELAP5-3D nodalization for the LOFT facility Experiment L3-7.

the gaps between the core filler blocks and the flow skirt (Component 235), and the leakage between the cold leg and hot leg nozzles. The gap between the filler plates in the downcomer (Component 223) was also modeled.

The intact loop model includes the hot leg, steam generator, two primary coolant pumps, and the cold leg. The pressurizer is connected to the intact loop hot leg, with spray flow from the cold leg. Charging and letdown flows are connected to the cold leg during steady state initialization only. The steam valve at the steam generator outlet (Component 540) was modeled with a minimum flow area of 0.00672 m^2 to simulate the steam leak during the experiment.

The broken loop model includes the hot and cold legs, the reflood assist bypass system piping, and the steam generator/pump simulator, which was attached to the hot leg for this cold leg break experiment. The break orifice was located at the junction between Components 345 and 350. A user-input loss coefficient of 1.0 was used at the break, and critical flow discharge coefficients of 1.2 were used for both subcooled liquid and two-phase flow. Loss coefficients of 50 were used for the reflood assist bypass valves (Component 375), which provided a reasonable simulation of the leakage through these valves during the blowdown.

The ECC systems modeled were the HPIS, accumulator, and LPIS. These were all connected to the intact loop cold leg for this experiment.

Heat structures in the reactor vessel represented the vessel itself, the fuel rods, filler blocks in the core and downcomer, the core support barrel, and other internal structures. Intact loop heat structures included the piping and steam generator tubes, along with the pressurizer vessel. The piping, pump and steam generator simulator walls were modeled in the broken loop. Heat structures were also used to model the steam generator shell. An environmental heat loss of 200 kW was modeled: 6 kW from the pressurizer, 174 kW from the rest of the primary coolant system, and 20 kW from the steam generator.

5.1.4 Data Comparisons and Results

A steady state calculation was performed to establish the desired initial conditions in the RELAP5-3D model. Table 5.1-1 provides a comparison of the measured and calculated initial and boundary conditions for Experiment L3-7; the core power was the only fixed value. All of the calculated values were in good agreement with the measurements except for the broken loop hot leg temperature, which was about 7 K lower than the data, and the feedwater flow rate, which was about 8% low. The low feedwater flow is not expected to have a noticeable effect on the simulation. Both the broken loop hot and cold leg temperatures were reset to the nominal measured values at the beginning of the transient calculation.

Table 5.1-2 provides a partial sequence of events for Experiment L3-7. The experiment was initiated by opening the quick-opening blowdown valve in the broken loop cold leg. The reactor scrammed on low hot leg pressure at 36 s. When the control rods were fully inserted, the primary coolant pumps were manually tripped. Natural circulation flow through the intact loop was established shortly after the pump coastdown was completed. HPIS flow to the intact loop cold leg was initiated automatically on low hot leg pressure (13.16 MPa), and was tripped manually at 1,805 s to allow the primary coolant system mass inventory to drop for the next portion of the experiment. Auxiliary feedwater flow to the steam generators was provided between 75 and 1,800 s. The experiment then continued until nearly 30,000 s, with the

Table 5.1-1. LOFT Experiment L3-7 initial conditions.

Parameter	Measured Value	Calculated Value
Intact Loop		
Mass flow (kg/s)	481.3 ± 6.3	481.3
Hot leg pressure (MPa)	14.90 ± 0.25	14.91
Cold leg temperature (K)	556 ± 3	556.0
Hot leg temperature (K)	576.1 ± 0.5	575.0
Pressurizer		
Liquid level (m)	1.10 ± 0.02	1.10
Broken Loop		
Cold leg temperature (K)	557.7 ± 2.5	555.9
Hot leg temperature (K)	561.4 ± 2.5	554.8
Reactor Vessel		
Core power (MW)	49 ± 1	48.9
Steam Generator		
Pressure (MPa)	5.576 ± 0.012	5.42
Liquid level (m)	3.20 ± 0.06	3.20
Feedwater flow rate (kg/s)	28.0 ± 0.4	25.6

objectives of establishing reflux cooling in the hot legs and investigating possible mitigating actions the operators could take in recovering from the small break LOCA.

Figures comparing the measured and calculated response of the LOFT system during the experiment are provided below. Both the semi- and nearly-implicit transient calculations used a requested time step size of 0.025 s. Data presented are from the NRC Data Bank. Measurement uncertainties provided on the figures were obtained from Reference 5.1-2 and generally represent the uncertainty for the largest measured value shown in the figure.

The measured and calculated reactor vessel upper plenum pressures are presented in Figure 5.1-3. In the experiment, the depressurization rate increased significantly when the reactor scrammed at 36 s because less heat was being added to the system. The depressurization rate then slowed when the primary coolant pumps were tripped near 39 s, as less energy was being removed through the steam generator as the flow coasted down. The depressurization rate increased again after the pressurizer emptied at 264 s, then decreased significantly when the pressure reached the saturation pressure for the liquid in the upper plenum and boiling began. The pressure decreased slightly faster after 1,100 s, the consequence of steam starting to flow out the break. The calculated pressure exhibited most of the same behavior as the experiment. The initial depressurization was slightly faster, causing an earlier scram. The upper plenum

Table 5.1-2. LOFT Experiment L3-7 sequence of events.

Event	Time after Experiment Initiation (s)
Experiment initiated	0.0
Reactor scrammed	36.0 ± 0.1
Control rods reached bottom	38.1 ± 0.1
Primary coolant pumps tripped	39.3 ± 0.5
Primary coolant pump coastdown completed	56.2 ± 0.1
Core natural circulation first indicated	60.8 ± 0.5
HPIS injection initiated	65.6 ± 0.1
Steam generator auxiliary feedwater initiated	75 ± 3
Pressurizer emptied	264 ± 7
Upper plenum reached saturation pressure	382 ± 6
End of subcooled break flow	1,037 ± 10
Steam generator auxiliary feedwater terminated	1,800 ± 5
HPIS flow terminated	1,805.3 ± 0.1

reached saturation a little earlier, after which the pressure decreased at a steady rate; steam was not calculated to flow through the break until after 1,800 s, after the HPIS flow was terminated. As the data trends and phenomenology were captured, and the calculation was within or near the data uncertainty bands through most of the simulation, the predicted pressure is judged to be in reasonable agreement with the experiment data.

Pressures in the steam generator secondary side are shown in Figure 5.1-4. In the experiment, there was leakage through the steam valve, which caused the pressure to decrease through most of the transient. Without the leakage, the pressure would have been expected to be maintained by safety relief valve cycling. Since there was no measurement of the leak rate, the steam control valve in the RELAP5-3D model was adjusted until it provided a reasonable approximation of the measured pressure response. Because the model was “tuned”, no judgment of the code prediction of the steam generator pressure is made. The leveling off in the measured pressure near 1,200 s appears to be the result of more steam entering the steam generator tubes as the primary system depressurized more rapidly. As this steam condensed, the heat transfer to the secondary side increased, delaying the continued pressure decrease for about 150 s. This behavior was not observed in the code calculation.

The pressurizer levels are compared in Figure 5.1-5. For this small break LOCA, the pressurizer level response is basically a reflection of the break flow rate, as the liquid flowing out the break is replaced in the primary coolant system by that draining from the pressurizer. The calculated level tailed off just before emptying, while the measured level did not. The predicted pressurized level is judged to be in reasonable agreement with the data.

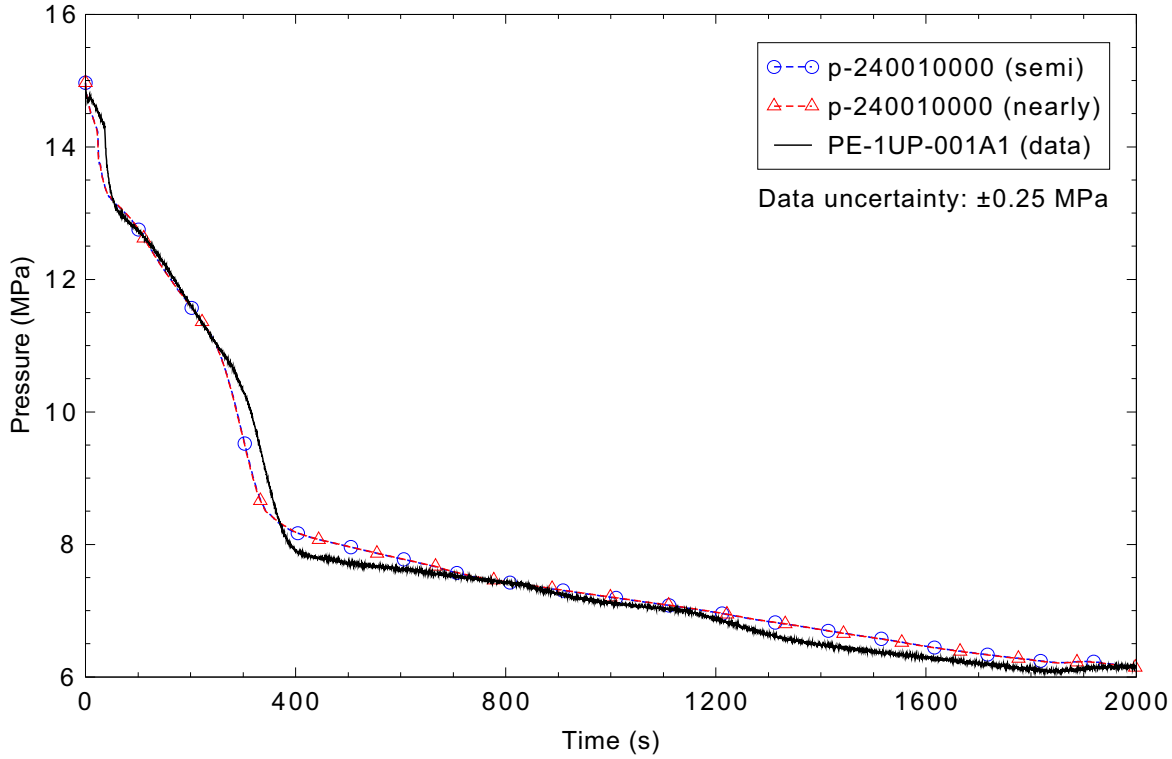

Figure 5.1-3. Measured and calculated reactor vessel upper plenum pressure for LOFT Experiment L3-7.

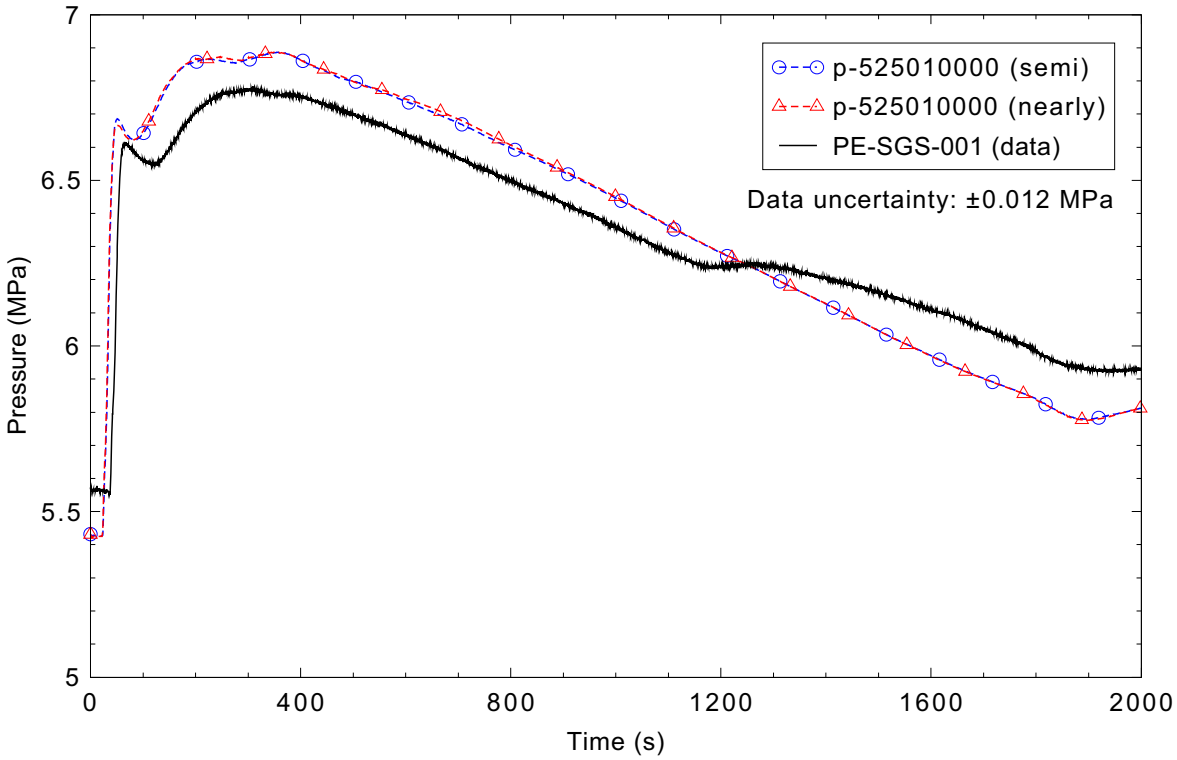

Figure 5.1-4. Measured and calculated steam generator secondary pressure for LOFT Experiment L3-7.

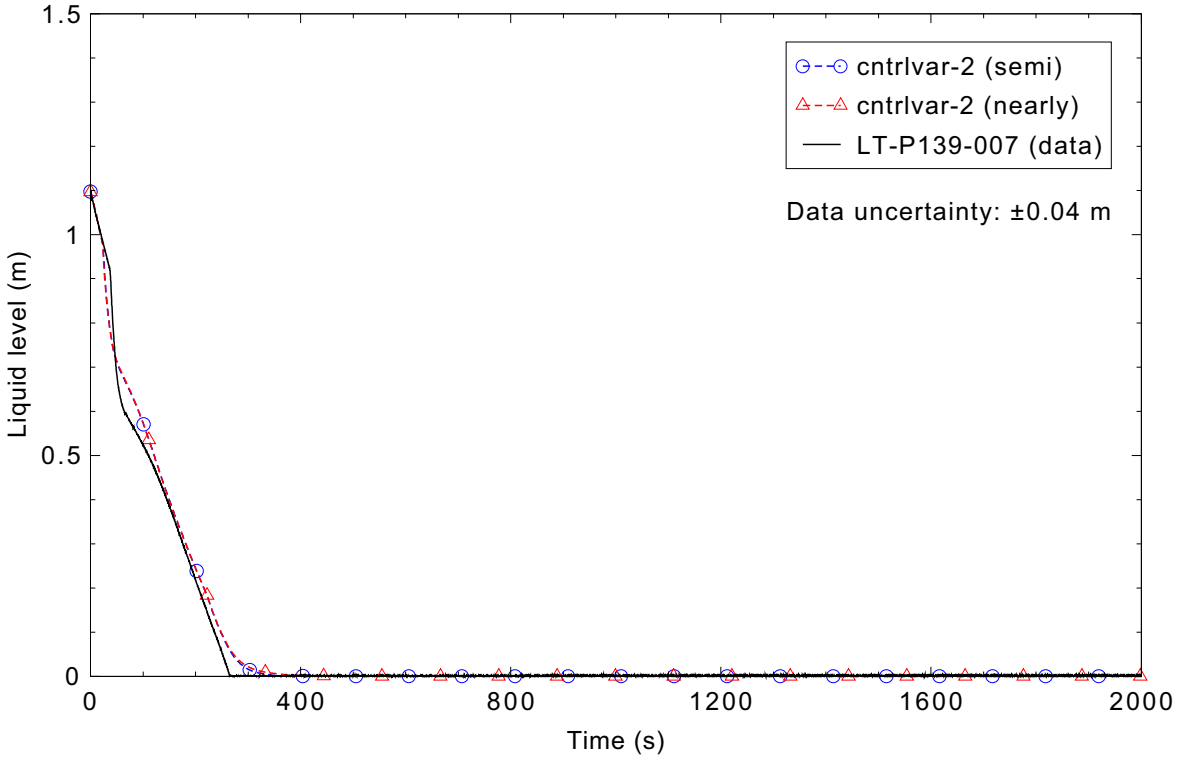

Figure 5.1-5. Measured and calculated pressurizer liquid level for LOFT Experiment L3-7.

Figure 5.1-6 presents the measured and calculated break flow rates. The measured data are a computed parameter based on the pressurizer level decrease during the first 25 s, a differentiation based on the level increase in the blowdown suppression tank from 75 to 1,800 s, and linear interpolation between 25 and 75 s. While the integral break flow is likely reasonably measured, differentiating the tank level measurement results in flow rates that are questionable. The code appears to be over predicting the break flow until about 300 s, then under predicting the flow after 400 s, even with a discharge coefficient of 1.2. The good prediction of the pressurizer level response indicates that the early break flow is not over predicted, but is reasonably simulated. The late appearance of steam at the break tends to confirm that the calculated break flow is too low after 400 s, keeping more liquid inventory in the primary coolant system. The lower calculated break flow between 1,200 and 1,400 s reflected a small amount of steam (α<0.05%) at the break. The brief increase around 1,280 s was caused by the flow regime changing to horizontally stratified for about 20 s, so that only liquid was flowing through the centrally-located break. Overall, the calculated break flow is judged to be minimal.

Figure 5.1-7 presents the fluid densities in the broken loop cold leg. There is a gap in the data between 1,100 and 1,400 s, during which a two-phase mixture appeared; based on the pressure response, this happened around 1,100 s. The density then slowly decreased until 1,800 s, when the termination of the HPIS flow allowed the liquid inventory in the pipe to be depleted more rapidly. The calculation was in excellent agreement with the data until the two-phase mixture appeared. Since the break flow rate was under predicted after about 400 s, more liquid was retained in the primary coolant system, and significant vapor did not appear in the cold leg until the HPIS flow was terminated. The calculated response after 1,800 s was a rapid decrease in density, as was measured. The overall prediction is judged to be in minimal

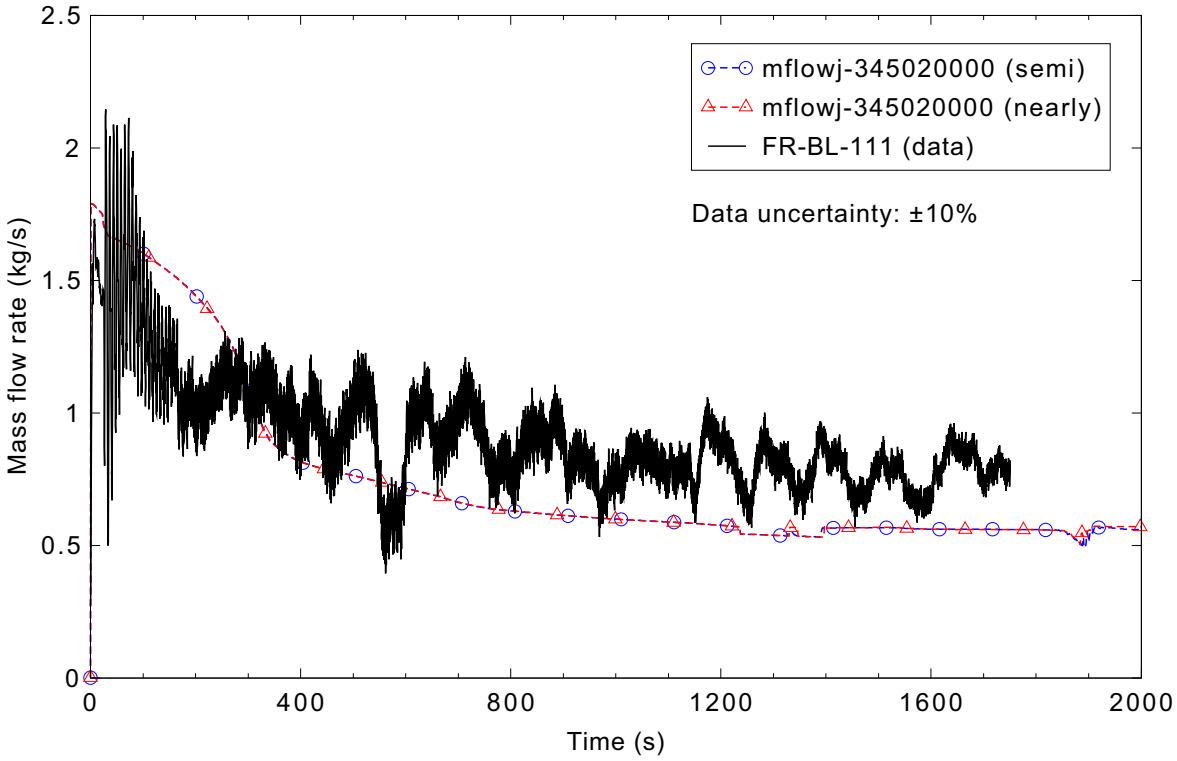

Figure 5.1-6. Measured and calculated break flow rate for LOFT Experiment L3-7.

agreement with the data because of the absence of two-phase fluid until after the HPIS flow was terminated.

Fluid densities in the intact loop cold leg are presented in Figure 5.1-8. An average density was not computed for the experiment data, so the available chordal densities are presented: chord C was near the top of the pipe, and chord B ran diagonally near the middle. Steam appeared in the cold leg by 900 s in the experiment. In the calculation, the combination of the low break flow and HPIS injection kept the cold leg liquid-filled. The predicted cold leg density is judged to be in minimal agreement with the data.

Figure 5.1-9 shows the fluid density in the intact loop hot leg. The density increased shortly after the transient began, as the power decrease associated with reactor scram reduced the temperature of the liquid entering the hot leg. The density quickly dropped again as natural circulation flow was established. The decrease in measured density near 300 s was probably steam from the pressurizer. The general decrease in density as vapor flowed from the reactor vessel started around 800 s. The relatively slight decrease in density indicates that the vapor flowed through the pipe, rather than collecting and causing the pipe to drain. (The lack of noise in the data from ~1,100-1,400 s indicates there was a problem with the data during that time.) In the calculation, the early density increase and decrease were well predicted, although steam did not appear in the hot leg until 1,150 s. A very slow decrease in the density then occurred until the HPIS flow was terminated, after which the density decreased more rapidly. The calculation is judged to be in reasonable agreement with the data, as the major trends were captured (although the voiding was late) and the prediction was within or near the data uncertainty through most of the transient.

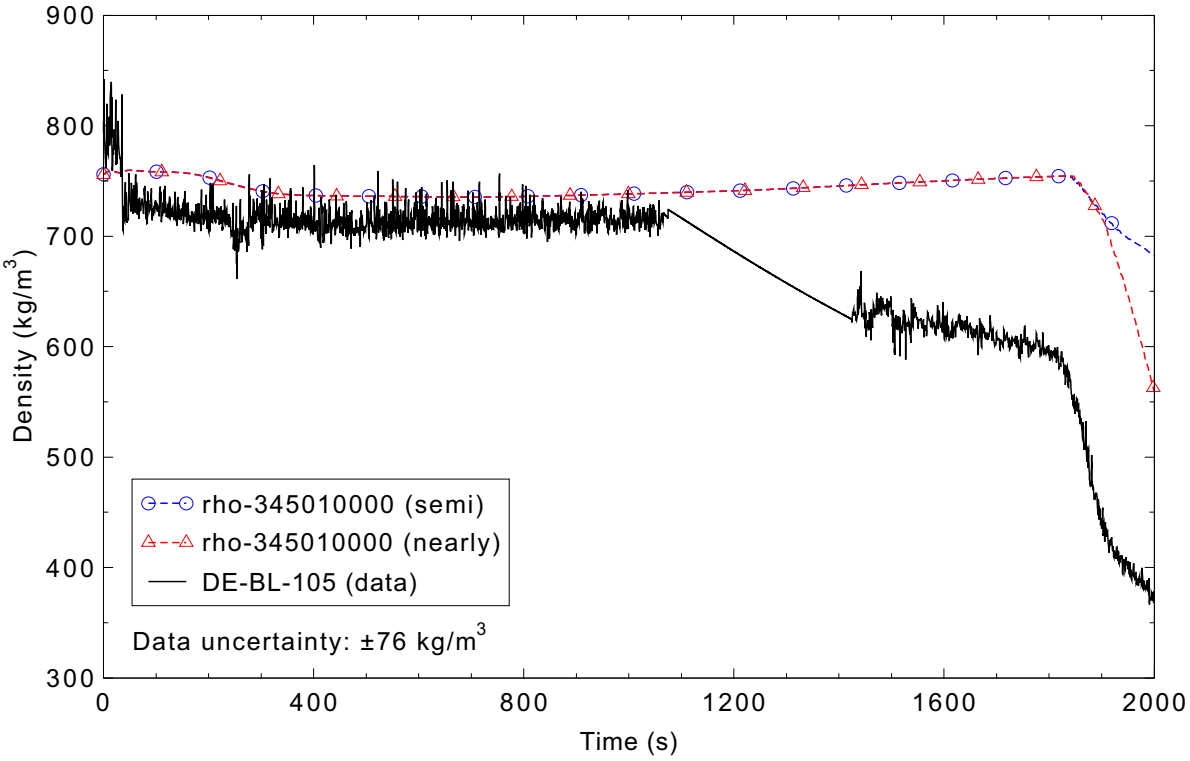

Figure 5.1-7. Measured and calculated broken loop cold leg fluid density for LOFT Experiment L3-7.

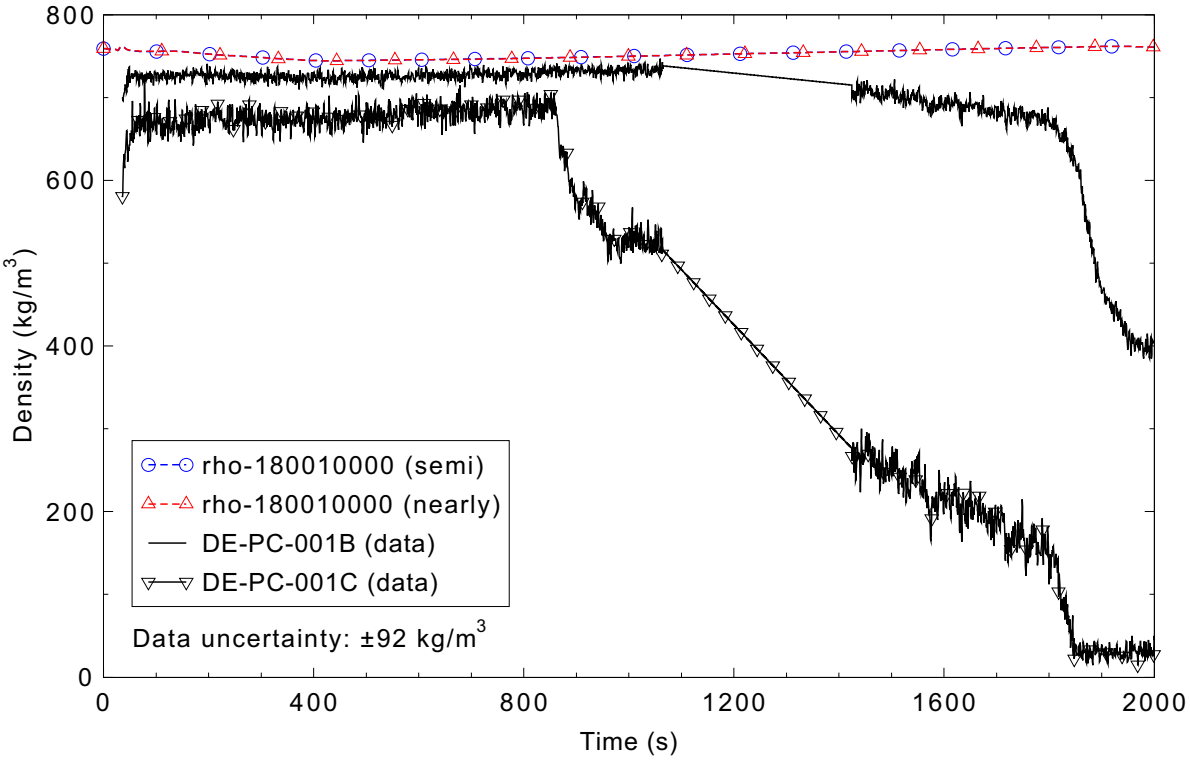

Figure 5.1-8. Measured and calculated intact loop cold leg fluid density for LOFT Experiment L3-7.

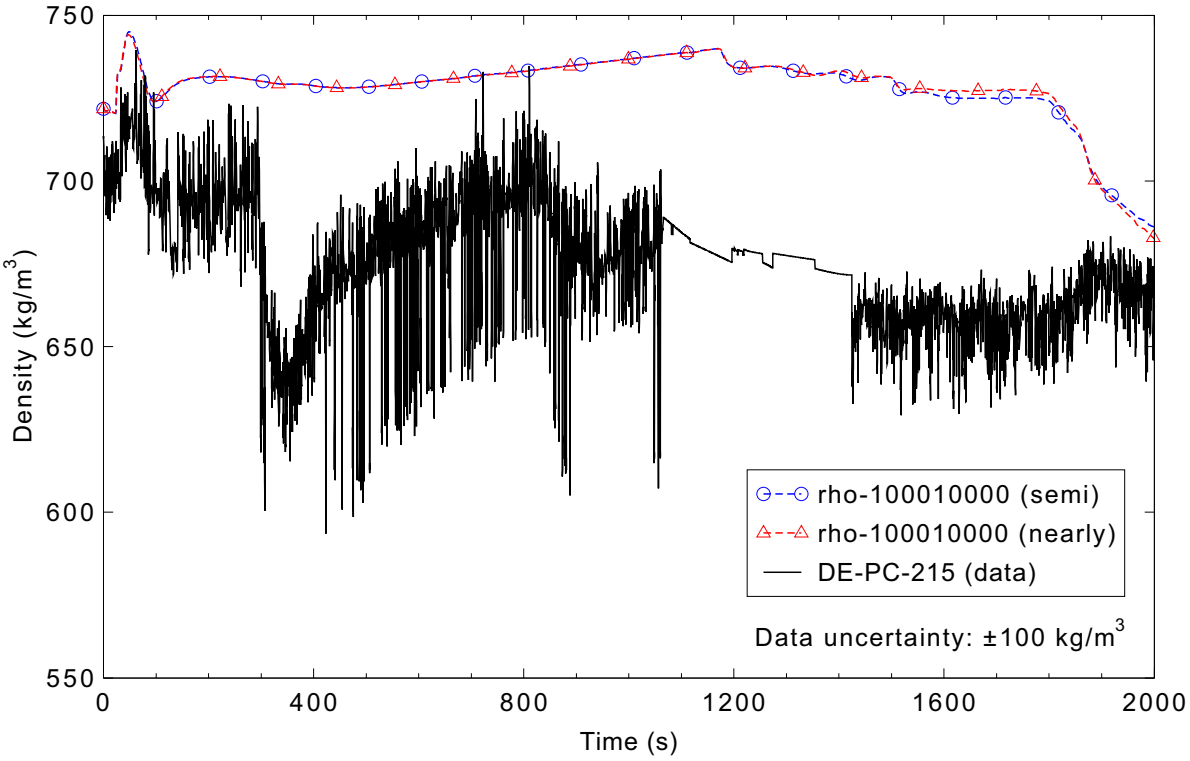

Figure 5.1-9. Measured and calculated intact loop hot leg fluid density for LOFT Experiment L3-7.

Coolant temperatures in the intact loop hot leg are shown in Figure 5.1-10. The initial conditions were different, in that the calculation was close to the nominal reported temperature and this particular thermocouple was near the high end of the uncertainty range. The temperature dropped early in the transient following the reactor scram, then increased again as natural circulation flow was established following the primary coolant pump trip and coastdown. The temperature then slowly decreased, generally following the saturation temperature, until about 1,800 s, when the auxiliary feedwater flow to the steam generator and the HPIS flow were terminated. This resulted in a steady increase in the measured temperature, but only a brief increase in the calculated temperature. The predicted temperature is judged to be in reasonable agreement with the data.

Coolant temperatures in the intact loop cold leg are presented in Figure 5.1-11. The initial temperature in the calculation was at the nominal reported cold leg temperature, while the data shown were at the high end of the reported uncertainty band. The temperatures dropped following scram, increased briefly as natural circulation was established, then dropped again. There was a gradual increase until about 400 s, then a slow decrease through most of the remainder of the transient. The temperature increased near 1,200 s in the experiment, the result of a slight increase in the natural circulation flow rate and an increase in the temperature of the liquid coming from the steam generator tubes. The calculated temperature was also influenced more by the cold HPIS injection than was the facility; this influence was confirmed by the increase in the calculated temperature when the HPIS flow was terminated shortly after 1,800 s. Note that the total temperature change was only about 10 K. The calculation is judged to be in reasonable agreement with the data until 1,200 s, then in minimal agreement.

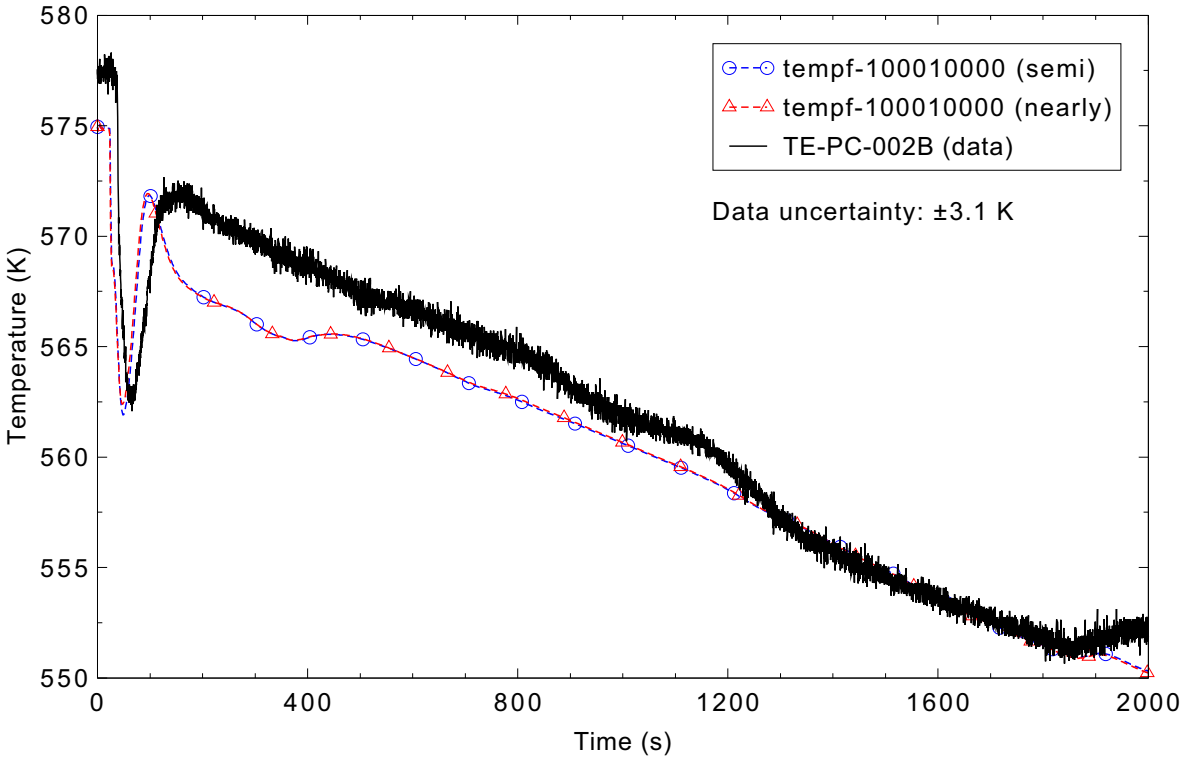

Figure 5.1-10. Measured and calculated intact loop hot leg fluid temperature for LOFT Experiment L3-7.

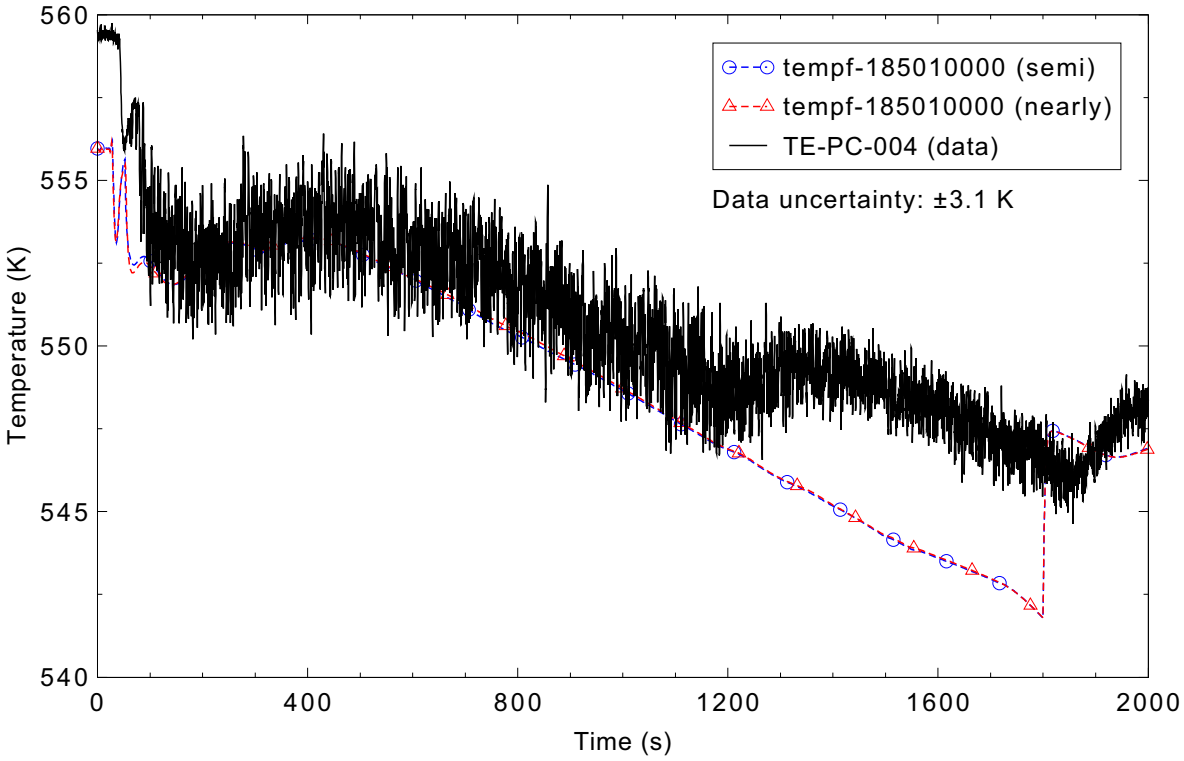

Figure 5.1-11. Measured and calculated intact loop cold leg fluid temperature for LOFT Experiment L3-7.

Fluid temperatures in the broken loop cold leg, upstream of the break, are shown in Figure 5.1-12. The general trend of the measured temperature was to increase during the first 1,100 s of the transient; this was followed by a decrease that followed the saturation temperature, as would be expected as a two-phase mixture was present (subcooled break flow ended at 1,037 s in the experiment). The fact that the temperature increased, while the intact loop cold leg temperature (Figure 5.1-11) decreased, indicates that hotter liquid from the broken loop hot leg was flowing through the reflood assist bypass lines into the broken loop cold leg. The calculated liquid temperature followed the general trend of the data, and was within the measurement uncertainty for most of the transient. It is therefore judged to be in reasonable agreement with the data.

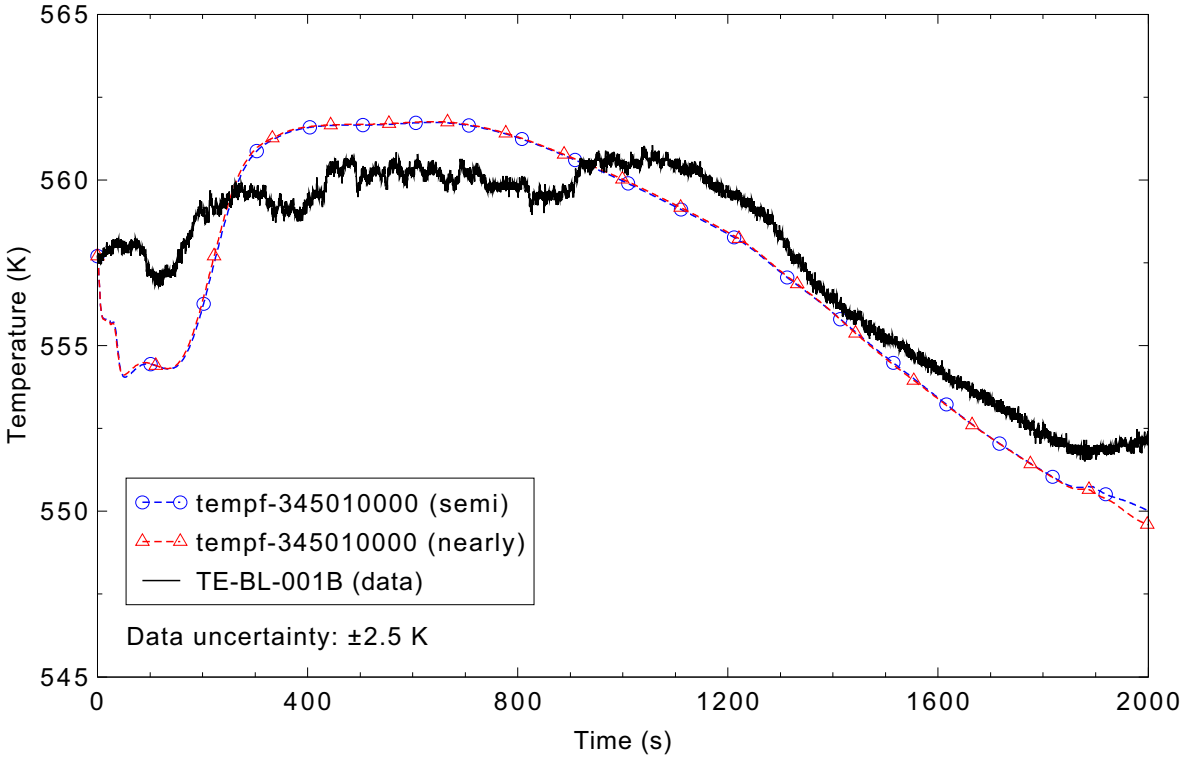

Figure 5.1-12. Measured and calculated broken loop cold leg fluid temperature for LOFT Experiment L3-7.

Fluid temperatures in the broken loop hot leg are compared in Figure 5.1-13. The slow decrease in the temperatures during the first 100 s indicates that this temperature is being affected by liquid flowing through the reflood assist bypass lines from the cold leg while the pumps are running. Once natural circulation cooling is established, the flow in these lines reverses, the broken loop hot leg temperature increases to the upper plenum temperature and then generally follows the saturation temperature through the rest of the transient. The response of the measurement to the flow changes is slower than in the calculation because the instrument is located in a more stagnant region of the hot leg, between the reflood assist bypass line and the quick-opening blowdown valve, whereas the calculated value shown is between the reactor vessel and the reflood assist bypass line. The calculated broken loop hot leg temperature is judged to be in reasonable agreement with the measured data.

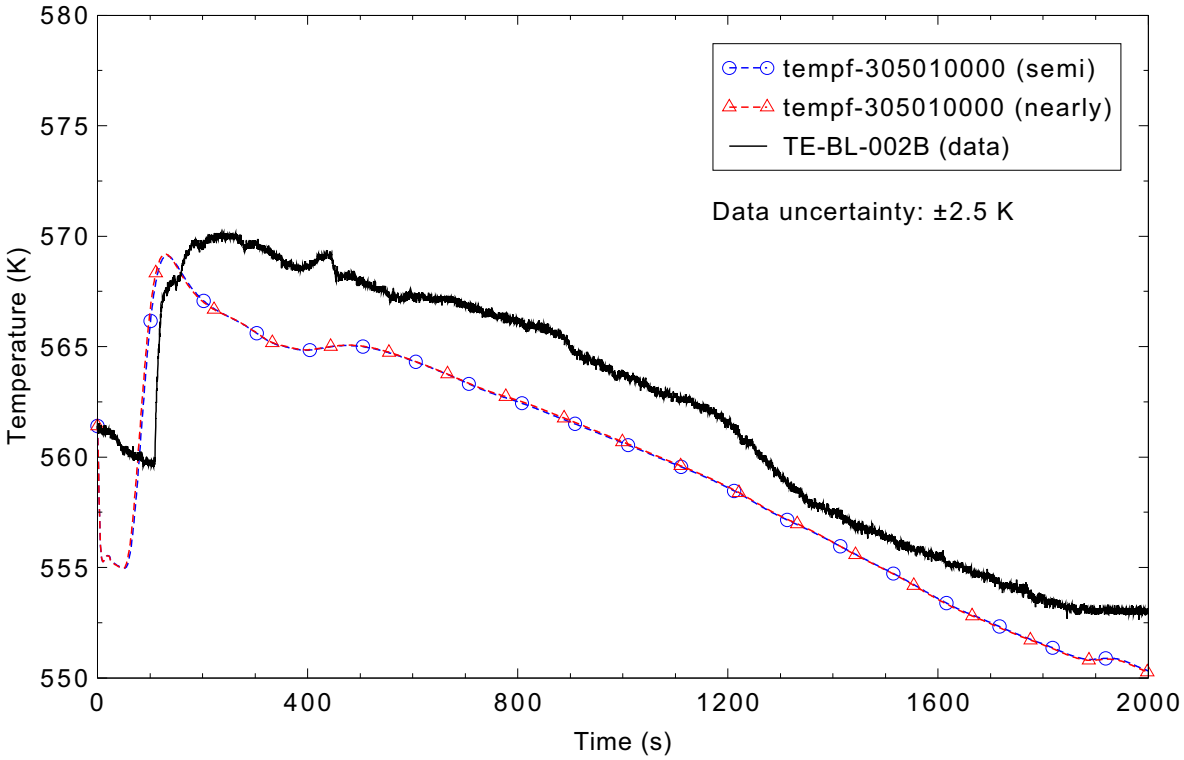

Figure 5.1-13. Measured and calculated broken loop hot leg fluid temperature for LOFT Experiment L3-7.

Fluid temperatures in the core inlet region are presented in Figure 5.1-14. The calculation did not show as much of an increase as the data from 50-100 s when natural circulation was being established. From 200-500 s, the measured temperature remained nearly constant while the predicted temperature increased slowly. Both the calculation and measurement then generally decreased until HPIS injection was terminated. As in the intact loop cold leg, the calculated core inlet temperature did not see the temperature increase near 1,200 s associated with the increase in natural circulation flow and was more influenced by the cold HPIS flow than was the measurement. The calculation is judged to be in reasonable agreement with the data until 1,200 s, as it was within the measurement uncertainty for most of the transient, but is judged to be minimal thereafter.

Figure 5.1-15 presents measured and calculated fluid temperatures in the reactor vessel upper plenum. The temperature decreased quickly following reactor scram, then increased as natural circulation flow was established. The temperature then decreased slowly, following the saturation temperature, until about 1850 s. The measured data then increased slightly before leveling off, while the calculated temperature increased very slightly before resuming its decrease. As the trends in the data were captured, and the calculation was within or near the data uncertainty band, the prediction is judged to be in reasonable agreement with the experiment.

Cladding surface temperatures near the top and bottom of the core are shown in Figures 5.1-16 and 5.1-17, respectively. Both temperatures decreased following reactor scram, increased as natural circulation was established, then decreased gradually until HPIS flow was terminated at 1,805 s. No core heatup was measured or predicted. The calculated core cladding surface temperatures are judged to be in reasonable agreement with the data.

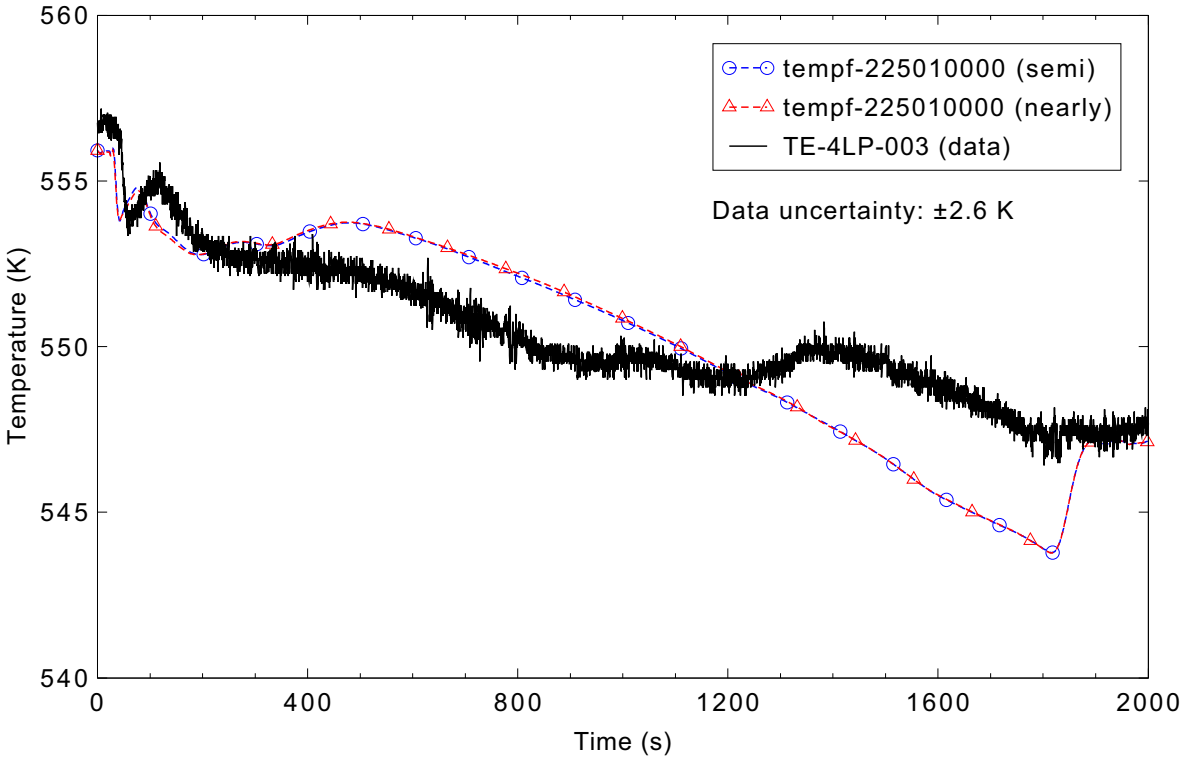

Figure 5.1-14. Measured and calculated core inlet fluid temperature for LOFT Experiment L3-7.

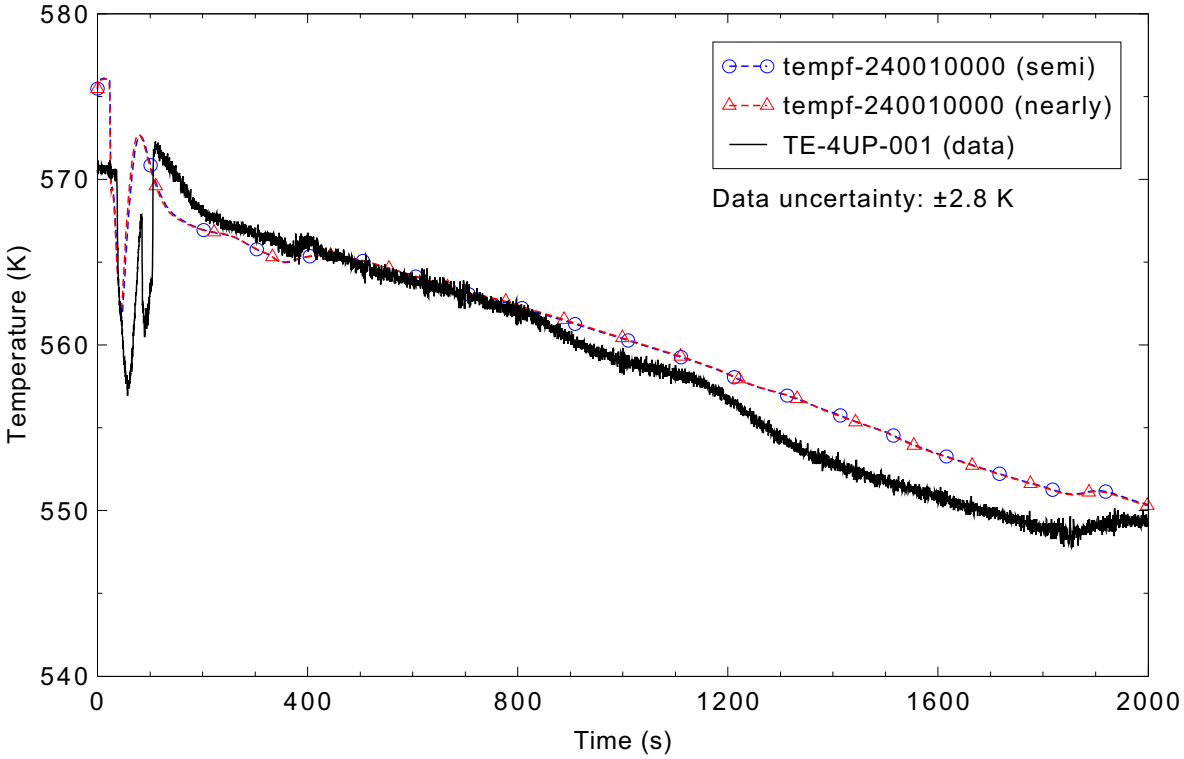

Figure 5.1-15. Measured and calculated reactor vessel upper plenum fluid temperature for LOFT Experiment L3-7.

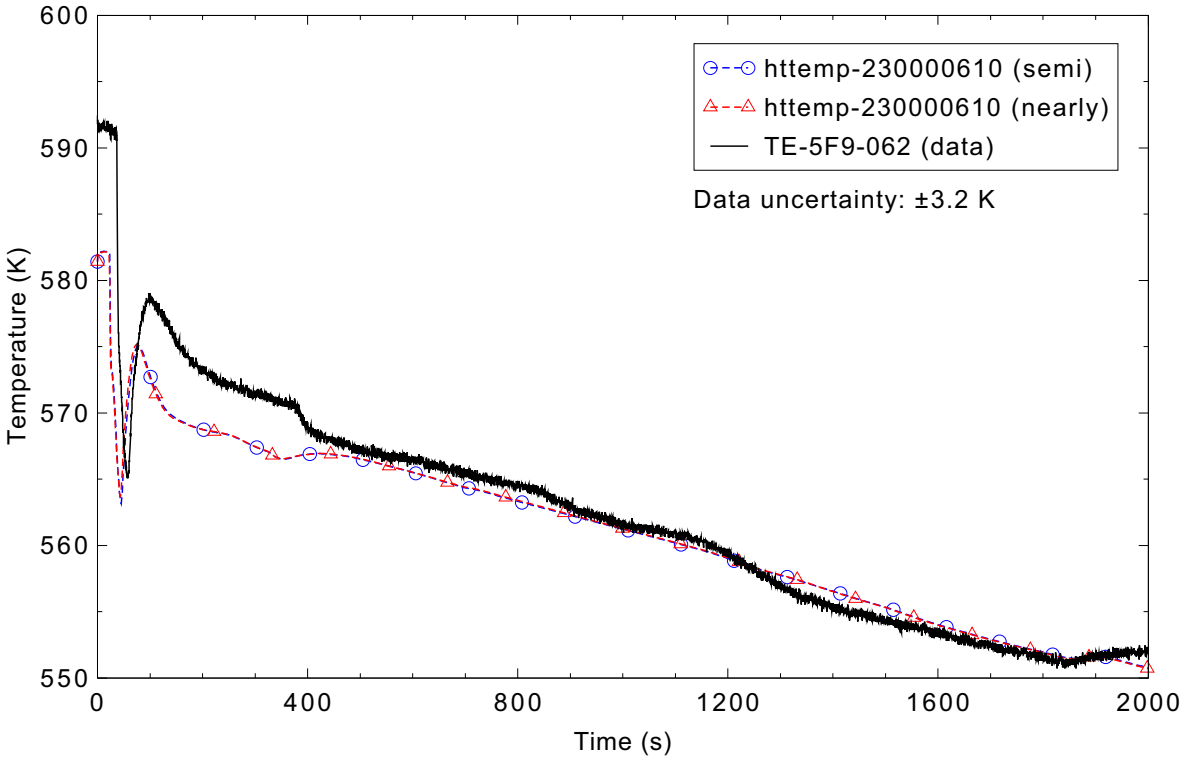

Figure 5.1-16. Measured and calculated fuel cladding surface temperature 1.57 m above the bottom of the fuel for LOFT Experiment L3-7.

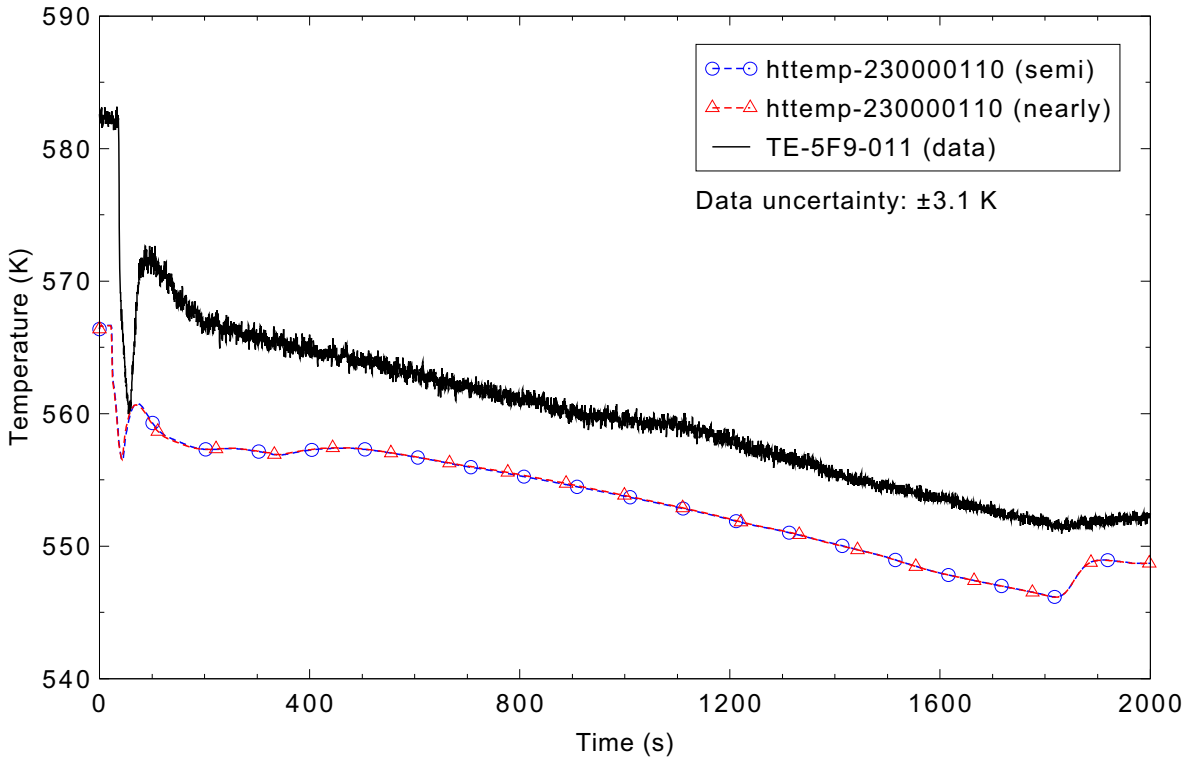

Figure 5.1-17. Measured and calculated fuel cladding surface temperature 0.28 m above the bottom of the fuel for LOFT Experiment L3-7.

Fluid velocities in the intact loop hot leg are shown in Figure 5.1-18. The calculated flow decreased earlier because the primary coolant pumps were tripped earlier. After that, the predicted flow rate was nearly identical to the measured value. There was a slight increase in the measured flow near 1,200 s. Increased steam flow into the steam generator tubes reduced the density on the upflow side of the tubes, which increased the density difference driving the natural circulation flow, causing the flow to increase. The hot leg fluid velocity is judged to be in excellent agreement with the data.

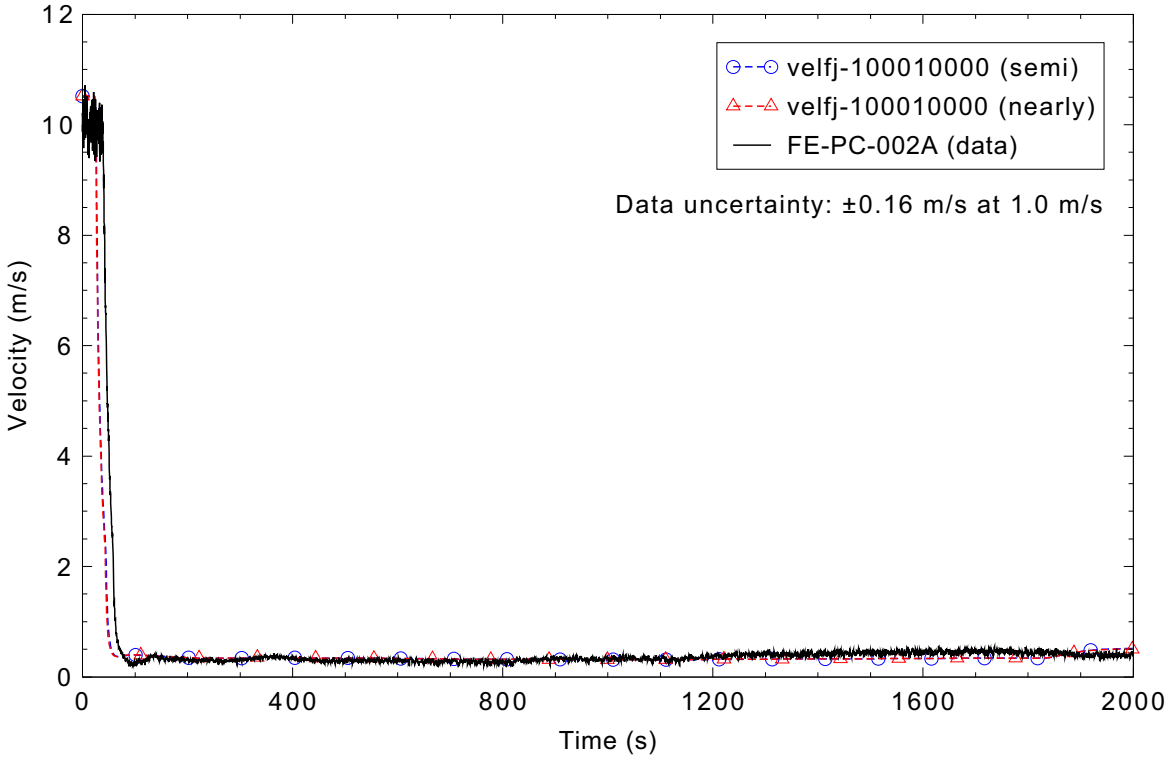

Figure 5.1-18. Measured and calculated hot leg fluid velocity for LOFT Experiment L3-7.

A comparison of the measured and calculated HPIS flow rates is provided in Figure 5.1-19. High pressure injection began a little earlier in the calculation, because the primary coolant system pressure was lower, allowing the trip setpoint to be reached earlier. The flow rates slowly increased as the transient progressed, reflecting the slowly decreasing primary coolant system pressure, until flow was terminated at 1,805 s. The calculation is judged to be in excellent agreement with the data.

5.1.5 Conclusions and Assessment Findings

Most of the small break phenomena were simulated well by the code. The primary coolant system pressure response, pressurizer liquid level, and cladding surface temperature calculations were reasonable. The coolant temperatures throughout the primary coolant system were judged to be reasonably simulated for most of the transient. Simulations of the HPIS flow and the fluid velocity in the hot leg were judged to be in excellent agreement with the experiment data.

The predictions of the break flow and the densities in the intact and broken loop cold legs were judged to be minimal, as were most of the coolant temperatures after 1,200 s. The break flow was simulated well

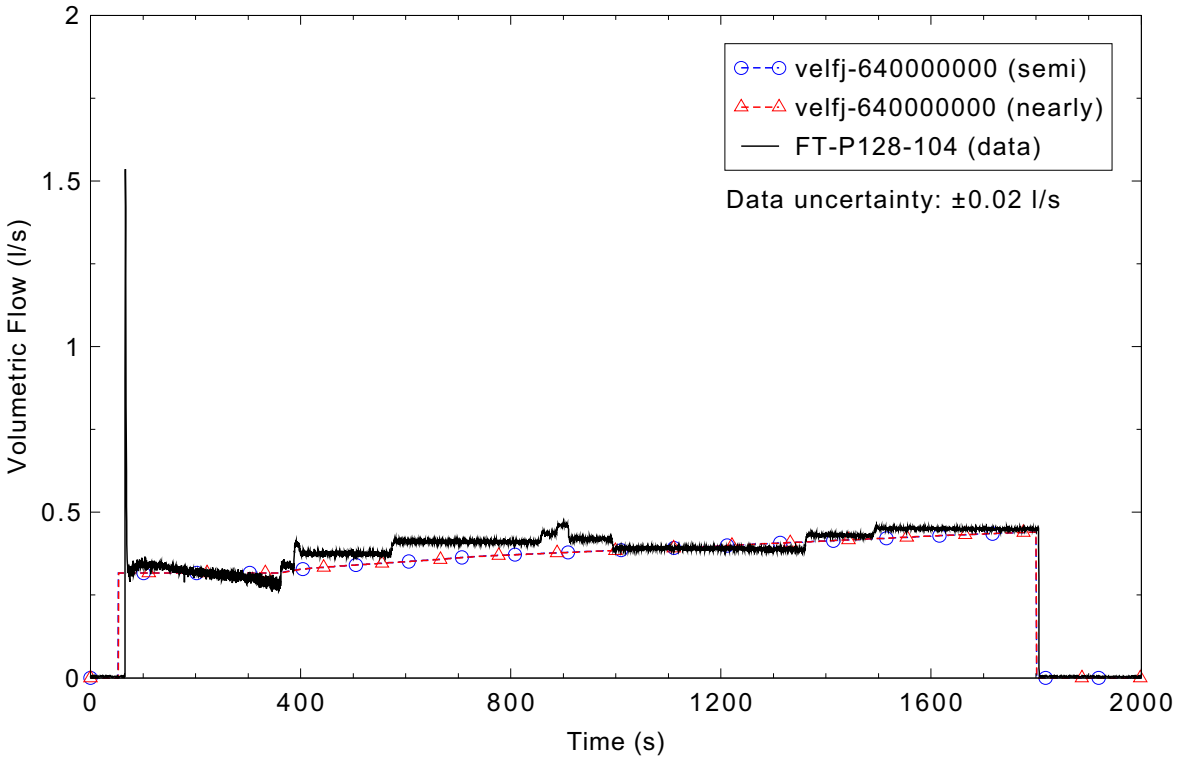

Figure 5.1-19. Measured and calculated HPIS volumetric flow for LOFT Experiment L3-7.

at the beginning of the transient, as evidenced by the response of the pressurizer liquid level, but was under predicted after about 400 s. The under prediction resulted in the calculation retaining more water in the system, which in turn led to an over prediction of the fluid densities in the cold legs. Because more liquid was retained in the system, voiding in the cold legs was predicted to occur much later than in the test, or not at all in the intact loop cold leg. Improvement of the break flow rate prediction would likely result in acceptable calculations of the densities throughout the system. This in turn would likely improve the pressure and coolant temperature predictions after 1,200 s.

The assessment findings apply equally to both simulations; there were no significant differences between the calculations using the semi- or nearly-implicit solution schemes.

5.1.6 References

5.1-1. D. L. Reeder, *LOFT System and Test Description (5.5 ft Nuclear Core 1 LOCEs)*, NUREG/CR-0247, TREE-1208, July 1978.

5.1-2. D. L. Gillas and J. M. Carpenter, *Experiment Data Report for LOFT Nuclear Small Break Experiment L3-7*, NUREG/CR-1570, EGG-2049, August 1980.

5.1-3. W. H. Grush and G. E. McCreery, *Posttest Analysis of Loss-of-Fluid Tests L3-2 and L3-7*, EGG-LOFT-5632, October 1981.

5.2 ROSA-IV Test SB-CL-18

The Rig of Safety Assessment (ROSA)-IV Large Scale Test Facility (LSTF)[5.2-1] is located at the Tokai Research Establishment of the Japan Atomic Energy Research Institute (JAERI). The LSTF is a 1/48 volumetrically-scaled, full-height, full-pressure simulator of a Westinghouse-type pressurized water reactor (PWR). Several series of tests were conducted at the ROSA-IV LSTF. Test SB-CL-18 was a 5% cold-leg small-break loss-of-coolant accident (SBLOCA). This test was also analyzed as International Standard Problem 26.[5.2-2]

5.2.1 Code Models Assessed

The capability of the RELAP5-3D code to model the effects of a SBLOCA in a PWR are assessed. Parameters of interest include the system pressure, break and injection flow rates, core liquid level, and peak core temperatures. This assessment compares results for the semi-implicit and nearly-implicit numerical schemes to the ROSA-IV SB-CL-18 test data.

5.2.2 Experiment Facility Description

The LSTF facility is described in detail in Reference 5.2-1. The electrically-heated core had a 3.66 m effective heating length with a 0.514 m diameter. The core contained 24 bundles and 1,064 heater rods that were representative of a commercial PWR. The reactor pressure vessel was operated at 16 MPa. As shown in Figure 5.2-1, the LSTF contained two primary coolant loops. The four primary loops of the reference PWR were represented by two equal-volume loops. The intact loop (loop A) contained a hot leg, steam generator, cold leg, a primary coolant pump, and the pressurizer. The broken loop (loop B) contained a hot leg, steam generator, cold leg, and a primary coolant pump. The crossover legs are referred to as the loop seals in subsequent discussions. The break location and size could be modified to model a number of different scenarios.

The emergency core coolant (ECC) system included a high-pressure injection system (HPIS), a low pressure injection system (LPIS), two accumulators (where accumulator A is also labeled as accumulator-cold and accumulator B is also labeled as accumulator-hot), and a residual heat removal (RHR) system. The ECC system was designed to allow injection to both cold legs, both hot legs, the reactor vessel lower plenum and upper plenum, and both loop seals.

Over 2,500 instruments were available for making various types of measurements in the LSTF. Fluid pressure, temperature, and flow rate were measured at key locations in the primary coolant, secondary coolant, and ECC systems.

Experiment SB-CL-18 was a 5% cold-leg small break LOCA. The break point was located in the broken loop cold leg between the reactor coolant pump and the reactor pressure vessel. The break orientation was horizontal.

5.2.3 Input Model Description

The RELAP5-3D input model used for the ROSA-IV SB-CL-18 simulation is shown in Figures 5.2-2 and 5.2-3. It includes the reactor vessel, the intact and broken loops, the steam generator secondary side for

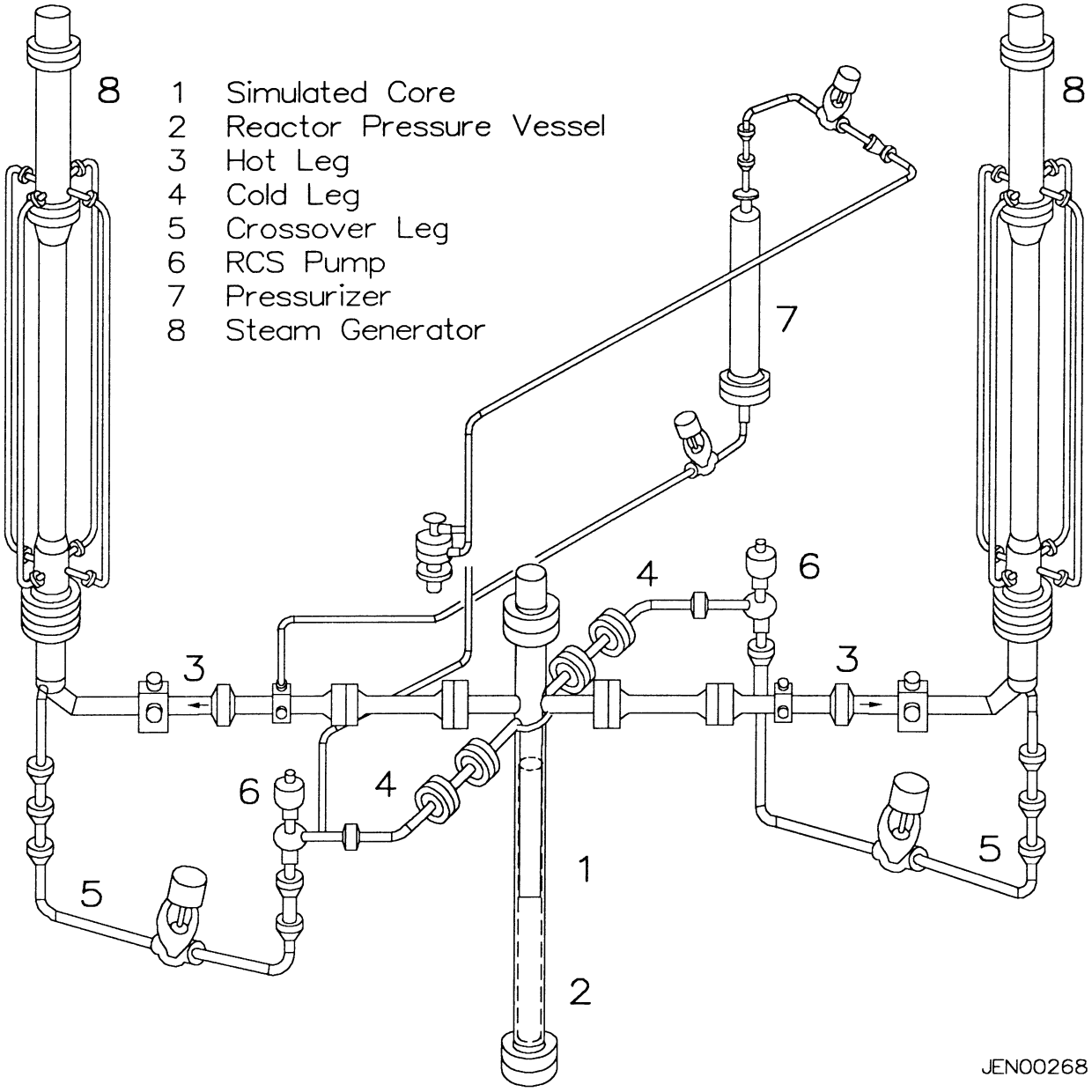

Figure 5.2-1. Schematic of the ROSA-IV Large Scale Test Facility.

both the intact and broken loops, the pressurizer, and the ECC systems. The model contains 193 control volumes, 201 junctions, and 177 heat structures.

The reactor vessel includes representations of the downcomer (Components 100-108), lower plenum (Components 112-116), core inlet (Component 120), core (Component 124), upper plenum (Components 126-140), and vessel upper head (Components 144-152). The core was modeled with eight axial nodes. Core bypass flow was modeled for the leakage between the cold leg and hot leg nozzles.

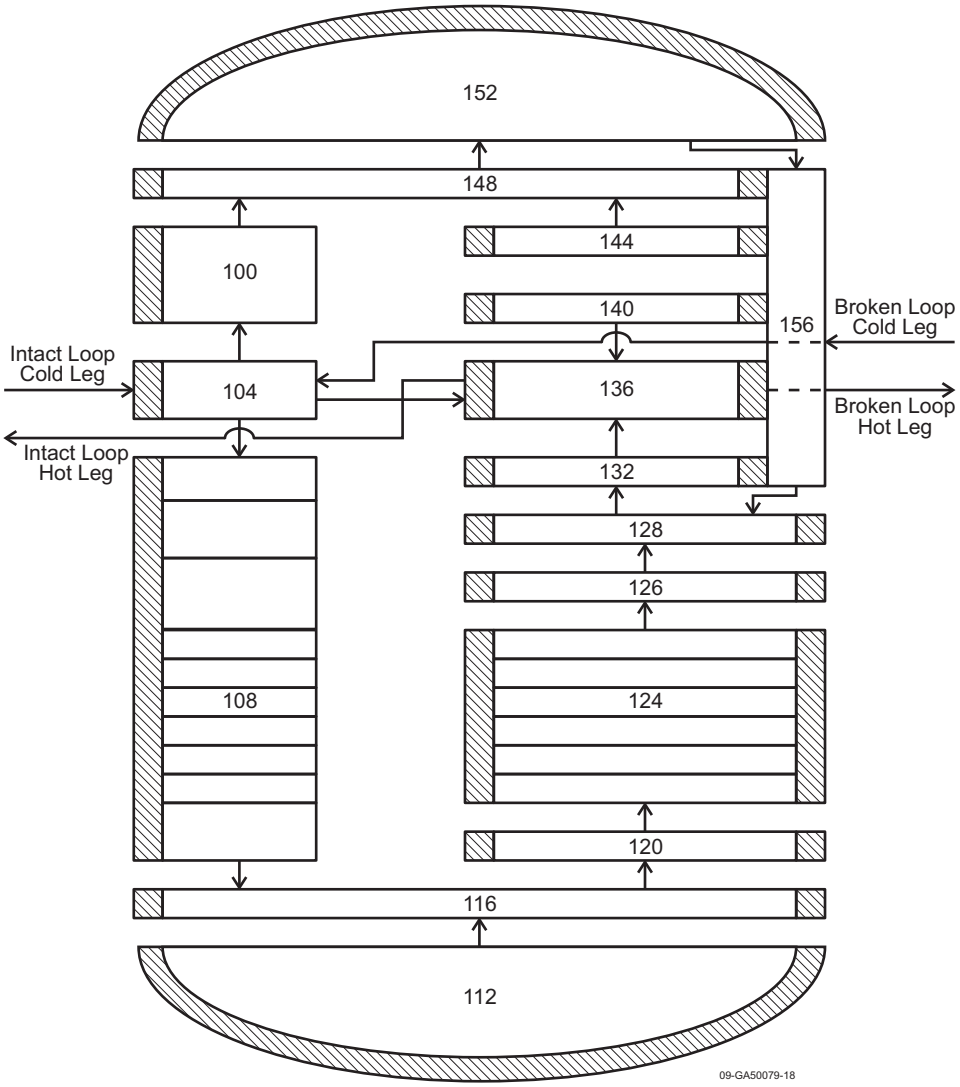

Figure 5.2-2. RELAP5 input model reactor vessel nodalization for ROSA-IV Test SB-CL-18.

The intact loop (400 & 500 component series) model includes the hot leg, steam generator, primary coolant pump, and the cold leg. The pressurizer (600 component series) is connected to the intact loop hot leg, with spray flow from the cold leg.

The broken loop (200 & 300 component series) model includes the hot leg, steam generator, primary coolant pump, and the cold leg. The break (Component 915) is connected to the cold leg downstream of the primary coolant pump.

The ECC systems modeled were the HPIS, two accumulators (Components 700 and 710), and the LPIS.

Heat structures in the model represented the core heater rods, the core support barrel, the reactor vessel, and the steam generator tubes.

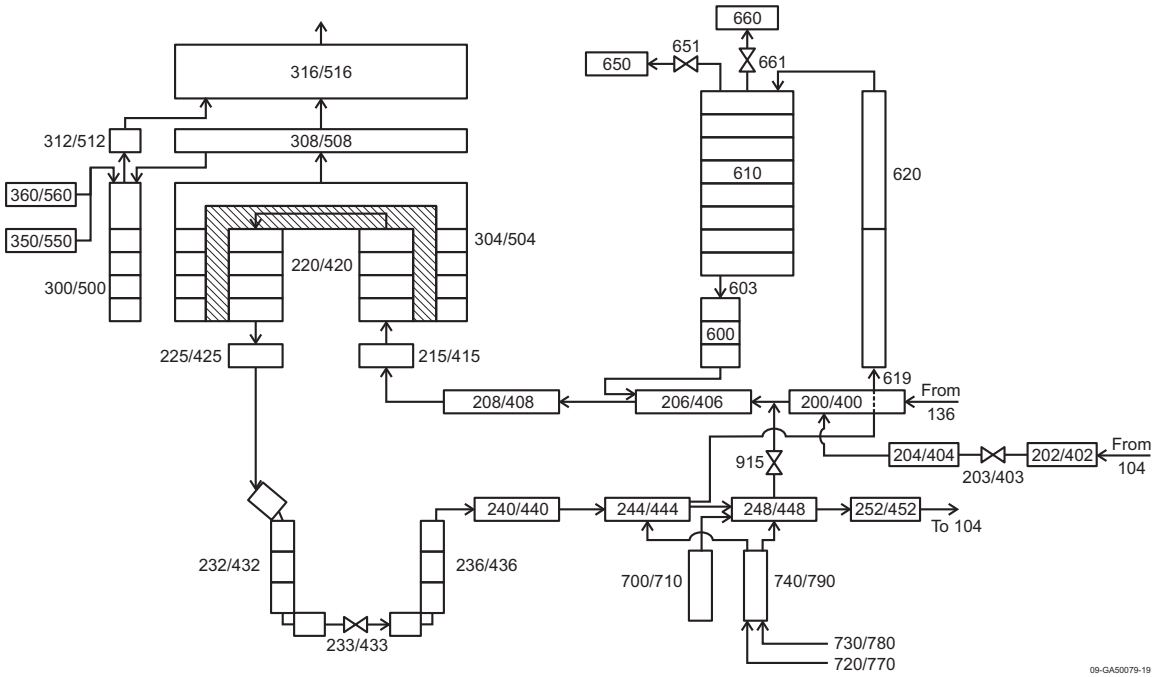

Figure 5.2-3. RELAP5-3D input model loop nodalization for ROSA-IV Test SB-CL-18.

5.2.4 Data Comparisons and Results

Table 5.2-1 provides a comparison of the measured and calculated initial and boundary conditions for Experiment SB-CL-18. All calculated values were in good agreement with the data.

The experiment was initiated by opening the break valve. The simulated reactor scram occurred when the pressurizer pressure reached 12.97 MPa, after about 10 s. Loss of offsite power was assumed to occur concurrently with the reactor scram; the primary coolant pumps were tripped to begin their coastdown, and the core power began to decrease along a pre-programmed curve. The reactor coolant pumps completely stopped at about 265 s. The safety injection signal was sent at a pressurizer pressure of 12.27 MPa, at about 12 s. However, the HPIS was not activated because it was assumed to fail for this experiment. There was a core heatup between about 120 and 155 s due to a loop seal-related core level depression. This caused significant heatup of the heater rods. At about 140 s, loop seal clearing occurred in both loops, resulting in a rewetting of the core heater rods. By about 180 s, the primary loop pressure decreased below the steam generator (SG) secondary side pressure. After this point the steam generators no longer served as heat sinks for the primary loop. The core was uncovered a second time starting at about 420 s due to coolant boiloff, causing some heatup in the upper part of the core. Depressurization of the primary system led to accumulator actuation at 455 s, helping fill the system with water. The core was covered with a two-phase mixture by about 540 s. The peak cladding temperature in the test was approximately 740 K, observed just before the loop seals cleared. The test measurements were recorded until 900 s.

Figures comparing the measured and calculated response of the ROSA-IV system during the experiment are provided below. The experiment data are from the NRC Data Bank. Both the semi- and

Table 5.2-1. ROSA-IV Test SB-CL-18 initial conditions.

Parameter	Measured Value	Calculated Value
Pressurizer		
Pressure (MPa)	15.5	15.5
Liquid level (m)	2.7	2.7
Intact Loop		
Hot leg temperature (K)	599	599.1
Cold leg temperature (K)	563	563.6
Broken Loop		
Hot leg temperature (K)	599	599.1
Cold leg temperature (K)	564	563.6
Core inlet mass flow rate (kg/s)	48.7	48.7
Pressure steam generator A (MPa)	7.3	7.2
Pressure steam generator B (MPa)	7.4	7.2

nearly-implicit calculations were run with a requested time step of 0.01 s. The nearly-implicit calculation failed around 30 s. Measurement uncertainty is presented where available.

Figure 5.2-4 shows the pressure in the pressurizer. The rapid depressurization in the first 38 s is due to subcooled break flow. The observed inflection in the calculation around 50 s was caused by boiling in the core. The depressurization rate increased near 150 s in the test and near 200 s in the calculation when the break transitioned to a two-phase flow, increasing the volumetric flow out of the system. A lower quality two-phase mixture at the break caused the depressurization rate to decrease near 500 s in the calculation and near 600 s in the test. The pressure was slightly over predicted from about 80 s to 300 s. The pressure was under predicted from 300 s to the end of the calculation. The differences in the inflection points in the curves were caused by differences in the break flow. Overall, the calculation was judged to be in reasonable agreement with the data.

The pressures in steam generators A and B are shown in Figures 5.2-5 and 5.2-6, respectively. Initially, the calculated pressure was about 150 kPa less than the measured value for both steam generators. From 20 to 170 s relief valve cycles were observed in both the measurements and the calculations, although the frequency was slightly different. After 170 s the pressures in steam generators A and B decreased below the primary coolant system pressure. As heat transfer was then into the primary system, rather than from it, the valve cycling ended and the pressure began to decrease. The calculation predicted that the primary and secondary pressures crossed at about 220 s, after which the pressures were predicted to decrease, albeit at a slower rate than measured. The slower calculated depressurization indicates that the code is under predicting the heat transfer back to the primary coolant system. The predicted decrease of the pressure in steam generator B is slightly better than the predicted decrease in pressure of steam generator A because the loop B loop seal clears, allowing more flow through the steam generator tubes; the loop A loop

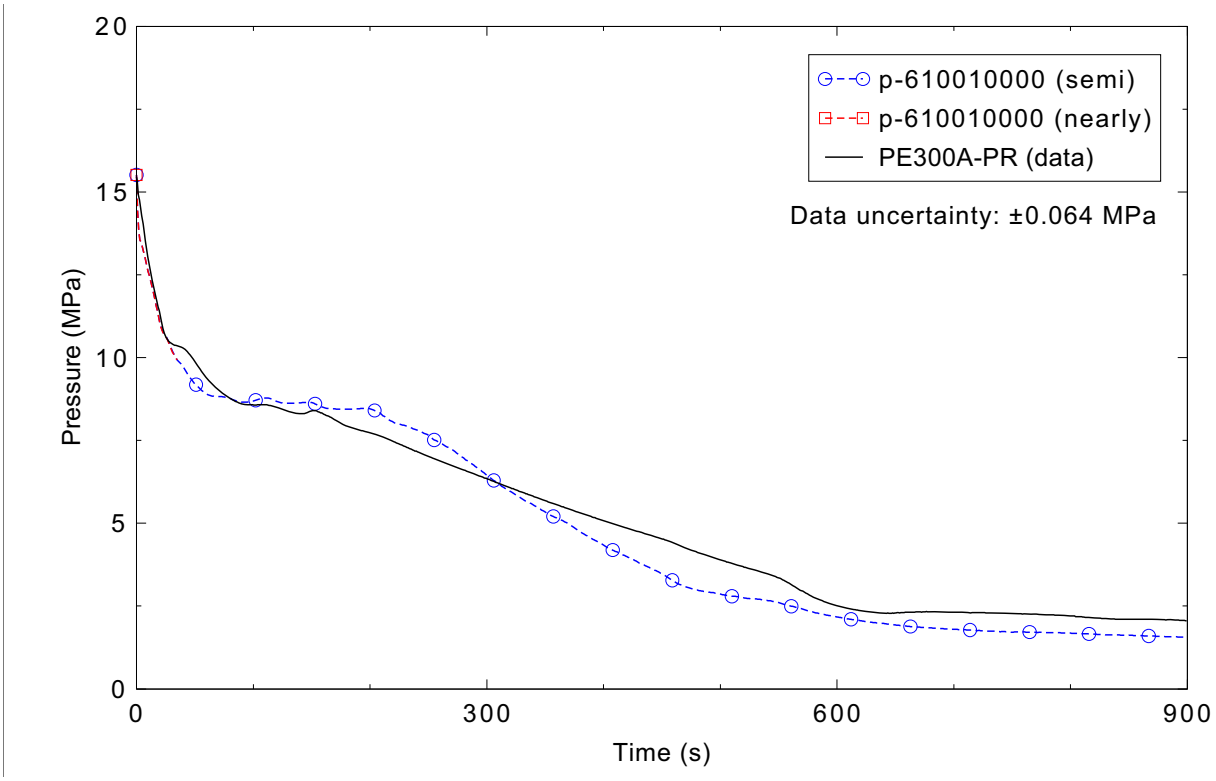

Figure 5.2-4. Measured and calculated pressurizer pressure for ROSA-IV Test SB-CL-18.

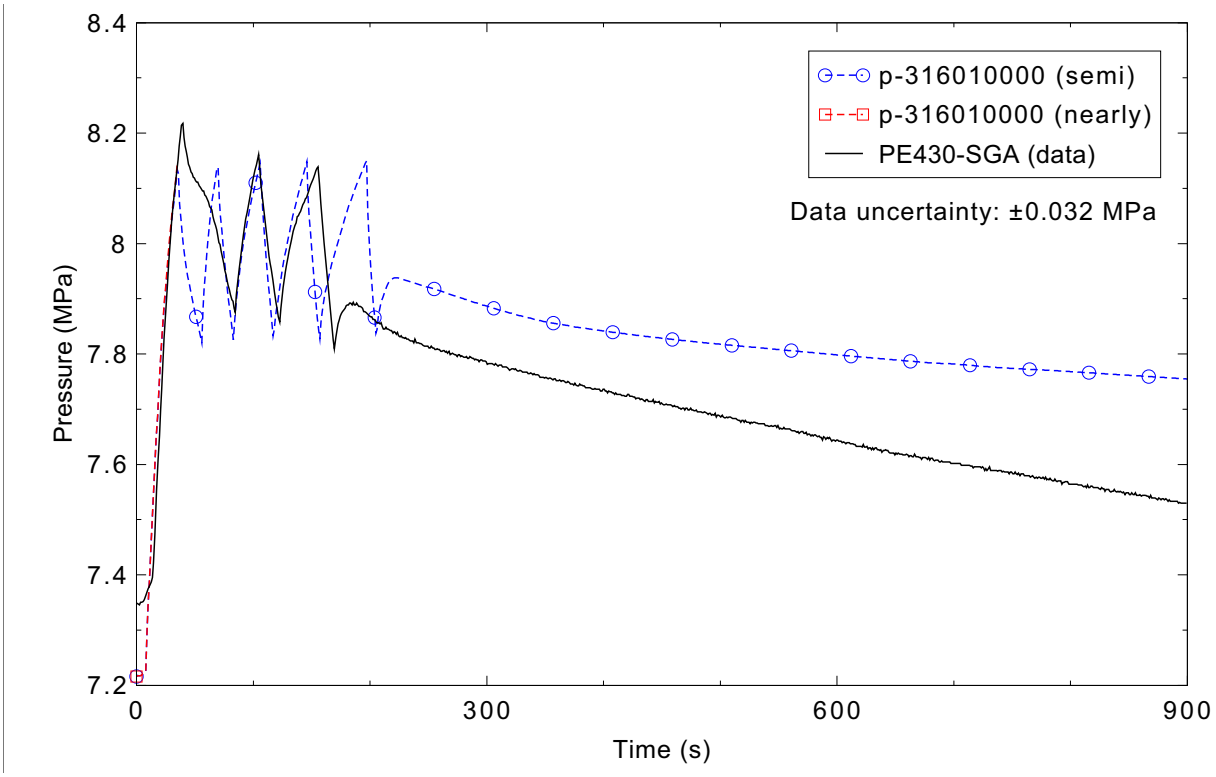

Figure 5.2-5. Measured and calculated pressure of steam generator A for ROSA-IV Test SB-CL-18.

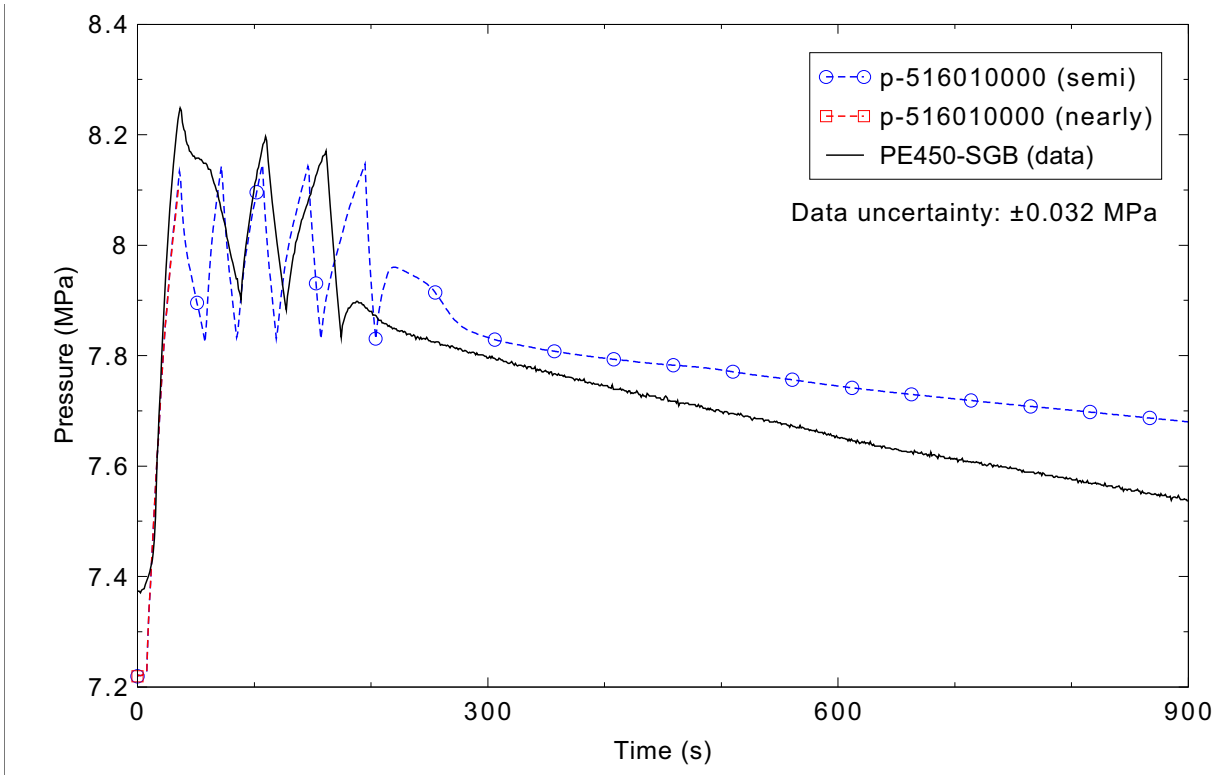

Figure 5.2-6. Measured and calculated pressure of steam generator B for ROSA-IV Test SB-CL-18.

seal was not predicted to clear (see discussion of Figures 5.2-10 and 5.2-11). The prediction of the pressures in the steam generators is judged to be in reasonable agreement with the data.

Figure 5.2-7 presents the pressurizer liquid level. The code predicted that the pressurizer emptied at the same rate as the experiment for the first about 20 s. The code predicted that the last of the water was emptied from the pressurizer more slowly than in the experiment. The calculated level is judged to be in reasonable agreement with the data.

The mass flow rate at the break is shown in Figure 5.2-8. Initially, the mass flow rate for the calculation is greater than the measured mass flow rate. The calculated mass flow rate quickly decreases and maintains a lower value, but the measurement remains relatively stable until about 150 s, despite a fairly large decrease in the primary system pressure. The measured mass flow rate drops quickly at around 150 s when the break flow transitions to high quality flow. This transition was predicted to occur at around 200 s in the calculation; up until then, the break flow reflected the primary system pressure response. From about 300 s through the end of the transient, the calculated mass flow rate at the break closely matches the measured mass flow rate. The calculation of the mass flow rate at the break is in minimal agreement with the data until a higher-quality two-phase flow is present, then is in reasonable agreement.

The vessel liquid level is shown in Figure 5.2-9. The calculated results initially follow the measurements reasonably well. There was a core level depression in the test at about 110 s that results in a core uncovery from about 120 to 155 s. The calculation predicted this uncovery about 60 s later. The calculated liquid level drops significantly below the measured value beginning around 220 s. This results in a predicted core uncovery that begins around 260 s and lasts for a good portion of the calculation. A

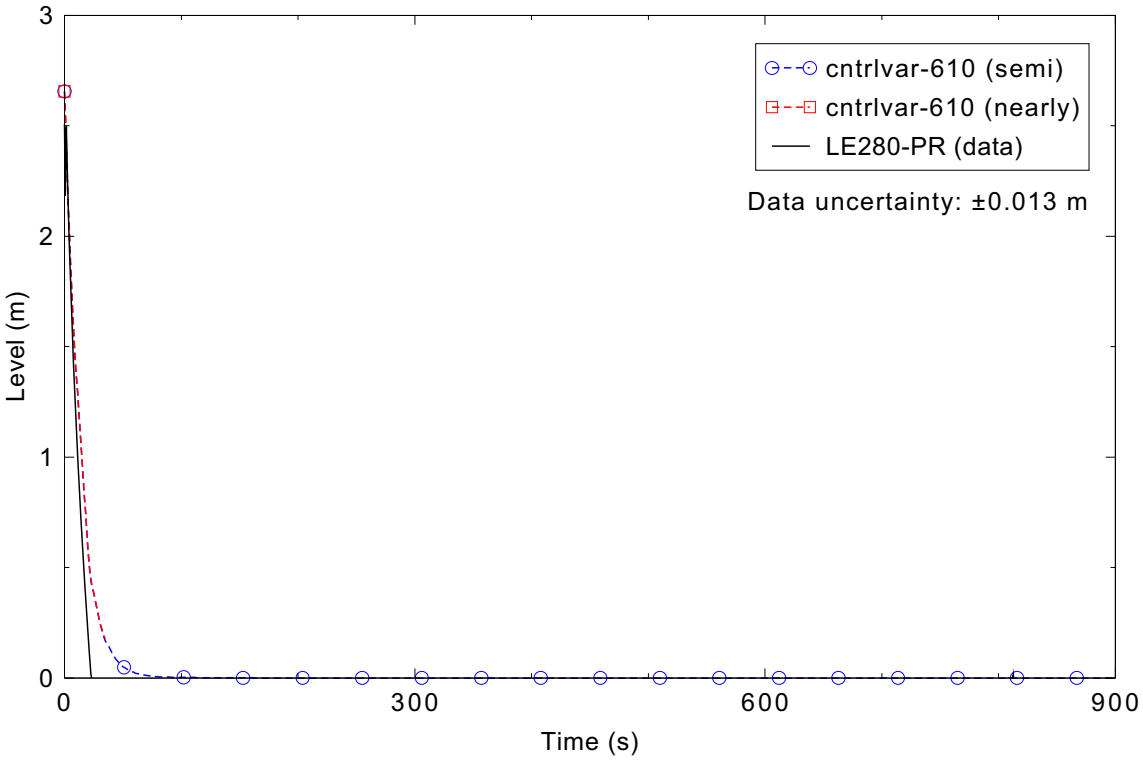

Figure 5.2-7. Measured and calculated pressurizer liquid level for ROSA-IV Test SB-CL-18.

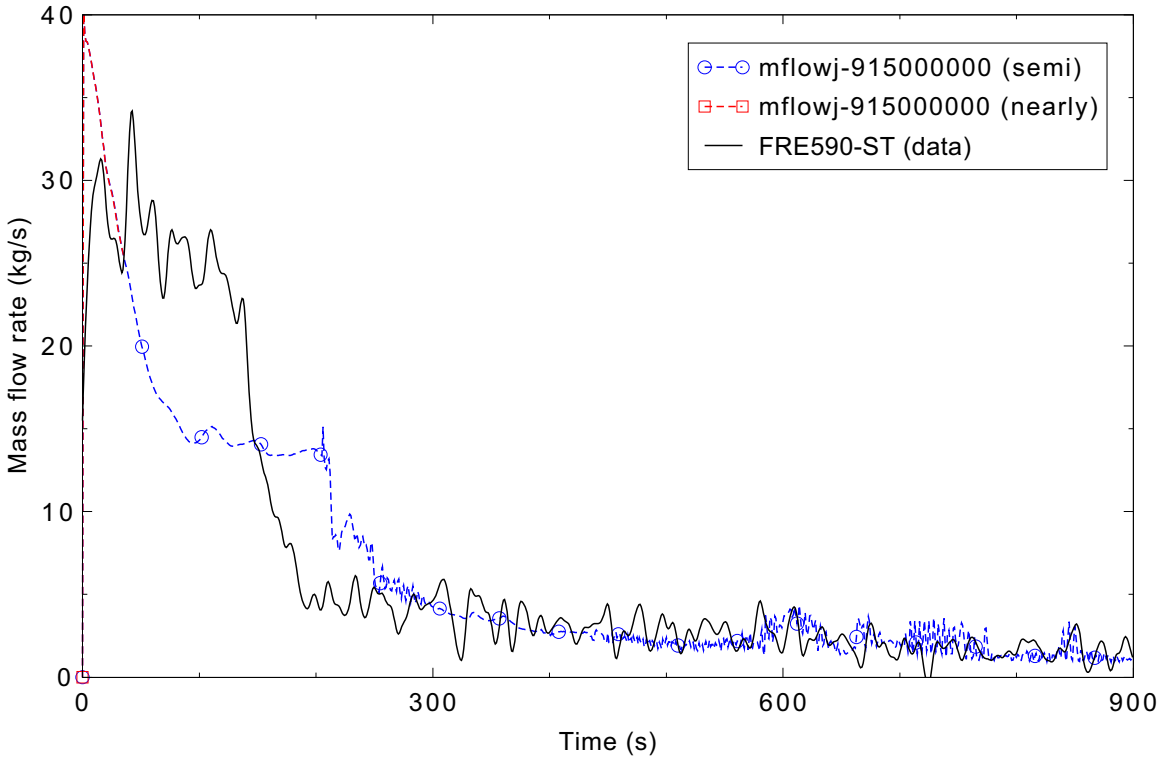

Figure 5.2-8. Measured and calculated break mass flow rate for ROSA-IV Test SB-CL-18.

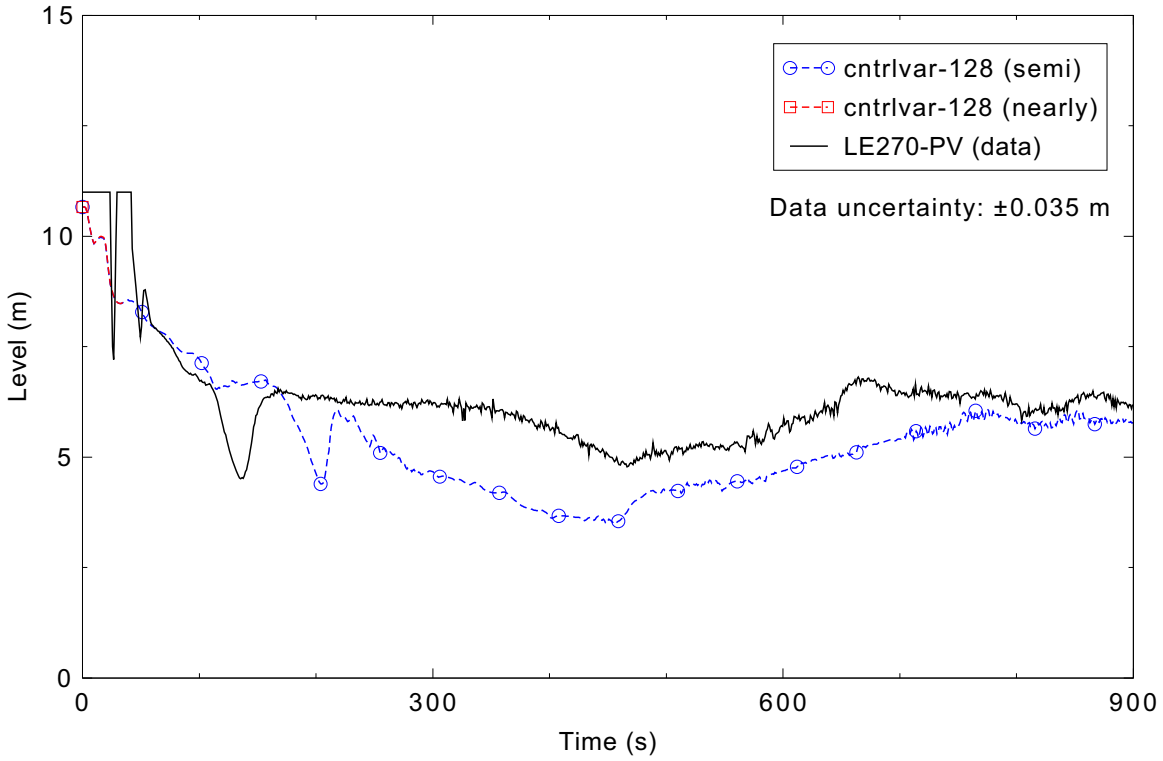

Figure 5.2-9. Measured and calculated vessel liquid level for ROSA-IV Test SB-CL-18.

second core uncovery occurred in the experiment which lasted from about 420 to 580 s. This under prediction of the vessel liquid level in the calculation results in a large core heatup. The overall prediction of the vessel liquid level is in minimal agreement; although the correct trends were predicted, the calculation was generally too far outside the published data uncertainty bands. If the loop A loop seal clearing had been predicted, the agreement likely would have been reasonable.

The differential pressures across loop seal A are shown in Figure 5.2-10, where DPE070-LSA is on the steam generator side of the loop seal and DPE080-LSA is on the coolant pump side of the loop seal. The differential pressure plot indicates that in the experiment, loop seal A cleared at about 140 s, whereas in the calculation the loop seal did not clear. This means that some water is still retained in loop seal A in the calculation. This is important, because otherwise this retained fluid could contribute to a greater core liquid level. The changing pressure drop in loop seal A indicates that the level is changing at this location. Overall the differential pressure is in minimal agreement with the data for loop seal A.

The differential pressures across loop seal B are shown in Figure 5.2-11, where DPE210-LSB is on the steam generator side of the loop seal and DPE220-LSB is on the coolant pump side of the loop seal. The differential pressure plot indicates that in the experiment loop seal B cleared at about 180 s, whereas in the calculation the loop seal cleared at about 210 s. Overall the differential pressure is in reasonable agreement with the data for loop seal B.

The mass flow rates in the broken loop cold leg between the break and the vessel are shown in Figure 5.2-12. The mass flow rate at this location experiences a flow reversal as the break opens, but soon

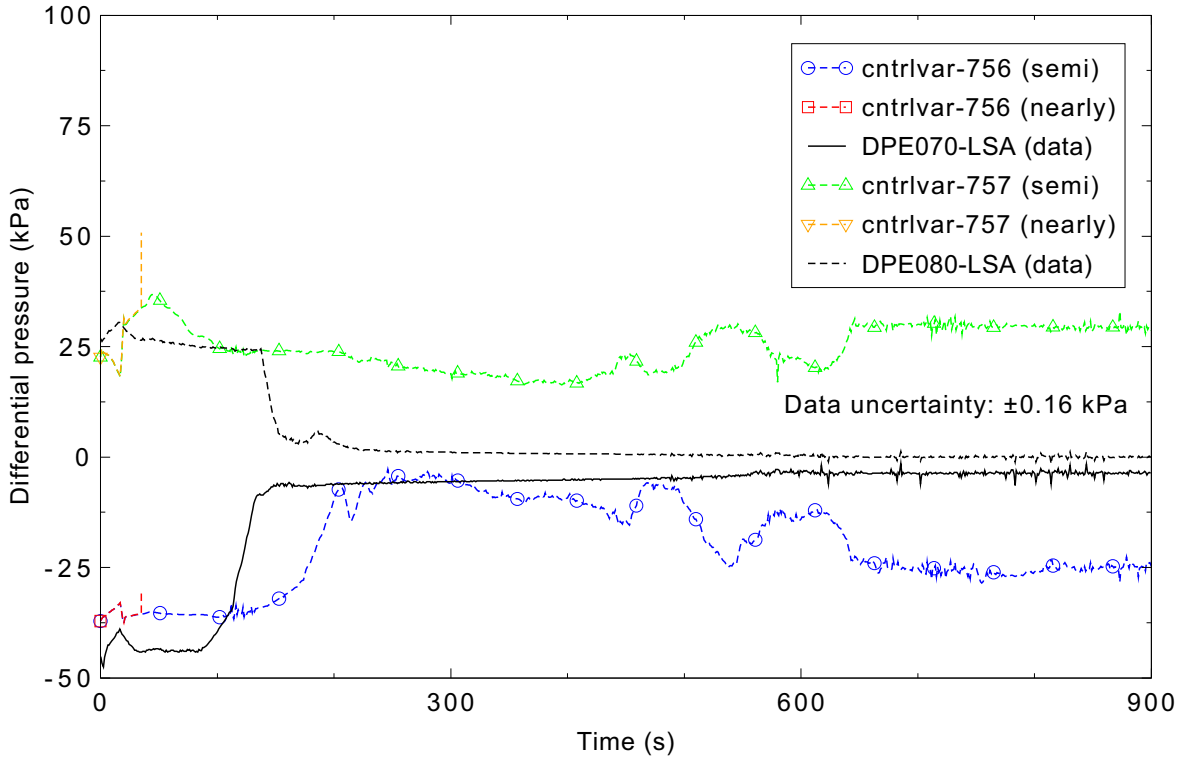

Figure 5.2-10. Measured and calculated differential pressures across loop seal A for ROSA-IV Test SB-CL-18.

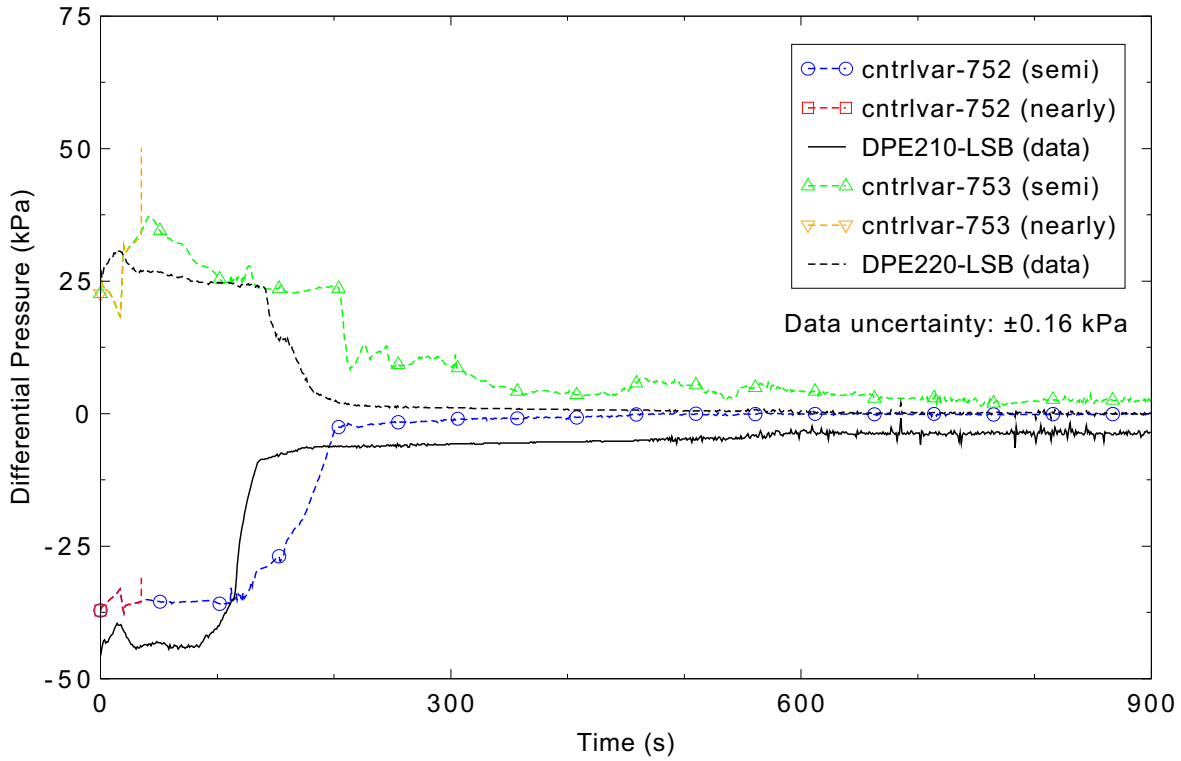

Figure 5.2-11. Measured and calculated differential pressures across loop seal B for ROSA-IV Test SB-CL-18.

thereafter the flow direction is reestablished due to forced convection from the pump. As pump coastdown occurs, the mass flow rate decreases and natural convection is established. When the flow through the broken loop drops below the break flow rate, flow reverses and is drawn from the vessel toward the break. The loop seals then clear and the mass flow rate through this section of the loop becomes virtually zero. After loop seal clearing, the mass flow to the break mostly travels through the hot leg, bypassing this section of the loop. At about 450 s, accumulator injection causes some flow in the cold leg again. The general trend of the mass flow rate in the broken loop cold leg is in good agreement with the data. However, there is a bit of a time lag in the flow reversal that occurs. Overall, the prediction is judged to be in reasonable agreement.

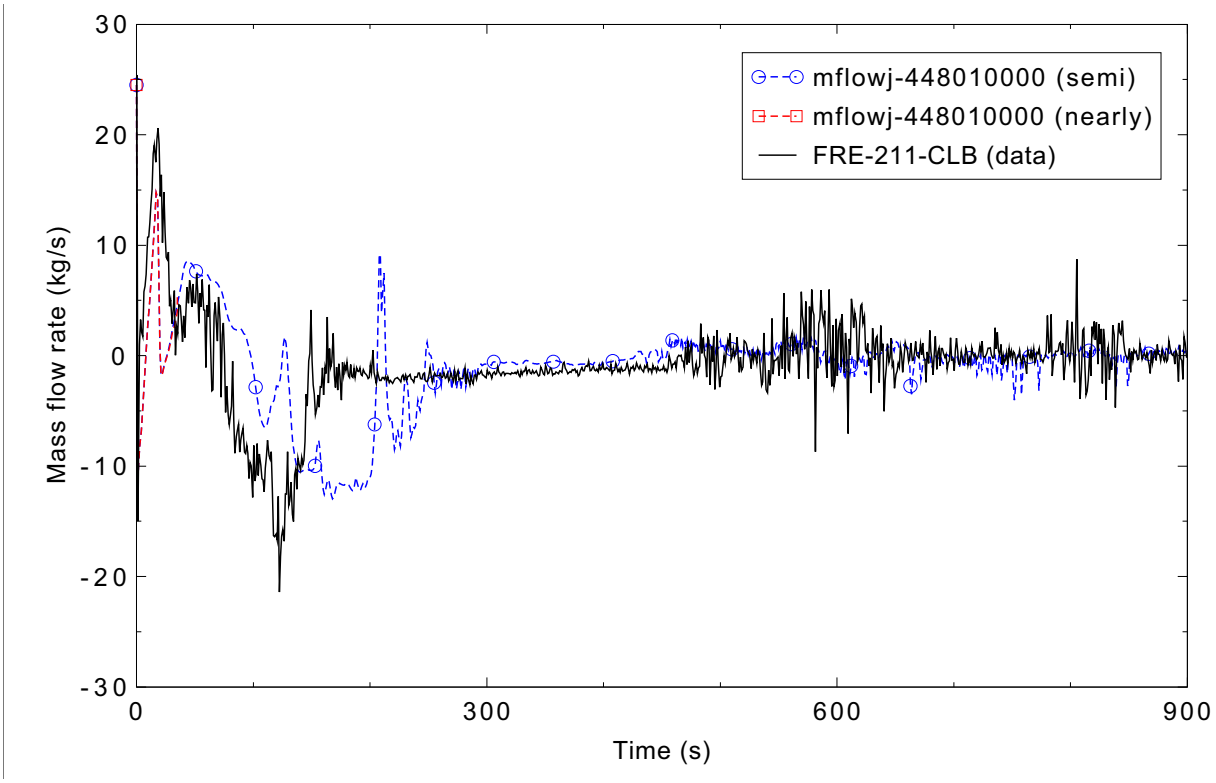

Figure 5.2-12. Measured and calculated mass flow rate in the broken loop cold leg for ROSA-IV Test SB-CL-18.

The mass flow rates in the broken loop hot leg are shown in Figure 5.2-13. Initially, the calculation follows the experiment data quite well, but begins to deviate at about 70 s. The mass flow rate is over predicted between 70 and 100 s. There is a large dip in the calculated mass flow rate from about 100 to 200 s, which is due to liquid draining from the steam generator. Negative flow is suspected in the test around this time because the density in the broken loop hot leg, shown in Figure 5.2-17, indicates that liquid is flowing back from the SG tubes. After 580 s the measured mass flow rate increased. This increase coincided with an increase in the core level, meaning that the increased core level is causing flow into the hot leg. This was not seen in the calculation due to the lower calculated core liquid level. The calculation is judged to be in reasonable agreement with the data.

The mass flow rates in the intact loop cold leg are shown in Figure 5.2-14. The predicted mass flow rate is in good agreement with the measurement. The calculation does not predict a large spike in mass

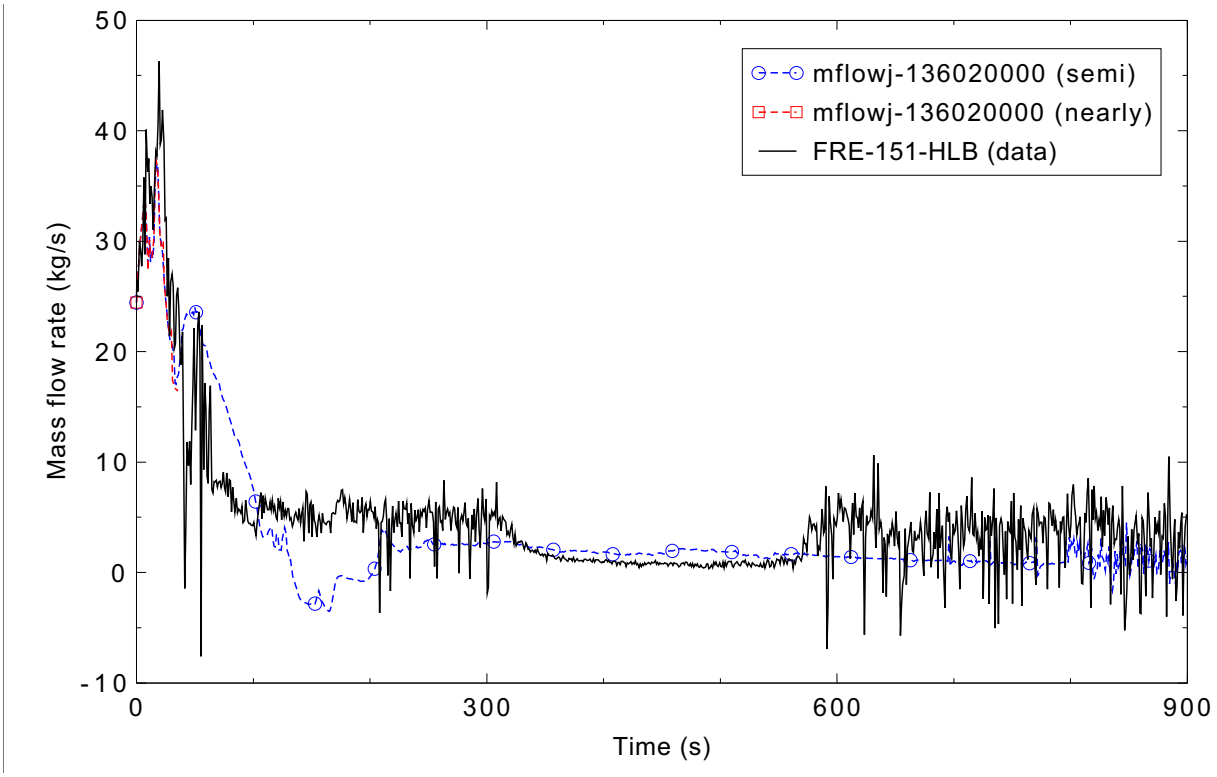

Figure 5.2-13. Measured and calculated mass flow rate in the broken loop hot leg for ROSA-IV Test SB-CL-18.

flow rate that occurs when the loop seal clears around 175 s. At about 450 s the experiment shows a small negative flow due to the accumulator injection. The calculated mass flow appears to show that the accumulator liquid was moving in the opposite direction from the experiment. The liquid in the test appears to be going to the loop seal, but Figure 5.2-10 shows that no incoming liquid is measured. Thus the measured mass flow direction is unclear. However the mass flow due to the accumulator was small on average, so any difference is minimal. Overall, the calculation is in reasonable agreement with the experiment.

Figure 5.2-15 presents the mass flow rate in the intact loop hot leg. The measurement and the calculation are in good agreement for about the first 70 s. The measured mass flow rate rapidly decreases around 70 s. Shortly thereafter the calculated mass flow rate decreases to a smaller value than the measurement and changes to a negative value for a short time. This negative value for the mass flow rate can be attributed to water draining from the steam generator. Again, negative flow is also suspected in the test around this time due to liquid draining from the SG tubes. Because loop seal A was not predicted to clear, the calculated mass flow rate goes to zero at about 250 s and stays there for the remainder of the calculation. The effect of the rising vessel level can be seen in the experiment results after about 580 s when a small positive flow resumes. The calculated vessel level is lower than the measurement, so this behavior is not seen in the calculation. The overall trend of the mass flow rate in the intact loop hot leg is in reasonable agreement.

The densities in the broken loop cold leg are shown in Figure 5.2-16. The code predicted the transition to a two-phase fluid later than it occurred in the experiment. The calculation captured the increase in

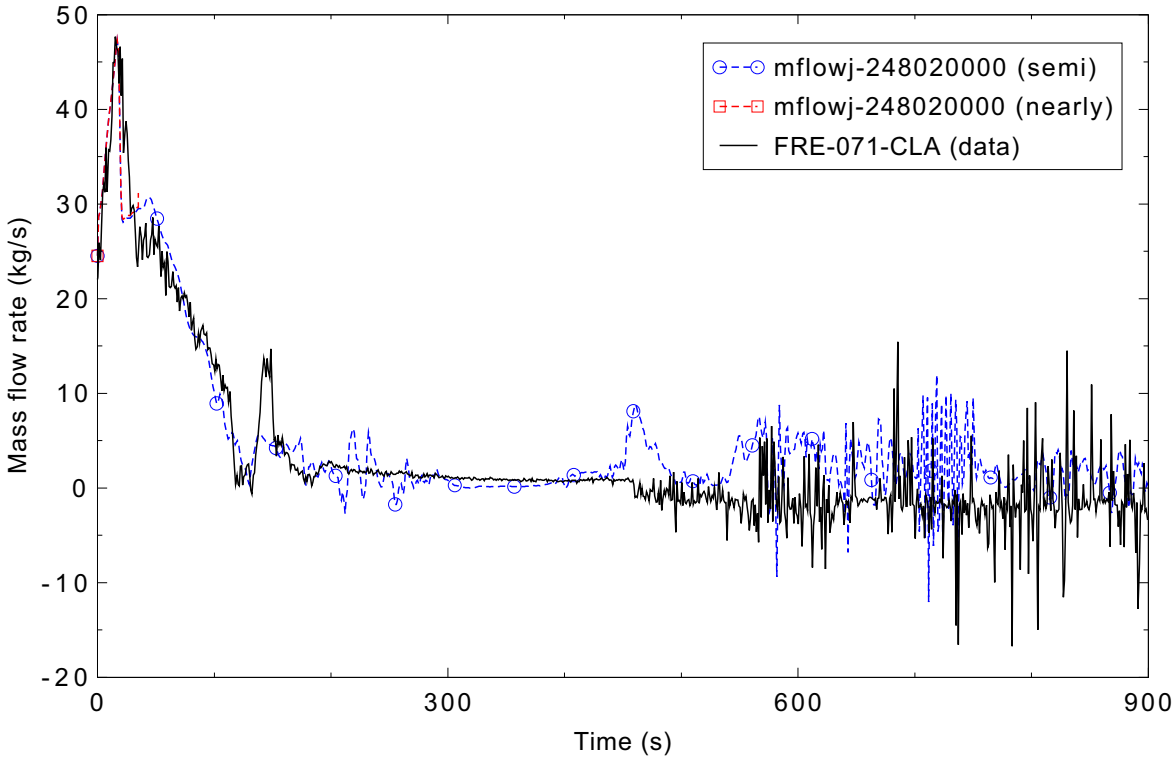

Figure 5.2-14. Measured and calculated mass flow rate in the intact loop cold leg for ROSA-IV Test SB-CL-18.

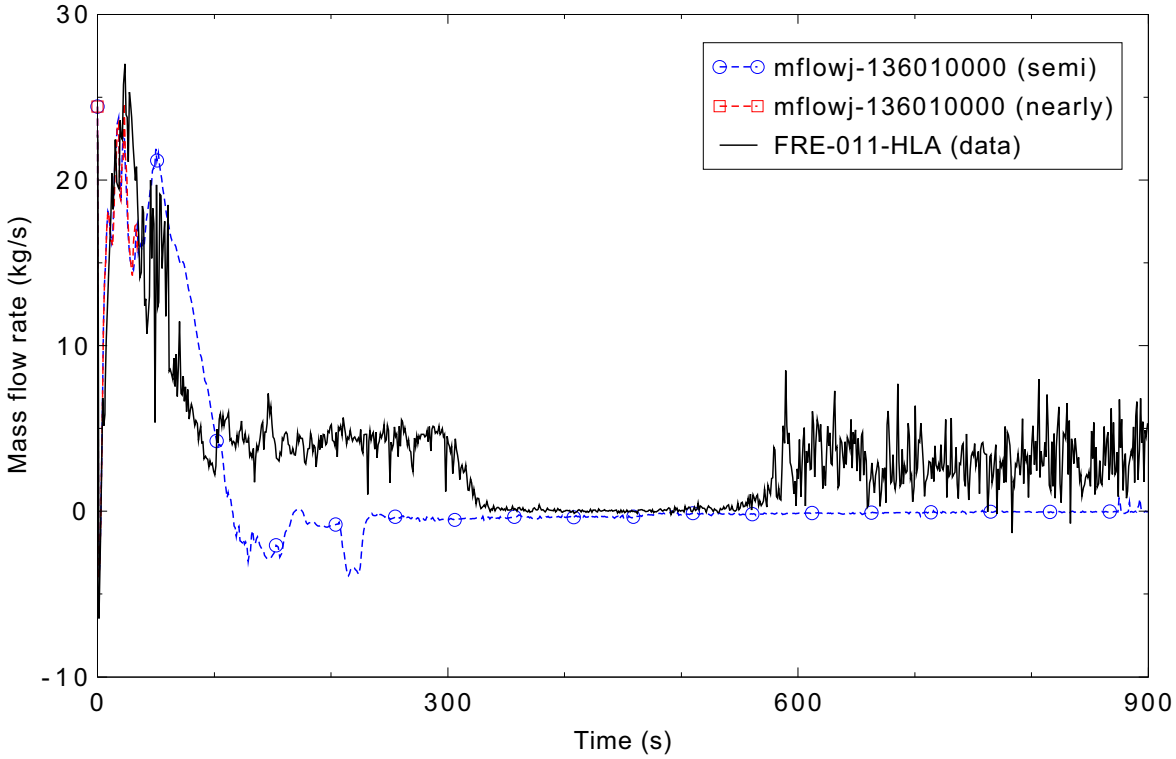

Figure 5.2-15. Measured and calculated mass flow rate in the intact loop hot leg for ROSA-IV Test SB-CL-18.

density that occurred from 550 to 650 s due to injection of liquid from the accumulator. Overall, the prediction is in reasonable agreement with the data.

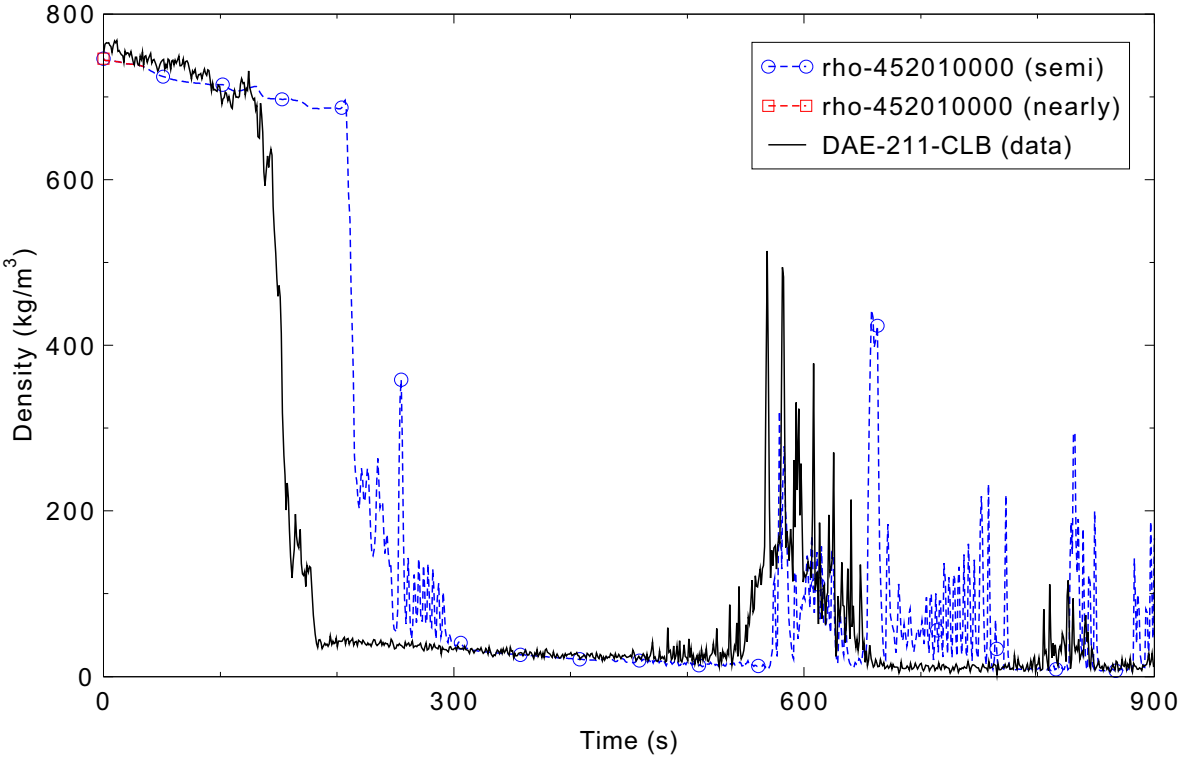

Figure 5.2-16. Measured and calculated density in the broken loop cold leg for ROSA-IV Test SB-CL-18.

Figure 5.2-17 shows the densities in the broken loop hot leg. The measured density and the calculation closely match until about 80 s. Around 80 s the measured density drops quickly, while the calculation predicts a slower decline in the density. At about 100 s the measured density increases sharply due to water draining from the steam generator as the loop seals cleared. A similar response was not observed in the calculation because most of the liquid in the SG tubes drained before the loop seal cleared. In the experiment, the water drains from hot leg B at about 350 s. The density remains small until about 560 s, when the measured density greatly increases due to the increase in the reactor vessel level. The code predicts that water begins to enter hot leg B at about 800 s. Overall, the calculated density in the broken loop hot leg is in minimal agreement with the data.

The densities in the intact loop cold leg are shown in Figure 5.2-18. The calculated and measured densities for the intact loop cold leg are in good agreement for about the first 450 s. There is a slight time lag in the rapid decrease in density between 180 and 220 s, when the loop seal clears (only the broken loop cleared in the calculation). The measured density increases around 450 s when water is injected from the accumulator. The calculated density shows that a great deal of water enters cold leg A. The predicted density is in minimal agreement with the data.

Figure 5.2-19 shows densities in the intact loop hot leg. The results for the calculation and the measurement are in good agreement for about the first 40 s. The measured density then drops quickly, while the calculated density descends more slowly. The slower decrease in the calculated density is due to

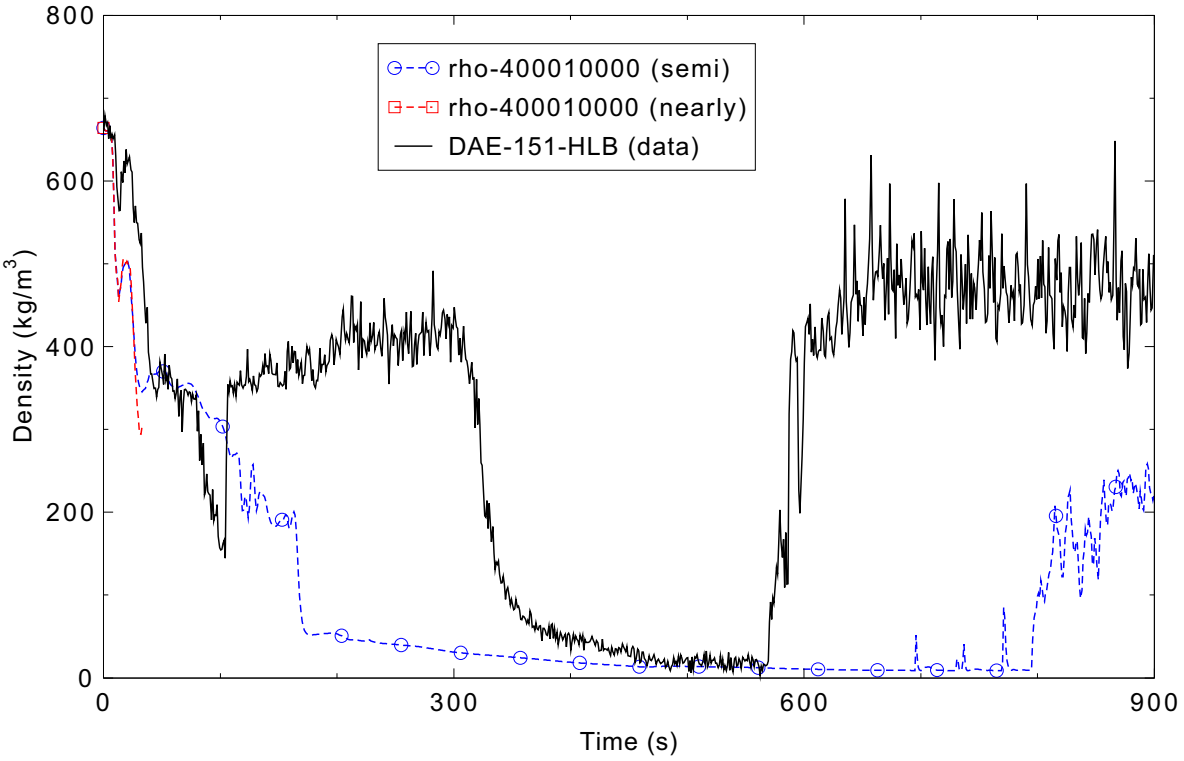

Figure 5.2-17. Measured and calculated density in the broken loop hot leg for ROSA-IV Test SB-CL-18.

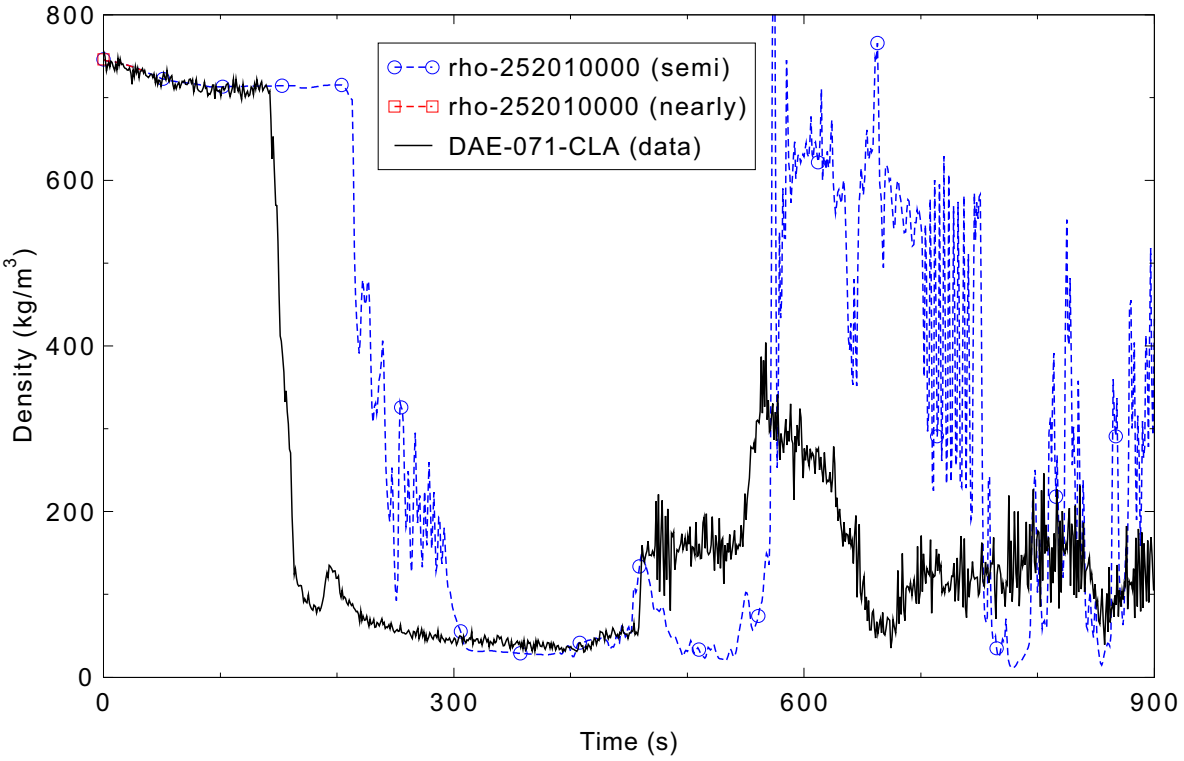

Figure 5.2-18. Measured and calculated density in the intact loop cold leg for ROSA-IV Test SB-CL-18.

the draining of the steam generator. In the measurement there is a quick rise and fall in the density due to loop seal clearing, however this is not seen in the calculation because the SG tubes drained before the loop seal cleared. At about 200 s the measured density rises due to draining from the steam generator, which lasted until about 300 s. The measured and calculated densities are in good agreement from about 320 to 600 s. The measured density then increases again as the vessel level rises high enough to allow liquid to enter the hot leg, but the calculation does not. Overall, the density in the intact loop hot leg is in minimal agreement with the data.

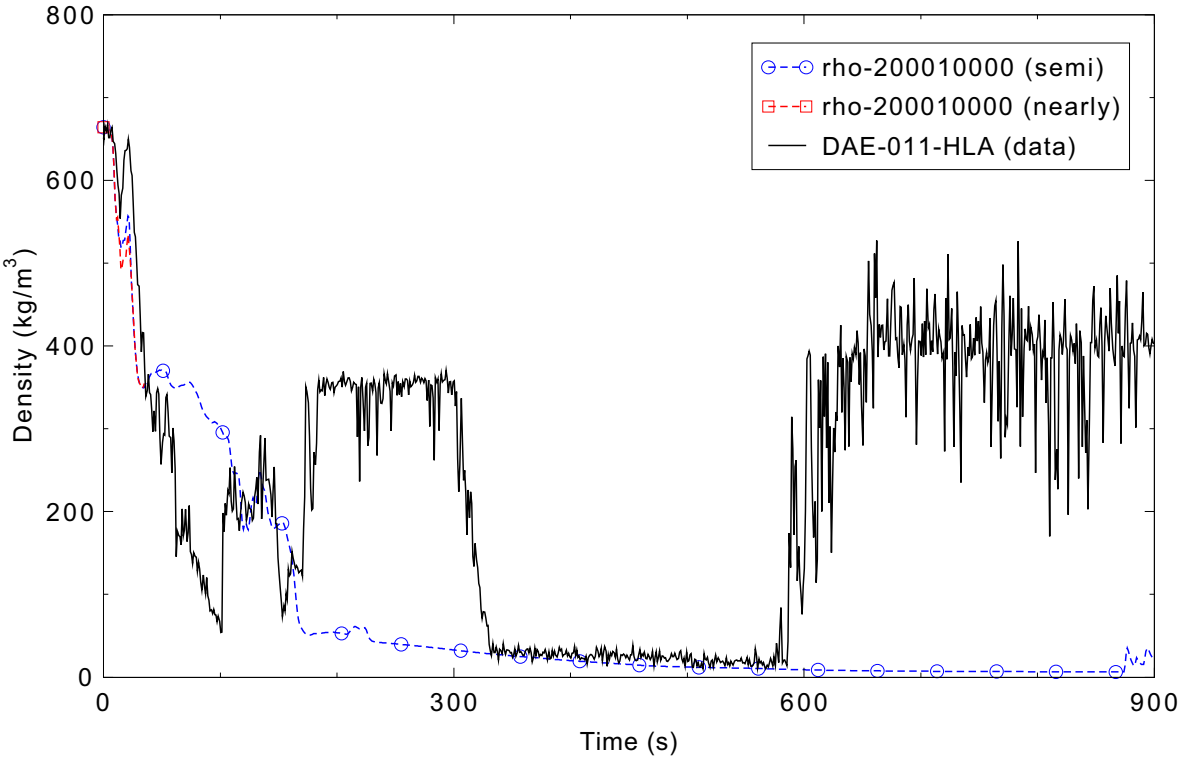

Figure 5.2-19. Measured and calculated density in the intact loop hot leg for ROSA-IV Test SB-CL-18.

The measured and calculated accumulator-cold and -hot mass flow rates are compared in Figures 5.2-20 and 5.2-21. The calculated mass flow rates in the two accumulators show that the accumulator injection began sooner in the calculation than in the test. The accumulators were activated when the pressurizer pressure reached a certain level. Due to the fact that the calculated primary coolant system pressure is lower than the measurement, the accumulators were activated earlier. The general trends of the mass flow rates in both accumulators are captured well. Overall, the mass flow rates in the accumulators are in reasonable agreement.

Heater rod surface temperatures at five axial levels are compared in Figures 5.2-22 through 5.2-24. The heater rod surface temperature for LSTF level 3 (1.018 m above the bottom of the core) is well captured overall, although the heatup that occurs around 150 s is not predicted even though a similar drop in the core liquid level was predicted. The results for level 5 (1.830 m above the bottom of the core) and level 6 (2.236 m above the bottom of the core) similarly don’t capture the heatup that occurred around 150 s. Level 8 (3.048 m above the bottom of the core) shows two temperature heatups that occurred earlier and were more extensive than that measured because the core remained uncovered longer at this elevation.

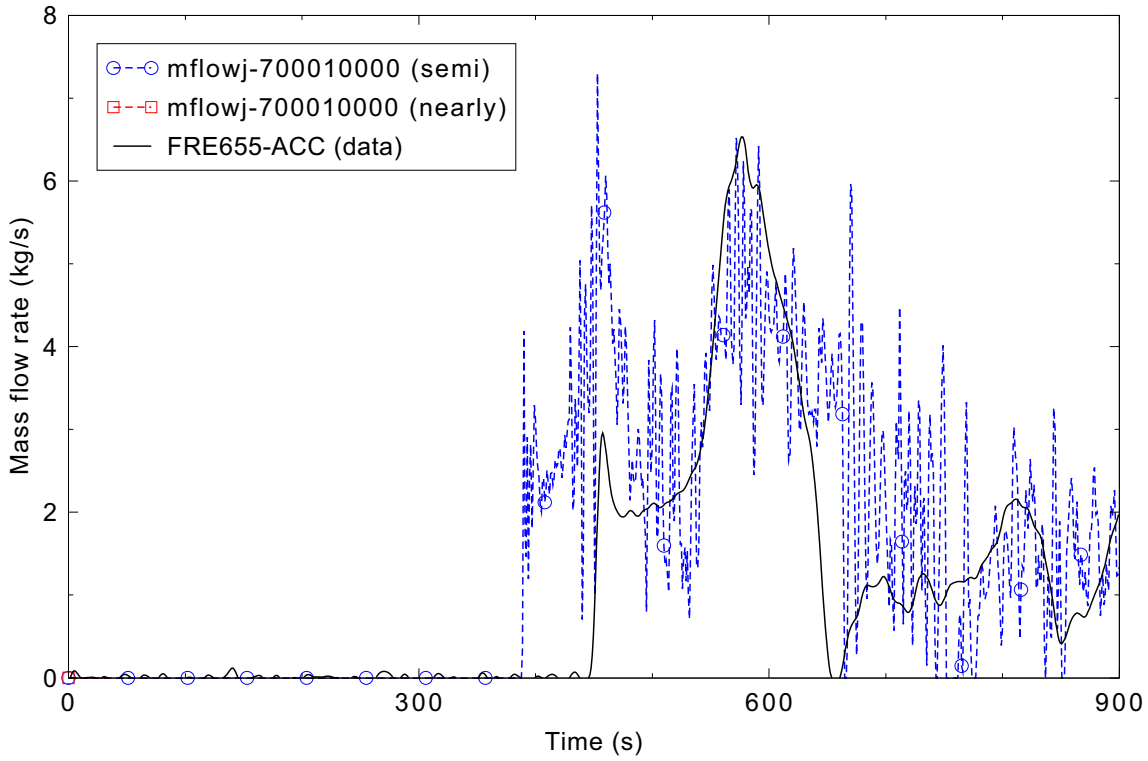

Figure 5.2-20. Measured and calculated mass flow rate accumulator-cold for ROSA-IV Test SB-CL-18.

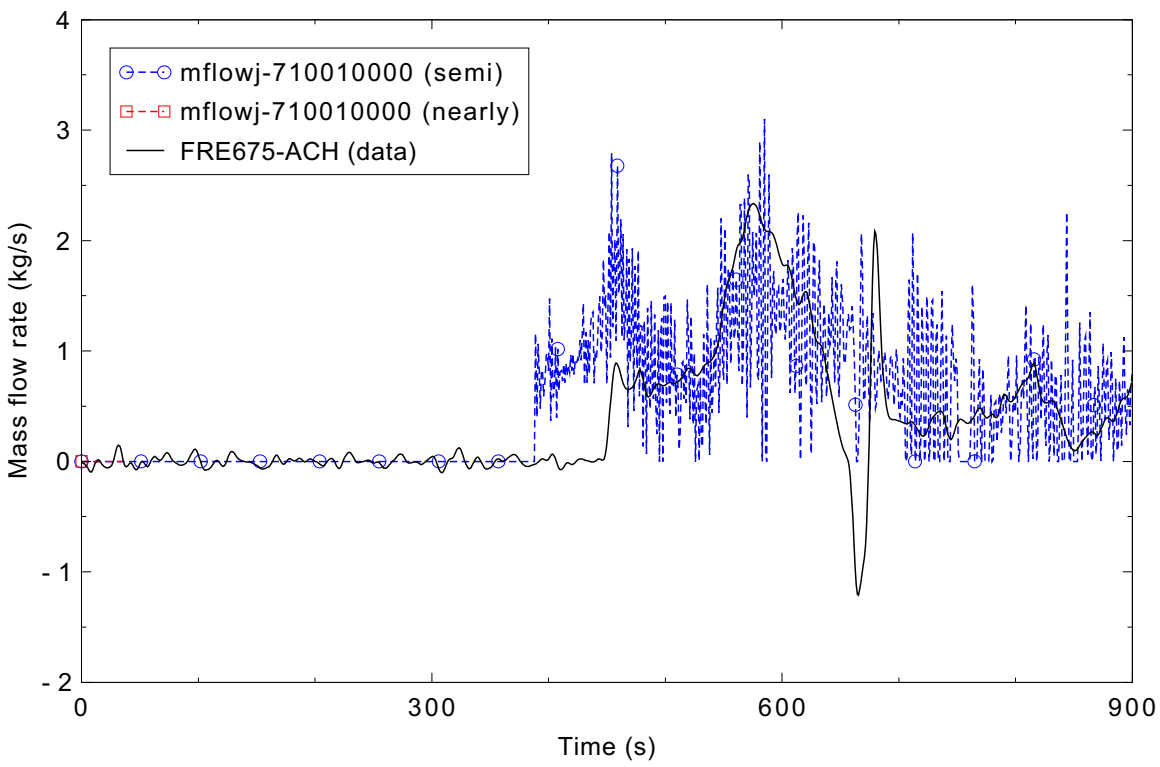

Figure 5.2-21. Measured and calculated mass flow rate accumulator-hot for ROSA-IV Test SB-CL-18.

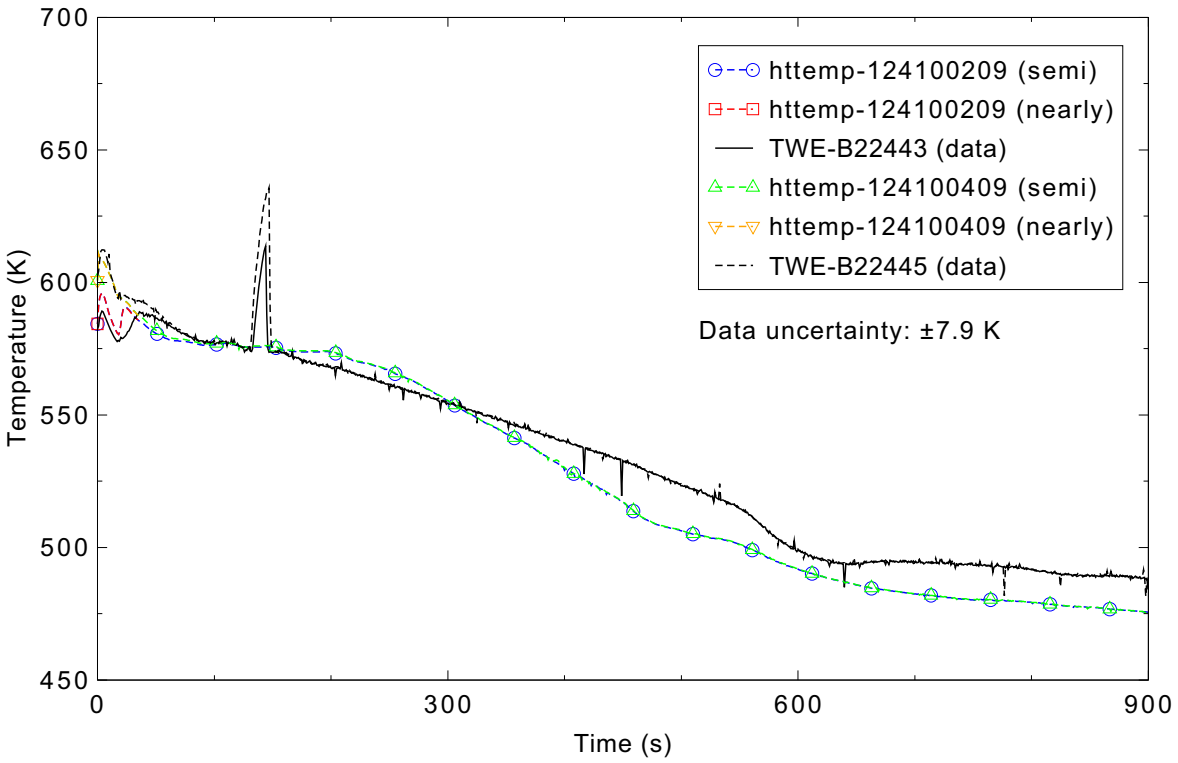

Figure 5.2-22. Measured and calculated heater rod surface temperature at axial levels 3 and 5 for ROSA-IV Test SB-CL-18.

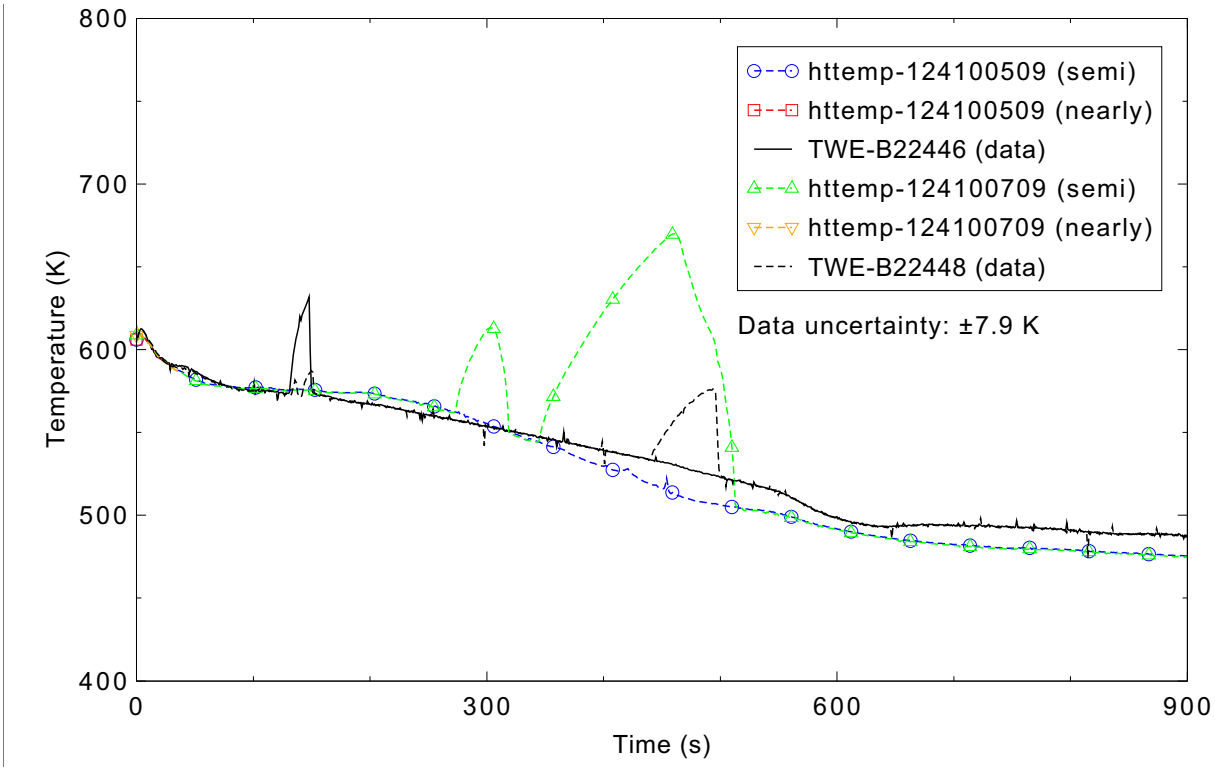

Figure 5.2-23. Measured and calculated heater rod surface temperature at axial levels 6 and 8 for ROSA-IV Test SB-CL-18.

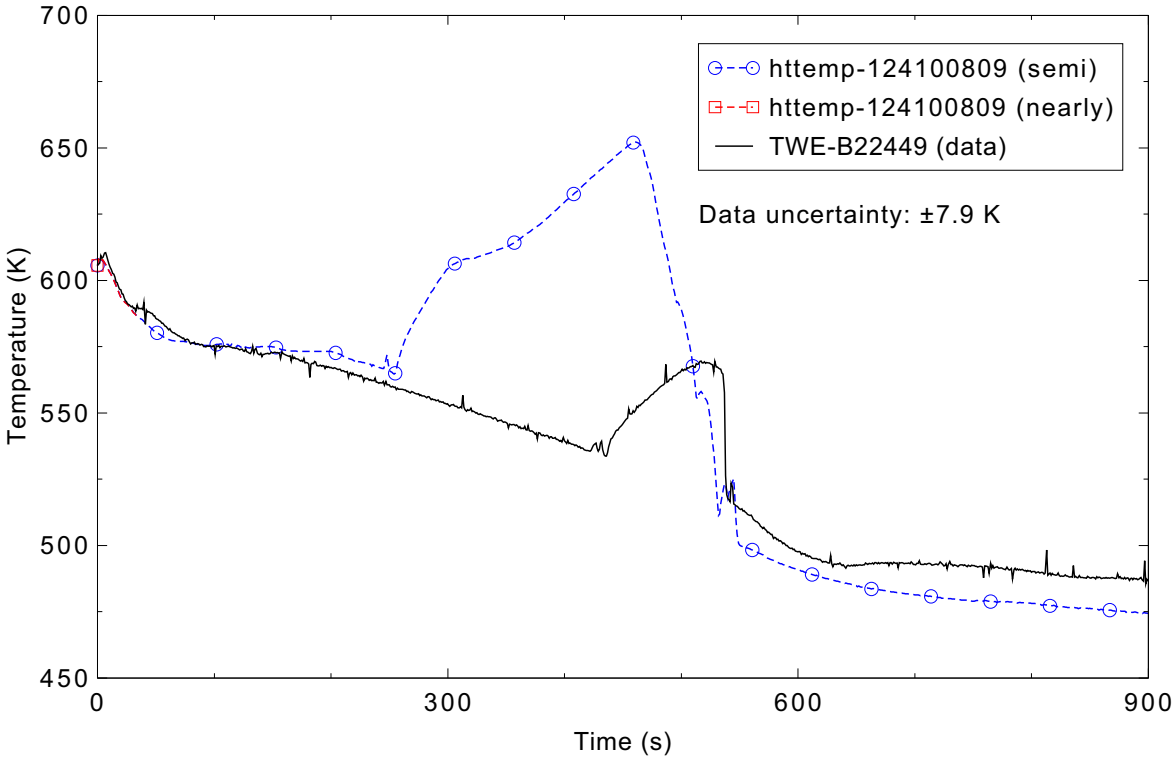

Figure 5.2-24. Measured and calculated heater rod surface temperature at axial level 9 for ROSA-IV Test SB-CL-18.

The calculation predicts that level 9 (3.610 m above the bottom of the core) at the top of the core has a large temperature heatup much sooner than the experiment. Due to the fact that loop seal A never truly clears in the calculation, a large amount of fluid is retained there and is not redistributed into the core. This causes the second core uncovery to occur prematurely, resulting in a large core heatup and an incorrect prediction of the heater rod surface temperature. The heater rod surface temperature is in good agreement toward the bottom of the core, but becomes increasingly worse at higher elevations. The heater rod surface temperatures for levels 3, 5, and 6 are in reasonable agreement with the data. The heater rod surface temperatures for levels 8 and 9 are in minimal agreement with the data.

5.2.5 Water Property Sensitivity Study

The default water property file in the code (h2o) is based on the 1967 steam tables. The ROSA-IV input deck was also run using the h2o95 (1995 steam tables) and h2on (1984 steam tables) options to assess the sensitivity of the code to different water property files. The semi-implicit results for the pressurizer pressure, the break mass flow rate, the vessel liquid level, and the heater rod temperatures for these runs are presented.

The pressurizer pressures are compared in Figure 5.2-25. There is no significant difference observed between the three calculations using different water property files.

The break mass flow rates are compared in Figure 5.2-26. There are small differences in the calculations after 600 s, but the observed differences are small.

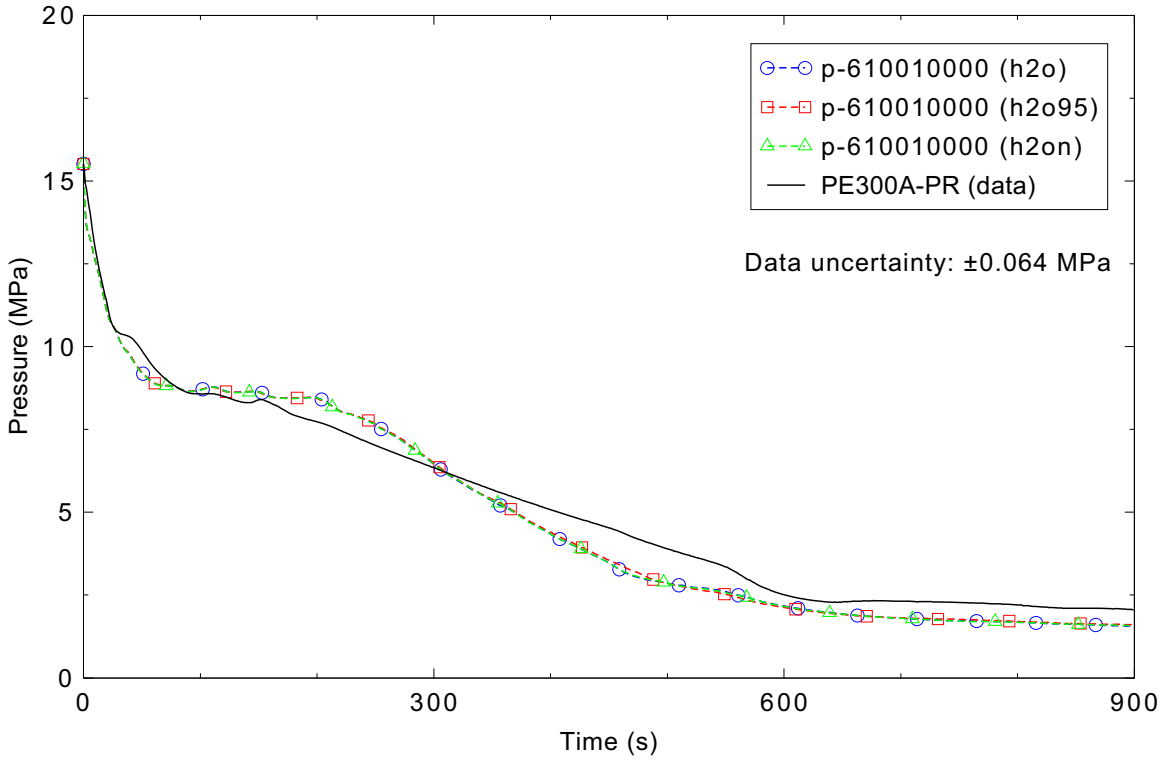

Figure 5.2-25. Measured and calculated pressurizer pressure using different water properties for ROSA-IV Test SB-CL-18.

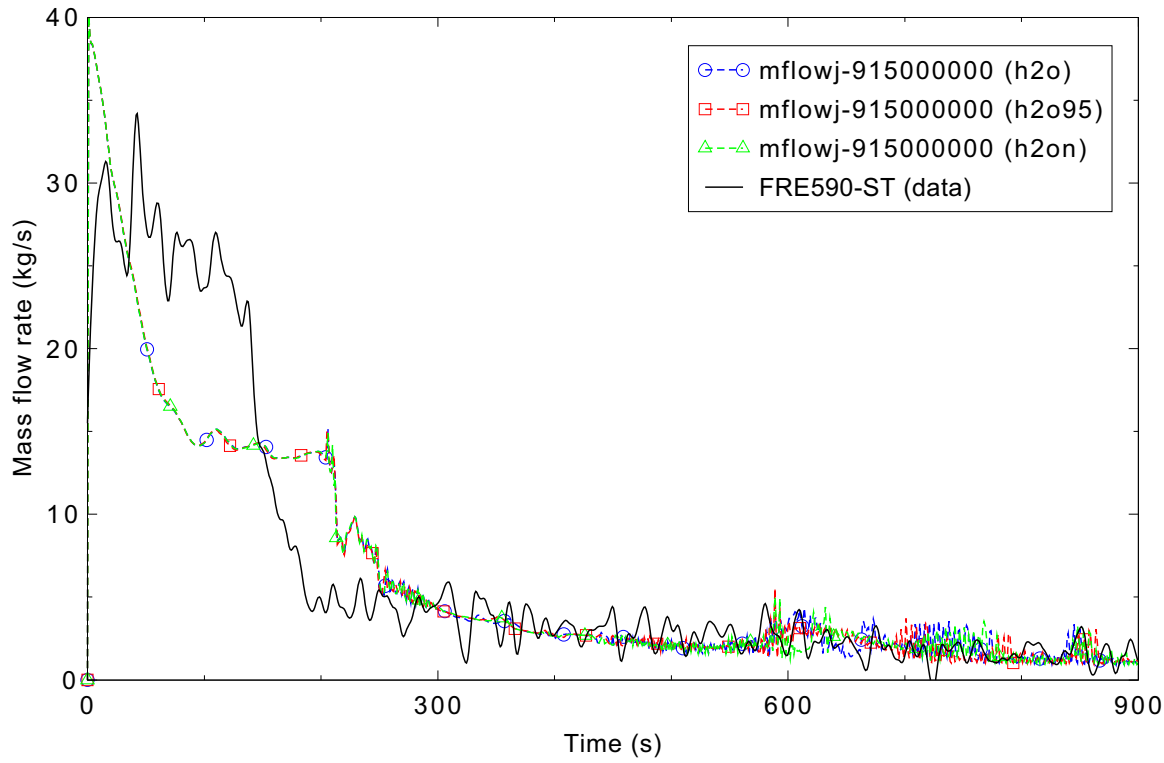

Figure 5.2-26. Measured and calculated break mass flow rate using different water properties for ROSA-IV Test SB-CL-18.

The vessel liquid levels are compared in Figure 5.2-27. Again the observed differences in the results are small.

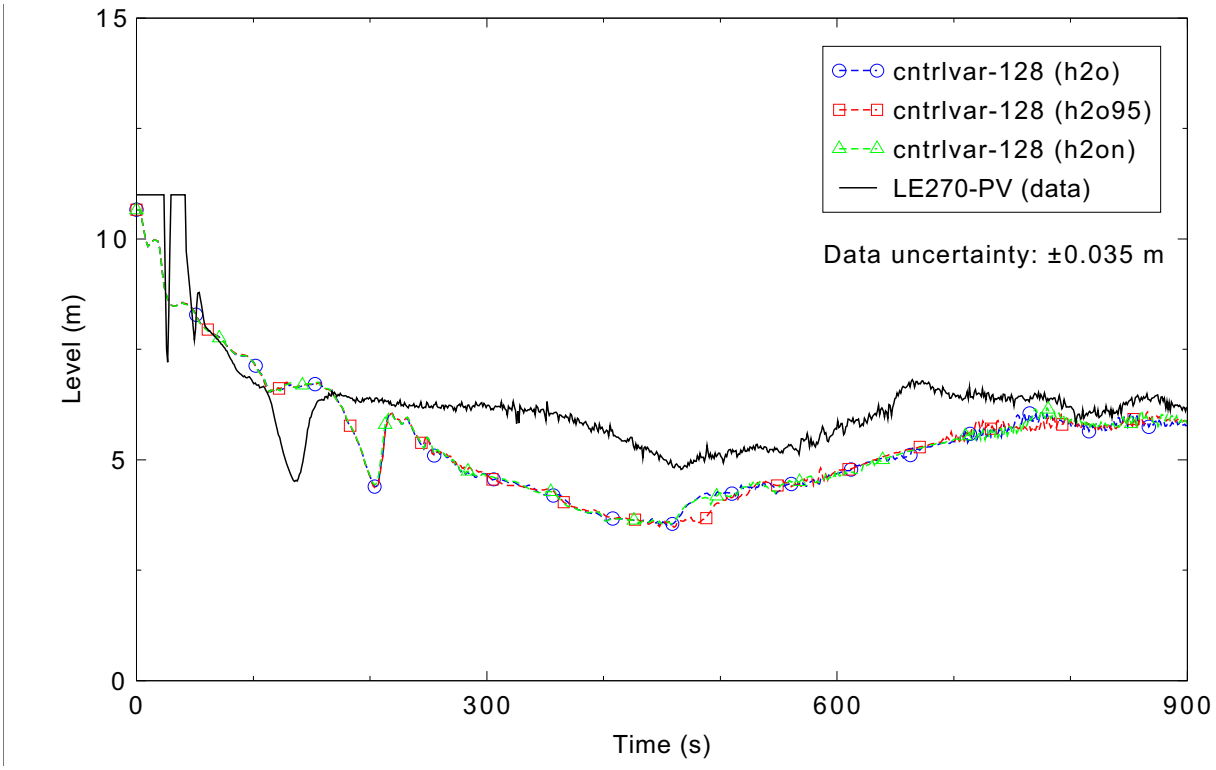

Figure 5.2-27. Measured and calculated vessel liquid level using different water properties for ROSA-IV Test SB-CL-18.

The heater rod surface temperatures at five different axial levels are compared in Figures 5.2-28 through 5.2-32. The heater rod surface temperatures that were calculated using the h2o and h2on water property files were nearly identical. The calculation with using the h2o95 water property file had a short heatup in axial level 6 that the other two calculations did not, and had lower peak temperatures in axial levels 8 and 9.

5.2.6 Conclusions and Assessment Findings

The majority of the parameters calculated by the code were in reasonable agreement with the measured data, although there were several significant parameters that were not.

The pressure in the primary coolant system was in reasonable agreement with the data, as was the pressure in the secondary coolant system. The mass flow rates in the hot and cold loops were judged to be reasonably predicted, although most of the loop densities were not. The accumulator mass flow rates were in reasonable agreement with the experiment, although they were activated earlier in the calculation than in the experiment.

The break mass flow rate was judged to be in minimal agreement with the data during the initial portion of the transient, but was in reasonable agreement after the transition to primarily steam flow. The heater rod temperatures toward the bottom of the core were in good agreement with the data, but became

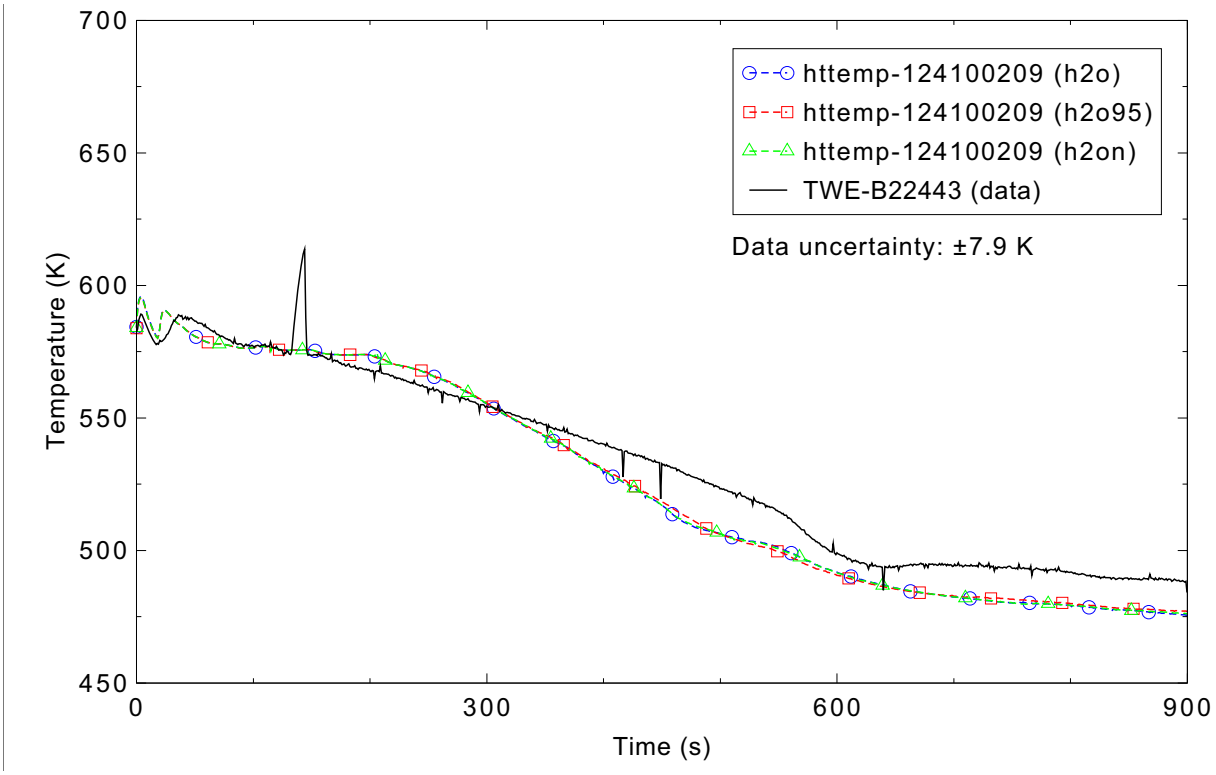

Figure 5.2-28. Measured and calculated heater rod surface temperature at axial level 3 using different water properties for ROSA-IV Test SB-CL-18.

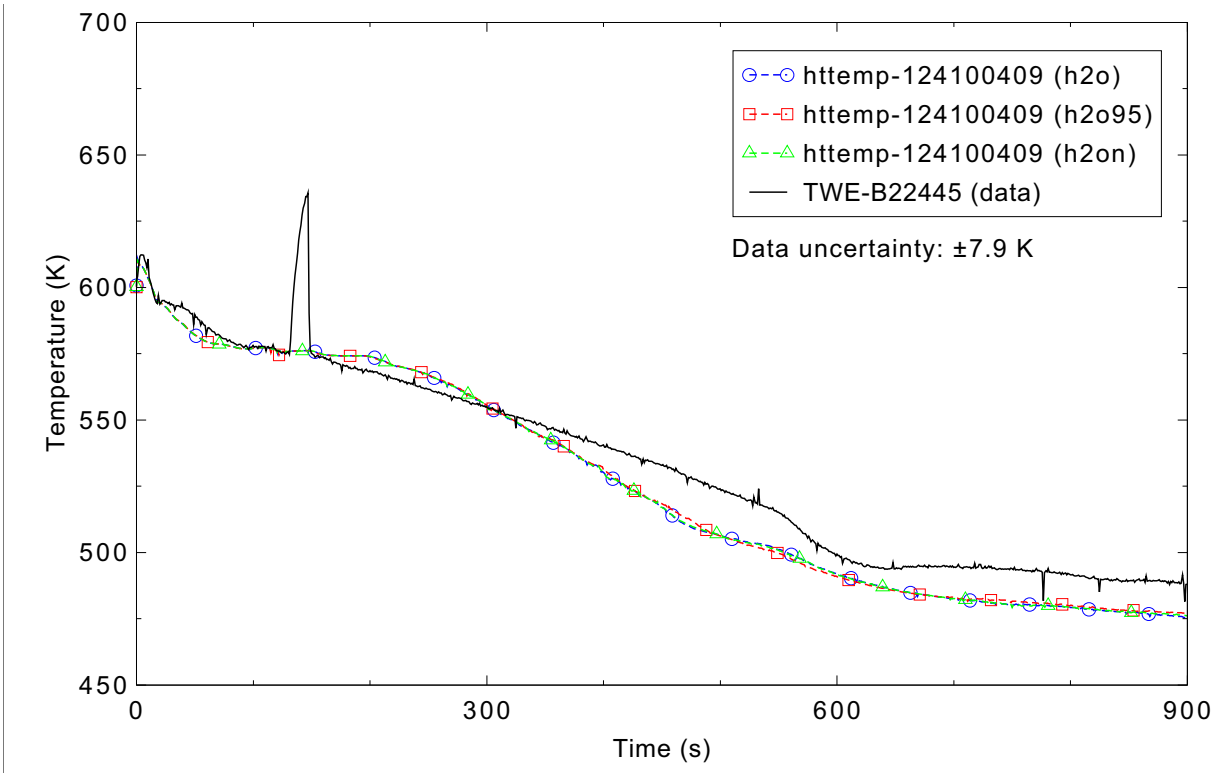

Figure 5.2-29. Measured and calculated heater rod surface temperature at axial level 5 using different water properties for ROSA-IV Test SB-CL-18.

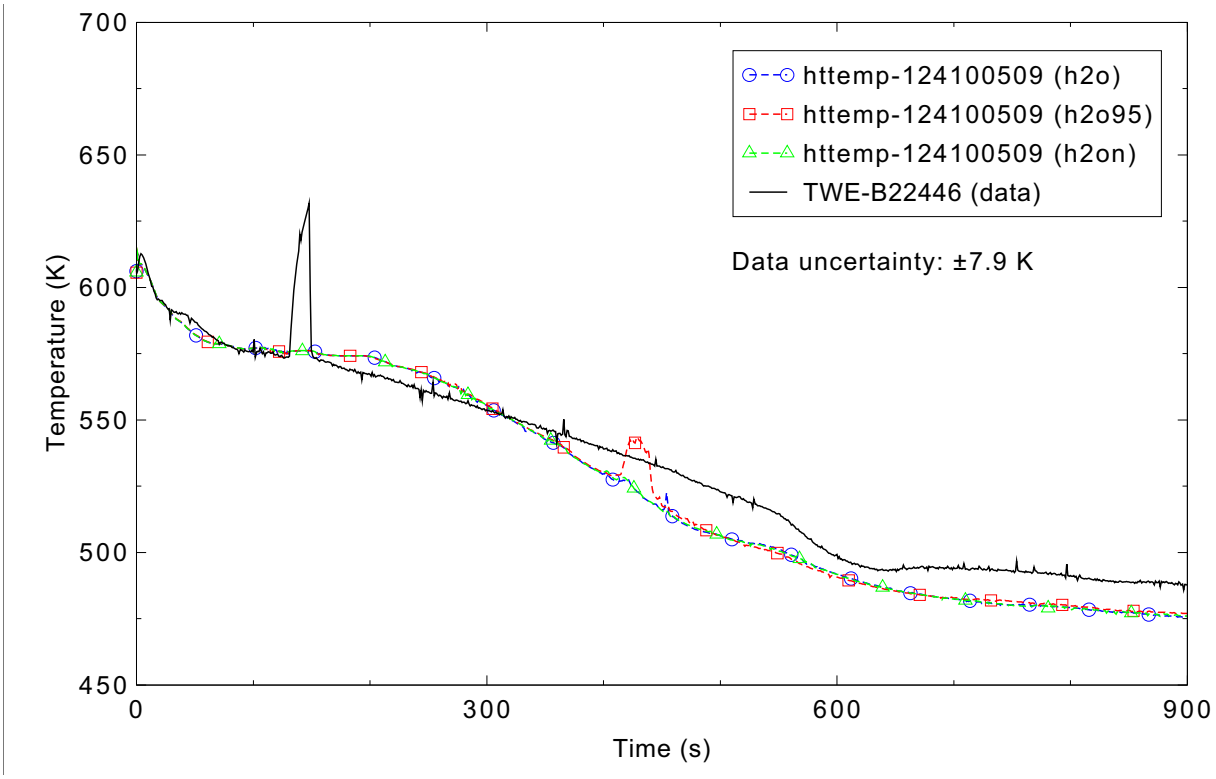

Figure 5.2-30. Measured and calculated heater rod surface temperature at axial level 6 using different water properties for ROSA-IV Test SB-CL-18.

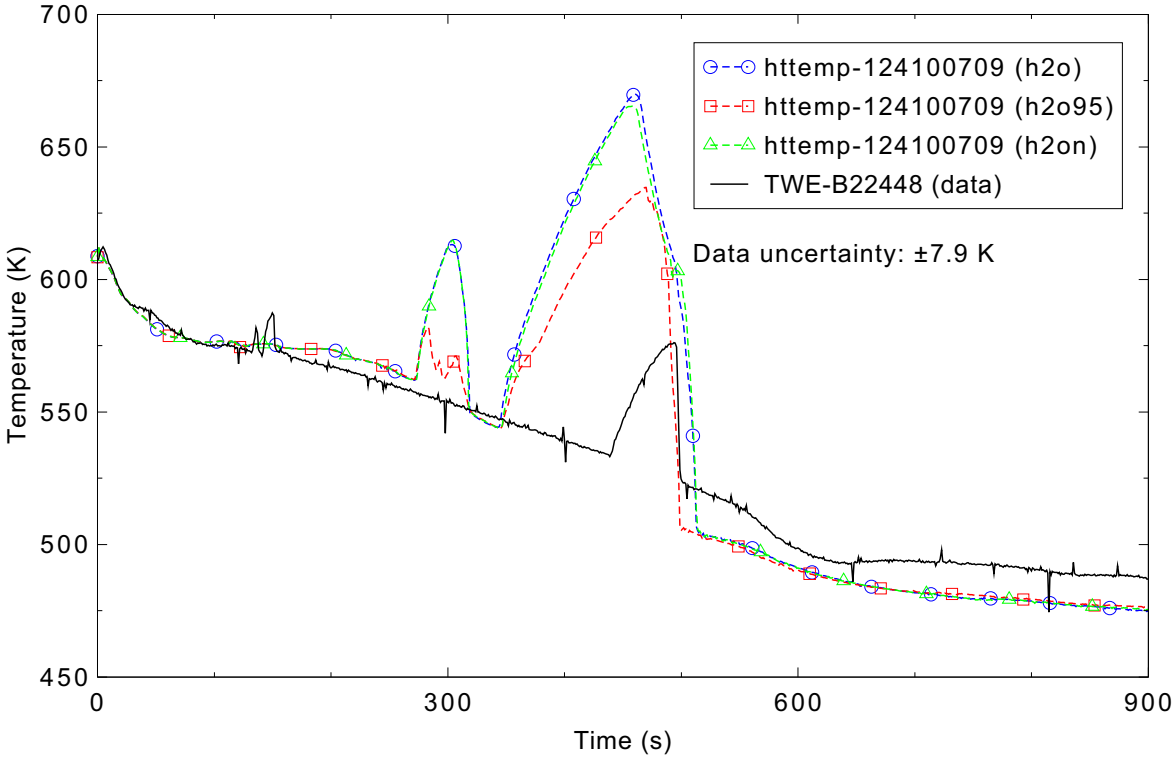

Figure 5.2-31. Measured and calculated heater rod surface temperature at axial level 8 using different water properties for ROSA-IV Test SB-CL-18.

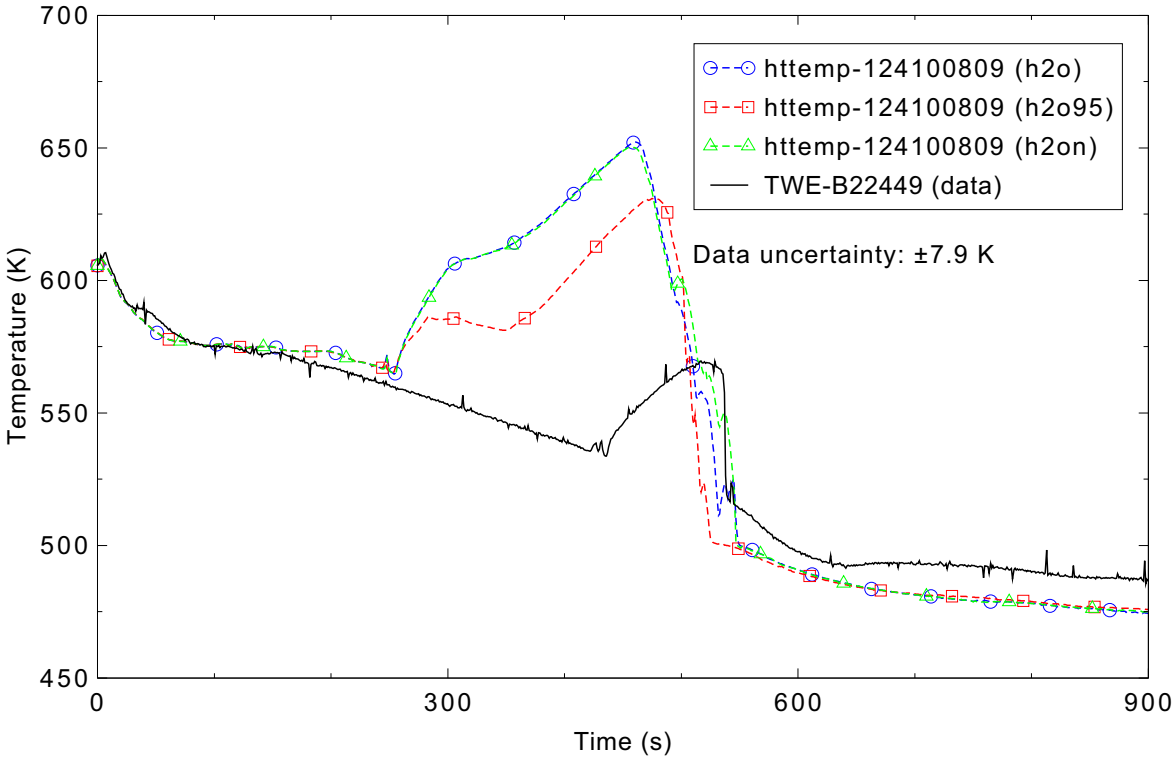

Figure 5.2-32. Measured and calculated heater rod surface temperature at axial level 9 using different water properties for ROSA-IV Test SB-CL-18.

worse with increasing height in the core. The core liquid level was under predicted for a portion of the calculation, which resulted in a longer-term core uncovery.

The primary deficiency in the calculation was that the code did not predict the clearing of the intact loop loop seal. This caused fluid to be retained in the intact loop. If this loop seal had cleared as it did in the experiment, the core liquid level would have been better predicted, and the core heatup would have been shorter. Also, there would have been flow through the intact loop steam generator tubes, which would have improved the prediction of the steam generator pressure.

Running the same input deck with the h2on water property file had a negligible effect on the calculations, but using the h2o95 water property file showed some differences in the heater rod temperatures toward the top of the core.

5.2.7 References

5.2-1. ROSA-IV Group, *ROSA-IV Large Scale Test Facility (LSTF) System Description*, JAERI-N 84-237, 1985.

5.2-2. *OECD/NEA/CSNI International Standard Problem No. 26 (ISP-26), ROSA-IV LSTF Cold-Leg Small-Break LOCA Experiment*, NEA/CSNI/R(91) 13, February 1992.

5.3 Semiscale NC Tests 1, 2, 3, and 10

A series of experiments was conducted by EG&G Idaho, Inc. in the Semiscale Mod-2A facility, a scaled model of a pressurized water reactor (PWR). The main objective of these experiments was to investigate natural circulation heat rejection under normal and abnormal operating conditions. Three distinct modes of natural circulation were found to occur as a function of primary coolant inventory: single-phase, two-phase (liquid continuous), and reflux condensation.

Of the ten tests in the series, four were simulated using the RELAP5-3D computer code and the calculated results were compared with the experiment data. The four tests are Test 1 (S-NC-1), Test 2 (S-NC-2), Test 3 (S-NC-3), and Test 10 (S-NC-10). Test S-NC-1 examined steady-state single-phase natural circulation behavior. Test S-NC-2 examined single-phase, two-phase, and reflux steady-state modes by varying the primary side system mass at different core powers (30, 60, and 100 kW) with a constant steam generator secondary side condition. The constant 60 kW power level cases were simulated and analyzed in this report. Test S-NC-3 examined primary side two-phase natural circulation behavior under varying steam generator secondary side mass inventory at a core power of 62 kW. Test S-NC-10 was designed to supplement data obtained in earlier tests of the natural circulation series, such that more precise statements could be made about single-phase and two-phase natural circulation behavior.

5.3.1 Code Models Assessed

Semiscale natural circulation Tests S-NC-1, S-NC-2, S-NC-3, and S-NC-10 assess the code capability for predicting the single- and two-phase natural circulation phenomena in an integral facility.

5.3.2 Experiment Facility Description

The Semiscale Mod-2A test facility was a full height, 1/1705 power-to-volume scaled model of the primary system of a four-loop PWR.[5.3-1] The Mod-2A system incorporated the major components of a PWR, including steam generators, reactor vessel, downcomer, pumps, pressurizer, and loop piping. For the bulk of the steady-state experiments, a single-loop configuration (shown in 5.3-1) was employed, using the intact loop. In the single-loop configuration, the intact-loop pump was replaced with a spool piece containing an orifice that simulated the hydraulic resistance of a locked pump rotor. In addition, the vessel was modified from the normal Mod-2A configuration by removing the vessel upper head to ensure a uniform heatup of the entire system and to avoid condensation on the upper head structure.

Detailed descriptions of the Semiscale Mod-2A test facility are given in Reference 5.3-1. All of the natural circulation experiments and the data are summarized in References 5.3-1 and 5.3-2. The data used in this report are from those references.

5.3.3 Input Model Description

5.3-2 shows the RELAP5-3D nodalization diagram for the Semiscale Mod-2A single-loop configuration. The model included the reactor vessel and downcomer, the hot leg, a steam generator, the pump suction piping, and the cold leg. The pressurizer was modeled with a time-dependent volume. The model consisted of 62 hydrodynamic components and 9 heat structures (35 heat structures for

Test S-NC-10 Part 1). The core heater rods were modeled using a heat structure (Structure 1500) extending over six hydrodynamic volumes.

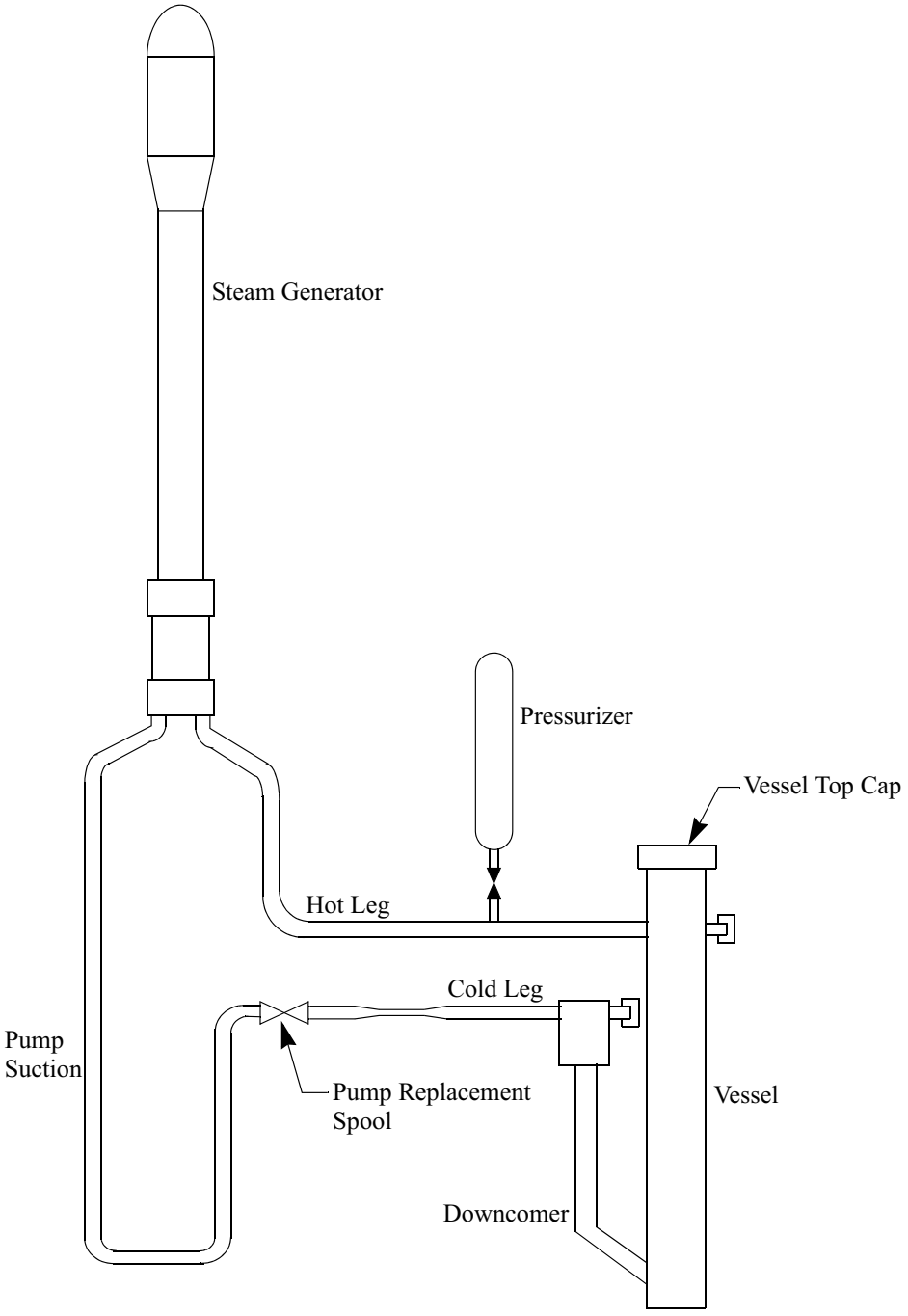

Figure 5.3-1. Semiscale Mod-2A single-loop configuration.

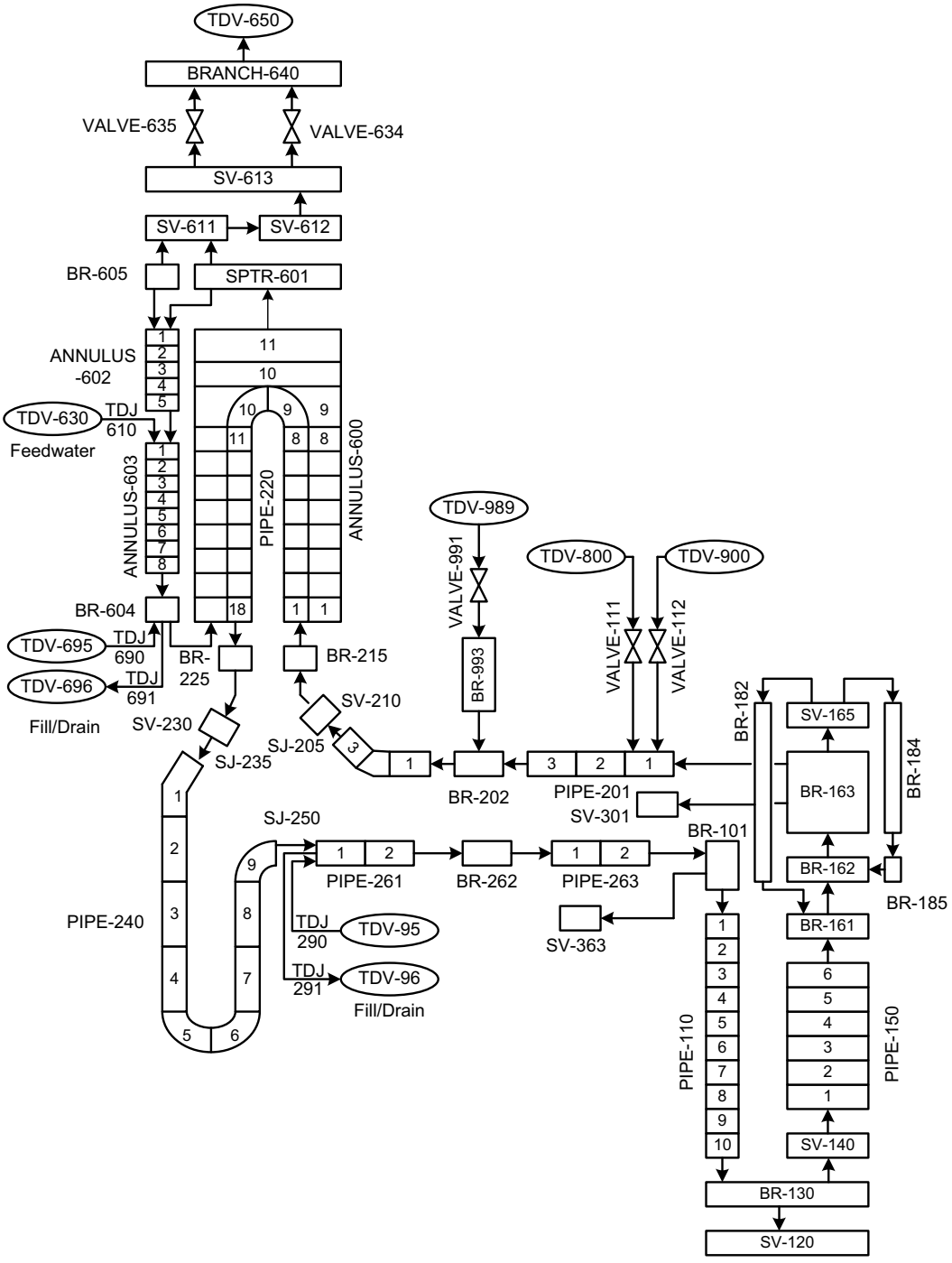

Figure 5.3-2. Nodalization of RELAP5-3D Semiscale natural circulation test model.

Two time-dependent junctions (Components 290 and 291) connect two time-dependent volumes (Components 95 and 96) to the cold leg (Component 261). These time-dependent junctions are used to adjust the mass inventory by filling or draining the primary system. These time-dependent junctions are

moved to be connected to the bottom of the lower plenum (Component 120) in the simulation of Test S-NC-10. There are two more time-dependent junctions (Components 690 and 691) in the secondary system, as shown in 5.3-2. They are used to fill and drain the secondary system.

Initial and boundary conditions for each test are discussed below.

5.3.3.1 Test S-NC-1 Conditions

Test S-NC-1 examined steady-state single-phase natural circulation behavior. The experiment consisted of five cases; Case 4 was simulated. Case 4 of S-NC-1 had the following test conditions. The primary and secondary system pressures were 10.1 MPa and 5.8 MPa, respectively. The core power was 60 kW. The liquid temperature in the hot leg was 577 K.

In the simulation, the steady-state pressure was maintained by the pressurizer. The time-dependent junctions for draining or filling the primary or secondary system inventory were not open during this simulation. Table 5.3-1 shows the simulation and test conditions.

Table 5.3-1. Comparison of simulation and test conditions of Semiscale Test S-NC-1.

Parameter	Experiment	Simulation
Primary system pressure (MPa)	10.1	10.1
Secondary system pressure (MPa)	5.8	5.8
Core power (kW)	60	60
Hot leg temperature (K)	577	576

5.3.3.2 Test S-NC-2 Conditions

Test S-NC-2 examined steady state single-phase, two-phase, and reflux modes of natural circulation by varying the primary system mass at core powers of 30 kW, 60 kW, and 100 kW with a constant steam generator secondary side condition. The 60 kW case was selected for the assessment. The initial primary system pressure was 10.4 MPa, and the primary system mass inventory was reduced from 100% to 61.2%. The secondary system pressure and mass inventory were 5.8 MPa and 100%, respectively. Table 5.3-2 summarizes the boundary conditions.

Table 5.3-2. Simulation conditions of Semiscale Test S-NC-2.

Parameter	Input Value
Primary system mass inventory	Drained from 100% to 61.2%
Secondary system mass inventory	100%
Initial primary system pressure	10.4 MPa
Secondary system pressure	5.8 MPa
Power	60 kW

In the calculation, the primary system mass was reduced by draining liquid from the cold leg after every 800 s of simulation time. A control system was used to make the desired primary side mass inventory adjustments, which took less than 10 s to accomplish.

5.3.3.3 Test S-NC-3 Conditions

Case 3 of Test S-NC-3 was simulated. This case investigated primary side two-phase natural circulation behavior with a varying steam generator secondary side mass inventory at a core power of 62 kW. The initial primary system pressure was 6.9 MPa and the mass inventory was 91.8%. The secondary system pressure was 5.9 MPa. Table 5.3-3 provides a summary of the simulation conditions.

Table 5.3-3. Simulation conditions of Semiscale Test S-NC-3.

Parameter	Input Value
Primary system mass inventory	91.8%
Secondary system mass inventory	Drained to reduce the SG effective heat transfer area from 100% to 15.2%
Initial primary system pressure	6.9 MPa
Secondary system pressure	5.9 MPa
Power	62 kW

In the calculation, the secondary system mass was reduced by draining liquid from the downcomer after every 500 s of simulation time. Mass was removed at each step to match the test conditions, in which the effective heat transfer area of the steam generator U-tubes changed from 100% to 15.2% over the course of the experiment. A control system was used to make the desired secondary side mass inventory adjustments.

5.3.3.4 Test S-NC-10 Conditions

Three cases of Test S-NC-10 were simulated, Parts 2 through 4. As discussed earlier, Test S-NC-10 was performed to supplement data obtained in the earlier tests of the natural circulation series.

Table 5.3-4 shows the simulation conditions of Test S-NC-10. In the simulation of Parts 2 and 4, the primary system mass inventory was reduced while the secondary system conditions were kept constant, as was done in Test S-NC-2. The mass was reduced after every 500 s of simulation time in Part 4 and after every 600 s in Part 2. In the simulation of Part 3, the secondary system mass inventory was reduced while the primary mass inventory was maintained, as was done in Test S-NC-3. The secondary mass was adjusted after every 500 s.

In Part 4 of the experiment, most of the data were taken at a core power of 100 kW. However, at primary system mass inventories of 81.93%, 78.97%, and 76.01%, data were taken at core powers of both 100 and 60 kW to investigate the effect of the power reduction on natural circulation behavior. The code assessment primarily considered the 100 kW portions of the experiment, as only three data points were taken at 60 kW.

Table 5.3-4. Simulation conditions of Semiscale Test S-NC-10.

Parameter	Part 2	Part 3	Part 4
Primary system mass inventory	Reduced from 100% to 74.44%	100%	Reduced from 100% to 76.01%
Secondary system mass inventory	100%	Reduced to change the SG tube effective heat transfer area from 100% to 74.44%	100%
Initial primary system pressure	8.6 MPa	7.7 MPa	11.1 MPa
Secondary system pressure	5.0 MPa	5.85 MPa	5.84 MPa
Power	33.54 kW	33.54 kW	100 kW and 60 kW
Heat loss	Not modeled	Not modeled	Not modeled

5.3.4 Data Comparisons and Results

The important parameters predicted by RELAP5-3D were compared with the measured data, which were obtained from the NRC Data Bank. The compared parameters are the mass flow rate in the primary system, the hot leg fluid temperature, the cold leg fluid temperature, and the primary system pressure. Discussions of each test are provided in the following sections.

5.3.4.1 Test S-NC-1

Test S-NC-1 was simulated to assess the capability of RELAP5-3D for predicting steady-state single-phase natural circulation behavior. Transient runs were made with the RELAP5-3D code using both the semi-implicit and the nearly-implicit advancement schemes. The requested time step size was 0.05 s for both cases.

The important parameters predicted with semi-implicit and nearly-implicit numerical methods are shown in Figures 5.3-3 through 5.3-6. The calculations reached steady state by 1,000 s. The semi- and nearly-implicit numerical schemes predicted almost identical results.

Table 5.3-5 compares parameters predicted by RELAP5-3D to the measured data. The predicted coolant temperatures and mass flow rate in the primary system compared well with the measured values. The code simulations are judged to be in excellent agreement with the data.

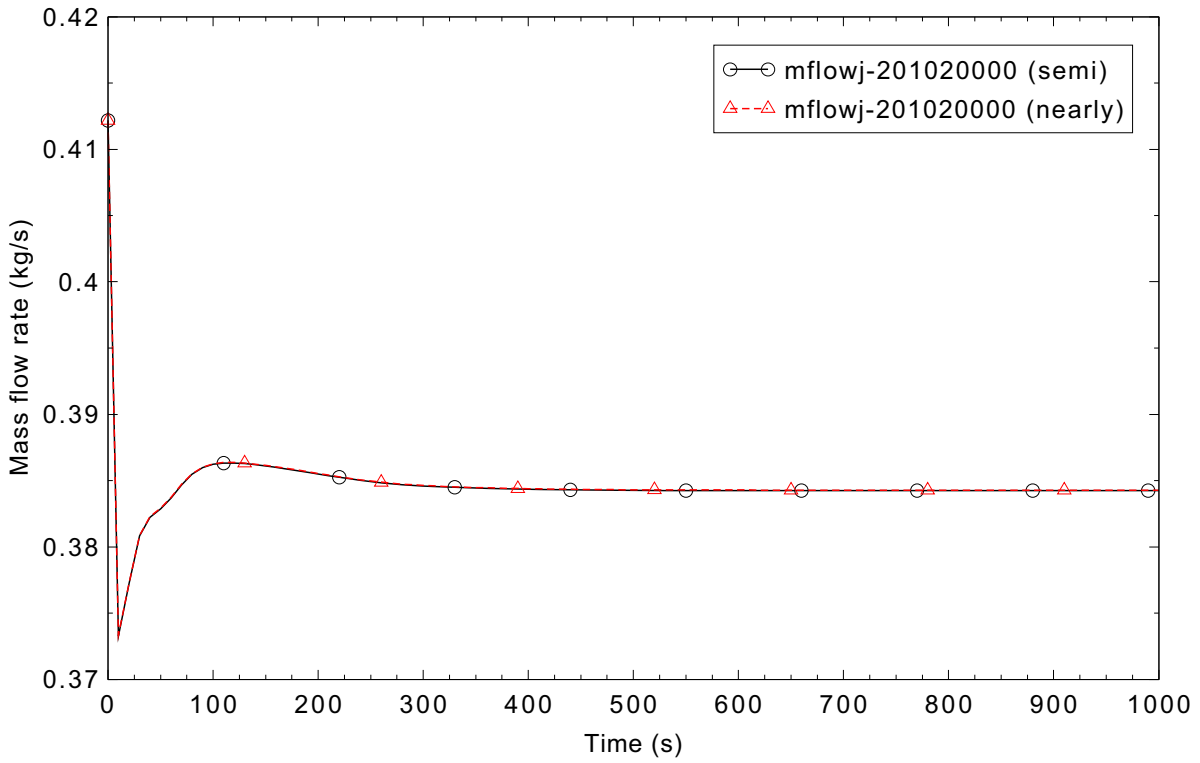

Figure 5.3-3. Calculated primary system mass flow rate at 60 kW core power for Semiscale Test S-NC-1.

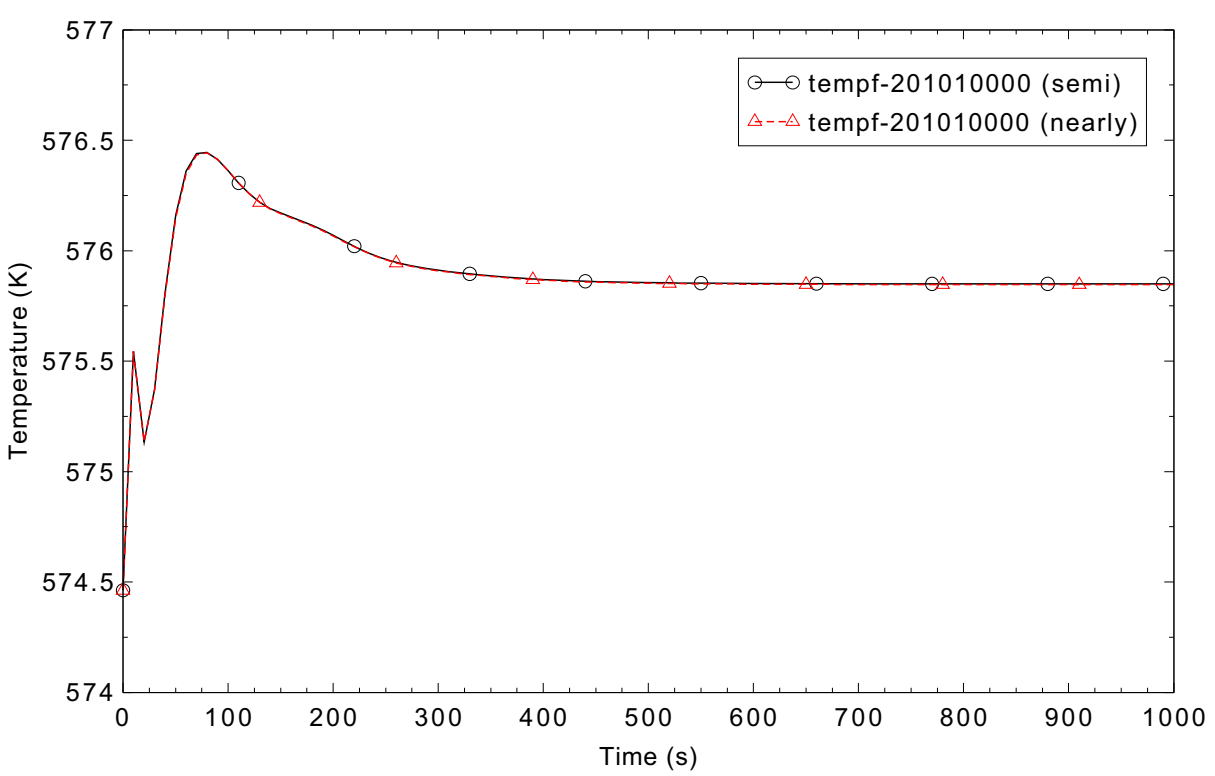

Figure 5.3-4. Calculated hot leg liquid temperature at 60 kW core power for Semiscale Test S-NC-1.

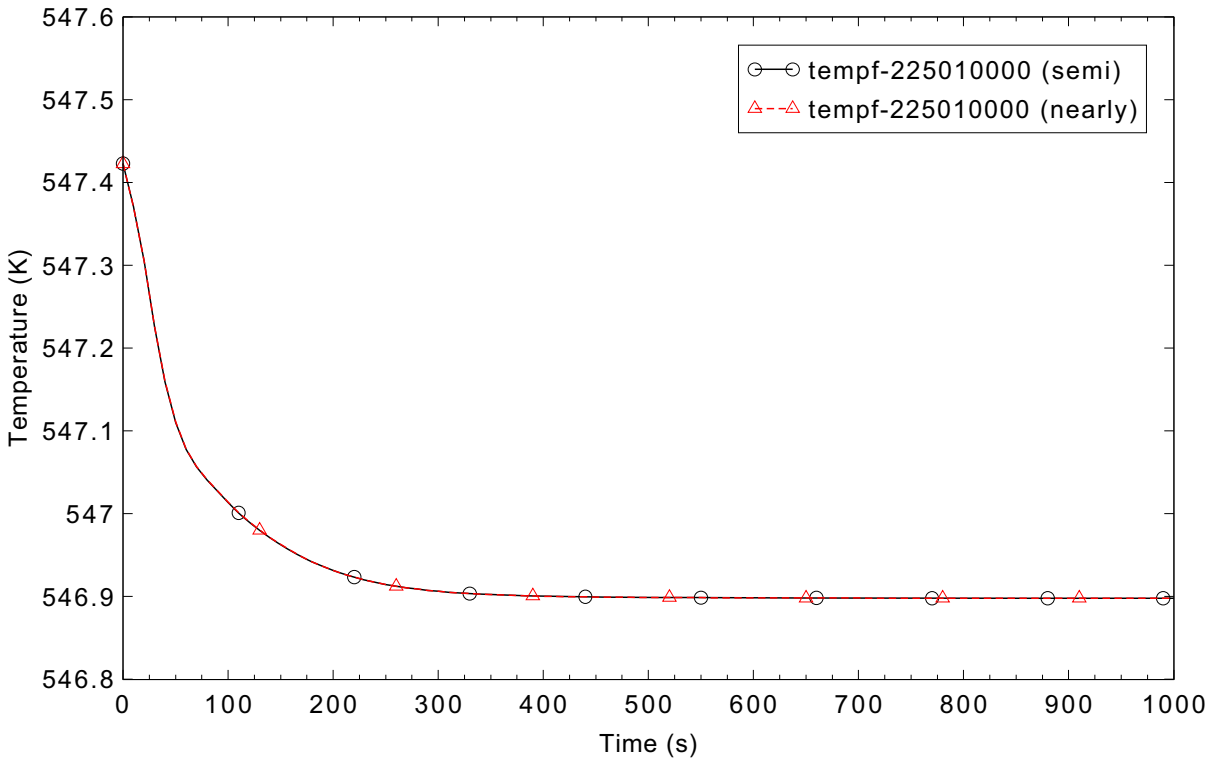

Figure 5.3-5. Calculated cold leg liquid temperature at 60 kW core power for Semiscale Test S-NC-1.

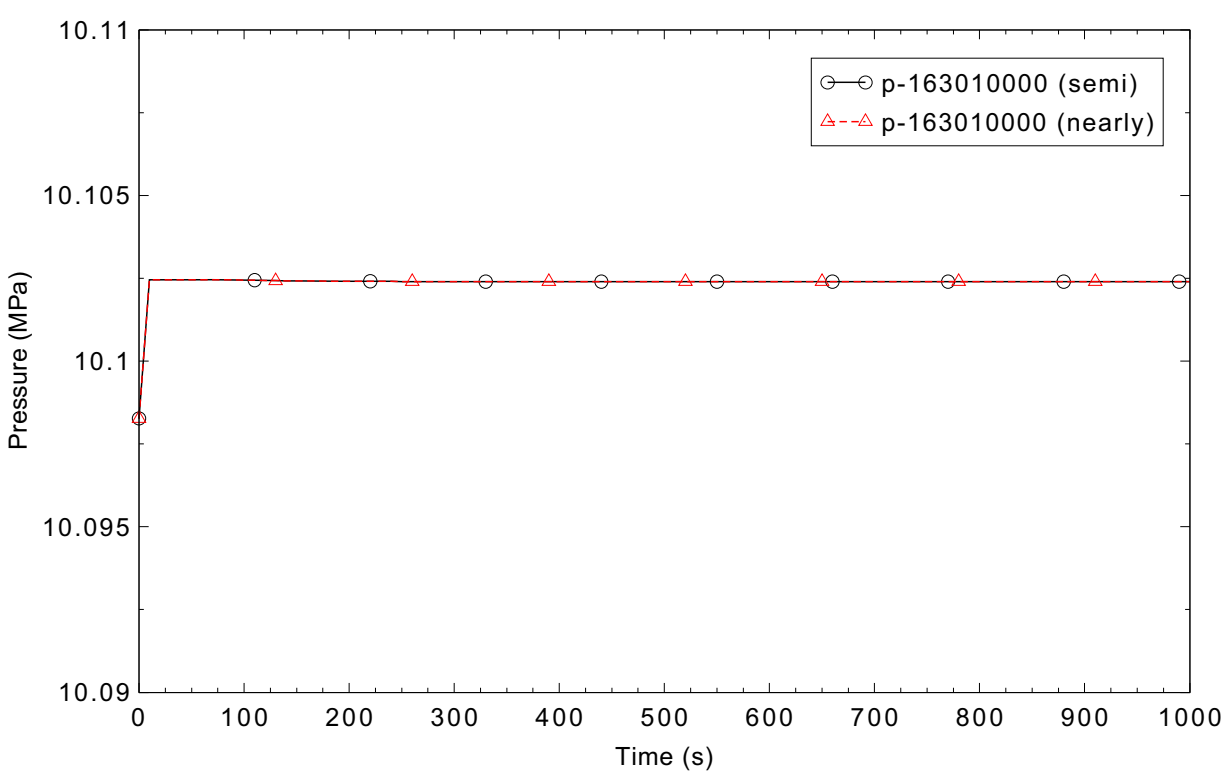

Figure 5.3-6. Calculated primary system pressure at 60 kW core power for Semiscale Test S-NC-1.

Table 5.3-5. Comparison of predicted parameters to measured data for Semiscale Test S-NC-1.

Parameter	Experiment	Simulation
Primary system pressure (MPa)	10.1	10.1
Secondary system pressure (MPa)	5.8	5.8
Core power (kW)	60	60
Hot leg temperature (K)	577	576
Cold leg temperature (K)	548	547
Mass flow rate in primary system (kg/s)	0.4	0.384

5.3.4.2 Test S-NC-2

Test S-NC-2 investigated steady state single-phase, two-phase, and reflux natural circulation by varying the primary system mass at a core power of 60 kW with constant steam generator secondary side conditions. Transient calculations were performed using both the semi-implicit and the nearly-implicit advancement schemes, with a requested time step size of 0.05 s. The nearly-implicit calculation was unable to maintain mass inventories above 93%. Sixteen different steady state conditions were achieved. Each steady state was at a different primary side mass inventory, ranging from 100% down to 61.2%. The primary system pressure was allowed to vary as the system was drained (the pressurizer was valved out) while the steam generator secondary pressure was held constant and acted as an effective heat sink throughout the test. It was noted in the experiment that for mass inventories between 94% and 100% the primary system behavior was similar to single-phase natural circulation. It was also noted that when the primary side mass inventory decreased below 66 to 70% the system transitioned from two-phase natural circulation to the reflux mode of cooling.

Figure 5.3-7 shows the calculated hot leg mass flow rate compared to the measured data. The calculated results compare well with the data in the 96% to 100% mass inventory range, in which the predicted void fraction in the hot leg was 0.0%. As the mass inventory was reduced further, steam began to be generated by boiling in the core and flashing. While there was some vapor in the down side of the steam generator U-tubes, more steam was present in the core, hot leg, and up side of the steam generator tubes. The reduced density in these regions resulted in an increased density difference to drive the natural circulation flow, which in turn increased. The peak flow rate occurred when the average density difference between the up and down sides of the tubes was at its maximum, near an inventory of 93% in the test and 87% in the simulation. The flow rate then decreased continuously as the primary system mass inventory was reduced further.

There were significant oscillations in the primary system mass flow rate and pressure for the mass inventory range between 71% and 85% in both the semi- and nearly-implicit calculations. The oscillations, which had a period of about 35 s, began when liquid was drained to reduce the primary system inventory to 85%. The flow into the core stagnated as liquid was drawn from the cold leg, allowing boiling to begin in the bottom core volume. The boiling caused the pressure to increase, and reduced the density in the core and up side of the steam generator tubes. This generated a larger density difference to drive the natural circulation flow, which then increased. As the flow continued to increase, enough colder liquid flowed into

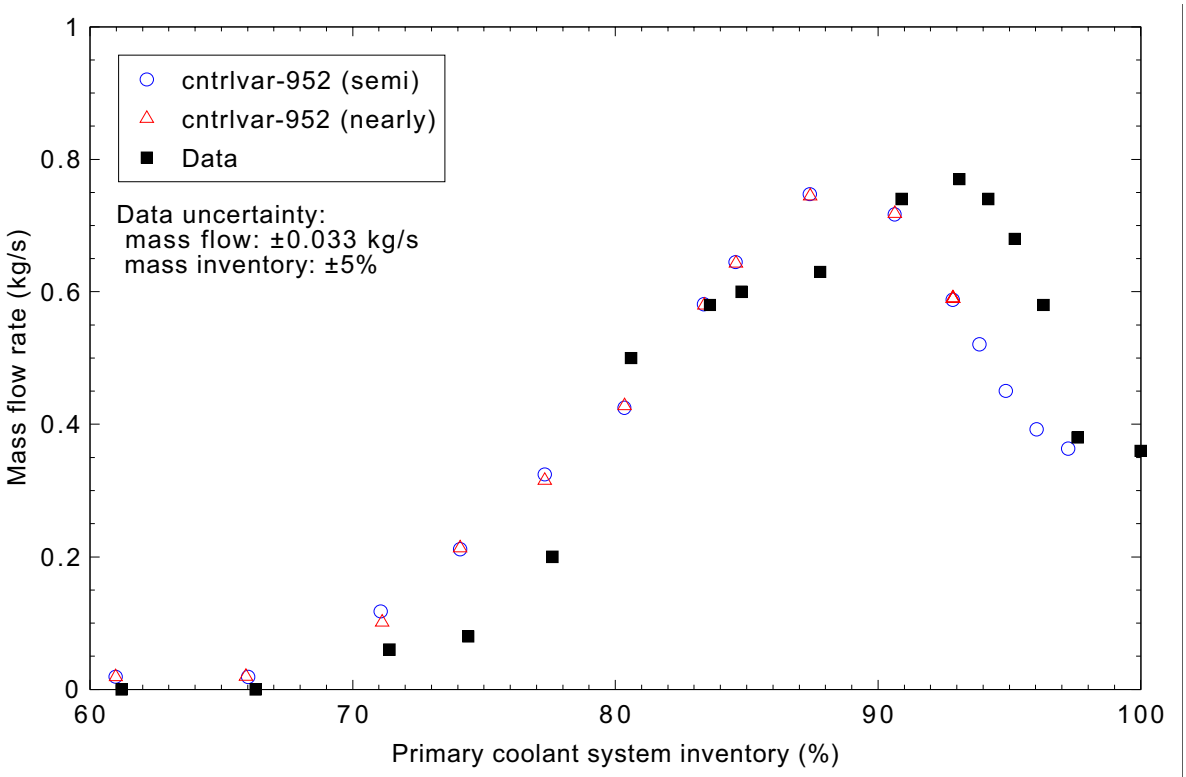

Figure 5.3-7. Measured and calculated primary system mass flow rate at 60 kW core power for Semiscale Test S-NC-2.

the core to reduce the boiling. The higher flow rate caused the up side of the steam generator tubes to start filling with liquid, and the down side to drain as more vapor was pulled over the top of the tubes, reducing the flow rate. When the flow rate dropped low enough, boiling started again near the bottom of the core, and the cycle repeated. The pressure oscillations were offset from the flow rate oscillations, and reflected the vapor generation balance between boiling in the core and condensation in the steam generator tubes. When the net vapor generation was positive, the pressure increased; when it was negative, the pressure decreased. Because of these oscillations, the predicted parameters shown in this section as well as the following sections were time averaged over 200 s.

The reflux condenser mode of natural circulation began when the mass inventory dropped below 70%. The large oscillations in the calculated mass flow rate disappeared. In this mode, vapor flowed to the steam generator and liquid returned to the reactor vessel through the hot leg, yielding a net mass flow rate of almost zero in both the experiment and the calculations. Figure 5.3-8 shows the predicted liquid and vapor mass flow rates at the hot leg region just below the steam generator inlet. In the legend ’mflowfj’ and ’mflowgj’ stand for the liquid and vapor flow rates, respectively. The primary system mass inventory was around 66% between 11,200 and 12,000 s and was around 61% from 12,000 to 12,800 s.

The predicted hot leg liquid temperatures are compared with the experiment data in Figure 5.3-9. The comparison shows that the prediction and the measurement are in generally good agreement. For mass inventories between 91% and 97%, the code predicted slightly higher liquid temperatures than were measured.

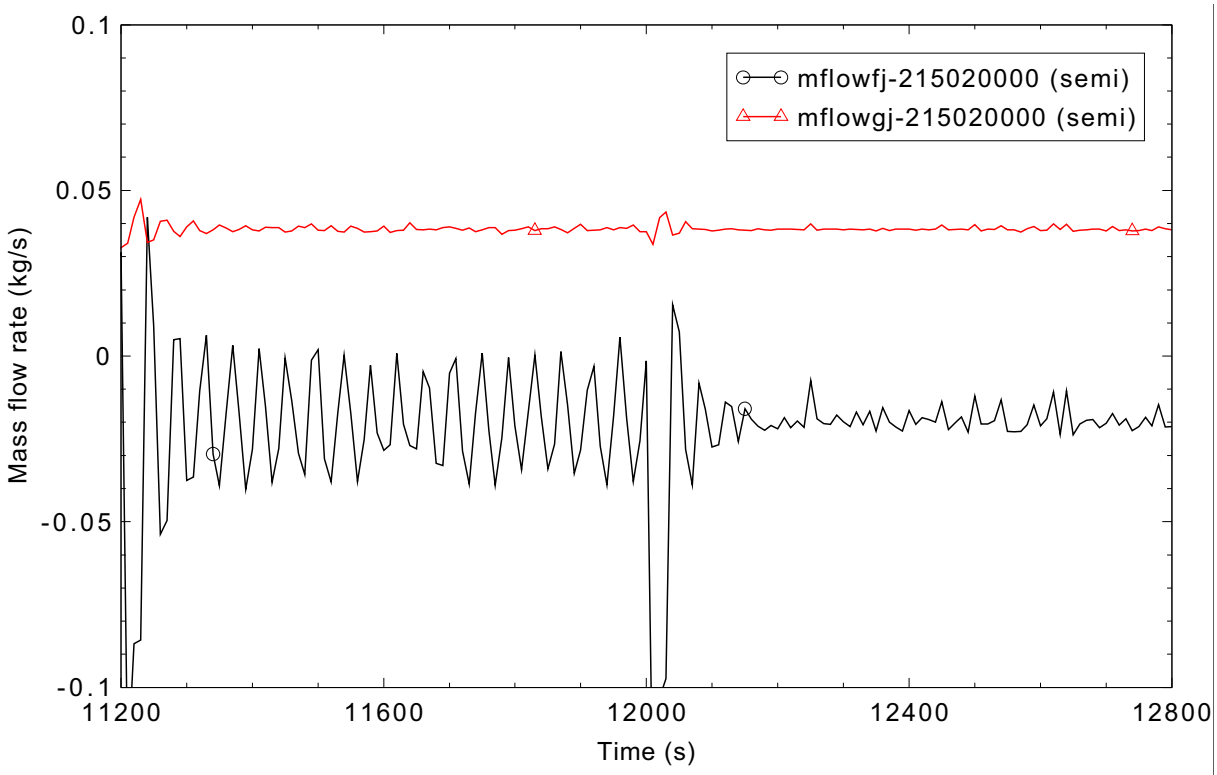

Figure 5.3-8. Calculated primary system liquid and vapor mass flow rates at 60 kW core power for Semiscale Test S-NC-2.

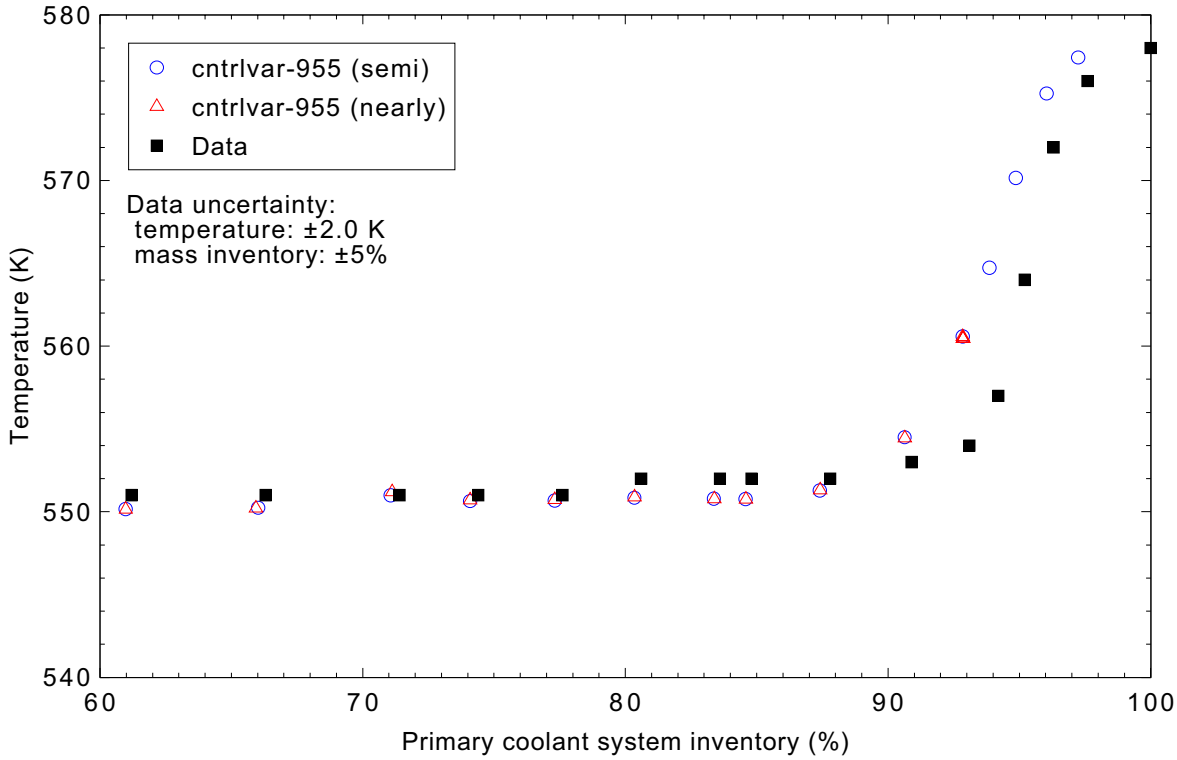

Figure 5.3-9. Measured and calculated hot leg liquid temperature at 60 kW core power for Semiscale Test S-NC-2.

Figure 5.3-10 shows the comparison of the predicted and the measured liquid temperatures in the cold leg. In the single-phase and reflux natural circulation ranges, the prediction and the measurement were in good agreement, but in the two-phase range RELAP5-3D predicted slightly lower liquid temperatures than were measured.

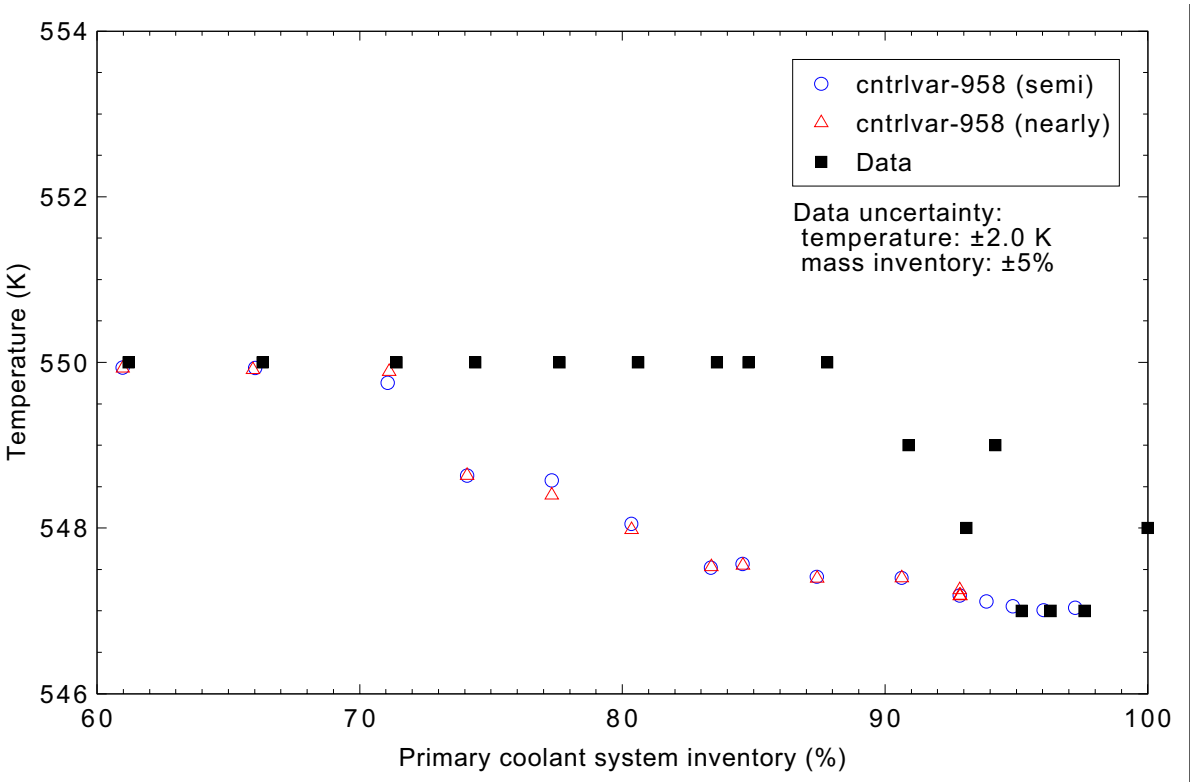

Figure 5.3-10. Measured and calculated cold leg liquid temperature at 60 kW core power for Semiscale Test S-NC-2.

The predicted reactor vessel upper plenum pressures are compared with the measured data in Figure 5.3-11. When the primary side mass inventory was in the range from 93% to 97%, RELAP5-3D predicted slightly higher pressures than were measured, while the pressure was slightly under predicted for mass inventories below 91%. In general, the predicted and measured pressures were in reasonable agreement.

5.3.4.3 Test S-NC-3

Transient calculations were performed using both the semi-implicit and the nearly-implicit advancement schemes. The requested time step size was 0.01 s for both calculations.

There were three cases involved with this test. Each case involved varying one parameter while holding two others constant; the parameters addressed were core power, primary system mass inventory, and secondary system mass inventory. This assessment used the third case, in which nine steady state conditions were established at different secondary system inventories at a core power of 62 kW and a primary system inventory of 91.8%. The effect of the test was to vary the effective heat transfer area during two-phase loop natural circulation.

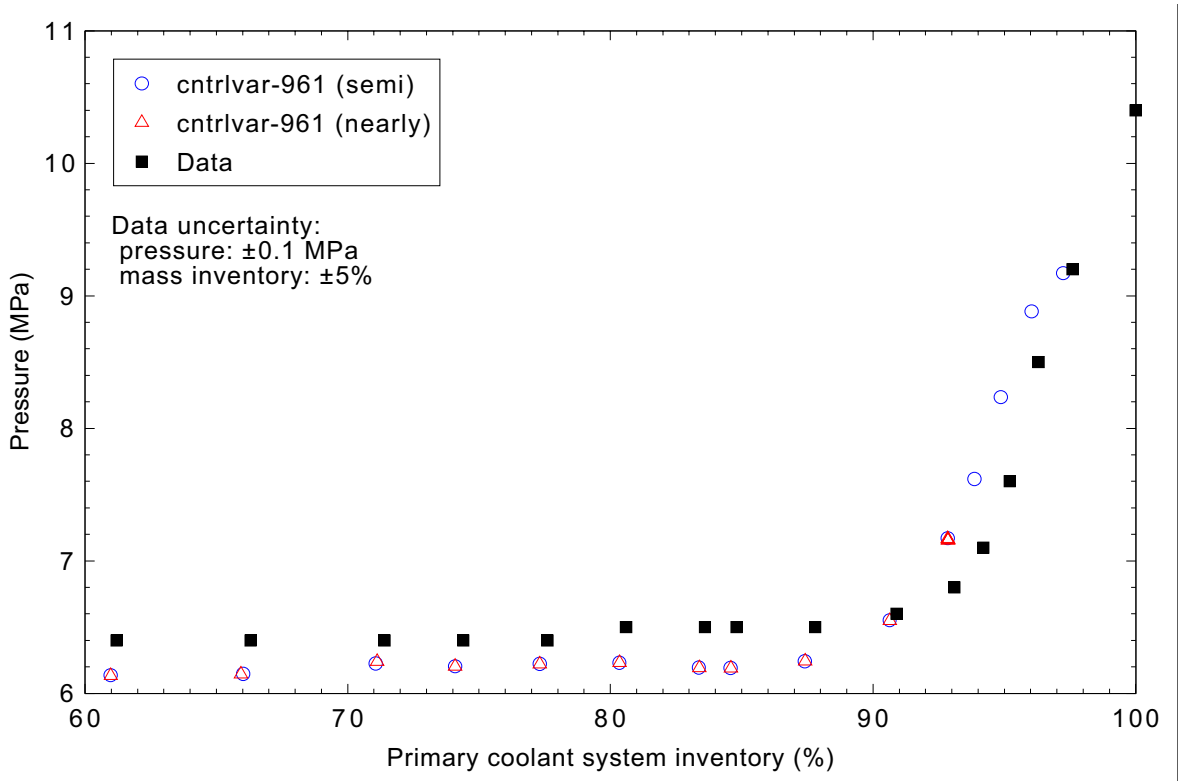

Figure 5.3-11. Measured and calculated reactor vessel upper plenum pressure at 60 kW core power for Semiscale Test S-NC-2.

FIgure 5.3-12 shows the measured and calculated primary system mass flow rates. The measured mass flow rate oscillated when the effective steam generator U-tube heat transfer area was less than 50%. Figure 5.3-12 shows the upper and lower bounds of the oscillations. RELAP5-3D predicted an oscillatory mass flow rate, and the parameters presented here were time-averaged over 200 s as was done in Test S-NC-2. These oscillations are high frequency numerically-driven, while those in Test S-NC-2 were low frequency physically-driven. The calculated mass flow rate compared relatively well with the data at effective heat transfer areas larger than 55%. Increasing differences in the mass flow rates occurred when the effective heat transfer area was below 45%. The calculated mass flow rate decreased from 0.73 kg/s to 0.58 kg/s as the effective heat transfer area was reduced from 68% to 15%, whereas the measured value decreased from 0.75 kg/s to 0.2 kg/s.

Figure 5.3-13 shows the predicted and measured primary system pressures. As expected, the primary side pressure increased in both the simulation and the experiment as less heat was transferred from the primary system to the secondary system with a constant heat source, especially when the effective heat transfer area was below 50%. The predicted pressures were similar to or a little higher than the measured pressures when the effective heat transfer area was above 50%. The predicted pressures were lower than the measured data when the effective area was below 50%, with the difference between the two pressures increasing as the effective area decreased.

Figure 5.3-14 presents the predicted and measured hot leg liquid temperatures. With the hot leg containing a two-phase mixture at the saturation temperature in both the test and calculation, the response

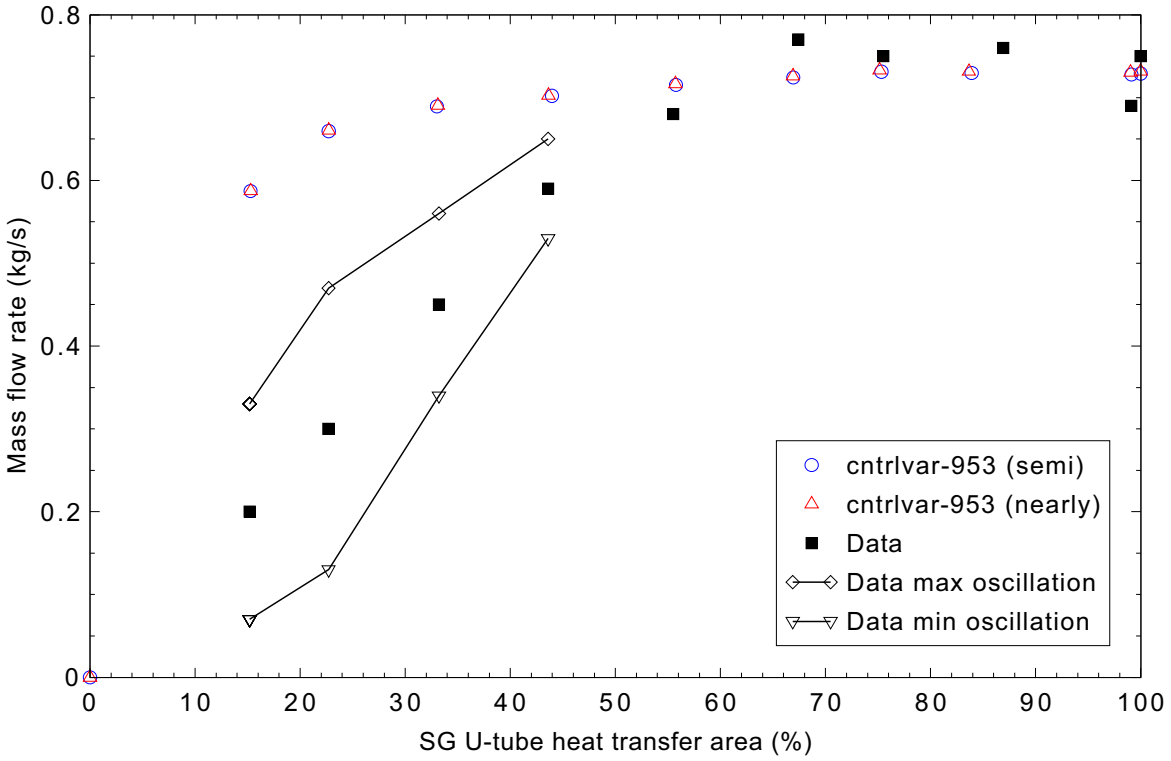

Figure 5.3-12. Measured and calculated primary system mass flow rate for Semiscale Test S-NC-3.

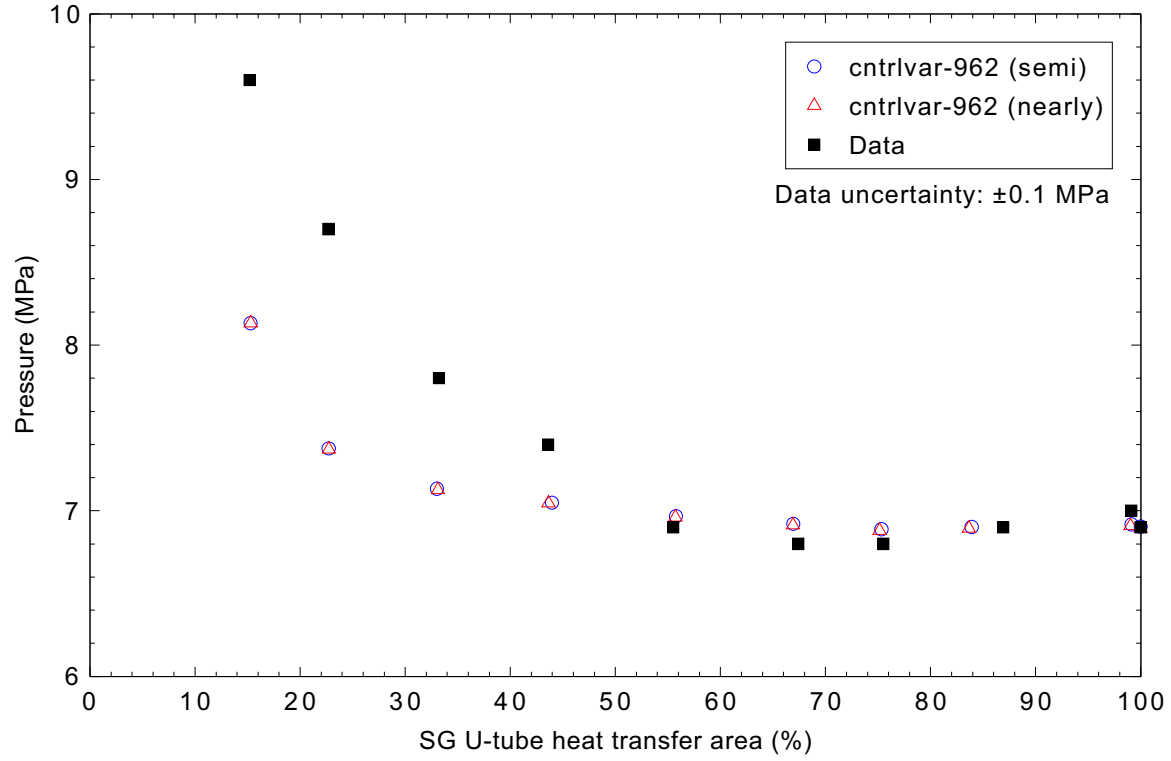

Figure 5.3-13. Measured and calculated primary system pressure for Semiscale Test S-NC-3.

was the same as for the pressure. When the effective heat transfer area was above 50%, the predicted temperatures were slightly higher than measured, but were lower than measured for effective areas below 50%.

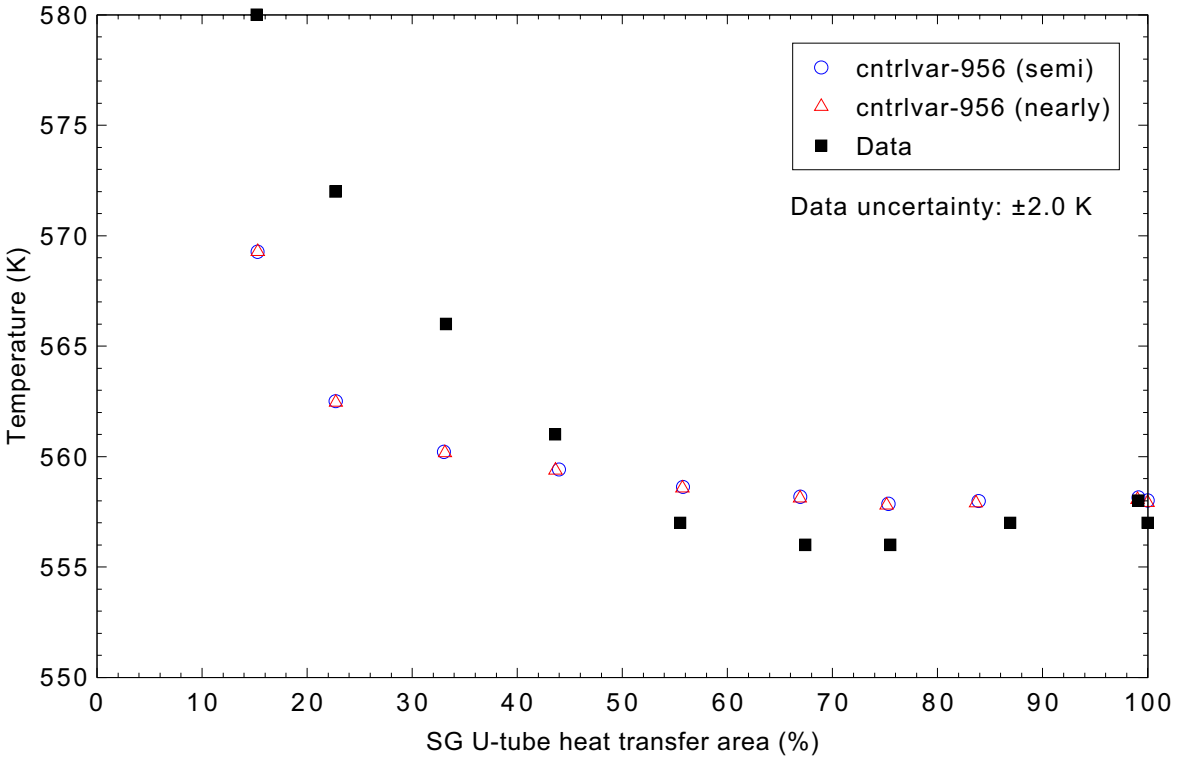

Figure 5.3-14. Measured and calculated hot leg liquid temperature for Semiscale Test S-NC-3.

The calculated and measured liquid temperatures in the cold leg are shown in Figure 5.3-15. In the test, the temperature oscillated when the effective heat transfer area was between 15% and 45%. The predicted and the measured temperatures were in a good agreement when the effective heat transfer area was larger than 50%. However, as it decreased below 50%, the temperatures were under predicted, with the difference between the two temperatures becoming larger as the effective heat transfer area decreased. Comparing Figures 5.3-14 and 5.3-15, the temperature differences between the measured and calculated temperatures are similar, indicating that the code is predicting nearly the same subcooling.

The under prediction of the pressure indicates that the heat transfer in the steam generator is over predicted. This is consistent with the higher predicted mass flow rate and similar temperature difference between the hot and cold legs, which show that the calculation is removing more energy from the coolant is it passes through the steam generator than was being removed in the test.

5.3.4.4 Test S-NC-10

Parts 2, 3, and 4 were included in the code assessment. It was hoped to use Part 1 as well, as it included environmental heat losses (Parts 2-4 and the other assessment cases did not), but there were some unknown boundary conditions that made that portion of the test unsuitable for code assessment.

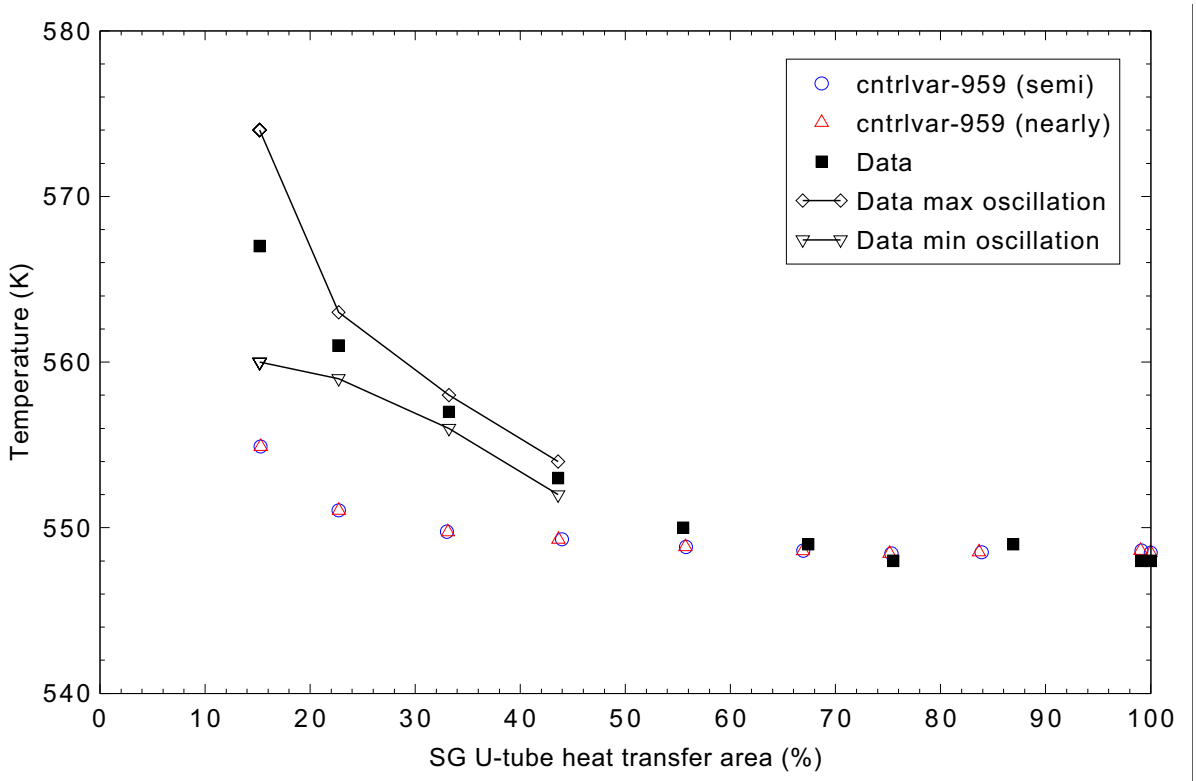

Figure 5.3-15. Measured and calculated cold leg liquid temperature for Semiscale Test S-NC-3.

5.3.4.4.1 Part 2

Transient calculations were performed using both the semi-implicit and the nearly-implicit advancement schemes. The requested time step size was 0.05 s for both cases. This test was similar to Test S-NC-2, but with a lower core power (33.54 kW vs. 60 kW).

Figure 5.3-16 shows the calculated and measured mass flow rates in the primary system. The code did not predict the mass flow rate well, especially when the primary system mass inventory was less than around 88%.

Figure 5.3-17 presents the primary system pressure comparison. The code generally under predicts the primary system pressure, with larger discrepancies at primary system inventories between 87 and 95%.

Figure 5.3-18 shows the predicted and measured hot leg liquid temperatures. The predicted temperature is in reasonably good agreement with the measured data. The under prediction at mass inventories from 91-95% is consistent with the pressure under prediction, as the hot leg contained a two-phase mixture at the saturation temperature in both the test and the calculation.

The calculated cold leg liquid temperatures were a little lower than the measured data, as shown in Figure 5.3-19, remaining at or slightly outside the measurement uncertainty band. The difference between the calculated and measured values increased at the lower end of the mass inventory range, consistent with the lower predicted mass flow rate.

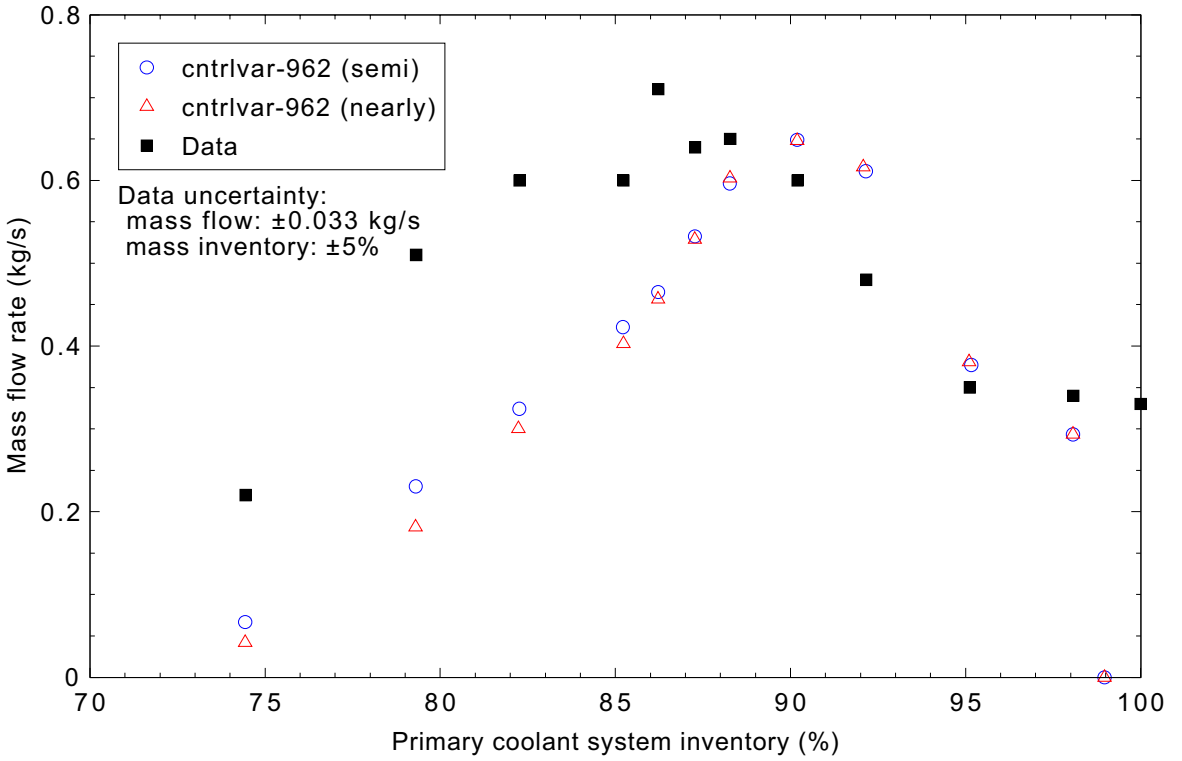

Figure 5.3-16. Measured and calculated primary system mass flow rate for Semiscale Test S-NC-10 Part 2.

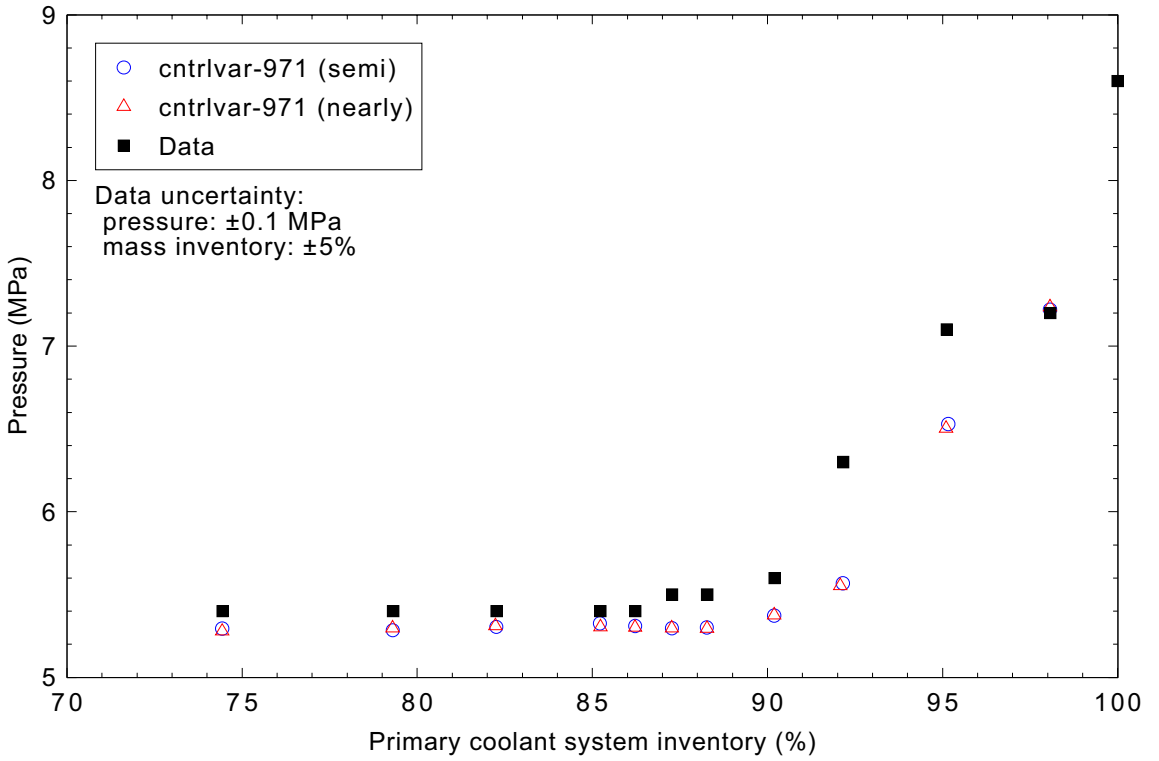

Figure 5.3-17. Measured and calculated primary system pressures for Semiscale Test S-NC-10 Part 2.

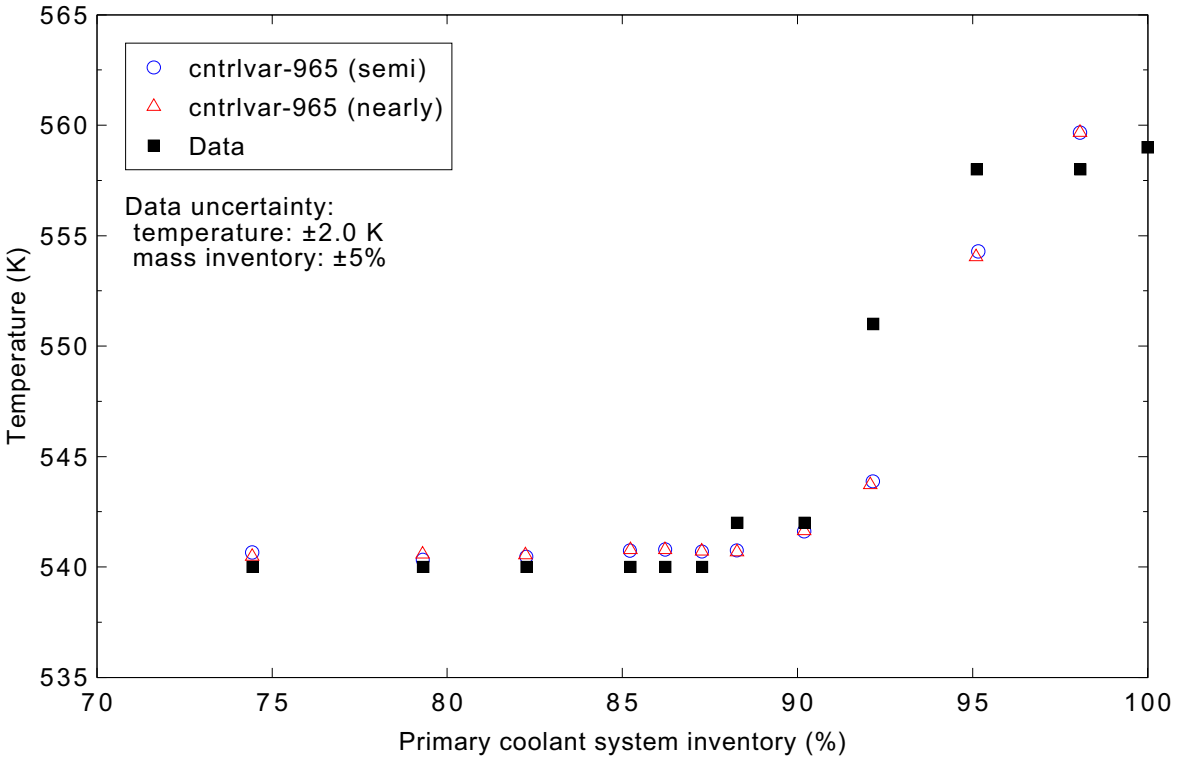

Figure 5.3-18. Measured and calculated hot leg liquid temperatures for Semiscale Test S-NC-10 Part 2.

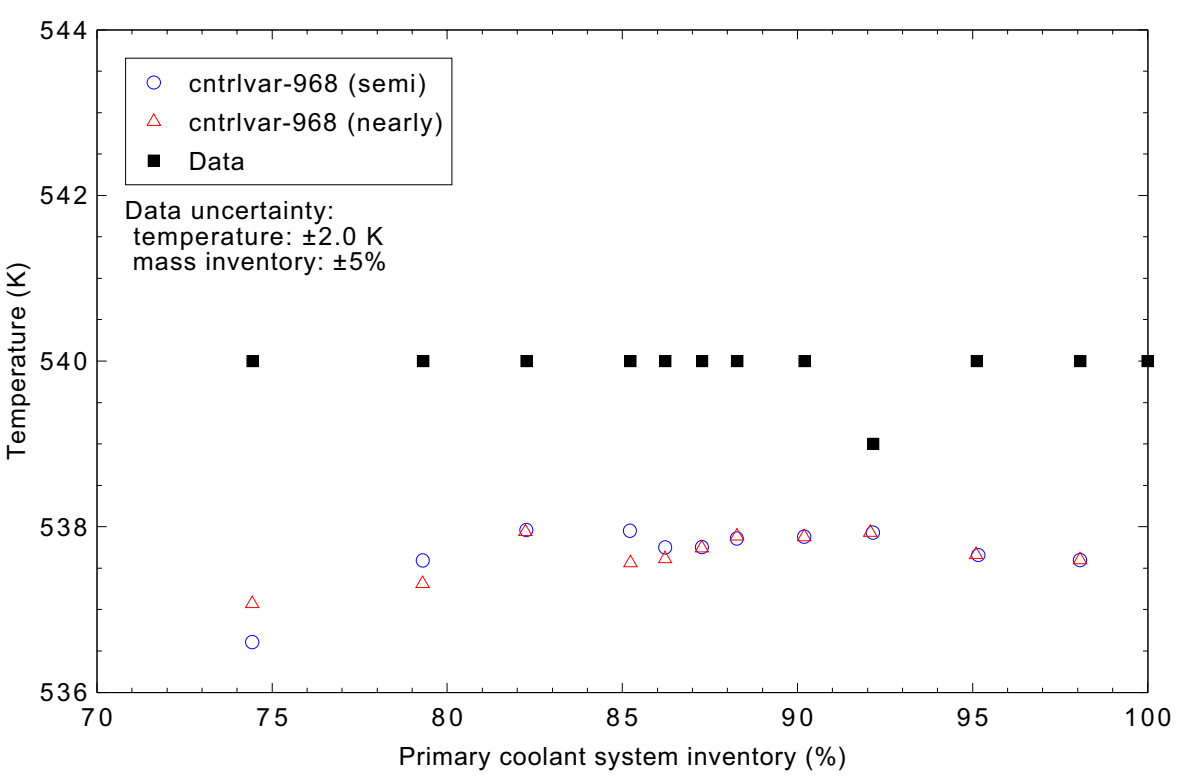

Figure 5.3-19. Measured and calculated cold leg liquid temperatures for Semiscale Test S-NC-10 Part 2.

5.3.4.4.2 Part 3

Transient calculations were performed using only the semi-implicit advancement scheme; the calculation using the nearly-implicit scheme hung up in an infinite loop. The requested time step size was 0.05 s. As in Test S-NC-3, the mass inventory of the secondary system was periodically reduced to vary the effective heat transfer area of the steam generator U-tubes. The core power and the primary system mass inventory were reduced compared to Test S-NC-3, from 62 kW and 91.8% to 33.54 kW and 86.95%. The secondary system pressure was very similar in both cases, around 5.9 MPa.

Figure 5.3-20 shows the calculated and measured primary system pressures, which exhibited similar behavior. As the heat transfer area is reduced, with a constant power and primary system mass inventory, there will be a point at which there is insufficient heat transfer to remove all of the core power. As the secondary inventory is reduced further, the primary system pressure increases as the steam generated in the core cannot be condensed completely in the steam generator tubes. This transition to an increasing pressure occurred near an effective heat transfer area of 70% in both the test and the calculation. The high value for the measured pressure at 100% inventory is inconsistent with the phenomenology described above, and therefore is suspect.

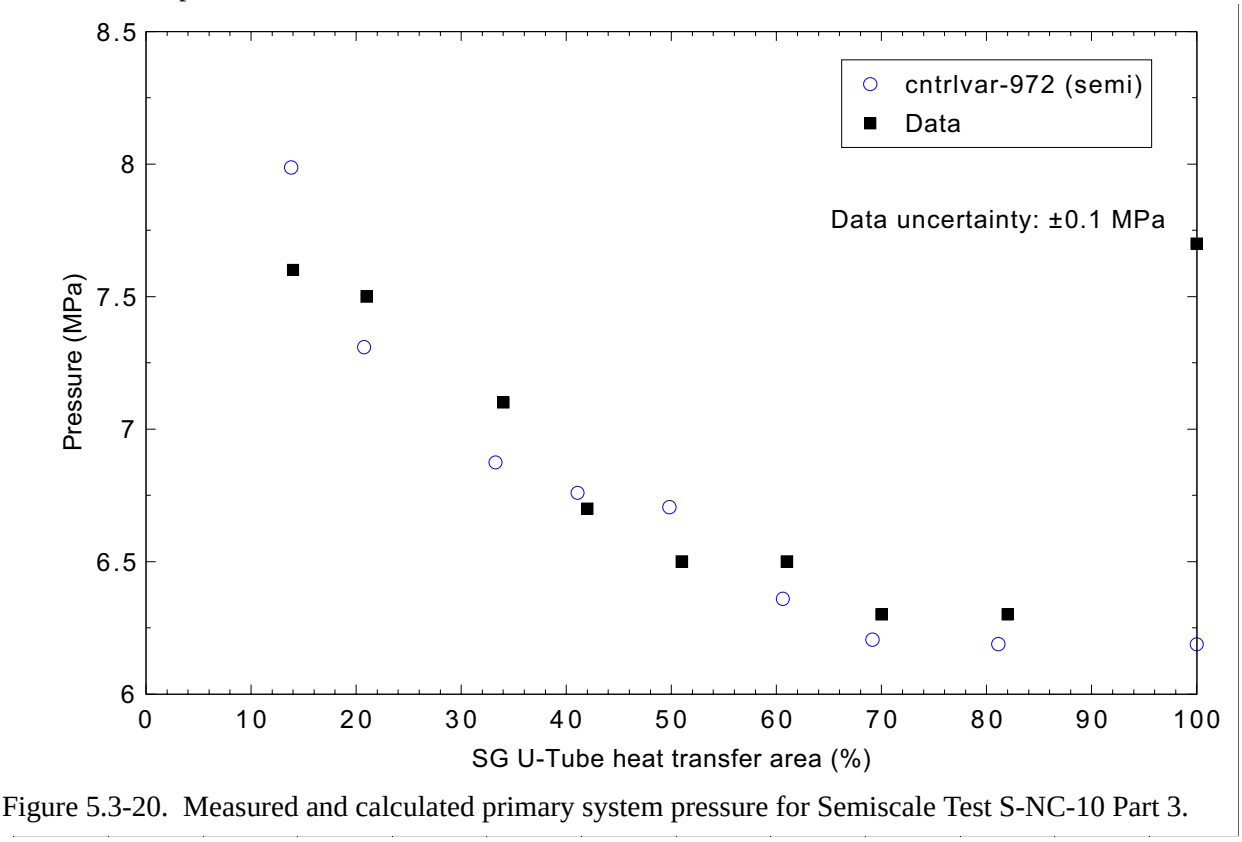

Figure 5.3-20. Measured and calculated primary system pressure for Semiscale Test S-NC-10 Part 3.

The primary system mass flow rate comparison is shown in Figure 5.3-21. The code tends to over predict the flow rate at effective heat transfer areas below 45% and under predict the flow at higher heat transfer areas. This is consistent with the behavior observed for Test S-NC-3.

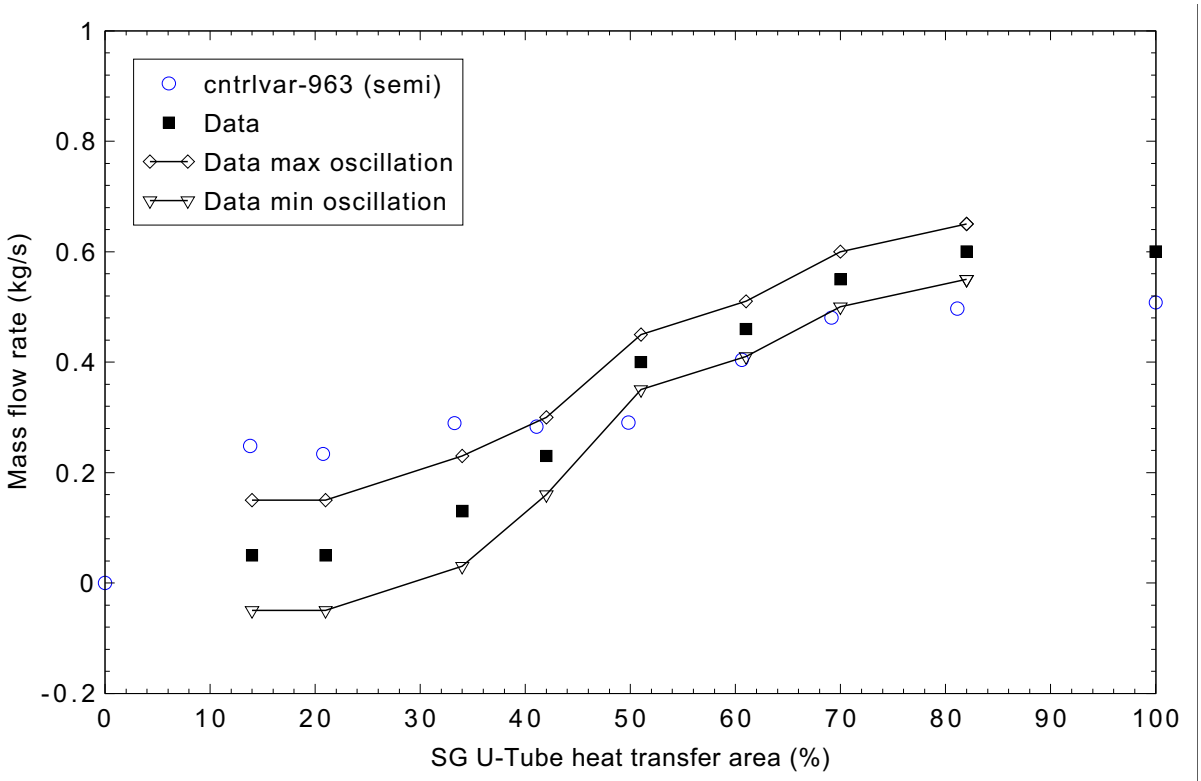

Figure 5.3-21. Measured and calculated primary system mass flow rate for Semiscale Test S-NC-10 Part 3.

Measured and calculated liquid temperatures in the hot and cold legs are shown in Figures 5.3-22 and 5.3-23, respectively. The measured hot leg temperatures are inconsistent with the measured pressures shown in Figure 5.3-20. As both the test and simulation had two-phase fluid in the hot legs, the liquid should be at the saturation temperature; it is in the code calculation, but it is below the saturation temperature in the test (by about 5 K at the 14% area point). The code generally calculates a lower cold leg temperature than was measured, with a larger difference between the calculated and measured values at lower effective heat transfer areas.

The combination of a higher primary system mass flow rate and a lower cold leg temperature indicate that the code is over predicting the heat transfer to the steam generator secondary side coolant.

5.3.4.4.3 Part 4

Transient calculations were performed using both the semi-implicit and nearly-implicit advancement schemes. The requested time step size was 0.05 s for both cases.

Figure 5.3-24 shows the calculated and measured mass flow rates in the primary system at a core power of 100 kW. There are two measured points at primary system mass inventories of around 82% and 79%. The higher values were measured before the power reduction to 60 kW and the lower values after the power was increased back to 100 kW. The code prediction is in good agreement with the data.

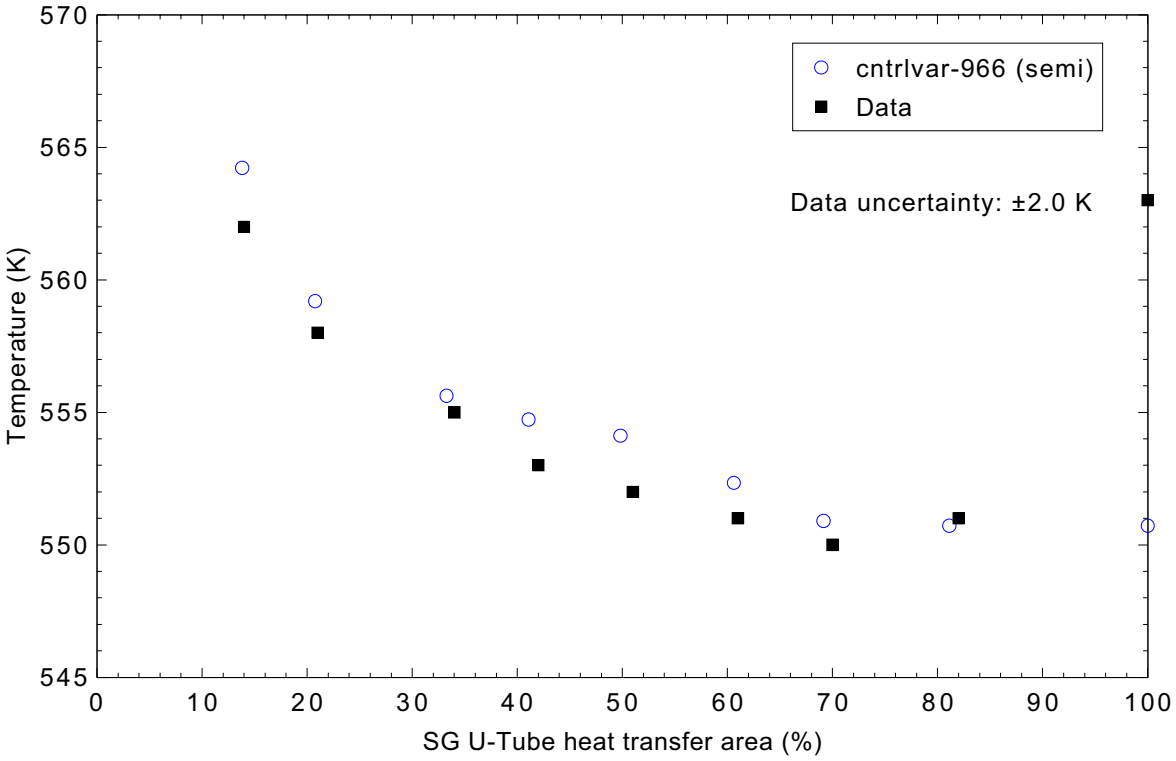

Figure 5.3-22. Measured and calculated hot leg liquid temperature for Semiscale Test S-NC-10 Part 3.

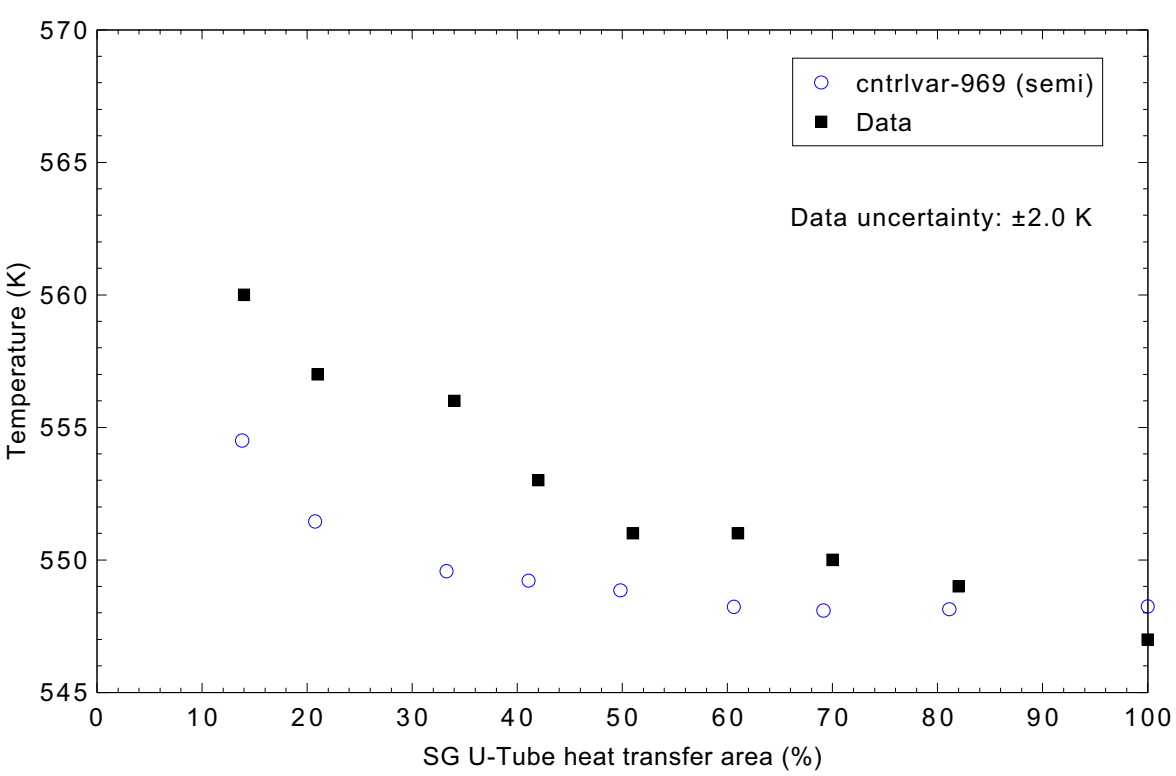

Figure 5.3-23. Measured and calculated cold leg liquid temperature for Semiscale Test S-NC-10 Part 3.

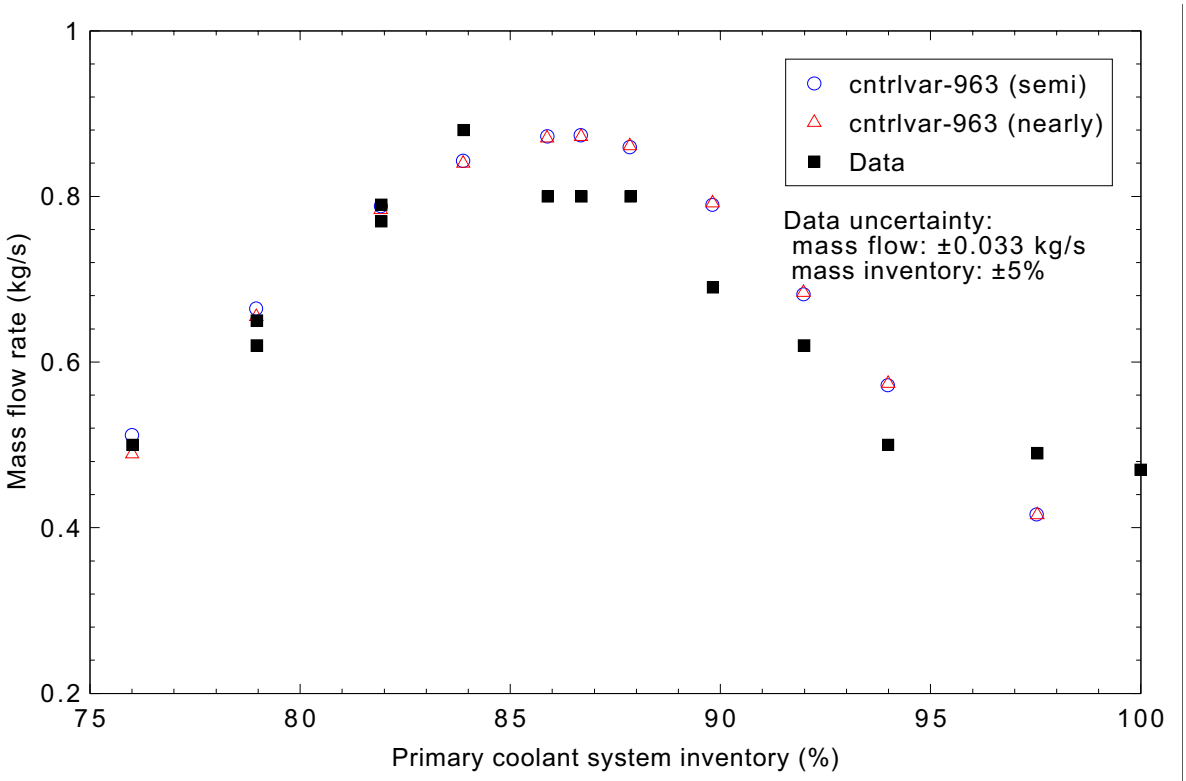

Figure 5.3-24. Measured and calculated primary system mass flow rate for Semiscale Test S-NC-10 Part 4 with core power of 100 kW.

Primary system mass flow rates from the 60 kW core power cases are presented in Figure 5.3-25. The predicted flow rates are much lower than those measured, and are judged to be in minimal agreement with the experiment data. This behavior is the opposite of that observed in Test S-NC-2, where the measured flow was over predicted. These two experiments had the same core power, steam generator pressure, and about the same initial pressure in the primary coolant system, yet the measured flow rates were very different. Using Figures 5.3-7 and 5.3-25, and interpolating where necessary, at a mass inventory of 83%, the measured flow rates are 0.58 kg/s (S-NC-2) and 0.63 kg/s (S-NC-10), and the calculated flow rate is 0.5 kg/s for both. At 76% inventory, the measured flow rates are 0.1 kg/s (S-NC-2) and 0.48 kg/s (S-NC-10), and the calculated flow rate is 0.28 kg/s for both. This discrepancy in the measured flow rates with similar conditions is not addressed in the references.

Figure 5.3-26 presents the measured and calculated primary system pressures with a power of 100 kW. As shown in these figures, RELAP5-3D under predicts the primary system pressure at mass inventories between 84 and 95%, with the difference between the measured and calculated values decreasing as the inventory dropped.

Hot leg fluid temperatures with a core power of 100 kW are compared in Figure 5.3-27. The calculated temperature is in good agreement with the data when the mass inventory is below about 90%. At mass inventories from 90-95%, the temperature is under predicted, consistent with the under prediction of the pressure (the fluid is at the saturation temperature in this two-phase natural circulation region). Overall, the prediction is judged to be in reasonable agreement with the data.

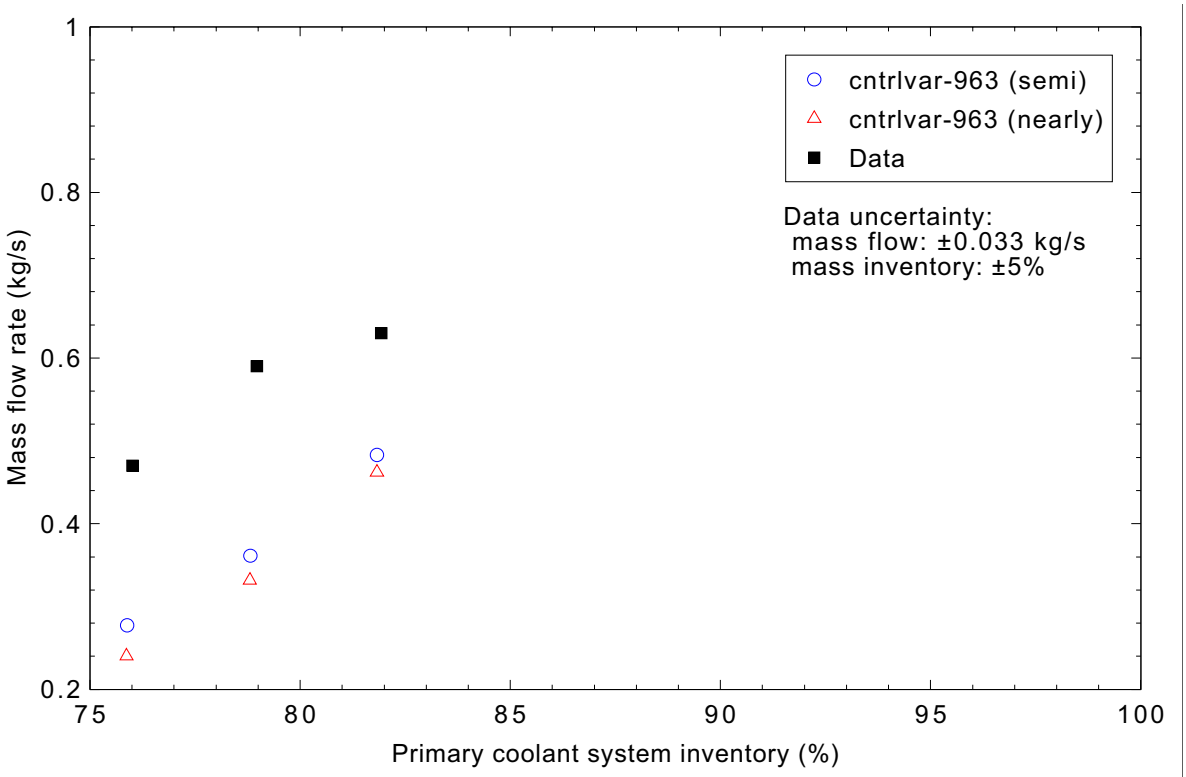

Figure 5.3-25. Measured and calculated primary system mass flow rate for Semiscale Test S-NC-10 Part 4 with core power of 60 kW.

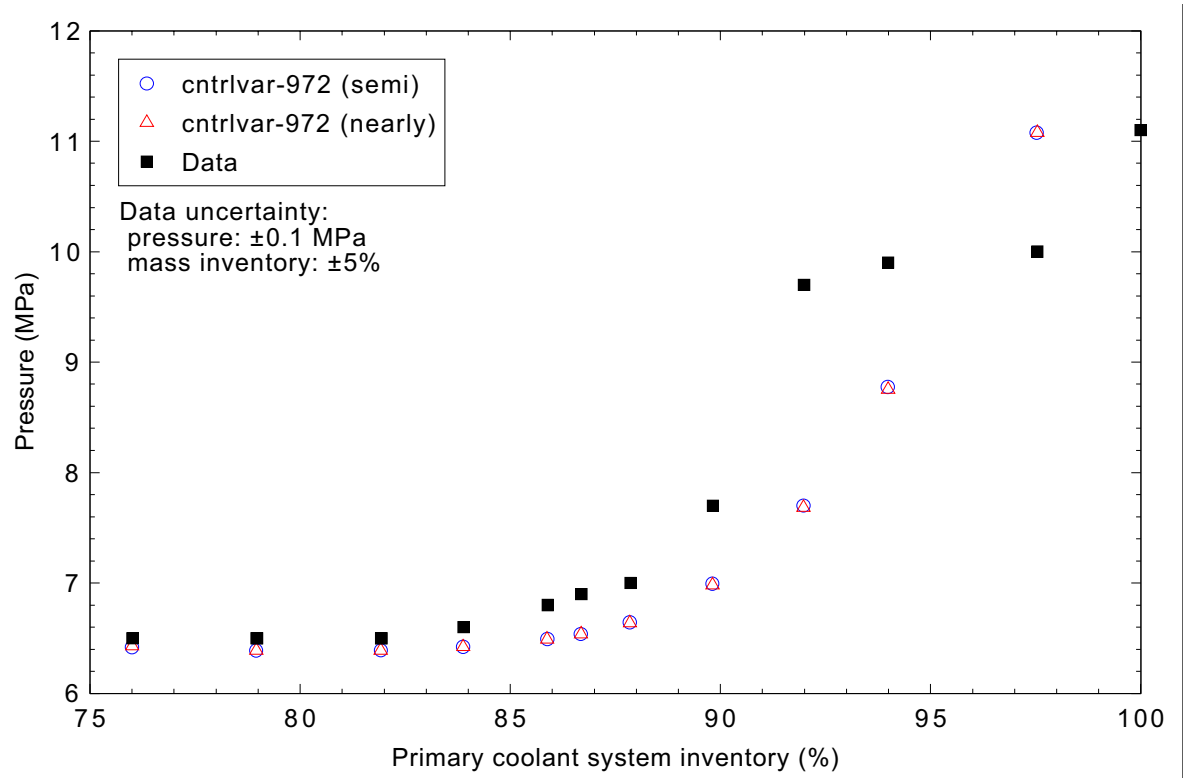

Figure 5.3-26. Measured and calculated primary system pressures for Semiscale Test S-NC-10 Part 4 with core power of 100 kW.

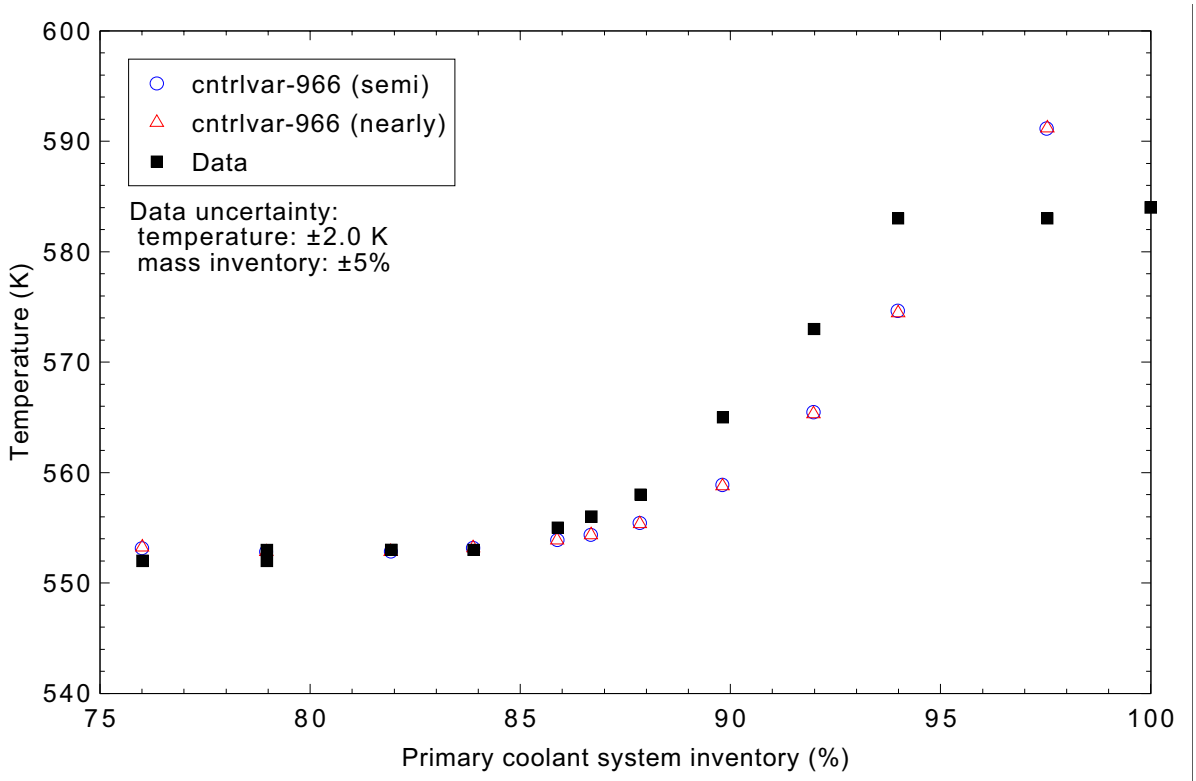

Figure 5.3-27. Measured and calculated hot leg liquid temperatures for Semiscale Test S-NC-10 Part 4 with core power of 100 kW.

Measured and calculated cold leg fluid temperatures are presented in Figure 5.3-28. The calculated temperatures are generally slightly lower than the measured values. The trend of the data is captured, and the predicted temperatures are within the uncertainty band of the measurement, so the code is judged to be in reasonable agreement with the data.

5.3.5 Conclusions and Assessment Findings

The code predictions of single-phase liquid natural circulation behavior were judged to be excellent. Under loop two-phase natural circulation conditions, the predictions were reasonable when the core power was high (100 kW, Test S-NC-10, Part 4), but degraded as the power decreased. In general, RELAP5-3D predicted reasonable two-phase natural circulation behavior with the high and intermediate core power (100 kW and 60 kW) but the predictions were minimal at low power (33.54 kW).

RELAP5-3D predicted reflux condenser mode of natural circulation when the core power was 60 kW and the primary system mass inventory was less than 67%, as observed in the experiment. This is in reasonable agreement with the experiment results.

When the secondary system mass inventory was high enough to make the effective heat transfer area larger than around 50%, the predicted natural circulation behavior was reasonable. However, at effective areas below 50%, the predicted mass flow rates in the primary system were higher than were measured, which was in minimal agreement with experiment results. The high mass flow rate was caused by an over prediction of the heat transfer from the primary system to the secondary system.

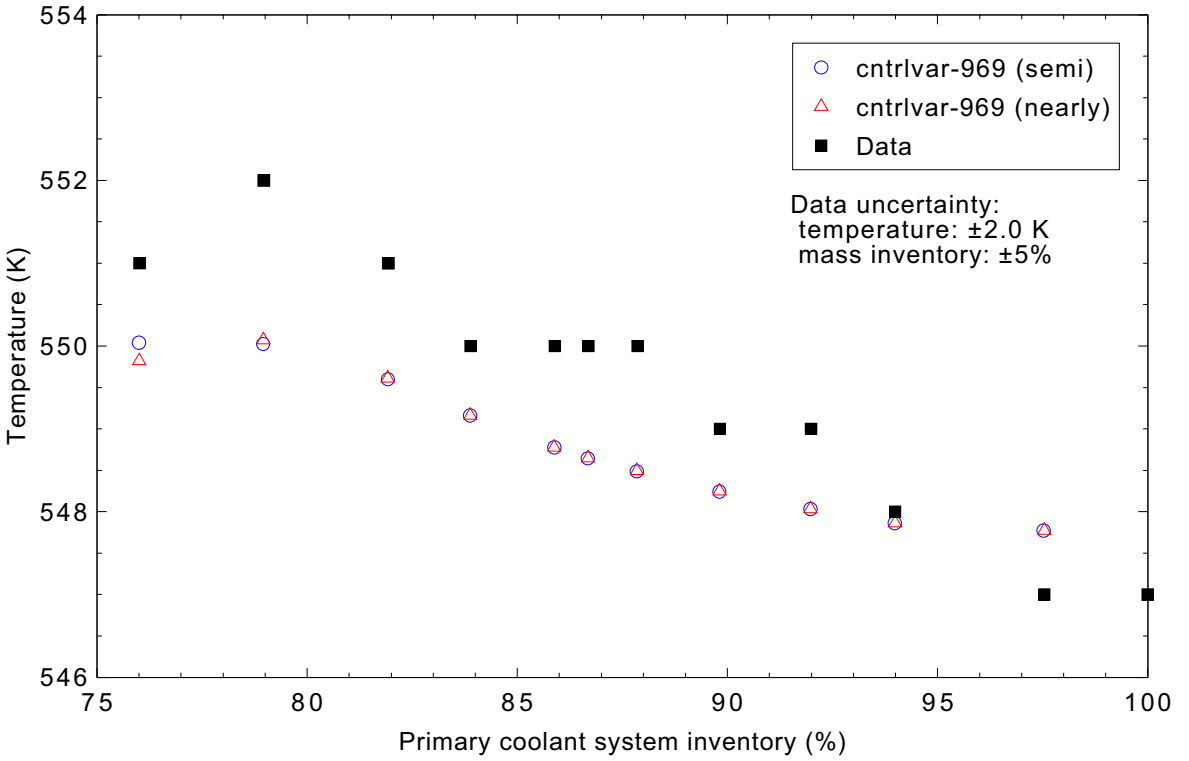

Figure 5.3-28. Measured and calculated cold leg liquid temperatures for Semiscale Test S-NC-10 Part 4 with core power of 100 kW.

5.3.6 References

5.3-1. Guy G. Loomis and Kunihisa Soda, *Results of the Semiscale MOD-2A Natural Circulation Experiments*, NUREG/CR-2335, EG&G Idaho Inc., September 1982.

5.3-2. Thomas M. O'Connell, *Experiment Data Report for Semiscale MOD-2A Natural Circulation Test S-NC-10,* NUREG/CR-2554, EG&G Idaho Inc., February 1982.

5.3-3. F. P. Incropera and D. P. DeWitt, *Fundamentals of Heat and Mass Transfer*, 4th Edition, John Wiley & Sons, 1990.

5.4 LOBI Test A1-04R

The Loop Blowdown Investigations (LOBI) test facility was a high pressure integral test facility built and operated in the Joint Research Centre, Ispra, Italy. In the LOBI experiments, the thermal-hydraulic behavior of the facility during various transients were investigated to provide an experimental basis for analytical model development and code validation. The facility was originally built to simulate the reflood portion of large break loss-of-coolant accidents (LOCAs), and was later reconfigured to investigate small break LOCAs and other transients. Test A1-04R simulated a large cold leg break.

5.4.1 Code Models Assessed

The LOBI test was used to assess the code performance during the blowdown phase of a large break LOCA in a pressurized water reactor (PWR). Models tested are related to large-break LOCA blowdown.

5.4.2 Experiment Facility Description

The LOBI facility[5.4-1] is a 1/712-scale model of a four loop PWR. A schematic of the LOBI facility is shown in 5.4-1. The facility has two loops: the intact loop represents three loops in the plant and contains the pressurizer; the broken loop represents one plant loop and contains the break. The reactor vessel model contains an electrically-heated rod bundle with 64 rods with a heated length of 3.9 m. The nominal heating power is 5.3 MW. The downcomer is shaped as an annulus. An upper head simulator is connected to the vessel. Each of the two primary loops contains a pump and a steam generator. The different mass flows in the loops are established by adjusting the pump speeds, since the two pumps are identical. Heat is removed from the steam generators by a secondary system. Emergency core cooling (ECC) water can be supplied from two accumulators, one for each loop. Cold or hot leg as well as combined injection can be simulated. For Test A1-04R, injection was to the cold leg only.

5.4.3 Input Model Description

The nodalization diagrams are shown in Figures 5.4-2 through 5.4-4. Both loops are modeled with the intact loop on the left and the broken loop on the right. There are a total of 187 volumes, 194 junctions, and 198 heat slabs in the LOBI facility input model. Some items that are not shown on the nodalization diagrams include the single-volume recirculation pipes connecting the individual hot and cold leg downcomers on each steam generator and the time-dependent volume/junction pair for pump seal water injection and drainage.

A 2000 s steady state calculation was performed. A summary of the values of key parameters at the end of the steady state run based on the semi-implicit results is given in Table 5.4-1 The nearly-implict results were identical except for a small difference in the pressurizer pressure that is negligible for the large break LOCA simulation.

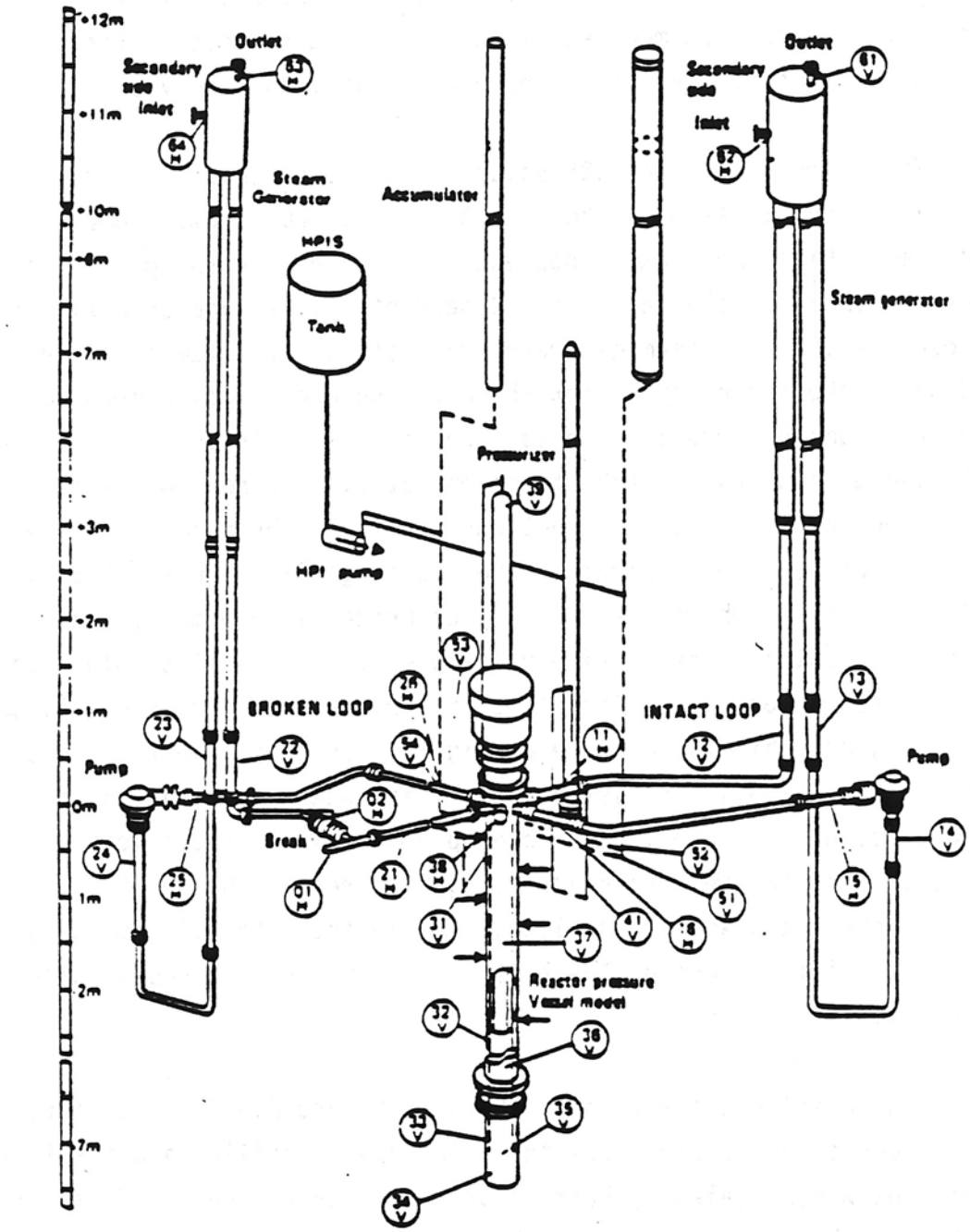

Figure 5.4-1. Schematic of the LOBI facility.

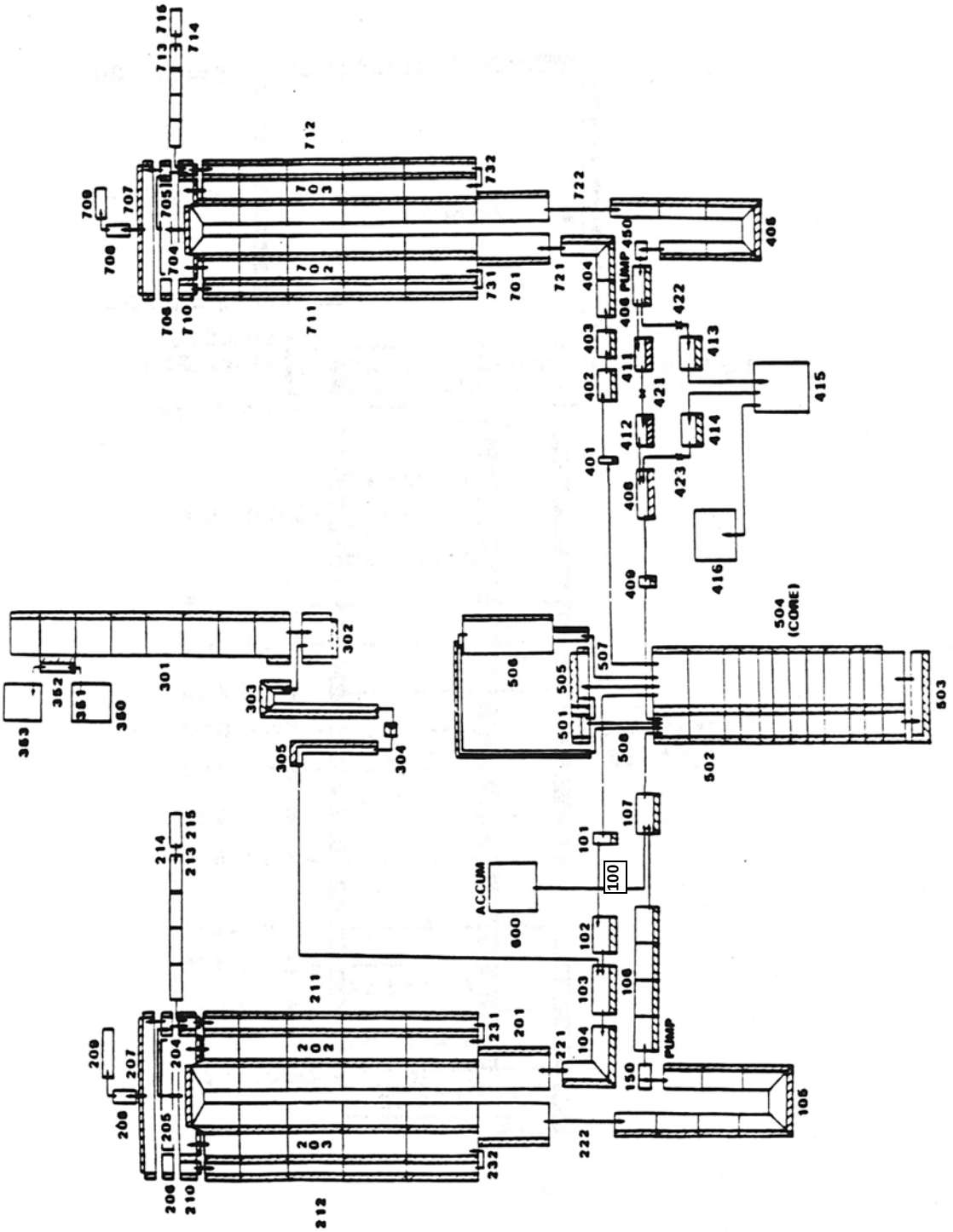

Figure 5.4-2. Noding diagram for the LOBI facility.

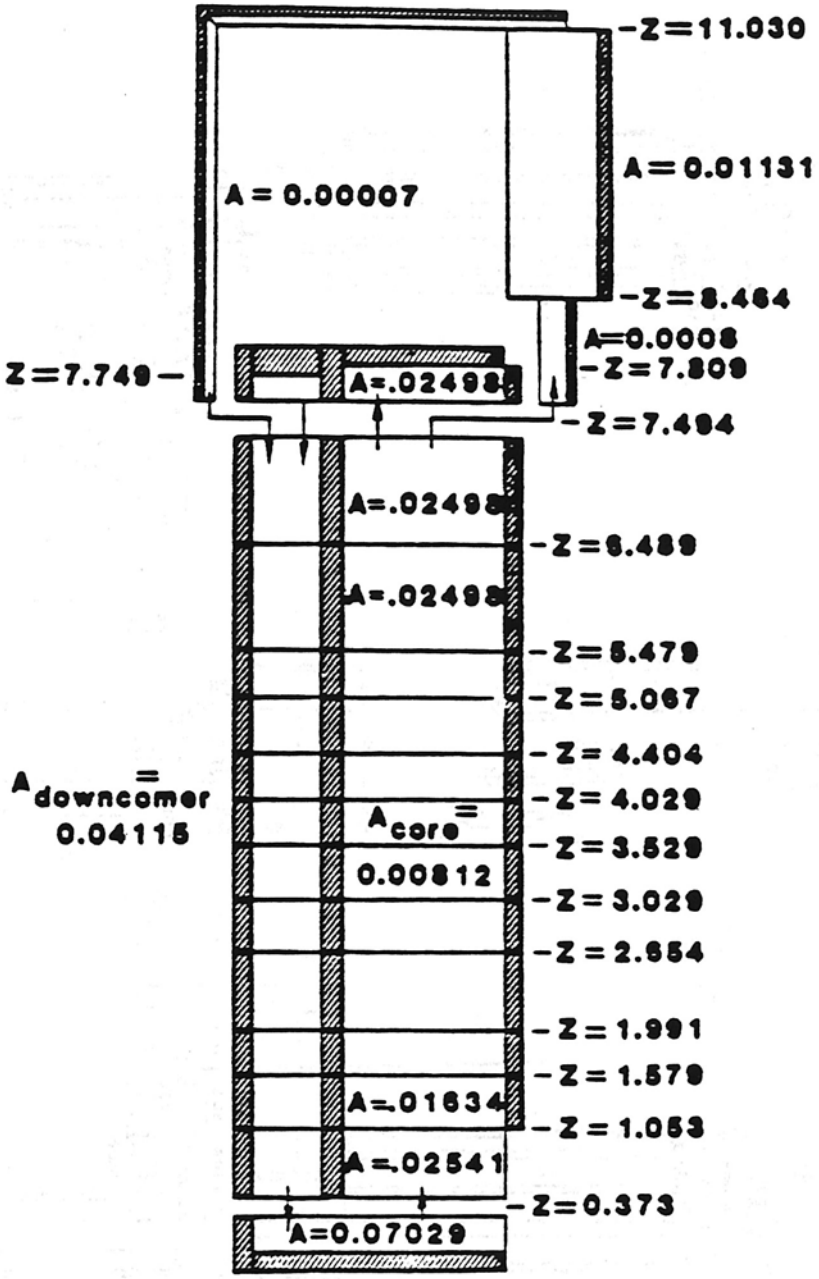

Figure 5.4-3. LOBI reactor vessel nodalization.

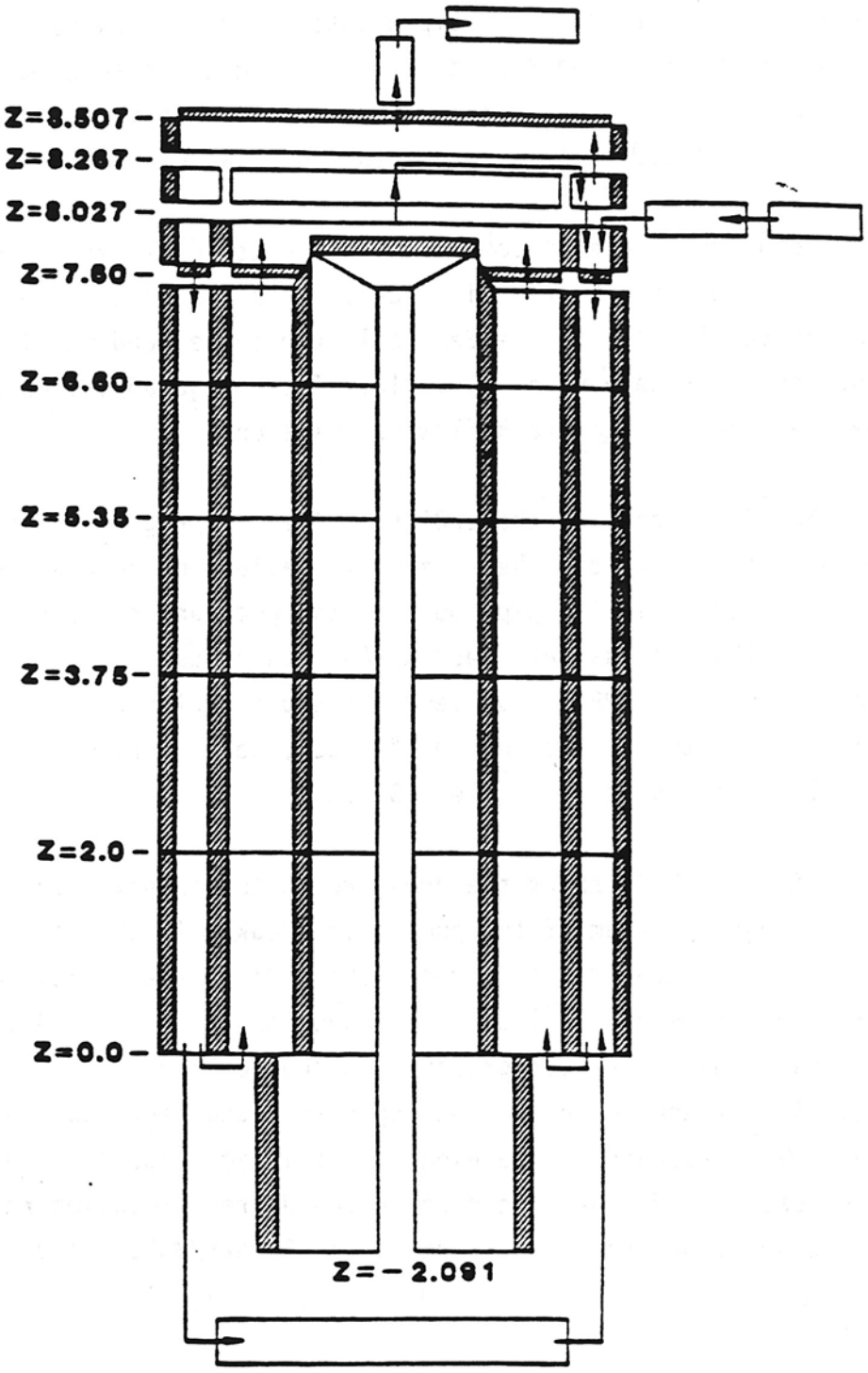

Figure 5.4-4. LOBI steam generator nodalization.

Table 5.4-1. Summary of steady state conditions for LOBI Test A1-04R.

Parameter	Intact Loop		Broken Loop	
	Data	RELAP5-3D	Data	RELAP5-3D
Core power (MW)	5.12	5.12	5.12	5.12
Loop pressure (MPa)	15.3	15.3	15.3	15.3
Primary system:				
Mass flow (kg/s)	21.1	20.8	7.0	6.9
Hot leg temperature (K)	600	604	606	604
Cold leg temperature (K)	571	574	571	574
Secondary System:				
Feedwater flow (kg/s)	2.07	2.07	0.8	0.8
Feedwater temperature (K)	493	493	501	493
Steam temperature (K)	553	554	553	556
Pressure (MPa)	6.4	6.5	6.4	6.7

5.4.4 Data Comparisons and Results

Transient runs were made with the RELAP5-3D code using both the semi-implicit and the nearly-implicit advancement schemes. Both calculations had a requested time step size of 0.025 s. Experiment data shown in the plots came from the NRC Data Bank.

The LOBI large break LOCA simulation is initiated as a double-ended guillotine break in the cold leg downstream of the reactor coolant pump. The simulation time for both the semi- and nearly- implicit calculations is 60 s. Results from -10 to 0 s shown in each plot are the steady state results before break initiation.

Figures 5.4-5 and 5.4-6 present the pressures in the cold legs at the pump outlets. A comparison of the RELAP5-3D results to the LOBI data shows excellent agreement for both the semi- and nearly-implicit cases. The calculated bump in the broken loop pressure at 5 s is caused by increased mass flow in the broken loop resulting from liquid draining from the upper portion of the reactor vessel. The effect of the liquid draining was not as significant in the test, causing the pressure to level off but not increase.

The broken loop mass flow rates from the pump side and the vessel side are shown in Figures 5.4-7 and 5.4-8, respectively. The calculated broken loop mass flow rates are in reasonable agreement with the data for both the semi-implicit and nearly-implicit cases. As mentioned above, the flow increase at 5 s is the result of liquid draining from the upper portion of the reactor vessel, entering the hot leg, and flowing

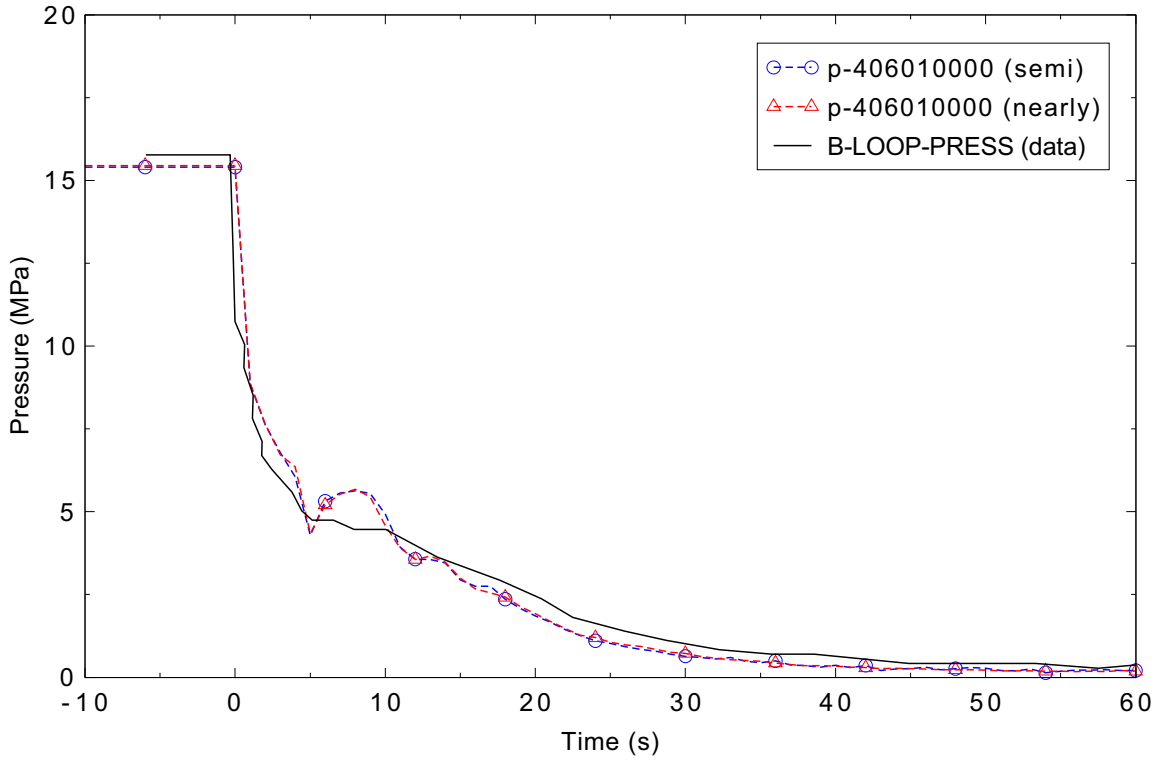

Figure 5.4-5. Measured and calculated broken loop pump outlet pressure for LOBI Test A1-04R.

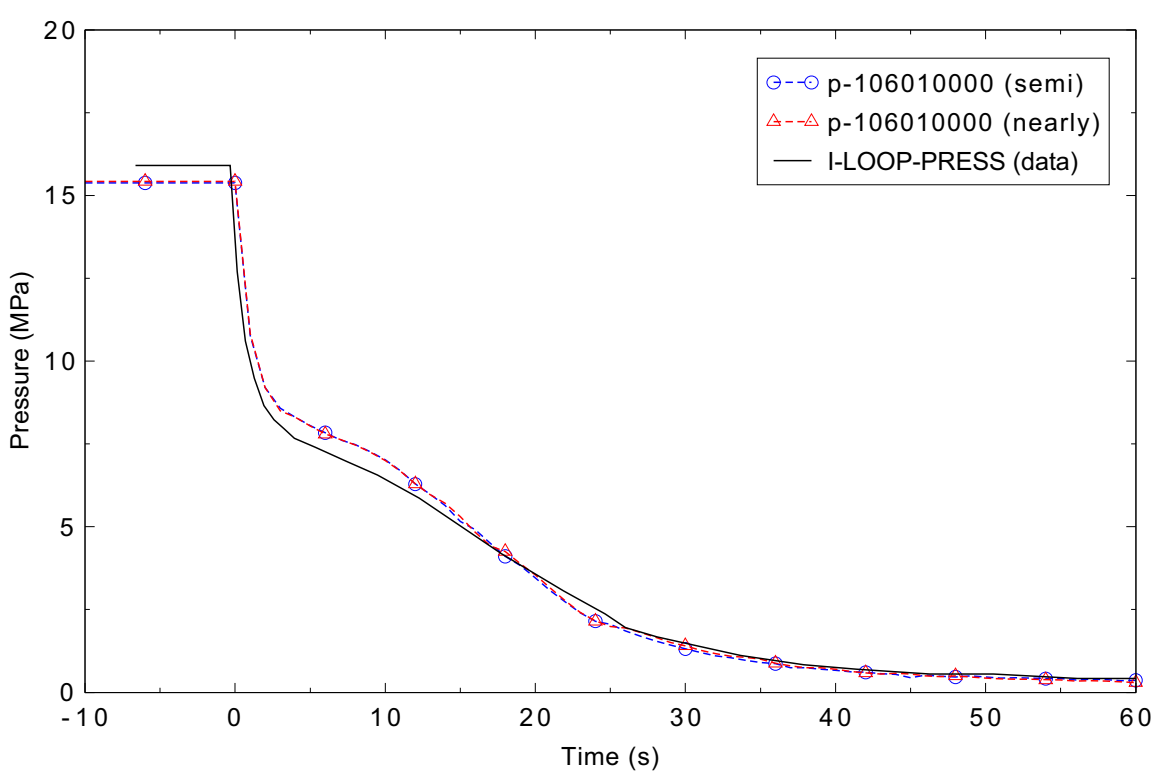

Figure 5.4-6. Measured and calculated intact loop pump outlet pressure for LOBI Test A1-04R.

to the break. Note that the discrepancy in steady-state break flow rates is due to instrumentation bias in the data; there is zero break flow to begin the transient.

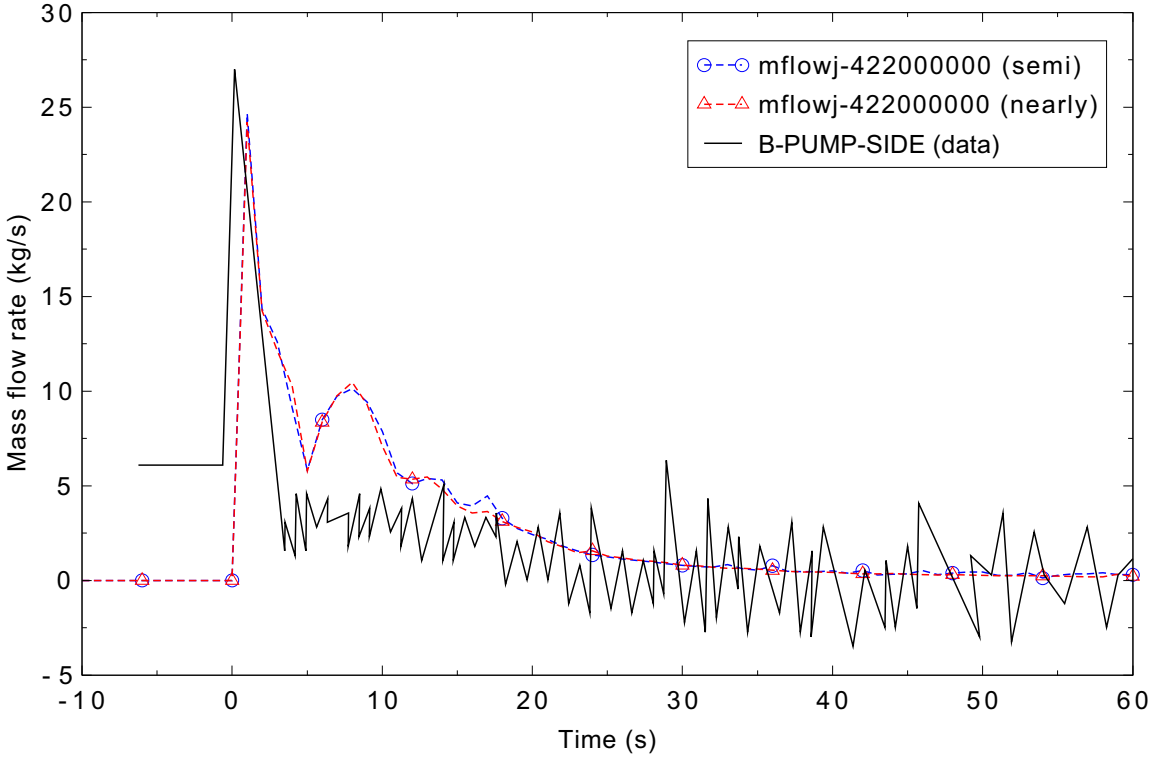

Figure 5.4-7. Measured and calculated broken loop mass flow rate (pump side) for LOBI Test A1-04R.

As the system depressurizes, the accumulators will discharge when the pressure in the intact loop falls below 2.7 MPa, which is the accumulator pressure. This occurs at about 22 s in both calculations. In the LOBI test, accumulator discharge begins near 24 s. The intact accumulator discharge flow rate, shown in Figure 5.4-9, indicates that RELAP5-3D significantly over predicts the flow rate. The maximum flow rate predicted by RELAP5-3D is about 5.2 kg/s, while the maximum flow rate measured during the experiment is about 3.3 kg/s. Oscillatory behavior is also observed in the nearly-implicit results. The reason for the RELAP5-3D over prediction of the accumulator flow rate is not known at this point. There were no accumulator pressure or level data from the test to use in determining whether the problem is in the data, the input model, or the physical model in the code. Figure 5.4-10 presents a plot of the fluid density at the intact accumulator injection point. As shown in the plot, RELAP5-3D does an excellent job of matching the data up to 25 s and is in reasonable agreement thereafter when the accumulator begins to drain. The data indicate that the cold leg was liquid-filled in the test, while both calculations had two-phase conditions until the end of the calculation.

Figure 5.4-11 presents the measured and calculated liquid temperatures at the accumulator injection point. The temperature generally follows the saturation temperature until the accumulator injection begins, after which the liquid is highly subcooled. The predicted temperature is slightly lower than the test data for both the semi- and nearly-implicit cases.

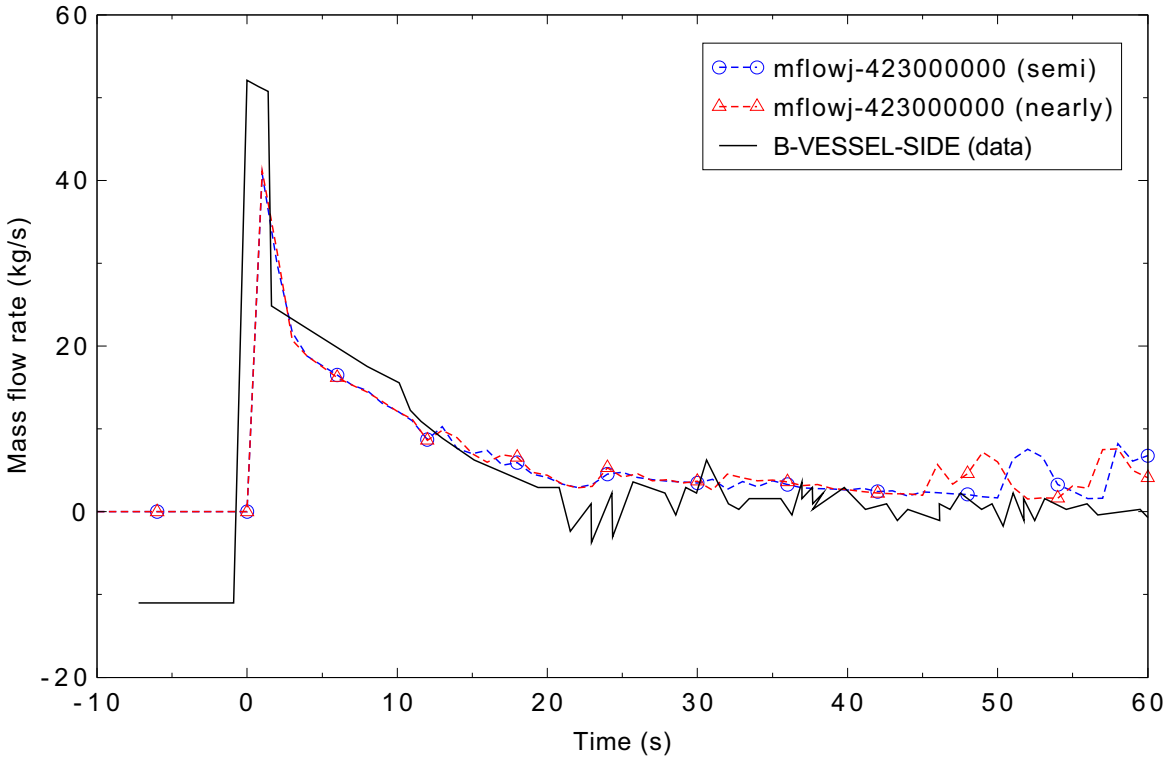

Figure 5.4-8. Measured and calculated broken loop mass flow rate (vessel side) for LOBI Test A1-04R.

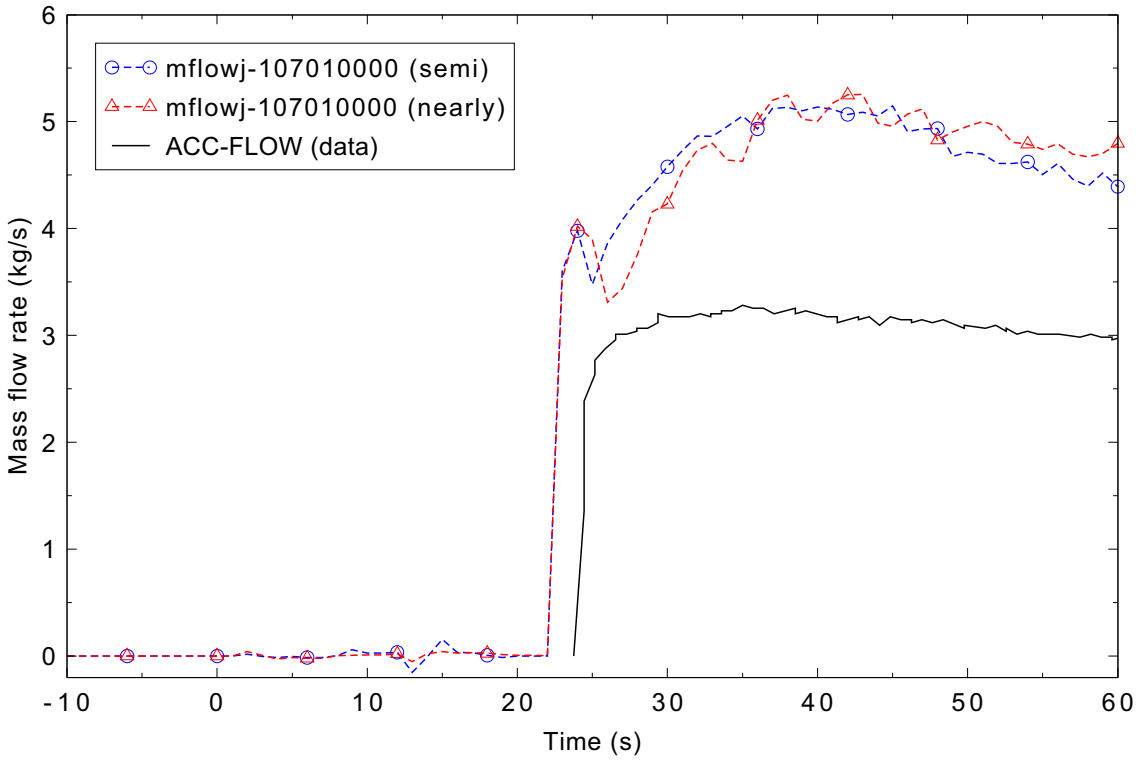

Figure 5.4-9. Measured and calculated accumulator discharge flow rate for LOBI Test A1-04R.

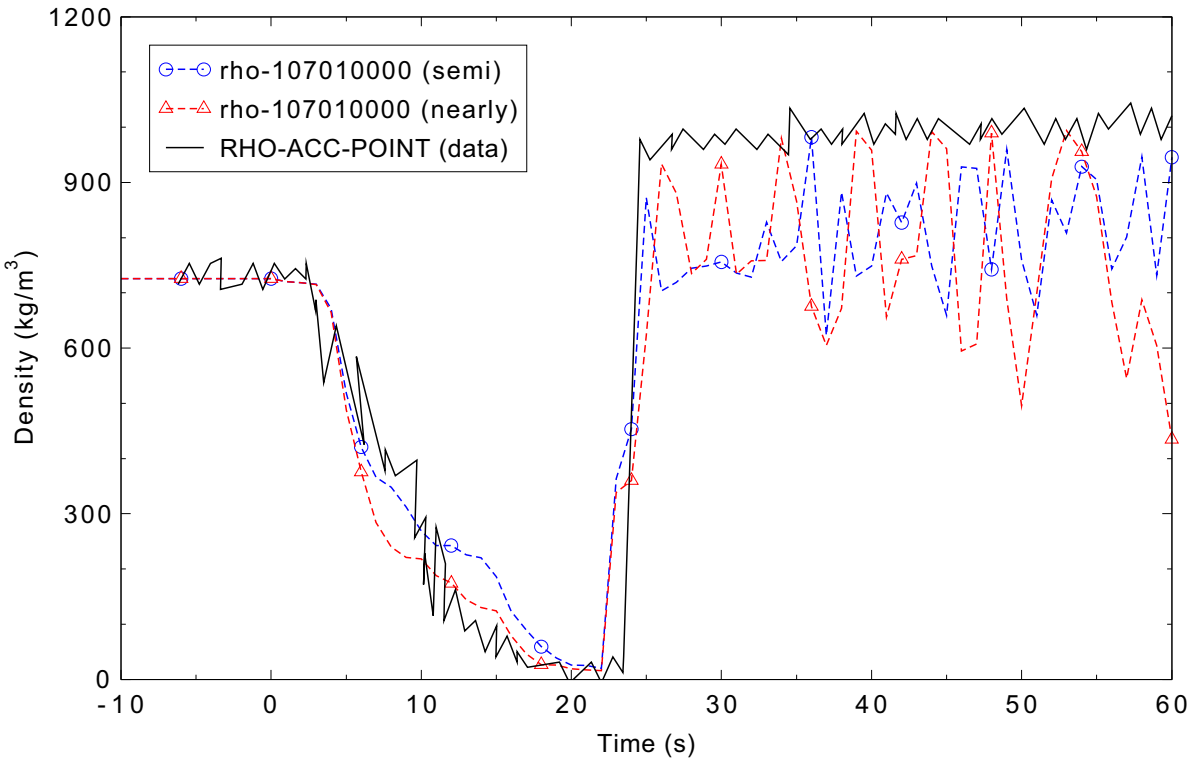

Figure 5.4-10. Measured and calculated fluid density at the accumulator injection point for LOBI Test A1-04R.

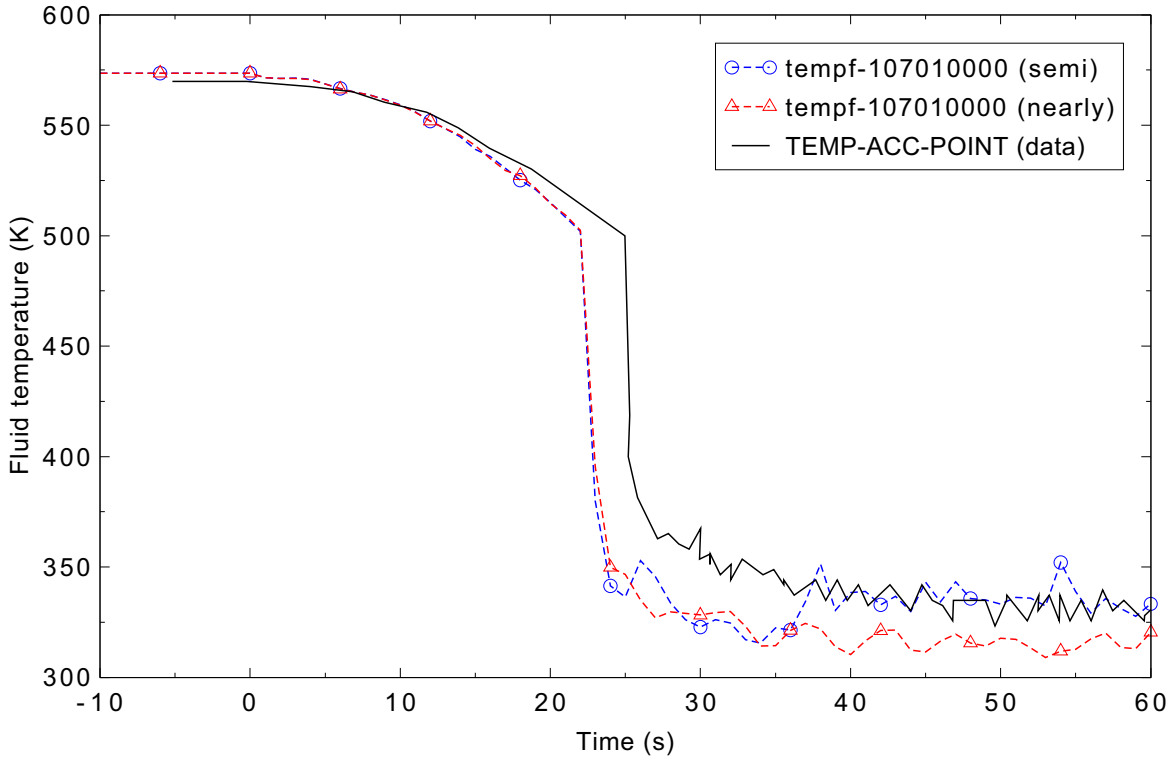

Figure 5.4-11. Measured and calculated fluid temperature at the accumulator injection point for LOBI Test A1-04R.

Figure 5.4-12 presents a comparison of the core differential pressure calculated by RELAP5-3D to the LOBI test results. In general, the code results are in excellent agreement with the experiment data for both the semi- and nearly-implicit cases.

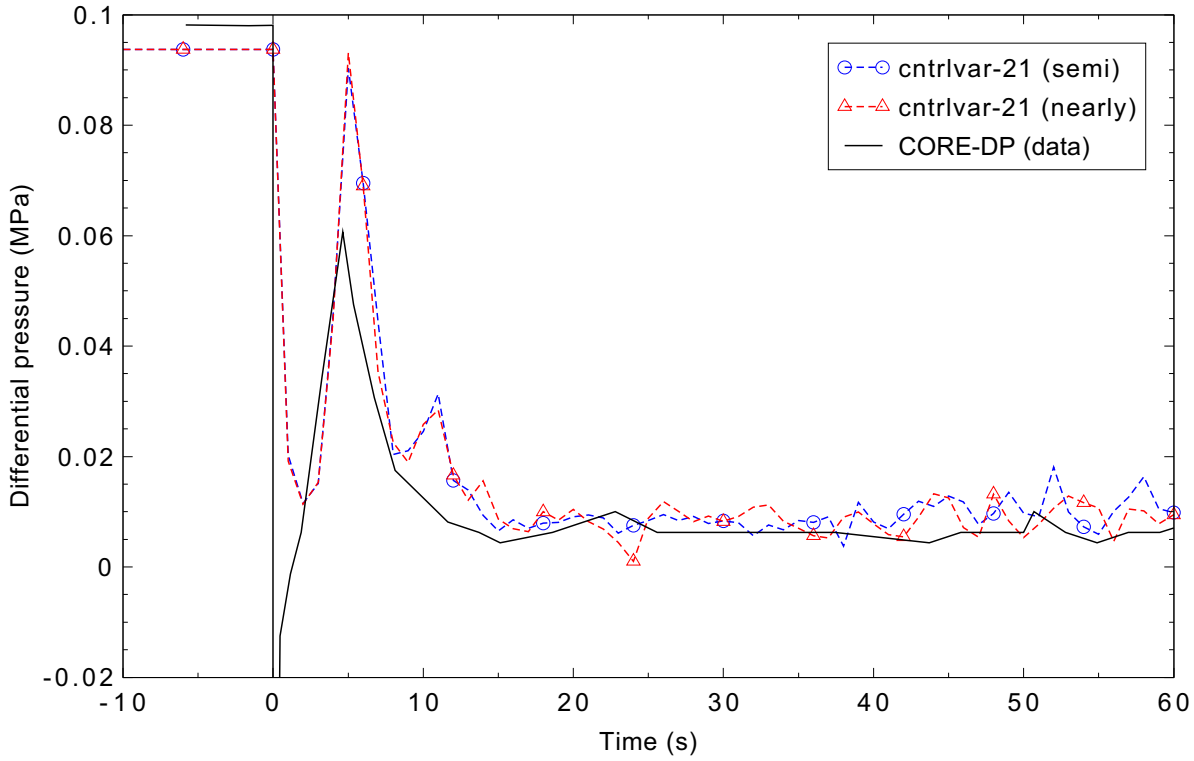

Figure 5.4-12. Measured and calculated core differential pressure for LOBI Test A1-04R.

Comparisons of the measured and calculated heater rod temperatures are presented in Figures 5.4-13 through 5.4-20. The measured data were taken at 12 axial levels that were not equally spaced; the data presented in these figures are from measurements at 0.5-m axial intervals, starting with Level 2, which is 0.2 m above the bottom of the heated length, through Level 11, which is 3.7 m above the bottom of the heated length. In the experiment, the initial blowdown resulted in a bundle-wide heatup, followed by a full or partial rewet by about 12 s from both the bottom and top of the core. This was followed by a second heatup over most of the core height, after which only some portions of the core quenched. The code did a very good job simulating the initial core heatup, and the first rewet was primarily from the bottom of the core.

The data presented in Reference 5.4-2 show no significant variation across the bundle up through Level 5. Above Level 5, however, the data report shows significant radial variations in the temperature response that are not captured in the data available from the NRC Data Bank. Some of the measurements showed a complete rewet after the initial heatup, some showed partial cooling, and some remained near the peak temperatures before slowly decreasing. These radial variations will not be captured in the one-dimensional RELAP5-3D model of the core. The data presented in the data report also indicate that the Data Bank channels for Levels 6 and 7 are mislabeled and should be reversed.

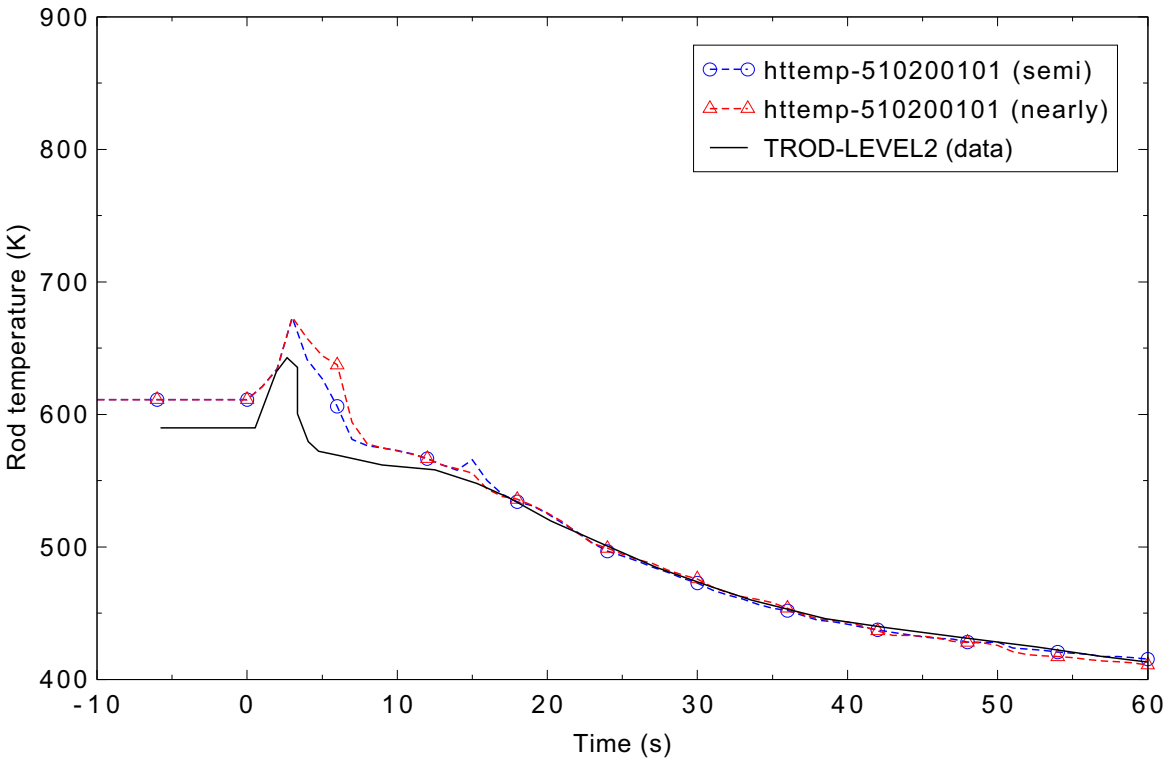

Figure 5.4-13. Measured and calculated lower core heater rod temperature (Level 2) for LOBI Test A1-04R.

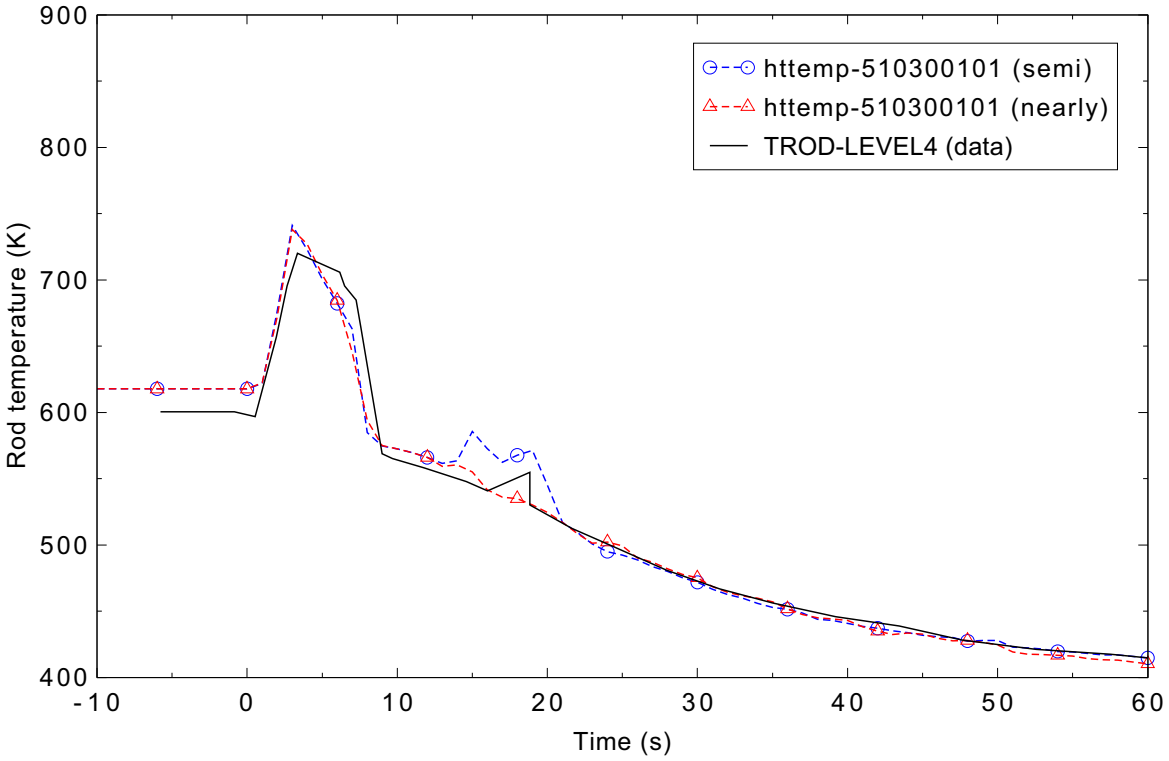

Figure 5.4-14. Measured and calculated lower core heater rod temperature (Level 4) for LOBI Test A1-04R.

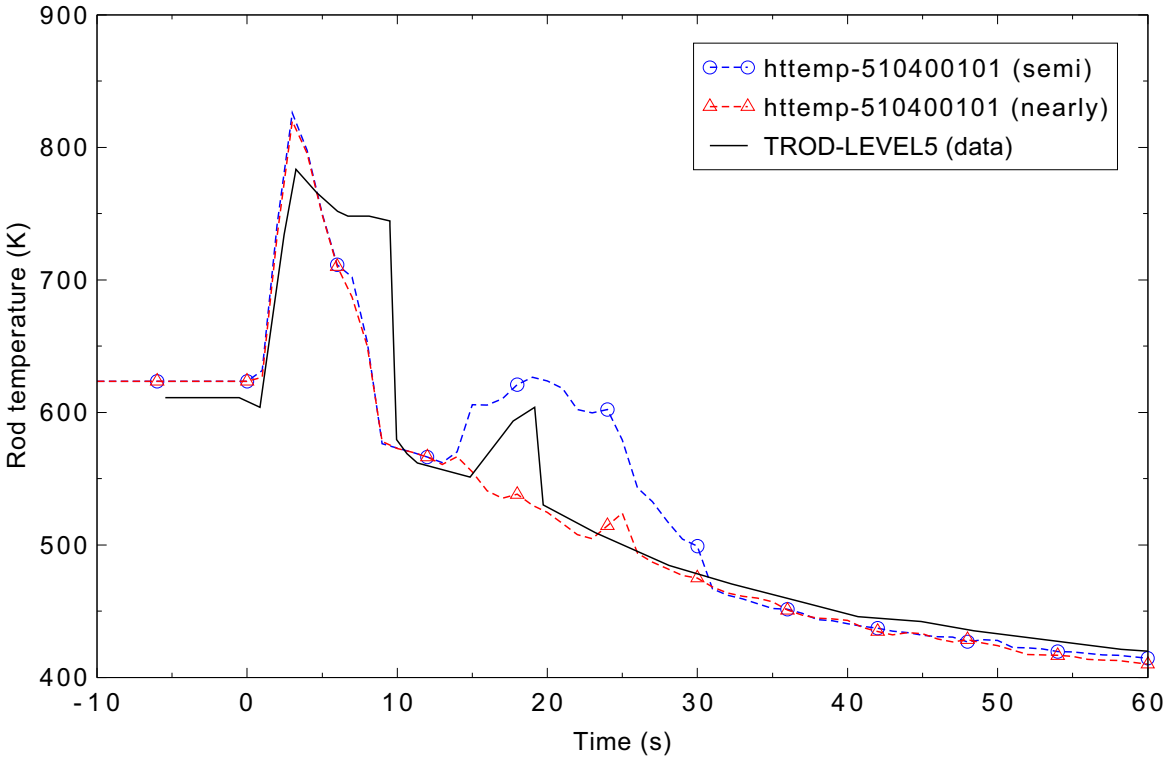

Figure 5.4-15. Measured and calculated mid-core heater rod temperature (Level 5) for LOBI Test A1-04R.

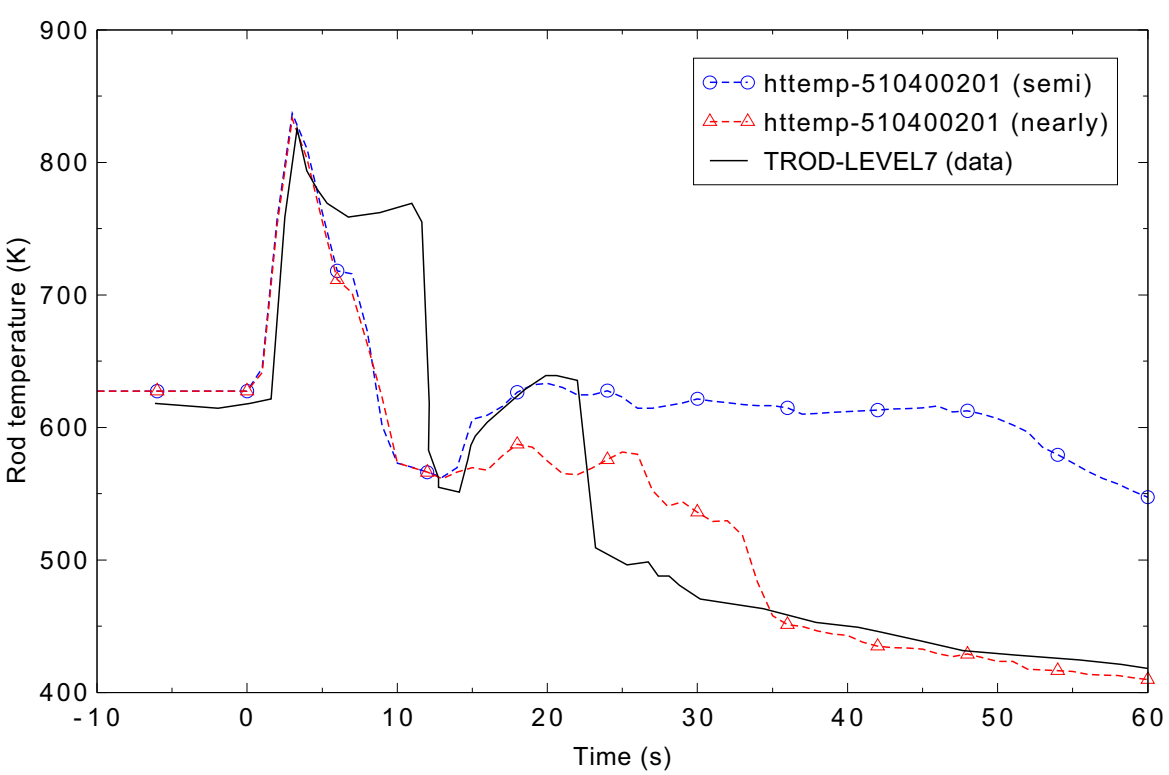

Figure 5.4-16. Measured and calculated mid-core heater rod temperature (Level 6) for LOBI Test A1-04R.

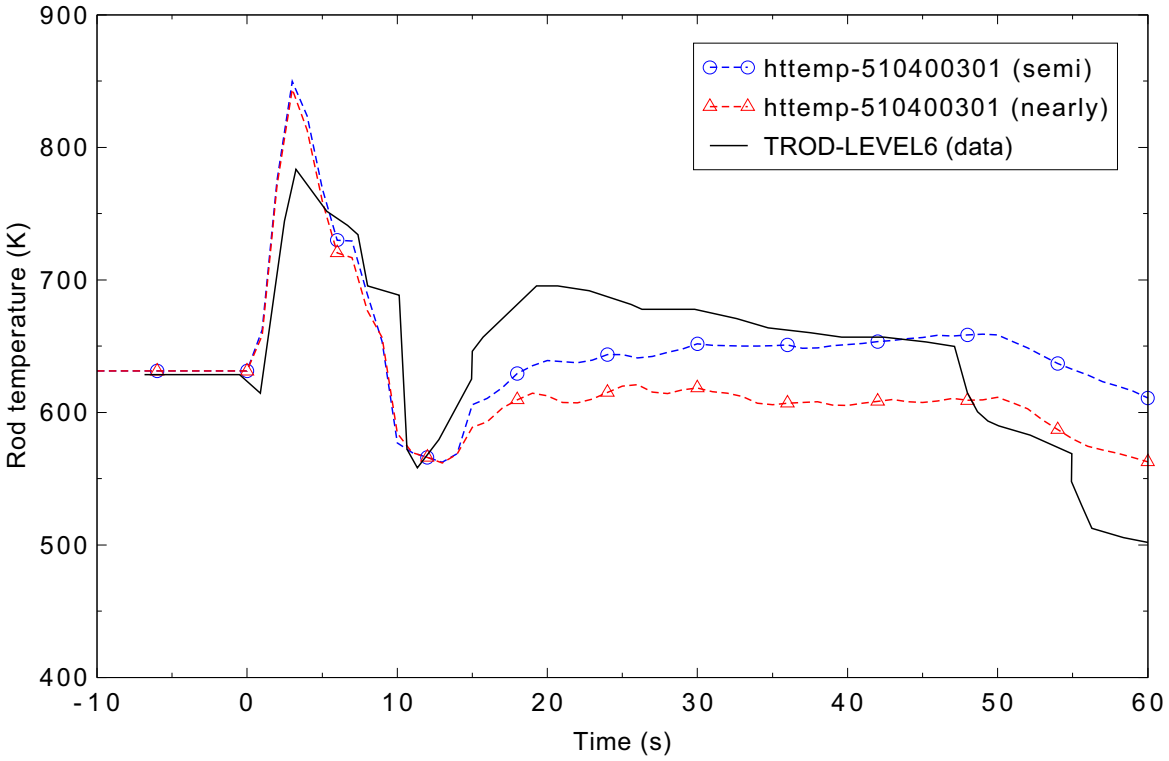

Figure 5.4-17. Measured and calculated mid-core heater rod temperature (Level 7) for LOBI Test A1-04R.

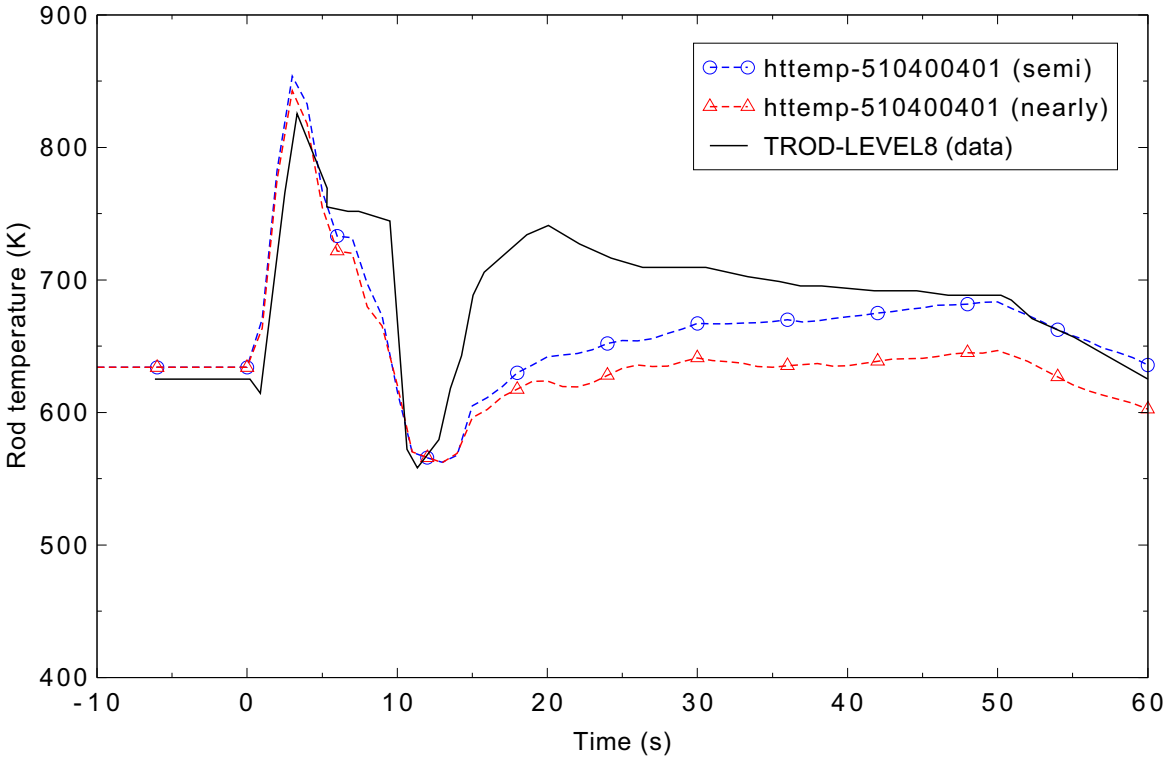

Figure 5.4-18. Measured and calculated mid-core heater temperature (Level 8) for LOBI Test A1-04R.

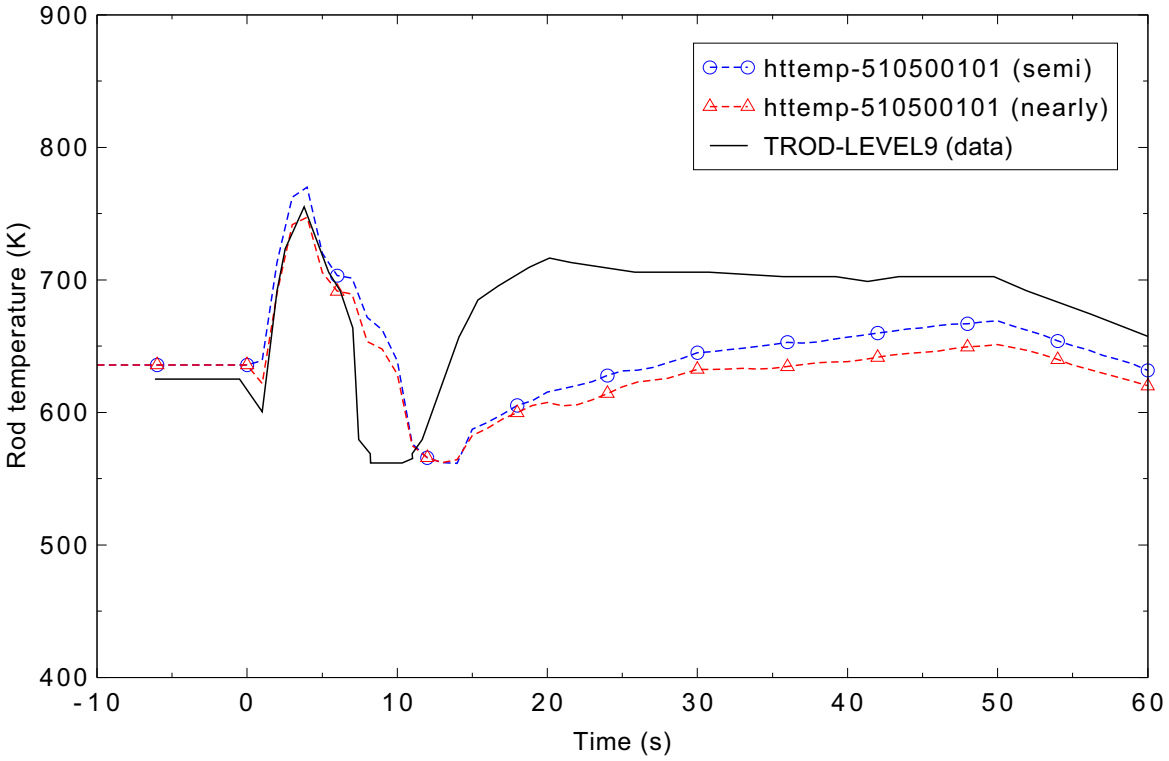

Figure 5.4-19. Measured and calculated upper core heater rod temperature (Level 9) for LOBI Test A1-04R.

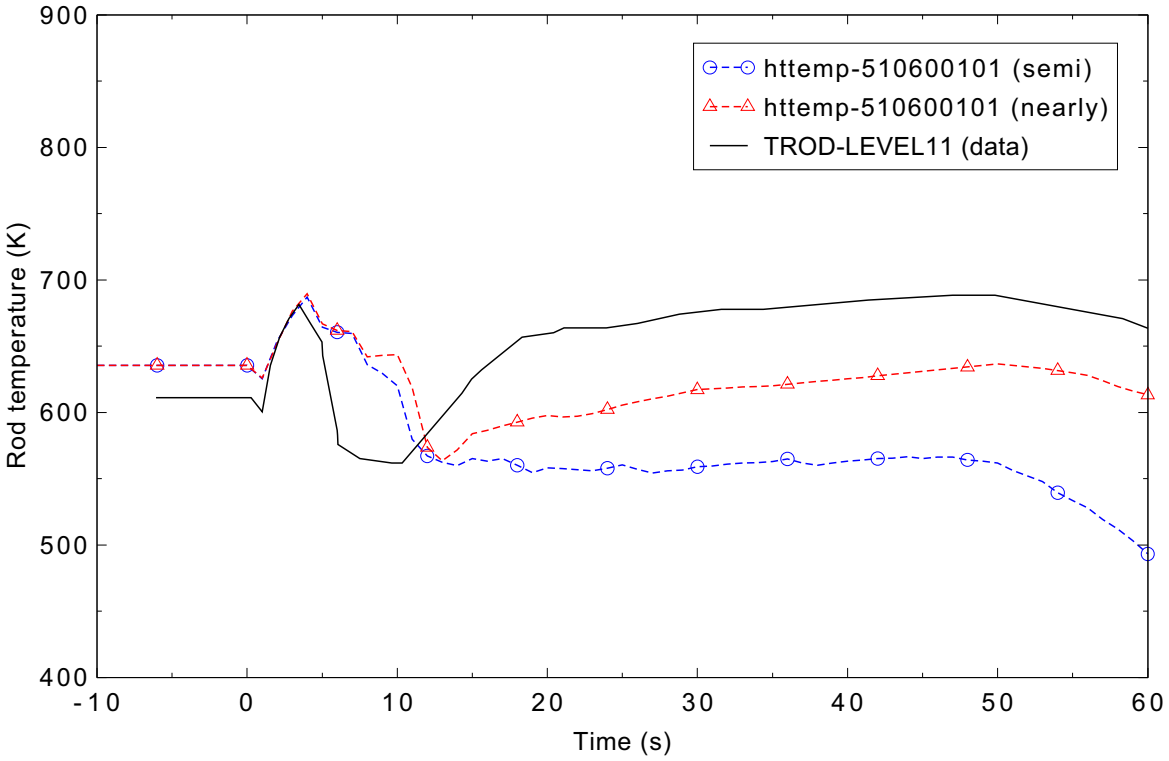

Figure 5.4-20. Measured and calculated upper core heater rod temperature (Level 11) for LOBI Test A1-04R.

The code simulations were in good agreement with the data up through Level 5, predicting both the timing and magnitudes of the initial and second heatups. At Level 6, while there is some radial variation in the measured data, all of the heater rods have quenched by 30 s; the semi-implicit calculation did not quench after the second heatup, while the nearly-implicit calculation did. The code simulated well the brief rewet near 10 s at Levels 7 and 8, but under predicted the rapid temperature increase that followed, and generally under predicted the temperature after that. The rewet in Level 9 was calculated to occur slightly late, and again the rapid temperature increase after the brief cooling was under predicted. At Level 11, the longer rewet, driven partially by liquid draining from the upper portion of the reactor vessel, was predicted to occur later. The semi-implicit calculation showed only small temperature increases after the rewet, remaining mostly near the saturation temperature, while the nearly-implicit calculation predicted temperatures about 50 K below those measured.

5.4.5 Conclusions and Assessment Findings

Based on the discussion above, it is concluded that RELAP5-3D is in excellent agreement for the system pressure and is in reasonable agreement for the loop mass flow using both the semi-implicit and nearly-implicit numerical schemes. The RELAP5-3D results for the accumulator flow rate are in minimal agreement with the experiment results for both the semi- and nearly-implicit numerical schemes, although it is possible that the data are in error since the code does such an excellent job in predicting the pressure response.

The rod temperatures are judged to be in reasonable agreement for the lower levels where there was no radial variation in the temperature response. At higher levels, the calculations are judged to be in reasonable agreement through the initial rewet, then are generally in minimal agreement after the second heatup starts.

5.4.6 References

5.4-1. Nuclear Energy Agency, *LOBI/B-R1M, Loop for Blowdown Investigation, PWR Single-Ended Cold-Leg Break Experiment B,* CSNI0003 LOBI/B-R1M, October 1988.

5.4-2. E. Ohlmer, et al., *Experimental Data Report on LOBI Test A1-04R*, Joint Research Centre, Ispra Establishment – Italy, 1981 [Proprietary].

5.5 LOFT Experiment L2-5 (1-D)

Experiments were performed in the 1970s and 1980s in the Loss-of-Fluid Test (LOFT) facility, a 50 MWt power/volume-scaled nuclear reactor designed to investigate the response of a commercial pressurized water reactor (PWR) to loss-of-coolant accidents (LOCAs) and operational transients. Experiment L2-5 simulated a double-ended cold leg break with a maximum core linear heat generation rate of 40.1 kW/m (12.2 kW/ft).

5.5.1 Code Models Assessed

As an integral test facility, multiple code models are addressed. The principal interest is in the core behavior: fuel rod heatup and quench, and peak cladding temperature. Other parameters of significance are the break flow rates, system pressure, and emergency core coolant (ECC) system response.

5.5.2 Experiment Facility Description

The LOFT facility is described in detail in Reference 5.5-1. The nuclear core was 1.68 m high with a 0.61 m diameter. The core contained nine fuel assemblies and 1,300 fuel rods that were representative of a commercial PWR. As shown in Figure 5.5-1, the facility contained two primary coolant loops. The intact loop represented three loops of a commercial plant, containing a hot leg, steam generator, cold leg, two primary coolant pumps, and the pressurizer. The broken loop represented a single loop, and included steam generator and primary coolant pump simulators, which modeled the flow resistance of these components. The broken loop could be configured to model either hot or cold leg breaks. Quick-opening blowdown valves (adjustable opening times of approximately 20 to 50 ms) simulated the initiation of primary coolant pipe ruptures, and orifices were used to model different break sizes. The break effluent was collected in a blowdown suppression tank.

The ECC system included a pumped high-pressure injection system (HPIS), a nitrogen-pressurized accumulator, and a pumped low-pressure injection system (LPIS). The accumulator was equipped with an adjustable height standpipe, which allowed the effective liquid volume to be varied between experiments. The ECC system was designed to allow injection to the intact loop hot leg, intact loop cold leg, reactor vessel upper plenum, lower plenum, or downcomer.

The LOFT facility was extensively instrumented. Fluid pressure, temperature, and flow rate were measured at key locations in the primary coolant, secondary coolant, and ECC systems. Three-beam gamma densitometers were used to measure fluid density at two locations in the intact and broken loops. Thermocouples measured fuel rod cladding and support tube temperatures at 196 core locations. Several fuel rod internal temperatures (fuel and plenum) were also measured. Neutron flux was measured with four fixed detectors, which were designed to measure power transients, and four traversing in-core probes, which were designed to measure steady-state axial flux distributions at four different locations in the core.

Experiment L2-5 simulated a double-ended offset shear of a cold leg pipe with an immediate primary coolant pump trip. For this experiment, the primary coolant pumps were disconnected from their flywheels, resulting in a much faster pump coastdown. ECC injection was to the intact loop cold leg. Reference 5.5-2 presents the data from this experiment.

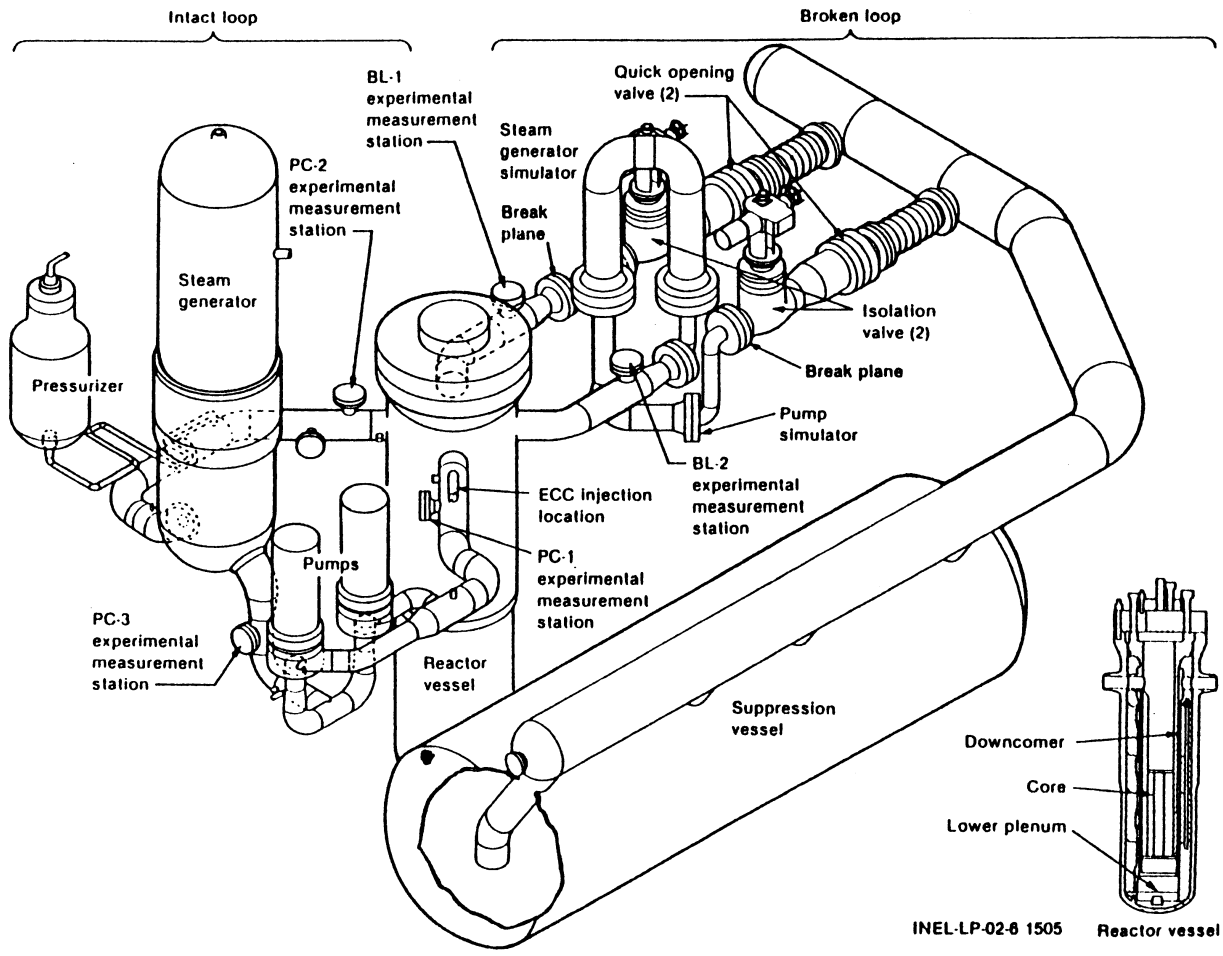

Figure 5.5-1. Schematic of the LOFT facility.

5.5.3 Input Model Description

The RELAP5-3D input model used for the L2-5 simulation is shown in Figure 5.5-2. It includes the reactor vessel, the intact and broken loops, the intact loop steam generator secondary side, the pressurizer, the ECC systems, and charging and letdown flows. The model contains 128 control volumes, 138 junctions, and 75 heat structures.

The reactor vessel includes representations of the downcomer (Components 700-740), lower plenum (Components 215-220), core inlet (Component 225), core (Component 230), and upper plenum (Components 240-260). The downcomer was split into two sectors, each connected to one cold leg. These two sectors were connected in crossflow at each elevation except at the level of the cold legs, where the hot leg nozzles were assumed to prevent azimuthal flow. The core was modeled with twelve axial nodes. Two core bypass paths were modeled: the gaps between the core filler blocks and the flow skirt (Component 235), and the leakage between the cold leg and hot leg nozzles.

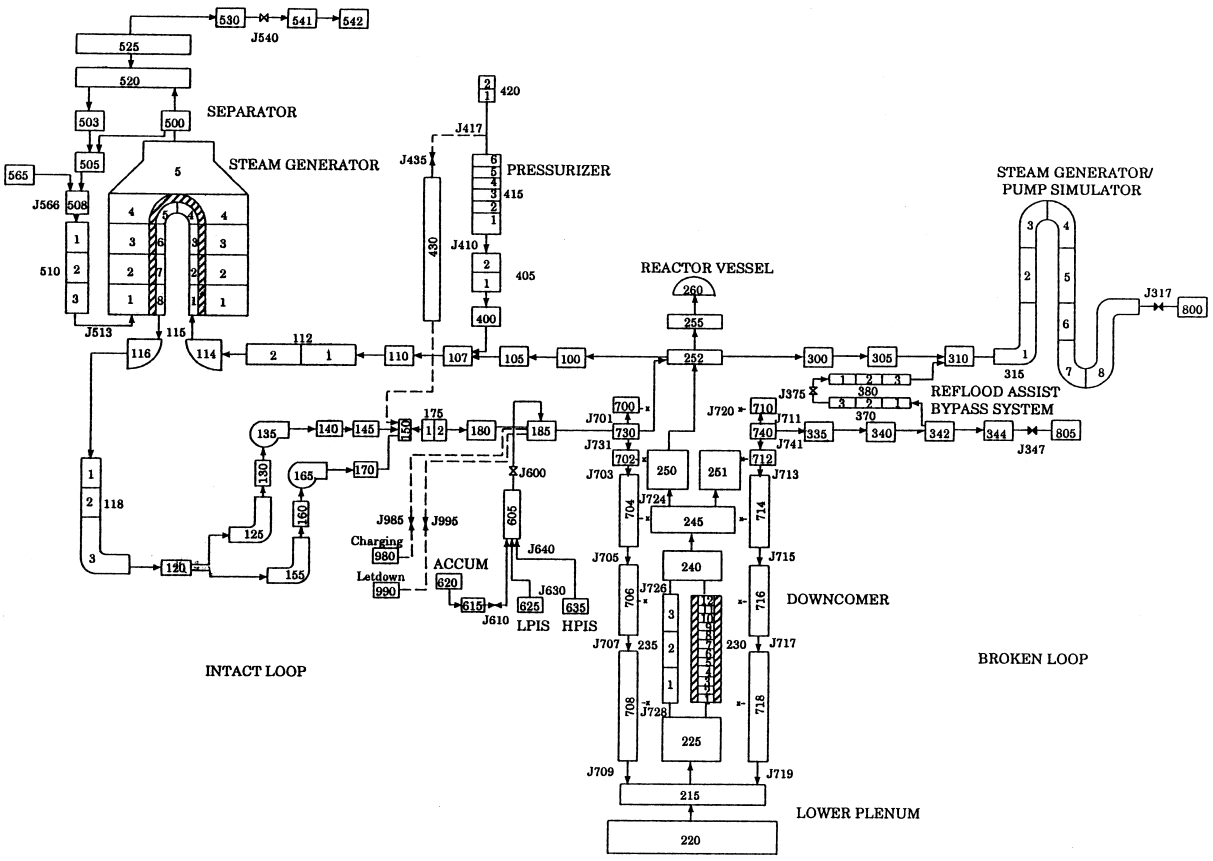

Figure 5.5-2. RELAP5-3D nodalization for the LOFT facility Experiment L2-5 (1-D vessel).

The intact loop model includes the hot leg, steam generator, two primary coolant pumps, and the cold leg. The pressurizer is connected to the intact loop hot leg, with spray flow from the cold leg. Charging and letdown flows are connected to the cold leg.

The broken loop model includes the hot and cold legs, the reflood assist bypass system piping, and the steam generator/pump simulator, which was attached to the hot leg for this cold leg break experiment. The break junctions had subcooled and two-phase discharge coefficients of 0.93 and 0.84, respectively. The time-dependent volumes downstream of the breaks were controlled to provide the back pressure measured in the blowdown suppression tank during the experiment.

The ECC systems modeled were the HPIS, accumulator, and LPIS. These were all connected to the intact loop cold leg for this experiment.

Heat structures in the model represented the central fuel assembly fuel rods, the peripheral fuel assembly fuel rods, the steam generator tubes, filler blocks in the core and downcomer, the core support barrel, and the reactor vessel lower head. An environmental heat loss of 174 kW from the primary coolant system was also modeled on the reactor vessel lower head heat structure. The reflood model was used for the fuel rod heat structures, starting at 25 s, when the pressure had dropped low enough to make the model applicable.

5.5.4 Data Comparisons and Results

A steady state calculation was performed to establish the desired initial conditions in the RELAP5-3D model. Table 5.5-1 provides a comparison of the measured and calculated initial and boundary conditions for Experiment L2-5; the core power, feedwater temperature, and accumulator conditions were the only fixed values. All of the calculated values were in good agreement with the measurements except for the broken loop hot leg temperature, which was about 5 K lower than the data; this is not expected to have a noticeable effect on the simulation.

Table 5.5-1. LOFT Experiment L2-5 initial conditions.

Parameter	Measured Value	Calculated Value
Intact Loop		
Mass flow (kg/s)	192.4 ± 7.8	192.4
Hot leg pressure (MPa)	14.94 ± 0.06	14.92
Cold leg temperature (K)	556.6 ± 4.0	556.5
Hot leg temperature (K)	589.7 ± 1.6	590.4
Pressurizer		
Liquid level (m)	1.14 ± 0.03	1.14
Broken Loop		
Cold leg temperature (K)	554.3 ± 4.2	556.5
Hot leg temperature (K)	561.9 ± 4.3	556.5
Reactor Vessel		
Core power (MW)	36.0 ± 1.2	36.0
Maximum fuel centerline temperature (K)	1,660 ± 57	1,710
Steam Generator		
Pressure (MPa)	5.85 ± 0.06	5.84
Feedwater flow rate (kg/s)	19.1 ± 0.4	19.1
Feedwater temperature (K)	482.0 ± 1.2	482.0
Accumulator		
Pressure (MPa)	4.29 ± 0.06	4.29
Liquid temperature (K)	303.2 ± 6.1	303.2
Liquid level above standpipe (m)	1.17 ± 0.01	1.16

Table 5.5-2 provides the sequence of events for Experiment L2-5. The experiment was initiated by opening the quick-opening blowdown valves in the broken loop hot and cold legs. Within the first second,

the reactor scrammed on low hot leg pressure, the primary coolant pumps were tripped, and the fuel began to heat up. The primary coolant pump trip in the experiment resulted in the power being supplied to the pumps being reduced to zero after about 1.3 s; this was simulated in the RELAP5-3D calculation by tripping the pumps at 1.6 s, near the midpoint of the power decrease. A partial rewet of the fuel occurred between 12.1 and 22.7 s in the experiment. The pressurizer emptied at 15.4 s, and accumulator injection began at 16.8 s. HPIS and LPIS injection began at 23.9 and 37.3 s, respectively, with their start being delayed to simulate the time required to load the diesel generators in a commercial power plant. The accumulator emptied near 50 s. The peak cladding temperature occurred at 28.47 s, and all of the cladding was quenched by 65 s. The experiment was effectively terminated at 107.1 s by stopping the LPIS injection; the calculation was terminated at 100 s.

Table 5.5-2. LOFT Experiment L2-5 sequence of events.

Event	Time after Experiment Initiation (s)
Experiment initiated	0.0
Subcooled blowdown ended	0.043 ± 0.01
Reactor scrammed	0.24 ± 0.01
Cladding temperatures initially deviated from saturation	0.91 ± 0.2
Primary coolant pumps tripped	0.94 ± 0.01
Subcooled break flow ended (cold leg)	3.4 ± 0.5
Partial rewet initiated	12.1 ± 1.0
Pressurizer emptied	15.4 ± 1.0
Accumulator A injection initiated	16.8 ± 0.1
Partial rewet ended	22.7 ± 1.0
HPIS injection initiated	23.90 ± 0.02
Maximum cladding temperature attained	28.47 ± 0.02
LPIS injection initiated	37.32 ± 0.02
Accumulator emptied	49.6 ± 0.1
Core cladding quenched	65 ± 2
LPIS injection terminated	107.1 ± 0.4

Figures comparing the measured and calculated response of the LOFT system during the experiment are provided below. Data uncertainties provided on the figures are for the maximum measured value during the experiment. Both the semi- and nearly-implicit calculations had requested time steps of 0.01 s. Data are from the NRC Data Bank.

Figure 5.5-3 presents the pressure in the reactor vessel upper plenum. The rapid depressurization in the first 4 s, during which both subcooled blowdown and subcooled break flow ended, was calculated very

well. The pressure was then under predicted slightly until about 20 s, then slightly over predicted until 36 s. The differences in the inflection points in the curves were caused by differences in the break flow. Overall, the calculation was judged to be in reasonable agreement with the data.

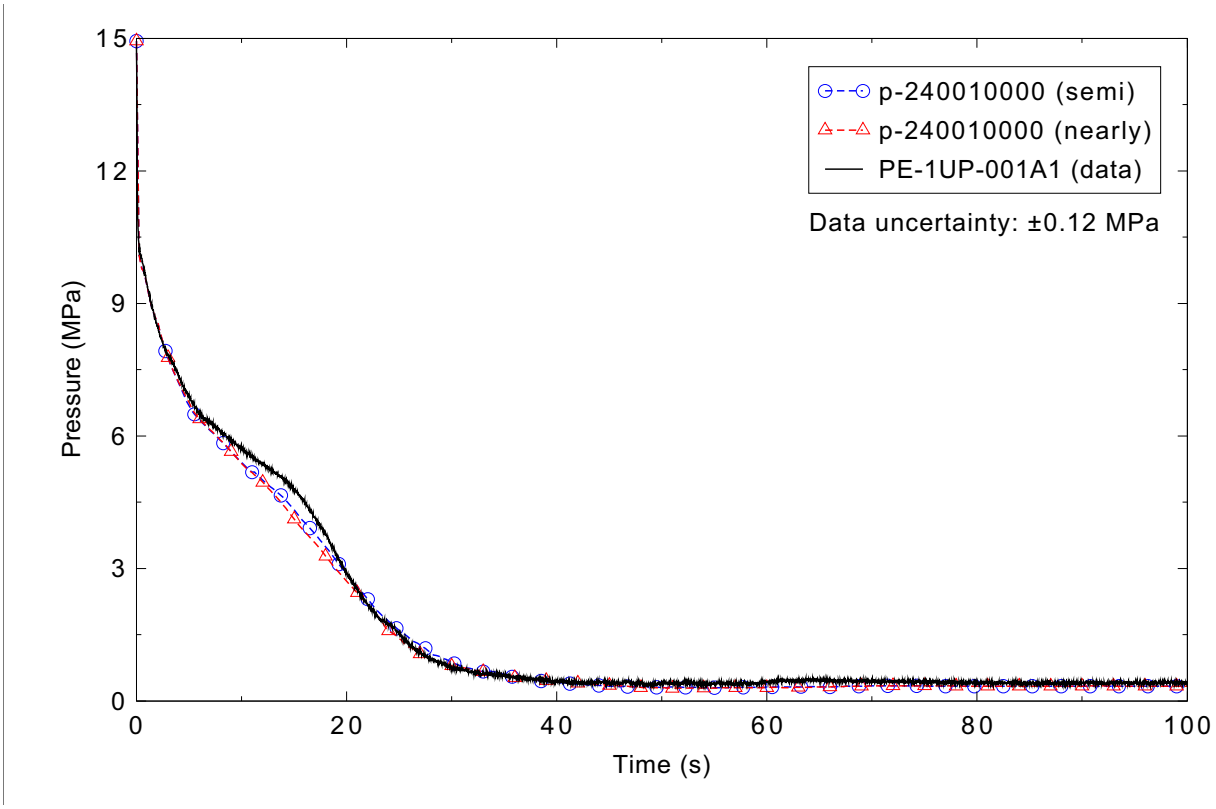

Figure 5.5-3. Measured and calculated reactor vessel upper plenum pressure for the LOFT Experiment L2-5 1-D case.

The steam generator pressure is shown in Figure 5.5-4. The calculation was in excellent agreement with the data until 60 s. After that, the measured pressure continued to decrease, while the calculated pressure remained nearly constant. The constant pressure is indicative of an isolated system, while the decreasing pressure is evidence that energy is still being removed from the secondary side. This may be caused by continuing heat transfer to the primary coolant, which ended near 60 s in the calculation. The calculation is judged to be in reasonable agreement with the data, based on the performance during the critical portion of the transient.

Figure 5.5-5 presents the pressurizer liquid level. The pressurizer emptied later in the calculation than in the experiment. In both the experiment and calculation, choked flow occurred in the surge line, keeping the pressurizer pressure well above the hot leg pressure until after the pressurizer emptied. Better agreement between the calculation and data could be achieved by reducing the flow loss coefficients in the surge line. With no changes to the input model, the prediction is judged to be reasonable, as the data trend is correct, appropriate phenomena are being modeled, and the calculation lies within the measurement uncertainty for most of the time.

Figure 5.5-6 shows the mass flow rate in the broken loop cold leg. Most of the calculation is in excellent agreement with the measured data. The peak flow rate and the transition from subcooled to

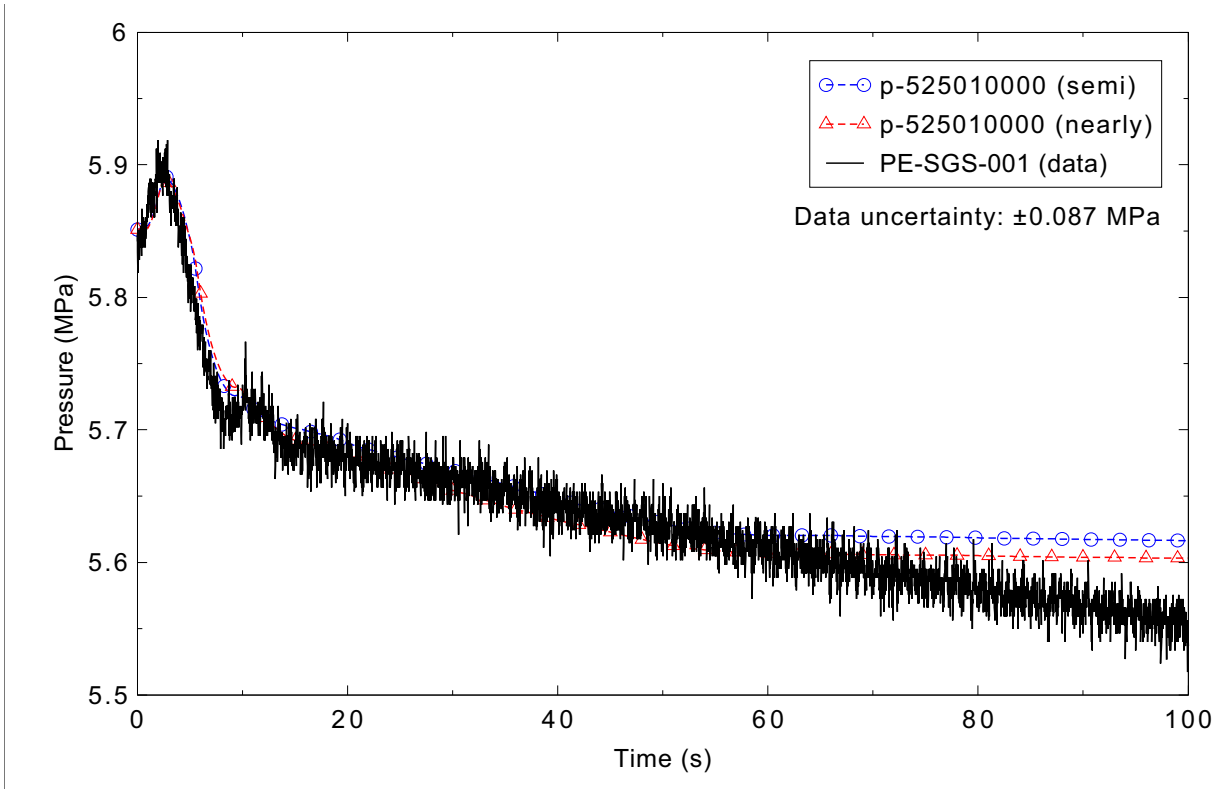

Figure 5.5-4. Measured and calculated steam generator pressure for the LOFT Experiment L2-5 1-D case.

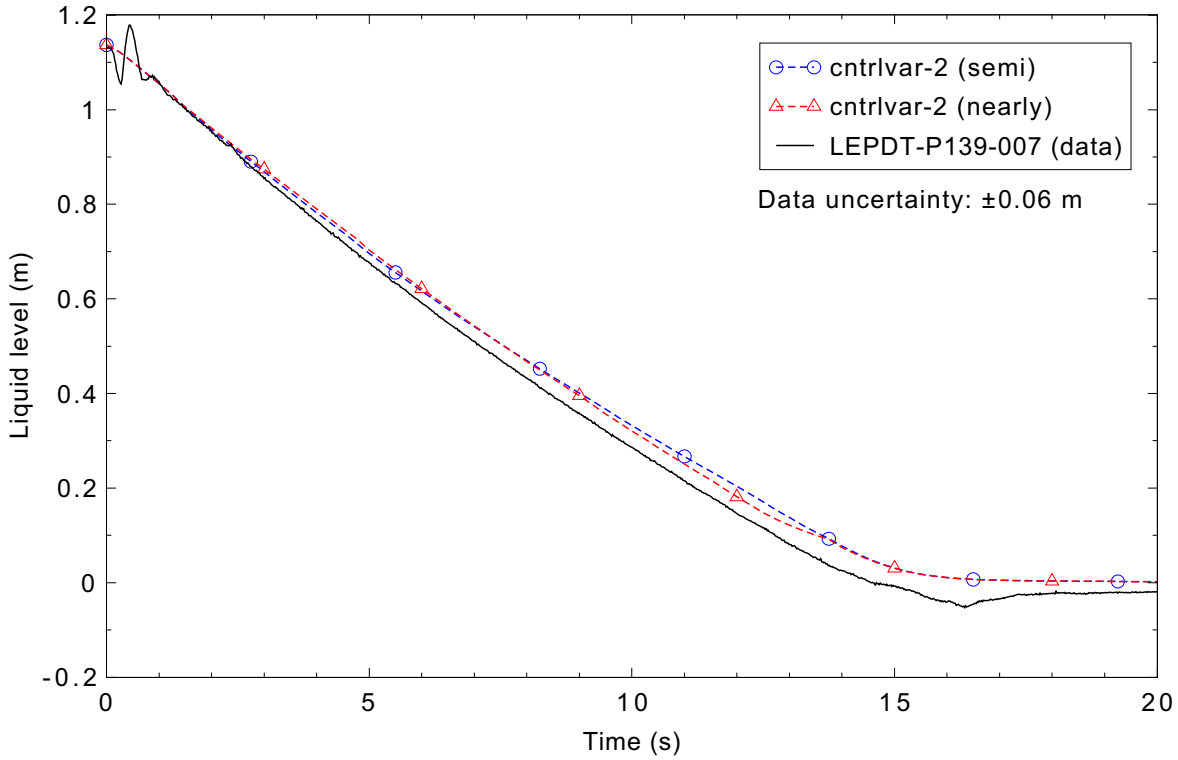

Figure 5.5-5. Measured and calculated pressurizer liquid level for the LOFT Experiment L2-5 1-D case.

two-phase critical flow are calculated well. The flow rate is over predicted between about 13 and 21 s, as the code leg fluid density is higher in the calculation than in the experiment. The large calculated flow spikes near 30 s reflected similar increases in density. Overall, the prediction is judged to be reasonable.

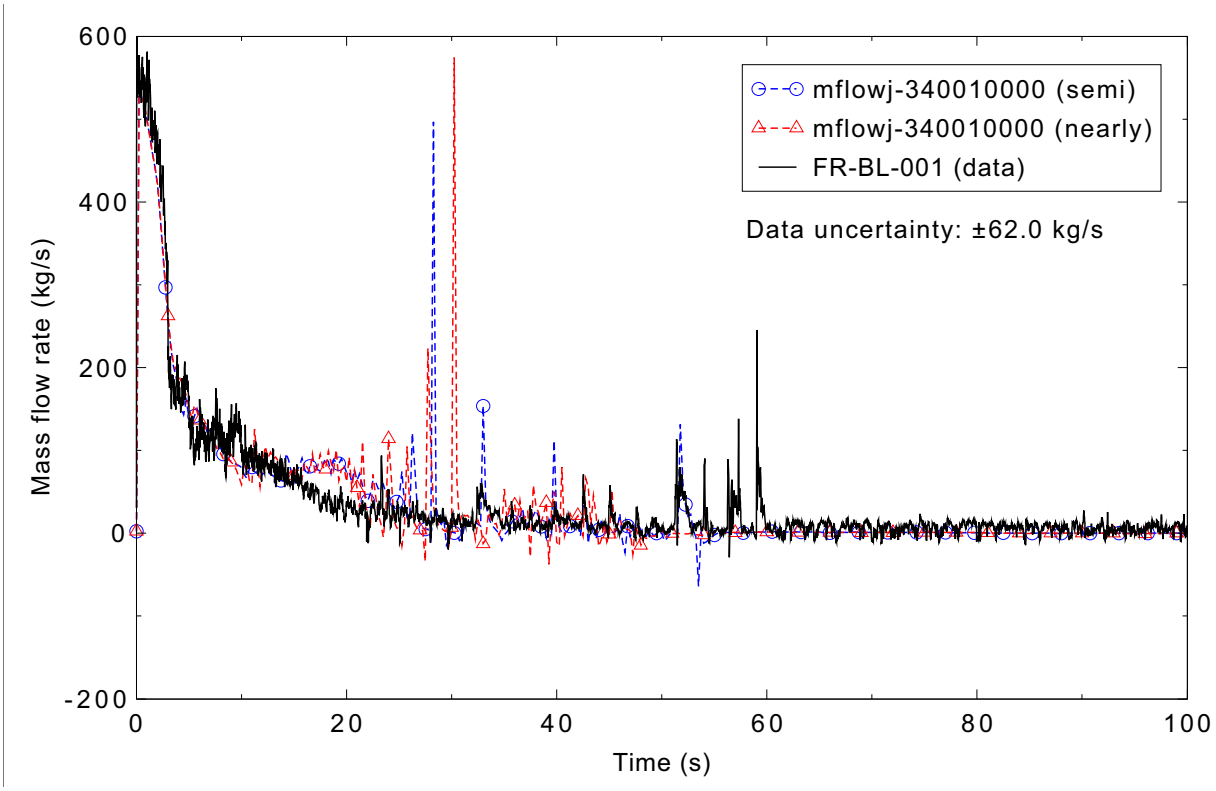

Figure 5.5-6. Measured and calculated mass flow rate in the broken loop cold leg for the LOFT Experiment L2-5 1-D case.

Flow rates in the broken loop hot leg are shown in Figure 5.5-7. Other than a brief under prediction near 10 s, the calculated flow is very close to the measured flow. Therefore, the prediction is judged to be in excellent agreement with the data.

Figure 5.5-8 presents the flow rate in the intact loop hot leg. The measurement did not indicate the direction of the flow; between 5 and 30 s the flow should have been negative, toward the break. [To compare the magnitudes of the flow rates, an additional curve on the plot shows the absolute value of the calculated flow rate. This is in good agreement with the data through most of the transient.] The data indicate that there may have been more flow in the hot leg in the experiment than in the prediction between 45 and 60 s, although the flow rate was small. Overall, the calculation of the flow rate is judged to be reasonable.

The mass flow rates in the intact loop cold leg are shown in Figure 5.5-9. The flow coastdown during the first 20 s is generally well simulated, with the calculation having a little higher flow rate near 20 s because it had more liquid in the cold leg. The flow oscillations from 30 to 70 s reflected slugs of liquid moving through the cold leg; evidence of this is seen in Figure 5.5-14 below. There appear to be more oscillations in the data than in the prediction. Overall, the code is judged to reasonably predict the intact loop cold leg flow.

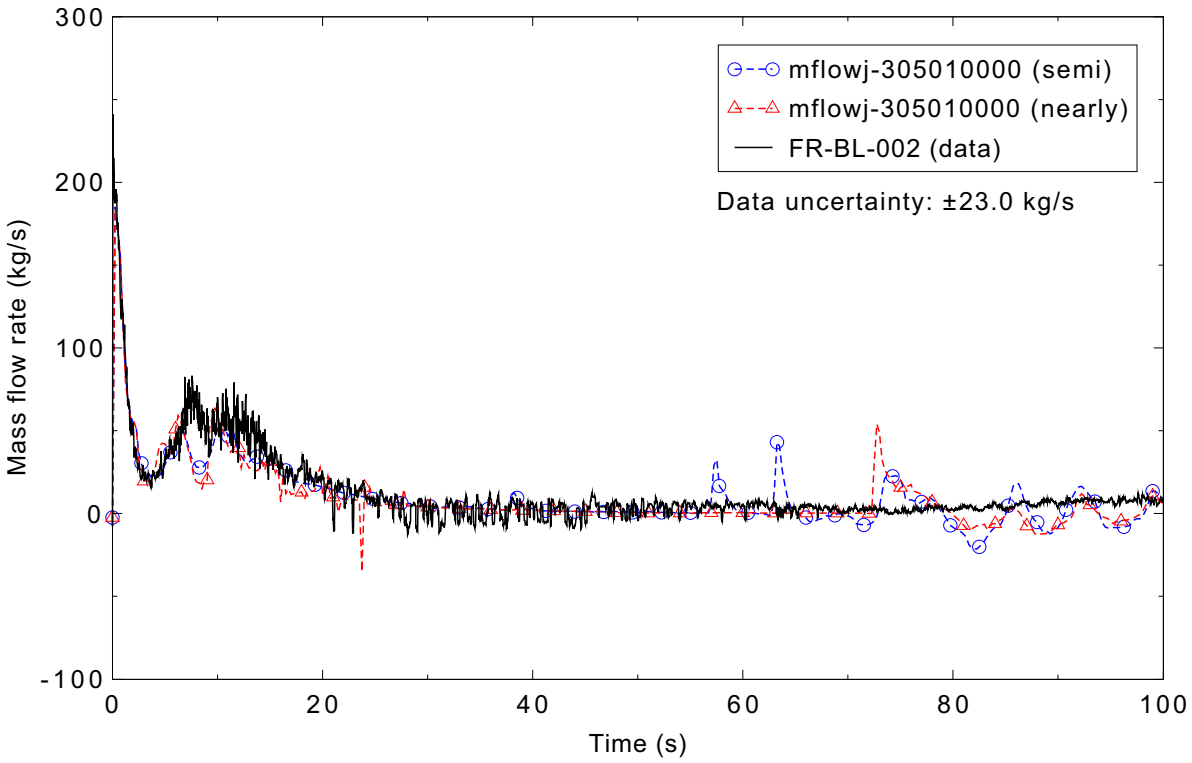

Figure 5.5-7. Measured and calculated mass flow rate in the broken loop hot leg for the LOFT Experiment L2-5 1-D case.

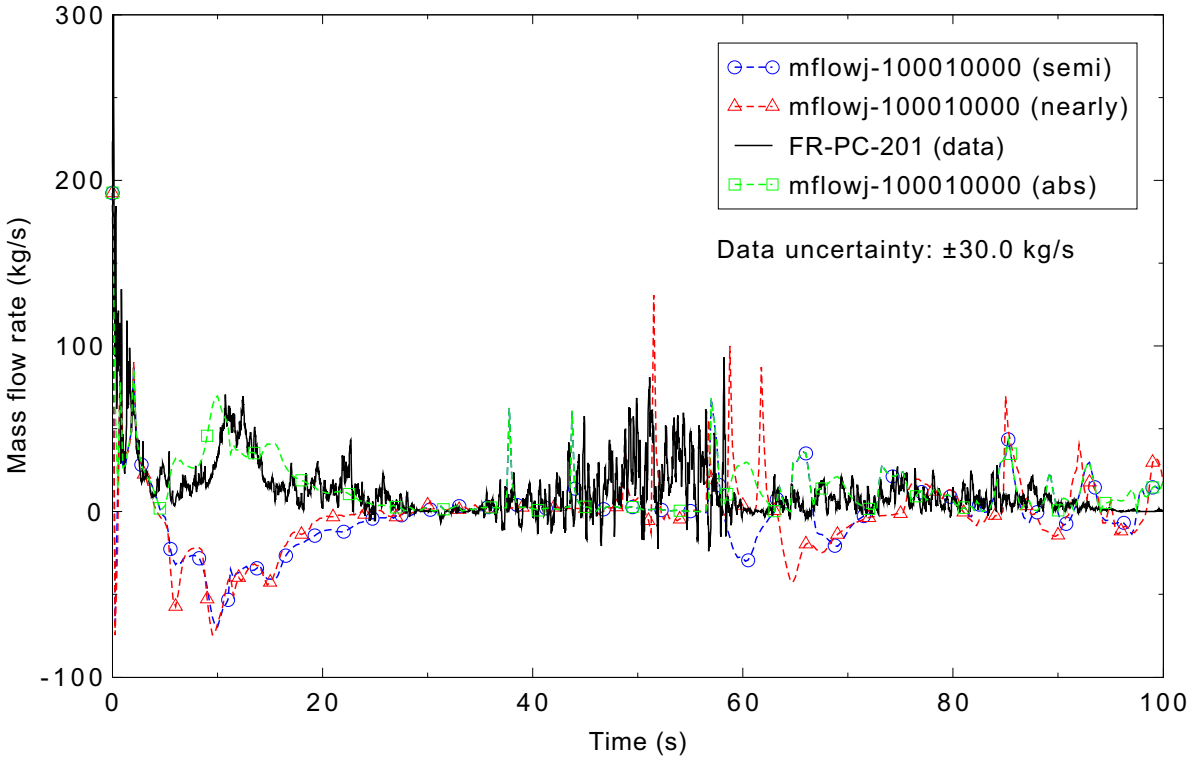

Figure 5.5-8. Measured and calculated mass flow rate in the intact loop hot leg for the LOFT Experiment L2-5 1-D case.

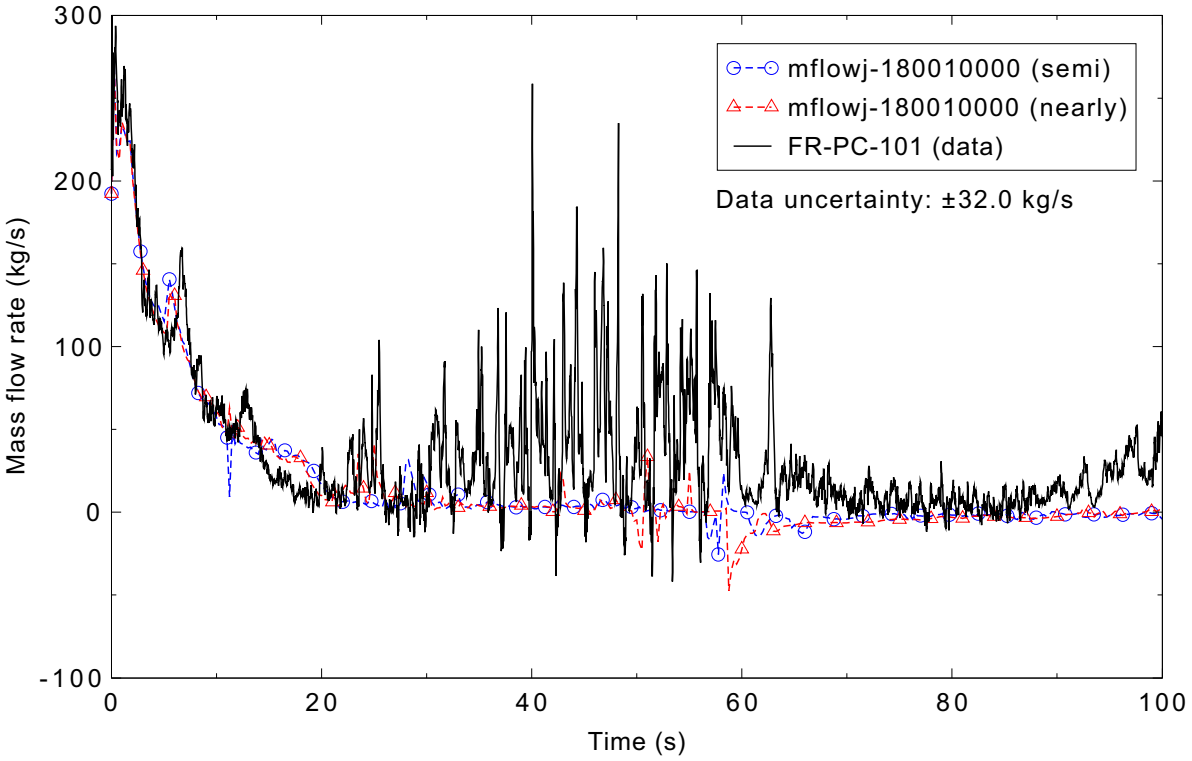

Figure 5.5-9. Measured and calculated mass flow rate in the intact loop cold leg for the LOFT Experiment L2-5 1-D case.

The rotational speed of one of the two primary coolant pumps is presented in Figure 5.5-10. The code prediction of the initial coastdown was excellent, but the freewheeling response of the pump was not well predicted, especially in the nearly-implicit calculation. Overall, the prediction is judged to be in minimal agreement with the data.

Densities in the broken loop cold leg are compared in Figure 5.5-11. The code predicted an earlier transition to two-phase conditions in the cold leg in the first few seconds, followed by a more gradual decrease than the nearly step decrease in density seen in the data. The calculation appears to have a little more liquid in the cold leg than the experiment between 15 and 20 s, although it is within the measurement uncertainty. Both the experiment and calculation had intermittent slugs of liquid in the cold leg between 30 and 60 s, before the pipe became steam-filled. The calculation is judged to be in reasonable agreement with the measured data.

Figure 5.5-12 shows densities in the broken loop hot leg. The data at this location are for two of the three densitometer beams; these are in the lower (DE-BL-002A) and upper (DE-BL-002C) portions of the pipe. (The other experiment densities presented are for pipe-average values calculated from the three chordal densities.) The calculated density lies between the measured values until after the core quench. More liquid returned to the hot leg earlier in the calculation than in the experiment. The agreement with the experiment data is judged to be reasonable until 60 s, then minimal afterwards.

The intact loop hot leg density is presented in Figure 5.5-13. The measured density increase near 5 s was predicted late and with a smaller magnitude, and the increase between 10 and 15 s was not predicted,

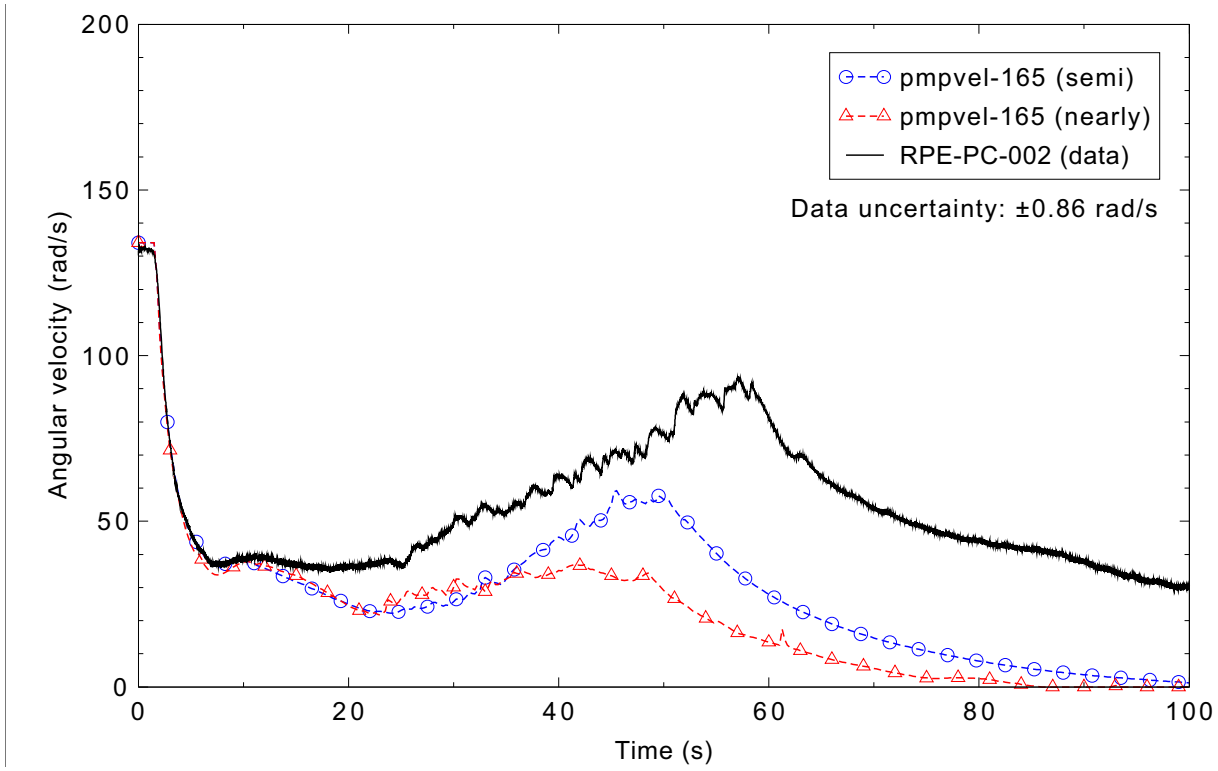

Figure 5.5-10. Measured and calculated speed for primary coolant pump 2 for the LOFT Experiment L2-5 1-D case.

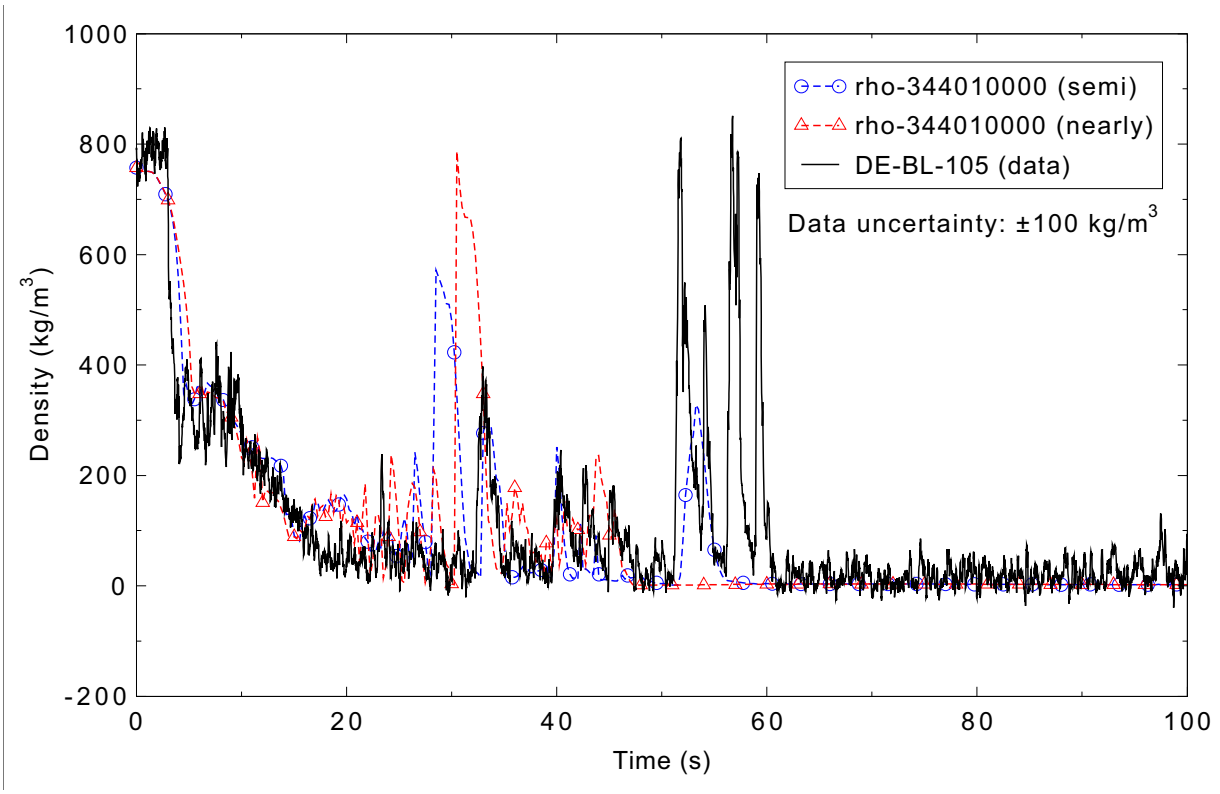

Figure 5.5-11. Measured and calculated density in the broken loop cold leg for the LOFT Experiment L2-5 1-D case.

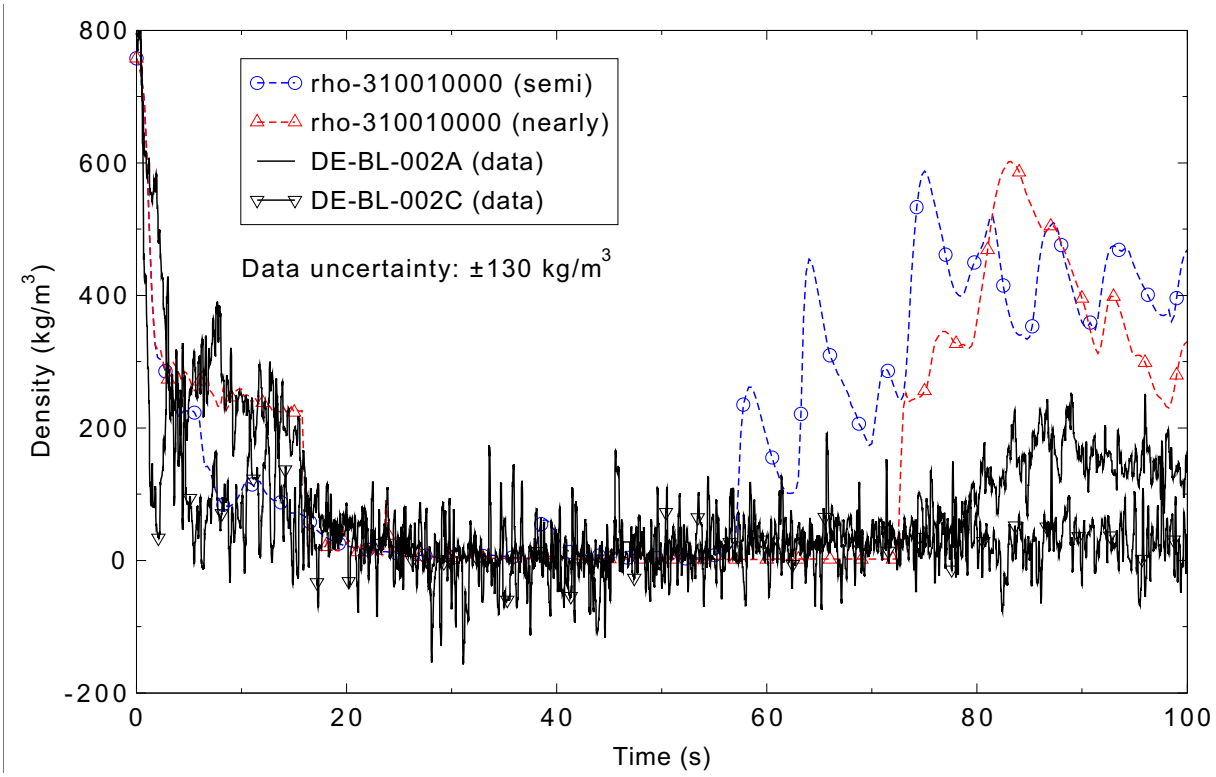

Figure 5.5-12. Measured and calculated density in the broken loop hot leg for the LOFT Experiment L2-5 1-D case.

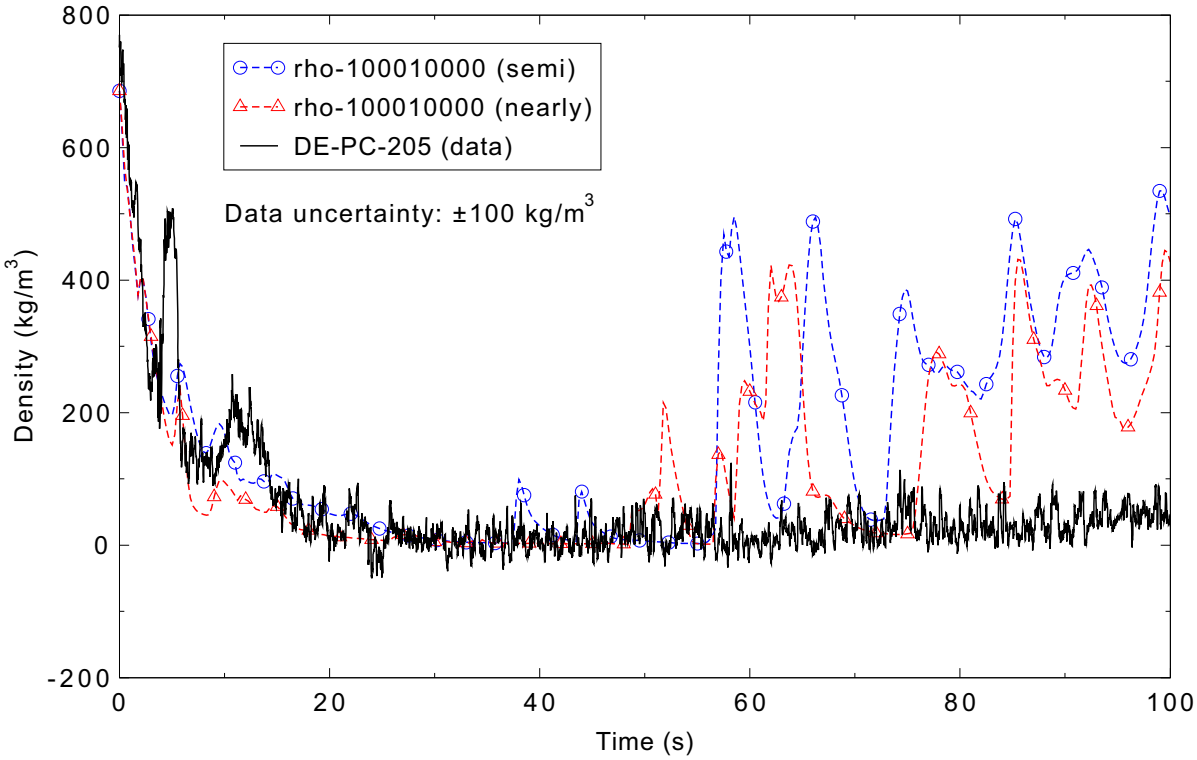

Figure 5.5-13. Measured and calculated density in the intact loop hot leg for the LOFT Experiment L2-5 1-D case.

although the calculated density did stop decreasing during that time. In the experiment, the density gradually increased after about 40 s. The calculated density exhibited larger, intermittent increases. Most of the deviation occurred after 55 s, after the core was completely quenched in the calculation. While the overall judgment is that the calculated density is in minimal agreement with the data, reasonable agreement was achieved during the more critical portion of the large break LOCA.

Figure 5.5-14 shows the intact loop cold leg densities. The initial density decrease in the first 15 s was reasonably simulated. In the experiment, the cold leg then became nearly steam-filled, while the simulation retained more liquid in the pipe. Large oscillations occurred in both the experiment and the calculation between 30 and 60 s. The density then settled out in both, although with more liquid in the simulation than in the test. While the general trends of the data are captured, the semi-implicit calculation is judged to be in minimal agreement with the experiment because too much liquid is being retained in the cold legs; the nearly-implicit calculation is judged to be in reasonable agreement.

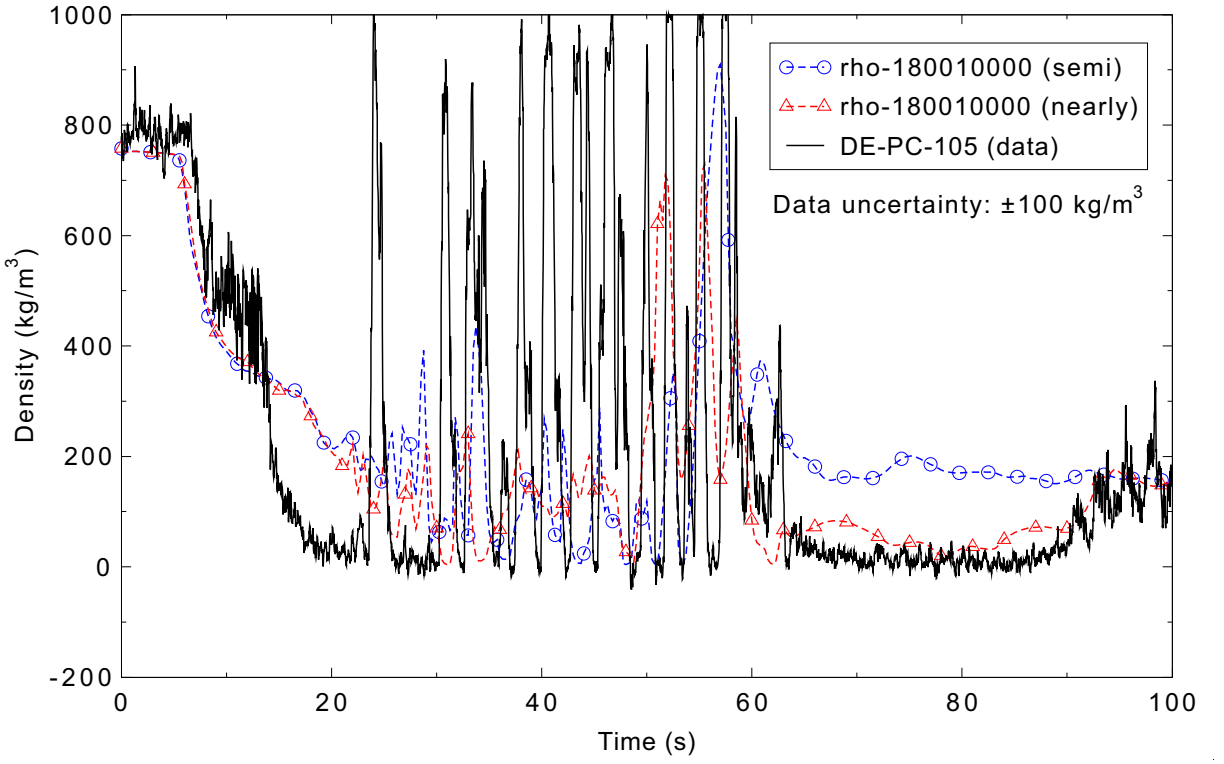

Figure 5.5-14. Measured and calculated density in the intact loop cold leg for the LOFT Experiment L2-5 1-D case.

The measured and calculated accumulator liquid levels are compared in Figure 5.5-15. The calculation is judged to be in excellent agreement with the data.

Figures 5.5-16 and 5.5-17 present the high- and low-pressure injection system flow rates, respectively. (Control variables are used to calculate the volumetric flow rates.) There appears to be an overshoot in the data when the HPIS flow begins, as it then settles out to a nearly constant value; the time-dependent junction in the RELAP5-3D input model is set to provide the nearly constant flow. As this is essentially a boundary condition, no assessment judgment is made. The drop in the measured LPIS flow between 50 and 60 s has no obvious cause - the primary coolant system pressure is not increasing, so the pump flow should

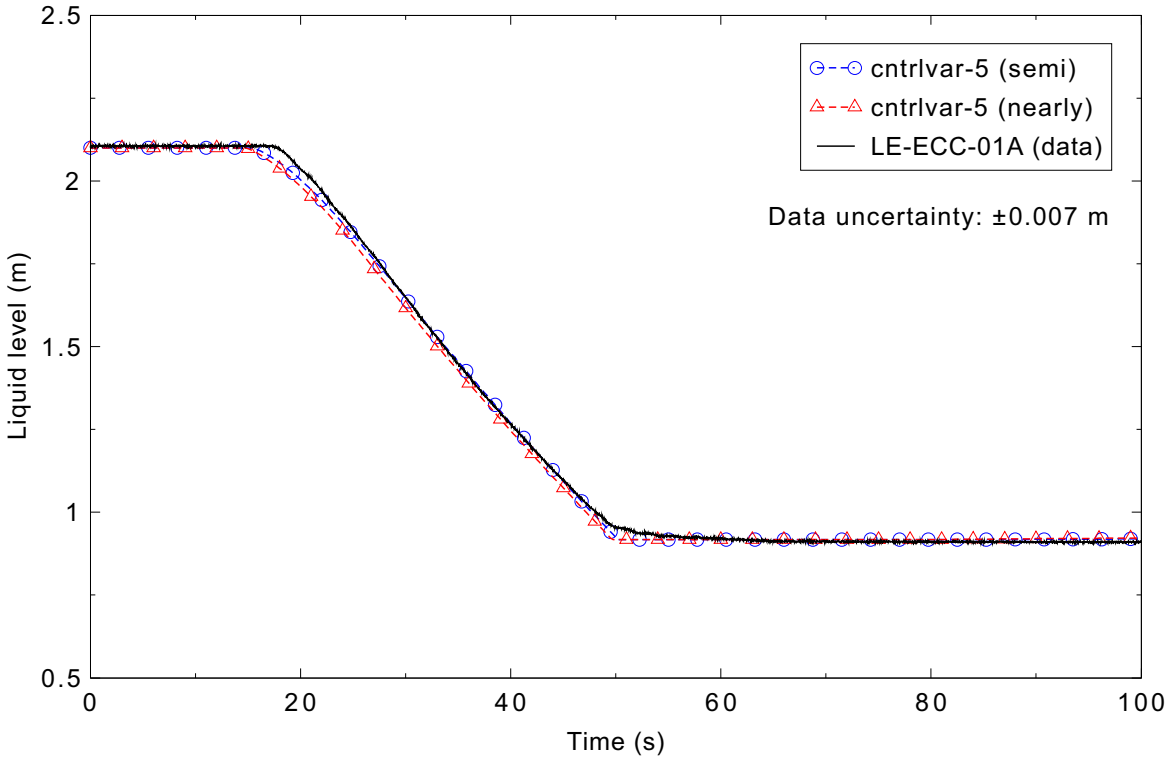

Figure 5.5-15. Measured and calculated accumulator liquid level for the LOFT Experiment L2-5 1-D case.

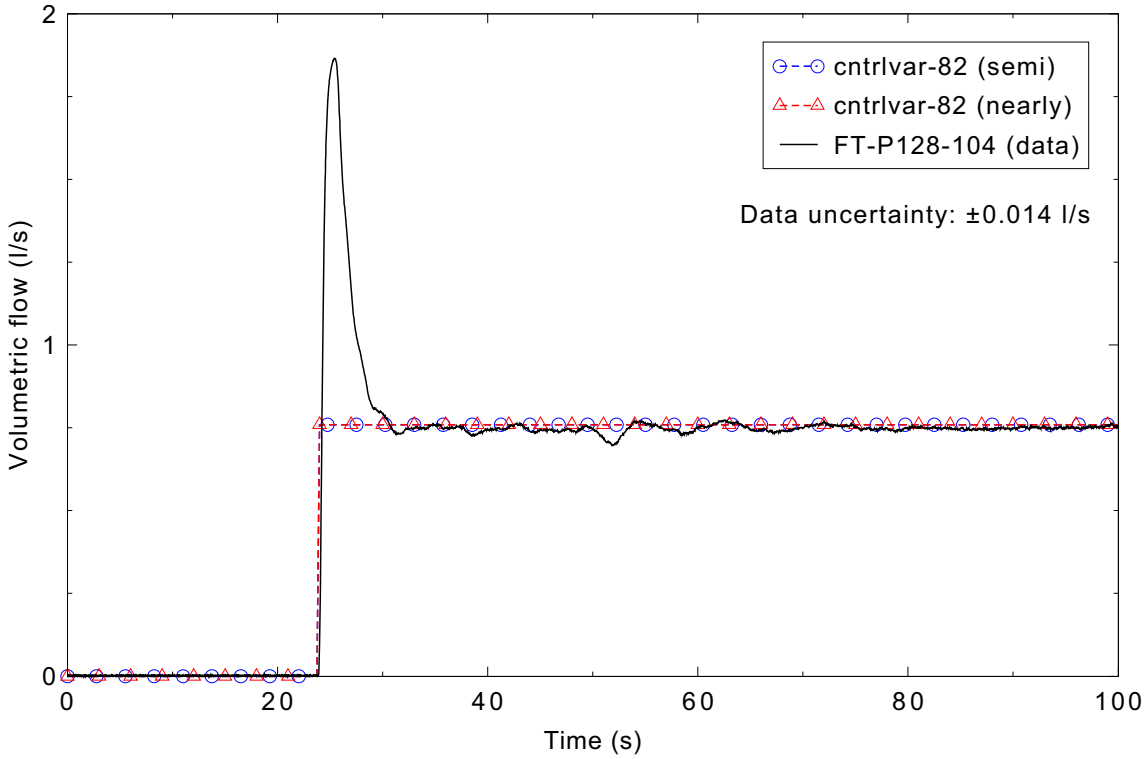

Figure 5.5-16. Measured and calculated HPIS flow for the LOFT Experiment L2-5 1-D case.

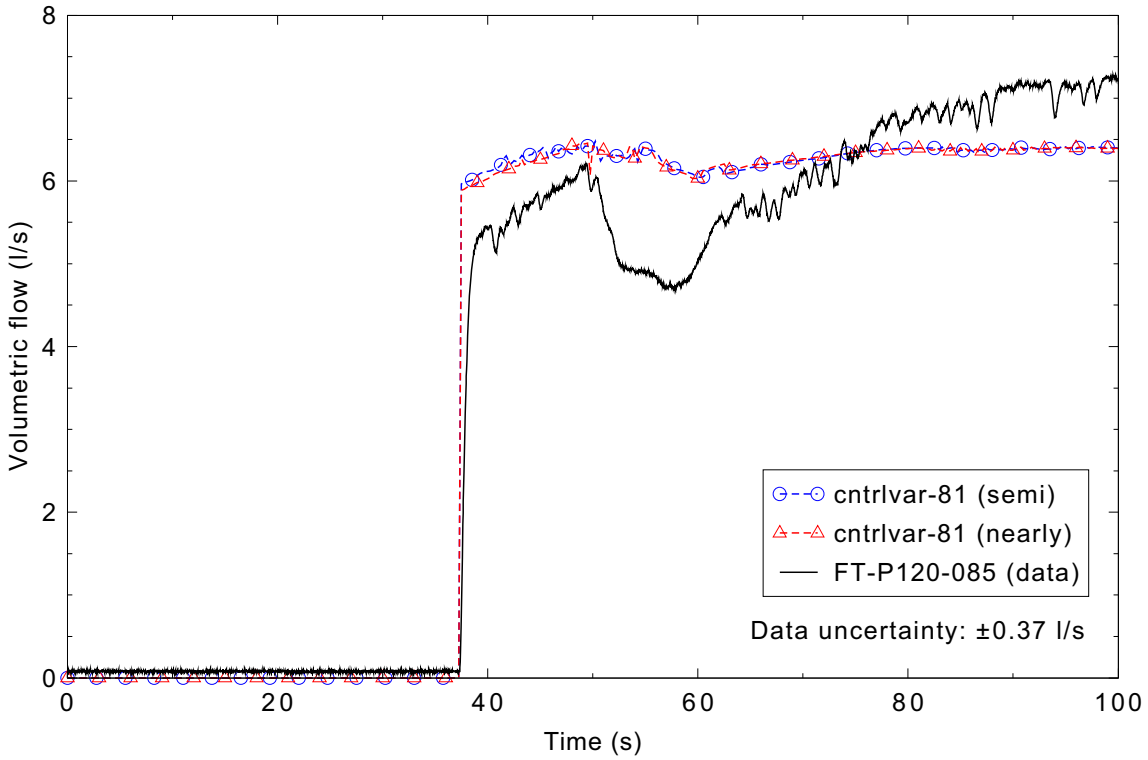

Figure 5.5-17. Measured and calculated LPIS flow for the LOFT Experiment L2-5 1-D case.

not be decreasing. The differences between the calculated and measured flow rates are attributed to differences in the primary coolant system pressure. The LPIS flow is judged to be in reasonable agreement with the data.

Figure 5.5-18 shows the measured reactor vessel upper plenum fluid temperature, as well as the calculated liquid and vapor temperatures. The calculation showed sustained superheated vapor between 20 and 50 s, while the measurement appears to show superheat beginning around 30 s. After 60 s, both the calculated and measured fluid temperatures are near the saturation temperature. However, the saturation temperature in the calculation is depressed, as it was lowered by the presence of nitrogen from the accumulator; the code uses the partial pressure of the steam to calculate the saturation temperature for the water. The prediction of the upper plenum fluid temperature is judged to be in reasonable agreement with the data.

The lower plenum liquid temperature is shown in Figure 5.5-19. The temperatures are at saturation through most of the transient, with the calculated values being lower because of the presence of the accumulator nitrogen. (The liquid saturation temperature is based on the steam partial pressure.) The prediction of the lower plenum liquid temperature is judged to be in reasonable agreement, as the data are well predicted prior to the accumulator emptying, and the correct trends are predicted after that.

Figure 5.5-20 presents a comparison of the fuel centerline temperatures in the central fuel assembly. The difference in the initial value is not considered significant, as the experiment is measuring a point value and the calculation is the average value over a 14-cm long segment of fuel; the calculation also only models a bundle-average fuel rod whose specific power may be lower than that of the measured fuel rod.

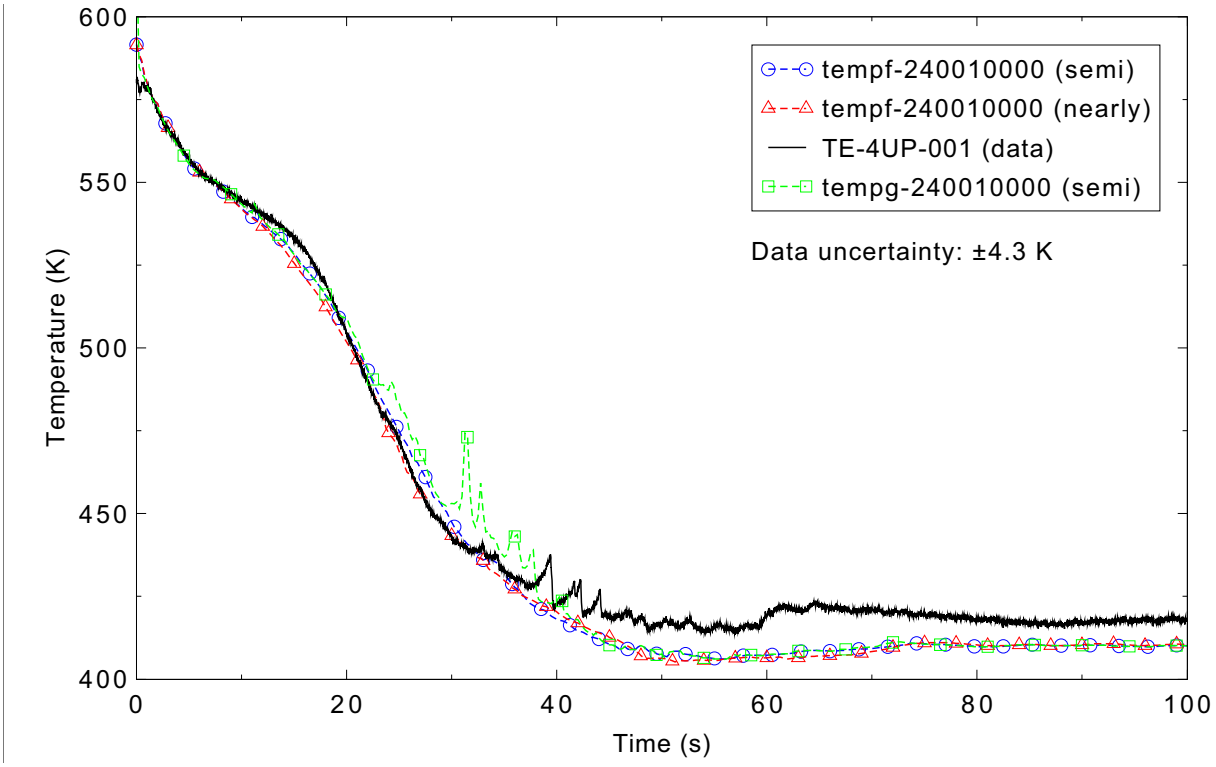

Figure 5.5-18. Measured and calculated reactor vessel upper plenum coolant temperature for the LOFT Experiment L2-5 1-D case.

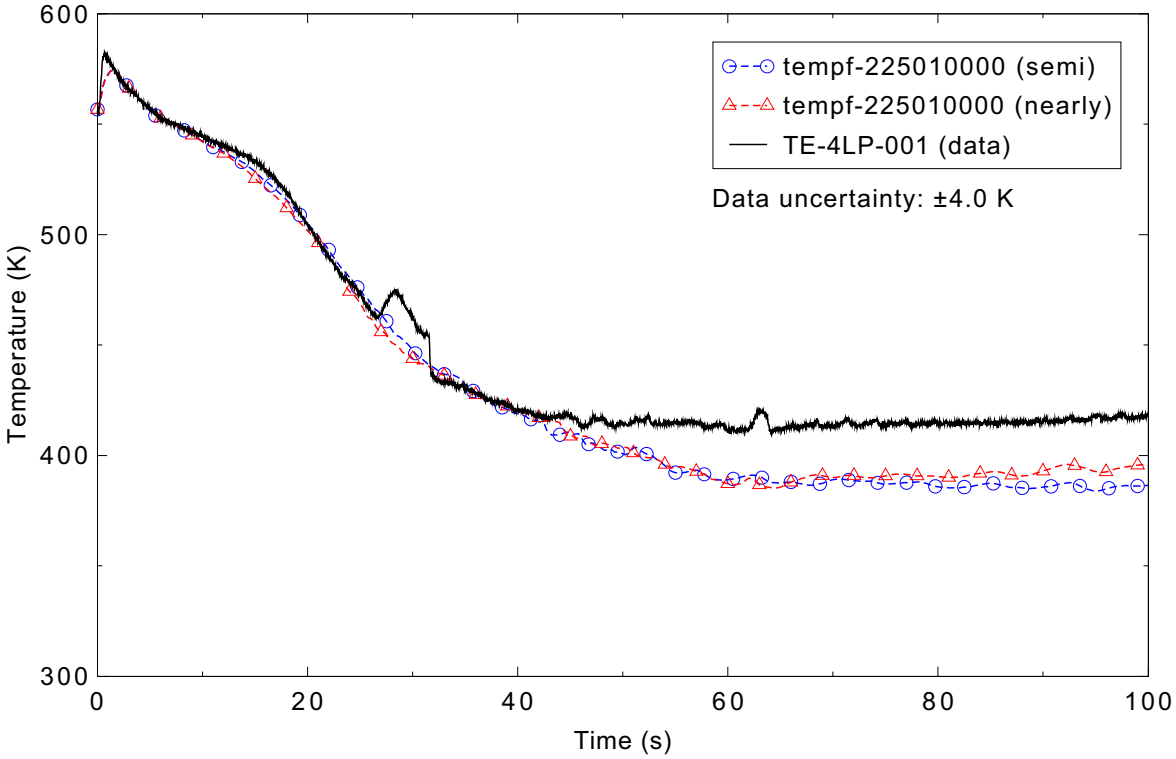

Figure 5.5-19. Measured and calculated reactor vessel lower plenum coolant temperature for the LOFT Experiment L2-5 1-D case.

The two major inflection points, for the initial core heatup near 10 s and for the final quench near 65 s, were predicted to occur at about the same times as were measured. The trend between these two times was not particularly well simulated, with the calculation steadily decreasing while the data remained fairly constant. The prediction of the fuel centerline temperature is judged to be reasonable.

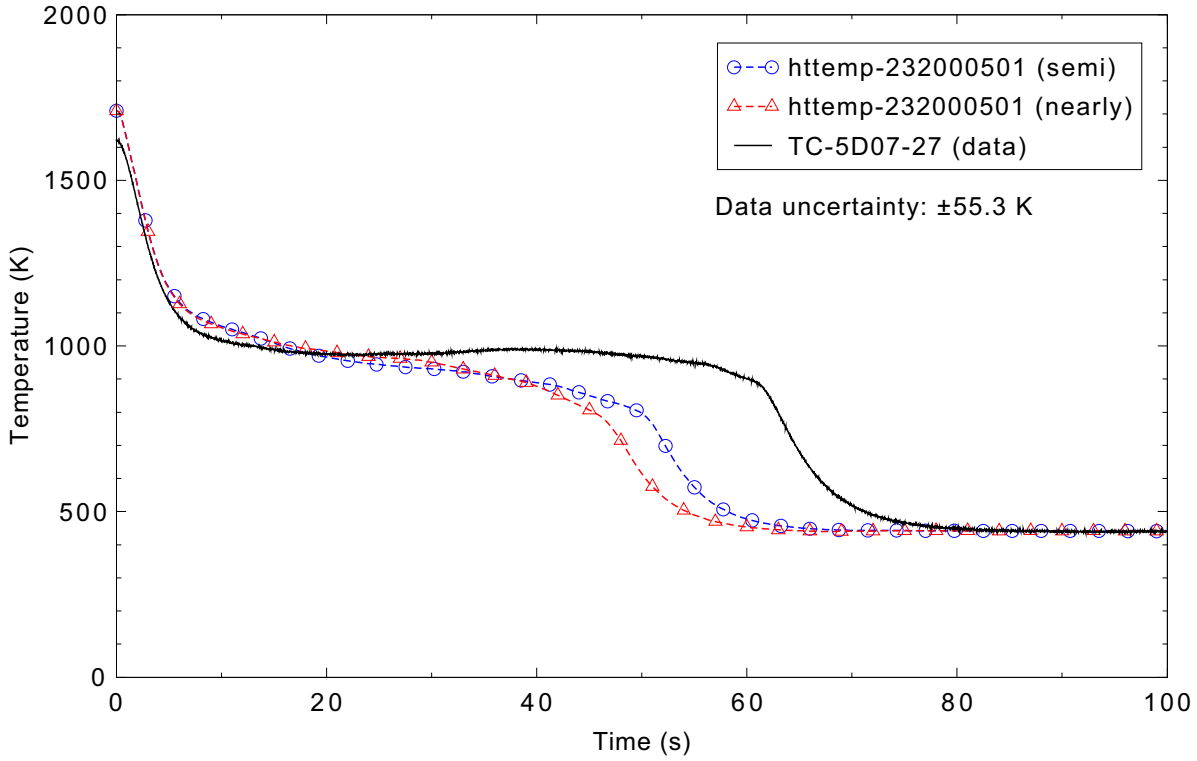

Figure 5.5-20. Measured and calculated fuel centerline temperature 0.69 m above the bottom of the fuel rod for the LOFT Experiment L2-5 1-D case.

Fuel cladding surface temperatures for each of the 12 axial levels in the RELAP5-3D model hot assembly are compared to the data in Figures 5.5-21 through 5.5-32. The timing of the initial cladding heatup was well predicted for the bottom seven levels in the RELAP5-3D model, although the peak temperatures were under predicted. No heatup was predicted for the top five axial levels, whereas heatups were measured. The second heatup in the upper portion of the core, starting around 20 s in the experiment, was generally not predicted, as the calculations showed only a few short temperature excursions. With only an average coolant channel modeled, it is not surprising that the cladding temperatures were somewhat under predicted. There was a partial top-down core rewet in the experiment that was not predicted by the code; Figures 5.5-25 and 5.5-26 illustrate that the rewet did not affect all of the fuel rods. The calculated peak cladding temperature of 985 K occurred at 6.3 s in axial level 4, the center of which is 0.49 m above the bottom of the fuel rod. The measured peak cladding temperature of 1,078 K occurred at 28.5 s in rod 5H06 0.61 m above the bottom of the fuel rod. The lower calculated peak temperature is expected, as the RELAP5-3D input model did not include a separate heat structure for the hot fuel pin. The data indicate that the final core quenching occurred from both the bottom and top of the core, with node 5 quenching last. This behavior is reflected in the calculation as well, with node 6 quenching last. The timing of the quench was predicted well in axial nodes 6 and 7, but was early in the other nodes. The overall prediction of the cladding surface temperatures is judged to be reasonable. The general heatup and quench behavior was predicted, including the final quench from both the bottom and top of the core. While the initial heatup

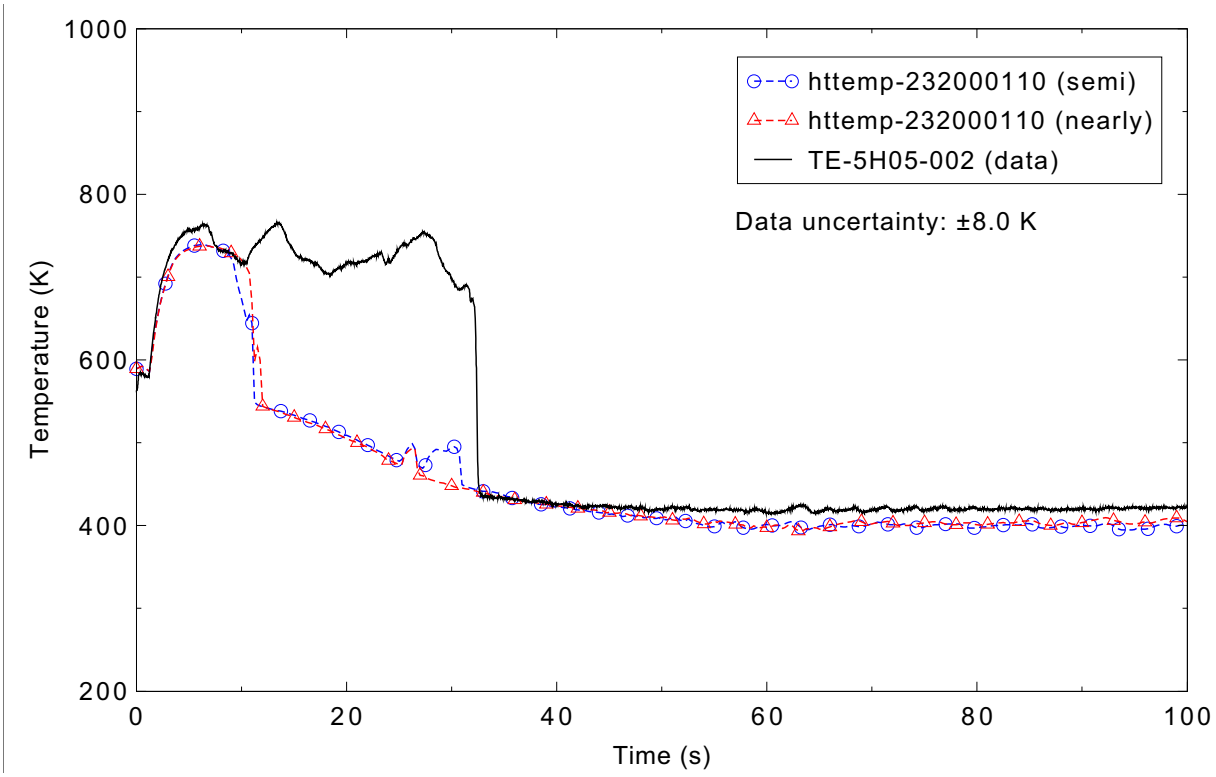

Figure 5.5-21. Measured and calculated fuel cladding surface temperature 0.05 m above the bottom of the fuel rod for the LOFT Experiment L2-5 1-D case.

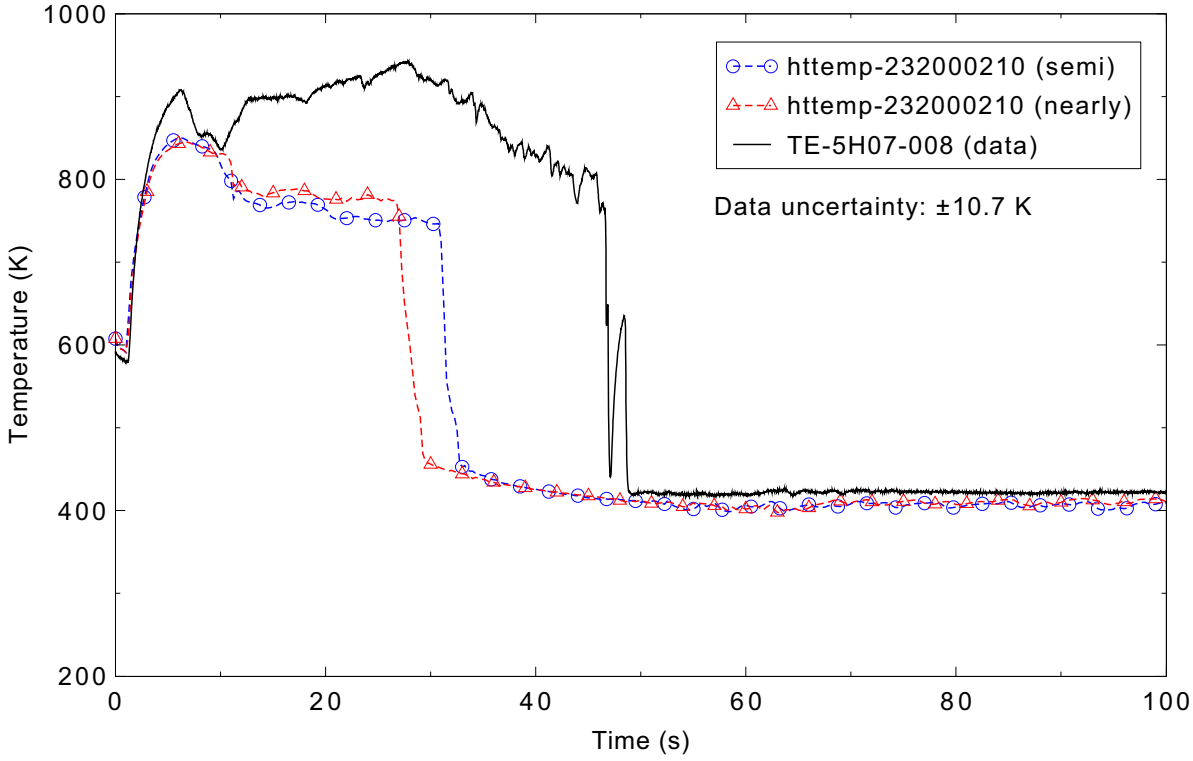

Figure 5.5-22. Measured and calculated fuel cladding surface temperature 0.20 m above the bottom of the fuel rod for the LOFT Experiment L2-5 1-D case.

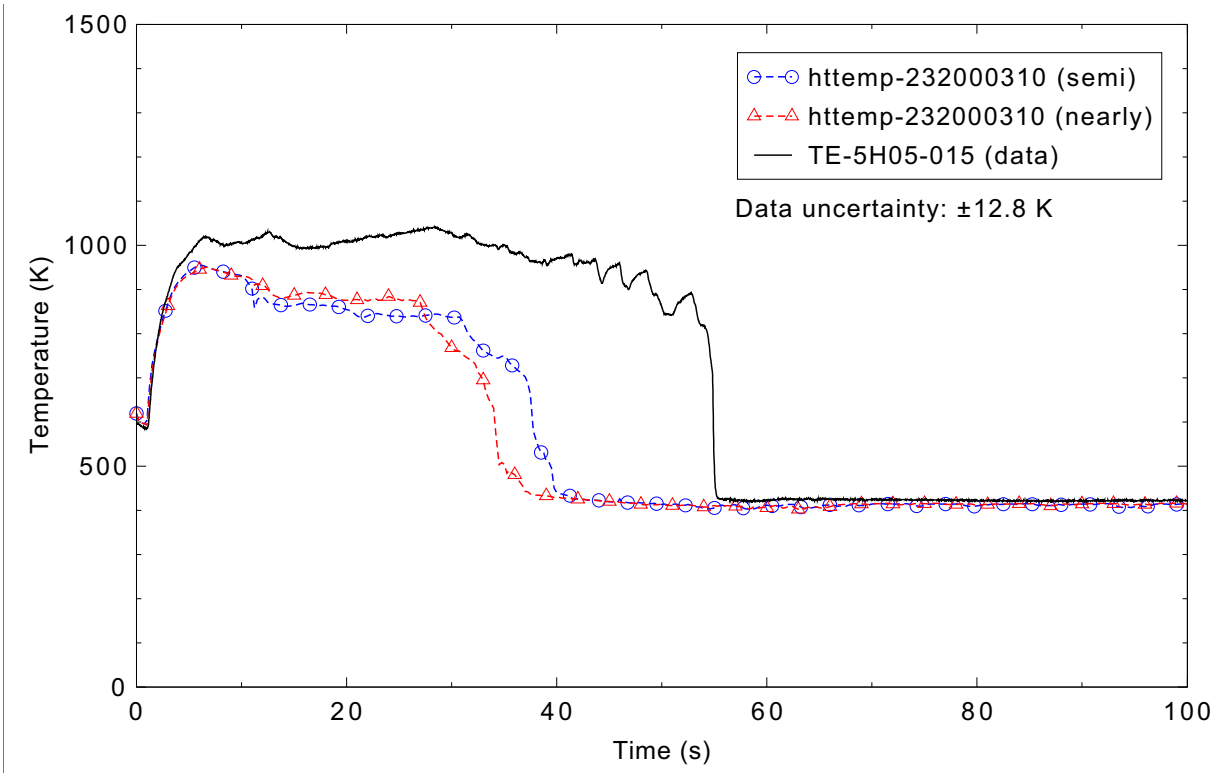

Figure 5.5-23. Measured and calculated fuel cladding surface temperature 0.38 m above the bottom of the fuel rod for the LOFT Experiment L2-5 1-D case.

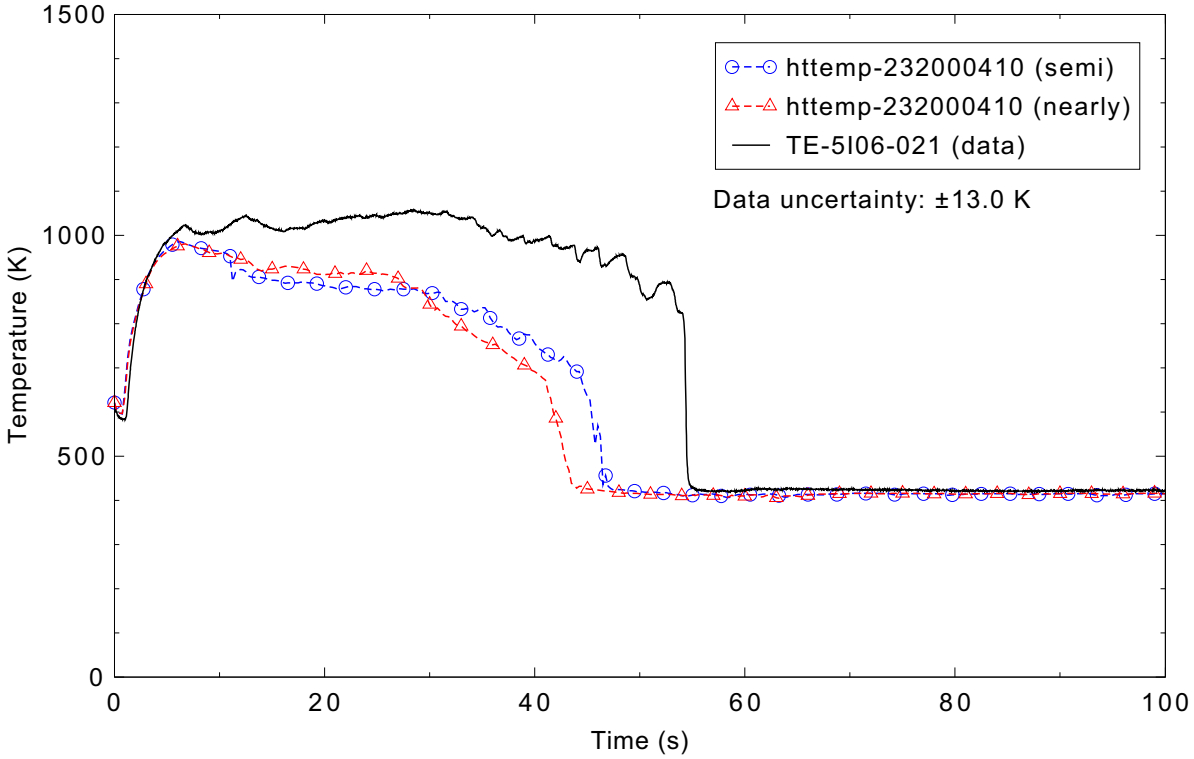

Figure 5.5-24. Measured and calculated fuel cladding surface temperature 0.53 m above the bottom of the fuel rod for the LOFT Experiment L2-5 1-D case.

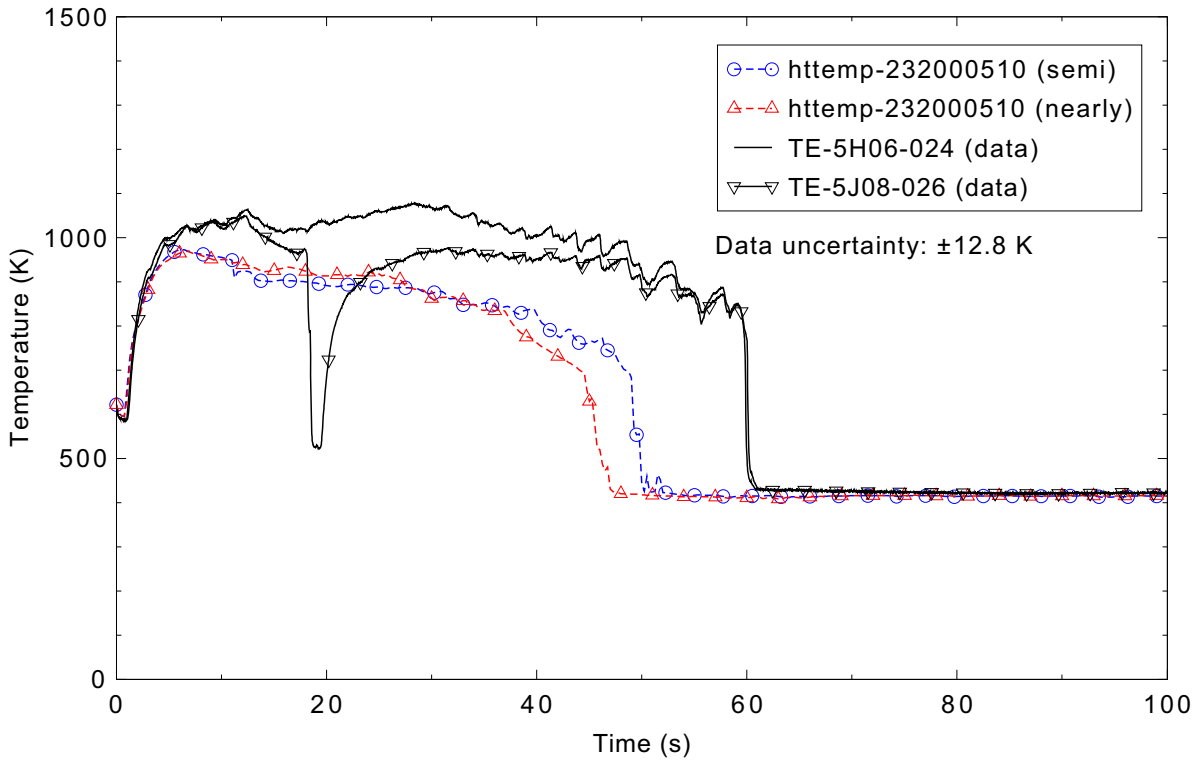

Figure 5.5-25. Measured and calculated fuel cladding surface temperature 0.64 m above the bottom of the fuel rod for the LOFT Experiment L2-5 1-D case.

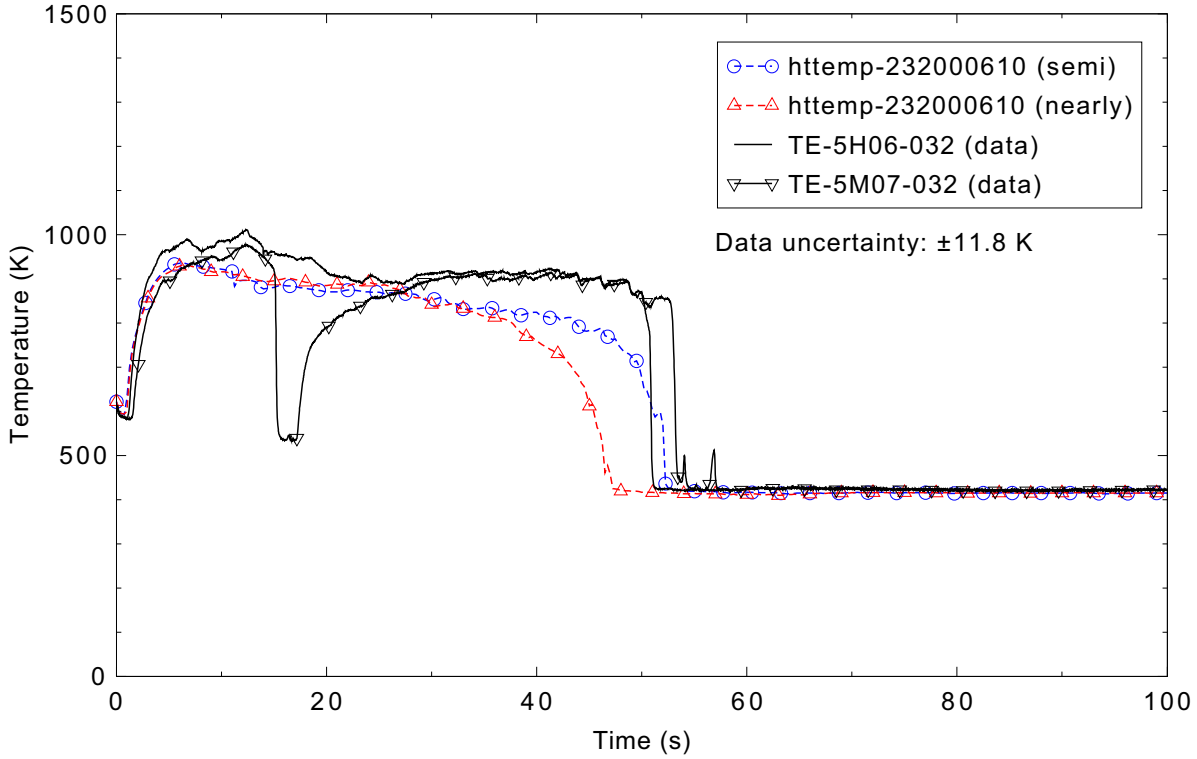

Figure 5.5-26. Measured and calculated fuel cladding surface temperature 0.81 m above the bottom of the fuel rod for the LOFT Experiment L2-5 1-D case.

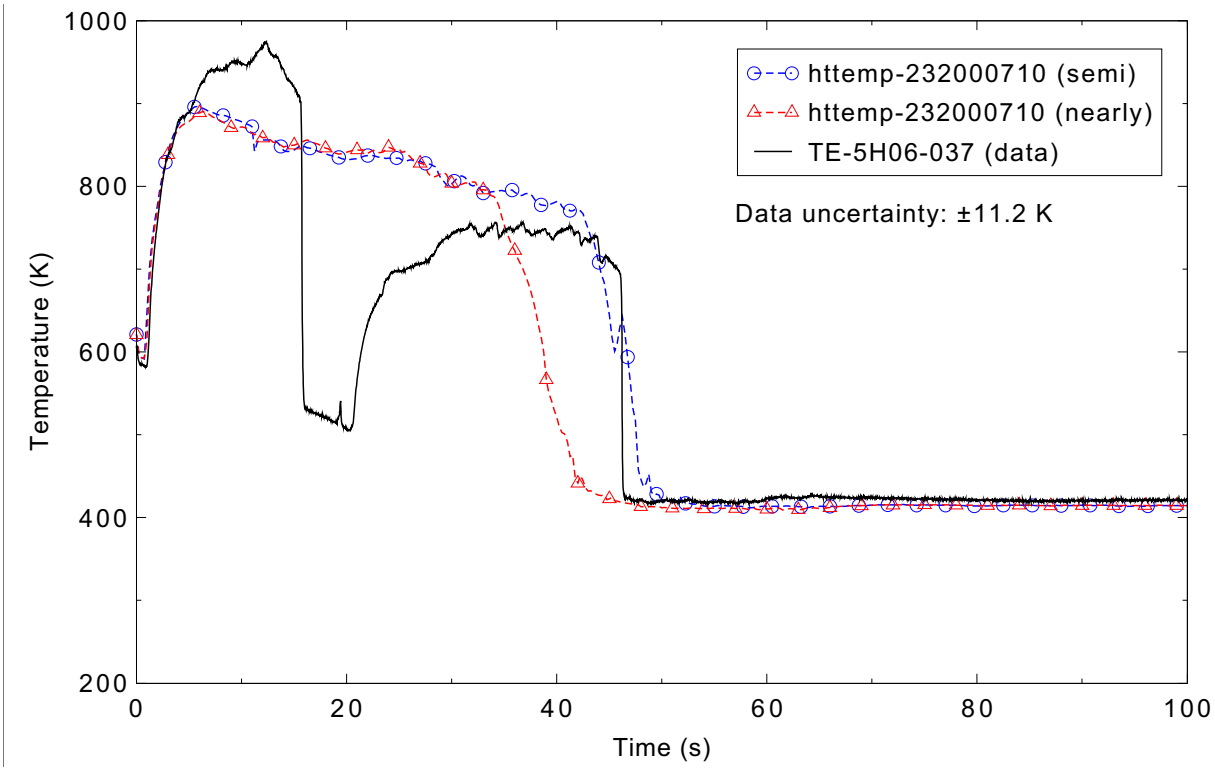

Figure 5.5-27. Measured and calculated fuel cladding surface temperature 0.94 m above the bottom of the fuel rod for the LOFT Experiment L2-5 1-D case.

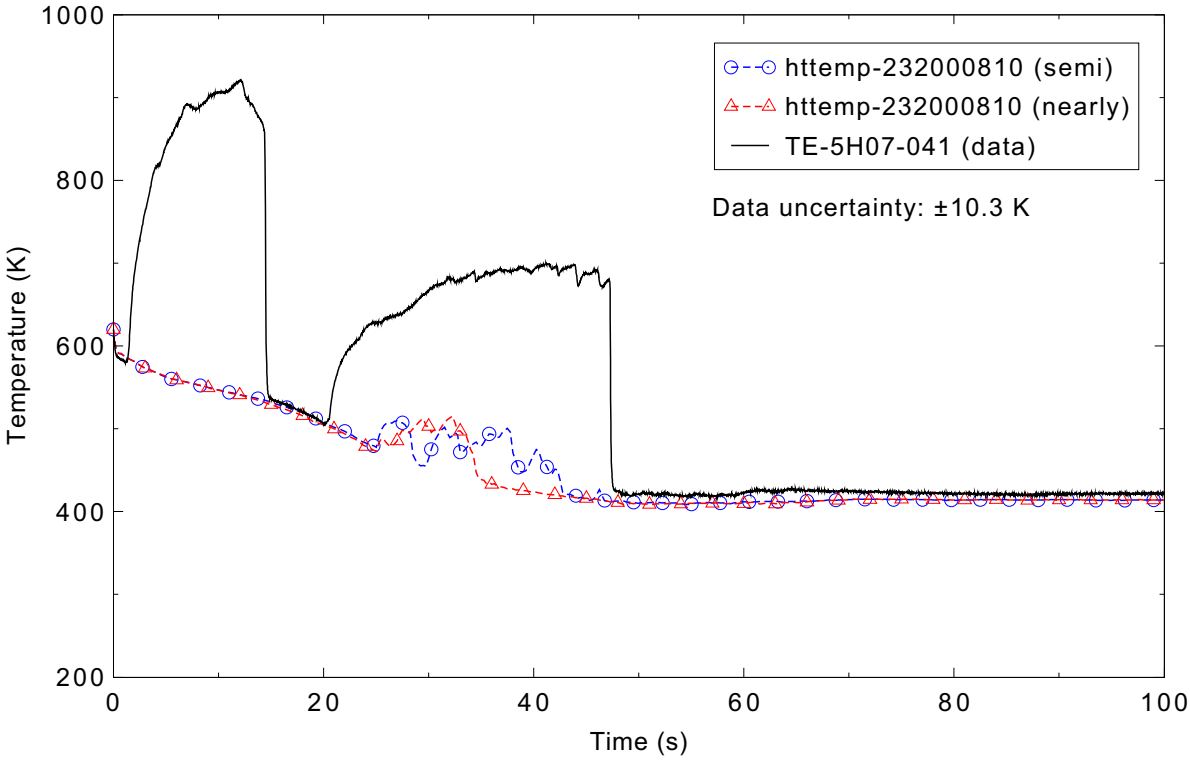

Figure 5.5-28. Measured and calculated fuel cladding surface temperature 1.04 m above the bottom of the fuel rod for the LOFT Experiment L2-5 1-D case.

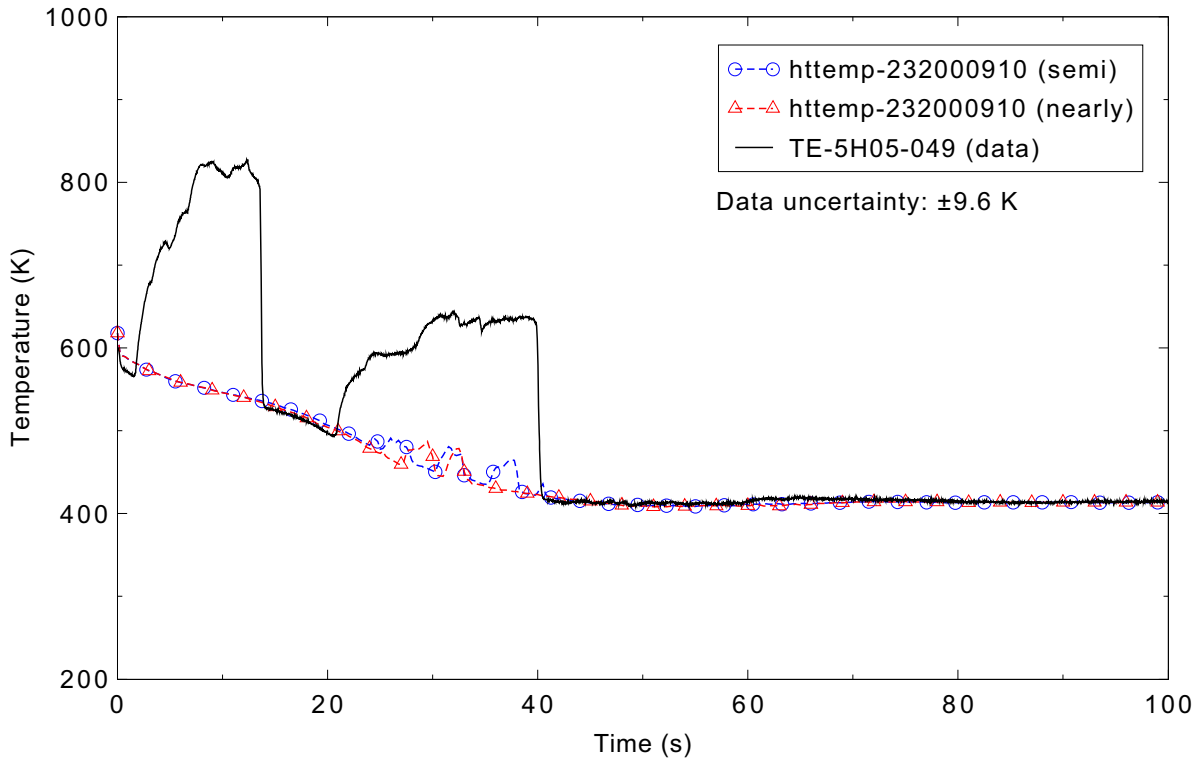

Figure 5.5-29. Measured and calculated fuel cladding surface temperature 1.25 m above the bottom of the fuel rod for the LOFT Experiment L2-5 1-D case.

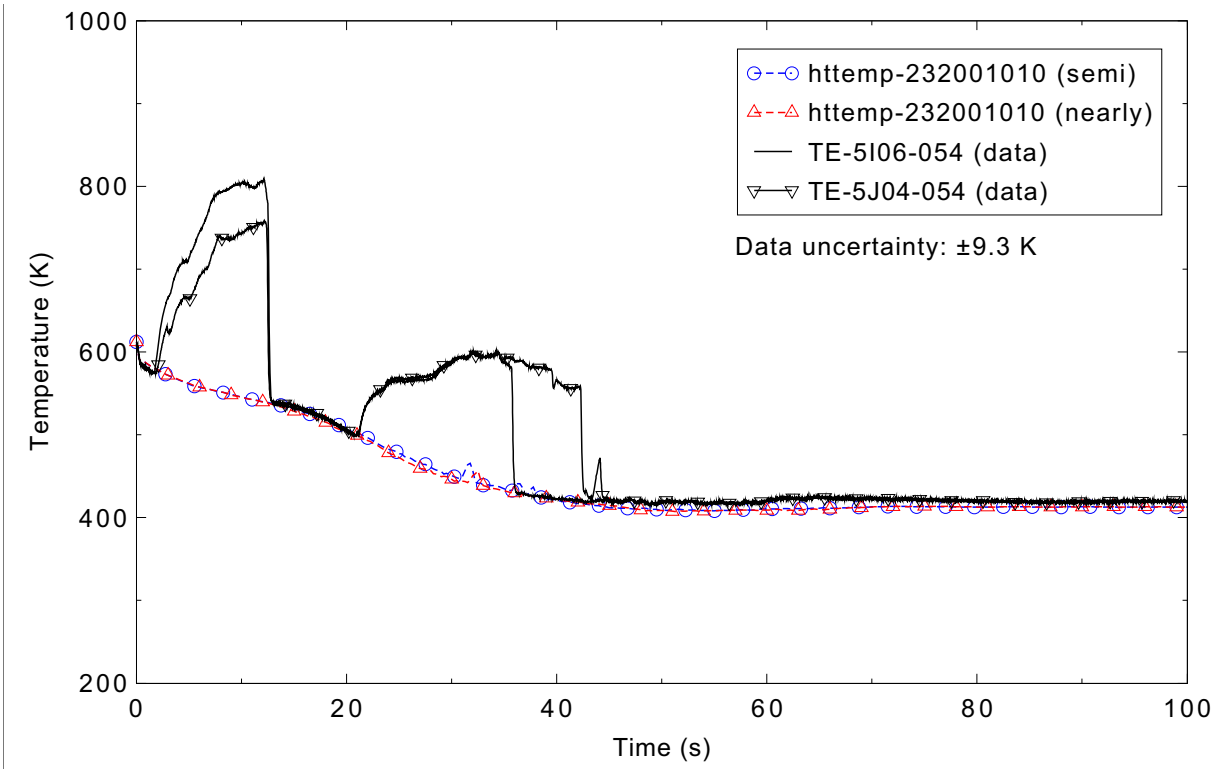

Figure 5.5-30. Measured and calculated fuel cladding surface temperature 1.37 m above the bottom of the fuel rod for the LOFT Experiment L2-5 1-D case.

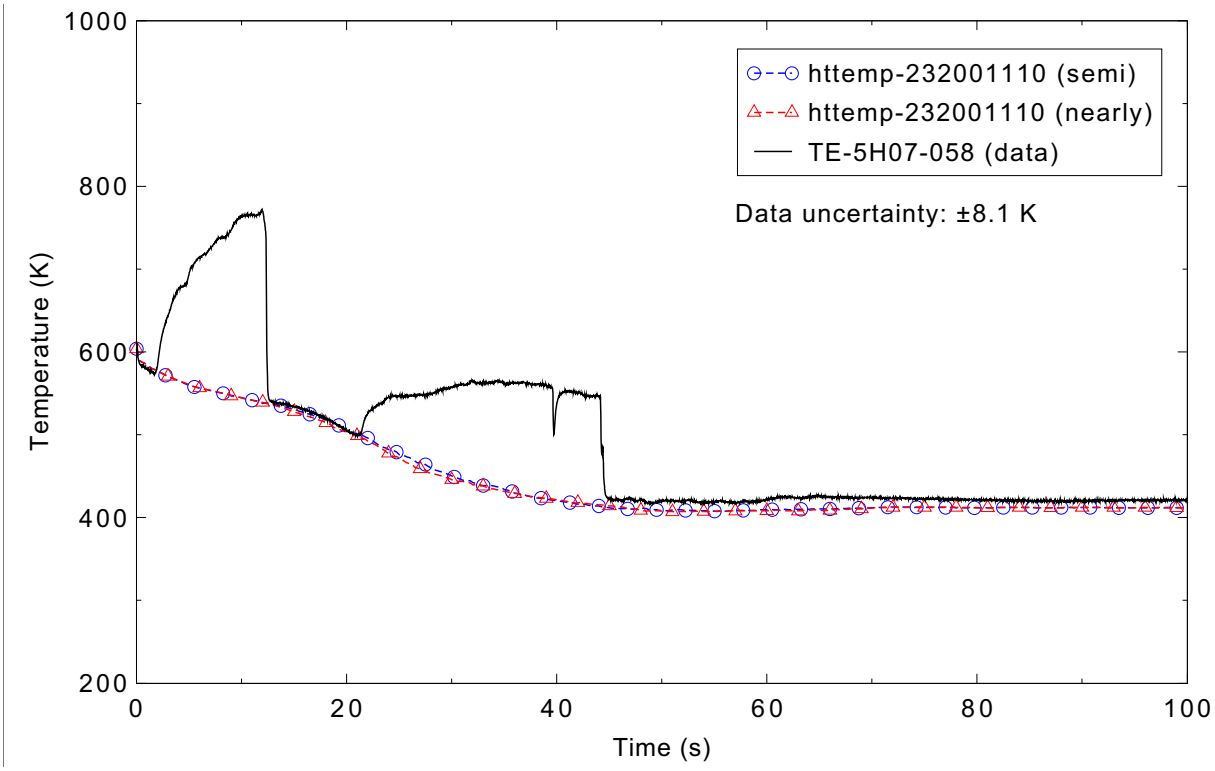

Figure 5.5-31. Measured and calculated fuel cladding surface temperature 1.47 m above the bottom of the fuel rod for the LOFT Experiment L2-5 1-D case.

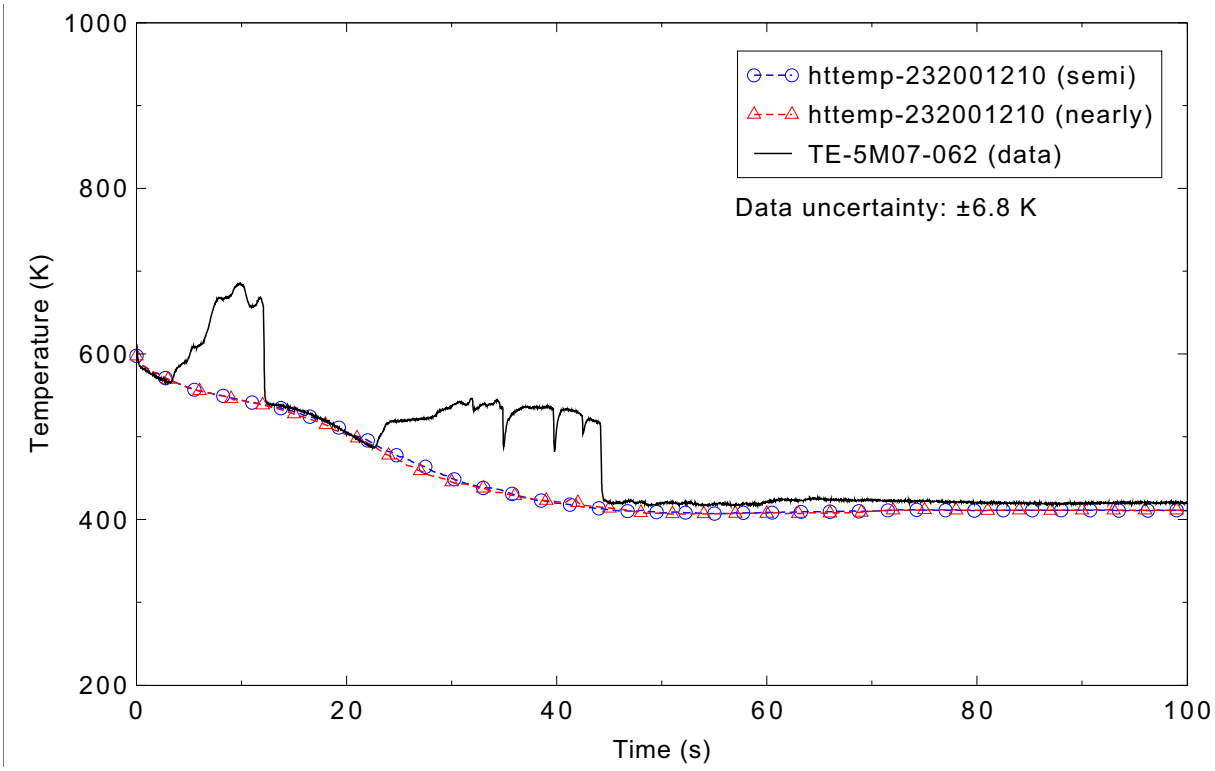

Figure 5.5-32. Measured and calculated fuel cladding surface temperature 1.57 m above the bottom of the fuel rod for the LOFT Experiment L2-5 1-D case.

of the top portion of the center fuel assembly was not predicted, it may have been influenced by the single channel core nodalization. The partial top-down rewet was not a core-wide event, and therefore may not be seen in a one-dimensional core model.

5.5.5 Conclusions and Assessment Findings

Most of the significant parameters calculated by the code were in good agreement with the measured data. Three notable exceptions were the fluid densities in the intact loop hot and cold legs and the broken loop hot leg. All of the assessment judgments applied to both the semi- and nearly-implicit calculations except for the prediction of the intact loop cold leg density, which was judged to be reasonably simulated in the nearly-implicit calculation but only minimally simulated in the semi-implicit calculation.

The pressures in both the primary and secondary coolant systems were found to be reasonably predicted. The ECC behavior was well simulated, with the calculated accumulator level in excellent agreement with the data and the LPIS flow in reasonable agreement; no judgment on the HPIS flow was made since it was essentially a constant flow boundary condition. It can be inferred that the break flows were reasonably simulated, as the flow rates and fluid densities in the broken loop hot and cold legs were well predicted (excellent agreement in the broken loop hot leg flow, reasonable agreement for the three other measurements until after the core quenched). In the intact loop, the flow rates were reasonably simulated, but the calculated densities were in minimal agreement with the data, generally retaining more water in the loops than was measured; also, the pump speed was in minimal agreement for most of the transient, although it was in good agreement during the initial coastdown. Fluid temperatures in the reactor vessel upper and lower plena were predicted reasonably, although the presence of accumulator nitrogen reduced the calculated saturation temperature.

Both the fuel centerline and cladding surface temperatures were judged to be reasonably predicted. In the experiment, there was a partial top-down rewet of some of the fuel rods; this was not predicted by the code. The final quench of the core was both bottom-up and top-down in the experiment and in the calculation. The data showed some early heatup in the center fuel assembly over the entire length of the core, but in the code calculation the top third of the core did not show any early cladding temperature excursions. The peak cladding temperature was predicted to be 93 K below the measured value, which is not unexpected as this is a comparison between a hot fuel rod and an assembly-average rod; the peak temperature also occurred earlier in the calculation than was measured (6 vs. 28 s).

5.5.6 References

5.5-1. D. L. Reeder, *LOFT System and Test Description (5.5 ft Nuclear Core 1 LOCEs)*, NUREG/CR-0247, TREE-1208, July 1978.

5.5-2. P. D. Bayless and J. M. Divine, *Experiment Data Report for LOFT Large Break Loss-of-Coolant Experiment L2-5*, NUREG/CR-2826, EGG-2210, August 1982.

5.6 LOFT Experiment L2-5 (3-D)

Experiments were performed in the 1970s and 1980s in the Loss-of-Fluid Test (LOFT) facility, a 50 MWt power/volume-scaled nuclear reactor designed to investigate the response of a commercial pressurized water reactor (PWR) to loss-of-coolant accidents and operational transients. Experiment L2-5 simulated a double-ended cold leg break with a maximum core linear heat generation rate of 40.1 kW/m (12.2 kW/ft).

5.6.1 Code Models Assessed

As an integral test facility, multiple code models are addressed. The principal interest is in the core behavior: fuel rod heatup and quench, and peak cladding temperature. Other parameters of significance are the break flow rates, system pressure, and emergency core coolant (ECC) system response.

5.6.2 Experiment Facility Description

The LOFT facility is described in detail in Reference 5.6-1. The nuclear core was 1.68 m high with a 0.61 m diameter. The core contained nine fuel assemblies and 1,300 fuel rods that were representative of a commercial PWR. As shown in Figure 5.6-1, the facility contained two primary coolant loops. The intact loop represented three loops of a commercial plant, containing a hot leg, steam generator, cold leg, two primary coolant pumps, and the pressurizer. The broken loop represented a single loop, and included steam generator and primary coolant pump simulators, which modeled the flow resistance of these components. The broken loop could be configured to model either hot or cold leg breaks. Quick-opening blowdown valves (adjustable opening times of approximately 20 to 50 ms) simulated the initiation of primary coolant pipe ruptures, and orifices were used to model different break sizes. The break effluent was collected in a blowdown suppression tank.

The ECC system included a pumped high-pressure injection system (HPIS), a nitrogen-pressurized accumulator, and a pumped low-pressure injection system (LPIS). The accumulator was equipped with an adjustable height standpipe, which allowed the effective liquid volume to be varied between experiments. The ECC system was designed to allow injection to the intact loop hot leg, intact loop cold leg, reactor vessel upper plenum, lower plenum, or downcomer.

The LOFT facility was extensively instrumented. Fluid pressure, temperature, and flow rate were measured at key locations in the primary coolant, secondary coolant, and ECC systems. Three-beam gamma densitometers were used to measure fluid density at two locations in the intact and broken loops. Thermocouples measured fuel rod cladding and support tube temperatures at 196 core locations. Several fuel rod internal temperatures (fuel and plenum) were also measured. Neutron flux was measured with four fixed detectors, which were designed to measure power transients, and four traversing in-core probes, which were designed to measure steady-state axial flux distributions at four different locations in the core.

Experiment L2-5 simulated a double-ended offset shear of a cold leg pipe with an immediate primary coolant pump trip. For this experiment, the primary coolant pumps were disconnected from their flywheels, resulting in a much faster pump coastdown. ECC injection was to the intact loop cold leg. Reference 5.6-2 presents the data from this experiment.

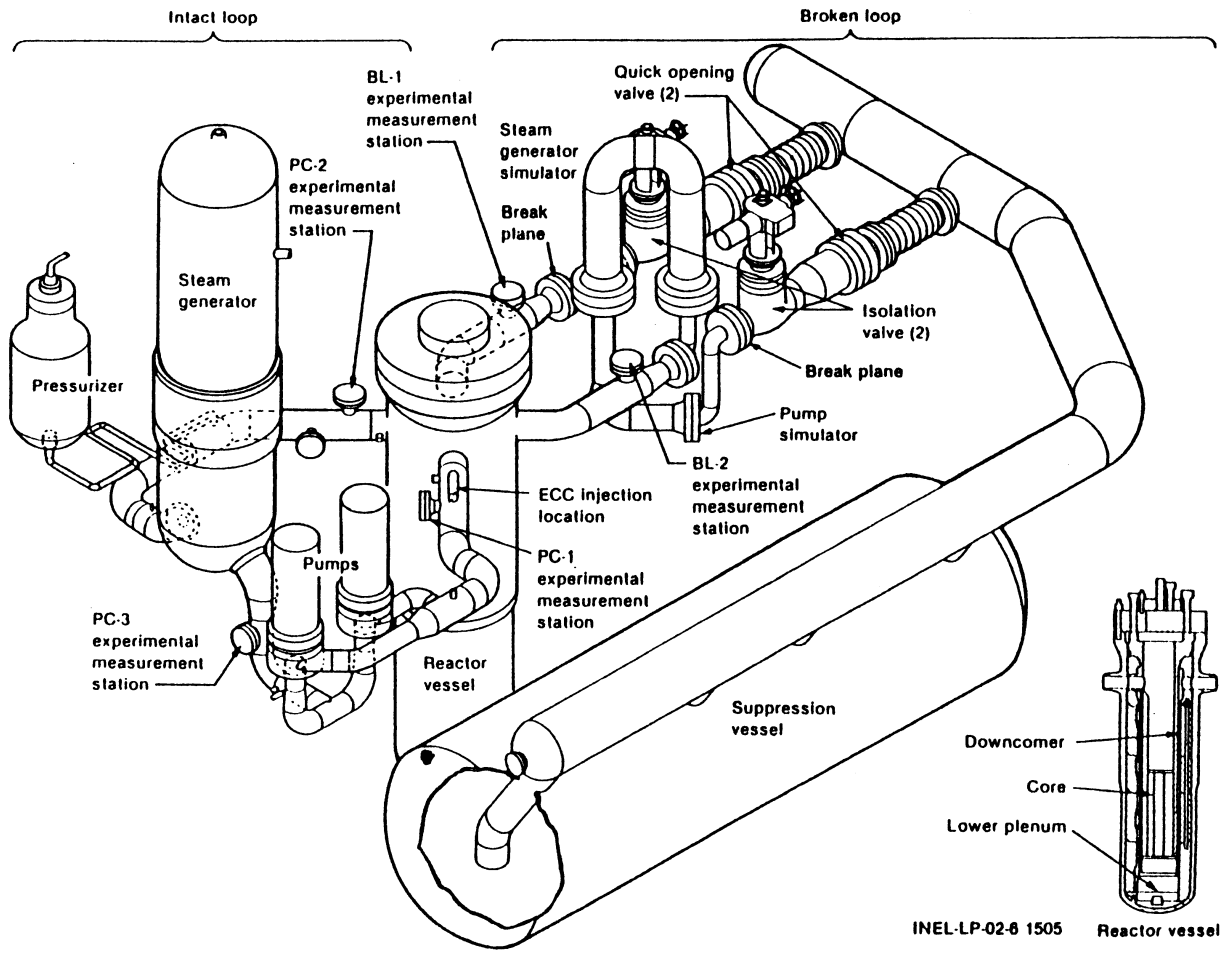

Figure 5.6-1. Schematic of the LOFT facility.

5.6.3 Input Model Description

The RELAP5-3D input model used for the 1-D L2-5 simulation is shown in Figure 5.6-2. It includes the reactor vessel, the intact and broken loops, the intact loop steam generator secondary side, the pressurizer, the ECC systems, and charging and letdown flows. For the 3-D model, most of the reactor vessel was modeled with three-dimensional components, and the remainder of the system model was unchanged. The model contains 370 control volumes, 817 junctions, and 284 heat structures.

The reactor vessel includes representations of the downcomer, lower plenum, core inlet, core, and upper plenum. Two core bypass paths were modeled: the gaps between the core filler blocks and the flow skirt, and the leakage between the cold leg and hot leg nozzles.The downcomer was modeled using a 3-D component (700) with four 90-degree azimuthal sectors, one radial ring, and six axial levels; the nodalization is shown in Figure 5.6-3. The azimuthal sectors were oriented so that each contained one of the reactor vessel nozzles: the intact loop cold leg in sector 1, the broken loop hot leg in sector 2, the broken loop cold leg in sector 3, and the intact loop hot leg in sector 4. The second 3-D component (200) modeled the lower plenum, core inlet, core, and upper plenum with four azimuthal sectors, three radial rings (corresponding to high, medium, and low power regions of the core), and 21 axial levels (12 in the

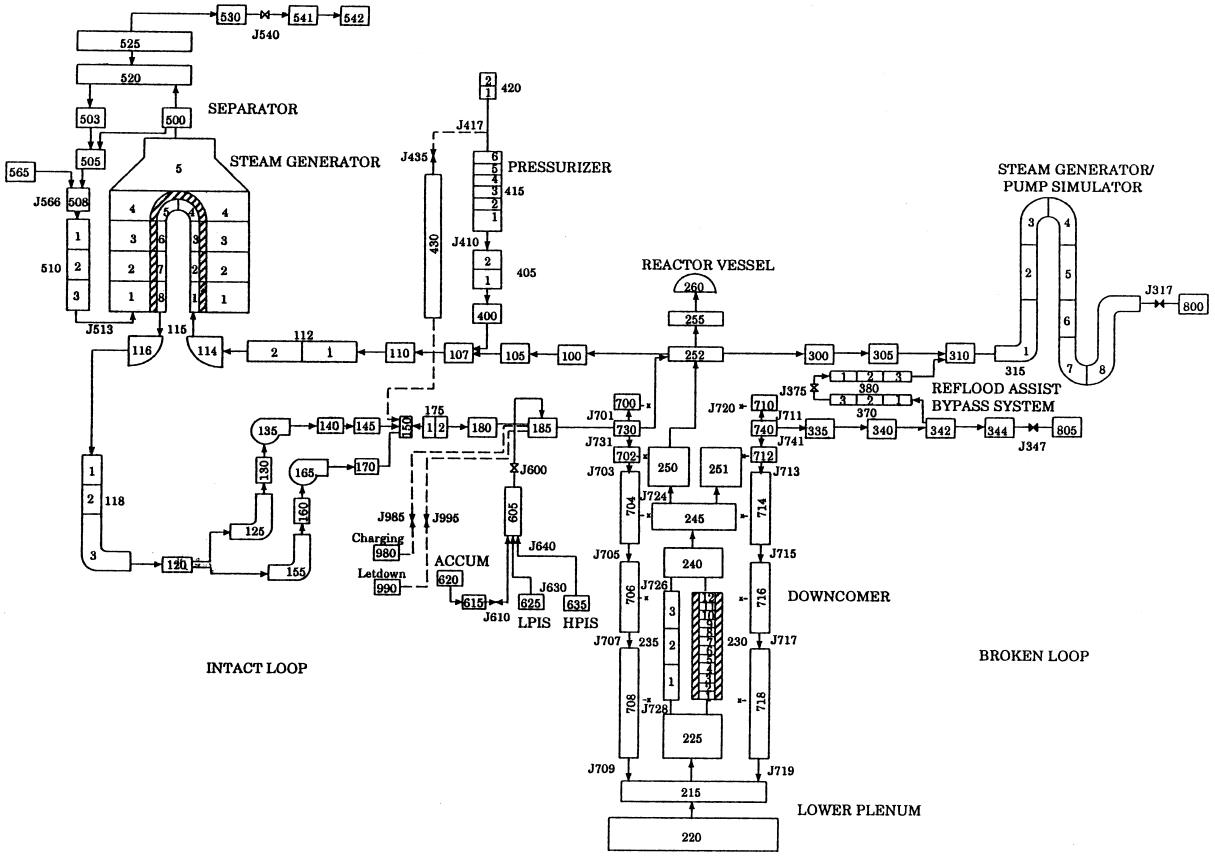

Figure 5.6-2. RELAP5-3D nodalization for the LOFT facility Experiment L2-5 (1-D vessel).

core). Figure 5.6-4 shows the nodalization for this component. A multiple junction (Component 709) connected the bottom of the downcomer to the top of the third ring in the lower plenum.

The intact loop model includes the hot leg, steam generator, two primary coolant pumps, and the cold leg. The pressurizer is connected to the intact loop hot leg, with spray flow from the cold leg. Charging and letdown flows are connected to the cold leg.

The broken loop model includes the hot and cold legs, the reflood assist bypass system piping, and the steam generator/pump simulator, which was attached to the hot leg for this cold leg break experiment. The break junctions had subcooled and two-phase discharge coefficients of 0.93 and 0.84, respectively. The time-dependent volumes downstream of the breaks were controlled to provide the back pressure measured in the blowdown suppression tank during the experiment.

The ECC systems modeled were the HPIS, accumulator, and LPIS. These were all connected to the intact loop cold leg for this experiment.

The fuel rods were modeled with 12 heat structure geometries, each representing the fuel rods in a given ring and sector. The fuel rod structures had 12 axial nodes, corresponding to the core hydraulic nodalization. The radial peaking factors were 1.31 for the inner ring, 1.13 for the middle ring, and 0.81 for

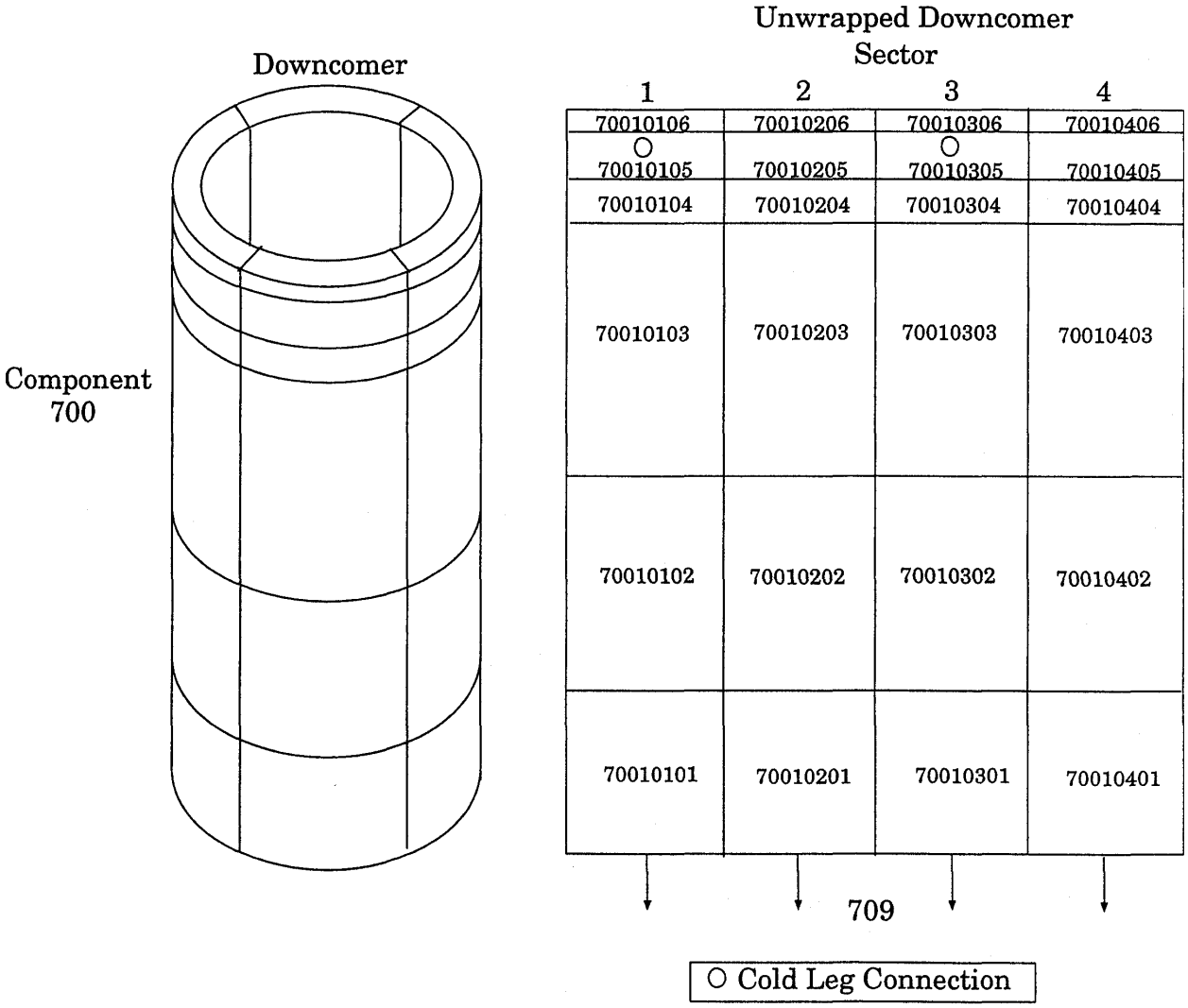

Figure 5.6-3. RELAP-3D nodalization for the LOFT reactor vessel downcomer (3-D vessel).

the outer ring. The reflood model was used for the fuel rod heat structures, starting at 25 s, when the pressure had dropped low enough to make the model applicable. Other heat structures in the model represented the steam generator tubes, filler blocks in the core and downcomer, the core support barrel, and the reactor vessel lower head. An environmental heat loss of 174 kW from the primary coolant system was also modeled on the reactor vessel lower head heat structure.

5.6.4 Data Comparisons and Results

A steady state calculation was performed to establish the desired initial conditions in the RELAP5-3D model. Table 5.6-1 provides a comparison of the measured and calculated initial and boundary conditions for Experiment L2-5; the core power, feedwater temperature, and accumulator conditions were the only fixed values. Most of the calculated values were in good agreement with the measurements. The broken loop hot leg temperature was about 5 K lower than the data, but this is not expected to have a noticeable effect on the simulation. The peak fuel centerline temperature was 87 K higher in the calculation, but this

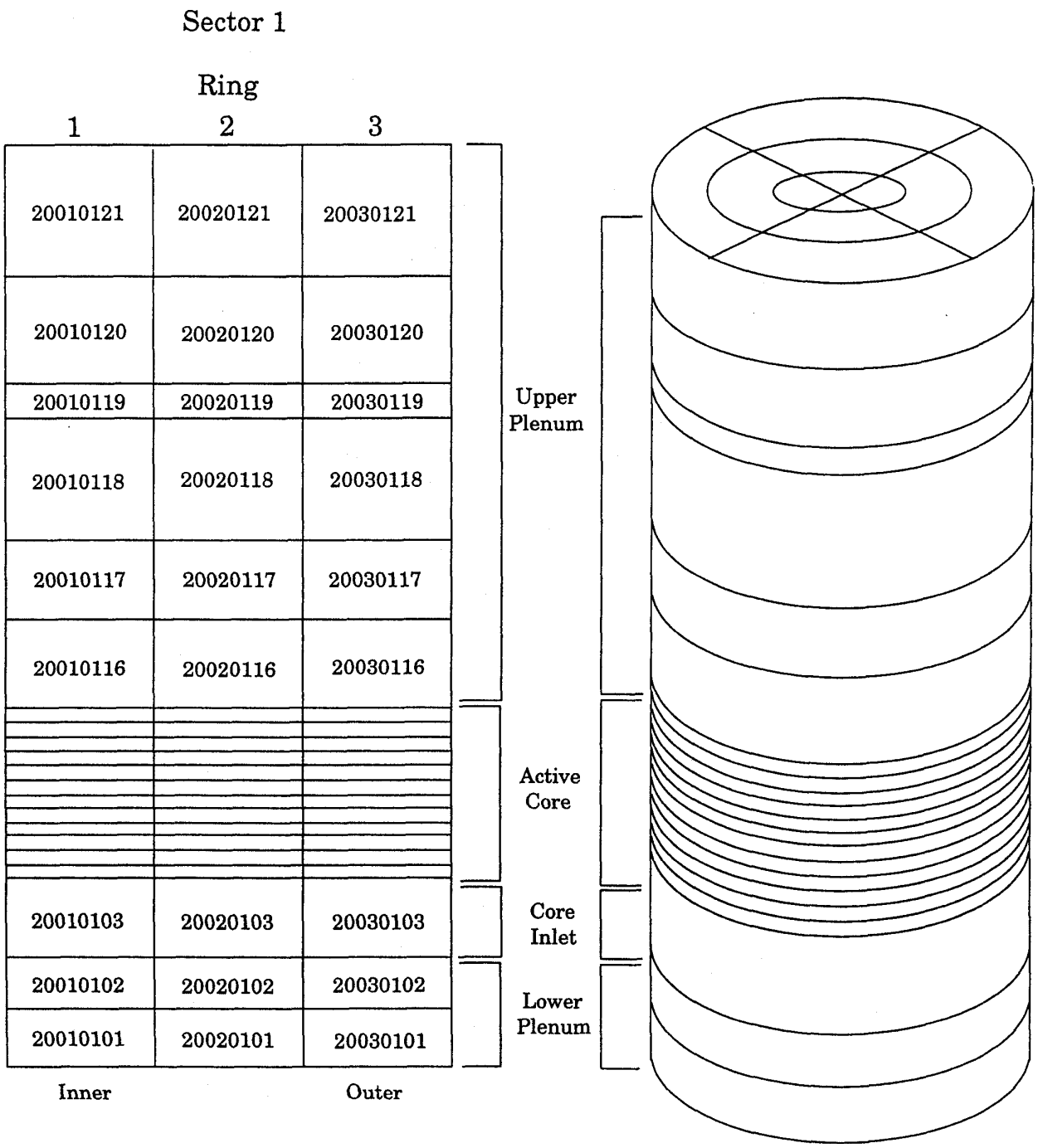

Figure 5.6-4. RELAP5-3D nodalization for the LOFT reactor vessel core region (3-D vessel).

is misleading because there were only a few centerline temperatures measured, and they may not have been located where the peak temperature occurred; no significant impact is expected.

Table 5.6-2 provides the sequence of events for Experiment L2-5. The experiment was initiated by opening the quick-opening blowdown valves in the broken loop hot and cold legs. Within the first second, the reactor scrammed on low hot leg pressure, the primary coolant pumps were tripped, and the fuel began to heat up. The primary coolant pump trip in the experiment resulted in the power being supplied to the

Table 5.6-1. LOFT Experiment L2-5 initial conditions.

Parameter	Measured Value	Calculated Value
Intact Loop		
Mass flow (kg/s)	192.4 ± 7.8	192.4
Hot leg pressure (MPa)	14.94 ± 0.06	14.92
Cold leg temperature (K)	556.6 ± 4.0	556.7
Hot leg temperature (K)	589.7 ± 1.6	590.5
Pressurizer		
Liquid level (m)	1.14 ± 0.03	1.14
Broken Loop		
Cold leg temperature (K)	554.3 ± 4.2	556.7
Hot leg temperature (K)	561.9 ± 4.3	556.7
Reactor Vessel		
Core power (MW)	36.0 ± 1.2	36.0
Maximum fuel centerline temperature (K)	1,660 ± 57	1,747
Steam Generator		
Pressure (MPa)	5.85 ± 0.06	5.86
Feedwater flow rate (kg/s)	19.1 ± 0.4	19.1
Feedwater temperature (K)	482.0 ± 1.2	482.0
Accumulator		
Pressure (MPa)	4.29 ± 0.06	4.29
Liquid temperature (K)	303.2 ± 6.1	303.2
Liquid level above standpipe (m)	1.17 ± 0.01	1.16

pumps being reduced to zero after about 1.3 s; this was simulated in the RELAP5-3D calculation by tripping the pumps at 1.6 s, near the midpoint of the power decrease. A partial rewet of the fuel occurred between 12.1 and 22.7 s in the experiment. The pressurizer emptied at 15.4 s, and accumulator injection began at 16.8 s. HPIS and LPIS injection began at 23.9 and 37.3 s, respectively, with their start being delayed to simulate the time required to load the diesel generators in a commercial power plant. The accumulator emptied near 50 s. The peak cladding temperature occurred at 28.47 s, and all of the cladding was quenched by 65 s. The experiment was effectively terminated at 107.1 s by stopping the LPIS injection; the calculation was terminated at 100 s.

Figures comparing the measured and calculated response of the LOFT system during the experiment are provided below. Data uncertainties provided on the figures are for the maximum measured value

Table 5.6-2. LOFT Experiment L2-5 sequence of events.

Event	Time after Experiment Initiation (s)
Experiment initiated	0.0
Subcooled blowdown ended	0.043 ± 0.01
Reactor scrammed	0.24 ± 0.01
Cladding temperatures initially deviated from saturation	0.91 ± 0.2
Primary coolant pumps tripped	0.94 ± 0.01
Subcooled break flow ended (cold leg)	3.4 ± 0.5
Partial rewet initiated	12.1 ± 1.0
Pressurizer emptied	15.4 ± 1.0
Accumulator A injection initiated	16.8 ± 0.1
Partial rewet ended	22.7 ± 1.0
HPIS injection initiated	23.90 ± 0.02
Maximum cladding temperature attained	28.47 ± 0.02
LPIS injection initiated	37.32 ± 0.02
Accumulator emptied	49.6 ± 0.1
Core cladding quenched	65 ± 2
LPIS injection terminated	107.1 ± 0.4

during the experiment. Both the semi- and nearly-implicit calculations had requested time steps of 0.01 s. Data are from the NRC Data Bank. Problems with the multi-dimensional component allowed the nearly-implicit calculation to run for less than 3 s; results up to the time of failure are included in the figures. The specific errors in the code causing the problem have not been identified.

Figure 5.6-5 presents the pressure in the reactor vessel upper plenum. The rapid depressurization in the first 4 s, during which both subcooled blowdown and subcooled break flow ended, was calculated very well. The pressure was then under predicted slightly until about 20 s, then slightly over predicted until 36 s. The differences in the inflection points in the curves were caused by differences in the break flow. Overall, the calculation was judged to be in reasonable agreement with the data.

The steam generator pressure is shown in Figure 5.6-6. The calculation was in excellent agreement with the data until 60 s. After that, the measured pressure continued to decrease, while the calculated pressure remained nearly constant. The constant pressure is indicative of an isolated system, while the decreasing pressure is evidence that energy is still being removed from the secondary side. This may be caused by continuing heat transfer to the primary coolant, which ended near 60 s in the calculation. The calculation is judged to be in reasonable agreement with the data, based on the performance during the critical portion of the transient.

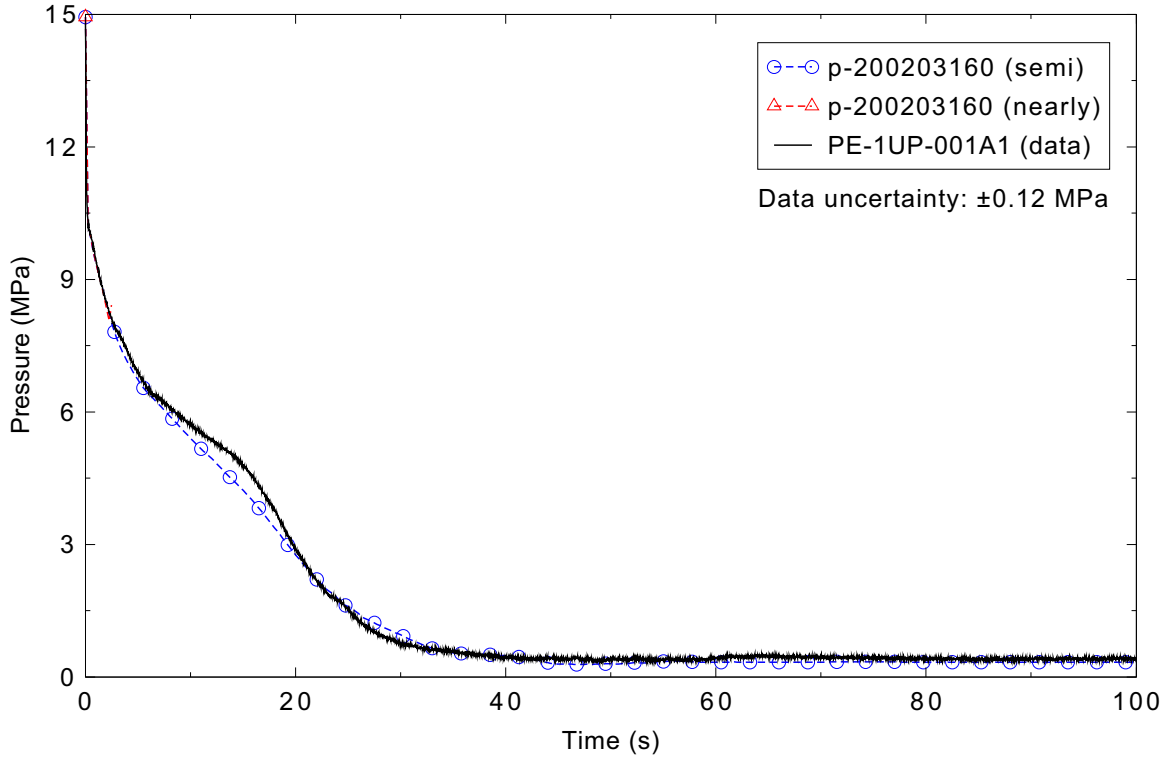

Figure 5.6-5. Measured and calculated reactor vessel upper plenum pressure for the LOFT Experiment L2-5 3-D case.

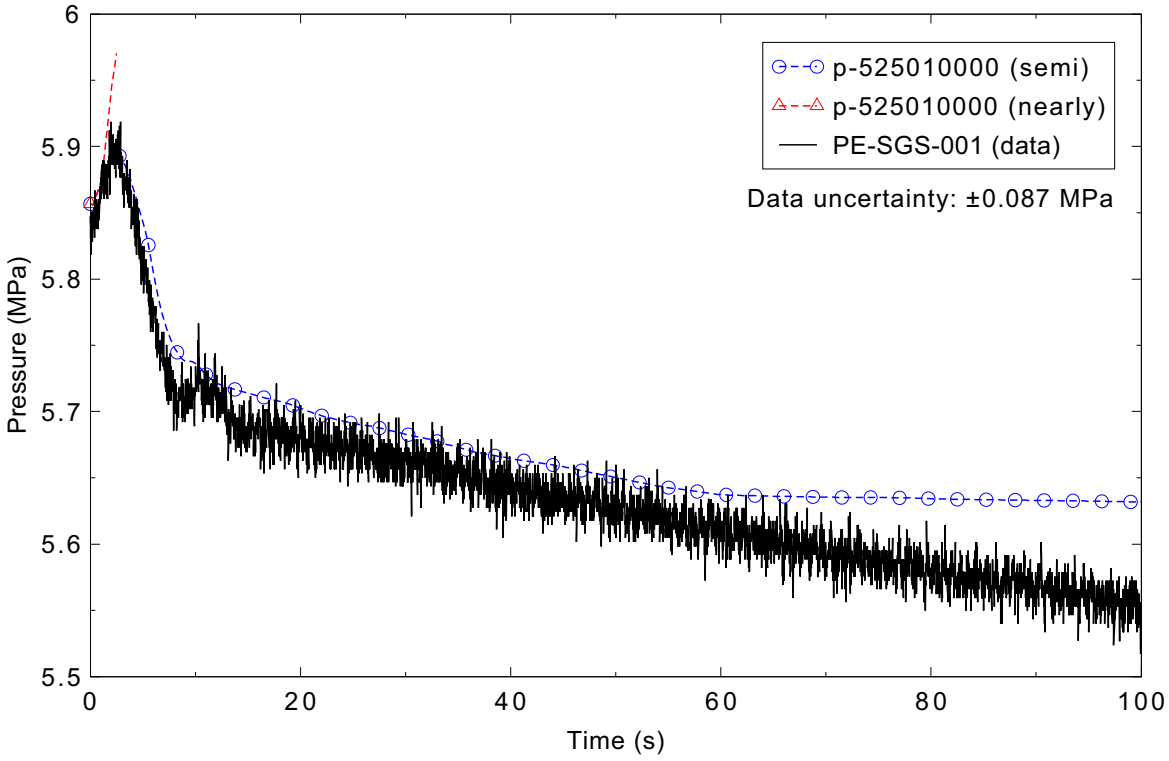

Figure 5.6-6. Measured and calculated steam generator pressure for the LOFT Experiment L2-5 3-D case.

Figure 5.6-7 presents the pressurizer liquid level. The pressurizer emptied later in the calculation than in the experiment. In both the experiment and calculation, choked flow occurred in the surge line, keeping the pressurizer pressure well above the hot leg pressure until after the pressurizer emptied. Better agreement between the calculation and data could be achieved by reducing the flow loss coefficients in the surge line. With no changes to the input model, the prediction is judged to be reasonable, as the data trend is correct, appropriate phenomena are being modeled, and the calculation lies within the measurement uncertainty for most of the time.

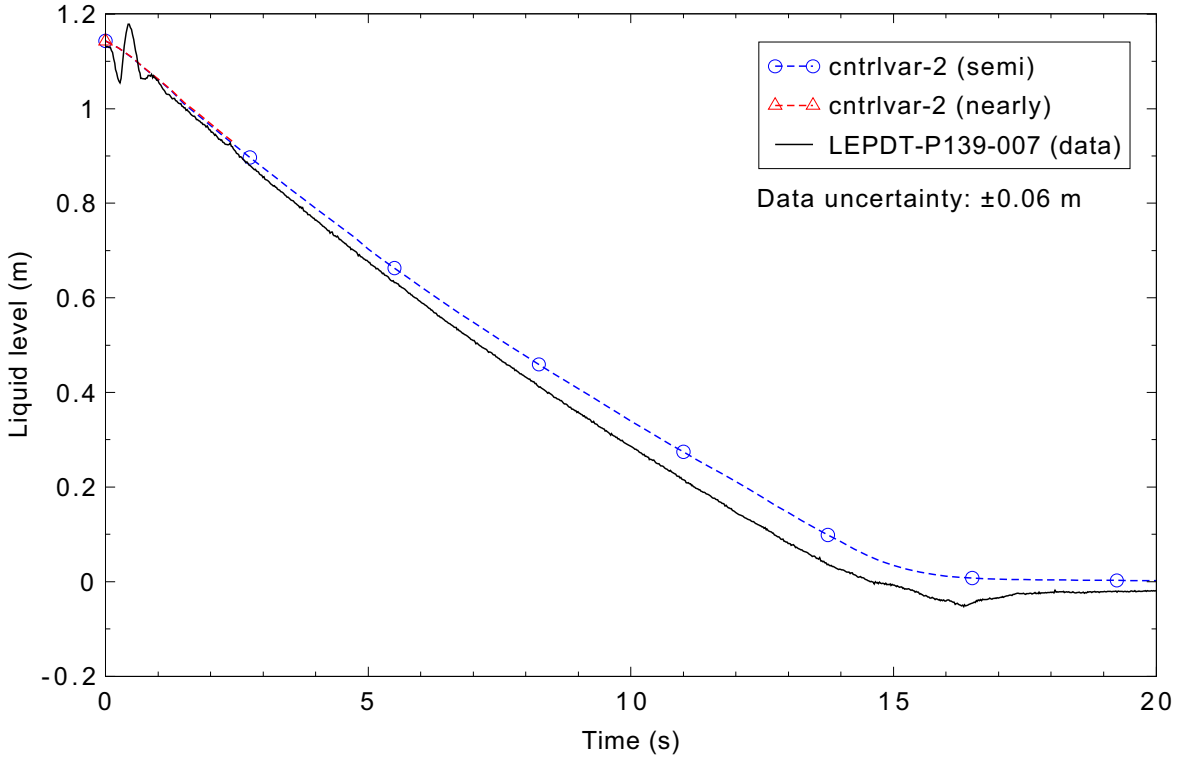

Figure 5.6-7. Measured and calculated pressurizer liquid level for the LOFT Experiment L2-5 3-D case.

Figure 5.6-8 shows the mass flow rate in the broken loop cold leg. Most of the calculation is in excellent agreement with the measured data. The peak flow rate and the transition from subcooled to two-phase critical flow are calculated well. The flow rate is over predicted between about 15 and 25 s, as the code leg fluid density is higher in the calculation than in the experiment. Overall, the prediction is judged to be reasonable.

Flow rates in the broken loop hot leg are shown in Figure 5.6-9. Other than a brief under prediction near 10 s, the calculated flow is very close to the measured flow. Therefore, the prediction is judged to be in excellent agreement with the data.

Figure 5.6-10 presents the flow rate in the intact loop hot leg. The measurement did not indicate the direction of the flow; between 5 and 30 s the flow should have been negative, toward the break. [To compare the magnitudes of the flow rates, an additional curve on the plot shows the absolute value of the calculated flow rate. This is in good agreement with the data through most of the transient.] The data indicate that there may have been more flow in the hot leg in the experiment than in the prediction between

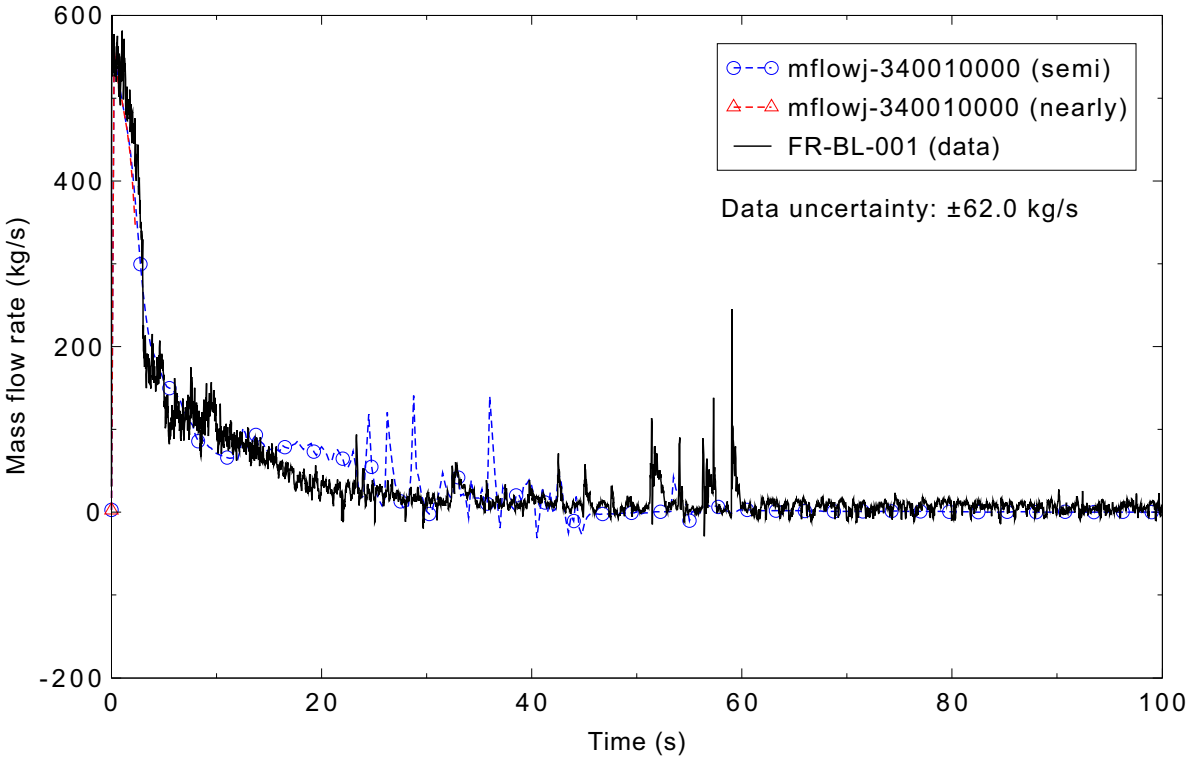

Figure 5.6-8. Measured and calculated mass flow rate in the broken loop cold leg for the LOFT Experiment L2-5 3-D case.

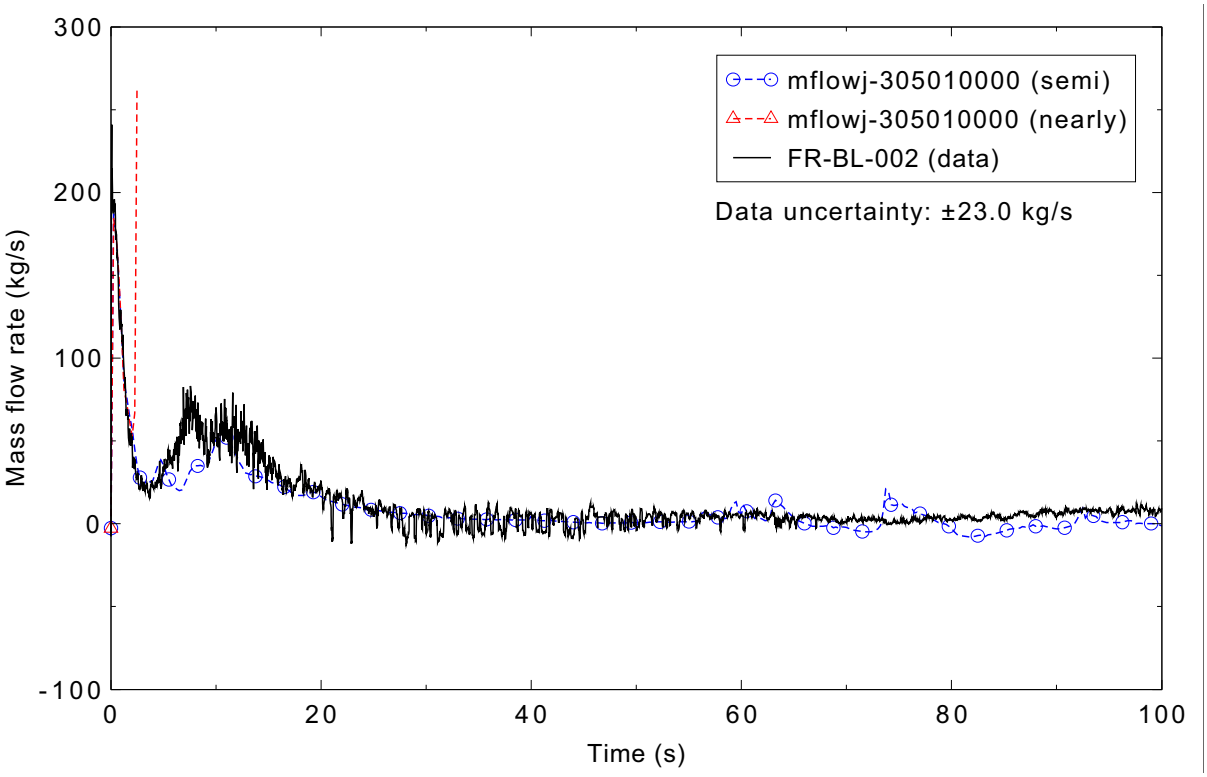

Figure 5.6-9. Measured and calculated mass flow rate in the broken loop hot leg for the LOFT Experiment L2-5 3-D case.

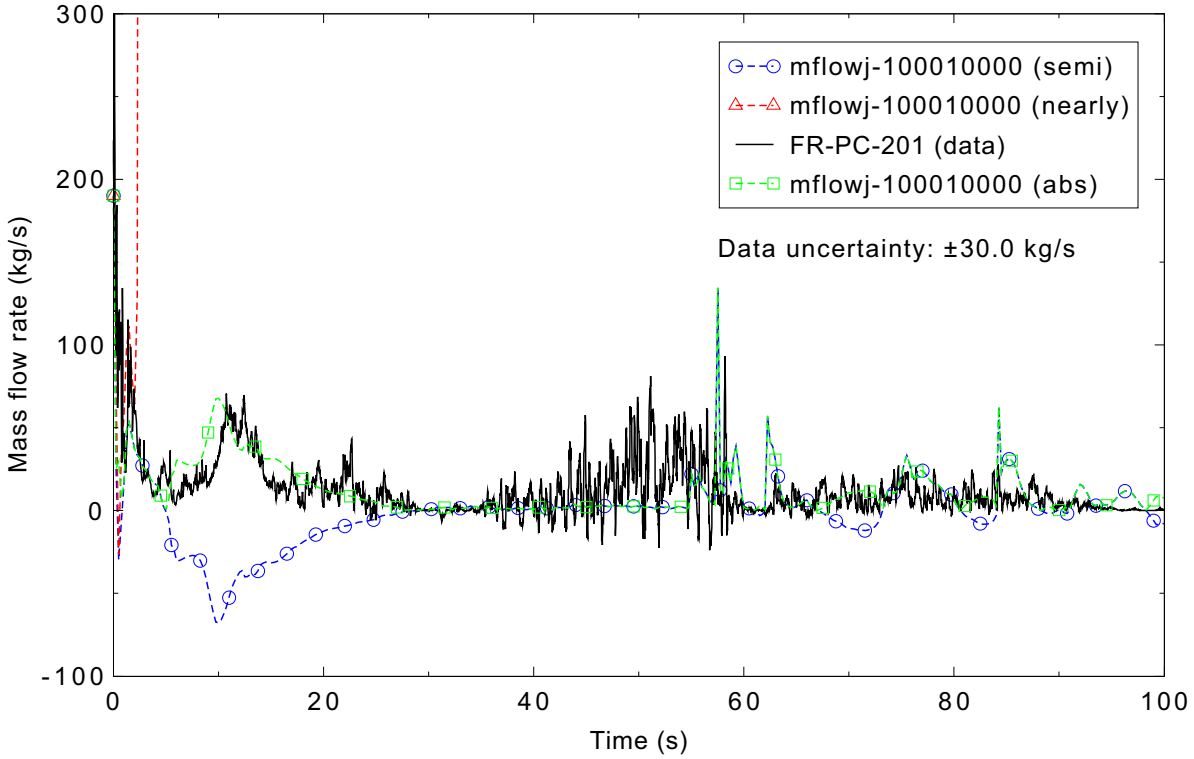

Figure 5.6-10. Measured and calculated mass flow rate in the intact loop hot leg for the LOFT Experiment L2-5 3-D case.

45 and 60 s, although the flow rate was small. Overall, the calculation of the flow rate is judged to be reasonable.

The mass flow rates in the intact loop cold leg are shown in Figure 5.6-11. The flow coastdown during the first 20 s is generally well simulated, with the calculation having a little higher flow rate near 20 s because it had more liquid in the cold leg. The flow oscillations from 30 to 70 s reflected slugs of liquid moving through the cold leg; evidence of this is seen in Figure 5.6-16 below. There appear to be more oscillations in the data than in the prediction. Overall, the code is judged to reasonably predict the intact loop cold leg flow.

The rotational speed of one of the two primary coolant pumps is presented in Figure 5.6-12. The code prediction of the initial coastdown was excellent, but the freewheeling response of the pump was not well predicted. Overall, the prediction is judged to be in minimal agreement with the data.

Densities in the broken loop cold leg are compared in Figure 5.6-13. The code predicted an earlier transition to two-phase conditions in the cold leg in the first few seconds, followed by a more gradual decrease than the nearly step decrease in density seen in the data. The calculation appears to have a little more liquid in the cold leg than the experiment between 15 and 30 s, although it is within the measurement uncertainty. Both the experiment and calculation had intermittent slugs of liquid in the cold leg between 30 and 60 s, before the pipe became steam-filled. The calculation is judged to be in reasonable agreement with the measured data.

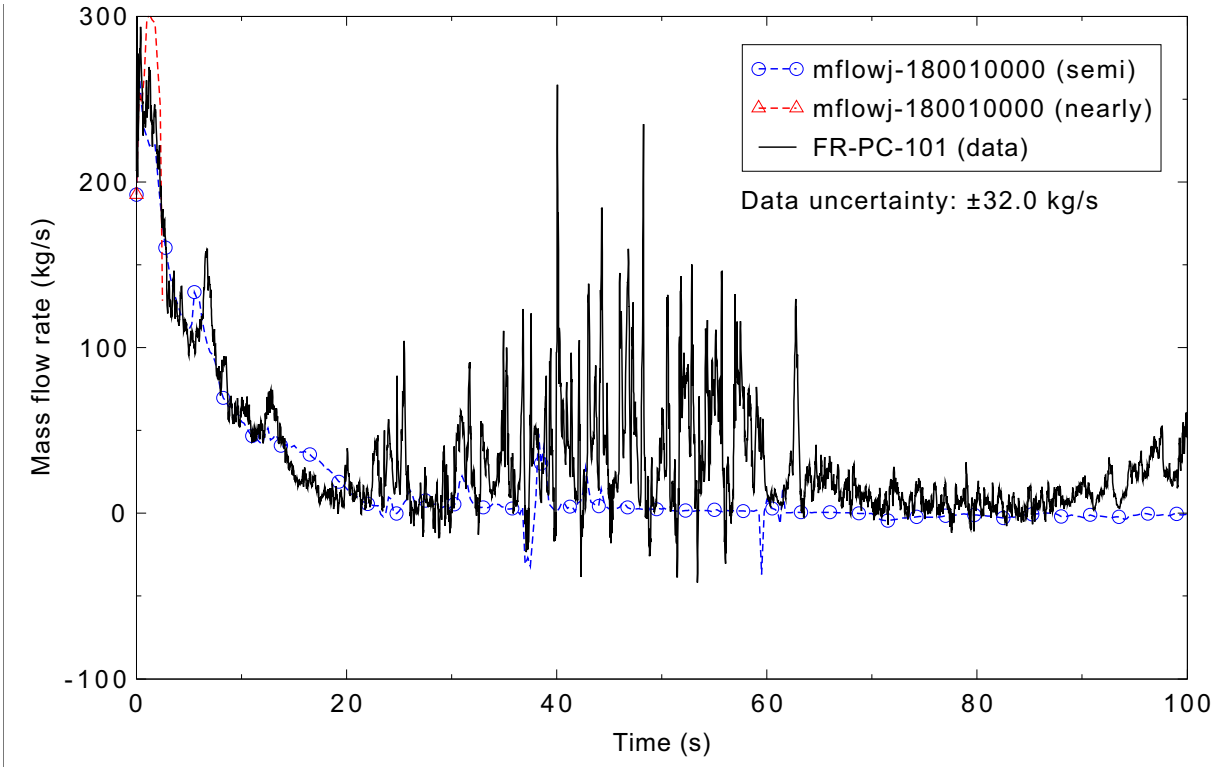

Figure 5.6-11. Measured and calculated mass flow rate in the intact loop cold leg for the LOFT Experiment L2-5 3-D case.

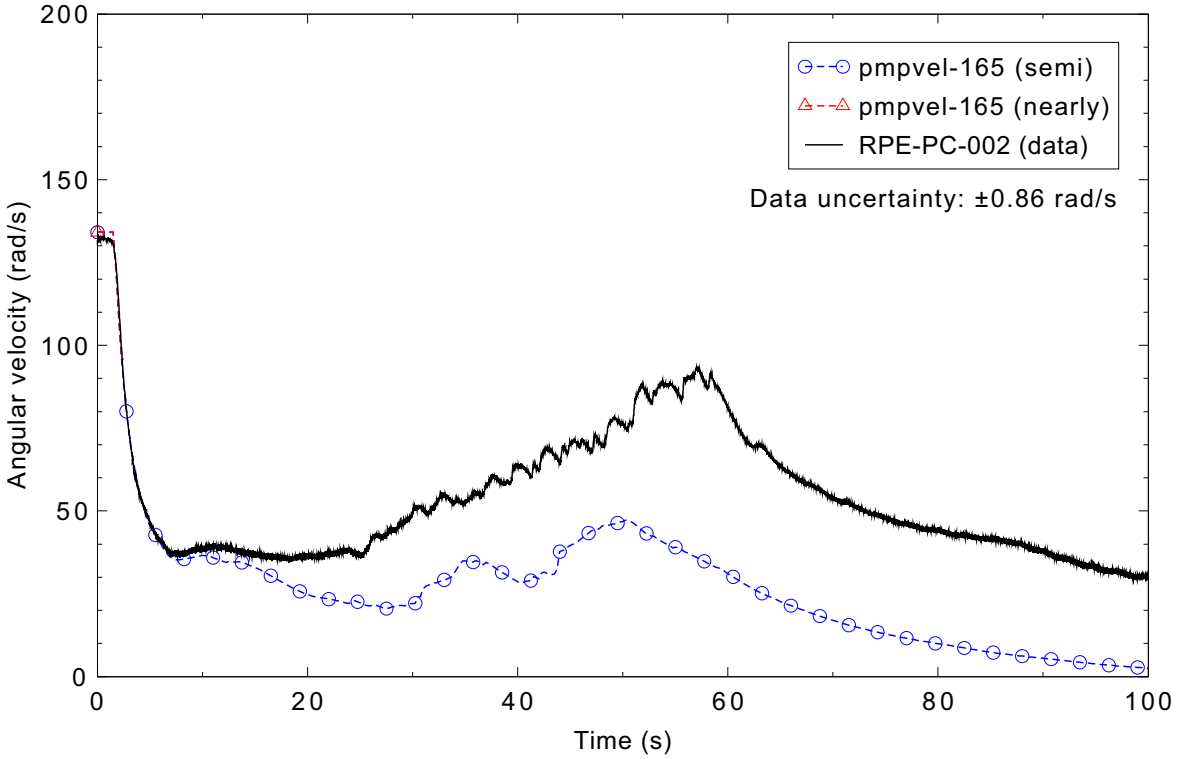

Figure 5.6-12. Measured and calculated speed for primary coolant pump 2 for the LOFT Experiment L2-5 3-D case.

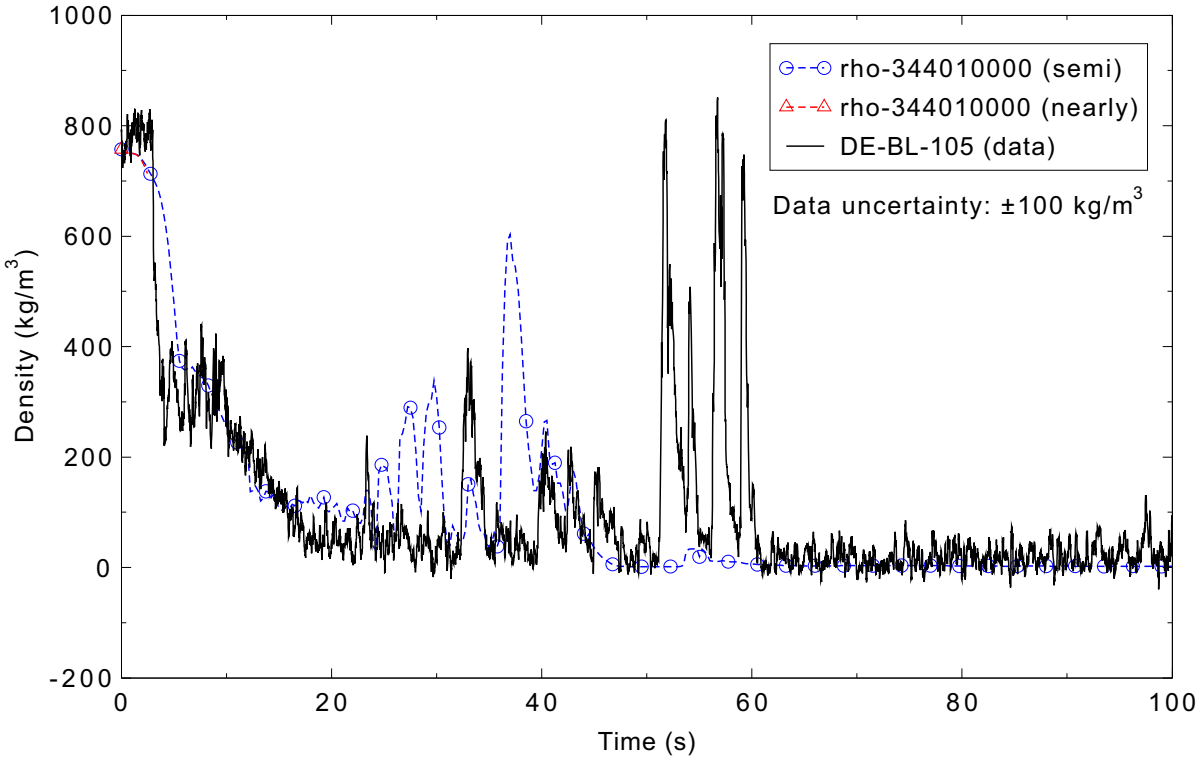

Figure 5.6-13. Measured and calculated density in the broken loop cold leg for the LOFT Experiment L2-5 3-D case.

Figure 5.6-14 shows densities in the broken loop hot leg. The data at this location are for two of the three densitometer beams; these are in the lower (DE-BL-002A) and upper (DE-BL-002C) portions of the pipe. (The other experiment densities presented are for pipe-average values calculated from the three chordal densities.) The calculated density lies between the measured values through most of the transient. Liquid returning to the hot leg occurred earlier in the calculation than in the experiment. The prediction is judged to be in reasonable agreement with the experiment data.

The intact loop hot leg density is presented in Figure 5.6-15. The measured density increase near 5 s was predicted late and with a smaller magnitude, and the increase between 10 and 15 s was not predicted, although the calculated density did stop decreasing during that time. In the experiment, the density gradually increased after about 40 s. The calculated density exhibited larger, intermittent increases. Most of the deviation occurred after 75 s, after the core was completely quenched in the calculation. While the overall judgment is that the calculated density is in minimal agreement with the data, reasonable agreement was achieved during the more critical portion of the large break LOCA.

Figure 5.6-16 shows the intact loop cold leg densities. The initial density decrease in the first 15 s was reasonably simulated. In the experiment, the cold leg then became nearly steam-filled, while the simulation retained more liquid in the pipe. Large oscillations occurred in both the experiment and the calculation between 30 and 60 s. The density then settled out in both, although with more liquid in the simulation than in the test. While the general trends of the data are captured, the calculation is judged to be in minimal agreement with the experiment because too much liquid is being retained in the cold legs.

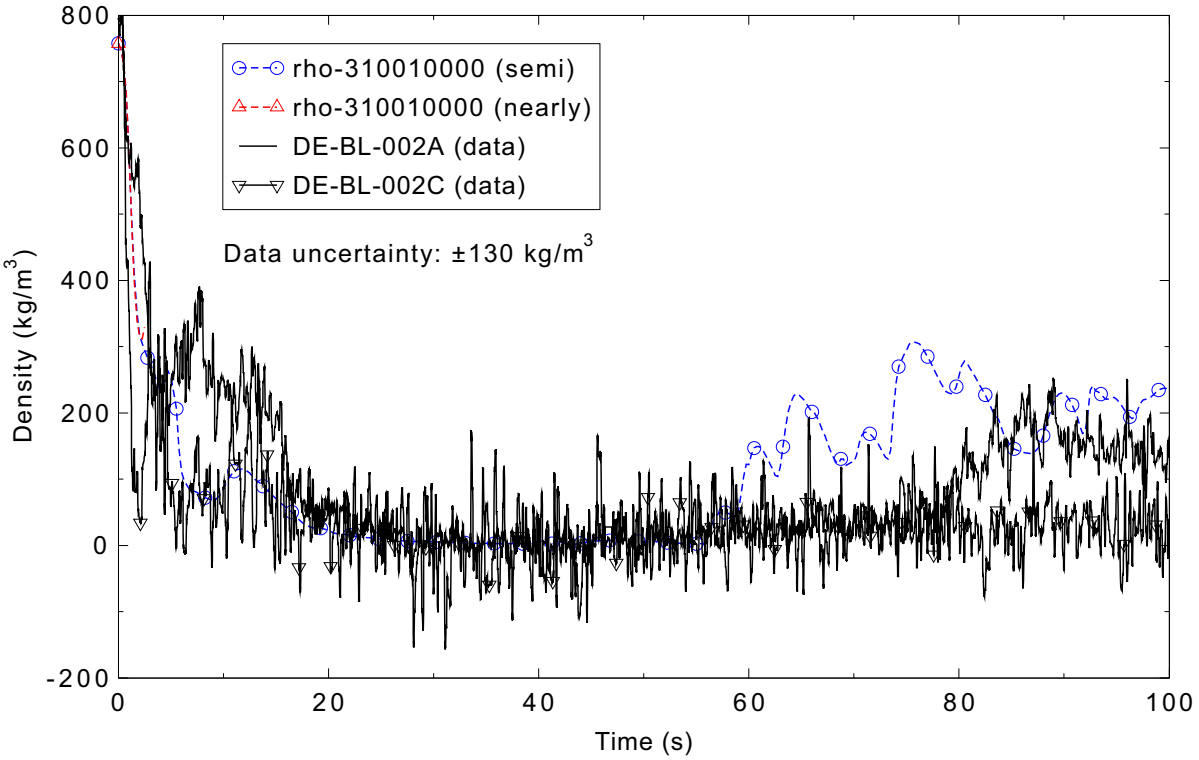

Figure 5.6-14. Measured and calculated density in the broken loop hot leg for the LOFT Experiment L2-5 3-D case.

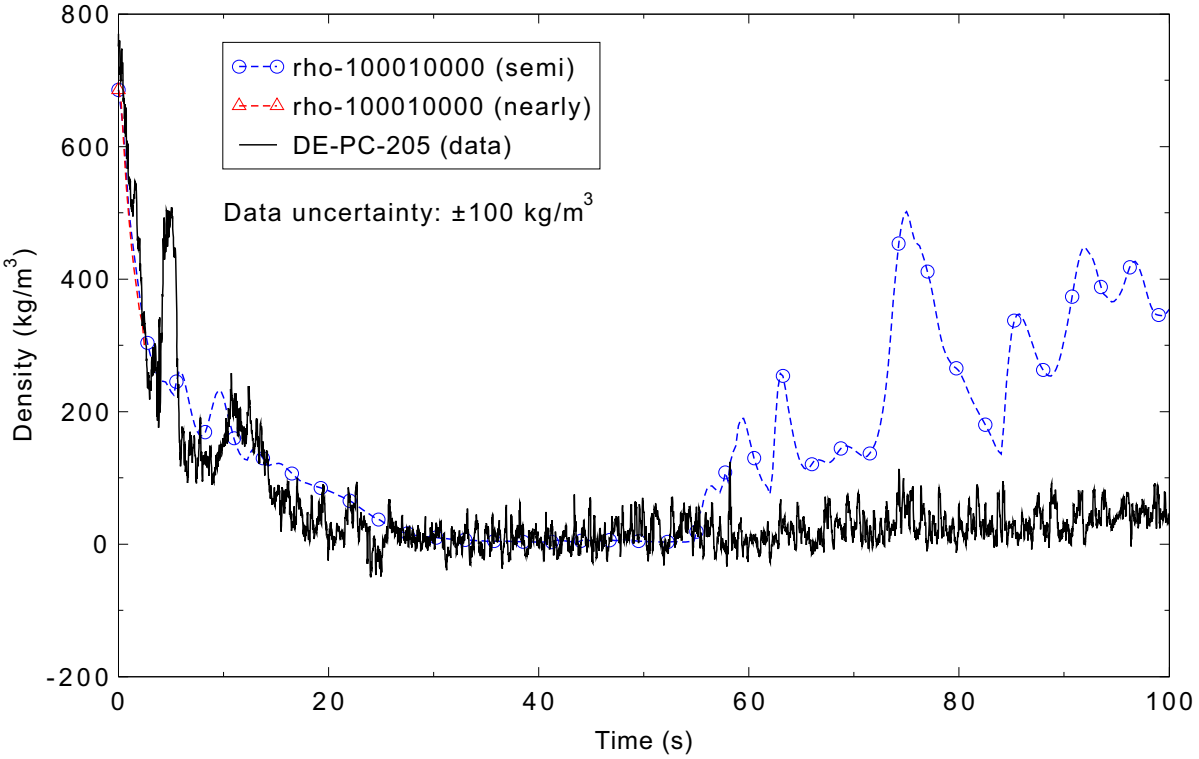

Figure 5.6-15. Measured and calculated density in the intact loop hot leg for the LOFT Experiment L2-5 3-D case.

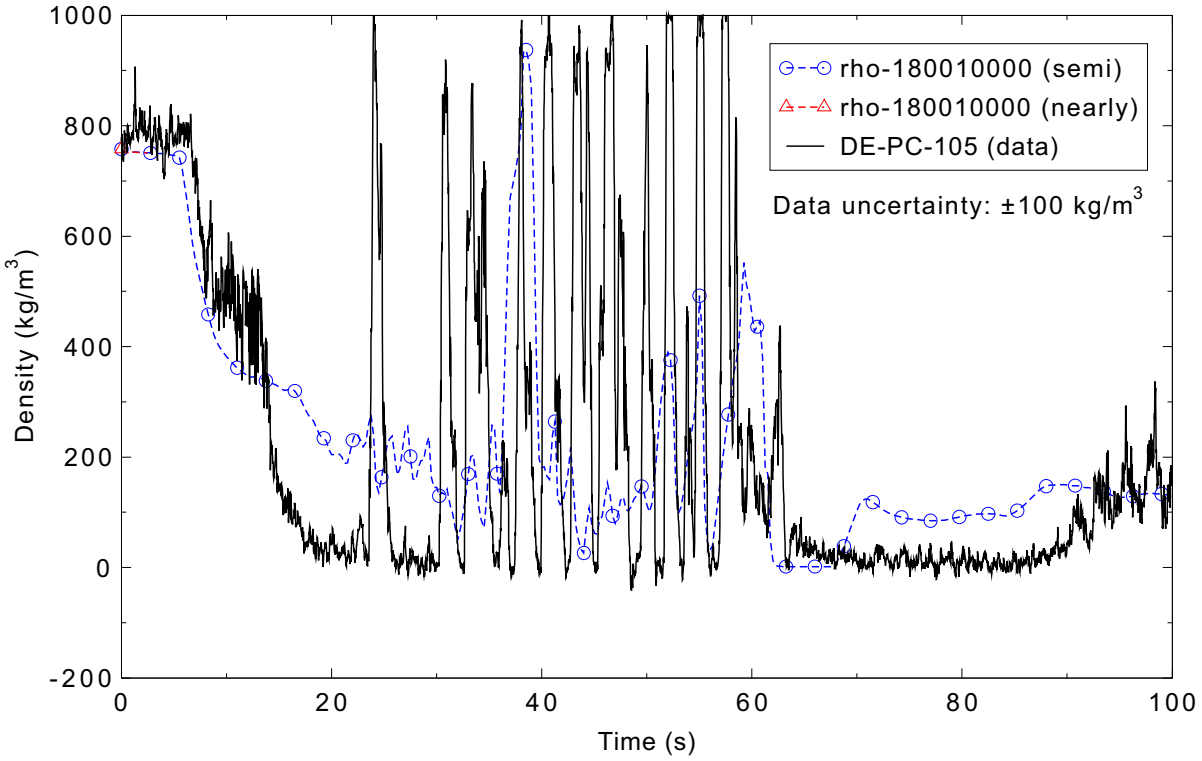

Figure 5.6-16. Measured and calculated density in the intact loop cold leg for the LOFT Experiment L2-5 3-D case.

The measured and calculated accumulator liquid levels are compared in Figure 5.6-17. The calculation is judged to be in excellent agreement with the data.

Figures 5.6-18 and 5.6-19 present the high- and low-pressure injection system flow rates, respectively. (Control variables are used to calculate the volumetric flow rates.) There appears to be an overshoot in the data when the HPIS flow begins, as it then settles out to a nearly constant value; the time-dependent junction in the RELAP5-3D input model is set to provide the nearly constant flow. As this is essentially a boundary condition, no assessment judgment is made. The drop in the measured LPIS flow between 50 and 60 s has no obvious cause - the primary coolant system pressure is not increasing, so the pump flow should not be decreasing. The differences between the calculated and measured flow rates are attributed to differences in the primary coolant system pressure. The LPIS flow is judged to be in reasonable agreement with the data.

Figure 5.6-20 shows the measured reactor vessel upper plenum fluid temperature, as well as the calculated liquid and vapor temperatures. The calculation showed sustained superheated vapor between 20 and 50 s, while the measurement appears to show superheat beginning around 30 s. After 60 s, both the calculated and measured fluid temperatures are near the saturation temperature. However, the saturation temperature in the calculation is depressed, as it was lowered by the presence of nitrogen from the accumulator; the code uses the partial pressure of the steam to calculate the saturation temperature for the water. The prediction of the upper plenum fluid temperature is judged to be in reasonable agreement with the data.

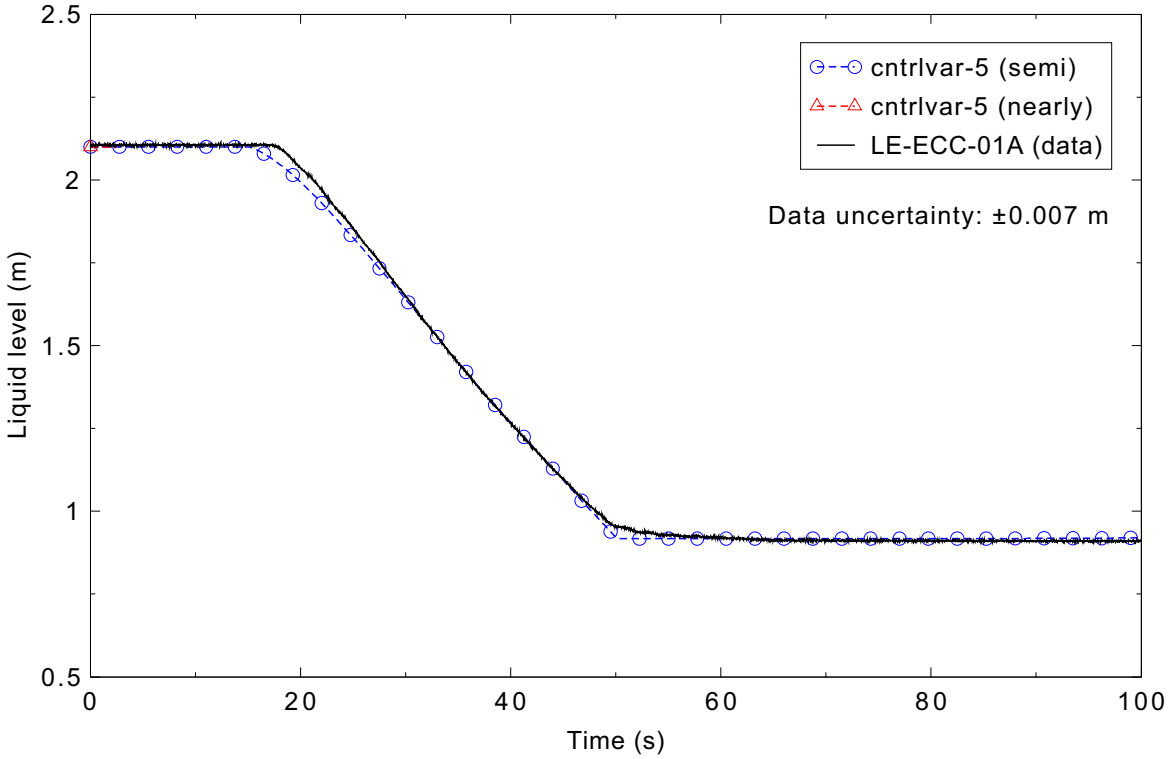

Figure 5.6-17. Measured and calculated accumulator liquid level for the LOFT Experiment L2-5 3-D case.

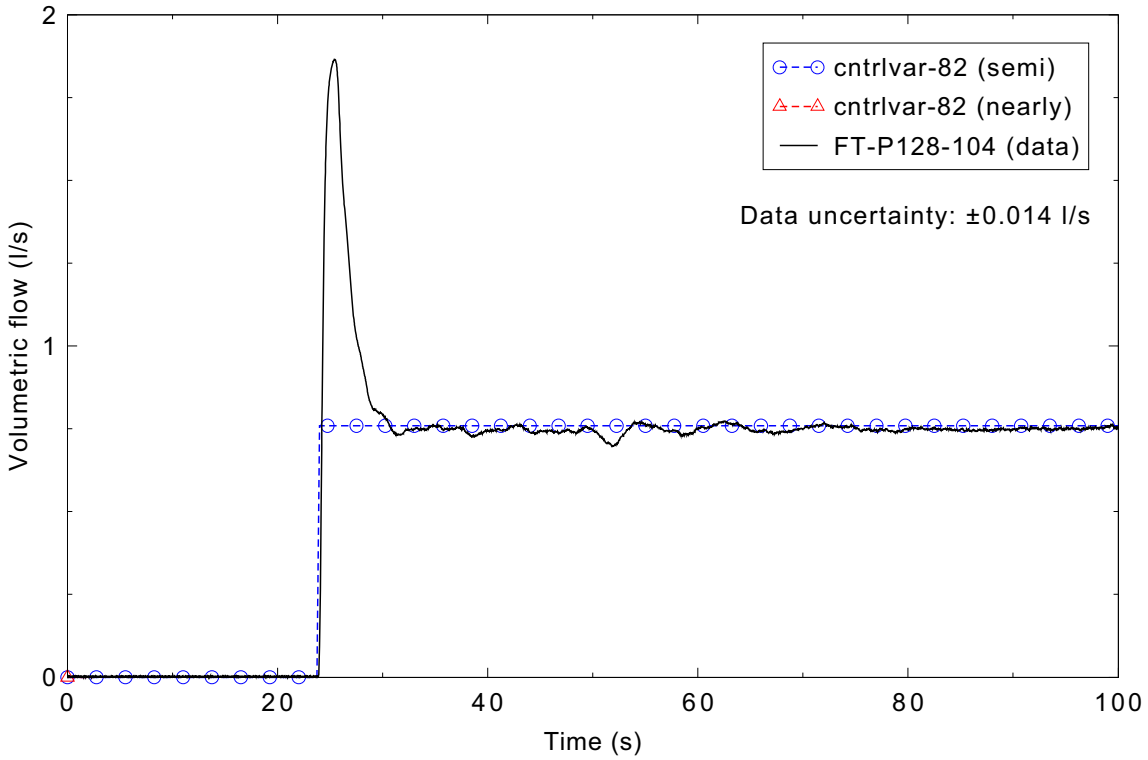

Figure 5.6-18. Measured and calculated HPIS flow for the LOFT Experiment L2-5 3-D case.

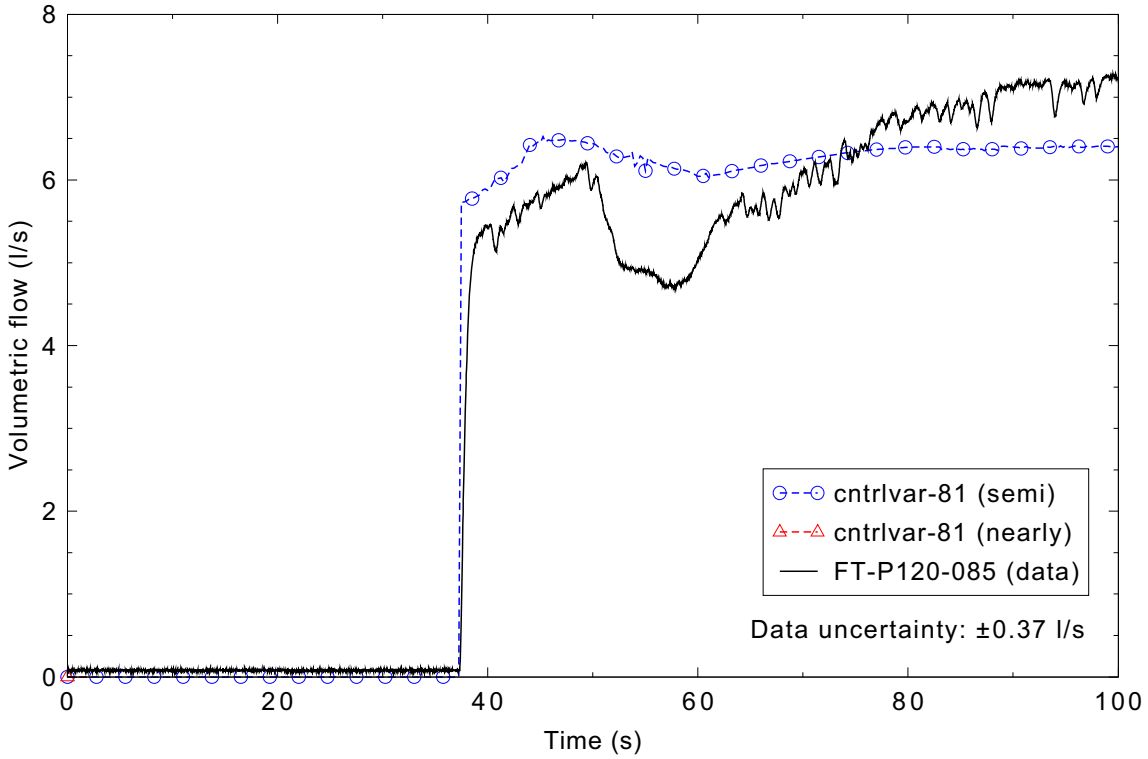

Figure 5.6-19. Measured and calculated LPIS flow for the LOFT Experiment L2-5 3-D case.

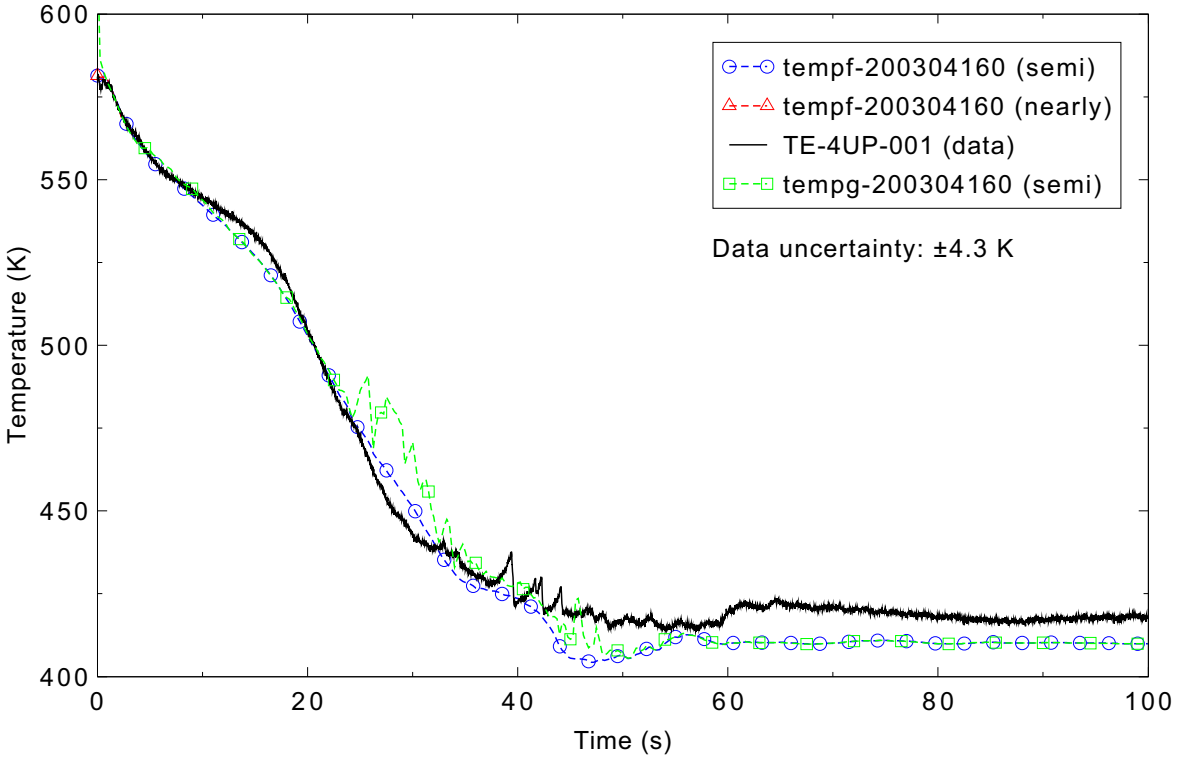

Figure 5.6-20. Measured and calculated reactor vessel upper plenum coolant temperature for the LOFT Experiment L2-5 3-D case.

The lower plenum liquid temperature is shown in Figure 5.6-21. The temperatures are at saturation through most of the transient, with the calculated values being lower because of the presence of the accumulator nitrogen. (The liquid saturation temperature is based on the steam partial pressure.) The prediction of the lower plenum liquid temperature is judged to be in reasonable agreement, as the data are well predicted prior to the accumulator emptying, and the correct trends are predicted after that.

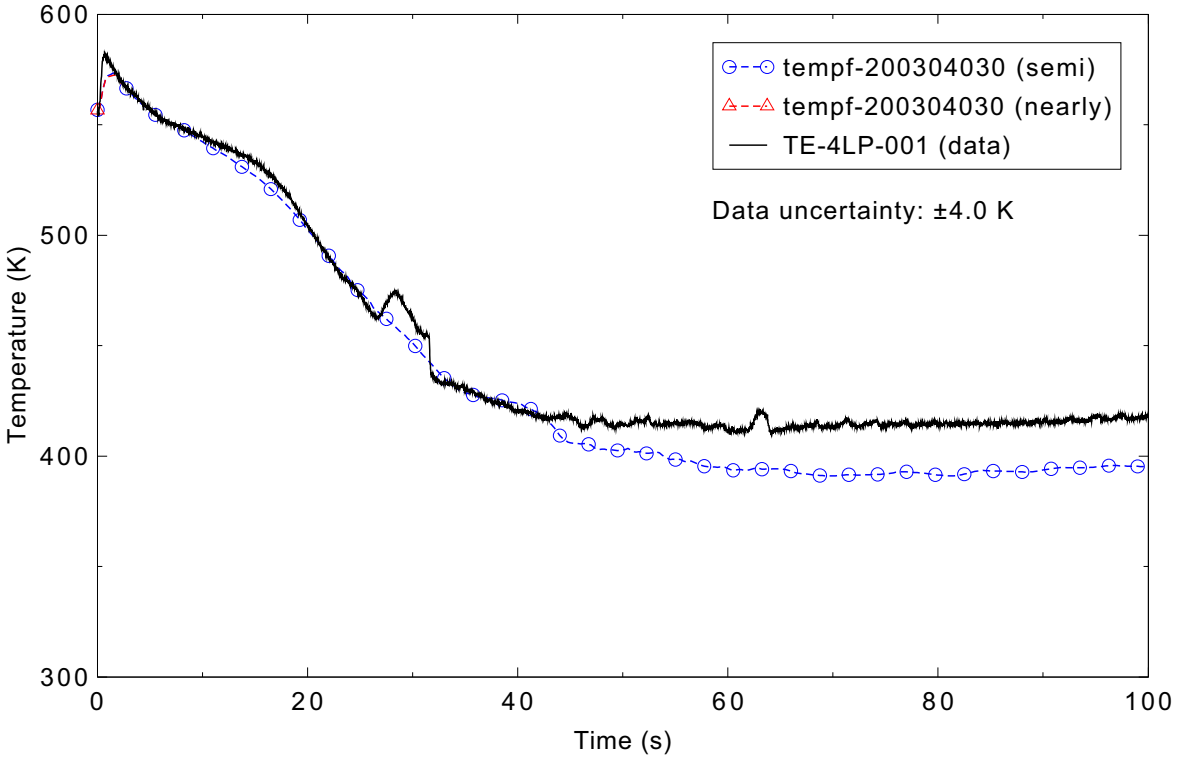

Figure 5.6-21. Measured and calculated reactor vessel lower plenum coolant temperature for the LOFT Experiment L2-5 3-D case.

Figure 5.6-22 presents a comparison of the fuel centerline temperatures in an inner ring fuel assembly. The difference in the initial value is not considered significant, as the experiment is measuring a value in a single rod that may have a different peaking factor than the 1.31 value used in the calculation. The two major inflection points, for the initial core heatup near 10 s and for the final quench near 65 s, were predicted to occur, although the quench in the calculation occurred about 10 s earlier than measured. The trend between these two times was not particularly well simulated, with the calculation steadily decreasing while the data remained fairly constant. Still, the prediction of the fuel centerline temperature is judged to be reasonable.

Fuel cladding surface temperatures for each of the 12 axial levels in one sector of the RELAP5-3D model inner ring are compared to the data in Figures 5.6-23 through 5.6-34. Compared to the data, the initial cladding heatup was predicted to occur a little late in core levels 1-3 and 9, a little early in levels 4-8, and not at all in the top three levels. (Very slight heatups were predicted to occur in the top three levels between 30 and 40 s.) The delayed (or missing) heatups led to an under prediction of the peak temperatures in the three levels at both the top and bottom of the core, while the peak temperatures in the middle six levels were predicted reasonably well. That is important since the overall peak temperature occurs in these levels. The measured peak cladding temperature of 1,078 K occurred at 28.5 s in rod 5H06, 0.61 m above

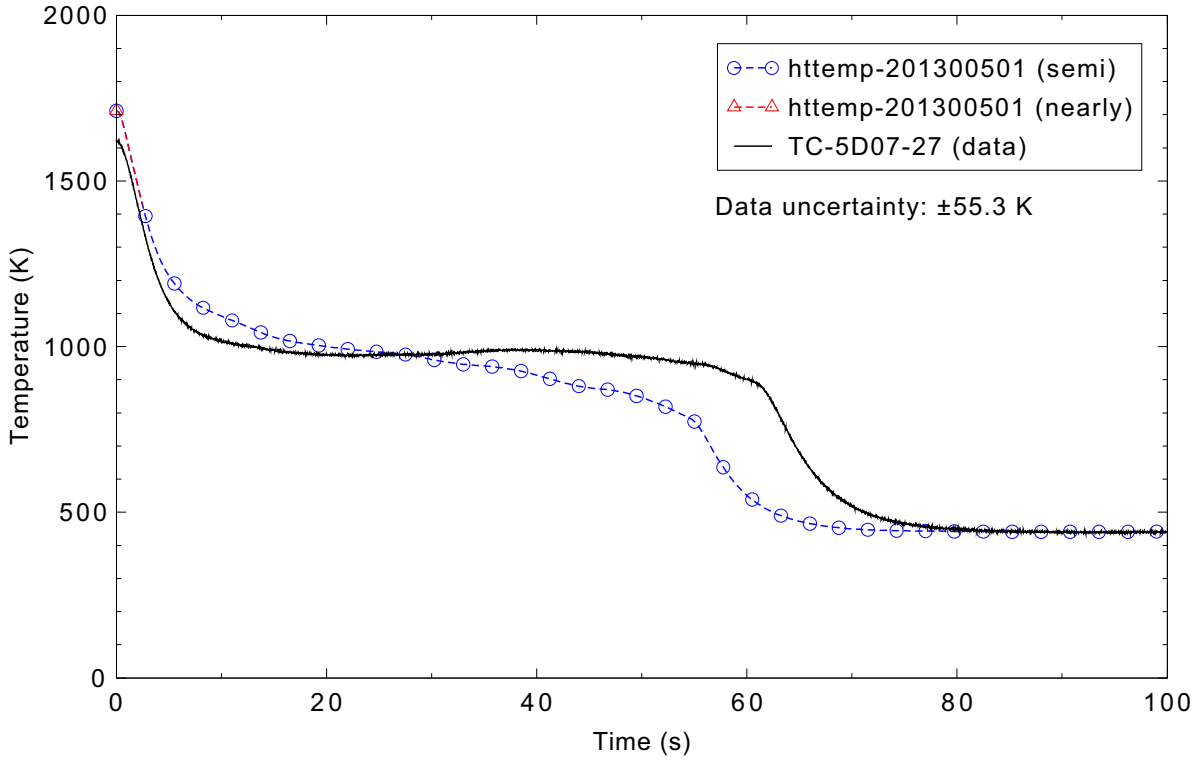

Figure 5.6-22. Measured and calculated fuel centerline temperature in Ring 1, Sector 3, 0.69 m above the bottom of the fuel rod for the LOFT Experiment L2-5 3-D case.

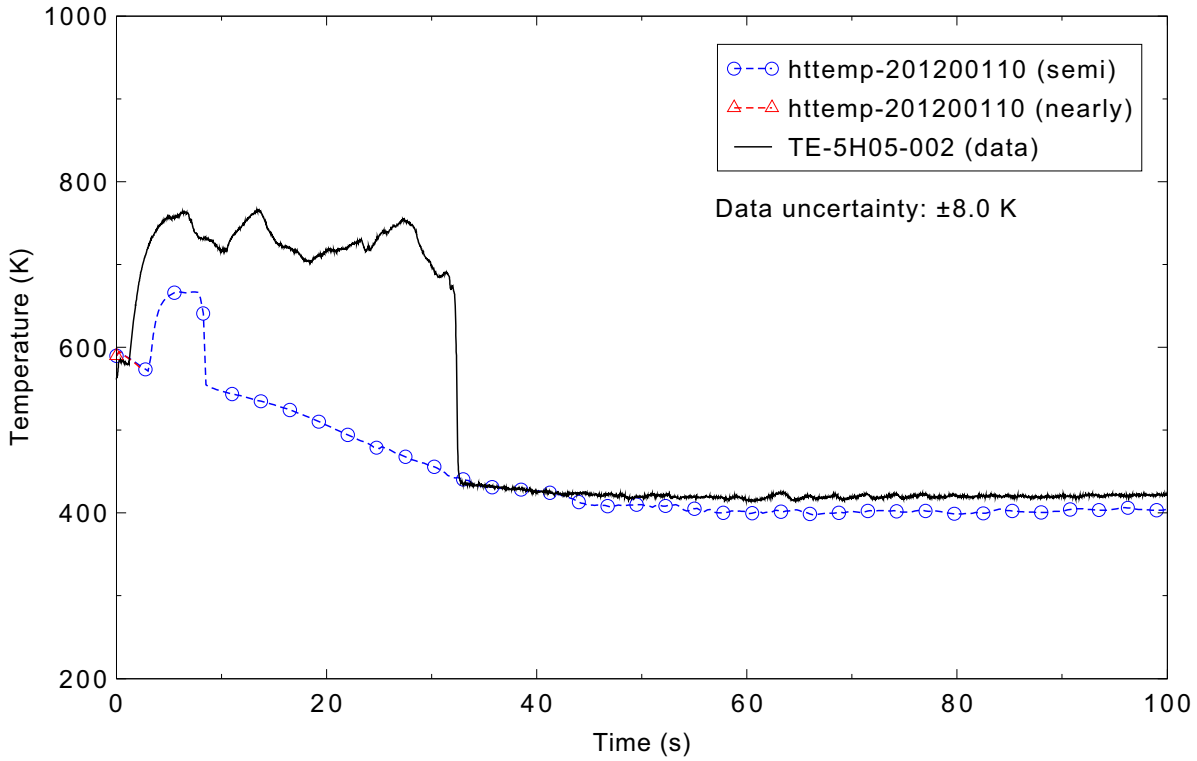

Figure 5.6-23. Measured and calculated fuel cladding surface temperature in Ring 1, Sector 2, 0.05 m above the bottom of the fuel rod for the LOFT Experiment L2-5 3-D case.

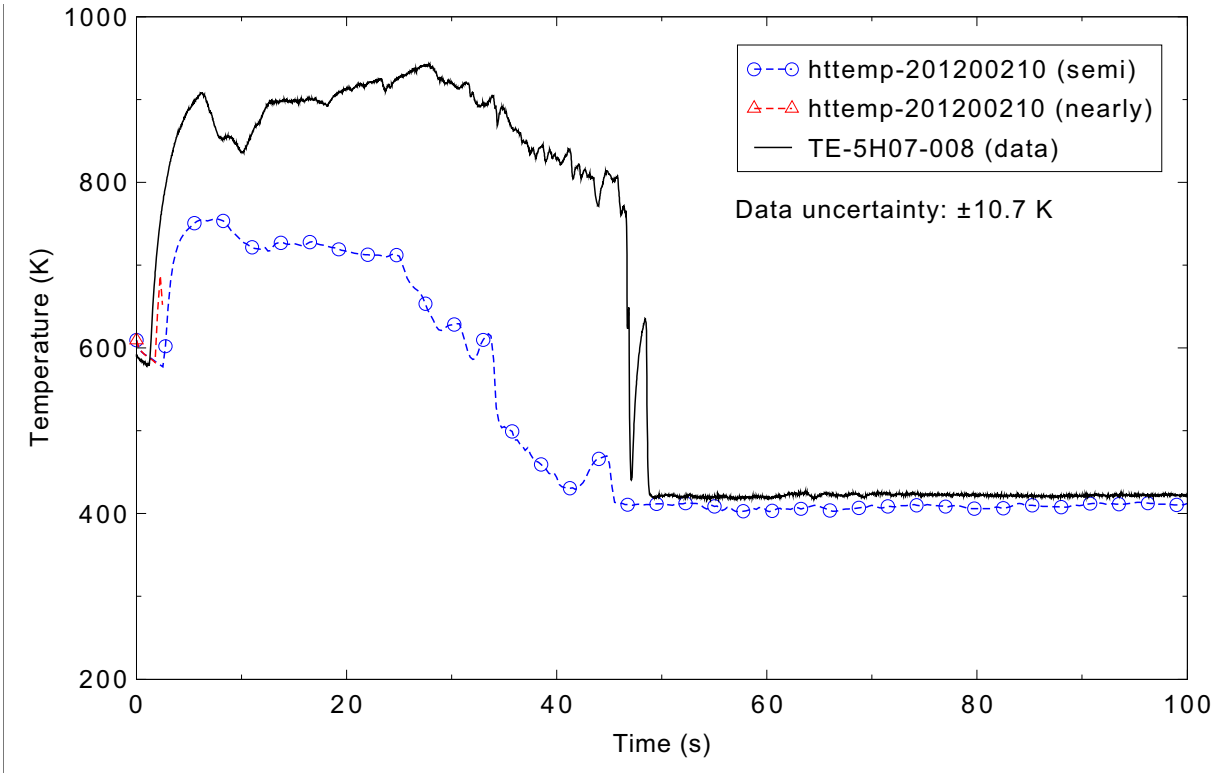

Figure 5.6-24. Measured and calculated fuel cladding surface temperature in Ring 1, Sector 2, 0.20 m above the bottom of the fuel rod for the LOFT Experiment L2-5 3-D case.

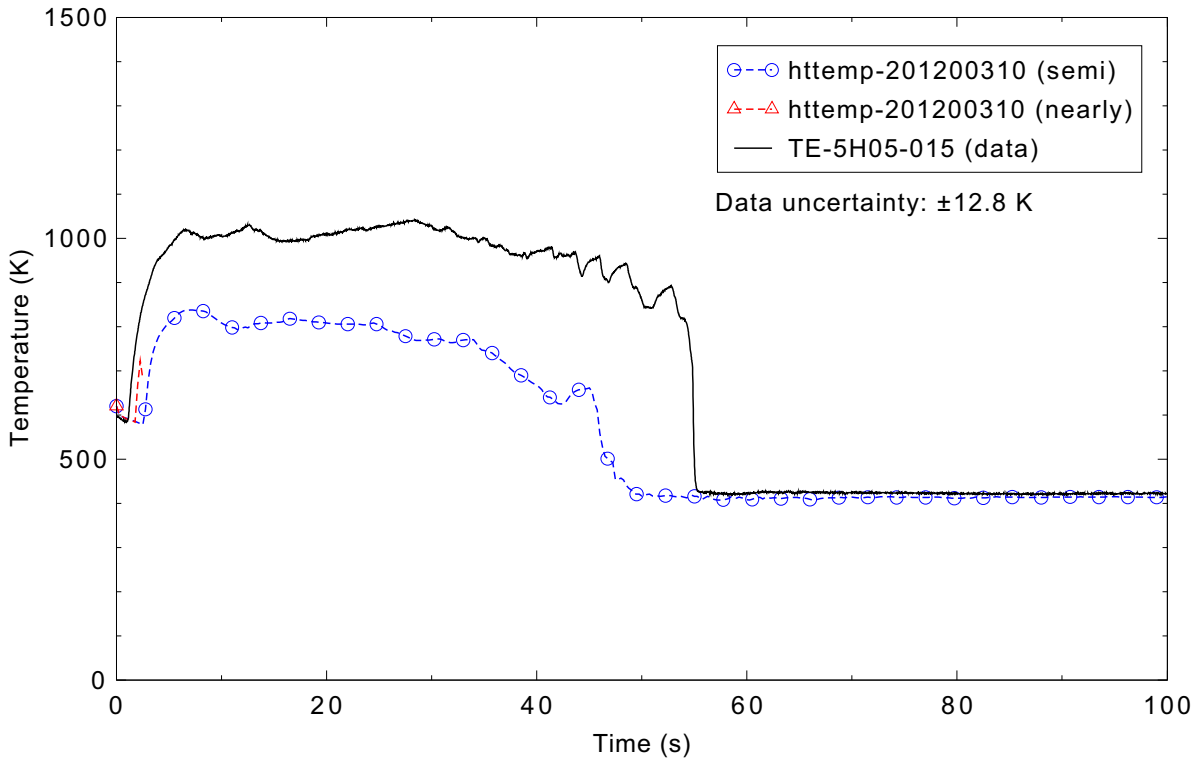

Figure 5.6-25. Measured and calculated fuel cladding surface temperature in Ring 1, Sector 2, 0.38 m above the bottom of the fuel rod for the LOFT Experiment L2-5 3-D case.

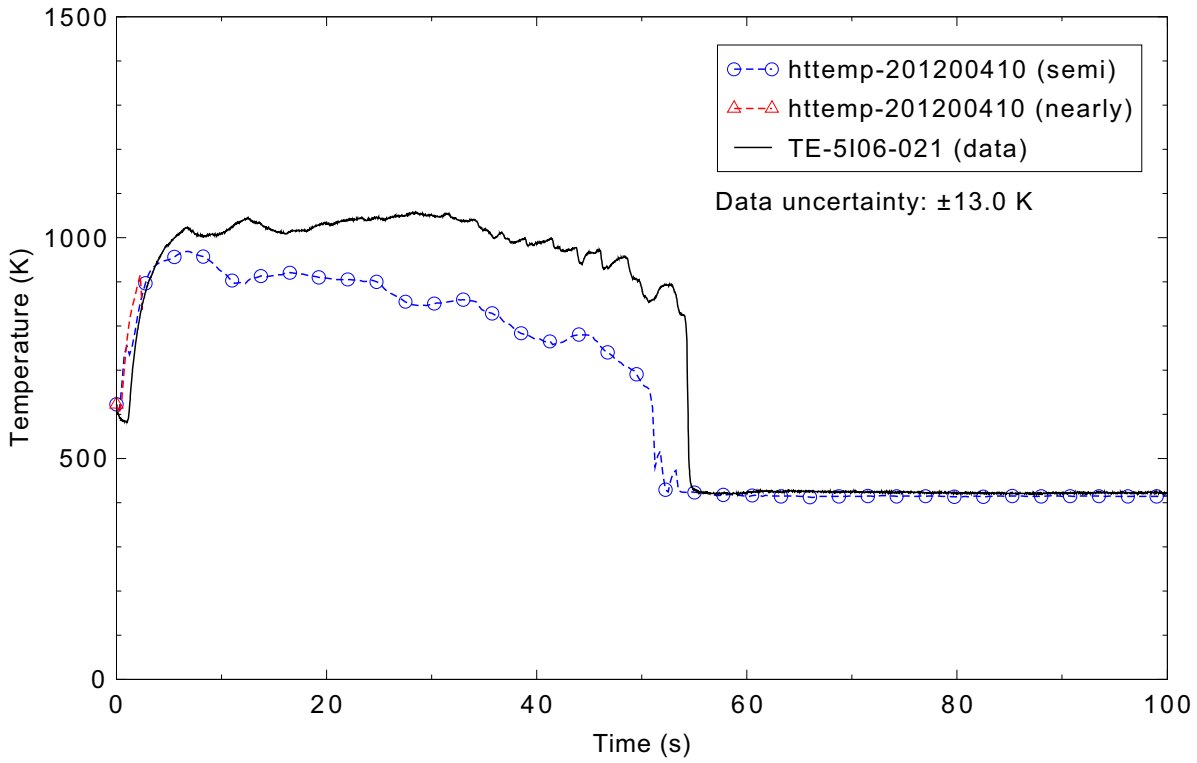

Figure 5.6-26. Measured and calculated fuel cladding surface temperature in Ring 1, Sector 2, 0.53 m above the bottom of the fuel rod for the LOFT Experiment L2-5 3-D case.

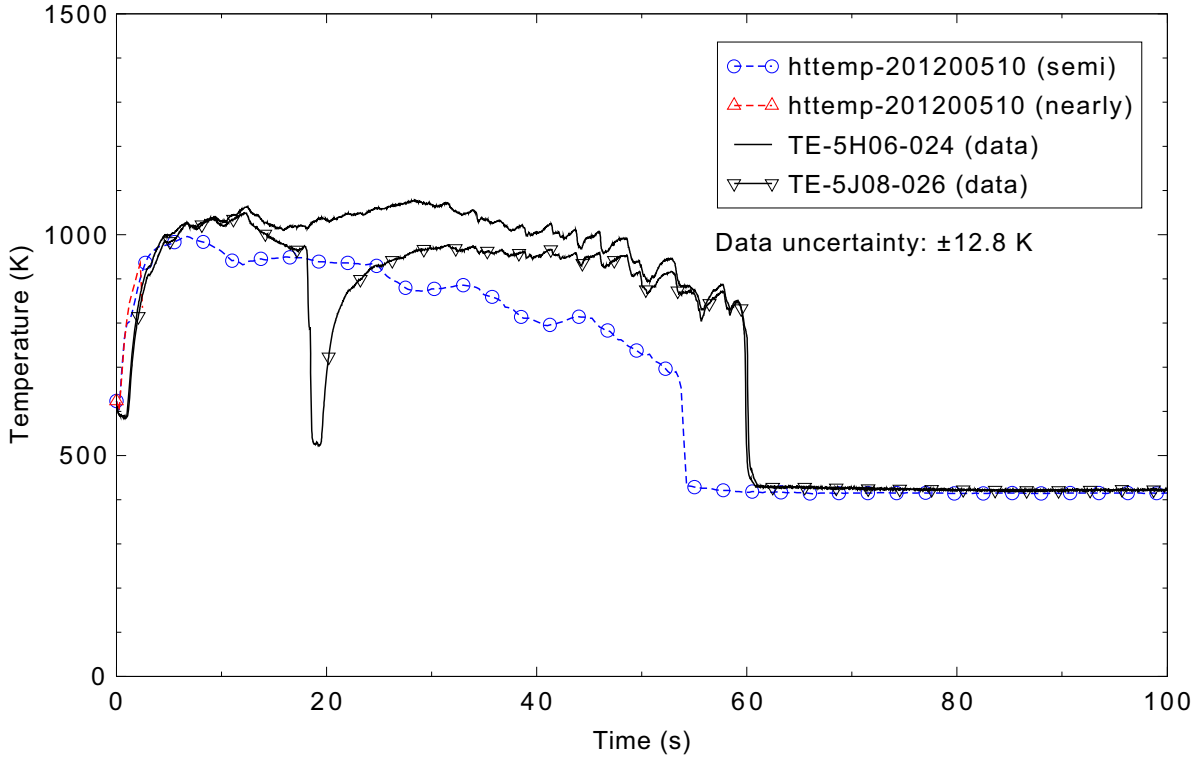

Figure 5.6-27. Measured and calculated fuel cladding surface temperature in Ring 1, Sector 2, 0.64 m above the bottom of the fuel rod for the LOFT Experiment L2-5 3-D case.

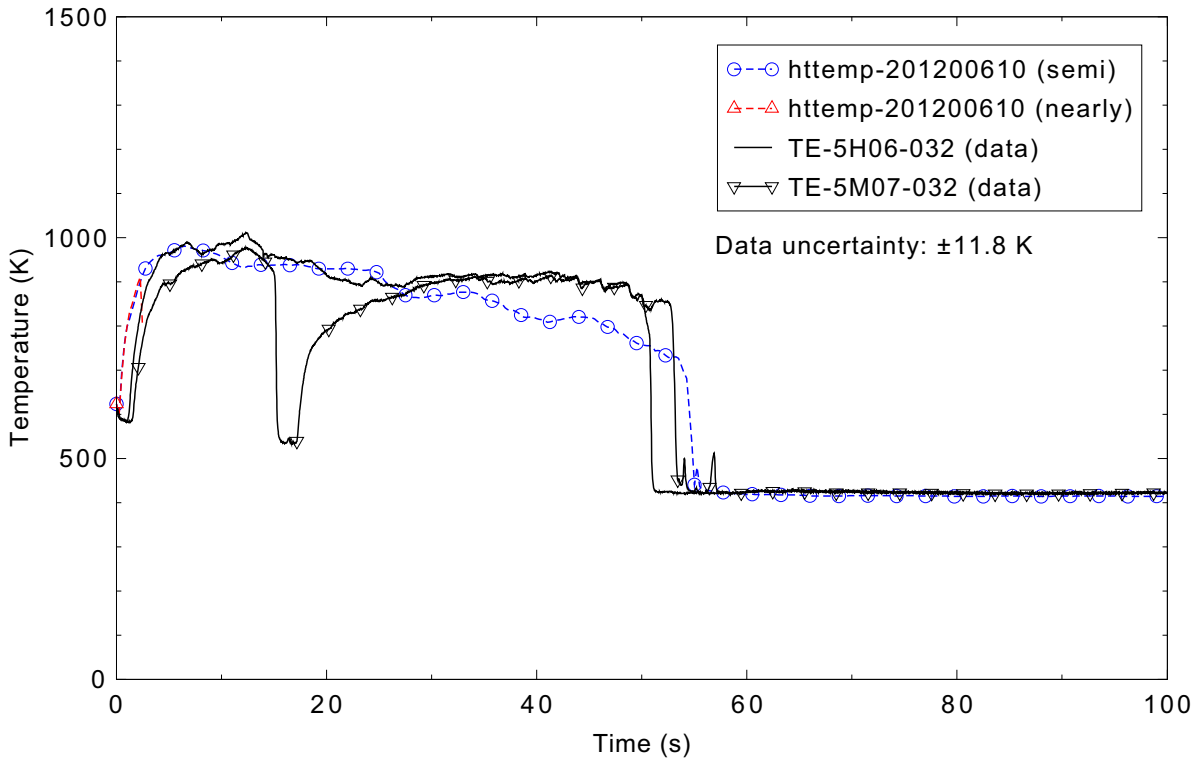

Figure 5.6-28. Measured and calculated fuel cladding surface temperature in Ring 1, Sector 2, 0.81 m above the bottom of the fuel rod for the LOFT Experiment L2-5 3-D case.

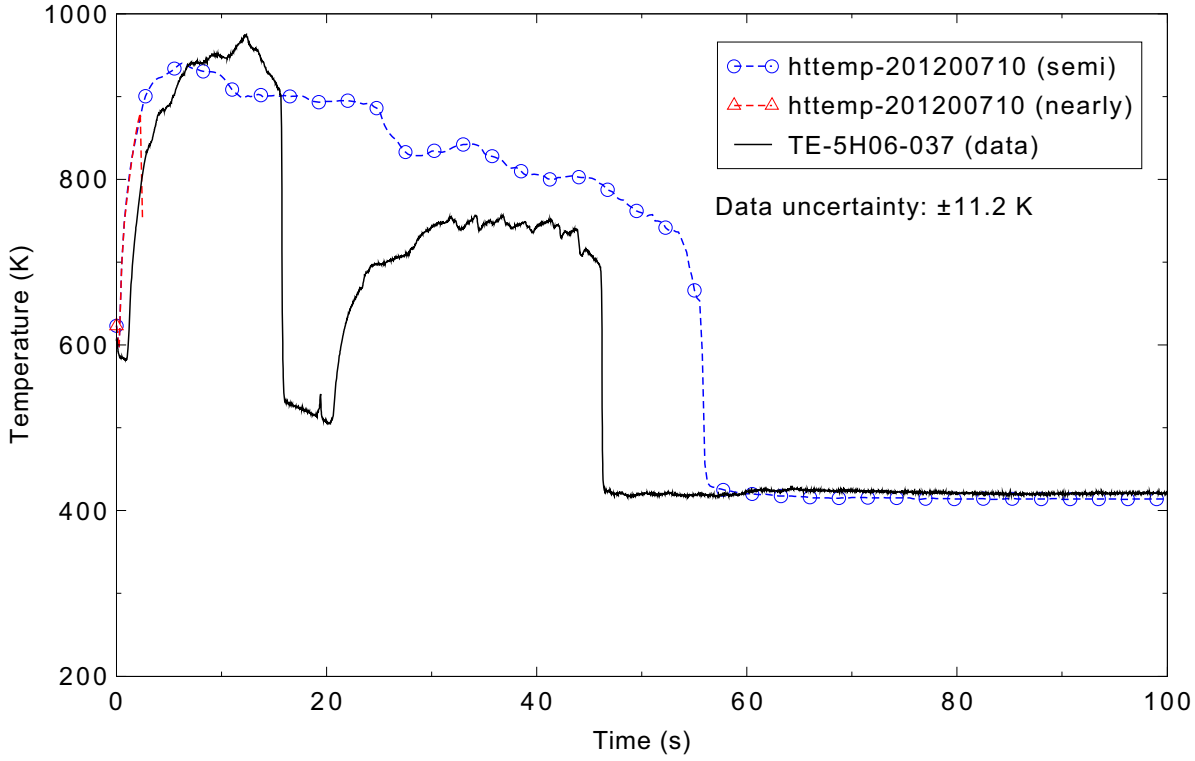

Figure 5.6-29. Measured and calculated fuel cladding surface temperature in Ring 1, Sector 2, 0.94 m above the bottom of the fuel rod for the LOFT Experiment L2-5 3-D case.

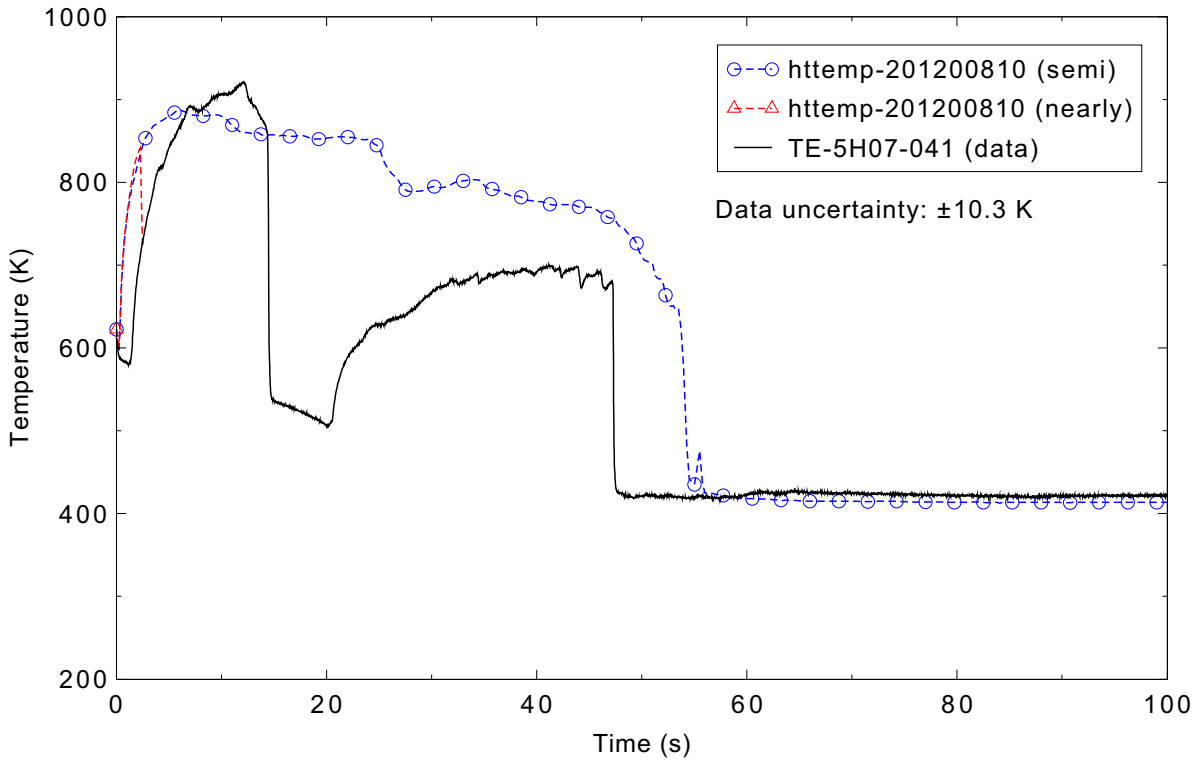

Figure 5.6-30. Measured and calculated fuel cladding surface temperature in Ring 1, Sector 2, 1.04 m above the bottom of the fuel rod for the LOFT Experiment L2-5 3-D case.

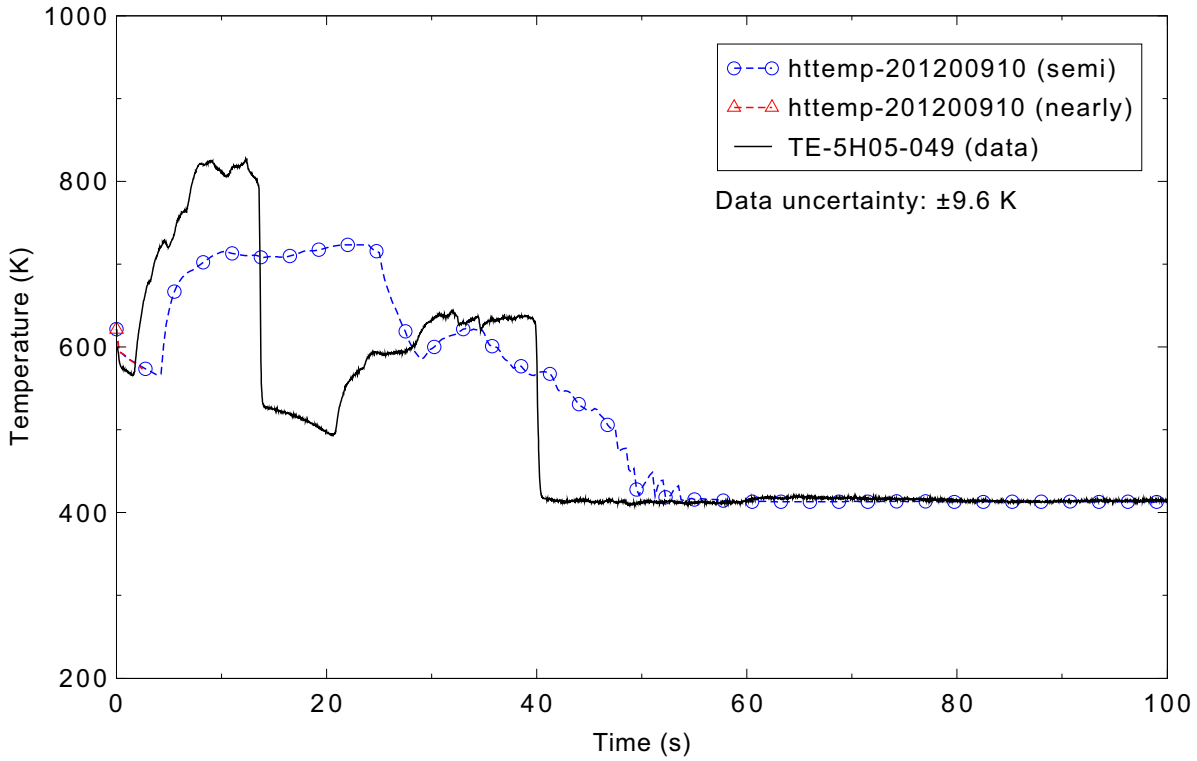

Figure 5.6-31. Measured and calculated fuel cladding surface temperature in Ring 1, Sector 2, 1.25 m above the bottom of the fuel rod for the LOFT Experiment L2-5 3-D case.

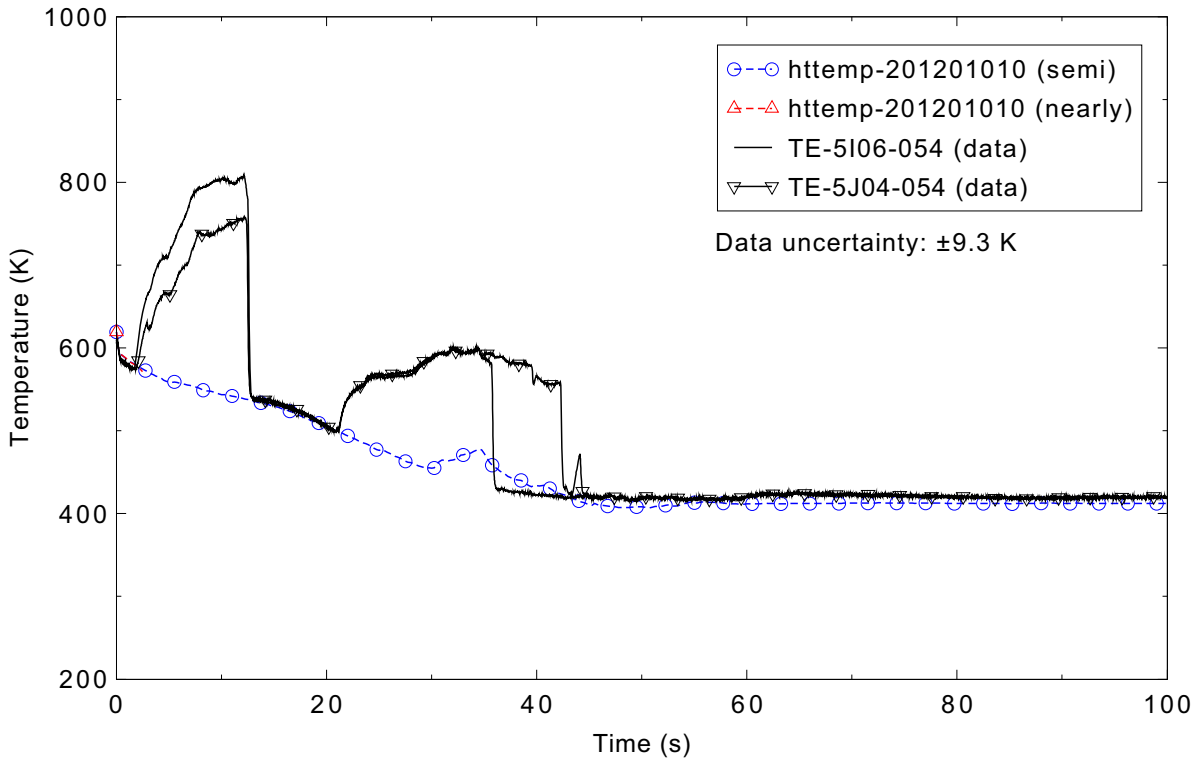

Figure 5.6-32. Measured and calculated fuel cladding surface temperature in Ring 1, Sector 2, 1.37 m above the bottom of the fuel rod for the LOFT Experiment L2-5 3-D case.

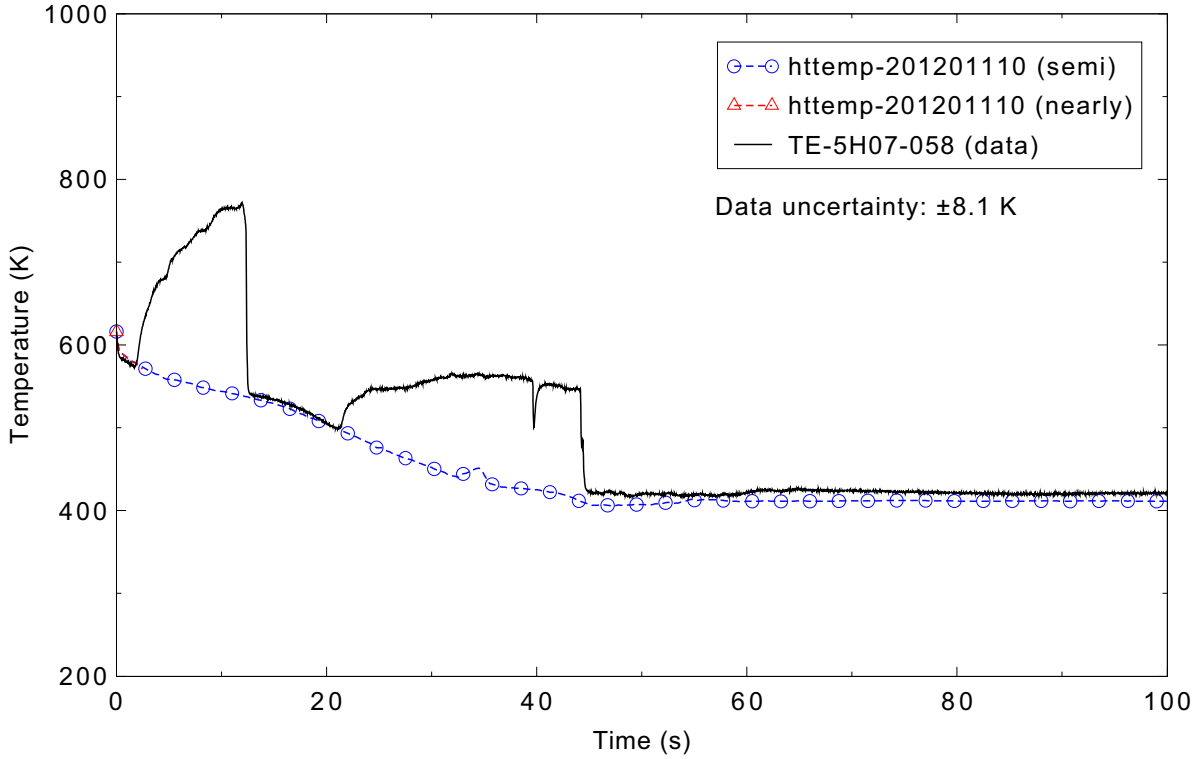

Figure 5.6-33. Measured and calculated fuel cladding surface temperature in Ring 1, Sector 2, 1.47 m above the bottom of the fuel rod for the LOFT Experiment L2-5 3-D case.

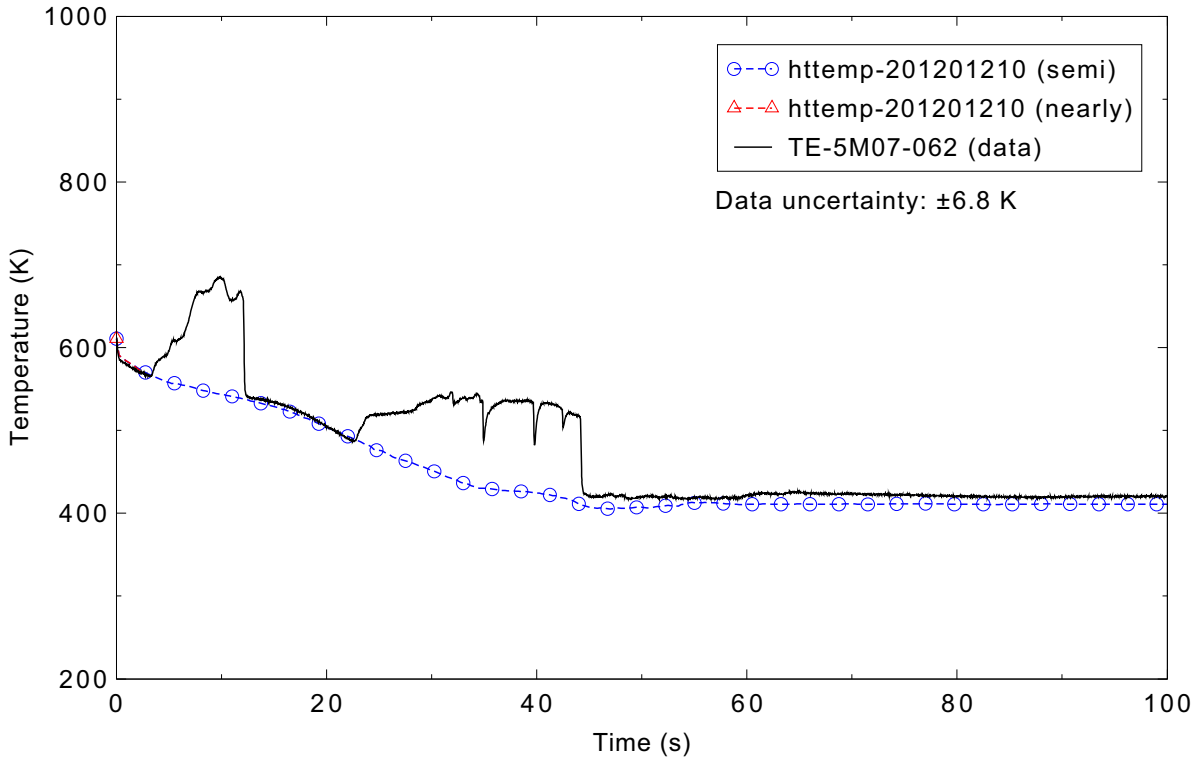

Figure 5.6-34. Measured and calculated fuel cladding surface temperature in Ring 1, Sector 2, 1.57 m above the bottom of the fuel rod for the LOFT Experiment L2-5 3-D case.

the bottom of the fuel rod, while in the calculation the peak value of 995 K occurred at 6.8 s in axial level 5, the center of which is 0.63 m above the bottom of the fuel rod. There was a partial top-down core rewet in the experiment that was not predicted by the code; Figures 5.6-27 and 5.6-28 illustrate that the rewet did not affect all of the fuel rods. The data indicate that the final core quenching occurred from both the bottom and top of the core, with level 5 quenching last. This behavior is reflected in the calculation as well, with level 7 quenching last. The timing of the quench was predicted well in axial level 6, was early in levels 2 through 5, and was late in levels 7-9. The overall prediction of the cladding surface temperatures is judged to be reasonable. The general heatup and quench behavior was predicted, including the final quench from both the bottom and top of the core, although the partial top-down rewet was not predicted. While the initial heatup of the top portion of the center fuel assembly was not predicted, it did not impact the peak cladding temperature.

The effects of the three-dimensional core modeling are shown in Figures 5.6-35 through 5.6-40. The first two pairs of figures illustrate the radial variation in the cladding surface temperature at two different elevations in the core; for each pair, the data are in the first (top) figure and the corresponding semi-implicit calculation values are in the second (bottom) figure. Large radial temperature variations were observed in both the test and the calculations because of the radial power peaking. In core axial level 4, the data (Figure 5.6-35) showed an early quench in the outer two rings. The final quench in the two outer rings also occurred at the same time, about 20 s earlier than the inner ring. In the calculation (Figure 5.6-36), no early quench was predicted and the final quench of the two outer rings occurred only a few seconds before that of the inner ring. In core axial level 6, the data (Figure 5.6-37) showed that there was an early heatup and quench in Ring 2, but only a late heatup in Ring 3, with the final quench in the

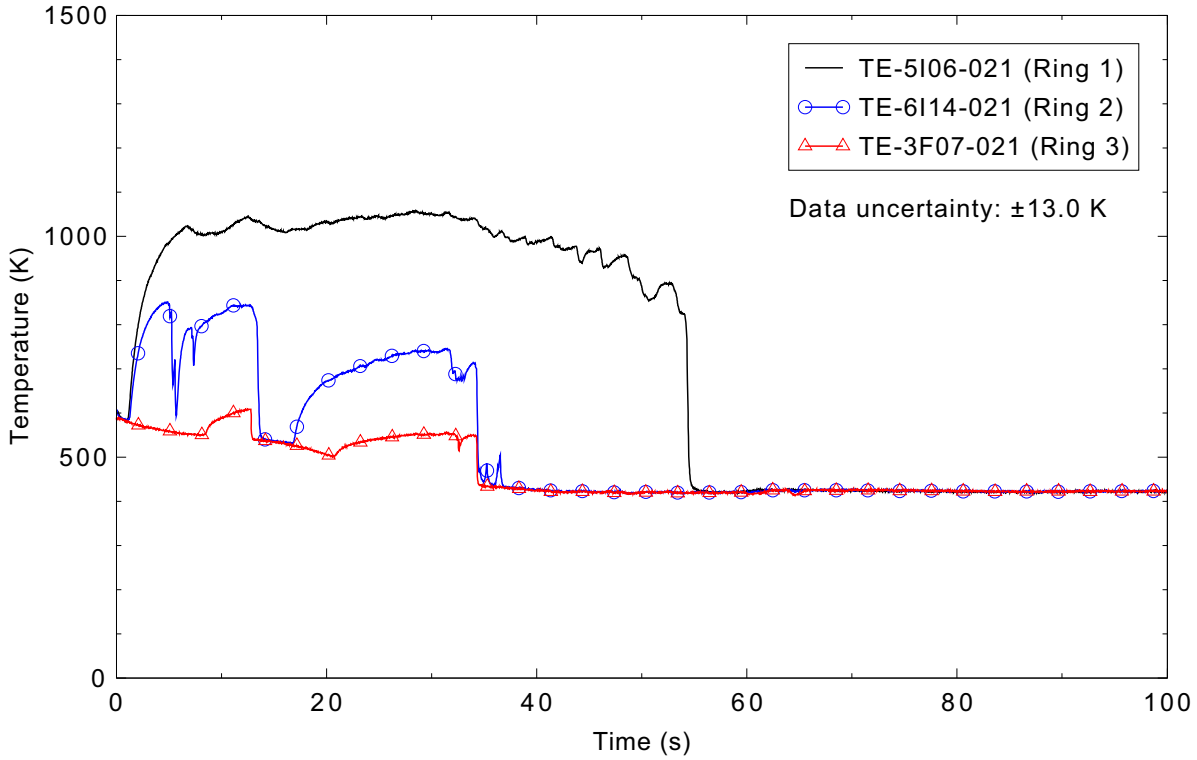

Figure 5.6-35. Measured values showing radial variation in the fuel cladding surface temperature 0.53 m above the bottom of the fuel rod for the LOFT Experiment L2-5 3-D case.

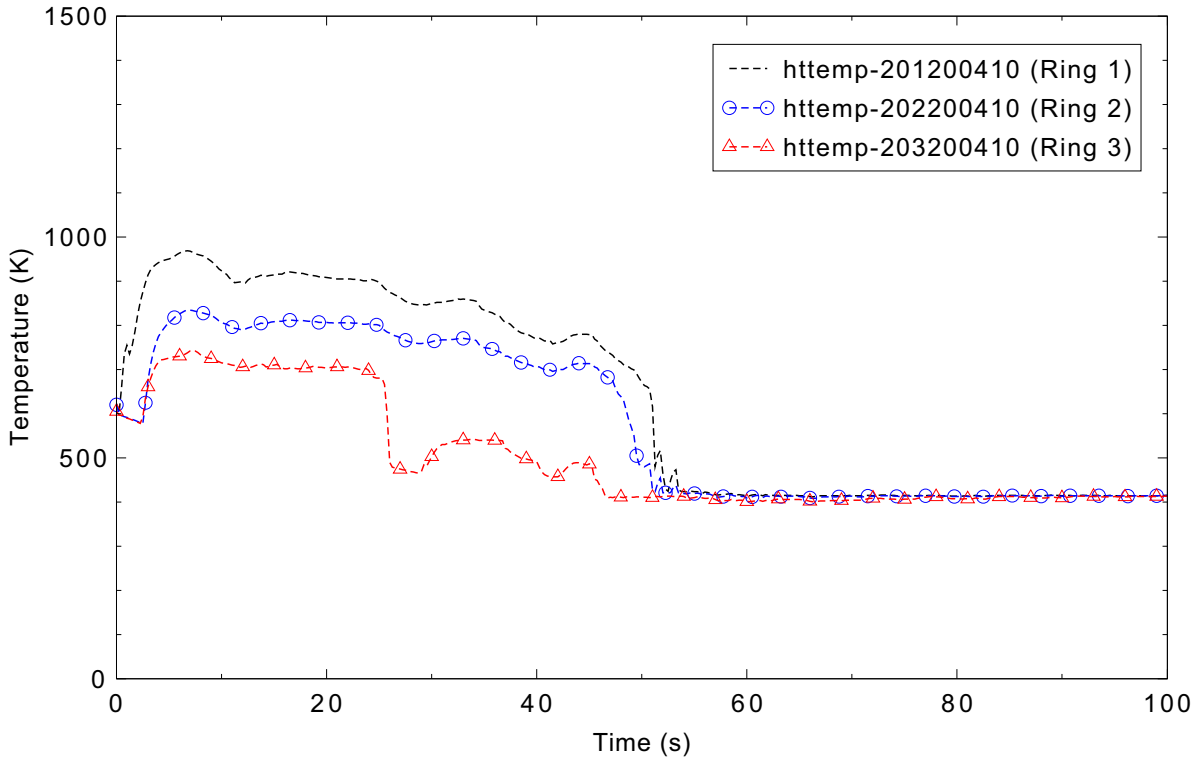

Figure 5.6-36. Calculated values showing radial variation in the fuel cladding surface temperature 0.53 m above the bottom of the fuel rod for the LOFT Experiment L2-5 3-D case.

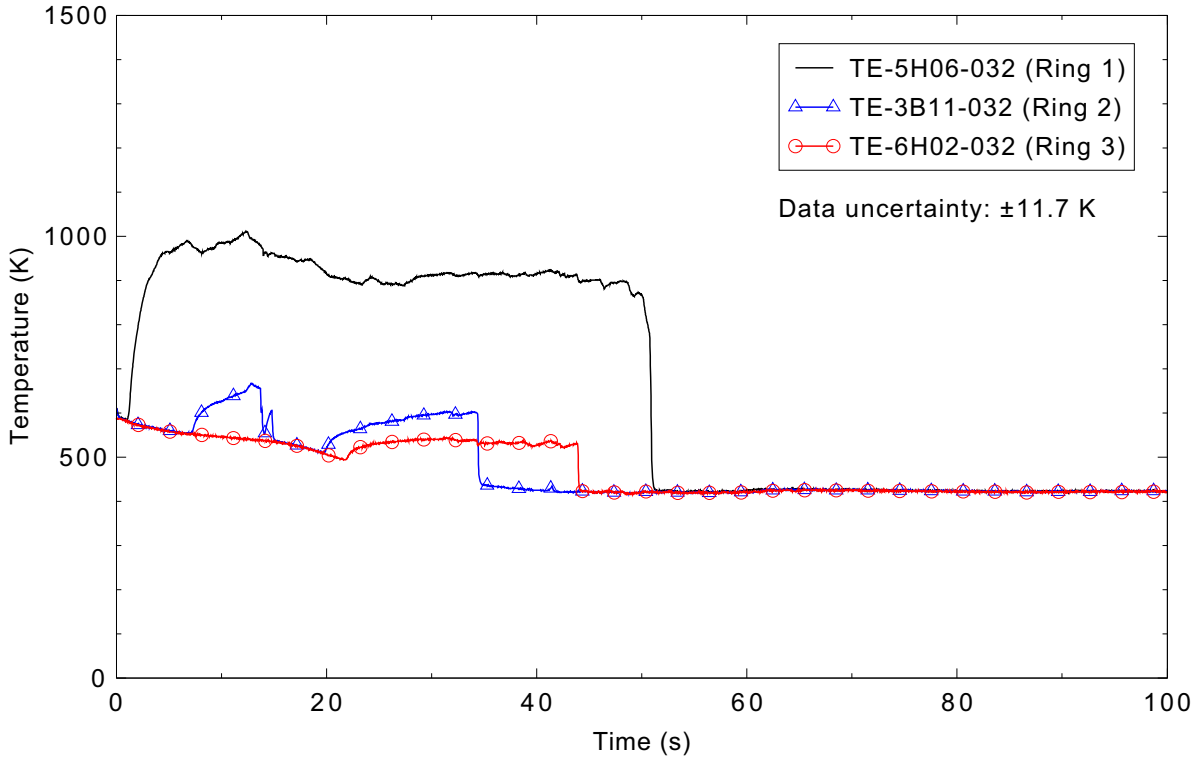

Figure 5.6-37. Measured values showing radial variation in the fuel cladding surface temperature 0.81 m above the bottom of the fuel rod for the LOFT Experiment L2-5 3-D case.

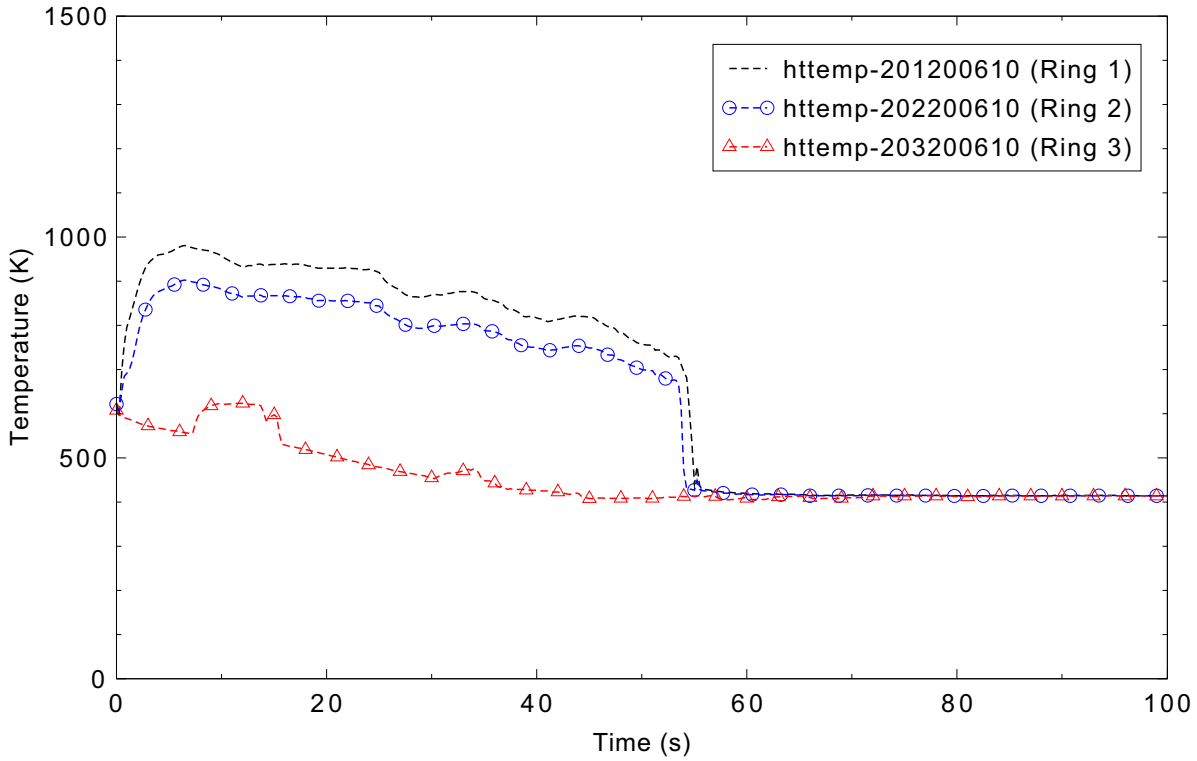

Figure 5.6-38. Calculated values showing radial variation in the fuel cladding surface temperature 0.81 m above the bottom of the fuel rod for the LOFT Experiment L2-5 3-D case.

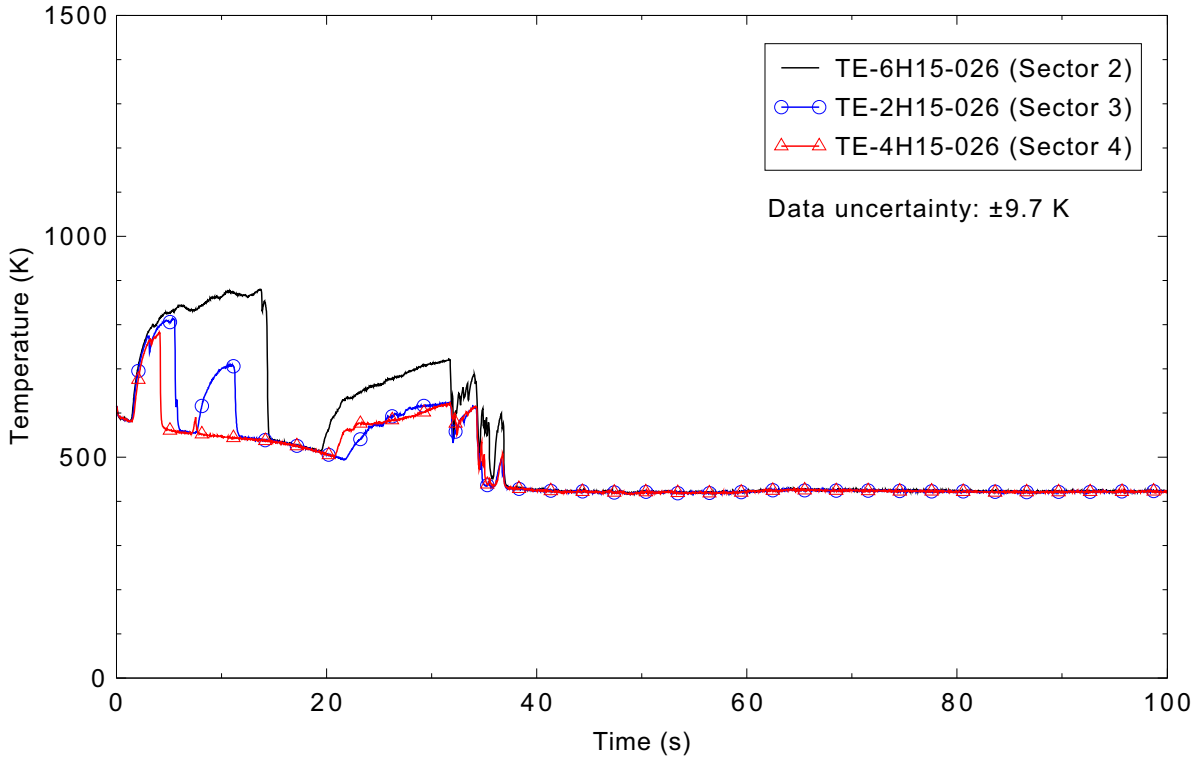

Figure 5.6-39. Measured values showing azimuthal variation in fuel cladding surface temperatures 0.66 m above the bottom of the fuel rod for the LOFT Experiment L2-5 3-D case.

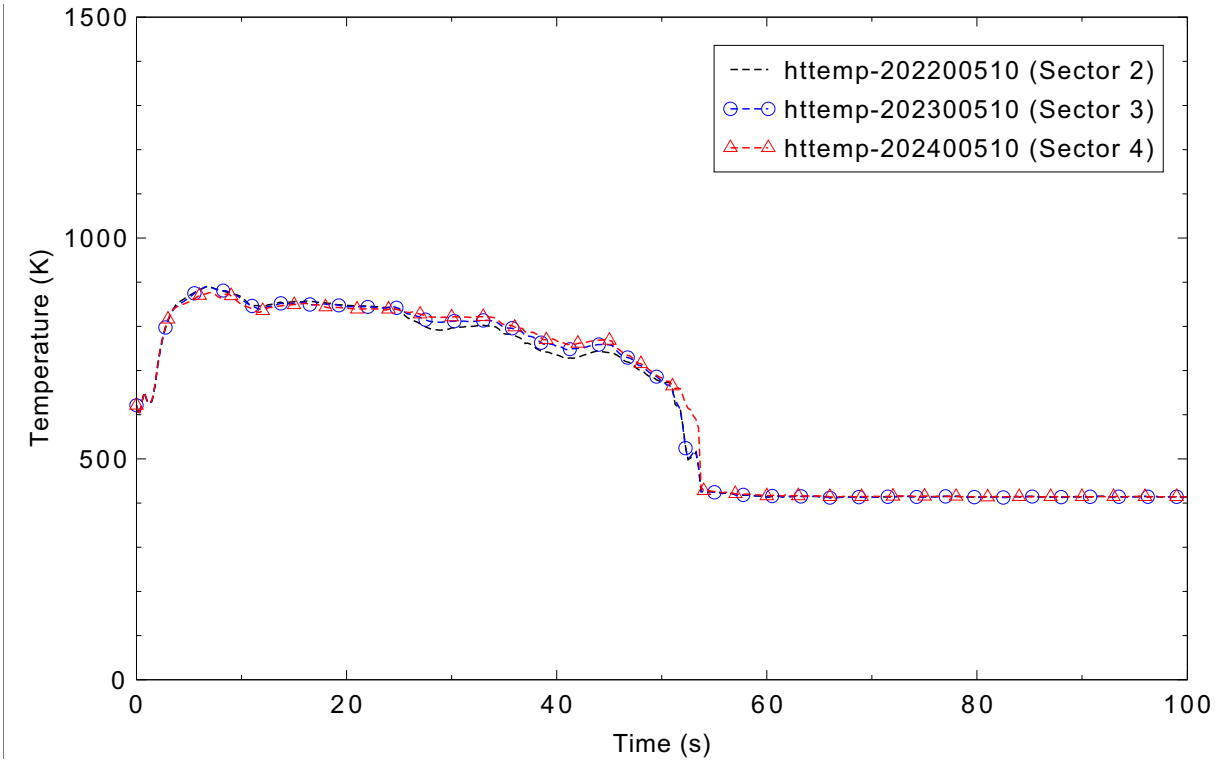

Figure 5.6-40. Calculated values showing azimuthal variation in fuel cladding surface temperatures 0.66 m above the bottom of the fuel rod for the LOFT Experiment L2-5 3-D case.

middle ring occurring first. In the calculation (Figure 5.6-38), there was an early heatup and quench in only the outer ring, and the final quench was from the outer ring inward. The final pair of figures, 5.6-39 and 5.6-40, show the azimuthal variation in the cladding surface temperature in three sectors of the middle ring. The measurements were taken at the same radial distance from the center of the core; a corresponding measurement was not available in Sector 1. The data showed an early rewet starting in Sector 4, which is under the intact loop hot leg, and then working around the vessel. The subsequent heatups were similar, with the final quench occurring about the same time in each sector. The calculation displayed almost no azimuthal variations. The first quench was not predicted, although there was a slight depression in the temperature around 15 s. The final quench occurred about 15 s later than was measured.

5.6.5 Conclusions and Assessment Findings

Most of the significant parameters calculated by the code were in good agreement with the measured data. The two notable exceptions were the fluid densities in the intact loop hot and cold legs. The assessment findings apply to the semi-implicit calculation only, as the nearly-implicit calculation failed before 3 s because of undetermined errors that appear to be associated with the multi-dimensional hydrodynamic component.

The pressures in both the primary and secondary coolant systems were found to be reasonably predicted. The ECC behavior was well simulated, with the calculated accumulator level in excellent agreement with the data and the LPIS flow in reasonable agreement; no judgment on the HPIS flow was made since it was essentially a constant flow boundary condition. It can be inferred that the break flows were reasonably simulated, as the flow rates and fluid densities in the broken loop hot and cold legs were well predicted (excellent agreement in the broken loop hot leg flow, reasonable agreement for the three other measurements). In the intact loop, the flow rates were reasonably simulated, but the calculated densities were in minimal agreement with the data, generally retaining more water in the loops than was measured; also, the pump speed was in minimal agreement for most of the transient, although it was in good agreement during the initial coastdown. Fluid temperatures in the reactor vessel upper and lower plena were predicted reasonably, although the presence of accumulator nitrogen reduced the calculated saturation temperature.

Both the fuel centerline and cladding surface temperatures were judged to be reasonably predicted. In the experiment, there was a partial top-down rewet of some of the fuel rods; this was not predicted by the code. The final quench of the core was both bottom-up and top-down in the experiment and in the calculation. The data showed some early heatup in the center fuel assembly over the entire length of the core, but in the code calculation the top two (of twelve) axial levels in the core did not show any early cladding temperature excursions. The peak cladding temperature was predicted to be 83 K below the measured value, and it occurred earlier than was measured (6.8 vs. 28.5 s).

Three-dimensional effects in the experiment were more pronounced than in the calculation. The essential behavior in the radial variations in the core temperatures was predicted by the code, but the azimuthal variations were not.

5.6.6 References

5.6-1. D. L. Reeder, *LOFT System and Test Description (5.5 ft Nuclear Core 1 LOCEs)*, NUREG/CR-0247, TREE-1208, July 1978.

5.6-2. P. D. Bayless and J. M. Divine, *Experiment Data Report for LOFT Large Break Loss-of-Coolant Experiment L2-5*, NUREG/CR-2826, EGG-2210, August 1982.

6. SUMMARY AND CONCLUSIONS

A developmental assessment has been performed for the RELAP5-3D computer code. This assessment used a combination of phenomenological, separate effects, and integral effects cases to investigate how well selected code models perform. The specific cases used comprise an assessment matrix that addresses most of the code models that are important when performing safety analyses for light water reactors.

Judgments were made on how well the code calculations predicted the important parameters from each of the assessment cases. These judgments used criteria that evaluated the trends and magnitudes of the data and calculations to determine whether the code results were acceptable or not. Assessment findings of "excellent" or "reasonable" are considered acceptable, while "minimal" or "insufficient" indicate that additional work on the code models may be needed.

The code calculations were performed with both the semi- and nearly-implicit solutions schemes. Assessment judgments for both sets of calculations were made, although no attempts were made to explain differences between the two calculations for a given assessment case. Default code options were generally used, although some card 1 options were required to define specific assessment cases. The calculations were run in 64-bit mode on a personal computer using the Linux operating system.

The phenomenological cases are generally simple problems that test one or two code models. They are thought problems that often have analytical solutions. Seventeen cases were included in the assessment. Unless the case had a closed-form solution, the assessment ranking could be no higher than reasonable.

The water faucet is water falling through a vertical pipe. Both the fluid velocity and liquid fraction were correctly predicted over the entire pipe length, resulting in an assessment judgment of excellent. There were no differences between the semi- and nearly-implicit calculations.

The water over steam problem is a vertical pipe that starts with saturated water at the top and saturated steam at the bottom; the water then falls to the bottom. The code calculations using a one-dimensional pipe component were reasonable using both the semi- and nearly-implicit methods. With a three-dimensional model, the semi-implicit method was judged to give reasonable results, while a failure was encountered using the nearly-implicit method, leading to a judgment of insufficient.

The fill-drain problem is a vertical pipe that is filled, then drained, to assess liquid level tracking. The calculation for the semi-implicit advancement scheme was judged to be in excellent agreement with the analytical solution, while the nearly-implicit simulation was judged to be in reasonable agreement.

The bubbling steam through liquid case injects steam with increasing velocity at the bottom of a water column to investigate mixture level tracking and liquid entrainment. The calculated results agreed qualitatively with the expected behavior. Mixture levels were established at lower steam mass flow rates, more liquid was entrained at higher steam flow rates. The code performance was judged to be reasonable using the semi-implicit solution scheme. For the nearly-implicit method, the performance was reasonable except between 800 and 1100 s, where the performance was minimal.

The manometer problem models water flowing between two vertical columns. With the mixture level tracking model on, the semi-implicit calculations were in excellent agreement with the analytical solution,

while the nearly-implicit calculations were in minimal agreement. With the mixture level tracking model off, the semi-implicit calculation was in minimal agreement with the analytical solution, and the nearly-implicit calculation was insufficient.

The gravity wave problem is a horizontal pipe that has water at a slightly increasing height along the length, causing a sloshing flow back and forth. The code performance was judged to be reasonable using both one- and three-dimensional components, generating an oscillating wave at nearly the analytic solution speed. The semi-implicit solution scheme exhibited a small instability in the pressure solution later in time that was not present with the nearly-implicit solution scheme.

The Pryor pressure problem is a steam-filled horizontal pipe that is filled from one end with water to investigate the water packing phenomenon. Both the semi- and nearly-implicit advancement schemes were judged to calculate reasonable results. Several pressure spikes were observed due to the presence of over-condensation and the resulting water-packing of the volumes.

The core power case used three individual problems to assess the 1979 decay heat model. Both the semi- and nearly-implicit calculations were found to be in excellent agreement with the standard.

The point kinetics ramp problem assessed the point kinetics model response to a reactivity insertion. Assessment judgments of excellent were assigned for both the semi- and nearly-implicit calculations except at small time steps. With a sufficiently small time step, a code error causes a large over prediction of the fission power, resulting in an insufficient assessment judgment.

Three problems were used to test the numerics for the multi-dimensional hydraulic component. For the pure radial flow case, both calculations were in excellent agreement with the exact solution for the radial velocity and pressure distributions.

For the rigid body rotation case, the semi-implicit calculation agreed with the exact solution for the radial and azimuthal velocities. Although the calculated radial pressure distribution did not exactly match the exact solution, the results were judged to be in excellent agreement. The nearly-implicit calculation did not agree with the exact solutions, particularly for the pressure distribution. The results were also not symmetric in the azimuthal direction, which indicates that there is an error in the nearly-implicit numerical scheme for the multi-dimensional component.

For the r-theta symmetric flow case, the semi-implicit calculation was in excellent agreement with the exact solution for the radial velocity, azimuthal velocity, and radial pressure distributions. The nearly-implicit calculation did not agree with the exact solutions, particularly for the pressure distribution. The results were also not symmetric in the azimuthal direction, which indicates that there is an error in the nearly-implicit numerical scheme for the multi-dimensional component. The velocity comparisons were judged to be reasonable, while the pressure prediction was minimal.

Three cases addressed the conduction enclosure model; as pure heat transfer tests, only the semi-implicit solution scheme was used for the comparisons. The conduction enclosure problem was a two-dimensional, steady-state heat conduction problem. There was excellent agreement between the analytical solution and the code calculation, with a relatively small number of nodes being able to give an approximation for the steady state temperature of the plate with less than 1% error throughout the domain.

The conduction enclosure one-dimensional transient simulated axial conduction in a cylinder. Overall, the agreement between the calculation and the analytical solution was excellent.

Transient cooling of a two-dimension plate was simulated by the final conduction enclosure problem. Overall, the agreement between the calculation and the analytical solution is excellent. At one hour, the maximum error was less than 0.9%, and by three hours the error dropped to less than 0.07%.

The separate effects cases are experiments that address one or a few code models. Twenty six individual tests were included in the assessment.

The objective of Edwards pipe problem is to validate the code capability to calculate basic rapid blowdown phenomena given a simple straight pipe geometry. The code assessment includes two predominant transient flow regimes and behavior. The initial part of the transient involves single-phase choked flow at the break location while the pipe undergoes rapid depressurization and propagation of a pressure wave along the pipe. As the pipe rapidly depressurizes, flashing occurs along the pipe, resulting in two-phase break flow until the pipe is depressurized and essentially empty. Both the semi- and nearly-implicit calculated pressure results were in reasonable agreement with the test data. Although measured break flow data were not available for this test, the fact that the pressure was well-calculated indicates that the break flow was likely well-calculated also.

Four critical flow tests performed in the Marviken facility were used to investigate various aspects of the critical flow model. Test 21 assessed the subcooled choked flow model. Both the semi- and nearly-implicit solution scheme calculations were in reasonable agreement with the data overall, although during the first 15 s the agreement was judged to be excellent.

Tests 22 addressed subcooled and saturated choked flow. Both the semi- and nearly-implicit solution scheme calculations were in reasonable agreement with the data. The mass flow rate was somewhat over predicted early in the transient, and over predicted later, with an overall assessment judgment of reasonable. As a consequence of the mass flow rate prediction, the vessel pressure was under predicted in the early portion of the transient and over predicted later, but again the overall judgment was reasonable agreement. The code did an excellent job predicting the temperature profile in the test vessel, and did a reasonable job predicting the mixture density.

Test 24 also addressed subcooled and saturated choked flow. Results using the semi- and nearly-implicit solution schemes were very similar. The code under predicted the vessel pressure in the early portion of the transient and over predicted the pressure during the remaining portion of the test, but was judged to do a reasonable job predicting the vessel pressure. The calculations were in excellent agreement with the maximum flow rate, but under predicted the mass flow rate somewhat for the majority of the transient; the overall mass flow rate was judged to be in reasonable agreement with the data. The code also did a reasonable job predicting the temperature profile in the test vessel and did a reasonable job predicting the mixture density until 24 s, after which the calculations were in minimal agreement with the data.

Marviken JIT 11 assessed high quality vapor choked flow. The calculated results for both the semi- and nearly-implicit solution schemes were very similar, and were judged to be in excellent agreement with

the test data. With the specified pressure boundary condition, the code did an excellent job of matching the critical flow data.

The final critical flow assessment used a Moby Dick air-water experiment to investigate two-phase, two-component flow. Both calculations were judged to minimally predict the pressure drop near the choking plane in the presence of an air-water mixture because of a significant under prediction of the two-phase pressure drop upstream of the choking plane. The unavailability of detailed information on the facility or experiment resulted in larger uncertainties for this test than most others.

Christensen Test 15 assessed the interphase mass transfer and wall heat flux partitioning models. The calculations were judged to be in excellent agreement with the measured data, correctly predicting the void fractions over the entire length of the test section.

Two GE level swell experiments were used to evaluate the performance of the vapor generation, interphase drag, and two-phase level models. For the 1-ft test, both the semi- and nearly-implicit calculations were in reasonable agreement with the experiment data. All major trends and phenomena were correctly modeled. Void fractions in the liquid region tended to be slightly over predicted, while the void fraction in the vicinity of the mixture level was generally low. The code correctly reproduced the initial level swell. Users should be aware of the possibility of localized unphysical flow regime inversion in the region around the mixture level.

For the 4-ft test, both calculated results were judged to be in reasonable agreement with the experimental data. The code tended to predict a sharper mixture level for most of this transient, with a lower void below the level and a higher void above. However, the major trends were correctly predicted. A limited sensitivity study indicated that the results were not significantly different whether the mixture level tracking model was used or not.

Bennett heated tube Tests 5358, 5294, and 5394 assessed the CHF model in RELAP5-3D. Both the semi- and nearly-implicit calculations did a reasonable job in predicting the CHF position even though they predicted the position slightly earlier than the measured data in the cases of the low and high mass fluxes and slightly later in the case of the intermediate mass flux.

The ORNL THTF tests assessed the CHF and film boiling heat transfer models in RELAP5-3D. With one exception, the CHF and film boiling heat transfer predicted by both solution schemes were in reasonable agreement with the experiment data for the four ORNL THTF tests. For the ORNL 3.07.9N and 3.07.9W test cases, the predicted rod temperatures were in reasonable agreement with the experiment data, and the code did a reasonable job of predicting CHF. For the 3.07.9B case, the CHF was reasonably predicted but the rod temperatures were only in minimal agreement with the measured data. For the ORNL 3.09.10I test, the predicted void fraction and gas temperature were in excellent agreement with the experiment data, and the rod surface temperature was in reasonable agreement.Grid spacers were only accounted for in the RELAP5-3D model through the CHF correlation. The grid spacers appeared to have a significant effect on the rod surface temperatures in the ORNL tests, leading to discontinuities in the temperature response.

RIT Tube Test 216 was used to assess the default CHF and PG-CHF (“power” form) models in RELAP5-3D. Both the semi- and nearly-implicit calculations did a reasonable job in predicting the CHF

position, even though it predicted the position slightly later in the case of the default CHF model and earlier in the case of the PG-CHF model than the measured data.

FLECHT SEASET Test 31504 investigated the performance of the reflood model at a low flooding rate. Both code calculations were judged to be in reasonable agreement with the measured data. Predicted rod surface temperatures in the lower half of the rod bundle were in excellent agreement with the data. Above the core midplane, the code adequately predicted the initial cladding temperature rise and peak temperature, but under predicted the cool down and rod quench behavior. For the most part, the code tended to under predict vapor temperatures in the early part of the transient and over predict vapor temperatures in the latter part of the reflood transient. The under prediction of the cool-down and quench behavior of the upper half of the core, coupled with the under prediction of vapor temperatures in the early part of the transient and the over prediction of vapor temperatures in the latter part of the transient, indicates a weakness in the current reflood model that needs to be addressed. Overall, measured and calculated void fractions were generally in good agreement. The code predicted mass inventory and distribution were in excellent agreement during the first 70 s of the transient, but after 70 s, the calculated mass inventory was under predicted by about 10%.

FLECHT SEASET Test 31701 investigated the performance of the reflood model at a high flooding rate. Both code calculations were judged to be in reasonable agreement with the measured data. Predicted rod surface temperatures in the lower two-thirds of the rod bundle were in good agreement with the data. Above this, the code adequately predicted the initial cladding temperature rise and peak temperature, but calculated an earlier quench than was measured in the experiment using the semi-implicit numerical scheme. The earlier quench of the upper portion of the bundle was the result of a calculated top-down quenching of the upper regions of the bundle that was not observed in the experiment. For the most part, the code tended to over predict vapor temperatures in the latter part of the reflood transient. The difference between measured and predicted fluid temperatures may be due in part to thermocouples measuring a combination of superheated steam and saturated liquid as the quench front approaches the measurement location. The top-down and bottom-up calculated quench behavior resulted in increased steam generation in the bundle and a reduction in the rate of increase in bundle mass inventory than was observed during the initial 100 s of the reflood experiment. However, when the entire core was calculated to quench at about 100 s, the calculated core mass inventory rapidly increased, filling the core with liquid by about 110 s into the transient.

The Dukler-Smith air-water flooding experiments assessed the Wallis CCFL model. Semi- and nearly-implicit predictions were in reasonable agreement with the Dukler-Smith experiment data for countercurrent air-water flow in a single tube over the range of air flows from 0.0126 to 0.126 kg/s. The assessment also shows that the Wallis correlation is implemented correctly.

UPTF downcomer CCFL Test 6, Run 131 was used to compare the relative performance of the annulus and pipe components for simulating the refill of the lower plenum during a loss-of-coolant accident. Only the semi-implicit solution ran to completion (100 s); the nearly-implicit calculation failed near 25 s. The annulus and pipe components are similar except that all the liquid is placed in the film, with no liquid allowed in drops, in the annulus component when in the annular-mist flow regime. Liquid is allowed in both the film and drops in the annular-mist flow regime in the pipe component. The semi-implicit calculations were judged to be in reasonable agreement with the measured liquid level data for UPTF Test 6, Run 131. The calculated refill was similar to that observed in the test, but started about 7 s earlier. The

RELAP5-3D calculation in which the downcomer was modeled with annulus components was in better agreement with the measured results than when pipe components were used. The flow regime model in the annulus component, which puts all the liquid in the film, resulted in a better prediction of the lower plenum refill for the UPTF test. The pipe component provided a conservative prediction of the amount of liquid in the lower plenum.

The MIT Pressurizer test was used to assess the code capability to simulate pressurizer behavior under inflow and outflow conditions. The models tested during this simulation are steam condensation on the pressurizer wall and interfacial heat transfer between the stratified liquid and the vapor above the liquid. The MIT Pressurizer test that is used for this assessment case is ST4. The code did a reasonable job of predicting the pressure response along with the axial temperature profile using both the semi-implicit and nearly-implicit advancement schemes, both with and without the mixture level tracking model, although use of that model improved the node boundary crossing response.

Neptunus Test Y05 simulated pressurizer transient behavior involving surge line flows and pressurizer spray. The code-calculated pressurizer pressure and temperature results were judged to be in reasonable agreement with the Neptunus pressurizer test data for test Y05 using either solution scheme. It was concluded that the pressurizer model appropriately calculated the expected two-phase, two-region, non-equilibrium behavior required to simulate pressurizer transient response.

MB2 Test 1712 was used to evaluate the performance of the code in modeling steady-state steam generator behavior. The overall results from the calculation were in reasonable agreement with the data. The primary temperature drop through the U-tube bundle showed reasonable agreement, indicating that the model correctly predicted the amount of energy transferred from the primary to the secondary system. Some other calculated steady-state conditions (e.g., narrow range level) lie outside the uncertainty range of the data, but not far enough to warrant concern.

The LOFT L3-1 accumulator case assessed the performance of the accumulator model during a slow depressurization associated with a small break loss-of-coolant accident. The calculations with both solution schemes were judged to be in excellent agreement with the measured data.

The performance of the jet pump model was evaluated using GE 1/6-scale jet pump data. Both the semi- and nearly-implicit calculations were judged to be in reasonable agreement with the measured data. For most of the measurement ranges, the code predictions were in excellent agreement with the data. However, for forward drive flows with flow ratios above 3.0, and for reverse drive flows with flow ratios below -2.5, the calculations were outside the measurement uncertainties, and the trends were away from the data. Most of the data taken were within the range that the code was performing well, suggesting that the regions where the code predictions were suspect may be encountered only in extreme cases. However, users should be aware of the potential problem.

The integral effects cases use data from large experimental facilities. These cases are generally of greater interest because they provide an indication of how well the code performs overall in modeling transients with a large number of phenomena. Nine cases addressing eight experiments were included in the assessment.

LOFT Experiment L3-7 simulated a small break LOCA in a PWR. For this test, the interest was in the overall system response, not that of the core, as there was no heatup. Parameters of significance are the break flow rates, system pressure, emergency core coolant (ECC) system response, and system mass distribution. Most of the small break phenomena were simulated well by the code. The primary coolant system pressure response, pressurizer liquid level, and cladding surface temperature calculations were reasonable. The coolant temperatures throughout the primary coolant system were judged to be reasonably simulated for most of the transient. Simulations of the HPIS flow and the fluid velocity in the hot leg were judged to be in excellent agreement with the experiment data. The predictions of the break flow and the densities in the intact and broken loop cold legs were judged to be minimal, as were most of the coolant temperatures after 1200 s. The break flow was simulated well at the beginning of the transient, but was under predicted after about 400 s. Most of the problems in the calculation were attributed to the break flow. Improvement of the break flow rate prediction would likely result in acceptable calculations of the densities throughout the system. This in turn would likely improve the pressure and coolant temperature predictions after 1200 s. The assessment findings apply equally to both simulations; there were no significant differences between the calculations using the semi- or nearly-implicit solution schemes.

ROSA LSTF Test SB-CL-18 also simulated a small break LOCA in a PWR. Parameters of interest included the system pressure, break and injection flow rates, core liquid level, and peak core temperatures. The nearly-implicit calculation failed early in the transient simulation, so assessments were only made of the semi-implicit calculation. The majority of the parameters calculated by the code were in reasonable agreement with the measured data, although there were several significant parameters that were not. The pressure in the primary coolant system was in reasonable agreement with the data, as was the pressure in the secondary coolant system. The mass flow rates in the hot and cold loops were judged to be reasonably predicted. The accumulator mass flow rates were in reasonable agreement with the experiment, although they were activated earlier in the calculation than in the experiment. The break mass flow rate was judged to be in minimal agreement with the data during the initial portion of the transient, but was in reasonable agreement after the transition to primarily steam flow. Most of the loop densities were judged to be in minimal agreement. The heater rod temperatures toward the bottom of the core were in good agreement with the data, but became worse with increasing height in the core. The core liquid level was under predicted for a portion of the calculation, which resulted in a longer-term core uncovery. The primary deficiency in the calculation was that the code did not predict the clearing of the intact loop loop seal. This caused fluid to be retained in the intact loop. If this loop seal had cleared as it did in the experiment, the core liquid level would have been better predicted, and the core heatup would have been shorter. Also, there would have been flow through the intact loop steam generator tubes, which would have improved the prediction of the steam generator pressure.

Running the ROSA case with the h2on water property file showed that the water property file had a negligible effect on the calculations. The h2o95 water property file showed a notable decrease in the maximum heater rod temperatures at the top of the core, although there were no noticeable differences in any of the other parameters.

Semiscale natural circulation Tests S-NC-1, S-NC-2, S-NC-3, and S-NC-10 were used to assess the code capability for predicting the single- and two-phase natural circulation phenomena. Both solution scheme predictions were excellent for single-phase liquid natural circulation. For two-phase natural circulation, the prediction was reasonable when the core power was high (100 kW, Test S-NC-10, Part 4) but became minimal as the power decreased. However, it was judged that the code predicted reasonable

two-phase natural circulation behavior with the high and intermediate core power (100 kW and 60 kW) but the discrepancy between the predicted and the measured natural circulation behavior was large with the low power (33.54 kW). A reasonable prediction of reflux condenser mode of natural circulation was provided when the core power was 60 kW and the primary system mass inventory was less than 67%. When the secondary system mass inventory was high enough to make the effective heat transfer area larger than around 50%, reasonable natural circulation was predicted. However, when it decreased to be smaller than 50%, the code predicted much higher mass flow rates in the primary system than were measured, which was in minimal agreement with experimental results.

LOBI Test A1-04R was used to assess the code capability during the blowdown phase of a large-break LOCA in a PWR. Both the semi- and nearly-explicit calculations were in excellent agreement for the system pressure and in reasonable agreement for the loop mass flow. The calculated results for the accumulator flow rate were significantly different from the LOBI data for both the nearly- and semi-implicit numerical schemes, although it is possible that the data are in error since the code does such an excellent job in predicting the pressure response. The rod temperatures were judged to be in excellent agreement for the lower levels where the code predicts nucleate boiling, were judged to be in minimal agreement at the mid-level where the code is predicting transition boiling, and were judged to be in reasonable agreement for the upper levels where the code is predicting film boiling.

LOFT Experiment L2-5 simulated a double-ended cold leg break in a PWR. The principal interest is in the core behavior: fuel rod heatup and quench, peak cladding temperature. Other parameters of significance are the break flow rates, system pressure, and emergency core coolant (ECC) system response. For this case, the reactor vessel was modeled using one-dimensional components. Most of the significant parameters calculated by the code were in good agreement with the measured data. The three notable exceptions were the fluid densities in the broken and intact loop hot legs, and in the intact loop cold leg (semi-implicit only at this location; the nearly-implicit calculation was reasonable). The pressures in both the primary and secondary coolant systems were found to be reasonably predicted. The ECC behavior was well simulated, with the calculated accumulator level in excellent agreement with the data and the LPIS flow in reasonable agreement; no judgment on the HPIS flow was made since it was essentially a constant flow boundary condition. The flow rates in the broken loop hot and cold legs were well predicted (excellent agreement in the broken loop hot leg flow, reasonable agreement in the cold leg). In the intact loop, the flow rates were reasonably simulated, but the calculated densities were in minimal agreement with the data, generally retaining more water in the loops than was measured; also, the pump speed was in minimal agreement for most of the transient, although it was in good agreement during the initial coastdown. Fluid temperatures in the reactor vessel upper and lower plena were predicted reasonably, although the presence of accumulator nitrogen in the calculation reduced the saturation temperature more than was indicated in the experiment. Both the fuel centerline and cladding surface temperatures were judged to be reasonably predicted. In the experiment, there was a partial top-down rewet of some of the fuel rods; this was not predicted by the code. The final quench of the core was both bottom-up and top-down in the experiment and in the calculation. The data showed some early heatup in the center fuel assembly over the entire length of the core, but in the code calculation the top third of the core did not show any early cladding temperature excursions. The peak cladding temperature was predicted to be 93 K below the measured value, which is not unexpected as this is a comparison between a hot fuel rod and an assembly-average rod; the peak temperature also occurred earlier in the calculation than was measured (6 vs. 28 s). The assessment findings apply to both the semi- and nearly-implicit calculations, as there were no substantive differences between the two calculations.

LOFT Experiment L2-5 was also simulated using two multi-dimensional components in the reactor vessel, one for the downcomer and one for the region inside the core barrel. For this case, the nearly-implicit calculation failed relatively early in the transient and no assessment judgments were made. The results for the semi-implicit calculation were essentially the same as for the one-dimensional case, except that the broken loop hot leg density prediction was judged to be reasonable. The early heatup of the core extended higher than in the one-dimensional case, and the peak cladding temperature was 10 K higher. The three-dimensional effects in the experiment were more pronounced than in the calculation. The essential behavior in the radial variations in the core temperatures was predicted by the code, but the azimuthal variations were not.

Most of the assessment cases showed essentially no differences in results between calculations using either the semi- or nearly-implicit solution scheme. However, there appear to be errors in the nearly-implicit solution scheme associated with the multi-dimensional hydrodynamic component. Until these issues are resolved, users should account for this in determining how best to apply the code to specific facility simulations.